

Texts in Applied Mathematics 66

Christoph Börgers

An Introduction to Modeling Neuronal Dynamics

EXTRAS ONLINE

 Springer

Texts in Applied Mathematics

Volume 66

Editors-in-chief:

S.S. Antman, University of Maryland, College Park, USA
L. Greengard, New York University, New York City, USA
P.J. Holmes, Princeton University, Princeton, USA

Series Editors:

J. Bell, Lawrence Berkeley National Lab, Berkeley, USA
J. Keller, Stanford University, Stanford, USA
R. Kohn, New York University, New York City, USA
P. Newton, University of Southern California, Los Angeles, USA
C. Peskin, New York University, New York City, USA
R. Pego, Carnegie Mellon University, Pittsburgh, USA
L. Ryzhik, Stanford University, Stanford, USA
A. Singer, Princeton University, Princeton, USA
A. Stevens, Universität Münster, Münster, Germany
A. Stuart, University of Warwick, Coventry, UK
T. Witelski, Duke University, Durham, USA
S. Wright, University of Wisconsin-Madison, Madison, USA

Christoph Börgers

An Introduction to Modeling Neuronal Dynamics

Christoph Börgers
Department of Mathematics
Tufts University
Medford, MA, USA

ISSN 0939-2475 ISSN 2196-9949 (electronic)
Texts in Applied Mathematics ISBN 978-3-319-51171-9 (eBook)
ISBN 978-3-319-51170-2
DOI 10.1007/978-3-319-51171-9

Library of Congress Control Number: 2016962460

Mathematics Subject Classification (2010): 37N25, 92C20, 92C42, 97M60

© Springer International Publishing AG 2017

This work is subject to copyright. All rights are reserved by the Publisher, whether the whole or part of the material is concerned, specifically the rights of translation, reprinting, reuse of illustrations, recitation, broadcasting, reproduction on microfilms or in any other physical way, and transmission or information storage and retrieval, electronic adaptation, computer software, or by similar or dissimilar methodology now known or hereafter developed.

The use of general descriptive names, registered names, trademarks, service marks, etc. in this publication does not imply, even in the absence of a specific statement, that such names are exempt from the relevant protective laws and regulations and therefore free for general use.

The publisher, the authors and the editors are safe to assume that the advice and information in this book are believed to be true and accurate at the date of publication. Neither the publisher nor the authors or the editors give a warranty, express or implied, with respect to the material contained herein or for any errors or omissions that may have been made. The publisher remains neutral with regard to jurisdictional claims in published maps and institutional affiliations.

Printed on acid-free paper

This Springer imprint is published by Springer Nature
The registered company is Springer International Publishing AG
The registered company address is: Gwerbestrasse 11, 6330 Cham, Switzerland

Preface

This book is intended as a text for a one-semester course on mathematical and computational neuroscience for upper-level undergraduate and first-year graduate students of mathematics, the natural sciences, engineering, or computer science. An undergraduate introduction to differential equations is more than enough mathematical background. Only a slim, high school-level background in physics is assumed and none in biology.

Each chapter is intended to be studied, with some omissions of course, in a 50-minute class. Not all topics discussed in earlier chapters reappear in later chapters. For instance, Chapters 15, 16, 19, 22, 27, 28, 33, and 34 could be skipped without loss of continuity. I have attempted to write in such a way that the students will be able to read the chapters on their own before coming to class, so that class time can be used for answering questions and discussing the material.

The programs generating the figures of the book are available online. To the caption of each figure generated by a MATLAB code, I have added in brackets the name of the directory in which the code generating the figure can be found. (For a very small number of figures that serve illustrative purposes only, but don't show results of substantial computations, the code is not made available.)

Exercises labeled (*) require MATLAB programming, often using one of the MATLAB programs generating one of the figures as a starting point. Exercises labeled (†) are more difficult than the others. The exercises are deliberately at a fairly wide range of levels of difficulty. Which to assign (or whether to assign others) must of course depend on who are the students who take the course.

Very many topics have been omitted, in an effort to make the book short enough so that one can (with moderate selectivity) teach a one-semester course out of it. My decisions on what to include reflect what I find interesting, of course, but also what I know. In particular, I do not comment on how "macroscopic" behavior emerges: locomotion, decision-making, memory recall, value judgements, etc. The reason is that I don't know. Most of the book is about basic differential equations, models of neurons, synapses, and oscillating networks.

Oscillations in neuronal networks have been of great interest to neuroscientists for many decades. They arguably represent the simplest form of coherent network behavior in the brain. One of the most interesting facts about brain

oscillations is that they provide a possible mechanism by which Hebbian cell assemblies, thought to be the basic unit of information storage in the brain, can be created and held together. Some of the later chapters are directly or indirectly about this topic. I included two chapters about plasticity, since plasticity, i.e., the ability to learn, is clearly the most interesting property of brain matter and also because it seems plausible that plasticity would play a role in the creation of oscillatory cell assemblies.

Models as simple as those discussed in this book obviously don't come close to reproducing the complexities of real brains. This criticism applies to all of computational neuroscience, even when the models are much more complex than those in this book. The complexity of the brain is staggering, and we cannot currently reproduce it faithfully in mathematical models or computational simulations, both because many aspects are just not sufficiently well known experimentally and because computers are not (yet) powerful enough. It is my view that computational modeling in neuroscience should not (yet) be viewed as a way of simulating brain circuits, but as a way of (1) suggesting hypotheses that can be tested experimentally or (2) *refuting* heuristic biological arguments. For these purposes, fully faithful, realistic modeling is clearly not required. In particular, while it is impossible to *prove* a heuristic, biological argument using simulations of a simplifying model, it is possible to *refute* such an argument by creating a model satisfying all assumptions used in the heuristic argument and showing that the conclusion of the argument fails to hold in the model.

I would like to thank Nancy Kopell, from whom I have learned much of what I know about dynamics in neuroscience and with whom I have collaborated on many research projects over the years. I am very grateful to the many people who made helpful comments and suggestions on drafts of this book, including Nancy Kopell, Horacio Rotstein, several students at Tufts University (in particular Jeffrey Carlson, Elise Ewing, and Melody Takeuchi), and several students at Boston University (in particular Julia Chartove, Alex Gelastopoulos, and Erik Roberts). Last but not least, I would like to thank my friends behind the counter at the True Grounds Cafe in Somerville, Massachusetts, where much of the work on this book was done.

Medford, MA, USA
September 2016

Christoph Börgers

Contents

Preface	v
1 Vocabulary and Notation	1
1.1 Biological Vocabulary	1
1.2 Mathematical Notation	6
1.3 Physical Units	7
I Modeling a Single Neuron	9
2 The Nernst Equilibrium	11
Exercises	14
3 The Classical Hodgkin-Huxley ODEs	15
3.1 The Hodgkin-Huxley Model	15
3.2 Activation, Inactivation, De-activation, and De-inactivation	20
Exercises	20
4 Numerical Solution of the Hodgkin-Huxley ODEs	23
Exercises	27
5 Three Simple Models of Neurons in Rodent Brains	31
5.1 Reduced Traub-Miles Model of a Pyramidal Neuron in Rat Hippocampus	32
5.2 Wang-Buzsáki Model of an Inhibitory Interneuron in Rat Hippocampus	33
5.3 Erisir Model of an Inhibitory Interneuron in Mouse Cortex	34
Exercises	36
6 The Classical Hodgkin-Huxley PDEs	39
Exercises	42

7	Linear Integrate-and-Fire (LIF) Neurons	45
	Exercises	50
8	Quadratic Integrate-and-Fire (QIF) and Theta Neurons	51
	Exercises	54
9	Spike Frequency Adaptation	57
9.1	A Model M-Current	58
9.2	Calcium-Dependent AHP Currents	60
9.3	Analysis in an Idealized Setting	60
	Exercises	68
II	Dynamics of Single Neuron Models	71
10	The Slow-Fast Phase Plane	73
10.1	A Two-Dimensional Reduction of the Classical Hodgkin-Huxley Model	73
10.2	The FitzHugh-Nagumo Model	76
	Exercises	77
11	Saddle-Node Collisions	79
	Exercises	83
12	Model Neurons of Bifurcation Type 1	85
	Exercises	89
13	Hopf Bifurcations	91
	Exercises	97
14	Model Neurons of Bifurcation Type 2	99
	Exercises	102
15	Canard Explosions	105
15.1	A Supercritical Canard Explosion	105
15.2	A Subcritical Canard Explosion	109
	Exercises	110
16	Model Neurons of Bifurcation Type 3	111
16.1	Izhikevich's $I_{Na,p}$ - I_K Model	111
16.2	The Self-Exciting Theta Neuron	114
	Exercises	118

17 Frequency-Current Curves	119
17.1 Computation of f-I-Curves	119
17.2 Examples of Continuous, Single-Valued f-I Curves	121
17.3 Examples of f-I Curves with Discontinuities and an Interval of Bistability	124
Exercises	128
18 Bistability Resulting from Rebound Firing	131
18.1 Classical Hodgkin-Huxley Model	132
18.2 Erisir Model	133
18.3 RTM Model with an M-Current	134
18.4 RTM Neuron with an h-Current	135
Exercises	139
19 Bursting	141
19.1 Hysteresis-Loop Bursting	141
19.2 A Concrete Example	143
19.3 Analysis in an Idealized Setting	145
19.4 Comparison of the Idealized Analysis with Biophysical Models	147
Exercises	149
III Modeling Neuronal Communication	151
20 Chemical Synapses	153
20.1 Nearly Instantaneous Rise	154
20.2 Gradual Rise	157
20.3 The Self-Exciting RTM Neuron	160
20.4 The Jahr-Stevens Model of NMDA Receptor-Mediated Synapses	161
20.5 Buildup of the Synaptic Gating Variable over Multiple Action Potentials	162
Exercises	164
21 Gap Junctions	165
Exercises	171
22 A Wilson-Cowan Model of an Oscillatory E-I Network	175
Exercises	180
IV Entrainment, Synchronization, and Oscillations	181
23 Entrainment by Excitatory Input Pulses	183
23.1 Simulations for a WB Neuron	184
23.2 Analysis for a LIF Neuron	187
Exercises	191

24	Synchronization by Fast Recurrent Excitation	193
24.1	Asynchronous Initialization	193
24.2	Simulations	195
	Exercises	197
25	Phase Response Curves (PRCs)	199
25.1	Input Pulses of Positive Strength and Duration	199
25.2	Input Pulses That Are Infinitesimally Weak, Infinitesimally Brief, or Both	202
25.3	Type 1 vs. Type 2 Phase Response	204
25.4	The PRC of a Theta Neuron with an Infinitesimally Brief Input	205
	Exercises	210
26	Synchronization of Two Pulse-Coupled Oscillators	213
26.1	The Model	213
26.2	Abstract PRCs	214
26.3	Analysis	217
26.4	Diagonally Symmetric PRCs	220
26.5	A Borderline Case in Which the Infinitesimal PRC Leads to a False Conclusion	222
26.6	Pulse-Coupled RTM Neurons	224
	Exercises	224
27	Oscillators Coupled by Delayed Pulses	227
27.1	Two Abstract Oscillators	227
27.2	Two Theta Neurons	232
27.3	Larger Networks of Abstract Oscillators	234
	Exercises	234
28	Weakly Coupled Oscillators	235
28.1	Two Weakly Pulse-Coupled Identical Oscillators	235
28.2	Two Weakly Pulse-Coupled Non-identical Oscillators	239
	Exercises	241
29	Approximate Synchronization by a Single Inhibitory Pulse	243
29.1	Simulations for Normalized LIF Neurons	243
29.2	Simulations for RTM Neurons	248
29.3	The River Picture for Theta Neurons	249
	Exercises	252
30	The PING Model of Gamma Rhythms	255
30.1	Two-Cell PING	258
30.2	Basic Network Simulations	258
30.3	Sparse and Random Connectivity	260

30.4	Strengths of External Drives and the Suppression Boundary	263
30.5	Recurrent Inhibition	264
30.6	Recurrent Excitation	264
	Exercises	265
31	ING Rhythms	269
31.1	Single-Cell ING	271
31.2	Basic Network Simulations	271
31.3	Adding Gap Junctions	273
31.4	Clustering	273
31.5	Two Abstract Oscillators Coupled by Inhibitory Pulses	276
31.6	Entrainment of Excitatory Cells by ING Rhythms	277
	Exercises	278
32	Weak PING Rhythms	281
32.1	Stochastic Weak PING	282
32.2	Adaptation-Based, Deterministic Weak PING	286
32.3	Deterministic Weak PING Without Any Special Currents	289
	Exercises	292
33	Beta Rhythms	293
33.1	PING-Like Beta Rhythms	293
33.2	A Period-Skipping Beta Rhythm, and Cell Assemblies	295
33.3	A Non-synaptic Beta Rhythm	299
	Exercises	299
34	Nested Gamma-Theta Rhythms	301
34.1	Gamma Rhythms Riding on Externally Imposed Theta Rhythms	302
34.2	A Model O-LM Cell	303
34.3	An E-I-O Network Generating Nested Gamma-Theta Rhythms	309
	Exercises	309
V	Functional Significance of Synchrony and Oscillations	311
35	Rhythmic vs. Tonic Inhibition	313
35.1	Periodic Pulse Trains	314
35.2	LIF Neuron Subject to Synaptic Inhibition	315
35.3	RTM Neuron Subject to Synaptic Inhibition	320
	Exercises	320
36	Rhythmic vs. Tonic Excitation	323
36.1	Analysis in an Idealized Setting	323
36.2	Frequency-Current Curve of the RTM Neuron with Pulsed Input	325
	Exercises	326

37	Gamma Rhythms and Cell Assemblies	327
37.1	An Example	327
37.2	The Exponential Sharpness of Thresholding	328
37.3	Analysis in an Idealized Setting	329
	Exercises	331
38	Gamma Rhythms and Communication	333
38.1	Gamma Phase-Dependent Communication	333
38.2	Gamma Coherence-Dependent Communication	336
	Exercises	337
VI	Synaptic Plasticity	339
39	Short-Term Depression and Facilitation	341
39.1	The Tsodyks-Markram Model of Short-Term Depression	342
39.2	The Tsodyks-Markram Model of Short-Term Facilitation	342
39.3	Replacing Jumps by Transitions Governed by ODEs	343
	Exercises	348
40	Spike Timing-Dependent Plasticity (STDP)	349
40.1	The Song-Abbott Model	349
40.2	Replacing Jumps by Transitions Governed by ODEs	352
40.3	STDP in Three-Cell Networks	354
40.4	STDP in Larger PING Networks	356
	Exercises	357
A	The Bisection Method	361
B	Fixed Point Iteration	363
C	Elementary Probability Theory	367
C.1	Basic Vocabulary and Facts	367
C.2	Uniform Distributions	371
C.3	Uniform Distributions in Matlab	371
C.4	Gaussian Distributions	372
C.5	Gaussian Distributions in Matlab	373
C.6	Discrete Ornstein-Uhlenbeck Processes	373
C.7	Exponential Distributions and Lack of Memory	375
C.8	Exponentially Distributed Random Numbers in Matlab	376
C.9	Discrete Approximation of Exponential Distributions	376
C.10	Poisson Schedules	377
C.11	Discrete Approximation of Poisson Schedules	377

D	Smooth Approximations of Non-smooth Functions	379
D.1	Jump Discontinuities	379
D.2	Absolute Values	380
D.3	Maxima and Minima	381
E	Solutions to Selected Homework Problems	383
Bibliography		435
Index		451

Chapter 1

Vocabulary and Notation

1.1 Biological Vocabulary

We begin by introducing some of the vocabulary used throughout this book. A human brain consists of approximately 100 billion *neurons* (nerve cells), and perhaps an equal number of *glia* or *glial cells* (auxiliary cells) [5]. A neuron consists of a cell body or *soma*, and branching projections, the *dendrites* (input units) and the *axon* (output unit). Figure 1.1 shows a caricature. For a depiction of real cells in the *hippocampus*, a brain structure that is central in memory formation and spatial navigation, see Fig. 1.2.

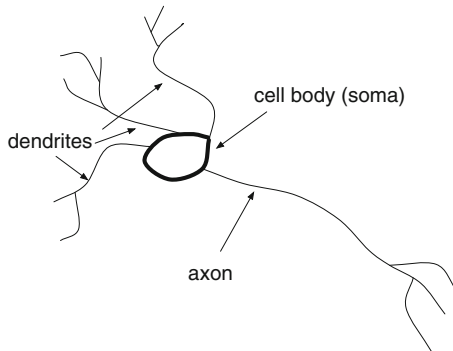


Figure 1.1. Caricature of a neuron.

Neurons and other cells are filled and surrounded by water in which ions such as sodium (Na^+), potassium (K^+), chloride (Cl^-), and calcium (Ca^{2+}) are

Electronic supplementary material: The online version of this chapter (doi: [10.1007/978-3-319-51171-9_1](https://doi.org/10.1007/978-3-319-51171-9_1)) contains supplementary material, which is available to authorized users.

dissolved. The superscripts indicate electrical charge. For instance, a chloride ion carries the charge $-q$, and a calcium ion carries the charge $2q$, where q denotes the *elementary charge*, i.e., the charge of a positron:

$$q \approx 1.60 \times 10^{-19} \text{ C.}$$

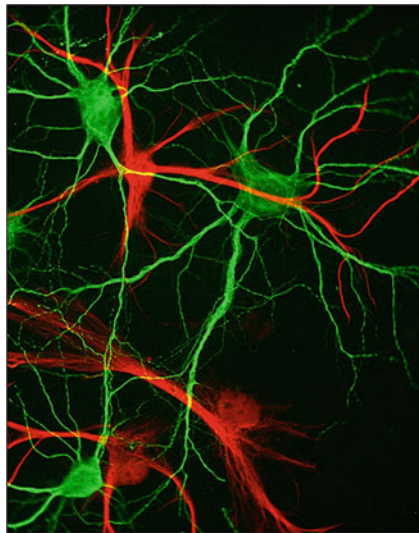


Figure 1.2. Hippocampal neurons (green) and glial cells (red). Copyright Paul De Koninck, Université Laval, www.greenspine.ca, reproduced with permission.

The charge of an electron is $-q$.

Most ion species can pass from the interior of the cell to its exterior or vice versa through *ion channels* in the cell membranes. Often these channels are *specific*: *Sodium channels* only let sodium pass, *potassium channels* only let potassium pass, and so on.

Since ions can pass from one side of the membrane to the other, one might expect their concentrations to become the same on both sides. However, this is not what happens because of two complications. First, some ions are *not* capable of crossing the membrane. There are, in particular, large negatively charged molecules present only in the cell interior, not in the extracellular fluid. Second, cell membranes contain pumps that actively transport ions from one side to the other. The most famous of these is the *sodium-potassium pump*, which removes sodium from the cell and brings in potassium — 2 potassium ions for 3 sodium ions.

As a result of these two complications, understanding the equilibrium state of a cell is not straightforward, and we will not attempt to do so here. Suffice it to say that in equilibrium, ion concentrations in the extracellular fluid are different from those in the cell interior, and there is an electrical potential jump across the cell membrane. We denote the concentrations of an ion species X in the intra- and extracellular fluids by $[X]_{\text{in}}$ and $[X]_{\text{ex}}$, respectively. Typically, $[\text{Na}^+]_{\text{ex}} \gg [\text{Na}^+]_{\text{in}}$,

$[K^+]_{\text{ex}} \ll [K^+]_{\text{in}}$, $[Cl^-]_{\text{ex}} \gg [Cl^-]_{\text{in}}$, and $[Ca^{2+}]_{\text{ex}} \gg [Ca^{2+}]_{\text{in}}$. (The symbols “ \gg ” and “ \ll ” stand for “is much greater than” and “is much less than,” respectively.) The difference in electrical potential between the interior and the exterior of the membrane is called the *membrane potential*, denoted by v . For a nerve cell in equilibrium, a typical value of v might be -70 mV , i.e., the potential on the interior side of the membrane is 70 mV below that in the extracellular fluid. Here mV stands for millivolt, the most commonly used unit of electrical potential in physiology. It is customary in neuroscience to use the word *hyperpolarization* for lowering v (making it more negative than it is in equilibrium), and *depolarization* for raising v (making it closer to zero, or even positive). We also associate the word *excitatory* with depolarization, and *inhibitory* with hyperpolarization; thus an excitatory input raises v , and an inhibitory one lowers v .

Nerve and muscle cells are *excitable*, i.e., they are capable of generating brief surges in the membrane potential called *action potentials* or *voltage spikes*; see Fig. 1.3 for a computer simulation, and Fig. 1.4 for an experimental recording. When a neuron generates an action potential, one also says that it *spikes* or *fires*. The intervals between action potentials are called the *inter-spike intervals*. Most action potentials are sodium-based; some are calcium-based. For sodium-based action potentials to arise, the cell membrane must include sodium channels that open up as v rises, for instance, as a result of input from other nerve cells (see below). Since sodium is more plentiful outside the cell than inside, sodium then enters the cell. Since sodium ions carry positive charge, this results in a further increase in v , further opening of sodium channels, and so on. The result may be a rapid self-accelerating rise in v , often to values above 0 mV . However, the sodium channels underlying the generation of action potentials do not remain open indefinitely at high membrane potentials; within a millisecond or two, they start closing again. One says that they *inactivate*. At the same time, the elevated value of v causes potassium channels to open. Just like the sodium channels, the potassium channels respond to rising v by opening, but they do so more sluggishly. Since potassium is more plentiful inside the cell than in the extracellular fluid, potassium leaves the cell, and since potassium carries positive charge, v falls. The current carried by the potassium ions is called the *delayed rectifier current* — delayed because the potassium channels open up with a delay, and rectifier because the potassium current results in the return of v to its equilibrium value.

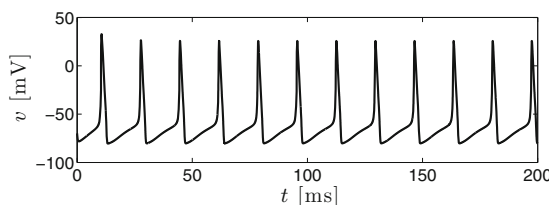


Figure 1.3. Computer simulation of a periodically firing neuron. (Simulation of the classical Hodgkin-Huxley model with $I = 7\text{ }\mu\text{A}/\text{cm}^2$, see Chapter 3.) [HH_VOLTAGE_TRACE]

In Figs. 1.3 and 1.4, it appears that the voltage gradually rises until it reaches a fairly sharply defined *threshold*, then all of the sudden rises rapidly; the threshold

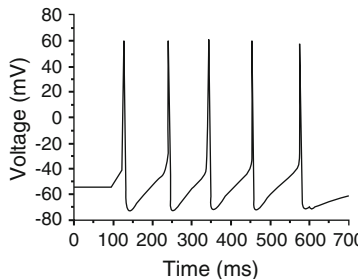


Figure 1.4. Recording of membrane potential from a neuron in the superior cervical ganglion (SCG) of a rat, from Fig. 7A of [70], reproduced with publisher's permission. (The SCG is part of the sympathetic nervous system, which controls the "fight or flight" response.)

seems to be a little bit lower than -60 mV in Fig. 1.3. One calls this the *firing threshold* or the *threshold voltage*. The fact that there often appears to be such a threshold is the basis of the integrate-and-fire models discussed in Chapters 7 and 8. However, in reality there is not usually a sharply defined threshold voltage; whether or not an action potential will occur depends not only on v , but also on other variables characterizing the state of the neuronal membrane.

The voltage spike is spatially local: It typically originates near the cell body on the axonal side, in a location called the *axon hillock*. It then travels down the axon until it reaches the tips of the branches of the axon, also called the *axon terminals*. The axon terminals come very close to the membranes of other neurons. The locations of such near-contacts are called *synapses*. The space between the *pre-synaptic* and *post-synaptic* membranes is called the *synaptic cleft*. It is on the order of 20 nm = 20×10^{-9} m wide. When an action potential arrives at an axon terminal, it often causes the release of a chemical called a *neurotransmitter*, which diffuses across the synaptic cleft to the post-synaptic membrane, where it binds to specialized receptors and leads to the opening of ion channels, thereby affecting the membrane potential of the post-synaptic neuron.

Different classes of neurons release different neurotransmitters. An important example of a neurotransmitter is *glutamate*. When glutamate binds to a receptor, the effect is a depolarization of the post-synaptic membrane, i.e., a rise in the membrane potential of the post-synaptic neuron. Therefore one calls glutamate an *excitatory neurotransmitter*. It is the most common excitatory neurotransmitter in the brain. Neurons that release an excitatory neurotransmitter are called *excitatory neurons*. Neurons that release glutamate are called *glutamatergic*. Many excitatory neurons in the brain have cell bodies of pyramidal shape, and are therefore called *pyramidal neurons*.

Two important glutamate receptor classes are the *AMPA receptors* and the *NMDA receptors*. They derive their names from synthetic substances that can

(artificially) activate them: α -amino-3-hydroxy-5-methyl-4-isoxazolepropionic acid, or AMPA, and N-methyl-D-aspartate, or NMDA. Both AMPA and NMDA receptors are *ionotropic*, which means that the receptor itself is an ion channel which opens when glutamate binds to it. Both are non-specific *cation* (positive ion) channels, i.e., they allow various different positive ions (sodium, potassium, and calcium) to pass.

A second important neurotransmitter is *GABA* (gamma-aminobutyric acid). It is usually *inhibitory*, i.e., when it binds to a receptor, the effect is a hyperpolarization of the post-synaptic membrane.^{1,2} GABA is the most common inhibitory neurotransmitter in the brain. Neurons that release an inhibitory neurotransmitter are called *inhibitory neurons*. They are typically *interneurons*, a phrase that refers to neurons whose axons connect only to nearby neurons, and don't project to distant brain regions. Neurons that release GABA are called *GABAergic*.

GABA acts on various types of GABA receptors. $GABA_A$ receptors are chloride channels that open up when GABA binds to them. Since chloride is more plentiful in the extracellular fluid than in the cell interior, the opening of chloride channels leads to an influx of chloride, and since chloride carries negative charge, this may result in the hyperpolarization of the post-synaptic cell. $GABA_B$ receptors, unlike the other receptors we have mentioned, are *metabotropic*, not ionotropic. This means that they are not ion channels. Instead, when GABA binds to a $GABA_B$ receptor, a signaling cascade, called a *second messenger* cascade, is set in motion that indirectly leads to the opening of potassium channels. This results in the flow of potassium out of the post-synaptic cell, and thereby in the hyperpolarization of the cell.

An earlier footnote indicated already that some neurotransmitters can act in both excitatory and inhibitory ways: GABA, for instance, can be excitatory, especially in early stages of development [35]. In [170], a single neurotransmitter (*acetylcholine*) at a single synapse is reported to have excitatory or inhibitory effects depending on whether the firing of the pre-synaptic neuron is slow or fast. There is also evidence indicating that a single neuron can release both glutamate and GABA; see, for instance, [140]. Thus neurotransmitters, synapses, and neurons cannot always be cleanly classified as excitatory or inhibitory.

The ion currents triggered by the binding of neurotransmitter to receptors in the post-synaptic membrane are called *post-synaptic currents*. They are transient. The ion channels that open as a result of neurotransmitter binding to the receptors close after a brief time. AMPA receptor-mediated post-synaptic currents last only for a few milliseconds, whereas NMDA receptor-mediated ones can last for tens or even hundreds of milliseconds. Similarly, $GABA_A$ receptor-mediated post-synaptic currents last only for ten milliseconds or less, whereas $GABA_B$ receptor-mediated ones last tens or hundreds of milliseconds.

¹One must say “usually” here because GABA can sometimes have a *shunting* effect, i.e., hold the membrane potential in place rather than lower it, or even be excitatory; see, for instance, [35].

²Hyperpolarization can also have an excitatory effect indirectly, by inducing depolarizing currents. An important example of a hyperpolarization-induced depolarizing current is the *h-current* discussed in Section 18.4.

The action potential-triggered release of neurotransmitters is a major mechanism of neuronal communication in the brain. It is called *synaptic* or *chemical* communication. A second important signaling mechanism involves *gap junctions*, i.e., locations at which neuronal membranes are in contact, with openings in both membranes allowing the direct flow of ions from one neuron into the other. This kind of neuronal communication is called *gap-junctional* or *electrical*.

Most of this book will be about modeling neurons and their connections using differential equations, and about the study of coherent activity, specifically oscillations, in neuronal tissue based on such models. However, the most striking property of brains is, of course, their ability to form memories and learn. This involves the strengthening and weakening of synaptic connections, referred to as *synaptic plasticity*. Mechanisms of synaptic plasticity include changes in the quantity of neurotransmitter released and changes in the number of post-synaptic receptors. The concluding chapters of the book briefly discuss this topic.

A detailed study of the anatomy of the brain is beyond the scope of this book, and is not necessary for our purposes. However, in several places we will refer to the *hippocampus*, which we mentioned earlier already, and the *neocortex*, the outer layer of the cerebral hemispheres, involved in sensory processing, motor commands, language, and other higher cognitive functions.

The neocortex is composed of six *layers*, called layers I, II, III, IV, V, and VI. Layer I is the outermost (most *superficial*) layer, and layer VI the innermost (*deepest*). Different layers serve different functions. For instance, the superficial layers II and III, often referred to as *layer II/III*, are important in communication between different parts of the neocortex, while the deep layers V and VI connect the neocortex with subcortical structures such as the brain stem and the spinal cord.

1.2 Mathematical Notation

This is much briefer than Section 1.1 because this book assumes some mathematical background, but no biological background.

For the exponential function, we often use the notation \exp :

$$\exp(x) = e^x.$$

One-sided limits will be denoted by notation such as

$$\lim_{t \searrow t_*} f(t) = f(t_* + 0) = \text{limit of } f(t) \text{ as } t \text{ tends to } t_* \text{ from above,}$$

$$\lim_{t \nearrow t_*} f(t) = f(t_* - 0) = \text{limit of } f(t) \text{ as } t \text{ tends to } t_* \text{ from below.}$$

Throughout the book, we will frequently be concerned with *asymptotics*. Asymptotic statements are statements referring to limits. For instance, if $f = f(t)$ and $g = g(t)$ are functions of t , we write

$$f(t) \sim g(t) \quad \text{as } t \rightarrow \infty$$

for

$$\lim_{t \rightarrow \infty} \frac{f(t)}{g(t)} = 1.$$

We write

$$f(t) \asymp g(t) \quad \text{as } t \rightarrow \infty$$

for

$$\lim_{t \rightarrow \infty} \frac{f(t)}{g(t)} \text{ exists and is positive and finite,}$$

that is, for

$$f(t) \sim Cg(t) \quad \text{for some constant } C \text{ with } 0 < C < \infty.$$

So $f \sim g$ is a stronger statement than $f \asymp g$. In both cases, f and g are “asymptotically similar,” but $f \asymp g$ means that they are asymptotically the same only up to a positive finite constant factor C , whereas $f \sim g$ means that furthermore, $C = 1$.

In some places we will use notation such as $O(x)$ and $o(x)$, sometimes referred to as *big-O* and *little-O notation*. Both $O(x)$ and $o(x)$ refer to a limit that is usually assumed to be clear from the context, for instance (and most typically), $x \rightarrow 0$ or $x \rightarrow \infty$. A quantity $q = q(x)$ is $O(x)$ if $|q(x)/x|$ remains bounded in the limit. More generally, we say that $q(x)$ is $O(x^p)$, for some $p > 0$, if $|q(x)/x^p|$ remains bounded in the limit. We will say that $q(x)$ is *exactly* $O(x^p)$ if $|q(x)/x^p|$ can be bounded from above and below by positive constants independent of x , for x sufficiently close to the limit (or sufficiently large, if the limit of interest is $x \rightarrow \infty$). We say that $q(x)$ is $o(x)$ if $|q(x)/x|$ tends to zero.

1.3 Physical Units

I am careful to include physical units often. However, there are places where specifying units is decidedly awkward, and in such cases, I allow myself to omit the units. For example, in Chapter 3, one finds the formula

$$\alpha_m(v) = \frac{(v + 45)/10}{1 - \exp(-(v + 45)/10)}.$$

The letter v denotes a voltage here, and α_m is a reciprocal time. With the proper physical units, the formula should be written like this:

$$\alpha_m(v) = \frac{(v + 45 \text{ mV})/10 \text{ mV}}{1 - \exp(-(v + 45 \text{ mV})/10 \text{ mV})} \text{ ms}^{-1}.$$

This looks ludicrous, and we will therefore make the convention that the unit of voltage is always the millivolt (mV), and the unit of time is always the millisecond (ms). Other physical quantities similarly have standard units that are implied when none are specified; see Table 1.1.

Even though it is assumed that the reader has a rudimentary knowledge of high school physics, I will review the definitions of these units briefly. To move a unit charge, i.e., the charge of a positron (which has the same charge as an electron, but with positive sign), from location A to location B requires 1 joule (J) of work if the electrical potential in B exceeds that in A by one volt (V). The joule, the

quantity	typical letter	unit
voltage	v	mV
time	t	ms
frequency	f	Hz = s ⁻¹
current density	I	μA/cm ²
conductance density	g	mS/cm ²
capacitance density	C	μF/cm ²

Table 1.1. Physical units used throughout this book.

standard unit of work (energy), is a newton (N) times a meter, and the newton is defined by the equation

$$N = \frac{\text{kg m}}{\text{s}^2}.$$

The “m” in mV, ms, and mS stands for “milli,” a factor of 10⁻³. The ampere (A) is the standard unit of current, defined by

$$A = \frac{C}{s},$$

where the letter C stands for coulomb (unit of charge). The “μ” in μA and μF stands for “micro,” a factor of 10⁻⁶. The siemens (S) is the standard unit of conductance, defined by

$$S = \frac{A}{V}.$$

Its reciprocal is the ohm (Ω),

$$\Omega = \frac{V}{A}$$

the standard unit of resistance. The siemens is therefore sometimes called the mho (ohm spelled backwards). The farad (F) is the standard unit of capacitance, defined by

$$F = \frac{C}{V}.$$

Neuroscientists work with current, conductance, and capacitance *densities* more often than with currents, conductances, and capacitances *per se*. This is why in Table 1.1, we have listed the units of current, conductance, and capacitance densities.

Notice that time is typically measured in ms in this book, but frequency in hertz (Hz), i.e., in s⁻¹, not in ms⁻¹. This incompatibility will cause factors of 1000 to appear in various formulas throughout the book.

Part I

Modeling a Single Neuron

Chapter 2

The Nernst Equilibrium

Charged particles, namely ions, diffuse in water in the brain. There is a field of study called *electro-diffusion theory* concerned with the diffusion of charged particles. In this chapter, we study one electro-diffusion problem that is crucial for understanding nerve cells.

As discussed in Chapter 1, ion concentrations and the electrical potential are different on the interior and exterior sides of the cell membrane. Following convention, we call the electrical potential in the extracellular fluid zero. (One is, in general, allowed to choose freely which electrical potential one calls zero; only potential *differences* have physical meaning.) With this convention, the membrane potential v is the electrical potential on the interior side.

It is instructive to think about what would happen if a membrane potential v were imposed artificially, for instance, by attaching a battery to the cell. Suppose that the ions of some species X could diffuse through the membrane through channels, but that there were no ion pumps actively transporting X-ions across the membrane. If $v = 0$, one would then expect $[X]_{\text{in}}$ and $[X]_{\text{ex}}$ to equalize. If $v \neq 0$, electrical forces come into play. Denote by z the number of unit charges carried by one X-ion: $z = 2$ for calcium, $z = -1$ for chloride, etc. If $z > 0$ and $v < 0$, for instance, X-ions are attracted into the cell, causing $[X]_{\text{in}}$ to rise. The rise, however, cannot continue indefinitely; as the discrepancy between $[X]_{\text{in}}$ and $[X]_{\text{ex}}$ increases, so does the net rate at which X-ions diffuse from the interior to the exterior.

We denote by W_e the amount of work done against the electrical field when moving one ion from the outside to the inside of the cell. (If $z > 0$ and $v < 0$, then $W_e < 0$, meaning that the electrical field does work.) Similarly we denote by W_d the amount of work done against the concentration jump when moving one ion from the outside to the inside. (If $[X]_{\text{ex}} > [X]_{\text{in}}$, then $W_d < 0$.) The diffusional and electrical effects are in equilibrium if

$$W_e + W_d = 0. \quad (2.1)$$

By the definition of electrical potential,

$$W_e = zqv, \quad (2.2)$$

where q is the unit charge, i.e., the charge of a positron. (In general, the electrical potential difference between two points in space is the work that needs to be done against the electrical field to move a positron from one point to the other.)

To derive a formula for W_d is not quite as straightforward. The diffusional effects are greater at higher temperature, and it is therefore not surprising that W_d is proportional to the temperature T . One would also expect that W_d increases as the ratio $[X]_{\text{in}}/[X]_{\text{ex}}$ increases. The formula for W_d is

$$W_d = kT \ln \frac{[X]_{\text{in}}}{[X]_{\text{ex}}}. \quad (2.3)$$

The letter k denotes *Boltzmann's constant*:

$$k \approx 1.38 \times 10^{-23} \text{ J/K},$$

where J stands for joule (unit of energy or work, $J=\text{Nm}=\text{kg m}^2/\text{s}^2$), and K stands for kelvin (unit of temperature). We will not justify (2.3) here. However, for motivation, we will derive the completely analogous and closely related formula for the work required to compress an ideal gas while keeping its temperature constant at the end of this chapter.

Using eqs. (2.2) and (2.3), eq. (2.1) becomes $v = v_X$, with

$$v_X = \frac{kT}{zq} \ln \frac{[X]_{\text{ex}}}{[X]_{\text{in}}}. \quad (2.4)$$

This quantity is called the *Nernst equilibrium potential* of ion species X, named after Walther Nernst (1864–1941), a physical chemist.

Human body temperature is about 37°C , or 310.15 K . For $T = 310.15\text{ K}$,

$$\frac{kT}{q} \approx 26.7 \text{ mV}. \quad (2.5)$$

Typical values of Nernst potentials for sodium, potassium, chloride, and calcium in mammalian nerve cells are on the order of

$$v_{\text{Na}} = 70 \text{ mV}, \quad v_{\text{K}} = -90 \text{ mV}, \quad v_{\text{Cl}} = -70 \text{ mV}, \quad v_{\text{Ca}} = 130 \text{ mV}.$$

The membrane potential never gets as high as v_{Na} , therefore sodium will flow into the cell whenever sodium channels are open. The same holds for calcium. In general, if $v \neq v_X$ and there are open X-channels, there is a flow of X-ions across the cell membrane, and therefore an electrical current, I_X , carried by the ions. This current is often assumed to obey *Ohm's law*:

$$I_X = g_X(v_X - v), \quad (2.6)$$

with $I_X > 0$ if the current is inward, and $I_X < 0$ if it is outward.³ In (2.6), g_X is a *conductance* (the reciprocal of a *resistance*); its value is proportional to the number of open X-channels.

We will now derive the formula for the work needed to compress an ideal gas. This formula is analogous to (2.3). The derivation will give the reader a sense for why the natural logarithm of the concentration ratio appears in (2.3).

When an ideal gas fills a container with volume V , the pressure P that the gas exerts on the container walls is proportional to the temperature T and the number N of gas molecules, and inversely proportional to the volume:

$$P = \frac{kNT}{V}. \quad (2.7)$$

Here k is Boltzmann's constant. Equation (2.7) is called the *ideal gas law*. Denoting by $[X]$ the number density of the gas (number of gas molecules per unit volume), i.e., $[X] = N/V$, we can also write $P = k[X]T$.

Suppose now that the gas filled a cylindrical container of cross-sectional area A and length L ; thus $V = AL$. We will compute how much work is needed to compress the cylinder to a length $L' < L$, thereby reducing the volume to $V' = AL'$ and increasing the number density to $[X]' = N/V'$, while keeping the temperature constant. In general, reduction of the length of the cylinder from some value $s > 0$ to $s - \Delta s$, where $\Delta s > 0$ is small, requires work

force \times distance over which force is applied =

$$\text{pressure} \times \text{area} \times \text{distance} = \frac{kNT}{As} \times A \times \Delta s = \frac{kNT}{s} \Delta s.$$

Therefore the work required to reduce the length from L to $L' < L$ is

$$\int_{L'}^L \frac{kNT}{s} ds = kNT \ln \frac{L}{L'} = kNT \ln \frac{V}{V'} = kNT \ln \frac{[X]'}{[X]}.$$

The work W per gas molecule is obtained by dividing by N :

$$W = kT \ln \frac{[X]'}{[X]}. \quad (2.8)$$

Notice the similarity between eqs. (2.8) and (2.3).

We derived (2.8) by thinking about compressing the gas by reducing the length of a cylindrical container. Suppose we compressed the gas in some other way. Might this require a different amount of work? The answer is no, for if there were a more energy-efficient method of accomplishing the compression, and a less energy-efficient one, we could compress the gas in the more energy-efficient way, then let it expand by reversing the less energy-efficient method, thereby gaining more energy from the expansion than had to be invested to achieve the compression. This

³The more common convention is to let a positive I_X denote an outward current. However, I find the sign convention that I am adopting here more natural.

would violate the first law of thermodynamics, the law of conservation of energy. In exercise 5, you will be asked to verify explicitly that one particular alternative way of compressing the gas leads to the same equation (2.8).

Exercises

- 2.1. Assume $z < 0$ and $[X]_{\text{ex}} > [X]_{\text{in}}$. In a sentence or two, explain why v_X , computed from (2.4), has the sign that one would intuitively expect it to have.
- 2.2. There are indications [3] that in schizophrenia, the activity of *NKCC1* (sodium-potassium-chloride cotransporter 1) may be increased in the prefrontal cortex, whereas that of *KCC2* (potassium-chloride cotransporter 2) may be decreased. *NKCC1* mediates chloride uptake by cells, whereas *KCC2* mediates chloride extrusion. Thus one would expect there to be an abnormally high chloride concentration in the cell interior. Would this raise or lower the Nernst potential of chloride?
- 2.3. Convince yourself that the right-hand side of (2.7) has the physical dimension of a pressure.
- 2.4. Before thinking much about (2.6), you might have guessed that an extra minus sign ought to appear in the equation if the ions were negatively charged, i.e., $z < 0$. Explain why in fact, the signs in (2.6) are precisely what you should intuitively expect them to be, regardless of whether $z > 0$ or $z < 0$.
- 2.5. We derived (2.8) by thinking about reducing the length of a cylindrical container. Suppose that instead, you accomplish the increase in the number density from $[X]$ to $[X]'$ by putting the gas into a spherical container, and shrinking the radius of the container. Show that this results in (2.8) as well.

Chapter 3

The Classical Hodgkin-Huxley ODEs

3.1 The Hodgkin-Huxley Model

In the 1940s, Alan Hodgkin and Andrew Huxley clarified the fundamental physical mechanism by which electrical impulses are generated by nerve cells, and travel along axons, in animals and humans. They experimented with isolated pieces of the giant axon of the squid. They summarized their conclusions in a series of publications in 1952; the last of these papers [76] is arguably the single most influential paper ever written in neuroscience, and forms the foundation of the field of mathematical and computational neuroscience. This chapter is an introduction to the Hodgkin-Huxley model.

Hodgkin and Huxley threaded a silver wire lengthwise through the axon, thereby eliminating spatial variations in the membrane potential v . This is called the *space clamp* technique, originally developed by George Marmont [113]. They conducted a series of experiments to clarify the mechanism underlying the action potentials in the space-clamped squid axon, and summarized the mechanism in the form of a system of ordinary differential equations⁴ (ODEs).

The equation describing how v evolves with time is based on the assumption that a nerve cell membrane acts like a *capacitor*, separating two charge layers of opposite signs. This *dipole layer* gives rise to a jump in the electrical potential; this jump is the membrane potential v . According to the fundamental equation of a capacitor,

$$Cv = Q, \tag{3.1}$$

Electronic supplementary material: The online version of this chapter (doi: [10.1007/978-3-319-51171-9_3](https://doi.org/10.1007/978-3-319-51171-9_3)) contains supplementary material, which is available to authorized users.

⁴An “ordinary differential equation” (ODE) involves derivatives of functions of one variable only. By contrast, a “partial differential equation” (PDE) involves partial derivatives of functions of several variables.

where Q is the separated charge (the charge carried by the two layers is $\pm Q$), and the constant of proportionality, C , is called the *capacitance*. If Q and v depend on time, t , we can differentiate both sides of (3.1) to obtain

$$C \frac{dv}{dt} = I_{\text{total}}, \quad (3.2)$$

where $I_{\text{total}} = dQ/dt$ is the total electrical current from one side of the capacitor to the other; this equation is the starting point for the Hodgkin-Huxley ODEs.

Based on experiments, Hodgkin and Huxley hypothesized that I_{total} was made up of four components: A sodium current I_{Na} , a potassium current I_{K} , a small additional current which they called the *leak current* and denoted by I_{L} , carried by chloride and other ions, and the current I that they themselves injected, using electrodes, in the course of their experiments. Thus

$$C \frac{dv}{dt} = I_{\text{Na}} + I_{\text{K}} + I_{\text{L}} + I. \quad (3.3)$$

The currents I_{Na} , I_{K} , and I_{L} are assumed to obey Ohm's law (see (2.6)):

$$I_{\text{Na}} = g_{\text{Na}}(v_{\text{Na}} - v), \quad I_{\text{K}} = g_{\text{K}}(v_{\text{K}} - v), \quad I_{\text{L}} = g_{\text{L}}(v_{\text{L}} - v).$$

Here v_{Na} and v_{K} are the Nernst potentials of sodium and potassium, respectively. If the leak current were exclusively carried by chloride, v_{L} would be the Nernst potential of chloride, but since it is carried by a mixture of ion species, v_{L} is a weighted average of the Nernst potentials of those ion species. Since I_{Na} , I_{K} , and I_{L} change sign when v passes v_{Na} , v_{K} , and v_{L} , one also refers to v_{Na} , v_{K} , and v_{L} as *reversal potentials*.

Hodgkin and Huxley derived from their experiments that, and how, the conductances g_{Na} and g_{K} track changes in v . Their descriptions of g_{Na} and g_{K} take the following forms:

$$g_{\text{Na}} = \bar{g}_{\text{Na}} m^3 h, \quad g_{\text{K}} = \bar{g}_{\text{K}} n^4, \quad (3.4)$$

where \bar{g}_{Na} and \bar{g}_{K} are constant conductances, and m , h , and n are time-dependent dimensionless quantities varying between 0 and 1. Hodgkin and Huxley proposed the following physical interpretation of eqs. (3.4). Suppose that each sodium channel is guarded by four *gates* in series, that these gates open and close independently of each other, and that all four gates must be open for the channel to be open. Suppose further that there are three gates of one type, let us call them the *m-gates*, and one gate of another type, let us call it the *h-gate*. If m and h denote the fractions of open *m*- and *h*-gates, respectively, then the fraction of open sodium channels is $m^3 h$. Similarly, if a potassium channel has four identical independent gates in series, with the channel open only if all four gates are open, and if n denotes the fraction of open potassium gates, then the fraction of open potassium channels is n^4 . This physical interpretation is not to be taken literally.⁵ The observation is simply that if it were true, the sodium and potassium conductances would in fact

⁵However, when a potassium channel was imaged in detail for the first time [39], decades after the work of Hodgkin and Huxley, the channel turned out to have four identical subunits.

be described by eqs. (3.4), with \bar{g}_{Na} and \bar{g}_{K} equal to the largest possible sodium and potassium conductances, realized when all channels are open. The variables m , h , and n are therefore called *gating variables*.

In the Hodgkin-Huxley model, m , h , and n obey simple first-order ODEs of the form

$$\frac{dm}{dt} = \frac{m_\infty(v) - m}{\tau_m(v)}, \quad \frac{dh}{dt} = \frac{h_\infty(v) - h}{\tau_h(v)}, \quad \frac{dn}{dt} = \frac{n_\infty(v) - n}{\tau_n(v)}, \quad (3.5)$$

where m_∞ , τ_m , h_∞ , τ_h , n_∞ , and τ_n are functions of v yet to be discussed. Instead of explicitly spelling out the three equations for m , h , and n , we will from now on briefly write

$$\frac{dx}{dt} = \frac{x_\infty(v) - x}{\tau_x(v)} \quad \text{for } x = m, h, n. \quad (3.6)$$

If x_∞ and τ_x were constants, independent of v , (3.6) would be equivalent to

$$x(t) = x(0)e^{-t/\tau_x} + x_\infty(1 - e^{-t/\tau_x}). \quad (3.7)$$

We always assume τ_x to be positive. The right-hand side of (3.7) is then a weighted average of $x(0)$ and x_∞ . The weight multiplying $x(0)$ starts out, at $t = 0$, at 1, and decays to 0 exponentially fast. The weight multiplying x_∞ starts out at 0, and converges to 1 exponentially fast. Thus $x(t)$ moves from $x(0)$ to x_∞ (its limit as $t \rightarrow \infty$) exponentially fast. The time it takes for $x(t)$ to make “substantial progress” towards x_∞ , namely, the time it takes for the weight in front of $x(0)$ to decay by a factor of $1/e$, is τ_x . We say that $x(t)$ converges to x_∞ *exponentially with time constant* τ_x . Thus eqs. (3.5) express that m , h , and n move towards m_∞ , h_∞ , and n_∞ , exponentially with time constants τ_m , τ_h , and τ_n . Note, however, that m_∞ , h_∞ , and n_∞ are “moving targets” — they change as v changes. How quickly m , h , and n respond to changes in v , and therefore in m_∞ , h_∞ , and n_∞ , is measured by τ_m , τ_h , and τ_n .

The functions $x_\infty(v)$ and $\tau_x(v)$, $x = m, h, n$, were defined by Hodgkin and Huxley so that the resulting ODEs would match their experimental data. Figure 3.1 shows the graphs of these functions. The formulas given by Hodgkin and Huxley will be listed at the end of this chapter. First we will make a few observations based on the graphs.

1. τ_m is approximately 10 times smaller than τ_h and τ_n . Thus m responds to changes in v much faster than h and n . The Hodgkin-Huxley equations are a *slow-fast system*, that is, there are two significantly different time scales, a slow one and a fast one.
2. m_∞ and n_∞ are increasing functions of v . One therefore calls m and n *activation variables*. In the language of the hypothesized physical interpretation discussed earlier, as v rises, m -gates open, and so do n -gates, although on a ten times slower time scale. One also says that the m - and n -gates are *activation gates*.

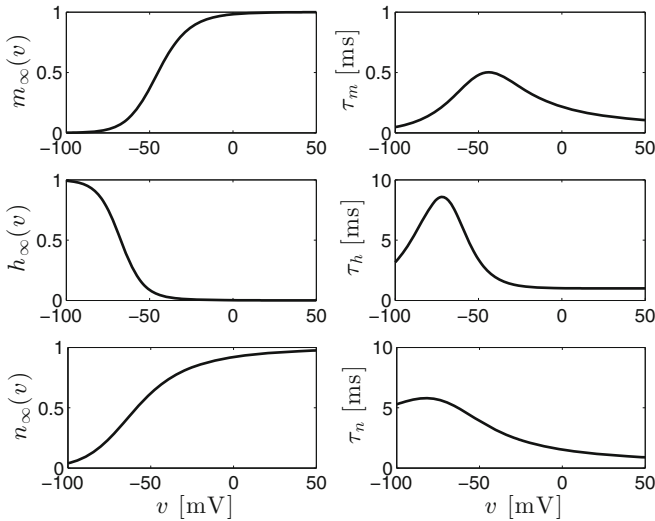


Figure 3.1. The functions $x_\infty(v)$ and $\tau_x(v)$, $x = m$, h , and n , in the Hodgkin-Huxley model. [\[HH_GATING_VARIABLES\]](#)

3. h_∞ is a decreasing function of v . One therefore calls h an *inactivation variable*. As v rises, h -gates close, but ten times slower than m -gates open. One also says that the h -gate is an *inactivation gate*.

By contrast with the sodium and potassium conductances, the *leak conductance* g_L is constant. For aesthetic reasons, we write

$$g_L = \bar{g}_L.$$

We summarize the Hodgkin-Huxley model of the space-clamped squid axon:

$$C \frac{dv}{dt} = \bar{g}_{Na} m^3 h (v_{Na} - v) + \bar{g}_K n^4 (v_K - v) + \bar{g}_L (v_L - v) + I, \quad (3.8)$$

$$\frac{dx}{dt} = \frac{x_\infty(v) - x}{\tau_x(v)}, \quad x = m, h, n. \quad (3.9)$$

This is a system of four ODEs for the four unknown functions v , m , h , and n . Up to now, we have thought of C as capacitance, \bar{g}_{Na} , \bar{g}_K , and \bar{g}_L as conductances, and I as a current. However, dividing both sides of (3.8), by the total membrane area, we see that the precisely same equation holds if we think of C , \bar{g}_{Na} , \bar{g}_K , \bar{g}_L , and I as capacitance, conductance, and current *per unit membrane area*, i.e., as capacitance, conductance, and current *densities*. Following Hodgkin and Huxley, this is how we will interpret these quantities from here on.

All that is left to do to specify the model completely is to specify the constants C , v_{Na} , v_K , v_L , \bar{g}_{Na} , \bar{g}_K , and \bar{g}_L , and the formulas for $x_\infty(v)$ and $\tau_x(v)$, $x = m, h, n$. The constants are

$$C = 1 \mu\text{F}/\text{cm}^2, \quad v_{\text{Na}} = 45 \text{ mV}, \quad v_{\text{K}} = -82 \text{ mV}, \quad v_{\text{L}} = -59 \text{ mV},$$

$$\bar{g}_{\text{Na}} = 120 \text{ mS}/\text{cm}^2, \quad \bar{g}_{\text{K}} = 36 \text{ mS}/\text{cm}^2, \quad \bar{g}_{\text{L}} = 0.3 \text{ mS}/\text{cm}^2,$$

See Section 1.3 for a discussion of the units used here and throughout this book.

Note that \bar{g}_{L} is very much smaller than \bar{g}_{Na} and \bar{g}_{K} . Nonetheless the leak conductance is crucial for the behavior of the model. The reason is that between voltage spikes, \bar{g}_{L} is *not* very small in comparison with $\bar{g}_{\text{Na}}m^3h$ and $\bar{g}_{\text{K}}n^4$; see exercise 3. Sodium and potassium channels are largely closed between voltage spikes, while the leak channels remain open.

We now specify $x_\infty(v)$ and $\tau_x(v)$, $x = m, h, n$. First, we observe that (3.6) can be re-written in the form

$$\frac{dx}{dt} = \alpha_x(v)(1-x) - \beta_x(v)x. \quad (3.10)$$

The relation between the parameters x_∞ and τ_x in (3.6), and the parameters α_x and β_x in (3.10), is

$$x_\infty = \frac{\alpha_x}{\alpha_x + \beta_x}, \quad \tau_x = \frac{1}{\alpha_x + \beta_x}, \quad (3.11)$$

or, equivalently,

$$\alpha_x = \frac{x_\infty}{\tau_x}, \quad \beta_x = \frac{1 - x_\infty}{\tau_x}. \quad (3.12)$$

Thinking of gates guarding channels as before, and assuming that open gates close and closed gates open at random times, with time rates dependent on v , one can interpret α_x as the time rate at which closed gates open, and β_x as the time rate at which open gates close. That is, in a short time Δt , the probability that a closed gate opens is approximately $\alpha_x \Delta t$, and the probability that an open gate closes is approximately $\beta_x \Delta t$. The differential equation governing x can be described either by specifying x_∞ and τ_x , or equivalently by specifying α_x and β_x .

Hodgkin and Huxley measured the quantities x_∞ and τ_x and computed from them the time rates α_x and β_x (measured in ms^{-1}) as functions of v (measured in mV). It is easier to fit α_x and β_x with simple formulas than to fit x_∞ and τ_x directly, because all α_x and β_x are monotonic functions of v , while the τ_x are not. Up to notation⁶, Hodgkin and Huxley's formulas are

$$\begin{aligned} \alpha_m(v) &= \frac{(v + 45)/10}{1 - \exp(-(v + 45)/10)}, & \beta_m(v) &= 4 \exp(-(v + 70)/18), \\ \alpha_h(v) &= 0.07 \exp(-(v + 70)/20), & \beta_h(v) &= \frac{1}{\exp(-(v + 40)/10) + 1}, \\ \alpha_n(v) &= \frac{1}{100} \frac{v + 60}{1 - \exp(-(v + 60)/10)}, & \beta_n(v) &= \frac{1}{8} \exp(-(v + 70)/80). \end{aligned}$$

(See Section 1.3 for a discussion of the physical units that are implied here.) Note that in the formulas for α_m and α_n , the denominators become zero for special values

⁶Denoting by v_{HH} the “ v ” of Hodgkin and Huxley, our “ v ” is $-v_{HH} - 70$ mV, in line with the notation that is now common.

of v : $v = -45$ for α_m , and $v = -60$ for α_n . L'Hospital's rule needs to be used to evaluate α_m and α_n for those values of v (exercise 4).

We already discussed *action potentials* or *voltage spikes* in Section 1.1; they are illustrated in Figs. 1.3 and 1.4, for instance. In the Hodgkin-Huxley model, action potentials are generated when the m -gates open up in response to an initial depolarization, causing a sodium current into the cell. This sodium current raises v further, and a sort of chain reaction ensues. The rise in v is terminated when the h -gates close, thereby ending the inflow of sodium, and the n -gates open, leading to an outflow of potassium. It is crucial here that τ_m is much smaller than τ_h and τ_n ; see Fig. 3.1. If the time constants were all equal, the closing of the h -gates and the opening of the n -gates could cancel the opening of the m -gates immediately, thereby preventing the voltage spike.

3.2 Activation, Inactivation, De-activation, and De-inactivation

The purpose of this brief section is to clarify some potentially confusing, but common and occasionally convenient terminology.

In Hodgkin-Huxley-like models, a gating variable x is generally called an *activation variable* if x_∞ is an increasing function of v , and an *inactivation variable* if x_∞ is a decreasing function of v . As mentioned earlier, in the classical Hodgkin-Huxley model, m and n are activation variables, and h is an inactivation variable.

An increase in an activation variable as a result of depolarization causes *activation* of the current. A decrease in an activation variable as a result of hyperpolarization causes *de-activation* of the current. A decrease in an inactivation variable as a result of depolarization causes *inactivation*, and an increase in an inactivation variable as a result of hyperpolarization causes *de-inactivation* of the current. Note in particular that de-activation is not the same as inactivation, and de-inactivation is not the same as activation.

We also sometimes use the word “induced.” For instance, a current with an inactivation gate that is de-inactivated in response to hyperpolarization might be called “hyperpolarization-induced.” A current with an activation gate that is activated in response to firing might be called “firing-induced.”

Exercises

- 3.1. Using separation of variables, derive (3.7) from (3.6).
- 3.2. Suppose that

$$\frac{dx}{dt} = \frac{2-x}{4}, \quad x(0) = 1.$$

What is $x(3)$?

- 3.3. Suppose that $v = -75$ mV is held fixed until the values of m , h , and n reach equilibrium. What are the sodium, potassium, and leak conductance densities now?

- 3.4. Using l'Hospital's rule, compute $\lim_{v \rightarrow -45} \alpha_m(v)$ and $\lim_{v \rightarrow -60} \alpha_n(v)$.
- 3.5. (*) Using a computer, plot α_x and β_x , $x = m, h$, and n . You can use the code that generates Fig. 3.1 as a starting point, if you like.

Chapter 4

Numerical Solution of the Hodgkin-Huxley ODEs

In practice, complicated differential equations such as the Hodgkin-Huxley ODEs are almost always solved *numerically*, that is, approximate solutions are obtained on a computer.⁷ The study of methods for the numerical solution of differential equations is the subject of a large and highly sophisticated branch of mathematics. However, here we will study only the two simplest methods: *Euler's method* and the *midpoint method*. Euler's method is explained here merely as a stepping stone to the midpoint method. For all simulations of this book, we will use the midpoint method, since it is far more efficient, and not much more complicated than Euler's method.

We write the Hodgkin-Huxley ODEs briefly as

$$\frac{dy}{dt} = F(y), \quad (4.1)$$

with

$$y = \begin{bmatrix} v \\ m \\ h \\ n \end{bmatrix}, \quad F(y) = \begin{bmatrix} (\bar{g}_{\text{Na}}m^3h(v_{\text{Na}} - v) + \bar{g}_K n^4(v_K - v) + \bar{g}_L(v_L - v) + I) / C \\ (m_\infty(v) - m) / \tau_m(v) \\ (h_\infty(v) - h) / \tau_h(v) \\ (n_\infty(v) - n) / \tau_n(v) \end{bmatrix}.$$

Suppose that in addition to the system of ODEs, (4.1), we are given the *initial condition*

$$y(0) = y_0, \quad (4.2)$$

Electronic supplementary material: The online version of this chapter (doi: [10.1007/978-3-319-51171-9_4](https://doi.org/10.1007/978-3-319-51171-9_4)) contains supplementary material, which is available to authorized users.

⁷This certainly does not mean that there are not mathematical methods that yield very valuable insight. You will see some of them later in this book. However, for most differential equations it is impossible to write down “explicit” solutions, that is, formulas representing solutions symbolically, and even when it is possible it may not always be useful.

i.e., we are given v , m , h , and n at time $t = 0$, and that we want to find $y(t)$, $0 \leq t \leq T$, for some $T > 0$.

The simplest idea for computing solutions to this problem is as follows. Choose a large integer M , and define $\Delta t = T/M$ and $t_k = k\Delta t$, $k = 0, 1, 2, \dots, M$. Compute approximations

$$y_k \approx y(t_k), \quad k = 1, 2, \dots, M,$$

from the equation

$$\frac{y_k - y_{k-1}}{\Delta t} = F(y_{k-1}), \quad k = 1, 2, \dots, M. \quad (4.3)$$

This is called *Euler's method*, named after Leonhard Euler (1707–1783). Note the similarity between eqs. (4.1) and (4.3): One obtains (4.3) by replacing the derivative in (4.1) by a difference quotient. This is motivated by the fact that

$$\frac{y(t_k) - y(t_{k-1})}{\Delta t} \approx \frac{dy}{dt}(t_{k-1}) \quad (4.4)$$

for small Δt .

A small modification leads to a much more effective method: Write $t_{k-1/2} = (k - 1/2)\Delta t$, $k = 1, 2, \dots, M$, and compute approximations

$$\hat{y}_{k-1/2} \approx y(t_{k-1/2}) \quad \text{and} \quad \hat{y}_k \approx y(t_k), \quad k = 1, 2, \dots, M,$$

by

$$\frac{\hat{y}_{k-1/2} - \hat{y}_{k-1}}{\Delta t/2} = F(\hat{y}_{k-1}) \quad \text{and} \quad (4.5)$$

$$\frac{\hat{y}_k - \hat{y}_{k-1}}{\Delta t} = F(\hat{y}_{k-1/2}), \quad k = 1, 2, \dots, M. \quad (4.6)$$

This is called the *midpoint method*. Equation (4.5) describes a step of Euler's method, with Δt replaced by $\Delta t/2$. Equation (4.6) is motivated by the fact that

$$\frac{y(t_k) - y(t_{k-1})}{\Delta t} \approx \frac{dy}{dt}(t_{k-1/2}) \quad (4.7)$$

for small Δt . The *central* difference approximation in (4.7) is much more accurate than the *one-sided* approximation in (4.4); see exercise 3. You might be concerned that whichever advantage is derived from using the central difference approximation in (4.6) is essentially squandered by using Euler's method to compute $\hat{y}_{k-1/2}$. However, this is not the case; the reason is, loosely speaking, that the right-hand side of eq. (4.6) is multiplied by Δt in the process of solving the equation for \hat{y}_k .

The theoretical analysis of Euler's method and the midpoint method relies on two assumptions. First, F must be sufficiently often differentiable.

(Twice is enough, but that is unimportant here: The right-hand side of the Hodgkin-Huxley equations is infinitely often differentiable with respect to v , m , h , and n .) In addition, one must assume that the solution $y(t)$ is defined for $0 \leq t \leq T$. See exercise 4 for an example illustrating that $y(t)$ is not guaranteed to be defined for $0 \leq t \leq T$ even if F is infinitely often differentiable. However, for the Hodgkin-Huxley equations, one can prove that all solutions are defined for all times; see exercise 5.

To characterize the accuracy of the approximations obtained using Euler's method and the midpoint method, we note first that y_k and \hat{y}_k depend not only on k , but also on Δt , and we make this dependence clear now by writing $y_{k,\Delta t}$ and $\hat{y}_{k,\Delta t}$ instead of y_k and \hat{y}_k .

For Euler's method, there exists a constant $C > 0$ independent of Δt (but dependent on F , y_0 , and T) so that

$$\max_{0 \leq k \leq M} |y(k\Delta t) - y_{k,\Delta t}| \leq C\Delta t. \quad (4.8)$$

Similarly, for the midpoint method,

$$\max_{0 \leq k \leq M} |y(k\Delta t) - \hat{y}_{k,\Delta t}| \leq \hat{C}\Delta t^2 \quad (4.9)$$

for a constant $\hat{C} > 0$ independent of Δt . The proofs of these results can be found in most textbooks on numerical analysis, for instance, in [78].

For small Δt , $\hat{C}\Delta t^2$ is much smaller than $C\Delta t$. (If Δt is small, Δt^2 is much smaller than Δt .) Therefore the midpoint method gives much better accuracy than Euler's method when Δt is small. One says that Euler's method is *first-order accurate*, and the midpoint method is *second-order accurate*. This terminology refers to the powers of Δt in eqs. (4.8) and (4.9).

Suppose that we want to compute the solution y up to some small error $\epsilon > 0$. If we use Euler's method, we should make sure that $C\Delta t \leq \epsilon$, so $\Delta t \leq \epsilon/C$. If we use the midpoint method, we need $\hat{C}\Delta t^2 \leq \epsilon$, so $\Delta t \leq \sqrt{\epsilon/\hat{C}}$. For small ϵ , the bound $\sqrt{\epsilon/\hat{C}}$ is much larger than the bound ϵ/C . This means that at least for stringent accuracy requirements (namely, for small ϵ), the midpoint method is much more efficient than Euler's method, since it allows much larger time steps than Euler's method.

In many places in this book, we will present computed solutions of systems of ODEs. All of these solutions were obtained using the midpoint method, most typically with $\Delta t = 0.01$ ms.

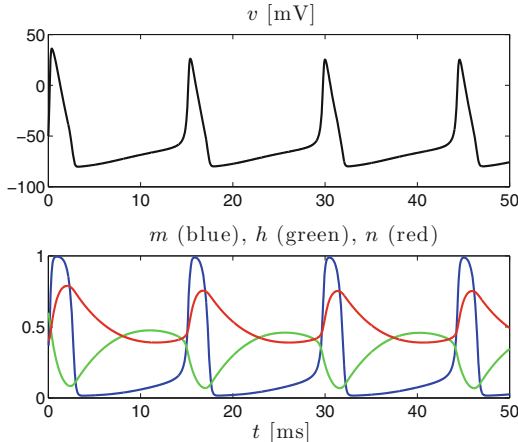


Figure 4.1. A solution of the Hodgkin-Huxley ODEs with $I = 10 \mu\text{A}/\text{cm}^2$.
[\[HH_SOLUTION\]](#)

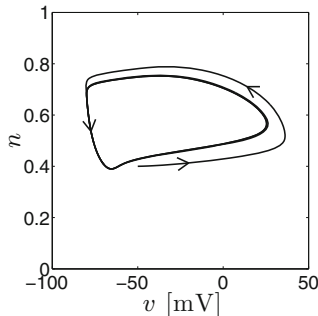


Figure 4.2. Projection into the (v, n) -plane of the solution shown in Fig. 4.1. The arrows indicate the direction in which the point (v, n) moves.
[\[HH_LIMIT_CYCLE\]](#)

Figure 4.1 shows an example of a solution of the Hodgkin-Huxley ODEs, demonstrating that the model produces voltage spikes. We gave a heuristic explanation of the origins of the voltage spikes in Section 1.1 already. From a mathematical point of view, the spikes will be discussed in later sections.

Figure 4.2 shows, for the same solution, the curve $(v(t), n(t))$ in the (v, n) -plane. Periodic firing corresponds to a periodic solution of the Hodgkin-Huxley ODEs, represented by a closed loop in (v, m, h, n) -space. Solutions that start near the periodic solution converge to it. One therefore calls the periodic solution an *attracting limit cycle*.

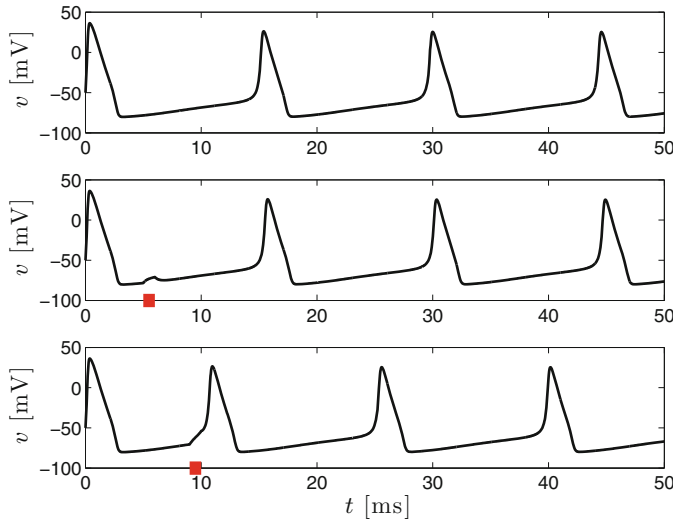


Figure 4.3. An illustration of the refractoriness of the Hodgkin-Huxley neuron following an action potential. Top panel: Solution already shown in Fig. 4.1. Middle panel: Solution obtained when a brief strong pulse of input is added, raising I from 10 to $40 \mu\text{A}/\text{cm}^2$ for t between 5 and 6 ms. Bottom panel: Same, with additional input pulse arriving later, between 9 and 10 ms. The time of the additional input pulse is indicated by a red bar in the middle and bottom panels.

[HH_REFRACTORINESS]

Figure 4.1 shows that it takes the gating variable, n , of the delayed rectifier current a few milliseconds to decay following a spike. This has an important consequence: Input arriving within a few milliseconds following a spike has very little effect. Positive charge injected at this time immediately leaks out. This is illustrated by Fig. 4.3. When the pulse comes soon after a spike (middle panel), it has almost no effect. When it comes just a few milliseconds later (bottom panel), it instantly triggers a new spike. One says that the neuron is *refractory* for a brief time following an action potential, the *refractory period*. It is not a sharply defined time interval: Immediately after a spike, the neuron is nearly insensitive even to strong input, then its input sensitivity gradually recovers.

Exercises

- 4.1. Consider an initial-value problem

$$\frac{dy}{dt} = -cy \quad \text{for } t \geq 0, \quad y(0) = y_0,$$

with $c > 0$ and y_0 given.

- (a) Write down a formula for $y(t)$, and show that $\lim_{t \rightarrow \infty} y(t) = 0$.
- (b) Denote by y_k , $k = 1, 2, 3, \dots$, the approximations to $y(k\Delta t)$ obtained using Euler's method. Write down an explicit, simple formula for y_k .
- (c) Prove that

$$\lim_{k \rightarrow \infty} y_k = 0 \quad \text{if } \Delta t < 2/c,$$

but

$$\lim_{k \rightarrow \infty} |y_k| = \infty \quad \text{if } \Delta t > 2/c.$$

One says that $2/c$ is a *stability threshold*.

- (d) We write $y_{k,\Delta t}$ instead of y_k to make clear that y_k does not only depend on k , but also on Δt . Let $T > 0$ and $\Delta t = T/M$, where M is a positive integer. Then $y_{M,\Delta t} = y_{M,T/M}$ is an approximation for $y(T)$. Show explicitly, without using (4.8), that

$$\lim_{M \rightarrow \infty} y_{M,T/M} = y(T).$$

(L'Hospital's rule will be useful here.)

- 4.2. For the initial-value problem in exercise 1, denote by \hat{y}_k , $k = 1, 2, 3, \dots$, the approximations of $y(k\Delta t)$ obtained using the midpoint method. Write down an explicit, simple formula for \hat{y}_k .
- 4.3. Let $y = y(t)$ be a function that is as often differentiable as you wish. (Three times will be enough, but that is unimportant here. Solutions of the Hodgkin-Huxley equations are infinitely often differentiable.) Let t be fixed, and let $\Delta t_{\max} > 0$ be any positive number.

- (a) Using Taylor's theorem, show that there exists a constant C , independent of Δt , so that

$$\left| \frac{y(t) - y(t - \Delta t)}{\Delta t} - y'(t - \Delta t) \right| \leq C\Delta t$$

for all Δt with $0 < \Delta t \leq \Delta t_{\max}$, where $y' = dy/dt$.

- (b) Using Taylor's theorem, show that there exists a constant \hat{C} , independent of Δt , so that

$$\left| \frac{y(t) - y(t - \Delta t)}{\Delta t} - y'(t - \Delta t/2) \right| \leq \hat{C}\Delta t^2$$

for all Δt with $0 < \Delta t \leq \Delta t_{\max}$, where again $y' = dy/dt$.

- 4.4. Using separation of variables, find a solution of the initial-value problem

$$\frac{dy}{dt} = y^2, \quad y(0) = 1.$$

Show that the limit of $y(t)$ as $t \rightarrow 1$ from the left is ∞ . This is called *blow-up in finite time*.

- 4.5. Suppose that v , m , h , and n solve the Hodgkin-Huxley ODEs, eqs. (3.8) and (3.9). Define

$$A = \min \left(v_K, v_L + \frac{I}{g_L} \right), \quad B = \max \left(v_{Na}, v_L + \frac{I}{g_L} \right).$$

Explain: If $A \leq v(0) \leq B$ and $0 \leq x \leq 1$ for $x = m$, h , and n , then $A \leq v(t) \leq B$ and $0 \leq x \leq 1$ for all $t \geq 0$. So there is no blow-up in finite time (see exercise 4) for the Hodgkin-Huxley ODEs.

Chapter 5

Three Simple Models of Neurons in Rodent Brains

Hodgkin and Huxley modeled the giant axon of the squid. Since then, many similar models of neurons in mammalian brains have been proposed. In this chapter, we list three examples, which will be used throughout the book.

In Chapter 3, the current density I reflected current injected by an experimenter. For a neuron in the brain, usually there is no experimenter injecting current. Nonetheless, the Hodgkin-Huxley-like models described here include a term I . It might represent input currents originating from other neurons, or currents not explicitly modeled. We call I the *external drive* or the *external input*.

The models discussed in this chapter are called the *RTM model*, *WB*, and *Erisir* models. All three are of the form of the classical Hodgkin-Huxley model, eqs. (3.8) and (3.9), but with different parameter values, different functions α_x and β_x (remember that α_x and β_x determine the functions x_∞ and τ_x), and with the assumption that “ $\tau_m = 0$,” that is, $m = m_\infty(v)$. Thus m is not a dependent variable any more, but a direct function of v . This assumption is justified by the fact that

$$\tau_m(v) = \frac{1}{\alpha_m(v) + \beta_m(v)}$$

is very small for all v ; see exercise 1, and compare also Fig. 3.1.

Sections 5.1–5.3 specify details, including formulas for the α_x and β_x . The graphs of the functions x_∞ and τ_x for all three models are given in Fig. 5.1, and the constants in Table 5.1.

Electronic supplementary material: The online version of this chapter (doi: [10.1007/978-3-319-51171-9_5](https://doi.org/10.1007/978-3-319-51171-9_5)) contains supplementary material, which is available to authorized users.

	C	v_{Na}	v_{K}	v_{L}	\bar{g}_{Na}	\bar{g}_{K}	\bar{g}_{L}
RTM	1	50	-100	-67	100	80	0.1
WB	1	55	-90	-65	35	9	0.1
Erisir	1	60	-90	-70	112	224	0.5

Table 5.1. Constants in the three Hodgkin-Huxley-like models discussed in this chapter. See Section 1.3 for the units implied here.

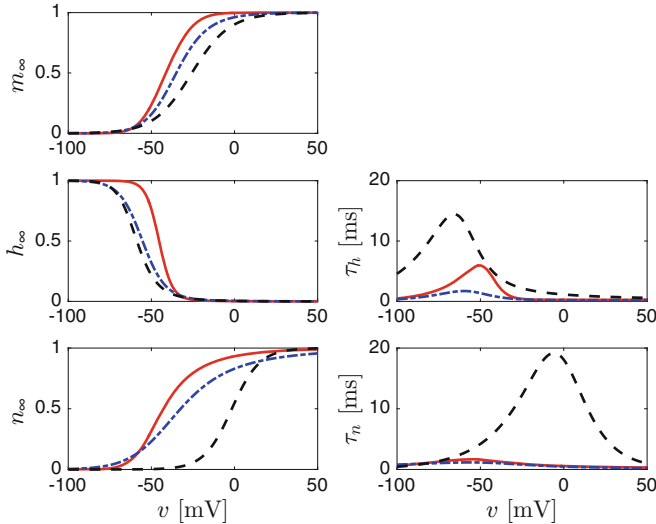


Figure 5.1. The functions x_∞ and τ_x for the RTM neuron (red and solid), WB neuron (blue, dash-dots), and Erisir neuron (black, dashes). We left out τ_m because $m = m_\infty(v)$ in all three of these models. [THREE_MODELS_GATING_VARIABLES]

5.1 Reduced Traub-Miles Model of a Pyramidal Neuron in Rat Hippocampus

This is a slight modification of a model due to Ermentrout and Kopell [50], which in turn is a substantial simplification of a model of a pyramidal excitatory cell in rat hippocampus due to Traub and Miles [161]. The constants are specified in Table 5.1. The functions α_x and β_x are

$$\begin{aligned} \alpha_m(v) &= \frac{0.32(v + 54)}{1 - \exp(-(v + 54)/4)}, & \beta_m(v) &= \frac{0.28(v + 27)}{\exp((v + 27)/5) - 1}, \\ \alpha_h(v) &= 0.128 \exp(-(v + 50)/18), & \beta_h(v) &= \frac{4}{1 + \exp(-(v + 27)/5)}, \\ \alpha_n(v) &= \frac{0.032(v + 52)}{1 - \exp(-(v + 52)/5)}, & \beta_n(v) &= 0.5 \exp(-(v + 57)/40). \end{aligned}$$

The red, solid curves in Fig. 5.1 show the graphs of x_∞ and τ_x , $x = m, h$, and n . Figure 5.2 shows a voltage trace with $I = 1.5 \mu\text{A}/\text{cm}^2$.

5.2 Wang-Buzsáki Model of an Inhibitory Interneuron in Rat Hippocampus

Wang and Buzsáki [174] proposed a model of an *inhibitory basket cell* in rat hippocampus. Basket cells derive their name from the fact that the branches of their axonal arbors form basket-like structures surrounding the cell bodies of other cells.

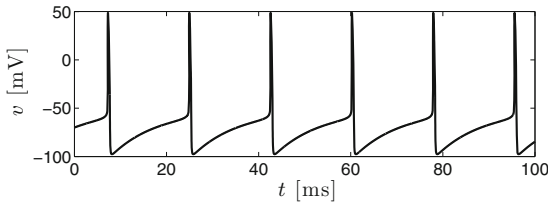


Figure 5.2. Voltage trace of the RTM neuron with $I = 1.5 \mu\text{A}/\text{cm}^2$.
[RTM_VOLTAGE_TRACE]

Two different classes of inhibitory basket cells are ubiquitous in the brain, the *parvalbumin-positive* (PV+) basket cells, which contain the protein *parvalbumin*, and the *cholecystokinin-positive* (CCK+) basket cells [55], which contain the hormone *cholecystokinin*. The PV+ basket cells are called *fast-firing* because they are capable of sustained high-frequency firing, and are known to play a central role in the generation of gamma frequency (30–80 Hz) oscillations. It is thought that gamma rhythms are important for sensory processing, attention, and working memory. The WB model is patterned after the fast-firing PV+ basket cells.

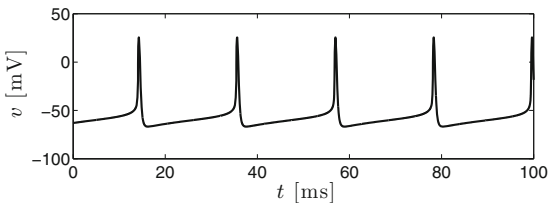


Figure 5.3. Voltage trace of the WB neuron with $I = 0.75 \mu\text{A}/\text{cm}^2$.
[WB_VOLTAGE_TRACE]

For the constants, see Table 5.1. The functions α_x and β_x are

$$\begin{aligned}\alpha_m(v) &= \frac{0.1(v + 35)}{1 - \exp(-(v + 35)/10)}, & \beta_m(v) &= 4 \exp(-(v + 60)/18), \\ \alpha_h(v) &= 0.35 \exp(-(v + 58)/20), & \beta_h(v) &= \frac{5}{1 + \exp(-0.1(v + 28))}, \\ \alpha_n(v) &= \frac{0.05(v + 34)}{1 - \exp(-0.1(v + 34))}, & \beta_n(v) &= 0.625 \exp(-(v + 44)/80).\end{aligned}$$

The blue, dash-dotted curves in Fig. 5.1 show the graphs of x_∞ and τ_x , $x = m, h$, and n . Figure 5.3 shows a voltage trace with $I = 0.75 \mu\text{A}/\text{cm}^2$.

The most striking difference between Figs. 5.2 and 5.3 is that the *spike afterhyperpolarization*, i.e., the hyperpolarization following an action potential, is far less deep in the WB model than in the RTM model. The difference between the lowest value of v and the firing threshold is about 15 mV in Fig. 5.3. This is in agreement with experimental results for fast-firing inhibitory interneurons; see references in [174]. (See, however, also the voltage traces of cortical interneurons and pyramidal cells in Figs. 1C and 1E of [148]. There the spike afterhyperpolarization is significantly *more* pronounced in the interneurons than in the pyramidal cells.)

The spike afterhyperpolarization is less pronounced for the WB model than for the RTM model because the maximal conductance densities \bar{g}_{Na} and \bar{g}_K are smaller. Deeper afterhyperpolarization would be obtained if \bar{g}_{Na} and \bar{g}_K were raised (exercise 5), or h and n made slower (exercise 6). In fact, the Wang-Buzsáki model as stated in [174] included a scaling factor ϕ in front of the formulas for α_h , β_h , α_n , and β_n . Wang and Buzsáki chose $\phi = 5$. This choice is built into the equations as stated above. However, they pointed out that reducing ϕ , which amounts to reducing α_h , β_h , α_n , and β_n , i.e., to slowing down h and n , makes spike afterhyperpolarization more pronounced.

5.3 Erisir Model of an Inhibitory Interneuron in Mouse Cortex

Erisir *et al.* [45] proposed a model of an inhibitory interneuron in mouse somatosensory cortex. With minor modifications discussed in detail in [17], the model takes the same form as the RTM and WB models, except that the potassium conductance is $\bar{g}_K n^2$, not $\bar{g}_K n^4$; the significance of this difference will be discussed at the end of this section. For the constants, see Table 5.1. The functions α_x and β_x are

$$\begin{aligned}\alpha_m(v) &= \frac{40(75.5 - v)}{\exp((75.5 - v)/13.5) - 1}, & \beta_m(v) &= 1.2262 \exp(-v/42.248), \\ \alpha_h(v) &= 0.0035 \exp(-v/24.186), & \beta_h(v) &= \frac{-0.017(v + 51.25)}{\exp(-(v + 51.25)/5.2) - 1}, \\ \alpha_n(v) &= \frac{95 - v}{\exp((95 - v)/11.8) - 1}, & \beta_n(v) &= 0.025 \exp(-v/22.222).\end{aligned}$$

The black, dashed curves in Fig. 5.1 show the graphs of x_∞ and τ_x , $x = m, h$, and n . Figure 5.4 shows a voltage trace with $I = 7 \mu\text{A}/\text{cm}^2$.

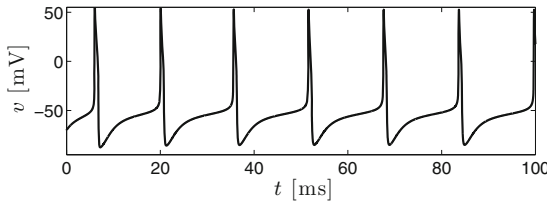


Figure 5.4. Voltage trace of Erisir neuron with $I = 7 \mu\text{A}/\text{cm}^2$.
[ERISIR_VOLTAGE_TRACE]

Note that \bar{g}_{Na} and \bar{g}_K are quite large in the Erisir model, even larger than in the RTM model. As a result, the voltage rises almost to v_{Na} during an action potential, and falls almost to v_K immediately following an action potential. The leak conductance density \bar{g}_L is large as well.

What is the significance of taking the potassium conductance to be $\bar{g}_K n^2$, not $\bar{g}_K n^4$? The main answer is that it does not appear to matter very much; compare Fig. 5.5, where we have used $\bar{g}_K n^4$ instead of $\bar{g}_K n^2$, with Fig. 5.4. In detail, using $\bar{g}_K n^2$ instead of $\bar{g}_K n^4$ has the following effects, which one can see when comparing Figs. 5.4 and 5.5.

1. As n rises to values near 1 during a spike, the potassium conductance responds more rapidly when the exponent is 2, not 4. Therefore the spike termination mechanism becomes faster, and the spikes become narrower.
2. As n falls to values near 0 following a spike, the potassium conductance follows less rapidly when the exponent is 2, not 4. This has the effect that the hyperpolarization following a spike is deeper.
3. Surprisingly, even though the potassium current is hyperpolarizing, and $\bar{g}_K n^2$ is greater than $\bar{g}_K n^4$ for $0 < n < 1$, firing is slightly faster with $\bar{g}_K n^2$ than with $\bar{g}_K n^4$. In essence, this is explained by the fact that the narrower action potentials in Fig. 5.4 allow less time for deep inactivation of the sodium current (Exercise 8).

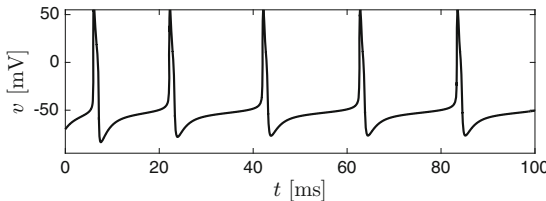


Figure 5.5. Voltage trace of modified Erisir neuron with potassium conductance equal to $\bar{g}_K n^4$ instead of $\bar{g}_K n^2$, $I = 7 \mu\text{A}/\text{cm}^2$. [[ERISIR_VOLTAGE_TRACE_2](#)]

Exercises

- 5.1. (*) Using Matlab, plot

$$\tau_m = \frac{1}{\alpha_m + \beta_m}$$

for the RTM neuron as a function of $v \in [-100, 50]$. You can use the code that generates the red, solid curves in Fig. 5.1 as a starting point.

- 5.2. (*) Using Matlab, plot $h + n$ for a solution of the RTM model equations. You can use the code generating Fig. 5.2 as a starting point. Convince yourself that $h + n$ varies approximately between 0.8 and 1.1.
- 5.3. (*) In the code used to generate Fig. 5.2, make the modification of setting $h = 1 - n$ instead of allowing h to be governed by its own differential equation. (This is motivated by the previous exercise.) Plot the analogue of Fig. 5.2 with this modification.
- 5.4. Exercise 3 shows that one can reproduce behavior that looks like neuronal firing with just two dependent variables: v and n . Explain why an equation with just the single dependent variable v , i.e., an equation of the form $dv/dt = F(v)$, could not model the periodic firing of a neuron.
- 5.5. (*) In the WB model, raise \bar{g}_{Na} to $100 \text{mS}/\text{cm}^2$ and \bar{g}_K to $50 \text{mS}/\text{cm}^2$. Using as a starting point the code that generates Fig. 5.3, plot a voltage trace obtained with the increased values of \bar{g}_{Na} and \bar{g}_K , and compare with Fig. 5.3.
- 5.6. (*) In the WB model, multiply α_h , β_h , α_n , and β_n by 0.2. Using as a starting point the code that generates Fig. 5.3, plot the voltage trace obtained, and compare with Fig. 5.3.
- 5.7. (*) Using as a starting point the codes that generate Figs. 5.2, 5.3, and 5.4, plot the sodium, potassium, and leak current densities as functions of time for the RTM, WB, and Erisir models. To see how large these current densities are, relative to each other, between spikes, use the `axis` command in Matlab to show only the range between $-5 \mu\text{A}/\text{cm}^2$ and $+5 \mu\text{A}/\text{cm}^2$ for the RTM and WB neurons, and the range between $-20 \mu\text{A}/\text{cm}^2$ and $+20 \mu\text{A}/\text{cm}^2$ for the Erisir neuron. In comparison with the leak current, are the sodium and potassium currents significant even between action potentials?

- 5.8. (*) (a) Demonstrate numerically that the sodium current inactivates more deeply when the potassium current in the Erisir neuron is taken to be $\bar{g}_K n^4$ than when it is taken to be $\bar{g}_K n^2$. (This is an effect of the broader spikes — the sodium current has more time to inactivate.) (b) Explain why deeper inactivation of the sodium current could lead to slower firing. (c) Re-compute Fig. 5.5 with $I = 7.4 \mu\text{A}/\text{cm}^2$ to convince yourself that the resulting voltage trace is very close to that of Fig. 5.4.

Chapter 6

The Classical Hodgkin-Huxley PDEs

The model proposed by Hodgkin and Huxley in 1952 is not a set of ODEs, but a set of PDEs — the dependent variables are not only functions of time, but also of space. This dependence will be neglected everywhere in this book, except in the present chapter. You can therefore safely skip this chapter, unless you are curious what the PDE-version of the Hodgkin-Huxley model looks like, and how it arises.

When there is no piece of silver wire threaded through the axon, that is, when there is no space clamp, the membrane potential v , as well as the gating variables m , h , and n , become dependent on the position on the neuronal membrane. It turns out that this adds one ingredient to the mechanism: diffusion of v along the neuronal membrane. In this chapter we explain what this means, and why it is true, for the simplest case, a cylindrical axon.

We consider a cylindrical piece of axon, and denote by “ z ” the coordinate along the axis of the cylinder. We still make a simplification: We allow the dependent variables to depend on z , but not on the angular variable. For symmetry reasons, this is sensible if the axon is a circular cylinder. We will develop a partial differential equation (PDE) describing the time evolution of v .

Suppose that $\Delta z > 0$ is small, and let us focus on the small piece of axon between $z - \Delta z/2$ and $z + \Delta z/2$; see Fig. 6.1. The current entering this piece through the cell membrane is approximately

$$I_m = 2\pi a \Delta z [\bar{g}_{\text{Na}} m(z, t)^3 h(z, t) (v_{\text{Na}} - v(z, t)) + \bar{g}_{\text{K}} n(z, t)^4 (v_{\text{K}} - v(z, t)) + \bar{g}_{\text{L}} (v_{\text{L}} - v(z, t)) + I(z, t)], \quad (6.1)$$

where a denotes the radius of the cylinder, the constants \bar{g}_{Na} , \bar{g}_{K} , and \bar{g}_{L} are conductance densities, and I denotes the applied current density. The factor $2\pi a \Delta z$ is the surface area of the small cylindrical piece. The subscript m in I_m stands for “membrane.”

The voltage difference between locations z and $z - \Delta z$ gives rise to a current. The value of this current at location $z - \Delta z/2$ is assumed to be given by Ohm's law:

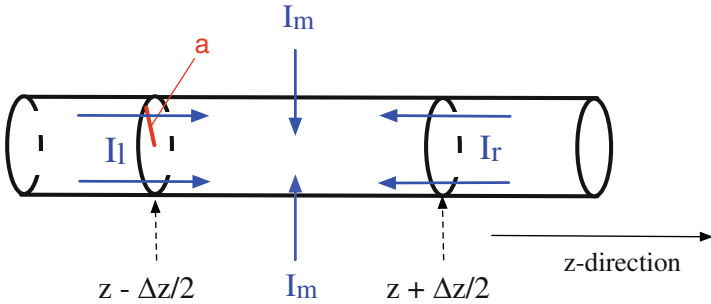


Figure 6.1. A cylindrical piece of axon of radius a with the transmembrane ionic current I_m and the currents entering from the left and the right, I_l and I_r .

law:

$$I_l = \frac{v(z - \Delta z, t) - v(z, t)}{r_i \Delta z}, \quad (6.2)$$

where r_i is the *longitudinal resistance of the cell interior per unit length*. (By convention, a current carried by charge entering the piece of axon between $z - \Delta z/2$ and $z + \Delta z/2$ is positive.) The subscript l stands for “left.” Similarly, the voltage difference between locations z and $z + \Delta z$ gives rise to a current into the piece of axon between $z - \Delta z/2$ and $z + \Delta z/2$ that is approximately equal to

$$I_r = \frac{v(z + \Delta z, t) - v(z, t)}{r_i \Delta z}. \quad (6.3)$$

The equation governing $v(z, t)$ is

$$2\pi a \Delta z C \frac{\partial v}{\partial t}(z, t) = I_m + I_l + I_r, \quad (6.4)$$

where C denotes capacitance density as before. Using eqs. (6.1), (6.2), and (6.3), and dividing (6.4) by $2\pi a \Delta z$, we find:

$$\begin{aligned} C \frac{\partial v}{\partial t}(z, t) &= \frac{1}{2\pi a r_i} \frac{v(z + \Delta z, t) - 2v(z, t) + v(z - \Delta z, t)}{\Delta z^2} + \\ &\quad \bar{g}_{\text{Na}} m(z, t)^3 h(z, t) (v_{\text{Na}} - v(z, t)) + \bar{g}_{\text{K}} n(z, t)^4 (v_{\text{K}} - v(z, t)) + \\ &\quad \bar{g}_{\text{L}} (v_{\text{L}} - v(z, t)) + I(z, t). \end{aligned} \quad (6.5)$$

We pass to the limit as $\Delta z \rightarrow 0$, and find, omitting the arguments z and t , and indicating partial derivatives with subscripts (see exercise 1):

$$C v_t = \frac{1}{2\pi a r_i} v_{zz} + \bar{g}_{\text{Na}} m^3 h (v_{\text{Na}} - v) + \bar{g}_{\text{K}} n^4 (v_{\text{K}} - v) + \bar{g}_{\text{L}} (v_{\text{L}} - v) + I. \quad (6.6)$$

The resistance of the cell interior per unit length, r_i , is usually assumed to be inversely proportional to the cross-sectional area of the axon [88, eq. (8.5)]:

$$r_i = \frac{R_i}{\pi a^2}, \quad (6.7)$$

where R_i is called the *resistivity* of the cell interior, independent of a . Using this relation in (6.6), we obtain the equation as written by Hodgkin and Huxley [76]:

$$Cv_t = \frac{a}{2R_i} v_{zz} + \bar{g}_{\text{Na}} m^3 h (v_{\text{Na}} - v) + \bar{g}_{\text{K}} n^4 (v_{\text{K}} - v) + \bar{g}_{\text{L}} (v_{\text{L}} - v) + I. \quad (6.8)$$

Even though the gating variables now depend on z , (3.9) remains unchanged.

Equation (6.8) is related to diffusion. To explain the connection, imagine a long thin rod filled with a water-ink mixture. The ink diffuses in the water. Let $\rho = \rho(z, t)$ denote the ink concentration (amount of ink per unit length) at position z at time t . It can then be shown that

$$\rho_t = \epsilon \rho_{zz}, \quad (6.9)$$

for some number $\epsilon > 0$; see exercise 2. Thus (6.8) can be stated as follows. The membrane potential obeys the Hodgkin-Huxley equations, but diffuses in space at the same time. The *diffusion coefficient*, $a/(2R)$, is a conductance (not a conductance density); see exercise 3. Hodgkin and Huxley measured $a = 0.0238$ cm, and $R = 35.4 \Omega \text{cm}$ (Ω stands for ohm, the unit of resistance, $\Omega = \text{V/A} = 1/\text{S}$), implying $a/(2R) \approx 0.34 \text{ mS}$.

To solve eqs. (6.8) and (3.9) numerically, one *discretizes* the z -axis, i.e., one computes the functions v , m , h , and n at a finite number of points z only, in effect returning to (6.5). Time can be s, for example, using the midpoint method described in Chapter 4. We omit the details here.

The model predicts the existence of sharp voltage *pulses* traveling along the axon. Qualitatively, the mechanism is as follows. When the voltage v is raised in one location, it *diffuses* into neighboring locations because of the diffusion term $(a/(2R))v_{zz}$ on the right-hand side of (6.8). This triggers the spike-generating mechanism — sodium channels opening up — in those neighboring locations, while the spike is ended in the original location by the opening of the potassium channels and the closing of the sodium channels. Thus the pulse travels. However, this discussion does not explain why the pulse typically travels uni-directionally. Action potentials typically originate in the axon near the cell body. Because the cell body is much larger in diameter than the axon, back-propagation into the cell body is more difficult than propagation away from it. Once uni-directional pulse propagation begins, it is easy to understand how it can be maintained: The tissue in the wake of the pulse is refractory; this is why the diffusion of v , which has no directional preference, causes the pulse to propagate forward, but not backward.

The modeling presented in this chapter, due to Hodgkin and Huxley, does not address all questions concerning the spatial propagation of action potentials in nerve cells. Real nerve cells may have approximately cylindrical pieces, but they are not overall of cylindrical shape. They are very complicated geometric objects.

A careful discussion of how to handle the complications arising from the geometry of nerve cells would go very far beyond the scope of this book. However, the principle discovered by Hodgkin and Huxley is correct even for nerve cells with realistic geometry: When the membrane potential is high at one location, it raises the membrane potential in neighboring locations via diffusion. This triggers the spike-generating mechanism based on sodium and potassium currents in the neighboring locations. Action potentials are traveling pulses generated in this way.

Often neurons of complicated shape are modeled as composed of cylindrical and spherical pieces, coupled by gap junctions, with each of the pieces satisfying a system of Hodgkin-Huxley-like ODEs. Models of this kind are called *multi-compartment models*. In this book, however, we will use single-compartment models only. That is, we will pretend that all neurons are space-clamped. This simplifying assumption is made frequently in mathematical neuroscience.

Axons are leaky cables immersed in salty water, a subject that was of interest to people even before the days of Hodgkin and Huxley. On August 15, 1858, a message was sent from Europe to North America through a transatlantic cable for the first time in history. The cable connected Valentia Harbor in Ireland with Trinity Bay in Newfoundland. It held up for only three weeks — but many new and improved transatlantic cables followed during the second half of the 19th century. In the early 1850s, the transatlantic cable project motivated the great Scottish physicist William Thomson, nowadays known as Lord Kelvin, to study the physics of leaky cables immersed in water. He showed that the voltage would diffuse along the length of the cable; thus he derived the term proportional to v_{zz} that appears in the Hodgkin–Huxley PDE.

Exercises

- 6.1. In deriving (6.8), we used that

$$\lim_{\Delta z \rightarrow 0} \frac{v(z + \Delta z, t) - 2v(z, t) + v(z - \Delta z, t)}{\Delta z^2} = \frac{\partial^2 v}{\partial z^2}(z, t) = v_{zz}(z, t).$$

Explain why this is true using l'Hospital's rule or, better, Taylor's theorem.

- 6.2. Here is a sketch of the derivation of (6.9). Fill in the details by answering the questions. Consider an interval $[a, b]$ along the z -axis, and assume that ink enters $[a, b]$ through the right boundary ($z = b$) at a rate proportional to $\rho_z(b, t)$. Denote the constant of proportionality by ϵ . So the rate at which ink enters $[a, b]$ through the right boundary is $\epsilon \rho_z(b, t)$.

(a) Explain why you would expect ϵ to be positive.

Assume also that ink enters $[a, b]$ through the left boundary ($z = a$) at rate $-\epsilon \rho_z(a, t)$.

(b) Explain what motivates the minus sign.

The total amount of ink in $[a, b]$ then changes at the rate

$$\frac{d}{dt} \int_a^b \rho(z, t) dz = \epsilon (\rho_z(b, t) - \rho_z(a, t))$$

(c) Explain why the above equation is equivalent to

$$\int_a^b (\rho_t - \epsilon \rho_{zz}) dz = 0. \quad (6.10)$$

(d) Explain: If we assume that $\rho_t - \epsilon \rho_{zz}$ is a continuous function of z , and if (6.10) holds for all intervals $[a, b]$, then (6.9) must hold.

- 6.3. (a) What is the physical dimension of r_i ? (b) What is the physical dimension of R_i ? (c) What is the physical dimension of ϵ in eq. (6.9)?
- 6.4. (†) Suppose that the axon is a circular cylinder of variable radius $a = a(z) > 0$. What do the Hodgkin-Huxley PDEs become in that case? To find out, rethink the derivation given in this chapter.

Chapter 7

Linear Integrate-and-Fire (LIF) Neurons

Nearly half a century before Hodgkin and Huxley, in 1907, Louis Édouard Lapicque proposed a mathematical model of nerve cells. Lapicque died in 1952, the year when the famous series of papers by Hodgkin and Huxley appeared in print. Lapicque's model is nowadays known as the integrate-and-fire neuron. We will refer to it as the LIF neuron. Most authors take the L in "LIF" to stand for "leaky," for reasons that will become clear shortly. We take it to stand for "linear," to distinguish it from the quadratic integrate-and-fire (QIF) neuron discussed in Chapter 8. The LIF neuron is useful because of its utter mathematical simplicity. It can lead to insight, but as we will demonstrate with examples in later chapters, reduced models such as the LIF neuron are also dangerous — they can lead to incorrect conclusions.

The LIF model can be described as follows. We assume that the ionic conductances are constant as long as the neuron does not fire, and that a spike is triggered if the membrane potential rises to a certain *threshold voltage*. We don't model the process of spike generation at all. Of course, in a *network* of LIF neurons, we would model the *effects* of neuronal firing on other neurons, but we won't discuss this topic here; see part III. As long as no spike is triggered, the equation governing the membrane potential v is assumed to be

$$C \frac{dv}{dt} = g_{\text{Na}}(v_{\text{Na}} - v) + g_{\text{K}}(v_{\text{K}} - v) + g_{\text{L}}(v_{\text{L}} - v) + I, \quad (7.1)$$

where g_{Na} , g_{K} , and g_{L} are constant (not to be confused with the quantities \bar{g}_{Na} , \bar{g}_{K} , and \bar{g}_{L} of earlier sections). Equation (7.1) can be written in the form

$$\frac{dv}{dt} = \frac{v_{\text{eq}} - v}{\tau_m} + \frac{I}{C}, \quad (7.2)$$

Electronic supplementary material: The online version of this chapter (doi: [10.1007/978-3-319-51171-9_7](https://doi.org/10.1007/978-3-319-51171-9_7)) contains supplementary material, which is available to authorized users.

where

$$\tau_m = \frac{C}{g_{\text{Na}} + g_{\text{K}} + g_{\text{L}}}$$

and

$$v_{\text{eq}} = \frac{g_{\text{Na}}v_{\text{Na}} + g_{\text{K}}v_{\text{K}} + g_{\text{L}}v_{\text{L}}}{g_{\text{Na}} + g_{\text{K}} + g_{\text{L}}}.$$

Here the subscript m in τ_m stands for “membrane” — τ_m is called the *membrane time constant*.

Equation (7.2) is supplemented by a condition of the form

$$v(t+0) = v_{\text{res}} \quad \text{if} \quad v(t-0) = v_{\text{thr}}, \quad (7.3)$$

where v_{thr} is called the *threshold voltage*, and $v_{\text{res}} < v_{\text{thr}}$ the *reset voltage*. Here “ $v(t-0)$ ” denotes the *left-sided limit* of v at t , and “ $v(t+0)$ ” denotes the *right-sided limit*. The assumption underlying (7.3) is that a very rapid voltage spike occurs when v reaches v_{thr} , and v then “resets” to a low value.

Equations (7.2) and (7.3), taken together, define the LIF model. One calls the LIF neuron *leaky* if $\tau_m < \infty$ (that is, $g_{\text{Na}} + g_{\text{K}} + g_{\text{L}} > 0$), and *non-leaky* if $\tau_m = \infty$ (that is, $g_{\text{Na}} + g_{\text{K}} + g_{\text{L}} = 0$).⁸ More generally, not only for the LIF model, the word *leakiness* refers to the density of open ion channels, and the reciprocal of the sum of all ion channel densities, multiplied by the capacitance density C , is the *membrane time constant* τ_m . In Hodgkin-Huxley-like models, the membrane time constant is C divided by the sum of all terms multiplying v on the right-hand side of the equation governing v .

Figure 7.1 shows a solution of (7.2) and (7.3) (blue), with a solution of the classical Hodgkin-Huxley equations superimposed (black). The non-leaky integrate-

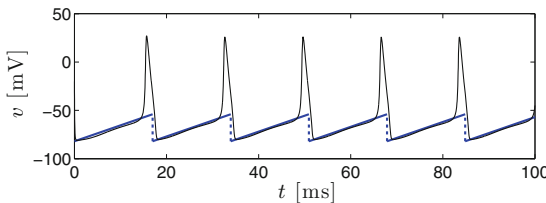


Figure 7.1. Classical Hodgkin-Huxley neuron with $I = 7$ (black), approximated by a non-leaky LIF neuron with $v_{\text{res}} = -82$, $v_{\text{thr}} = -54$, and $I = 1.65$ (blue). [\[LIF_NEURON_WITH_HH\]](#)

and-fire neuron appears to yield a good approximation of the voltage trace of the classical Hodgkin-Huxley neuron here. This might suggest that the classical Hodgkin-Huxley neuron is close to non-leaky below the threshold voltage. However, that is far from true, as demonstrated by Fig. 7.2, which shows

$$\tau_m = \frac{C}{\bar{g}_{\text{Na}}m^3h + \bar{g}_{\text{K}}n^4 + \bar{g}_{\text{L}}},$$

⁸As discussed earlier, we take the L in LIF to mean “linear,” not “leaky.” Therefore in our terminology, a LIF neuron keeps its L even when it isn’t leaky.

as a function of time: The membrane time constant is in fact very small, below 1 ms, along the entire limit cycle! The classical Hodgkin-Huxley has nearly linear voltage traces below threshold not because the sodium, potassium, and leak currents are small below threshold, but because their sum happens to be close to constant between spikes; see Fig. 7.3. Note that when the sum of the ion currents is approximately constant, dv/dt is approximately constant, and therefore v is approximately a linear function of t .

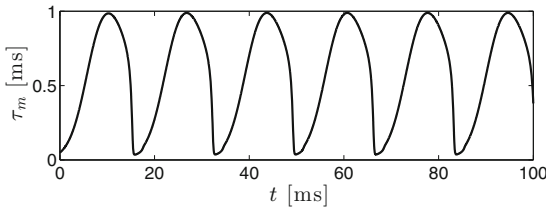


Figure 7.2. Membrane time constant, as a function of time, for the solution of the classical Hodgkin-Huxley neuron shown in Fig. 7.1. [TAU_M_FOR_HH]

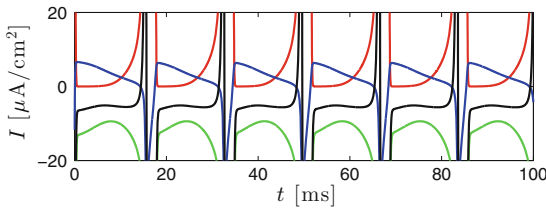


Figure 7.3. Sodium current (red), potassium current (green), leak current (blue), and their sum (black) for the solution of the classical Hodgkin-Huxley neuron shown in Fig. 7.1. [SUBTHR_FOR_HH]

To reduce the number of parameters in the LIF model, we shift and scale the voltage:

$$\tilde{v} = \frac{v - v_{\text{res}}}{v_{\text{thr}} - v_{\text{res}}}. \quad (7.4)$$

Equation (7.2) then becomes (after two lines of straightforward calculation, see exercise 1)

$$\frac{d\tilde{v}}{dt} = -\frac{\tilde{v}}{\tau_m} + \tilde{I}_{\text{ext}}, \quad \text{with} \quad \tilde{I}_{\text{ext}} = \frac{v_{\text{eq}} - v_{\text{res}}}{\tau_m(v_{\text{thr}} - v_{\text{res}})} + \frac{I}{C(v_{\text{thr}} - v_{\text{res}})}. \quad (7.5)$$

The reset potential is now $\tilde{v}_{\text{res}} = 0$, and the threshold voltage is $\tilde{v}_{\text{thr}} = 1$. In summary, we have found that the LIF model can be transformed, simply by shifting and scaling the membrane potential, into

$$\frac{dv}{dt} = -\frac{v}{\tau_m} + I, \quad (7.6)$$

$$v(t+0) = 0 \quad \text{if } v(t-0) = 1. \quad (7.7)$$

(We have now dropped the tildes in the notation, and the subscript “ext” in I .) Notice that the time has not been scaled — τ_m is the same membrane time constant, measured in milliseconds, as before. The new I (that is, \tilde{I}_{ext} as defined in (7.5)) is a reciprocal time.

When discussing Hodgkin-Huxley-like models, we usually specify units of physical quantities. In the context of the normalized LIF model (7.6), (7.7), as well as similar models discussed in future chapters, it often seems overly pedantic to insist on specifying times in ms, I in ms^{-1} , and so on. We will therefore usually drop units when discussing the normalized LIF model and similar future models, but keep in mind that t and τ_m are times (measured in ms), and therefore I has to be reciprocal time (measured in ms^{-1}).

If $v(t)$ satisfies (7.6) and $v(0) = 0$, then (see exercise 2)

$$v(t) = \left(1 - e^{-t/\tau_m}\right) \tau_m I. \quad (7.8)$$

$v(t)$ eventually reaches the threshold voltage 1 if and only if $\tau_m I > 1$, i.e., $I > 1/\tau_m$. We therefore call $1/\tau_m$ the *threshold drive*. Figure 7.4 shows an example of a voltage trace with $I > 1/\tau_m$.

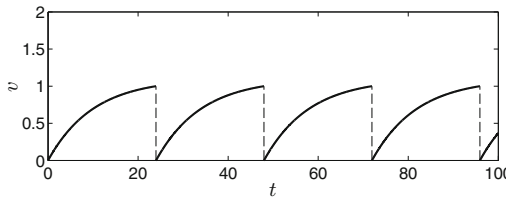


Figure 7.4. Voltage trace of a normalized LIF neuron with $\tau_m = 10$ and $I = 0.11$. [LIF_VOLTAGE_TRACE]

If $I > 1/\tau_m$, the time it takes for $v(t)$ to reach 1 equals

$$T = \tau_m \ln \frac{\tau_m I}{\tau_m I - 1}. \quad (7.9)$$

The frequency is the reciprocal of the period T . We always assume that time is measured in ms. Therefore $1/T$ is the number of spikes per ms. However, while milliseconds are a natural unit of time in neuroscience, the customary and natural unit of frequency is not the reciprocal millisecond, but the reciprocal second, namely the hertz (Hz). If f denotes the frequency of the LIF neuron in Hz, the relation between f and T (the period in ms) is

$$f = \frac{1000}{T}. \quad (7.10)$$

Figure 7.5 shows the voltage trace of a LIF neuron with $\tau_m = 2$, firing at 50 Hz. The figure shows that during a large fraction of the period, v is very close

to the threshold voltage, 1. As a result, the LIF neuron will be highly sensitive to noisily fluctuating input: While v is nearly at threshold, any small input fluctuation can cause a spike. In exercise 4, you will be asked to show that this is

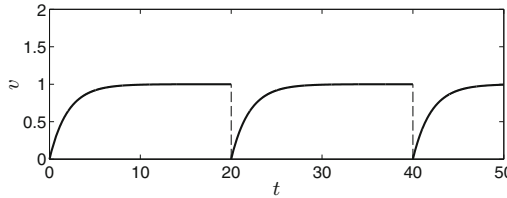


Figure 7.5. Voltage trace of a normalized LIF neuron with $\tau_m = 2$, I chosen so that the frequency becomes 50 Hz. [LIF_VOLTAGE_TRACE_2]

true whenever $T/\tau_m \gg 1$. When using the LIF model, τ_m should therefore not be chosen much smaller than the largest period T we are interested in to avoid excessive noise-sensitivity. Since the most typical firing periods are on the order of tens of milliseconds, τ_m should certainly not be much smaller than 10 ms.

One could argue that this reflects a flaw of the LIF model: Hodgkin-Huxley-like model neurons often do have very small membrane time constants (see Fig. 7.2 and exercise 5), yet they are not extremely sensitive to noisy input.

In the LIF model, the subthreshold dynamics of a neuron are replaced by one-dimensional linear dynamics. The LIF neuron is therefore not a good model of neurons with more complex subthreshold dynamics. For example, subthreshold voltage traces often have inflection points; see, for instance, Figs. 5.2 and 5.4. A one-dimensional linear equation describing subthreshold dynamics cannot reproduce this feature. However, inflection points can be obtained by making the subthreshold dynamics *quadratic*; this is the main topic of Chapter 8.

To reproduce subthreshold *oscillations*, or more generally, non-monotonic subthreshold voltage traces, a one-dimensional model of subthreshold dynamics is not sufficient; compare exercise 5.4. The model of [80] has in common with the LIF neuron that the subthreshold dynamics are linear, and there is a discontinuous reset as soon as v reaches a threshold, but the subthreshold dynamics are two-dimensional. The dependent variables are the membrane potential v , and an additional “recovery variable” which we will call u , representing, for instance, voltage-gated currents. When v reaches the threshold, both v and u may in general be reset; in [80, Fig. 5], in fact only u is reset. With two-dimensional subthreshold dynamics, non-monotonic voltage traces — oscillations, overshoots, undershoots, etc. — become possible.

In the Izhikevich neuron [81], the subthreshold dynamics are two-dimensional as well, with the same dependent variables v and u , but the evolution equation for v is *quadratic in v* . By this we mean that the term v^2 appears on the right-hand side of the evolution equation for v ; all other terms are linear in u and v . Characteristics of many different types of neurons can be reproduced with different model parameters;

see [81, Fig. 2]. For a detailed study of the link between Hodgkin-Huxley-like models and reduced two-dimensional models of subthreshold dynamics that are quadratic in v , see [131].

Exercises

- 7.1. Verify (7.5).
- 7.2. Assume that $v(0) = 0$ and $v(t)$ satisfies (7.6). Show:
 - (a) $v(t) = (1 - e^{-t/\tau_m}) \tau_m I$.
 - (b) $v(t)$ eventually reaches 1 if and only if $\tau_m I > 1$.
 - (c) If $\tau_m I > 1$, then the time it takes for $v(t)$ to reach 1 equals

$$T = \tau_m \ln \frac{\tau_m I}{\tau_m I - 1}.$$

- 7.3. Let T be the period of the LIF neuron, as given in exercise 2(c). Show that

$$T \sim \frac{1}{I}$$

as $I \rightarrow \infty$. (See Section 1.2 for the meaning of “~”.) Thus the membrane time constant τ_m becomes irrelevant for very large I .

- 7.4. Assume that $v(0) = 0$ and $v(t)$ satisfies (7.6). Let $v(\tilde{T}) = 0.95$ and $v(T) = 1$. Compute a formula for $(T - \tilde{T})/T$, the fraction of the period of the LIF neuron during which v exceeds 0.95. Your formula should reveal that $(T - \tilde{T})/T$ is a function of T/τ_m only. Plot it as a function of T/τ_m , and discuss what the plot tells you.
- 7.5. (*) Using as a starting point the codes generating Figs. 5.2, 5.3, and 5.4, plot

$$\tau_m = \frac{C}{\bar{g}_{\text{Na}} m^3 h + \bar{g}_{\text{K}} n^4 + \bar{g}_{\text{L}}}$$

as a function of t for the RTM, WB, and Erisir models.

Chapter 8

Quadratic Integrate-and-Fire (QIF) and Theta Neurons

As noted at the end of the preceding chapter, subthreshold voltage traces of neurons often have an inflection point; see, for instance, Figs. 5.2 and 5.4. Voltage traces of the LIF neuron (Fig. 7.4) don't have this feature. However, we can modify the LIF neuron to introduce an inflection point, as follows:

$$\frac{dv}{dt} = -\frac{v(1-v)}{\tau_m} + I \quad \text{for } v < 1, \quad (8.1)$$

$$v(t+0) = 0 \quad \text{if } v(t-0) = 1. \quad (8.2)$$

This is called the (normalized) *quadratic integrate-and-fire (QIF) model*. As in eqs. (7.6) and (7.7), v is a non-dimensionalized membrane potential, obtained from the actual membrane potential by shifting and scaling in such a way that $0 \leq v \leq 1$, whereas t and τ_m have the physical dimension of time, and I is a reciprocal time. The right-hand side of (8.1) is positive for all v if and only if $I > 1/(4\tau_m)$ (see exercise 1). Thus $1/(4\tau_m)$ is the *threshold drive* here. Figure 8.1 shows a voltage trace of a QIF neuron.

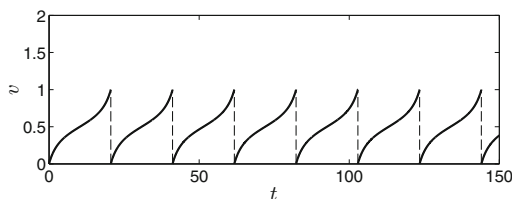


Figure 8.1. Voltage trace of a QIF neuron. [QIF_VOLTAGE_TRACE]

Electronic supplementary material: The online version of this chapter (doi: [10.1007/978-3-319-51171-9_8](https://doi.org/10.1007/978-3-319-51171-9_8)) contains supplementary material, which is available to authorized users.

Equation (8.1) can be solved explicitly using separation of variables. If

$$I > \frac{1}{4\tau_m} \quad (8.3)$$

and $v(0) = v_0$, then

$$v(t) = \frac{1}{2} + \sqrt{\tau_m I - \frac{1}{4}} \tan \left(\frac{\sqrt{\tau_m I - 1/4}}{\tau_m} t + \arctan \frac{v_0 - 1/2}{\sqrt{\tau_m I - 1/4}} \right) \quad (8.4)$$

(exercise 2). Although only values of v between 0 and 1 are relevant for the QIF model, we note that (8.4) is the solution of (8.1) with $v(0) = v_0$ for any v_0 between $-\infty$ and $+\infty$. Equation (8.4) implies that

$$\lim_{t \rightarrow t_-} v(t) = -\infty \quad \text{and} \quad \lim_{t \rightarrow t_+} v(t) = \infty,$$

with

$$t_{\pm} = \frac{\tau_m}{\sqrt{\tau_m I - 1/4}} \left(\pm \frac{\pi}{2} - \arctan \frac{v_0 - 1/2}{\sqrt{\tau_m I - 1/4}} \right). \quad (8.5)$$

Taking advantage of this observation, we modify the reset condition (8.2) by moving the threshold voltage to $+\infty$, and the reset voltage to $-\infty$:

$$v(t+0) = -\infty \quad \text{if} \quad v(t-0) = \infty. \quad (8.6)$$

There is no biological reason for doing this, but the modification leads to a more attractive mathematical model, as will be seen shortly. Figure 8.2 shows a voltage trace with the reset condition (8.6).

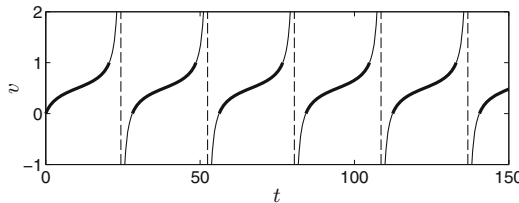


Figure 8.2. Voltage trace of a QIF neuron with threshold at $+\infty$ and reset at $-\infty$. The portion of the voltage trace with $0 \leq v \leq 1$ is bold.

[QIF_INFINITE_THRESHOLD]

We change coordinates now:

$$v = \frac{1}{2} + \frac{1}{2} \tan \frac{\theta}{2}. \quad (8.7)$$

Note that $\theta = 0$ corresponds to $v = 1/2$ (the value that minimizes dv/dt), and $\theta = \pm\pi$ correspond to $v = \pm\infty$. Inserting (8.7) into (8.1), we find

$$\frac{1}{4 \cos^2 \frac{\theta}{2}} \frac{d\theta}{dt} = -\frac{1}{4\tau_m} \left(1 - \tan^2 \frac{\theta}{2} \right) + I$$

$$\begin{aligned} \Leftrightarrow \quad & \frac{d\theta}{dt} = -\frac{1}{\tau_m} \left(\cos^2 \frac{\theta}{2} - \sin^2 \frac{\theta}{2} \right) + 4I \cos^2 \frac{\theta}{2} \\ \Leftrightarrow \quad & \frac{d\theta}{dt} = -\frac{\cos \theta}{\tau_m} + 2I(1 + \cos \theta). \end{aligned} \quad (8.8)$$

The reset condition (8.6) becomes

$$\theta(t+0) = -\pi \quad \text{if} \quad \theta(t-0) = \pi. \quad (8.9)$$

Eqs. (8.8) and (8.9) define a model called the *theta neuron*. It was first proposed by Ermentrout and Kopell [49], who used, in our notation, $\tau_m = 1/2$; see exercise 3. Notice that the reset (8.9) plays no role for subsequent calculations, since the right-hand side of (8.8) is periodic with period 2π ; it can therefore be omitted without consequence. Thus our model is now a differential equation, without any discontinuous reset.

Equation (8.8) can be viewed as an equation describing the motion of the point $(\cos \theta, \sin \theta)$ on the unit circle. If $I > 1/(4\tau_m)$, the right-hand side of (8.8) is positive for all θ , and the point therefore moves around the circle indefinitely in the counter-clockwise direction. However, if $I < 1/(4\tau_m)$, the right-hand side of (8.8) is zero at

$$\theta_{\pm} = \pm \arccos \frac{2I\tau_m}{1 - 2I\tau_m}. \quad (8.10)$$

Note that $0 < \theta_+ < \pi$ and $-\pi < \theta_- < 0$. Since the right-hand side of (8.8) is zero at θ_+ and θ_- , these are *fixed points* of (8.8): If $\theta(t_0) = \theta_{\pm}$ for some t_0 , then $\theta(t) = \theta_{\pm}$ for all t . For $\theta_- < \theta < \theta_+$, the right-hand side of (8.8) is negative, and therefore the motion of the point is clockwise. Figure 8.3 illustrates the motion on the unit circle.

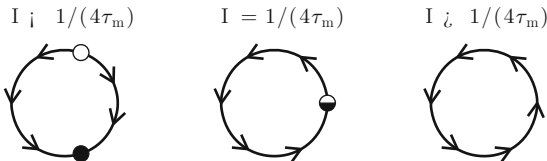


Figure 8.3. Motion on the unit circle described by (8.8). [[THREE_CIRCLES](#)]

We call the points $(\cos \theta_-, \sin \theta_-)$ and $(\cos \theta_+, \sin \theta_+)$ the fixed points of the flow on the circle. The fixed point $(\cos \theta_-, \sin \theta_-)$ is *stable*: If the moving point starts out near it, it approaches it. The fixed point $(\cos \theta_+, \sin \theta_+)$ is *unstable*: If the moving point starts out near it, it moves away from it. In the left-most panel of Fig. 8.3, the stable fixed point is indicated by a solid circle, and the unstable one by an open circle. As I approaches $1/(4\tau_m)$ from below, the two fixed points approach each other. They coalesce when $I = 1/(4\tau_m)$. The flow on the circle then has only one fixed point, at $(1, 0)$, and this fixed point is *semi-stable*: The moving point is attracted to it on one side, but repelled from it on the other side. We indicate

the semi-stable fixed point by a circle that is half-solid and half-open in the middle panel of Fig. 8.3.

To illustrate from a slightly different point of view that the theta model describes “periodic firing,” we show in Fig. 8.4 the quantity $1 - \cos \theta$ as a function of time. (This quantity has no biological interpretation, but it has narrow “spikes,” reaching its maxima when $\theta = \pi$ modulo 2π .)

The firing period is the time that it takes for v , given by (8.4), to move from $-\infty$ to $+\infty$. Equation (8.5) implies that this time is

$$T = \frac{\pi \tau_m}{\sqrt{\tau_m I - 1/4}}. \quad (8.11)$$

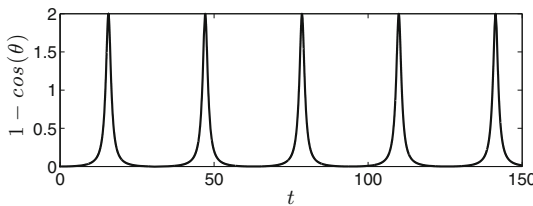


Figure 8.4. The “periodic firing” of a theta neuron, with $\tau_m = 1/2$ and $I = 0.505$. [THETA_FIRING]

Exercises

- 8.1. Prove that the right-hand side of (8.1) is positive for $0 \leq v \leq 1$ if and only if $I > 1/(4\tau_m)$.
- 8.2. Derive (8.4).
- 8.3. Show that (8.8) with $\tau_m = 1/2$ is equivalent to

$$\frac{d\theta}{dt} = 1 - \cos \theta + J(1 + \cos \theta),$$

where $J = 2I - 1$. This is the form in which Ermentrout and Kopell stated the theta model in [49].

- 8.4. (*) Using as a starting point the code that generates Fig. 8.1, plot the voltage trace of the normalized QIF neuron with $\tau_m = 1/2$, adjusting I by trial and error in such a way that the frequency becomes 20 Hz. Based on your plot, would you think that the noise-sensitivity of the normalized QIF neuron for small τ_m is as great as that of the normalized LIF neuron? (See the discussion at the end of Chapter 7.)
- 8.5. This exercise continues the theme of exercise 4. For the LIF neuron, the period is given by the formula

$$T = \tau_m \ln \frac{\tau_m I}{\tau_m I - 1}.$$

For the theta neuron,

$$T = \frac{2\pi\tau_m}{\sqrt{4\tau_m I - 1}}.$$

Instead of thinking about noise-sensitivity, as we did (in a rather non-rigorous way) at the end of Chapter 7 and in exercise 4, we now ask how sensitively T depends on I . A natural quantity to consider is the *condition number*

$$\kappa = \left| \frac{dT}{dI} \frac{I}{T} \right|.$$

To see why κ measures how sensitively T depends on I , write the definition of κ like this:

$$\kappa = \frac{|dT/T|}{|dI/I|}.$$

When I is perturbed by a small amount dI , the resulting perturbation of T is dT . The *relative* perturbations in I and T are dI/I and dT/T , respectively, and κ is the ratio of the absolute values of those relative perturbations. If $\kappa = 5$, one should expect a 1% change in I to cause a 5% change in T . Show that for the LIF neuron,

$$\kappa = \frac{e^{T/\tau_m} - 1}{T/\tau_m},$$

and for the theta neuron,

$$\kappa = \frac{1}{2} + \frac{(T/\tau_m)^2}{8\pi^2}.$$

Thus the sensitivity of T to perturbations in I becomes infinite as $T/\tau_m \rightarrow \infty$ in both cases, but it does so exponentially for the LIF neuron, and only quadratically for the theta neuron.

Chapter 9

Spike Frequency Adaptation

Many neurons, in particular the excitatory pyramidal cells, have *spike frequency adaptation currents*. These are hyperpolarizing currents, activated when the membrane potential is high, and de-activated, typically slowly, when the membrane potential is low. As a consequence, many neurons cannot sustain rapid firing over a long time; spike frequency adaptation currents act as “brakes,” preventing hyperactivity. In this chapter, we discuss two kinds of adaptation currents, called *M-currents* (Section 9.1) and *calcium-dependent afterhyperpolarization (AHP) currents* (Section 9.2). Both kinds are found in many neurons in the brain. They have different properties. In particular, M-currents are active even before the neuron fires, while calcium-dependent AHP currents are firing-activated. As a result, the two kinds of currents affect the dynamics of neurons and neuronal network in different ways; see, for instance, exercises 17.3 and 17.4.

Adaptation currents often make the inter-spike interval increase (at least approximately) monotonically; see Fig. 9.1 for an example. However, it is not clear that the increase in the inter-spike interval *must* be monotonic. One might think that a longer inter-spike interval would give the adaptation current more time to decay substantially, and might therefore be followed by a shorter inter-spike interval, which would give the adaptation less time to decay and therefore be followed by a longer inter-spike interval again, etc. In Section 9.3, we show that in a simple model problem, this sort of oscillatory behavior of the inter-spike interval is not possible.

Electronic supplementary material: The online version of this chapter (doi: [10.1007/978-3-319-51171-9_9](https://doi.org/10.1007/978-3-319-51171-9_9)) contains supplementary material, which is available to authorized users.

9.1 A Model M-Current

M-currents [19] are depolarization-activated, slowly decaying, hyperpolarizing potassium currents. The name comes from the fact that they are down-regulated by activation of the *muscarinic acetylcholine receptors* (the M stands for muscarinic). Acetylcholine is a neurotransmitter that plays many important roles in the brain, and is, for instance, known to be crucial for mechanisms underlying attention. The down-regulation of an M-current through activation of the muscarinic acetylcholine

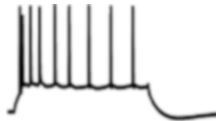


Figure 9.1. Voltage trace of a pyramidal cell in rat basolateral amygdala, from Fig. 3B of [127], reproduced with publisher's permission.

receptors may be one mechanism underlying this connection.

Crook *et al.* [31] proposed a model M-current which, in a slightly modified form due to Olufsen *et al.* [122], is given by

$$I_M = \bar{g}_M w(v_K - v) \quad (9.1)$$

with

$$\frac{dw}{dt} = \frac{w_\infty(v) - w}{\tau_w(v)}, \quad (9.2)$$

$$w_\infty(v) = \frac{1}{1 + \exp(-(v + 35)/10)}, \quad (9.3)$$

$$\tau_w(v) = \frac{400}{3.3 \exp((v + 35)/20) + \exp(-(v + 35)/20)}. \quad (9.4)$$

(One should think of I_M as a current *density*, not a current.) Figure 9.2 shows the graphs of w_∞ and τ_w . We add this model M-current to the right-hand side of the equation for v in the RTM model. Thus this equation now takes the form

$$C \frac{dv}{dt} = \bar{g}_{Na} m_\infty(v)^3 h(v_{Na} - v) + \bar{g}_K n^4 (v_K - v) + \bar{g}_L (v_L - v) + \bar{g}_M w(v_K - v) + I,$$

where everything other than the term $\bar{g}_M w(v_K - v)$ is as in Section 5.1. Figure 9.3 illustrates the resulting spike frequency adaptation, i.e., deceleration of firing.

The model M-current of Crook *et al.* does not only oppose prolonged rapid firing; it hyperpolarizes even at rest. To demonstrate this, we repeat the simulation of Fig. 9.3, but set I to zero, which has the effect that the neuron simply rests. The result is shown in Fig. 9.4. The M-current is not zero at rest. In fact, in the simulation of Fig. 9.4, the steady state value of w is 0.031, and therefore the steady state value of the conductance density of the M-current is $0.031 \bar{g}_M \approx 0.0078 \text{ mS/cm}^2$. Thus at rest, the M-current, as modeled here, gives rise to a weak but significant *tonic* (constant) potassium current. This is indeed biologically realistic [114].

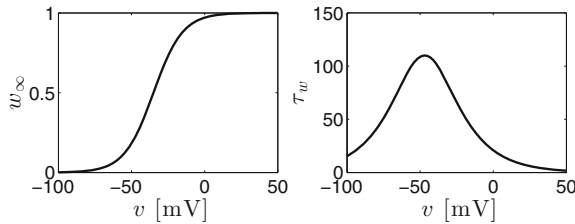


Figure 9.2. The functions w_∞ and τ_w in the definition of the model M-current. [M_CURRENT]

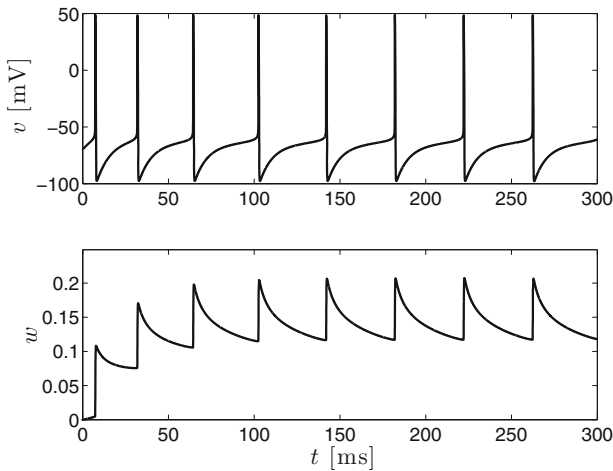


Figure 9.3. Buildup of the M-current decelerates firing of the RTM neuron. In this simulation, $\bar{g}_M = 0.25 \text{ mS/cm}^2$, and $I = 1.5 \mu\text{A/cm}^2$. [RTM_M]

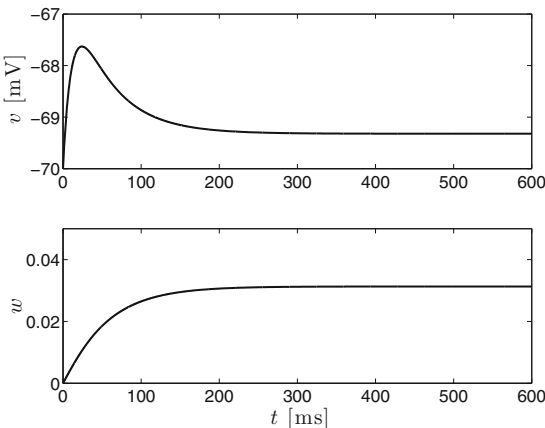


Figure 9.4. Same as Fig. 9.3, but with $I = 0$. The M-current gives rise to a weak but significant constant potassium conductance at rest. [RTM_M_RESTING]

9.2 Calcium-Dependent AHP Currents

Calcium-dependent AHP currents [2] are activated by the influx of calcium that results from firing. Unlike the M-current, they are therefore strictly *spiking*-activated, not more generally *depolarization*-activated. We will use a model of a calcium-dependent AHP current essentially due to Ermentrout [46]. We make two very minor modifications of Ermentrout's model; see exercise 4. Our model is defined as follows.

$$I_{\text{AHP}} = \bar{g}_{\text{AHP}} [\text{Ca}^{2+}]_{\text{in}} (v_K - v), \quad (9.5)$$

where $[\text{Ca}^{2+}]_{\text{in}}$ denotes calcium concentration in the intracellular fluid, assumed to satisfy

$$\frac{d [\text{Ca}^{2+}]_{\text{in}}}{dt} = \frac{c_\infty(v) - [\text{Ca}^{2+}]_{\text{in}}}{80}, \quad (9.6)$$

with

$$c_\infty(v) = \frac{4}{25} \frac{120 - v}{1 + e^{-(v+15)/5}}. \quad (9.7)$$

Figure 9.5 shows the graph of c_∞ as a function of v . The values of c_∞ are very close to zero unless v is above -40 mV.

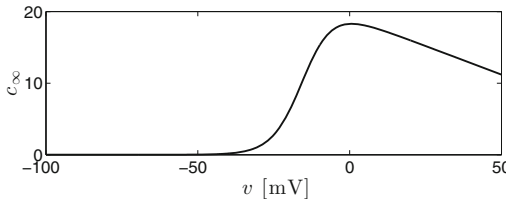


Figure 9.5. The function c_∞ defined in (9.7). [CALCIUM_RISE]

Figure 9.6 shows a voltage trace for the RTM neuron with I_{AHP} added. Note that Fig. 9.6 is quite similar to Fig. 9.3. However, when I is set to zero, the model with I_{AHP} behaves quite differently from the model with I_{M} ; see Fig. 9.7. Unlike the M-current, the calcium-dependent AHP current is essentially zero at rest.

9.3 Analysis in an Idealized Setting

In Figs. 9.1, 9.3, and 9.6, we see a monotonic increase in the inter-spike interval, until a limiting value is reached. One might wonder why it has to be that way. Is it possible that longer inter-spike intervals, during which the adaptation current has more time to decay, are followed by shorter ones, and vice versa? For a simple caricature model of spike frequency adaptation, we will now show that this cannot

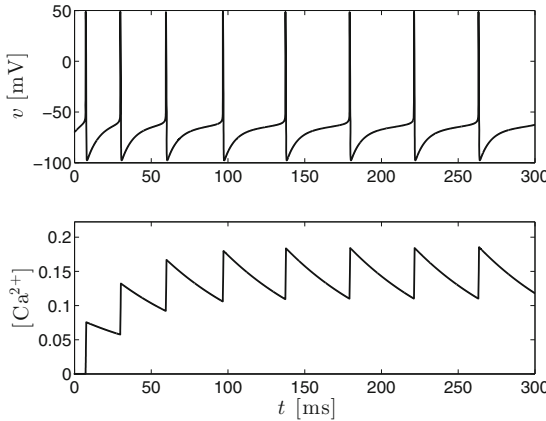


Figure 9.6. Buildup of the calcium concentration activates an AHP current, and thereby decelerates firing of the RTM neuron. In this simulation, $\bar{g}_{AHP} = 0.25 \text{ mS/cm}^2$ and $I = 1.5 \mu\text{A/cm}^2$. [RTM_AHP]

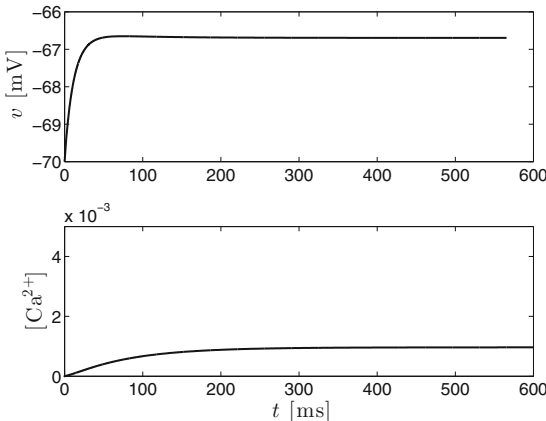


Figure 9.7. Same as Fig. 9.6, but with $I = 0$. At rest, the model calcium-dependent AHP current density is very close to zero. (Compare with Fig. 9.4, but notice that the vertical axes are scaled differently.) [RTM_AHP_RESTING]

happen: The convergence of the inter-spike intervals to their limiting value has to be monotonic, regardless of model parameter values. The caricature model will also allow an analysis of the number of spikes it takes to reach a nearly constant inter-spike interval; see exercise 6.

Our caricature model is given by the differential equations

$$\frac{dv}{dt} = -\frac{v}{\tau_m} + I - wv \quad \text{and} \quad \frac{dw}{dt} = -\frac{w}{\tau_w} \quad \text{for } v < 1, \quad (9.8)$$

together with the reset conditions

$$v(t+0) = 0 \quad \text{and} \quad w(t+0) = w(t-0) + \epsilon \quad \text{if } v(t-0) = 1, \quad (9.9)$$

where $\tau_w > 0$ and $\epsilon > 0$ are parameters. As for the normalized LIF and QIF models, we will think of v as dimensionless, t as a time measured in ms, but will usually omit specifying units. The *adaptation variable* w is analogous to $\bar{g}_M w$ in the model described by (9.1)–(9.4). It decays exponentially with time constant τ_w between spikes, and jumps by ϵ when the neuron fires. We assume that $\tau_m I > 1$. This implies that there is an infinite sequence of spikes: Following a spike, w decays exponentially, eventually becoming so small that the term $-wv$ cannot prevent v from reaching the threshold 1. Figure 9.8 shows v and w as functions of time for one particular choice of parameters.

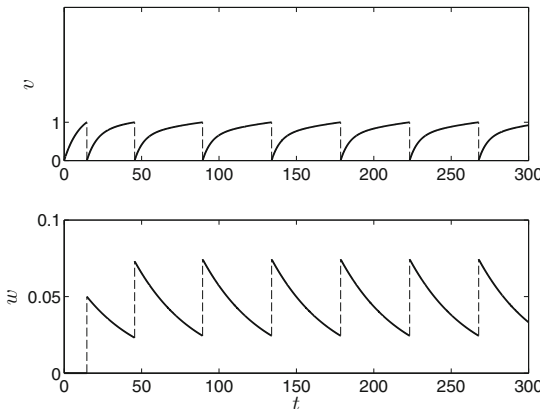


Figure 9.8. A solution of (9.8) and (9.9), with $\tau_m = 10$, $I = 0.13$, $\tau_w = 40$, $\epsilon = 0.05$, and $v(0) = 0$, $w(0) = 0$. [LIF_ADAPTER]

We assume $v(0) = 0$ and $w(0) = w_0 \geq 0$. We denote the times of spikes by

$$t_1 < t_2 < t_3 < \dots,$$

and the times between spikes by

$$T_k = t_{k+1} - t_k, \quad k = 1, 2, 3, \dots$$

We also write $t_0 = 0$ and $T_0 = t_1$. Our goal is to prove that the sequence $\{T_k\}_{k=0,1,2,\dots}$ is monotonic and convergent.

Note that $v(t_k + 0) = 0$. We write $w_k = w(t_k + 0)$ for $k = 0, 1, 2, \dots$, and note $w_k \geq \epsilon$ for $k \geq 1$. For given parameters $\tau_m > 0$, $I > 1/\tau_m$, and $\tau_w > 0$, we can compute T_k from w_k , simply by solving the initial-value problem

$$\begin{aligned} \frac{dv}{dt} &= -\frac{v}{\tau_m} + I - w_k e^{-(t-t_k)/\tau_w} v, \\ v(t_k) &= 0. \end{aligned}$$

The time at which the solution of this problem reaches 1 is $t_k + T_k$. Equivalently, of course, we can solve

$$\frac{dv}{dt} = -\frac{v}{\tau_m} + I - w_k e^{-t/\tau_w} v, \quad (9.10)$$

$$v(0) = 0, \quad (9.11)$$

and then T_k is the time at which the solution v of this problem reaches 1. For slight notational simplification, this is how we will say it.

Lemma 9.1. *For any $\tau_m > 0$, $I > 1/\tau_m$, $w_k \geq 0$, $\tau_w > 0$, if v solves (9.10), (9.11), then $dv/dt > 0$ for all $t > 0$.*

Proof. From eq. (9.10), $dv/dt = I$ when $v = 0$, so $dv/dt > 0$ initially. Suppose that $dv/dt \leq 0$ for some $t > 0$, and let t_0 be the smallest such t . Then $dv/dt = 0$ at $t = t_0$. Differentiating (9.10) once, we find

$$\frac{d^2v}{dt^2} = -\frac{1}{\tau_m} \frac{dv}{dt} - w_k e^{-t/\tau_w} \frac{dv}{dt} + \tau_w w_k e^{-t/\tau_w} v.$$

At time t_0 , since $dv/dt = 0$,

$$\frac{d^2v}{dt^2} = \tau_w w_k e^{-t_0/\tau_w} v > 0.$$

This implies that v has a strict local minimum at time t_0 , which is impossible since $dv/dt > 0$ for $t < t_0$. This contradiction proves our assertion. \square

Lemma 9.2. *For any $\tau_m > 0$, $I > 1/\tau_m$, $\tau_w > 0$, the solution v of (9.10), (9.11) depends on w_k continuously, and decreases with increasing w_k .*

Proof. This is a consequence of standard results on ordinary differential equations, using the fact that by Lemma (9.1), $v > 0$ for $t > 0$, and therefore the term $w_k e^{-t/\tau_w} v$ on the right-hand side of eq. (9.10) increases with increasing w_k . If this was a satisfactory explanation to you, you can skip the rest of this proof. However, since (9.10) is so simple, we will now argue explicitly, without invoking any “standard results.”

Assume that $0 \leq w_k < \tilde{w}_k$. We will compare the solutions v and \tilde{v} of

$$\frac{dv}{dt} = -\frac{v}{\tau_m} + I - w_k e^{-t/\tau_w} v, \quad v(0) = 0, \quad (9.12)$$

and

$$\frac{d\tilde{v}}{dt} = -\frac{\tilde{v}}{\tau_m} + I - \tilde{w}_k e^{-t/\tau_w} \tilde{v}, \quad \tilde{v}(0) = 0. \quad (9.13)$$

We will show that $v(t) > \tilde{v}(t)$ for $t > 0$. To do this, we write out the solutions to (9.12) and (9.13) explicitly, using, for instance, an *integrating factor*. The calculation is exercise 5; the result is

$$v(t) = \int_0^t \exp\left(-\frac{t-s}{\tau_m} - w_k \tau_w (e^{-s/\tau_w} - e^{-t/\tau_w})\right) ds, \quad (9.14)$$

and

$$\tilde{v}(t) = \int_0^t \exp\left(-\frac{t-s}{\tau_m} - \tilde{w}_k \tau_w (e^{-s/\tau_w} - e^{-t/\tau_w})\right) ds. \quad (9.15)$$

From these formulas, it is clear that $w_k < \tilde{w}_k$ implies $v(t) > \tilde{v}(t)$ for $t > 0$, and also that $v(t)$ depends continuously on w_k . \square

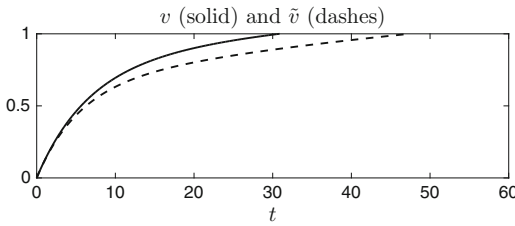


Figure 9.9. Solutions of eqs. (9.12) (solid) and (9.13) (dashes), with $\tau_m = 10$, $I = 0.13$, $w_k = 0.05$, $\tilde{w}_k = 0.08$, $\tau_w = 40$, and $t_k = 0$. [V_V_TILDE]

Figure 9.9 illustrates the result that we just proved, and makes the next lemma self-evident.

Lemma 9.3. T_k is an increasing continuous function of w_k .

Immediately after time t_k , the value of w is w_k . Then w decays for a time interval of duration T_k , and at time $t_{k+1} = t_k + T_k$, w jumps by ϵ , to w_{k+1} . So

$$w_{k+1} = e^{-T_k/\tau_w} w_k + \epsilon, \quad k = 0, 1, 2, \dots \quad (9.16)$$

We define a function T so that $T(w_k) = T_k$. For any $z \geq 0$, $T(z)$ is the time at which the solution of

$$\frac{dv}{dt} = -\frac{v}{\tau_m} + I - wv, \quad \frac{dw}{dt} = -\frac{w}{\tau_w}, \quad (9.17)$$

$$v(0) = 0, \quad w(0) = z \quad (9.18)$$

reaches $v = 1$. (The letter z is just an arbitrary letter that we choose to use for the independent variable of T ; think $z = w_k$.) We further define

$$\phi(z) = e^{-T(z)/\tau_w} z + \epsilon. \quad (9.19)$$

Then (9.16) can be written as

$$w_{k+1} = \phi(w_k), \quad k = 0, 1, 2, \dots \quad (9.20)$$

In spite of the simplicity of our model, it is not possible to find a useful explicit expression for ϕ . However, for any given parameters τ_m , I , τ_w , and ϵ , it is easy to evaluate this function numerically. Figure 9.10 shows the graph of ϕ for one particular choice of parameters; the 45° -line is indicated as a dashed line. The function ϕ depicted in Fig. 9.10 has exactly one fixed point z_* , which is indicated as well. The following lemma shows that qualitatively, the graph of ϕ looks like Fig. 9.10 for all parameter choices.

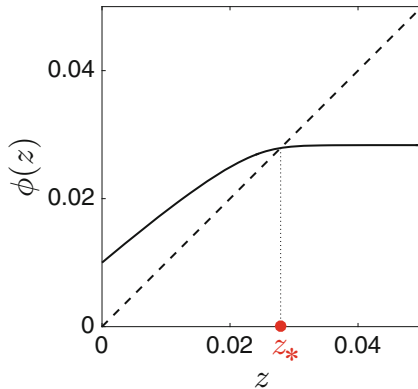


Figure 9.10. The map ϕ , with $\tau_m = 10$, $I = 0.12$, $\tau_w = 100$, $\epsilon = 0.01$. [ADAPTATION_MAP]

Lemma 9.4. Let $\tau_m > 0$, $I > 1/\tau_m$, $\tau_w > 0$, and $\epsilon > 0$. (a) $0 \leq \phi'(z) < 1$ for all $z \geq 0$. (b) $\phi(0) = \epsilon$. (c) $\lim_{z \rightarrow \infty} \phi(z) < \infty$. (d) There exists exactly one $z_* \geq 0$ with $\phi(z_*) = z_*$.

Proof. (a) From (9.19), it follows that the derivative of ϕ is

$$\phi'(z) = -\frac{T'(z)}{\tau_w} e^{-T(z)/\tau_w} z + e^{-T(z)/\tau_w} = e^{-T(z)/\tau_w} \left(1 - \frac{z T'(z)}{\tau_w} \right). \quad (9.21)$$

We know that $T'(z) \geq 0$, from Lemma 9.3. Therefore (9.21) immediately implies $\phi'(z) < 1$. To see why $\phi'(z) \geq 0$, note that this inequality is equivalent, by eq. (9.21), to

$$z T'(z) \leq \tau_w. \quad (9.22)$$

For $z = 0$, there is nothing to show. Let $z > 0$ and $\Delta z > 0$. Then $T(z + \Delta z)$ is the time it takes for v to reach 1, if v and w satisfy (9.8) with $v(0) = 0$ and $w(0) = z + \Delta z$. Therefore $T(z + \Delta z)$ is bounded by the time it takes for w to decay

from $z + \Delta z$ to z , plus $T(z)$. The time it takes for w to decay from $z + \Delta z$ to z is easy to calculate. It is the time t at which

$$(z + \Delta z)e^{-t/\tau_w} = z,$$

i.e., it is

$$\tau_w \ln \frac{z + \Delta z}{z}.$$

Therefore

$$T(z + \Delta z) \leq \tau_w \ln \frac{z + \Delta z}{z} + T(z).$$

Subtract $T(z)$ from both sides and divide by Δz :

$$\frac{T(z + \Delta z) - T(z)}{\Delta z} \leq \frac{\tau_w}{\Delta z} \ln \frac{z + \Delta z}{z}.$$

Taking the limit as $\Delta z \rightarrow 0$ on both sides, we find (9.22).

(b) This follows immediately from (9.19).

(c) To show that $\lim_{z \rightarrow \infty} \phi(z)$ exists, we must show that ϕ is bounded. Let $z \geq 0$. For the solution of (9.17), (9.18), we have $v = 1$, $w = ze^{-T(z)/\tau_w}$, and $dv/dt \geq 0$ at time $t = T(z)$, and therefore

$$-\frac{1}{\tau_m} + I - ze^{-T(z)/\tau_w} \geq 0.$$

This implies

$$\phi(z) = ze^{-T(z)/\tau_w} + \epsilon \leq I - \frac{1}{\tau_m} + \epsilon < \infty.$$

(d) The existence of z_* follows from $\phi(0) = \epsilon > 0$ and $\lim_{z \rightarrow \infty} \phi(z) < \infty$, by the intermediate value theorem: The graph of ϕ starts out above the 45°-line, and ends up (for large z) below it, so it must cross the line somewhere. The uniqueness follows from part (a): The function $\phi(z) - z$ can be zero at only one point, since its derivative is negative. \square

Lemma 9.5. *For any choice of the parameters $\tau_m > 0$, $I > 1/\tau_m$, $\tau_w > 0$, $\epsilon > 0$, assuming $v(0) = 0$ and $w(0) = w_0 \geq 0$, the sequence $\{w_k\}$ converges monotonically to a finite positive limit.*

Proof. Consider the plot in Fig. 9.10, and recall that the graph of ϕ qualitatively looks like the one in Fig. 9.10 for all parameter choices (Lemma 9.4). If $w_0 \leq z_*$, then $w_1 = \phi(w_0) \leq \phi(z_*)$ because ϕ is an increasing function, and therefore, since $\phi(z_*) = z_*$, $w_1 \leq z_*$. Repeating this reasoning, we find $w_k \leq z_*$ for all k . Furthermore, since the portion of the graph of ϕ to the left of $z = z_*$ lies above

the 45° -line, $w_{k+1} = \phi(w_k) \geq w_k$. Thus $\{w_k\}_{k=0,1,2,\dots}$ is an increasing function, bounded from above by z_* . This implies that $\{w_k\}$ has a limit, which we call w_∞ :

$$w_\infty = \lim_{k \rightarrow \infty} w_k.$$

We apply ϕ to both sides of this equation:

$$\phi(w_\infty) = \phi\left(\lim_{k \rightarrow \infty} w_k\right) = \lim_{k \rightarrow \infty} \phi(w_k) = \lim_{k \rightarrow \infty} w_{k+1} = w_\infty.$$

Thus w_∞ is a fixed point of ϕ (this simply means $\phi(w_\infty) = w_\infty$), and therefore, since z_* is the only fixed point of ϕ , $w_\infty = z_*$.

Similarly, one shows that if $w_0 \geq z_*$, then $\{w_k\}$ is monotonically decreasing and converges to z_* . \square

Finally, Lemma 9.5 implies what we wanted to prove:

Proposition 9.6. *For any choice of the parameters $\tau_m > 0$, $I > 1/\tau_m$, $\tau_w > 0$, $\epsilon > 0$, assuming $v(0) = 0$ and $w(0) = w_0 \geq 0$, the sequence $\{T_k\}$ converges monotonically to a finite positive limit.*

Proof. This follows immediately from Lemma 9.5, since $T_k = T(w_k)$ and T is monotonically increasing. \square

One unrealistic feature of the caricature model (9.8), (9.9) lies in the fact that the variable w does not *saturate*. It could, in principle, become arbitrarily large. This is, of course, not correct for real adaptation currents: Once all channels are open, the conductance cannot become larger any more. We might therefore modify the reset condition (9.9) as follows:

$$v(t+0) = 0 \text{ and } w(t+0) = w(t-0) + \epsilon(w_{\max} - w(t-0)) \text{ if } v(t-0) = 1, \quad (9.23)$$

where $w_{\max} > 0$ is a new parameter, and $0 < \epsilon \leq 1$. In this model, w cannot exceed w_{\max} , assuming it starts below w_{\max} .

Lemma 9.7. *The analogue of Lemma 9.5 holds for the modified model (9.8), (9.23).*

Proof. The function $T = T(z)$ is, of course, the same as in the analysis of the original model (9.8), (9.9). However, the function $\phi(z)$ is replaced by

$$\tilde{\phi}(z) = ze^{-T(z)/\tau_w} + \epsilon \left(w_{\max} - ze^{-T(z)/\tau_w} \right) = (1 - \epsilon) \left(ze^{-T(z)/\tau_w} + \frac{\epsilon}{1 - \epsilon} w_{\max} \right).$$

We write $\phi = \phi(z, \epsilon)$ to emphasize the dependence of ϕ on ϵ . Similarly, we write $\tilde{\phi} = \tilde{\phi}(z, \epsilon)$. With this notation,

$$\tilde{\phi}(z, \epsilon) = (1 - \epsilon)\phi\left(z, \frac{\epsilon}{1 - \epsilon} w_{\max}\right).$$

Lemma 9.4 then implies (a) $0 \leq \tilde{\phi}'(z) < 1 - \epsilon$ for all $z \geq 0$, (b) $\tilde{\phi}(0) = \epsilon w_{\max}$, (c) $\lim_{z \rightarrow \infty} \tilde{\phi}(z) < \infty$. These properties of $\tilde{\phi}$ imply that (d) there exists exactly one $\tilde{z}_* \geq 0$ with $\tilde{\phi}(\tilde{z}_*) = \tilde{z}_*$. The proof of Lemma 9.7 is then the same as that of Lemma 9.5, with ϕ replaced by $\tilde{\phi}$ and z_* replaced by \tilde{z}_* . \square

From Lemma 9.7, we obtain the following proposition.

Proposition 9.8. *The analogue of Proposition 9.6 holds for the modified model (9.8), (9.23).*

The caricature model (9.8), (9.9) can also be used to analyze how long it takes for the period to become steady when there is adaptation; see exercise 6. The main conclusion from exercise 6 is that it takes longer to reach a steady period when the neuron is driven more strongly, or adaptation is weaker.

Exercises

- 9.1. In the caricature model (9.8), (9.9), if the neuron fires at a constant frequency, the adaptation variable w varies from a maximal value w_{\max} to a minimal value w_{\min} . Express w_{\max} and w_{\min} in terms of parameters of the model.
- 9.2. (*) Starting with the code that generates Fig. 9.3, see how the solution changes if you (a) double \bar{g}_M , or (b) double τ_w .
- 9.3. (*) In Fig. 9.3, the variable w saturates rapidly: After three spikes, it is quite close to its maximal value already. As a result, the firing frequency stabilizes within about three spikes. Are there parameter values for which it takes more spikes for the frequency to stabilize? Try raising or lowering (a) I , (b) \bar{g}_M . You will discover that spike frequency adaptation is slower, in the sense that it takes more spikes for the frequency to stabilize, if the neuron is driven more strongly, and/or the adaptation is weaker. (Compare also with exercise 6.)
- 9.4. The model given by eqs. (9.5)–(9.7) differs from that proposed by Ermentrout in [46] in two regards.
 - (a) Instead of the factor $[\text{Ca}^{2+}]_{\text{in}}$ in eq. (9.5), Ermentrout used $[\text{Ca}^{2+}]_{\text{in}} / (30 + [\text{Ca}^{2+}]_{\text{in}})$. Explain why replacing $[\text{Ca}^{2+}]_{\text{in}}$ by $[\text{Ca}^{2+}]_{\text{in}} / (30 + [\text{Ca}^{2+}]_{\text{in}})$ in (9.5) amounts to dividing \bar{g}_{AHP} by 30 to very good approximation.
 - (b) Ermentrout used 25 in place of 15 in the exponent in eq. (9.7). Discuss how replacing 25 by 15 changes the model.
- 9.5. Derive (9.14). (Don't just verify it. That would be a pointless computation. Derive it, to remind yourself of the use of integrating factors.)
- 9.6. (*) (†) The purpose of this exercise is to think about how long it takes for the period to become steady in the presence of adaptation. We analyze this question for the caricature model (9.8), (9.9), which we simplify dramatically by letting τ_w tend to ∞ ; this simplification is motivated by the fact that adaptation currents typically recover slowly.

- (a) Starting with the code generating Fig. 9.10, reproduce Fig. 9.10 with $\tau_w = 1000$ and $\tau_w = 2000$. You will see that ϕ appears to have a limit, ϕ_∞ , as $\tau_w \rightarrow \infty$, and that ϕ_∞ appears to be of the form

$$\phi_\infty(z) = \begin{cases} z + \epsilon & \text{if } z \leq z_c, \\ z_c + \epsilon & \text{if } z > z_c, \end{cases}$$

where z_c is independent of τ_w .

- (b) Guess a formula expressing z_c in terms of parameters of the model. Verify your guess computationally.

- (c) Give a theoretical explanation of the formula for z_c that you guessed and verified in part (b). Your explanation will not likely be mathematically rigorous, but it should be plausible at least.

- (d) For large τ_w , how many times does the neuron have to fire, starting with $v(0) = 0$ and $w(0) = 0$, before w comes close to reaching its limiting value? (To answer this question, use the formula for z_c that you guessed and verified in part (b).)

- (e) Check your answer to part (d) numerically, using as a starting point the code generating Fig. 9.8. Is it accurate if $\tau_w = 100$, or does τ_w have to be much larger? (Adaptation currents may well have decay time constants of 100 ms, but decay time constants on the order of 1000 ms are probably not realistic.)

Part II

Dynamics of Single Neuron Models

Chapter 10

The Slow-Fast Phase Plane

In this chapter, we use phase plane pictures to understand the mechanism of neuronal firing more clearly. The key is the presence of two time scales, a slow one and a fast one: Neurons build up towards firing gradually, then fire all of the sudden. This is what is captured (and in fact this is *all* that is captured) by the integrate-and-fire model.

10.1 A Two-Dimensional Reduction of the Classical Hodgkin-Huxley Model

To understand the classical Hodgkin-Huxley equations better, we make two simplifications: We set $m = m_\infty(v)$, and $h = 0.83 - n$. The approximation $m = m_\infty(v)$ was already made in the RTM, WB, and Erisir models introduced in Chapter 5. It makes sense also for the classical Hodgkin-Huxley equations, since τ_m is much smaller than τ_h and τ_n ; see Fig. 3.1. The approximation $h = 0.83 - n$ is based on the observation that for solutions of the classical Hodgkin-Huxley equations, $h + n \approx 0.83$. (There is no profound reason for this, it just happens to be so.) For the solution of the classical Hodgkin-Huxley equations shown in Fig. 4.1, we plot $h + n$ in Fig. 10.1; the value 0.83 is indicated as a dashed red line. It turns out that $h + n \approx 0.83$ over a wide range of values of I ; see exercise 1. Figure 10.2 is analogous to Fig. 4.1, with the reductions $m = m_\infty(v)$ and $h = 0.83 - n$.

We summarize the reduced model:

$$C \frac{dv}{dt} = \bar{g}_{\text{Na}} m_\infty(v)^3 (0.83 - n)(v_{\text{Na}} - v) + \bar{g}_K n^4 (v_K - v) + \bar{g}_L (v_L - v) + I, \quad (10.1)$$

Electronic supplementary material: The online version of this chapter (doi: [10.1007/978-3-319-51171-9_10](https://doi.org/10.1007/978-3-319-51171-9_10)) contains supplementary material, which is available to authorized users.

$$\frac{dn}{dt} = \frac{n_\infty(v) - n}{\tau_n(v)}, \quad (10.2)$$

with n_∞ , τ_n , m_∞ , and all parameters defined in Chapter 3. This is a two-dimensional

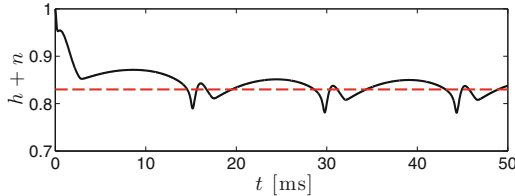


Figure 10.1. $h + n$ for the solution of the Hodgkin-Huxley equations with $I = 10 \mu A/cm^2$ shown in Fig. 4.1. The red dashed line is at 0.83. [HH_H_PLUS_N]

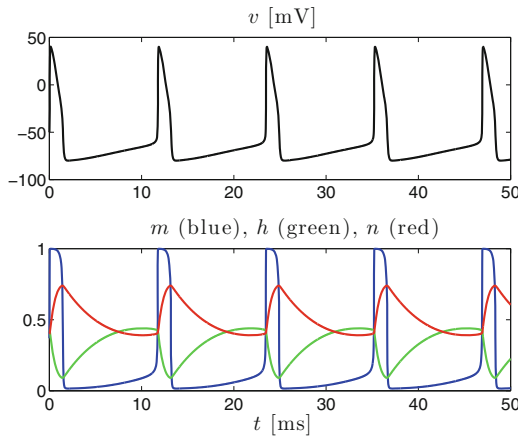


Figure 10.2. Same as Fig. 4.1, but with the reductions $m = m_\infty(v)$ and $h = 0.83 - n$. [REDUCED_HH]

system of ODEs, i.e., a system of the form

$$\frac{dv}{dt} = f(v, n), \quad (10.3)$$

$$\frac{dn}{dt} = g(v, n). \quad (10.4)$$

Solutions of a system of this form can be thought of as moving points in the (v, n) -plane, also called the *phase plane* in this context. The *phase space*, in general, is the space of dependent variables. Notice that the time t is not directly depicted in the phase plane — you can see information related to t only by watching the point move. If you only see the curve that it traces out, that gives you *some* information — like watching the white streaks in a blue sky left behind by an airplane — but it

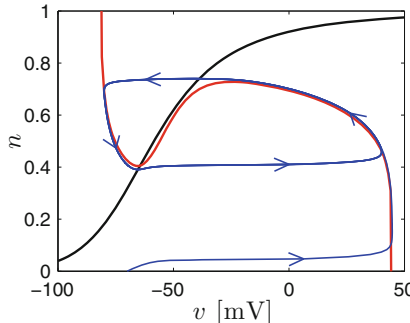


Figure 10.3. The n -nullcline (black) and the v -nullcline (red) of the reduced Hodgkin-Huxley equations for $I = 10 \mu\text{A}/\text{cm}^2$, together with a solution (blue).
[HH_NULLCLINES_PLUS_SOLUTION]

doesn't tell you everything about the motion. We also use the words *trajectory* or *orbit* for the solution of a system of ordinary differential equations, especially when we depict a solution as a curve in phase space.

One of the first things to do about a two-dimensional system of first-order ordinary differential equations is to study the *nullclines*, the curves along which the derivatives of the dependent variables are zero. The curve where $dn/dt = 0$, the n -nullcline, is very easy. It is given by $n = n_\infty(v)$. We plotted this curve in Chapter 3 already; it is also the black curve in Fig. 10.3. Notice that the n -nullcline is independent of the value of I . The curve where $dv/dt = 0$, the v -nullcline, is a little less easy to compute. It is implicitly defined by

$$\bar{g}_{\text{Na}} m_\infty(v)^3 (0.83 - n)(v_{\text{Na}} - v) + \bar{g}_K n^4 (v_K - v) + \bar{g}_L (v_L - v) + I = 0. \quad (10.5)$$

This equation cannot easily be solved by hand. However, it is easy to show that for a fixed v between v_K and v_{Na} , it has at most one solution $n \in [0, 1]$; see exercise 2. If there is a solution, it can be found with great accuracy using, for instance, the *bisection method*; see Appendix A. The reader can see the details by reading the code that generates Fig. 10.3. The red curve in that figure is the v -nullcline.

The moving point must pass through the black curve horizontally (since $dn/dt = 0$), and through the red curve vertically (since $dv/dt = 0$). In Fig. 10.3, a solution is shown in blue. The flow along this trajectory is counter-clockwise. You see here that the trajectory appears to be attracted to a closed loop, a *limit cycle*, corresponding to a periodic solution of eqs. (10.1) and (10.2).

Figure 10.3, like any phase plane plot, only shows *where* the solution moves, but not *how fast* it moves. In fact, the speed around the cycle is very far from constant. We define

$$s(t) = \sqrt{\left(\frac{dv/dt}{120 \text{ mV}}\right)^2 + \left(\frac{dn/dt}{0.35}\right)^2}.$$

(The scaling is motivated by the fact that on the limit cycle, $\max v - \min v \approx 120 \text{ mV}$, and $\max n - \min n \approx 0.35$.) We call the motion along the cycle *slow* when $s \leq M/50$,

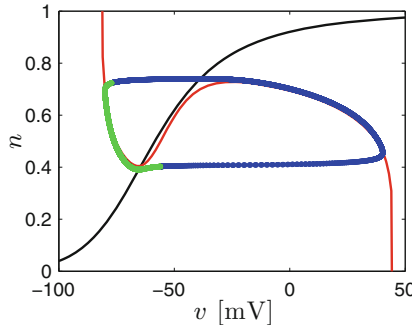


Figure 10.4. Slow portion of cycle in green, fast portion in blue. (See text for the precise definitions of “slow” and “fast” used here.) [HH_CYCLE_SPEED]

where M is the maximum of s over the entire cycle, and *fast* otherwise. Figure 10.4 shows the slow portion of the cycle in green and the fast portion in blue. The motion is slow during the left-most part of the cycle, when v changes little and n changes substantially, and fast during the remainder of the cycle, when v rises and falls. One calls n the *slow variable*, v the *fast variable*, and the reduction that we are considering here is also called the *slow-fast phase plane*.

The reduced, two-dimensional Hodgkin-Huxley model described in this chapter is an example of a *relaxation oscillator*. *Oscillator* because solutions oscillate (there is a limit cycle). *Relaxation* because v creeps up gradually first, while n falls, “building up tension” as it were, then all of the sudden the tension is “released” when the trajectory shoots over from the left branch of the v -nullcline to its right branch.

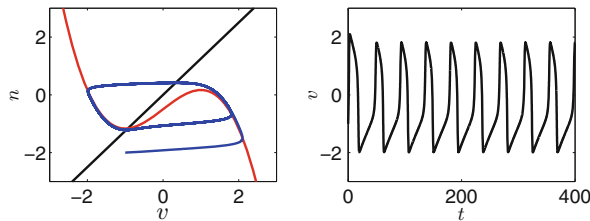


Figure 10.5. Left: The n -nullcline (black) and the v -nullcline (red) of the FitzHugh-Nagumo equations, with $a = 1.25$, $\tau_n = 25$, and $I = -0.5$, together with a solution (blue). Right: v as a function of t for the same equations. [FN]

10.2 The FitzHugh-Nagumo Model

Figure 10.3 suggests a simplified model, in which the n -nullcline is replaced by a straight line, and the v -nullcline by a cubic. This model is called the *FitzHugh-Nagumo* model. It was proposed by Richard FitzHugh in 1961 [54]. In 1962, Jin-Ichi

Nagumo proposed an electrical circuit governed by FitzHugh's equation [121]; this is why the model bears both names nowadays. The equations of the FitzHugh-Nagumo model can be written as follows:

$$\frac{dv}{dt} = v - \frac{v^3}{3} - n + I, \quad (10.6)$$

$$\frac{dn}{dt} = \frac{av - n}{\tau_n}, \quad (10.7)$$

where $a > 0$ and $\tau_n \gg 1$. All variables and parameters should be considered dimensionless here. FitzHugh's choices, translated into our notation, are $a = 1.25$ and $\tau_n = 15.625$. The left panel of Fig. 10.5 is the analogue of Fig. 10.3, but for the FitzHugh-Nagumo model, with $a = 1.25$ and $\tau_n = 25$. The right panel shows v as a function of time.

In spite of its simplicity, the FitzHugh-Nagumo model can reproduce aspects of the dynamics of the classical Hodgkin-Huxley model surprisingly well; for an example, see [86, Fig. 4].

Exercises

- 10.1. (*) Using the program that generated Fig. 10.1 as a starting point, make similar plots for $I = 7, 8, \dots, 14, 15 \mu\text{A}/\text{cm}^2$.
- 10.2. Show: For any v with $v_K \leq v \leq v_{\text{Na}}$, eq. (10.5) has at most one solution $n \in [0, 1]$.
- 10.3. Consider the downward-moving portion of the limit cycle in Fig. 10.3, following the crossing of the v -nullcline in the left upper “corner.” Explain why the limit cycle cannot cross the v -nullcline again before crossing the n -nullcline.
- 10.4. When you look closely at the portion of the spike of a Hodgkin-Huxley neuron when the voltage v decreases, you see a slight kink, about two-thirds of the way towards the minimum: From the maximum to the kink, the voltage decreases slightly less fast than from the kink to the minimum. Guess what this kink corresponds to in the phase plane.
- 10.5. In (10.6), assume that n is constant. (This is motivated by the assumption that $\tau_n \gg 1$.) Analyze the dynamics of v under this assumption.
- 10.6. Assume $a \geq 1$. (a) Show that the FitzHugh-Nagumo system has exactly one fixed point. (b) Show: If $I > a - 2/3$, the fixed point is stable. To do this, you have to remember that a fixed point is stable if and only if the *Jacobi matrix* at the fixed point has eigenvalues with negative real parts only; see [149] or, for a very brief review, Chapter 12.

Thus the FitzHugh-Nagumo system can rest at a stable fixed point if I is large enough; a similar phenomenon occurs in real neurons [9], and is called *depolarization block*.

Chapter 11

Saddle-Node Collisions

Model neurons, as well as real neurons, don't fire when they receive little or no input current, but fire periodically when they receive strong input current. The transition from rest to firing, as the input current is raised, is called a *bifurcation*. In general, a bifurcation is a sudden qualitative change in the solutions to a differential equation, or a system of differential equations, occurring as a parameter, called the *bifurcation parameter* in this context, is moved past a threshold value, also called the *critical value*. (To bifurcate, in general, means to divide or *fork* into two branches. This suggests that in a bifurcation, one thing turns into two. This is indeed the case in some bifurcations, but not in all.) Because the variation of drive to a neuron is the primary example we have in mind, we will denote the bifurcation parameter by I , and its threshold value by I_c , in this chapter.

Since we want to study the transition from (stable) rest to firing in a neuron, we will focus on bifurcations in which stable fixed points become unstable, or disappear altogether. In this chapter, we study the simplest such bifurcations, namely collisions between saddle points and stable nodes resulting in the disappearance of both fixed points. For more about this and other kinds of bifurcations, see, for instance, [74] or [149].

We begin with the differential equation

$$\frac{dx}{dt} = x^2 + I, \quad (11.1)$$

where I is given and $x = x(t)$ is the unknown function. One can find the solutions of this equation using separation of variables, but it is easier and more instructive to understand what the solutions look like by drawing a picture. Figure 11.1 shows the cases $I = -1$, $I = 0$, and $I = 1$. In each case, we plot $x^2 + I$ as a function of

Electronic supplementary material: The online version of this chapter (doi: [10.1007/978-3-319-51171-9_11](https://doi.org/10.1007/978-3-319-51171-9_11)) contains supplementary material, which is available to authorized users.

x , not $x(t)$ as a function of t . We think of $x(t)$ as describing a point moving along the real axis. Notice that the point must move to the right where $x^2 + I > 0$, and to the left where $x^2 + I < 0$.

For $I < 0$, there are two fixed points, i.e., points where the right-hand side of the differential equation is 0; they are $\pm\sqrt{-I}$. The fixed point $-\sqrt{-I}$ is *stable* or *attracting*: If $x(0) \approx -\sqrt{-I}$, then $x(t) \rightarrow -\sqrt{-I}$ as $t \rightarrow \infty$. The fixed point $\sqrt{-I}$ is *unstable*, and, to be precise, *repelling*: If $x(0) \approx \sqrt{-I}$ but $x(0) \neq \sqrt{-I}$, $x(t)$ moves away from $\sqrt{-I}$ as t increases, either to $-\sqrt{-I}$ or to ∞ , depending on which side of the fixed point $x(0)$ is on. We always indicate stable fixed points with solid circles, and unstable ones with open circles.

As I increases towards 0, the two fixed points approach each other. They collide when $I = 0$. For $I = 0$, there is a single fixed point at 0, and it is *semi-stable*: If $x(0) < 0$, then $x(t) \rightarrow 0$, but if $x(0) > 0$, then $x(t) \rightarrow \infty$. We indicate semi-stable fixed points with circles that are half-solid and half-open. For $I > 0$, there are no fixed points; all solutions $x(t)$ of the differential equation $dx/dt = x^2 + I$ satisfy $\lim_{t \rightarrow \infty} x(t) = \infty$.

The two fixed points collide and annihilate each other as I passes through $I_c = 0$ from below. For reasons that are not clear at this point, but will become clear shortly, the bifurcation shown in Fig. 11.1 is called a *saddle-node bifurcation*.

One can also think of lowering I . In that case, two fixed points appear as I passes through 0 from above, “out of the blue.” Saddle-node bifurcations are therefore also called *blue sky bifurcations*, especially when one thinks of the direction in which fixed points appear, rather than disappear.

The word bifurcation is somewhat justified for a saddle-node bifurcation: On one side of the critical value of the bifurcation parameter, there is a two-pronged “fork,” namely the two fixed points. The fork has no “handle,” though: On the other side of the critical value, there are no fixed points at all. Exercise 2 asks you to plot the fork.

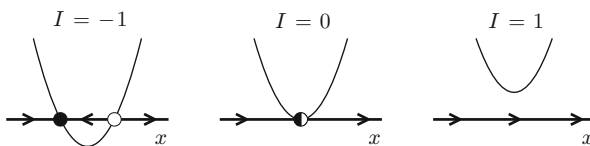


Figure 11.1. Two fixed points collide and annihilate each other. The equation is $dx/dt = x^2 + I$.

Notice the similarity between Figs. 11.1 and 8.3. The transition from rest to periodic firing in the theta neuron is a saddle-node bifurcation. In general, there is usually a saddle-node bifurcation in an equation of the form

$$\frac{dx}{dt} = f(x, I) \tag{11.2}$$

if f , as a function of x , has a *double zero*, i.e., $f(x_c, I_c) = 0$ and $f_x(x_c, I_c) = 0$ for some value, I_c , of the parameter and some point x_c . We assume that the fixed point is otherwise non-degenerate, i.e., that $f_{xx}(x_c, I_c) \neq 0$ and $f_I(x_c, I_c) \neq 0$. We then

replace the right-hand side in (11.2) by its leading-order Taylor approximation near (x_c, I_c) :

$$\frac{dx}{dt} = \frac{1}{2} f_{xx}(x_c, I_c)(x - x_c)^2 + f_I(x_c, I_c)(I - I_c). \quad (11.3)$$

We scale time as follows:

$$\tilde{t} = \frac{f_{xx}(x_c, I_c)}{2} t.$$

(If $f_{xx}(x_c, I_c) < 0$, this also reverses the direction of time.) Then

$$\frac{dx}{d\tilde{t}} = \frac{dx}{dt} \frac{dt}{d\tilde{t}} = (x - x_c)^2 + \frac{2f_I(x_c, I_c)}{f_{xx}(x_c, I_c)}(I - I_c).$$

If we also define

$$\tilde{x} = x - x_c, \quad \text{and} \quad \tilde{I} = \frac{2f_I(x_c, I_c)}{f_{xx}(x_c, I_c)}(I - I_c),$$

then

$$\frac{d\tilde{x}}{d\tilde{t}} = \tilde{x}^2 + \tilde{I}.$$

Thus up to shifting and/or re-scaling x , t , and I , (11.3) is the same as (11.1). One therefore calls (11.1) the *normal form* of a saddle-node bifurcation.

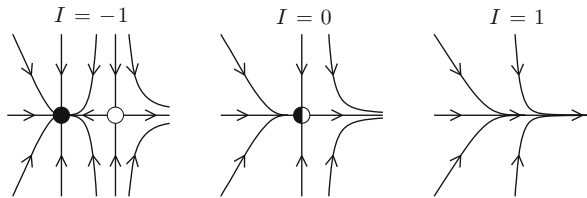


Figure 11.2. A saddle-node collision in two dimensions. The equations are $dx/dt = x^2 + I$, $dy/dt = -5y$.

The simplest way of writing down a two-dimensional analogue of (11.1) is to add a variable y that simply decays to 0, for instance, like this:

$$\frac{dx}{dt} = x^2 + I, \quad \frac{dy}{dt} = -5y. \quad (11.4)$$

Figure 11.2 shows resulting phase plane pictures. For $I = -1$, there are two fixed points: a stable one at $(-1, 0)$, and an unstable one at $(1, 0)$. The unstable fixed point has an attracting direction (the y -direction), and a repelling direction (the x -direction). Thus not all trajectories starting near the unstable fixed point move away from it; in fact, those that start directly above or below the unstable fixed point move towards it. A fixed point of this nature is called a *saddle point*. The vertical line through the fixed point is its *stable manifold*. In general, the stable

manifold is the set of all points (x_0, y_0) in the plane so that the trajectory with $(x(0), y(0)) = (x_0, y_0)$ converges to the saddle point. The set of points on the x -axis to the right of $x = -1$ is the *unstable manifold* of the saddle point. In general, the unstable manifold is the set of all points (x_0, y_0) in the plane so that the trajectory with $(x(0), y(0)) = (x_0, y_0)$ converges to the saddle point in *backward time*, that is, as $t \rightarrow -\infty$. Intuitively, one should think of the unstable manifold as composed of trajectories that emanate from the saddle at $t = -\infty$. The stable fixed point at $(-1, 0)$ attracts all trajectories in its vicinity in a non-oscillatory manner; such a fixed point is called a *stable node*.

As I rises, the saddle and the node approach each other, colliding when $I = 0$. Typical trajectories for $I = 0$ are shown in the middle panel of Fig. 11.2. The fixed point looks like a stable node on the left, and like a saddle on the right. For $I > 0$, there are no fixed points; the collision has annihilated both fixed points.

Saddle-node collisions are very common in the sciences. Figure 11.3 shows phase plane pictures for a system from [66], discussed also in [149, Example 8.1.1], which models a gene and a protein interacting with each other.

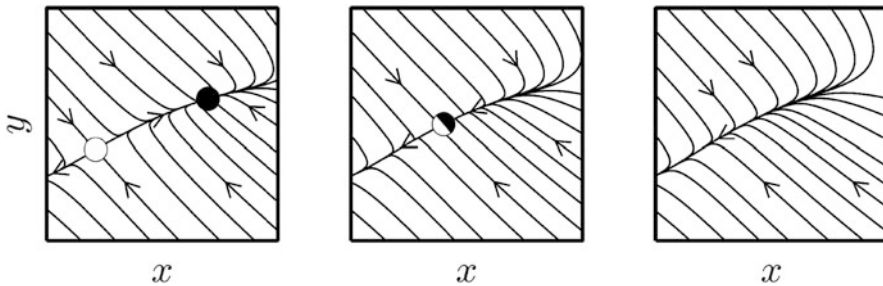


Figure 11.3. Phase plane pictures for the system discussed in [149, Example 8.1.1], originally from [66], modeling gene-protein interaction. The variables x and y are proportional to the concentrations of protein and messenger RNA, respectively. From left to right, the rate of degradation of x (denoted by a in [149, Example 8.1.1]) rises. [SADDLE_NODE_BIFURCATION]

Figures 11.2 and 11.3 motivate the name *saddle-node bifurcation*: The two fixed points colliding and annihilating each other are a saddle and a node. In the next paragraph, I will argue that this is the only “non-degenerate” possibility when two fixed points collide and annihilate each other. I will only discuss the case of a two-dimensional system, and use ideas explained in easily accessible ways in [149], but not in this book; readers unfamiliar with these ideas should simply skip the following paragraph.

Suppose that a continuous change in a bifurcation parameter makes two fixed points collide and annihilate each other. Consider a closed curve Γ surrounding the site of the collision. The index I_Γ of Γ [149, Section 6.8] with respect to the vector field defined by the right-hand side of the system of ordinary differential equations is zero after the fixed points have disappeared. Since I_Γ depends continuously on the bifurcation parameter and is an integer, it cannot depend on the bifurcation parameter at all. So $I_\Gamma = 0$ even prior to the collision of the two fixed points, thus

the sum of the indices of the two fixed points is zero, and therefore one of the two fixed points must be a saddle (index -1), while the other must be a non-saddle (index 1) [149, Section 6.8]. Because the collision must involve a saddle and a non-saddle, it must occur on the τ -axis of Figure 5.2.8 of [149], and therefore it must be a saddle-node collision, if we disregard the “degenerate” possibility of a collision that occurs at the origin of [149, Fig. 5.2.8].

Suppose now that $I > I_c$. We assume, as was the case in the examples of Figs. 11.1 and 11.2, that the fixed points exist for $I < I_c$, not for $I > I_c$. In the reverse case, the obvious sign changes need to be made in the following discussion. If $I \approx I_c$, the velocity is still small near the point where the saddle-node collision occurred, since the right-hand side changes continuously. To move past this point therefore takes a long time — as it turns out, on the order of $C/\sqrt{I - I_c}$, where C is a positive constant. One says that the saddle-node collision leaves a “ghost” behind: There are no fixed points any more when $I > I_c$, but trajectories still move slowly past the location where the fixed points disappeared. We will make this precise, and prove it, for the example shown in Fig. 11.1 only. Let $a > 0$ be an arbitrary number. For $I > 0$, the time needed for x to move from $-a$ to a is

$$\int_{-a}^a \frac{dt}{dx} dx = \int_{-a}^a \frac{1}{x^2 + I} dx = \frac{2 \arctan(a/\sqrt{I})}{\sqrt{I}} \sim \frac{\pi}{\sqrt{I}}.$$

(See Section 1.2 for the meaning of “ \sim ”.) Thus in the limit as $I \rightarrow 0$, the time it takes to move from $-a$ to a is approximately π/\sqrt{I} , regardless of the choice of a .

Exercises

- 11.1. This exercise is not directly related to the content of this chapter, but illustrates the usefulness of thinking of an equation of the form $dx/dt = f(x)$ as describing a point moving on the x -axis.

Logistic population growth is described by

$$\frac{dx}{dt} = rx \left(1 - \frac{x}{K}\right),$$

where x is the size of the population, $r > 0$ is the rate of growth when the population is small, and K is the maximal population size that can be supported by the environment, also called the *carrying capacity*. (Notice that dx/dt becomes 0 as x approaches K from below.) Without computing an expression for the solutions of the differential equation, show: (a) If $0 < x(0) < K$, then $\lim_{t \rightarrow \infty} x(t) = K$. (b) The graph of x is concave-up if $0 < x < K/2$, and concave-down if $K/2 < x < K$.

- 11.2. For the equation $dx/dt = x^2 + I$, plot the fixed points as a function of I , indicating stable fixed points by a solid curve, and unstable ones by a dashed curve. This plot is called the *bifurcation diagram* for the equation $dx/dt = x^2 + I$.

11.3. (*) The equations underlying Fig. 11.3 are

$$\frac{dx}{dt} = -Ix + y, \quad (11.5)$$

$$\frac{dy}{dt} = \frac{x^2}{1+x^2} - y. \quad (11.6)$$

The three panels of the figure show phase plane pictures for (from left to right) $I = 0.45$, $I = 0.5$, and $I = 0.55$. The critical value of I is $I_c = 0.5$. The two fixed points collide at $(x, y) = (1, 0.5)$.

For $I = 0.5 + 10^{-p}$, $p = 4, 5, 6$, compute the solution with $x(0) = 2$, $y(0) = 0.5$, and plot x as a function of t for $0 \leq t \leq 10,000$. (Use the midpoint method for these computations.) You will find that x is always a decreasing function of t , and converges to 0 as $t \rightarrow \infty$. For each of the three values of I , compute the time $T = T(I)$ that it takes for x to fall from 1.5 to 0.5. Demonstrate numerically that $T(I)\sqrt{I - I_c}$ is approximately independent of I .

11.4. Consider the equation

$$\frac{dx}{dt} = |x| + I.$$

- (a) Explain: As I rises above 0, two fixed points collide and annihilate each other.
- (b) Show: For $I > 0$, $I \approx 0$, the time needed to move past the ghost of the fixed points is $\sim 2 \ln(1/I)$.
- (c) Why is the time needed to move past the ghost not $\asymp 1/\sqrt{I}$, as suggested by the last paragraph of the chapter? (See Section 1.2 for the meaning of “ \asymp ”.)

Chapter 12

Model Neurons of Bifurcation Type 1

For a model neuron, there is typically a critical value I_c with the property that for $I < I_c$, there is a stable equilibrium with a low membrane potential, whereas periodic firing is the only stable behavior for $I > I_c$, as long as I is not too high.⁹

In this section, we discuss a class of model neurons in which a saddle-node bifurcation occurs as I crosses I_c . We begin with the two-dimensional reduction of the RTM neuron described in exercise 5.3. For this model, we will examine the transition from $I < I_c$ to $I > I_c$ numerically. The model is of the form

$$C \frac{dv}{dt} = \bar{g}_{\text{Na}} (m_\infty(v))^3 (1 - n)(v_{\text{Na}} - v) + \bar{g}_{\text{K}} n^4 (v_{\text{K}} - v) + \bar{g}_{\text{L}} (v_{\text{L}} - v) + I, \quad (12.1)$$

$$\frac{dn}{dt} = \frac{n_\infty(v) - n}{\tau_n(v)}, \quad (12.2)$$

with parameters and functions m_∞ , n_∞ , and τ_n defined as in the definition of the RTM neuron in Chapter 5. We call this the *two-dimensional RTM model*.

We denote the right-hand sides of (12.1) and (12.2) by $f(v, n)$ and $g(v, n)$, respectively, so our system is

$$\frac{dv}{dt} = f(v, n), \quad \frac{dn}{dt} = g(v, n). \quad (12.3)$$

Electronic supplementary material: The online version of this chapter (doi: [10.1007/978-3-319-51171-9_12](https://doi.org/10.1007/978-3-319-51171-9_12)) contains supplementary material, which is available to authorized users.

⁹For very high I , there is usually a stable equilibrium again, but at a high membrane potential. This is referred to as *depolarization block*, an observed phenomenon in real neurons driven very hard [9], but we don't discuss it here; see also exercises 10.6, 12.3, and 12.4.

A point (v_*, n_*) in the (v, n) -plane is a fixed point of this system if and only if $f(v_*, n_*) = 0$ and $g(v_*, n_*) = 0$, i.e., $n_* = n_\infty(v_*)$ and

$$\bar{g}_{\text{Na}} (m_\infty(v_*))^3 (1 - n_\infty(v_*))(v_{\text{Na}} - v_*) + \bar{g}_{\text{K}} (n_\infty(v_*))^4 (v_{\text{K}} - v_*) + \bar{g}_{\text{L}}(v_{\text{L}} - v_*) + I = 0. \quad (12.4)$$

Notice that (12.4) is one equation in one unknown, v_* . We prove next that this equation has at least one solution for any value of I , so that there is always at least one fixed point of (12.1), (12.2).

Proposition 12.1. *If v_* solves (12.4), then*

$$\min \left(v_{\text{K}}, v_{\text{L}} + \frac{I}{\bar{g}_{\text{L}}} \right) \leq v_* \leq \max \left(v_{\text{Na}}, v_{\text{L}} + \frac{I}{\bar{g}_{\text{L}}} \right). \quad (12.5)$$

There is at least one solution of (12.4).

Proof. We denote the left-hand side of (12.4) by $F(v_*)$, so

$$F(v) = \bar{g}_{\text{Na}} (m_\infty(v))^3 (1 - n_\infty(v))(v_{\text{Na}} - v) + \bar{g}_{\text{K}} (n_\infty(v))^4 (v_{\text{K}} - v) + \bar{g}_{\text{L}}(v_{\text{L}} - v) + I.$$

We will prove: (a) If $v < v_{\text{K}}$ and $v < v_{\text{L}} + I/\bar{g}_{\text{L}}$, then $F(v) > 0$. (b) If $v > v_{\text{Na}}$ and $v > v_{\text{L}} + I/\bar{g}_{\text{L}}$, then $F(v) < 0$. Together, (a) and (b) imply that any v_* with $F(v_*) = 0$ must satisfy inequalities (12.5). Furthermore, since $F(v) > 0$ for sufficiently small v and $F(v) < 0$ for sufficiently large v , F must be equal to zero in between at least once.

To prove (a), recall that $v_{\text{K}} < v_{\text{L}} < v_{\text{Na}}$. If $v < v_{\text{K}}$, then the terms $\bar{g}_{\text{Na}} (m_\infty(v))^3 (1 - n_\infty(v))(v_{\text{Na}} - v)$ and $\bar{g}_{\text{K}} (n_\infty(v))^4 (v_{\text{K}} - v)$ are positive. If furthermore $v < v_{\text{L}} + I/\bar{g}_{\text{L}}$, i.e., $\bar{g}_{\text{L}}(v_{\text{L}} - v) + I > 0$, then $F(v) > 0$. The proof of (b) is analogous. \square

It is easy to find the solutions of (12.4) numerically, using the bisection method (see Appendix A), and therefore we can determine all fixed points of (12.1), (12.2); we won't explain in detail how we do this, but refer the interested reader to the Matlab code generating Fig. 12.1.

We assume that the reader is familiar with the classification of fixed points of two-dimensional systems of ODEs [149, Chapters 5 and 6]. Nonetheless we will very briefly sketch the relevant ideas here. A fixed point (v_*, n_*) is *attracting* if solutions that start close enough to (v_*, n_*) remain close to (v_*, n_*) for all later times, and converge to (v_*, n_*) as $t \rightarrow \infty$; it is called a *stable node* if the approach to the fixed point is non-oscillatory, and a *stable spiral* if it involves damped oscillations that continue indefinitely. For examples of stable nodes, see the stable fixed points in Figs. 11.2 and 11.3. The fixed point (v_*, n_*) is *repelling* if it would become

attracting if the time direction were reversed; it is called an *unstable node* or an *unstable spiral*, depending on whether it would turn into a stable node or a stable spiral if the time direction were reversed. A fixed point (v_*, n_*) is called a *saddle* if some nearby trajectories are attracted by it, and others are repelled. For example, see the unstable fixed points in the left-most panels of Figs. 11.2 and 11.3. Fixed points can be classified by studying the eigenvalues of the *Jacobi matrix*

$$J = \begin{bmatrix} \partial f / \partial v & \partial f / \partial n \\ \partial g / \partial v & \partial g / \partial n \end{bmatrix}.$$

One evaluates J at the fixed point (v_*, n_*) , then computes its eigenvalues by finding zeros of the characteristic polynomial of J , using the quadratic formula. There are typically two eigenvalues, λ_+ and λ_- , with the subscripts + and – corresponding to the sign chosen in the quadratic formula. It is possible for λ_+ and λ_- to coincide;

properties of eigenvalues	type of fixed point
both real and negative	stable node
both real and positive	unstable node
complex-conjugate pair, negative real part	stable spiral
complex-conjugate pair, positive real part	unstable spiral
both real, one positive and one negative	saddle

Table 12.1. *Classifications of fixed points of a two-dimensional system.*

then J has only one eigenvalue, but it is of multiplicity 2. Table 12.1 shows how the eigenvalues are used to classify fixed points.

Non-real eigenvalues always come in complex-conjugate pairs. This is simply a consequence of the fact that the Jacobi matrix J is real. In fact, if J is any real $N \times N$ -matrix, with $N \geq 2$, and if λ is a complex number that is an eigenvalue of J , then the complex-conjugate $\bar{\lambda}$ is an eigenvalue of J as well; see exercise 5.

Using the eigenvalues, we can determine, for any fixed point of (12.1), (12.2), whether it is stable or unstable. Figure 12.1 shows the result of computing and classifying all fixed points for $0 \leq I \leq 0.2 \mu\text{A}/\text{cm}^2$. For $0 \leq I \leq I_c$, with $I_c \approx 0.13 \mu\text{A}/\text{cm}^2$, a stable node and a saddle exist. They collide when I reaches I_c , and don't exist for $I > I_c$. In addition, there is an unstable node for all I between 0 and $0.2 \mu\text{A}/\text{cm}^2$. For the third, unstable node, v_* appears to be independent of I , judging by the figure; this is in fact almost, but not strictly, true.

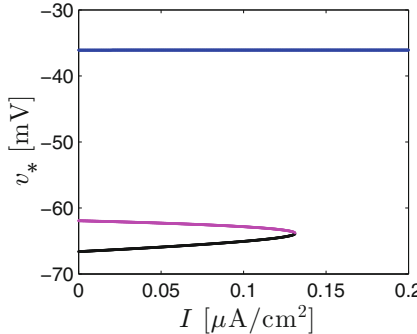


Figure 12.1. Fixed points of the two-dimensional RTM neuron, as a function of I . Black: stable node. Magenta: saddle. Blue: unstable node. [RTM_2D_FP]

How does a saddle-node bifurcation result in the onset of firing in this example? To understand, we compute solutions of (12.1), (12.2) for $I = 0$ (below threshold) and $I = 1$ (above threshold). The left panel of Fig. 12.2 shows the limit cycle for $I = 1$. The middle panel shows a solution for $I = 0$ which converges to the stable fixed point as $t \rightarrow \infty$ and to the saddle as $t \rightarrow -\infty$ — hence the gap. The right panel shows a close-up of the gap, with another solution connecting the unstable fixed point and the stable fixed point added in red. These pictures show that even for $I = 0$, there is an *invariant cycle*, i.e., a closed loop in the phase plane which a trajectory cannot leave. The stable node and the saddle lie on this invariant cycle. When they collide and annihilate each other, the invariant cycle turns into a limit cycle, and oscillations (that is, periodic voltage spikes) begin. One calls this a *saddle-node bifurcation on an invariant cycle (SNIC)*. The simplest example of a SNIC was depicted in Fig. 8.3 already.

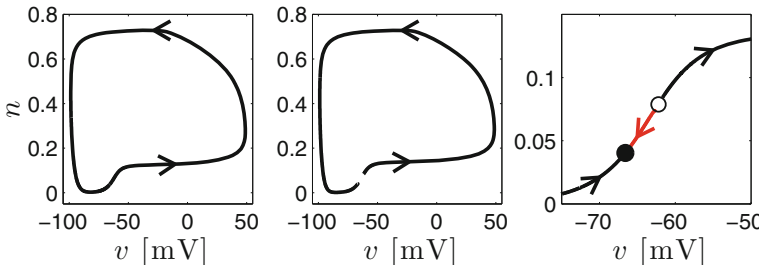


Figure 12.2. Solutions of (12.1), (12.2) for $I = 1$ (left-panel) and $I = 0$ (middle and right panels). [RTM_2D_INVARIANT_CYCLE]

A model neuron is called of *bifurcation type 1* if the passage from $I < I_c$ to $I > I_c$ involves a SNIC [47, 75, 129]. In this bifurcation, the stable fixed point is lost, and a stable limit cycle is established at the same time. The theta neuron is an example; see Fig. 8.3. The RTM and WB models discussed in Chapter 5 are

examples as well, although this is not straightforward to prove, nor even entirely easy to demonstrate convincingly using numerical computations.

There is another class of neuronal models, called models of *bifurcation type 3* in this book, in which the stable fixed point is abolished by a saddle-node bifurcation as well, but not by a SNIC; see Chapter 16.

Exercises

- 12.1. Think about an ODE of the form

$$\frac{dv}{dt} = F(v),$$

where F is a differentiable function with a continuous derivative. Explain: v_* is an attracting fixed point if $F(v_*) = 0$, $F'(v_*) < 0$, and a repelling one if $F(v_*) = 0$, $F'(v_*) > 0$.

- 12.2. If we replace n by $n_\infty(v)$ in (12.1), we obtain

$$\begin{aligned} C \frac{dv}{dt} = & \bar{g}_{\text{Na}} m_\infty(v)^3 (1 - n_\infty(v)) (v_{\text{Na}} - v) \\ & + \bar{g}_K n_\infty(v)^4 (v_K - v) + \bar{g}_L (v_L - v) + I. \end{aligned} \quad (12.6)$$

- (a) Explain: v_* is a fixed point of (12.6) if and only if $(v_*, n_\infty(v_*))$ is a fixed point of (12.1), (12.2).
- (b) (*) (†) Starting with Fig. 12.1, explain: If v_* is a stable fixed point of (12.6), the point $(v_*, n_\infty(v_*))$ may still be an unstable fixed point of (12.1), (12.2).
- 12.3. (*) Starting with the program that you wrote for problem 5.3, simulate the two-dimensional reduced Traub-Miles neuron for $I = 1000 \mu\text{A}/\text{cm}^2$, and for $I = 1500 \mu\text{A}/\text{cm}^2$. In each case, start with $v(0) = -70 \text{ mV}$ and $n(0) = n_\infty(v(0))$, simulate 100 ms, and show the time interval $90 \leq t \leq 100$ in your plot. You will find that for $I = 1000 \mu\text{A}/\text{cm}^2$, there is periodic spiking, but for $I = 1500 \mu\text{A}/\text{cm}^2$, the trajectory comes to rest at a stable fixed point. This is the phenomenon of depolarization block mentioned earlier, but it occurs at quite unrealistically large values of I only in this model.
- 12.4. (*) Make a plot similar to Fig. 12.1, but for $I \leq 2000 \mu\text{A}/\text{cm}^2$. (Use the code that generates Fig. 12.1 as a starting point.) Discuss how the plot matches with exercise 3.
- 12.5. Suppose that J is a real $N \times N$ -matrix, $N \geq 2$. Suppose that $\lambda = a + ib$ is an eigenvalue of J , with $a \in \mathbb{R}$ and $b \in \mathbb{R}$. Show: $\bar{\lambda} = a - ib$ is an eigenvalue of J as well.

Chapter 13

Hopf Bifurcations

In some neuronal models, the transition from $I < I_c$ to $I > I_c$ involves not a SNIC, as in Chapter 12, but a *Hopf bifurcation*. In this chapter, we give a very brief introduction to Hopf bifurcations.

In a Hopf bifurcation, a stable spiral becomes unstable as a bifurcation parameter crosses a critical value. As before, we denote the bifurcation parameter by the letter I , and the critical value by I_c ; in the examples of primary interest to us in this book, I is an input current into a model neuron. We assume that the spiral is stable for $I < I_c$, and unstable for $I > I_c$. (This is just a sign convention: If it were the other way around, we could use $\tilde{I} = -I$ as the bifurcation parameter.) The Jacobi matrix at the fixed point has a complex-conjugate pair of eigenvalues with negative real part for $I < I_c$, and positive real part for $I > I_c$.

Very loosely speaking, the *Hopf bifurcation theorem* states that the loss of stability of a spiral typically involves the creation of oscillations. The precise statement of the theorem is fairly technical, and we will not give it here; see, for instance, [41]. There are two kinds of Hopf bifurcations, called *supercritical* and *subcritical*. We will present the simple examples used in [149] to illustrate these two different kinds of Hopf bifurcations.

Example 13.1 We define a system of two ODEs for the two dependent variables $x = x(t)$, $y = y(t)$, in terms of polar coordinates r and θ (that is, $x = r \cos \theta$, $y = r \sin \theta$). Our equations are

$$\frac{dr}{dt} = Ir - r^3, \quad (13.1)$$

$$\frac{d\theta}{dt} = 1. \quad (13.2)$$

Electronic supplementary material: The online version of this chapter (doi: [10.1007/978-3-319-51171-9_13](https://doi.org/10.1007/978-3-319-51171-9_13)) contains supplementary material, which is available to authorized users.

Equation (13.2) means that the point (x, y) rotates around the origin in the positive (counter-clockwise) orientation at unit angular speed. To understand eq. (13.1), we

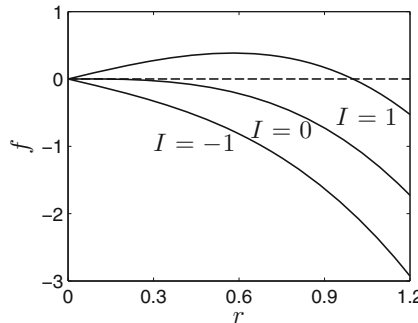


Figure 13.1. Graph of $f(r) = Ir - r^3$ for three different values of I . [HOPF_SUP]

show the graph of $f(r) = Ir - r^3$, $r \geq 0$, for three different values of I in Fig. 13.1. For $I \leq 0$, eq. (13.1) has a stable fixed point at $r = 0$, and no positive fixed points. For $I > 0$, eq. (13.1) has an unstable fixed point at $r = 0$, and a stable one at $r = \sqrt{I}$.

It is easy to translate these statements into statements about $(x(t), y(t))$; compare Fig. 13.2. For $I \leq 0$, $(x(t), y(t)) \rightarrow 0$ as $t \rightarrow \infty$. Thus the origin is a stable fixed point that attracts all solutions; one says that it is *globally attracting*. For $I > 0$ the origin is still a fixed point, but repelling. There is a trajectory traveling along the circle with radius \sqrt{I} centered at the origin.¹⁰ It is an *attracting limit cycle* because nearby trajectories converge to the circle. In fact, *all* trajectories converge to this circle, except for the one that rests at the origin at all times.

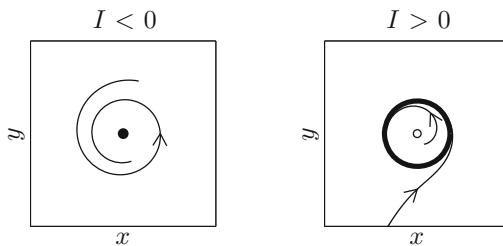


Figure 13.2. Solutions of (13.1), (13.2) for negative and positive I . [HOPF_SUP_PHASE_PLANE]

Fig. 13.3 shows a (somewhat symbolic) *bifurcation diagram*. The solid horizontal line signifies the fixed point at the origin, which is stable for $I \leq 0$ and unstable for $I > 0$. The solid curves for $I > 0$ ($\pm\sqrt{I}$) signify the radius of the attracting limit cycle.

¹⁰Strictly speaking, there are infinitely many such solutions: If $(x(t), y(t))$ is a solution, and if $\tau \in \mathbb{R}$, then $(x(t + \tau), y(t + \tau))$ is a solution as well. However, the distinction between $(x(t + \tau), y(t + \tau))$ and $(x(t), y(t))$ is not visible in a phase plane picture.

As I passes through $I_c = 0$ from below, a stable limit cycle of radius $R(I) = \sqrt{I}$ is created. We say that the limit cycle is created with an *infinitesimally small radius*, since $\lim_{I \rightarrow 0^+} R(I) = 0$. The oscillations in x and y have amplitude $R(I)$. Thus the oscillations are created with an infinitesimally small amplitude, but with a fixed frequency — one oscillation in time 2π . ■

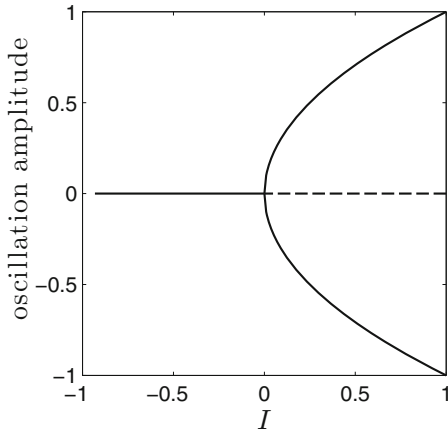


Figure 13.3. Bifurcation diagram for (13.1), (13.2). [HOPF_SUP_BIF_DIAG]

Example 13.2 We now change the sign of the cubic term:

$$\frac{dr}{dt} = Ir + r^3, \quad (13.3)$$

$$\frac{d\theta}{dt} = 1. \quad (13.4)$$

Again eq. (13.4) means that the point (x, y) moves around the origin in the positive (counter-clockwise) orientation at unit angular speed.

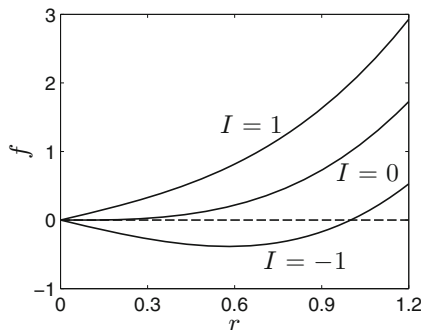


Figure 13.4. Graph of $f(r) = Ir + r^3$ for three different values of I . [HOPF_SUB]

To understand eq. (13.3), we show the graph of $f(r) = Ir + r^3$, $r \geq 0$, for three different values of I in Fig. 13.4. For $I < 0$, eq. (13.3) has a stable fixed point at $r = 0$, and an unstable fixed point at $r = \sqrt{-I}$. For $I \geq 0$, eq. (13.3) has an unstable fixed point at $r = 0$, and no positive fixed point.

We translate these statements into statements about $(x(t), y(t))$; compare Fig. 13.5. For $I < 0$, there is a stable fixed point at $(0, 0)$, and there is an unstable closed orbit traveling along the circle with radius $\sqrt{-I}$ centered at the origin. It is a *repelling limit cycle*, meaning that it would become an attracting limit cycle if the direction of time were reversed. Trajectories inside the circle converge to the origin, while trajectories outside the circle diverge to infinity. For $I \geq 0$, the origin is an unstable fixed point, and there are no other fixed points or closed orbits; all trajectories diverge to infinity, except of course for the one that rests at $(0, 0)$.

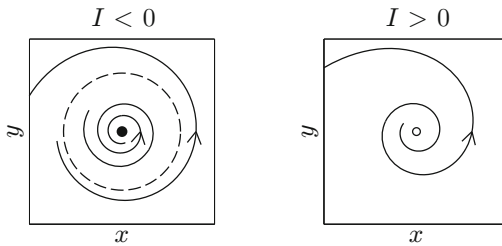


Figure 13.5. *Solutions of (13.3), (13.4) for negative and positive I .* [HOPF_SUB_PHASE_PLANE]

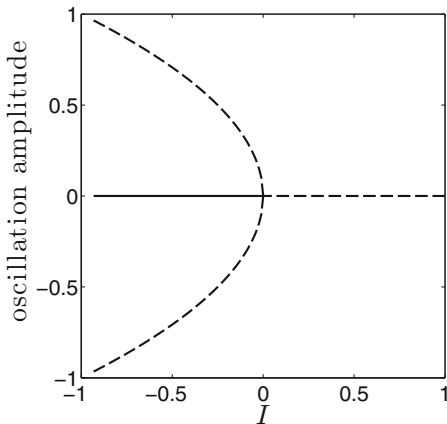


Figure 13.6. *Bifurcation diagram for (13.3), (13.4).* [HOPF_SUB_BIF_DIAG]

Figure 13.6 shows the bifurcation diagram. The horizontal line signifies the fixed point at the origin, which is stable for $I \leq 0$ and unstable for $I > 0$. The dashed curves for $I < 0$ ($\pm\sqrt{-I}$) signify the radius of the repelling limit cycle.

As I approaches $I_c = 0$ from below, the repelling limit cycle of radius $\sqrt{-I}$ encroaches upon the fixed point at the origin. When the repelling limit cycle reaches the origin, the fixed point becomes unstable, and the system is left without any stable structure (fixed point or limit cycle); trajectories diverge to infinity. ■

Note that in example 13.1, oscillations arise as the stable spiral at the origin becomes unstable, whereas no such thing happens in example 13.2. However, the following example shows that the mechanism in 13.2 *can* in fact give rise to oscillations.

Example 13.3 We add to eq. (13.3) a term that keeps the trajectories on the outside of the repelling limit cycle from diverging to infinity:

$$\frac{dr}{dt} = Ir + r^3 - r^5, \quad (13.5)$$

$$\frac{d\theta}{dt} = 1. \quad (13.6)$$

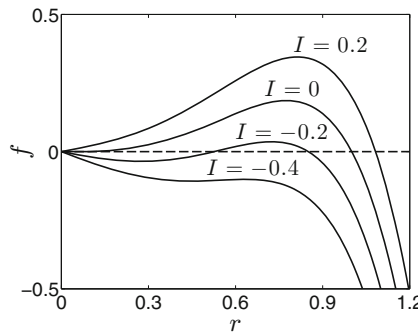


Figure 13.7. Graph of $f(r) = Ir + r^3 - r^5$ for four different values of I .
[HOPF_SUB_2]

To analyze (13.5), we show in Fig. 13.7 the graph of $f(r) = Ir + r^3 - r^5$ for four different values of I . Obviously $f(0) = 0$ always. In exercise 1, you will show:

1. For $I < -1/4$, $f'(0) < 0$, and there are no positive solutions of $f(r) = 0$.
2. For $-1/4 < I < 0$, there are exactly two positive solutions of $f(r) = 0$, namely

$$r_0 = \sqrt{1/2 - \sqrt{1/4 + I}}, \quad \text{and} \quad R_0 = \sqrt{1/2 + \sqrt{1/4 + I}},$$

and $f'(0) < 0$, $f'(r_0) > 0$, and $f'(R_0) < 0$.

3. For $I > 0$, there is exactly one positive solution of $f(r) = 0$, namely

$$R_0 = \sqrt{1/2 + \sqrt{1/4 + I}},$$

and $f'(0) > 0$, $f'(R_0) < 0$.

We translate these statements into statements about $(x(t), y(t))$; compare Fig. 13.8. For $I < -1/4$, $(x(t), y(t)) \rightarrow 0$ as $t \rightarrow \infty$. Thus the origin is a globally attracting fixed point. For $-1/4 < I < 0$, the origin is still a stable fixed point, but there is also an attracting limit cycle, along the circle with radius R_0 centered

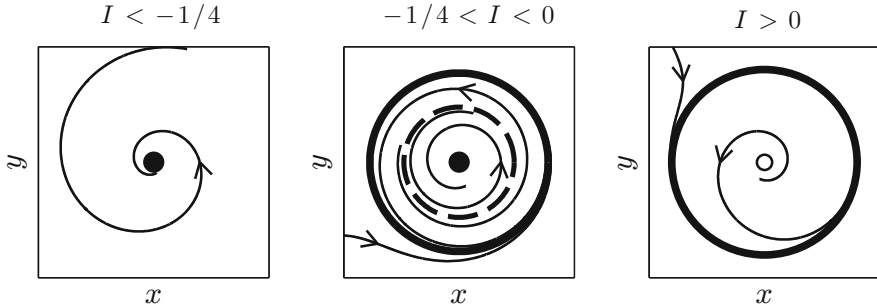


Figure 13.8. Solutions of (13.5), (13.6) for $I < -1/4$, $-1/4 < I < 0$, and $I > 0$. [HOPF_SUB_PHASE_PLANE_2]

at the origin, and there is an unstable closed orbit (a repelling limit cycle), along the circle with radius r_0 centered at the origin. If $(x(0), y(0))$ lies outside the circle with radius r_0 , then $(x(t), y(t))$ converges to the attracting limit cycle; if it lies inside, then $(x(t), y(t))$ converges to the origin. We say that there is *bistability* (the co-existence of two stable structures) for $-1/4 < I < 0$, and that the unstable closed orbit separates the *basins of attraction* of the stable fixed point and the attracting limit cycle. For $I > 0$, the origin is an unstable fixed point, and all trajectories converge to the circle with radius R_0 , of course with the exception of the one that rests at $(0,0)$ for all time.

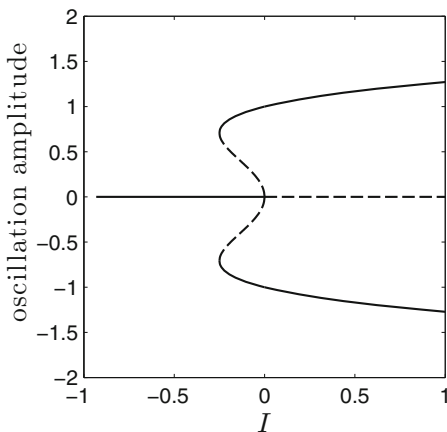


Figure 13.9. Bifurcation diagram for (13.5), (13.6). [HOPF_SUB_BIF_DIAG_2]

Fig. 13.9 shows the bifurcation diagram. The solid horizontal line signifies the fixed point at the origin, which is stable for $I < 0$ and unstable for $I \geq 0$. The

solid curves ($\pm R_0$) signify the stable limit cycle, and the dashed curves ($\pm r_0$) the unstable periodic orbit.

Two bifurcations occur in this example. When I crosses $-1/4$ from below, two limit cycles arise, an attracting and a repelling one. This type of bifurcation is called a *saddle-node bifurcation of cycles*; one might also call it a *blue sky bifurcation of cycles* here, since the two cycles appear “out of the blue” as I is raised. Then, as I crosses 0 from below, the origin becomes unstable just as it did in example 13.2. At that point, the only stable structure left in the system is the attracting limit cycle with radius R_0 .

In contrast with example 13.1, here the onset of oscillations occurs at a non-zero amplitude. In fact, the stable limit cycle always has radius greater than $1/\sqrt{2}$ (the value of $R_0 = r_0$ when $I = -1/4$).

Note that in this example, there are two critical values of I , corresponding to the two bifurcations: The blue sky bifurcation of cycles occurs as I rises above $I_* = -1/4$, and the Hopf bifurcation occurs as I rises above $I_c = 0$. ■

Example 13.1 exhibits a *supercritical* or *soft* Hopf bifurcation, whereas examples 13.2 and 13.3 exhibit *subcritical* or *hard* Hopf bifurcations. The words “soft” and “hard” are easy to understand: The onset of oscillations is at infinitesimally small amplitude in example 13.1, whereas it is at a positive amplitude in example 13.3, and trajectories simply diverge to infinity when $I > I_c$ in example 13.2. To understand the motivation for the words “supercritical” and “subcritical,” look at Figures 13.3 and 13.6. In Fig. 13.3, the “fork” is on the right, *above* I_c — hence *supercritical*. (The convention that “above I_c ” means “on the side of I_c where the fixed point is unstable” is crucial here.) In Fig. 13.6, the “fork” is on the left, *below* I_c — hence *subcritical*.

In fact, the classical Hodgkin-Huxley neuron exhibits both types of Hopf bifurcations as the external drive is varied: The transition from resting at a hyperpolarized membrane potential to periodic firing involves a hard Hopf bifurcation, and the transition from periodic firing to depolarization block, i.e., resting at a depolarized membrane potential, involves a soft Hopf bifurcation; see Fig. 5.7A of [88]. Evidence for the onset of firing via a hard Hopf bifurcation will be given in Chapter 14 for the two-dimensional reduction (10.1), (10.2), and in Fig. 17.1 for the full four-dimensional classical Hodgkin-Huxley model.

Exercises

- 13.1. Derive the properties of f in example 13.3.
- 13.2. Write (a) eqs. (13.1), (13.2) and (b) eqs. (13.3), (13.4) in terms of x and y .
- 13.3. Let $d\theta/dt = 1$ and (a) $dr/dt = Ir - r^2$, (b) $dr/dt = Ir + r^2$. Analyze the behavior of the solutions.
- 13.4. (a) Write the equations in the preceding exercise in terms of x and y .
(b) (†) Show that the right-hand side is once but not twice differentiable $(0, 0)$, whereas the right-hand side in exercise 2 is infinitely often differentiable.

Chapter 14

Model Neurons of Bifurcation Type 2

A neuron is said to be of *bifurcation type 2* if the transition that occurs as I crosses I_c is a Hopf bifurcation [47, 75, 129]. Examples of model neurons of bifurcation type 2 include the classical Hodgkin-Huxley model, and the Erisir model described in Section 5.3. The Hopf bifurcation in the classical Hodgkin-Huxley model is analyzed in great detail in [67]. For numerical evidence that the transition from rest to firing in the Erisir model involves a subcritical Hopf bifurcation, see [17], and also Fig. 17.9.

Here we will consider two-dimensional reductions of these two models, in which $m = m_\infty(v)$ (this assumption was made throughout Chapter 5), and $h = A - n$, where A is approximately the time average of $h + n$ over the limit cycle. (The value of A should then, strictly speaking, be somewhat dependent on I , but we neglect that.) We already discussed such a two-dimensional reduction for the classical Hodgkin-Huxley model in Chapter 10; see eqs. (10.1), (10.2). We will show here that for this model, the transition from rest to spiking involves a subcritical Hopf bifurcation, with a bifurcation structure qualitatively very much like that of example 13.3. We will also study a two-dimensional reduction of the Erisir model. Surprisingly, it turns out that the reduction changes the bifurcation type of the Erisir model: The reduced, two-dimensional Erisir model is of type 1.

We begin with eqs. (10.1), (10.2), the two-dimensional reduction of the classical Hodgkin-Huxley ODEs. First we determine the fixed points of eqs. (10.1), (10.2). Fixed points are points (v_*, n_*) , where $n_* = n_\infty(v_*)$ and $F(v_*) = 0$, with

$$F(v) = \bar{g}_{\text{Na}}m_\infty(v)^3(0.83 - n_\infty(v))(v_{\text{Na}} - v) + \bar{g}_{\text{K}}n_\infty(v)^4(v_{\text{K}} - v) + \bar{g}_{\text{L}}(v_{\text{L}} - v) + I.$$

Solutions of this equation are easy to determine numerically. For a given I between 0 and 15, there is exactly one solution. (A Matlab program that verifies this can

Electronic supplementary material: The online version of this chapter (doi: [10.1007/978-3-319-51171-9_14](https://doi.org/10.1007/978-3-319-51171-9_14)) contains supplementary material, which is available to authorized users.

be found in directory `HH_REDUCED_COUNT_FP`.) It is also easy to compute the Jacobi matrix, J_* , at (v_*, n_*) . We do this using analytic formulas; this is tedious but not hard, since we are given explicit formulas for $m_\infty(v)$, $n_\infty(v)$, and $\tau_n(v)$. One could do it using finite difference quotients approximating partial derivatives as well. We then compute the eigenvalues of J_* to classify the fixed point. The result is shown in Fig. 14.1. A stable spiral turns into an unstable one as I crosses a threshold $I_c \approx 7.4$. This suggests a Hopf bifurcation. The conclusion is confirmed by Fig. 14.2, which shows the eigenvalues of J_* as curves in the complex plane, parametrized by I . The real axis is crossed when I crosses I_c .

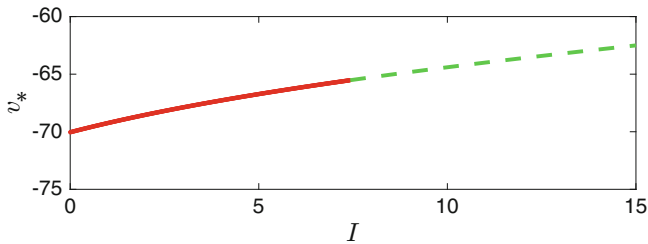


Figure 14.1. The v -coordinate, v_* , of the fixed point of eqs. (10.1), (10.2), as a function of I . The fixed point is a stable spiral for $I < I_c \approx 7.4$ (red, solid), and an unstable spiral for $I > I_c$ (green, dashes). [HH_REDUCED_FIXED_POINTS]

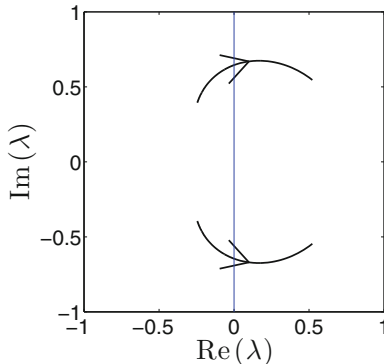


Figure 14.2. The eigenvalues of the fixed points in Fig. 14.1 in the complex plane. The imaginary axis (indicated in blue) is crossed when $I = I_c$. [HH_REDUCED_FP_EVS]

To see whether the Hopf bifurcation is subcritical or supercritical, we compute limit cycles. To compute a picture of an attracting limit cycle is easy: We compute a solution that starts in a point that we expect to be in the basin of attraction of the limit cycle, compute for $0 \leq t \leq T$, but plot the results only for $T - P \leq t \leq T$, where $0 \ll P \ll T$. (We find good choices of P and T by trial and error.) To compute repelling limit cycles is equally easy, since a repelling limit cycle becomes

attracting when the time direction is reversed. Reversing the time direction in a system of differential equations,

$$\frac{dy}{dt} = F(y), \quad (14.1)$$

simply means putting a minus sign in front of the right-hand side: $y = y(t)$ solves (14.1) if and only if $\tilde{y}(t) = y(-t)$ solves

$$\frac{d\tilde{y}}{dt} = -F(\tilde{y}). \quad (14.2)$$

We note that in general the computation of *unstable periodic orbits* is not so easy. In dimensions greater than 2, an unstable periodic orbit may be repelling in one direction, but attracting in another. Such a periodic orbit is said to be *of saddle type*, and does not become attracting when time is reversed; see exercise 1. In fact, we study the reduced, two-dimensional Hodgkin-Huxley model here precisely to avoid this complication.¹¹

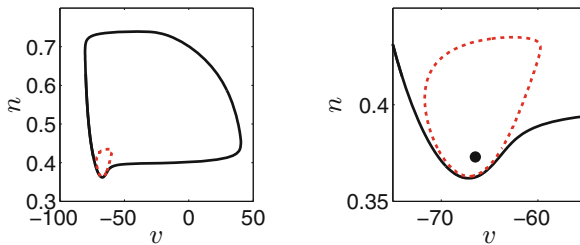


Figure 14.3. Two limit cycles for the reduced, two-dimensional Hodgkin-Huxley model given by eqs. (10.1), (10.2), with $I = 5.5$: An attracting one (solid, black), and a repelling one (red, dashes). The right panel is a close-up of the left. The dot in the right panel indicates the fixed point, which is a stable spiral. [HH_REDUCED_REPELLING_CYCLE]

For instance, for $I = 5.5 < I_c \approx 7.4$, we find an attracting limit cycle, and a repelling one, shown in Fig. 14.3. The diameter of the repelling limit cycle tends to zero as $I \nearrow I_c \approx 7.4$, and it grows as I decreases. As I falls below a second critical value, $I_* \approx 5.2$, both limit cycles disappear. The analogues of I_c and I_* in example 13.3 are 0 and $-1/4$, respectively. As in example 13.3, the distance between the two limit cycles tends to zero as $I \searrow I_*$; see Fig. 14.4.

We now turn to a two-dimensional reduction of the Erisir model. In the simulation shown in Fig. 5.4, the sum $h + n$ approximately varies between 0.27 and 0.40, with a mean of about 0.36. Figure 14.5 shows the voltage trace of Fig. 5.4, and a similar voltage trace computed with the simplification $h = 0.36 - n$. Figure 14.6 shows the fixed points as a function of I . For I between 0 and the critical value

¹¹There are general methods for computing unstable periodic orbits in higher dimensions (see, for instance, [144]), but we won't use them in this book.

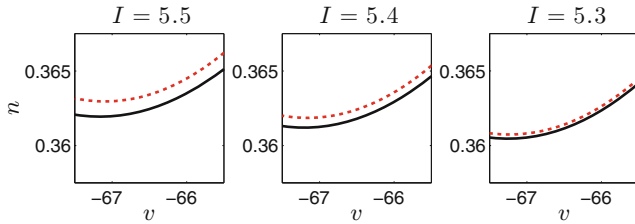


Figure 14.4. Close-up view of the stable and unstable limit cycles, near the “knee” (the lowest point of the stable limit cycle), as $I \searrow I_*$.

[HH_REDUCED_CYCLE_DISTANCE]

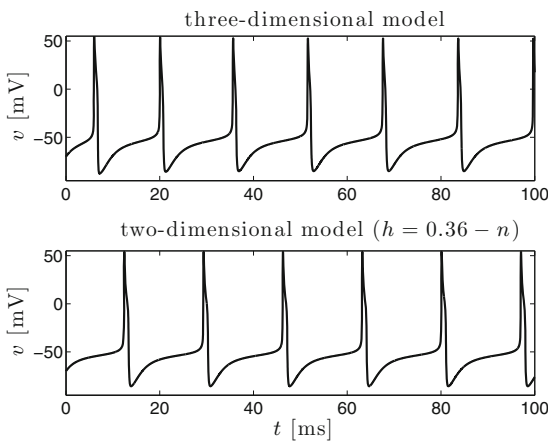


Figure 14.5. Voltage traces of the Erisir model as described in Section 5.3, and of the reduced, two-dimensional model in which $h = 0.36 - n$. [ERISIR_REDUCED]

$I_c \approx 6.3$, there are three fixed points. In order of increasing values of v_* , they are a stable fixed point, a saddle, and unstable node. For the unstable node, v_* is very close to independent of I . The stable fixed point is a stable node for some values of I (solid black), and a stable spiral for others (solid red). As I reaches I_c from below, the stable node and the saddle collide and annihilate each other, and the unstable node is the only fixed point left.

Exercises

14.1. Think about the system

$$\frac{dr}{dt} = r - r^3, \quad \frac{d\theta}{dt} = 1, \quad \frac{dz}{dt} = z,$$

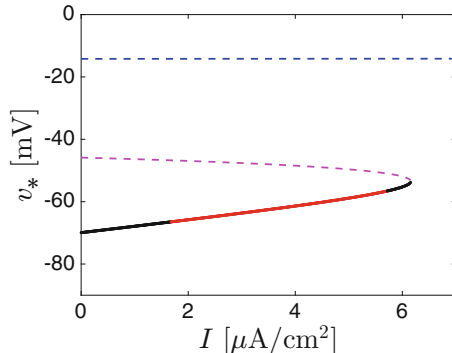


Figure 14.6. Fixed points of the reduced, two-dimensional Erisir model ($h = 0.36 - n$) as a function of I . Black, solid: stable node. Red, solid: stable spiral. Magenta, dashes: saddle. Blue, dashes: unstable node. [ERISIR_2D_FP]

where r and θ are the polar coordinates in the (x, y) -plane: $x = r \cos \theta$, $y = r \sin \theta$. (a) Explain why $x(t) = \text{cost}$, $y(t) = \sin t$, $z(t) = 0$ defines a periodic orbit. (b) Explain why this periodic orbit is unstable. (c) Explain why the periodic orbit would remain unstable if time were reversed.

- 14.2. (*) Think about the FitzHugh-Nagumo equations, (10.6) and (10.7), with $a = 1.25$ and $\tau_n = 25$. (These are the parameters of Fig. 10.5.) (a) Recall from exercise 10.6 that there is exactly one fixed point (v_*, n_*) . Plot v_* as a function of $I \in [-2, 0]$, using color to indicate the nature of the fixed point (stable/unstable node/spiral, or saddle). There is a critical value, $I = I_c$, in the interval $[-2, 0]$, with the property that the fixed point is stable for $I < I_c$, and unstable for $I > I_c$. Numerically compute I_c . (b) Give numerical evidence showing that the transition from $I < I_c$ to $I > I_c$ is a subcritical Hopf bifurcation.¹²

¹²See, however, also Section 15.1, where parameters a and τ_n are given that yield a *supercritical* Hopf bifurcation.

Chapter 15

Canard Explosions

The bifurcation diagrams of neuronal models of bifurcation type 2 usually do not at all look very similar to the idealized bifurcation diagrams in, for instance, Figs. 13.3 and 13.9. Those idealized pictures miss a feature called the *canard explosion*, a sudden extremely rapid growth in the amplitude of periodic spiking, resulting from the spike-generating mechanism of the neuron. What this has to do with “canard” (French for “duck”) will be explained near the end of Section 15.1. There is a very large literature on the theory of canards and their role in neuronal dynamics; see, for example, [8, 40, 99, 120, 134, 177]. The canard phenomenon plays a role in numerous other areas of science and engineering as well; see, for instance, [64, 112, 124, 141]. However, in this chapter, we will merely demonstrate the phenomenon in two very simple two-dimensional examples.

15.1 A Supercritical Canard Explosion

We consider the FitzHugh-Nagumo equations, written as before in the form

$$\frac{dv}{dt} = v - \frac{v^3}{3} - n + I, \quad (10.6)$$

$$\frac{dn}{dt} = \frac{av - n}{\tau_n}, \quad (10.7)$$

with $a = 5$ and $\tau_n = 60$.¹³ The equation has exactly one fixed point; see exercise 10.6a. We denote the fixed point by (v_*, n_*) . It is easy to compute, using

Electronic supplementary material: The online version of this chapter (doi: 10.1007/978-3-319-51171-9_15) contains supplementary material, which is available to authorized users.

¹³ This example is borrowed from [96, Fig. 3]. When the equations in [96] are translated into the form (10.6), (10.7) by scaling and shifting v , n , t , and I , the parameters used in [96, Fig. 3] become $a = 100/21$ and $\tau_n = 175/3$. We use $a = 100/20 = 5$ and $\tau_n = 180/3 = 60$ instead.

$$v_* - \frac{v_*^3}{3} - av_* + I = 0.$$

This equation can be solved using bisection. After that, n_* is obtained from $n_* = av_*$. The fixed point can be classified using the eigenvalues of the Jacobi matrix. Figure 15.1 shows v_* as a function of I , and indicates the classification of the fixed points. As I rises above $I_c \approx -4.29$, the fixed point turns from a stable spiral into an unstable one, in a Hopf bifurcation. In the range of values of I for which the fixed point is unstable, there is a stable limit cycle; we indicate the maximum and minimum of v along the limit cycle as functions of I .

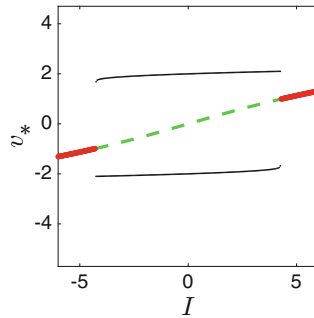


Figure 15.1. Fixed points of the FitzHugh-Nagumo model with $a = 5$ and $\tau_n = 60$. The fixed point is a stable spiral (red, solid) for $I < I_c \approx -4.29$ and $I > |I_c| \approx 4.29$, and an unstable spiral (green, dashes) for $I_c < I < |I_c|$. The thin black lines indicate the maximum and minimum of v along the stable limit cycle.

[FITZHUGH_NAGUMO_MACRO]

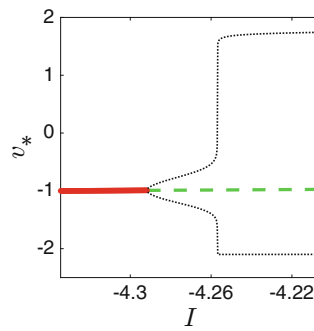


Figure 15.2. Fig. 15.1 under the microscope near $I = I_c$.

[FITZHUGH_NAGUMO_MICRO]

The blow-up of Fig. 15.1 shown in Fig. 15.2 demonstrates that the limit cycle is born at zero amplitude as I rises above I_c . (This is not visible in Fig. 15.1 because the resolution is not high enough.) Thus the Hopf bifurcation is

supercritical.¹⁴ However, the figure also shows something else: As I rises above another critical value, about -4.26 in this example and thus just barely greater than I_c , the amplitude of the periodic solution “explodes.” This abrupt transition from small- to large-amplitude oscillations is called a *canard explosion*.

The canard explosion is *not* a bifurcation. The same unstable fixed point and stable limit cycle exist on both sides of the explosion. Standard results about the continuous dependence of solutions of ordinary differential equations on the right-hand side imply that the diameter of the limit cycle depends on I continuously. However, the expansion of the diameter occurs on an interval of values of I with a width that tends to 0 exponentially fast as $\tau_n \rightarrow \infty$; see, for instance, [99]. We will not formulate this result precisely here, let alone prove it.

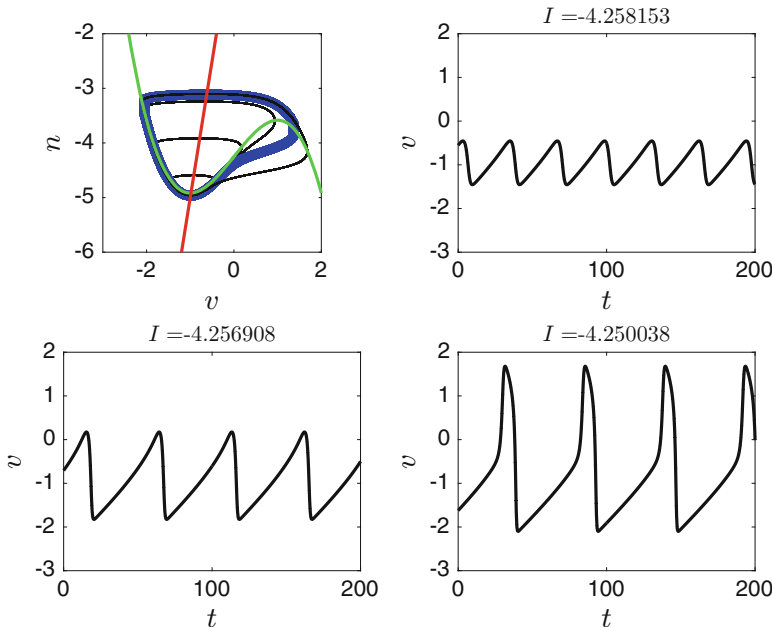


Figure 15.3. *Solutions of the FitzHugh-Nagumo equations with $a = 5$, $\tau_n = 60$, and five different values of I , yielding cycles of increasing diameters. The values of I are -4.258153 , -4.256908 , -4.256906 , -4.256889 (bold blue), and -4.250038 . Left upper panel: Phase plane. The cubic indicated in green is the v -nullcline. The straight line in red is the n -nullcline. Remaining three panels: v as a function of t , for the values of I indicated in the titles. The figure is not entirely Δt -independent; we used $\Delta t = 0.01$ here, as in most simulations in this book. Smaller values of Δt yield qualitatively similar pictures with very slightly different values of I . [CANARD]*

¹⁴This is the only neuronal model discussed in this book in which there is a *supercritical* (soft) Hopf bifurcation at I_c .

Figure 15.3 shows attracting limit cycles for several values of I that are extremely close to each other. For values just barely above I_c , small-amplitude oscillations are possible. As soon as the amplitude becomes somewhat larger, however, the “spike-generating” mechanism of the model is ignited, and the oscillation amplitude explodes. The limit cycle has a small diameter when $I \approx -4.258$, and it is of full size for $I \approx -4.250$.

In this example, one can argue that it is the canard explosion which justifies the idea that action potentials are “all-or-nothing events,” because it dramatically reduces the parameter range in which there are lower-amplitude oscillations instead of full action potentials.

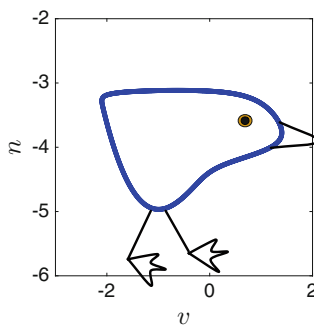


Figure 15.4. The intermediate-size cycle indicated in bold blue in Fig. 15.3, with a few artistic additions explaining what it has to do with a duck.

Some people think that a trajectory like that shown in bold blue in Fig. 15.3 is reminiscent of a duck; see Fig. 15.4 for my best attempt to persuade you. If this leaves you as unconvinced as it leaves me, you can also take “canard” to refer to the Merriam-Webster definition of “canard” [117] as “a false report or story” [176], perhaps because the canard explosion looks very much like a discontinuity, but isn’t one.

Canards are closely related to *mixed-mode oscillations*, i.e., alternation between low-amplitude, subthreshold oscillations, and action potentials; see, for instance, [134]. In fact, it is easy to turn the model discussed in this section into one that generates mixed-mode oscillations. The simplest way of doing this is to add to the external drive I a time-dependent “adaptation current” I_{adapt} , governed by equations of the form

$$I_{\text{adapt}}(t+0) = I_{\text{adapt}}(t-0) - \delta \quad \text{if } v(t-0) = 0, \frac{dv}{dt}(t-0) < 0, \quad (15.1)$$

$$\frac{dI_{\text{adapt}}}{dt} = -\frac{I_{\text{adapt}}}{\tau_{\text{adapt}}} \quad \text{otherwise,} \quad (15.2)$$

with $\delta > 0$ and $\tau_{\text{adapt}} > 0$. Thus I_{adapt} becomes more negative abruptly, by the amount, δ , with each action potential, and returns to zero exponentially with decay time constant τ_{adapt} otherwise. An example is shown in Fig. 15.5.

15.2 A Subcritical Canard Explosion

We return to the two-dimensional reduction of the classical Hodgkin-Huxley equations given by eqs. (10.1), (10.2). We demonstrated earlier that there is a subcritical Hopf bifurcation at $I = I_c$ in this model; see Figs. 14.1, 14.2, and 14.3. We now add to Fig. 14.1 the graphs of the maximum and minimum of v along the stable limit cycle, and along the unstable limit cycle for $I < I_c$, as functions of I . It is

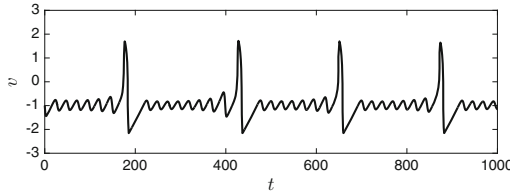


Figure 15.5. Mixed-mode oscillations obtained from the FitzHugh-Nagumo model of Section 15.1 with $I = -4.2$ by adding a simple adaptation current governed by (15.1), (15.2) with $\delta = 0.2$, $\tau_{\text{adapt}} = 150$, and $I_{\text{adapt}} = -\delta$ at time $t = 0$. [MMOS]

now the *unstable* limit cycle which grows as I decreases, then suddenly “explodes,” colliding with and destroying the stable limit cycle (Fig. 15.6). Like supercritical canards, subcritical ones can give rise to mixed-mode oscillations; see [132], and also exercise 6.

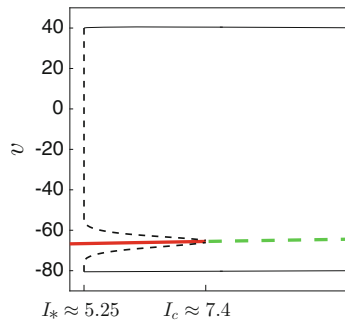


Figure 15.6. The bifurcation diagram for eqs. (10.1), (10.2). Stable spiral (red, solid), unstable spiral (green, dashed), stable limit cycle (black, solid), and unstable limit cycle (black, dashed). The nearly instantaneous rise in amplitude of the unstable limit cycle happens on such a narrow range of values of I that it is difficult to resolve with accuracy; in this figure we simply drew it into the figure as a vertical dashed line. [HH_REDUCED_BIF_DIAG]

Exercises

- 15.1. (a) How do the nullclines in Fig. 15.3 depend on τ_n ? (b) Sketch the nullclines and the solutions of (10.6), (10.7) for $\tau_n = \infty$. (c) The rising portion of the cubic nullcline is often called the *unstable* or *repelling* portion. Explain this terminology based on the sketch you made in part (b).
- 15.2. (†) Figure 15.7 again shows a portion of the “duck” trajectory indicated in bold blue in Fig. 15.3 and, with some artistic additions, in 15.4. The trajectory closely tracks the repelling portion (see exercise 1) of the v -nullcline for quite a while, before veering off to the right. You might first think that

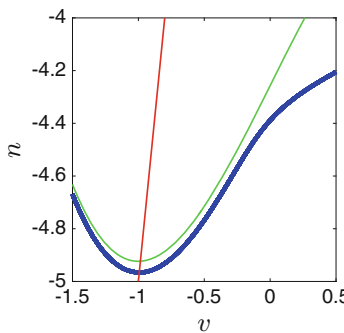


Figure 15.7. A portion of the bold blue trajectory from Figs. 15.3 and 15.4, together with the v -nullcline (green) and the n -nullcline (red straight line). [CANARD_2]

this is impossible: Why does the repelling portion of the cubic not repel the trajectory for such a long time? Explain why this can only happen if the trajectory tracks the v -nullcline at a distance that is exactly $O(1/\tau_n)$ as $\tau_n \rightarrow \infty$. (See Section 1.2 for the meaning of “exactly $O(1/\tau_n)$ ”.) Your explanation will not be rigorous, but it should be convincing.

- 15.3. (*) For the “duck” trajectory indicated in bold blue in Figs. 15.3 and 15.4, plot v as a function of t . You will see v rise linearly with t for a significant portion of the cycle, between action potentials. How is this reflected in Fig. 15.7?
- 15.4. (*) What happens if you increase τ_{adapt} in Fig. 15.5? What happens if you increase δ ? Guess before you try it.
- 15.5. (*) Can you choose parameters in Fig. 15.5 so that bursts of several action potentials (not just one) alternate with subthreshold oscillations?
- 15.6. (*) Can you generate mixed-mode oscillations by adding an adaptation current as in Section 15.1 to the reduced Hodgkin-Huxley model of Section 15.2? Would you choose a drive I just above I_* , or just above I_c ?

Chapter 16

Model Neurons of Bifurcation Type 3

In neuronal models of bifurcation type 2 (Chapter 14), the possibility of stable rest is abolished via a Hopf bifurcation as I rises above I_c , and the possibility of stable periodic firing is abolished via a collision of the stable limit cycle with an unstable periodic orbit as I falls below I_* , with $I_* < I_c$. In neuronal models of bifurcation type 1 (Chapter 12), there is no distinction between I_* and I_c ; stable rest is abolished as I rises above I_c , and stable periodic firing is abolished as I falls below I_c .

Here we discuss yet another class of neuronal models, which we will call *of bifurcation type 3*, in which the possibility of stable rest is abolished via a saddle-node bifurcation as I rises above I_c , and the possibility of stable periodic firing is abolished via a collision of the stable limit cycle with a saddle as I falls below I_* , with $I_* < I_c$. Models of this kind have been discussed in the literature; see in particular [82]. However, there is no universally adopted name for them; while “type 1” and “type 2” are standard terminology, “type 3” is not. We will study two examples of model neurons of bifurcation type 3.

16.1 Izhikevich’s $I_{\text{Na,p}}-I_K$ Model

This example is due to Eugene Izhikevich [82], and is called the *persistent sodium and potassium model* or $I_{\text{Na,p}}-I_K$ model. Action potentials in this model result from the interaction of two currents, a sodium and a potassium current, just as in the Hodgkin-Huxley-like models discussed earlier. However, here the sodium current is *persistent*.

In general, a voltage-activated current is called *persistent* or *non-inactivating* if the channel that the current passes through has no inactivation gate. A current

Electronic supplementary material: The online version of this chapter (doi: [10.1007/978-3-319-51171-9_16](https://doi.org/10.1007/978-3-319-51171-9_16)) contains supplementary material, which is available to authorized users.

that is not persistent is called *transient* or *inactivating*. In the classical Hodgkin-Huxley model, the sodium current is transient, while the potassium current is persistent. If the factor of h in the expression for the sodium current were absent, the sodium current would be persistent, too. Note that “persistent” does not mean “always present.” A persistent current can very well shut down as a result of hyperpolarization. (This is called *de-activation* to distinguish it from *inactivation*; see Section 3.2.) Persistent sodium currents are ubiquitous in the brain [30]. They raise the neurons’ excitability, and are thought to play a role in epilepsy [147].

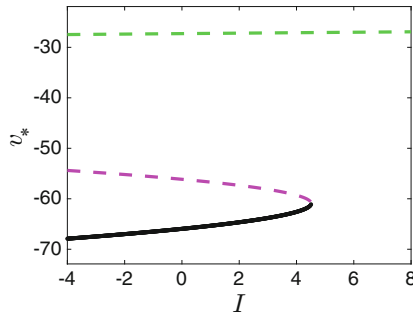


Figure 16.1. Fixed points of the $I_{\text{Na,p}}-I_{\text{K}}$ model as a function of I . For $I < I_c \approx 4.5$, there are a stable node (black, solid), a saddle (magenta, dashes), and an unstable spiral (green, dashes). When I reaches I_c , the saddle and the stable node collide and annihilate each other, and only the unstable spiral remains.
[INAPIK_FIXED_POINTS]

Izhikevich’s $I_{\text{Na,p}} - I_{\text{K}}$ model is of the form

$$C \frac{dv}{dt} = \bar{g}_{\text{Na}} m_\infty(v)(v_{\text{Na}} - v) + \bar{g}_{\text{K}} n(v_{\text{K}} - v) + \bar{g}_L(v_{\text{L}} - v) + I, \quad (16.1)$$

$$\frac{dn}{dt} = \frac{n_\infty(v) - n}{\tau_n}. \quad (16.2)$$

In contrast with all Hodgkin-Huxley-like models discussed earlier, no powers of gating variables appear in (16.1). The activation gate of the sodium current is assumed to be infinitely fast, i.e., a function of v , reducing the number of dependent variables to two (v and n). Izhikevich’s parameter choices are [82]

$$C = 1 \text{ } \mu\text{F}/\text{cm}^2, \quad \bar{g}_{\text{Na}} = 20 \text{ } \text{mS}/\text{cm}^2, \quad \bar{g}_{\text{K}} = 10 \text{ } \text{mS}/\text{cm}^2, \quad \bar{g}_L = 8 \text{ } \text{mS}/\text{cm}^2,$$

$$v_{\text{Na}} = 60 \text{ mV}, \quad v_{\text{K}} = -90 \text{ mV}, \quad v_{\text{L}} = -80 \text{ mV}.$$

We use $\tau_n = 0.15 \text{ ms}$ here, very close to the value used in [82, Fig. 4.23]. Thus the potassium activation gate, n , while not infinitely fast, is extremely fast. The functions m_∞ and n_∞ are

$$m_\infty(v) = \frac{1}{1 + \exp((-20 - v)/15)} \quad \text{and} \quad n_\infty(v) = \frac{1}{1 + \exp((-25 - v)/5)}. \quad (16.3)$$

Both are increasing functions of v , i.e., both the m -gate and the n -gate are activation gates.

To examine bifurcations in this model, we compute the fixed points of eqs. (16.1), (16.2), and classify them by computing the eigenvalues of the Jacobi matrix. For a given I , the fixed points are obtained by finding all solutions of the equation

$$\bar{g}_{\text{Na}} m_\infty(v)(v_{\text{Na}} - v) + \bar{g}_K n_\infty(v)(v_K - v) + \bar{g}_L(v_L - v) + I = 0.$$

(v_*, n_*) is a fixed point if and only if v_* solves this equation and $n_* = n_\infty(v_*)$. Figure 16.1 shows the result of this calculation. At $I = I_c \approx 4.5$, there is a saddle-node collision.

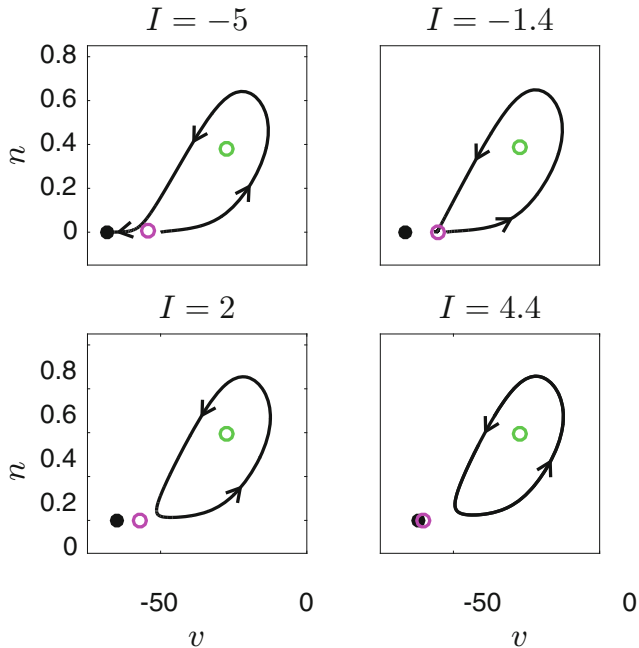


Figure 16.2. Phase plane picture for the $I_{\text{Na},p}$ - I_K model showing co-existence of a stable limit cycle, a stable node (black solid dot), a saddle (magenta open circle), and an unstable spiral (green open circle). The saddle and the node collide when $I = I_c \approx 4.5$ (right lower panel), and the saddle destroys the limit cycle by inserting itself into the cycle when $I = I_* \approx -1.4$ (right upper panel). [INAPIK_PHASE_PLANE]

The left lower panel of Fig. 16.2 shows the (v, n) -plane for $I = 2$. We see that a stable fixed point and stable limit cycle co-exist here. As $I \nearrow I_c \approx 4.5$, the saddle and the node collide and annihilate each other (right lower panel of the figure). As $I \searrow I_* \approx -1.4$, the saddle inserts itself into the limit cycle, and this abolishes the limit cycle (right upper panel), turning it into a trajectory that originates from the

saddle in the unstable direction and returns to the saddle in the stable direction. Such a trajectory is called *homoclinic*. The bifurcation in which a saddle inserts itself into a limit cycle, turning the limit cycle into a homoclinic trajectory, is also called a *homoclinic bifurcation* [149].

In summary, in this example the stable fixed point is abolished in a saddle-node collision *off* an invariant cycle as I rises above I_c . The limit cycle is abolished in a homoclinic bifurcation (a saddle-cycle collision) as I falls below I_* .

16.2 The Self-Exciting Theta Neuron

We consider a theta neuron as written by Ermentrout and Kopell in [49]:

$$\frac{d\theta}{dt} = 1 - \cos \theta + I(1 + \cos \theta). \quad (16.4)$$

Compare exercise 8.3, and note that we now write I for the quantity called J in exercise 8.3. We think of this neuron as representing a population of neurons firing in synchrony.

We add a time-dependent excitatory term:

$$\frac{d\theta}{dt} = 1 - \cos \theta + (I + z(t))(1 + \cos \theta), \quad (16.5)$$

which we assume to rise abruptly in response to a spike (passage through $\theta = \pi$ modulo 2π):

$$z(t+0) = z_{\max} \quad \text{if} \quad \theta(t-0) = \pi \text{ modulo } 2\pi, \quad (16.6)$$

with $z_{\max} > 0$, and decay exponentially otherwise:

$$\frac{dz}{dt} = -\frac{z}{\tau_z}, \quad (16.7)$$

with $\tau_z > 0$. For aesthetic appeal, we add a reset condition for θ :

$$\theta(t+0) = -\pi \quad \text{if} \quad \theta(t-0) = \pi \text{ modulo } 2\pi, \quad (16.8)$$

but note that this reset condition is in fact without any impact since the right-hand side of eq. (16.5) does not change when θ is replaced by $\theta \pm 2\pi$. We call the model defined by eqs. (16.5)–(16.8) the *self-exciting theta neuron*. For illustration, we show in Fig. 16.3 a solution for one particular choice of parameters.

Notice that our model is not a system of ordinary differential equations, because of the discontinuous reset of z . For readers who like differential equations models (as I do), we will later make the reset of z smooth, turning the model into a system of ordinary differential equations while keeping its essential behavior unchanged; see eqs. (16.9) and (16.10).

Just as we think of the single theta neuron as representing a synchronized population of neurons, we think of z as representing *recurrent excitation*, i.e., mutual excitation of the neurons in the population. One could therefore argue that discussion of the self-exciting theta neuron should be deferred to part III of this

book, where we will study mechanisms of neuronal communication; however, we discuss it here as a simple example of a model of bifurcation type 3.

Recurrent excitation is known to be important for the transient maintenance of neuronal activity representing *working memory*, i.e., items that are held in memory for just a few seconds for the purpose of completing a current task; see, for instance, [60]. Keeping in mind a phone number between looking it up and dialing it is an example. There is evidence that rhythmicity plays a role in working memory [1, 102, 188]. Rhythmicity of neuronal network activity is typically the result of synchronization; see part IV of this book. Taken together, these considerations motivate our interest in (16.5)–(16.8) as a very simple model of recurrent excitation in a synchronized network.

Eqs. (16.5) and (16.7) form a system of ordinary differential equations, which we will now study for $-\pi < \theta < \pi$. For $I < 0$, the system has the two fixed points $(\theta_{\pm}, 0)$, where θ_{\pm} are the fixed points of the theta neuron without self-excitation, given by eq. (8.10) with $\tau_m = 1/2$. It is easy to see that $(\theta_-, 0)$ is a stable node, and $(\theta_+, 0)$ a saddle; see exercise 1. As I rises above $I_c = 0$, the two fixed points collide and annihilate each other. Thus the possibility of stable rest is abolished by a saddle-node bifurcation in the self-exciting theta neuron.

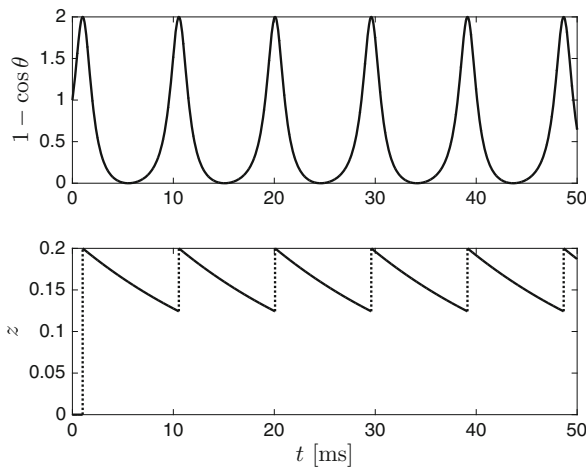


Figure 16.3. Solution of eqs. (16.5)–(8.9) with $I = -0.05$, $z_{\max} = 0.2$, $\tau_z = 20$, $\theta(0) = \pi/2$, and $z(0) = 0$. By setting $\theta(0) = \pi/2$, we force an initial spike (passage through $\theta = \pi$ modulo 2π), which raises z to z_{\max} , enabling sustained firing. We plot $1 - \cos \theta$ because it is a quantity that exhibits a spike when θ passes through π modulo 2π . [SELF_EXCITING_THETA_NEURON]

Even for $I < I_c$, periodic firing is possible for the self-exciting theta neuron, because of the self-excitation term. To understand how the possibility of periodic firing is abolished, it is instructive to plot examples of solutions of (16.5), (16.7) in the (θ, z) -plane for various values of I . Figure 16.4 shows solutions for $z_{\max} = 0.2$, $\tau_z = 20$. (Our choice of $\tau_z = 20$ will be discussed later in this section; see also

exercise 2.) For these parameter values, periodic firing is possible if and only if $I > I_*$, with $I_* = -0.1069\dots$. In each panel of the figure, we indicate in bold the trajectory that starts at $\theta = -\pi$ and $z = z_{\max}$, the point in the (θ, π) -plane to which the self-exciting theta neuron resets after firing. Periodic firing occurs if and only if this trajectory reaches $\theta = \pi$. In panel A of the figure, $I = -0.15$, significantly below I_* , and the trajectory starting at $(\theta, z) = (-\pi, z_{\max})$ ends in the stable node $(\theta_-, 0)$; there is no periodic firing. In panel B, the value of I is very slightly above I_* . The trajectory indicated in bold now reaches $\theta = \pi$, so there is periodic firing. Before it reaches $\theta = \pi$, it passes the saddle point $(\theta_+, 0)$ at a small distance. The range of values $I > I_*$ for which the periodic cycle comes close to the saddle is quite narrow, but if I were even closer to (but still greater than) I_* , the trajectory would come even closer to the saddle. In panel C, $I > I_*$, but $I < I_c = 0$. Periodic firing is possible, but the stable node and the saddle are still present. Panel D shows solutions for $I > I_c = 0$, when there are no fixed points any more.

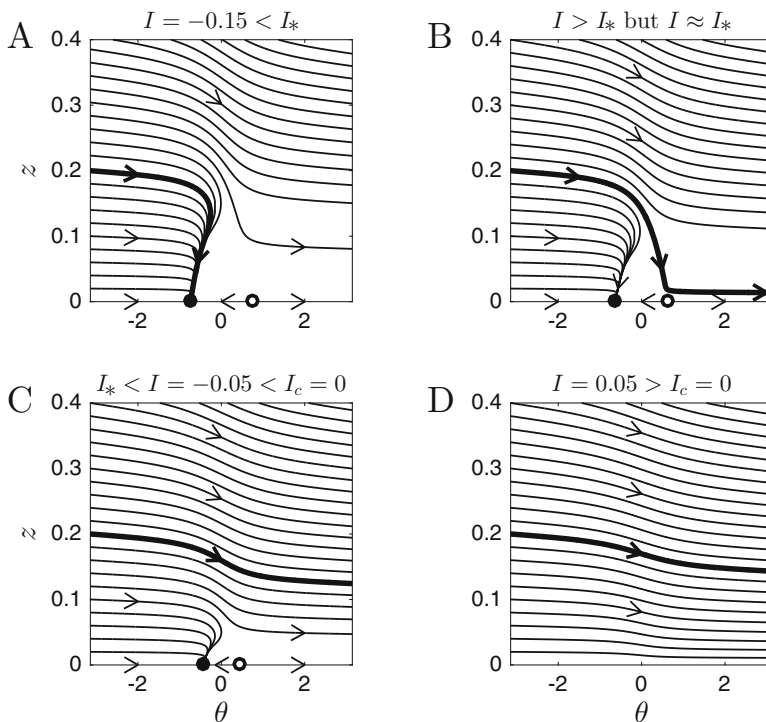


Figure 16.4. Solutions of eqs. (16.5) and (16.7) with $z_{\max} = 0.2$ and $\tau_z = 20$. For these parameter values, periodic firing is possible if and only if $I > I_* = -0.1069\dots$. In panel B, I is very slightly above I_* . The values of I in the three other panels are specified above those panels. In each panel, the trajectory starting at $\theta = -\pi$ and $z = z_{\max}$ is indicated as bold curve. [SETN_PHASE_PLANE]

Figure 16.4 clarifies what happens as I drops below I_* : The saddle inserts itself into the periodic cycle, turning it into a homoclinic trajectory when I is precisely equal to I_* , and then, for $I < I_*$, into a trajectory that converges to the stable node (panel A). For short, the self-exciting theta neuron is of bifurcation type 3.

We will now discuss our choice $\tau_z = 20$ for our illustrative figures in this section. As discussed earlier, the self-exciting theta neuron can be thought of as a caricature of rhythmic working memory activity driven by recurrent excitation. The recurrent excitation underlying working memory is known to be NMDA receptor-mediated [171]. NMDA receptor-mediated recurrent excitation is relatively slow; a decay time constant on the order of 100 ms or longer is typical (see Chapter 1). Since we always think of time as measured in ms, even when working with reduced models such as the theta model, it would have seemed natural to choose $\tau_z = 100$ in this section. We chose $\tau_z = 20$ because that makes it easier to obtain a picture convincingly demonstrating the saddle-cycle collision such as panel B of Fig. 16.4. The phase plane pictures for $\tau_z = 100$ look qualitatively just like those in Fig. 16.4 (see exercise 2), but the range of values of $I > I_*$ for which the periodic trajectory comes close to the saddle is extremely narrow for $\tau_z = 100$, even narrower than for $\tau_z = 20$.

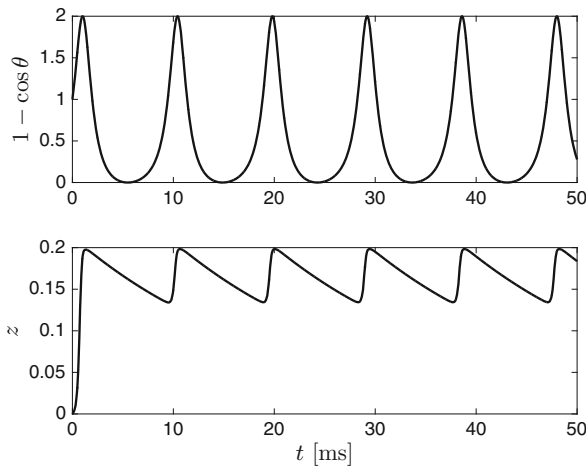


Figure 16.5. Solution of eqs. (16.9) and (16.10) with $I = -0.05$, $z_{\max} = 0.2$, $\tau_z = 20$, $\theta(0) = \pi/2$, and $z(0) = 0$. [SELF_EXCITING_THETA_SMOOTH]

As promised earlier, we turn the self-exciting theta neuron into a system of differential equations now:

$$\frac{d\theta}{dt} = 1 - \cos \theta + (I + z)(1 + \cos \theta), \quad (16.9)$$

$$\frac{dz}{dt} = -\frac{z}{\tau_z} + 10e^{-5(1+\cos\theta)}(z_{\max} - z). \quad (16.10)$$

When $\cos \theta \approx -1$, i.e., $\theta \approx \pi$ modulo 2π , then the term $10e^{-5(1+\cos\theta)}(z_{\max} - z)$ is close to $10(z_{\max} - z)$, and rapidly drives z towards z_{\max} . When $\cos \theta$ is not close

to -1 , then $10e^{-5(1+\cos\theta)}(z_{\max} - z) \approx 0$, and therefore eq. (16.10) approximately describes exponential decay of z with time constant τ_z . For illustration, we show in Fig. 16.5 a solution for one particular choice of parameters; compare this figure with Fig. 16.3. The model given by eqs. (16.9) and (16.10) is of bifurcation type 3 as well (exercise 3). Since $\theta = \theta(t)$ can be thought of as a moving point on the unit circle in the (x, y) -plane by writing $x = \cos\theta$ and $y = \sin\theta$, we can also think of (16.9) and (16.10) as describing motion of a point on the cylinder

$$\{(x, y, z) : x^2 + y^2 = 1, z \in \mathbb{R}\}.$$

If self-excitation triggered by firing is added to an RTM neuron, the resulting model becomes type 3 as well; see Section 20.3. It seems plausible that the same would be true for most if not all model neurons of bifurcation type 1. If we start with any model neuron, and add self-excitation that is (completely) absent in the absence of firing, it is in any case clear that in the resulting composite model, the possibility of stable rest is abolished by the same mechanism as in the original model, since the self-excitation remains dormant as long as the neuron rests. Thus adding firing-dependent self-excitation to a type 1 model neuron must always result in a model in which the possibility of stable rest is abolished by a saddle-node collision.

Exercises

- 16.1. Explain why for $I < 0$, the fixed point $(\theta_+, 0)$ of eqs. (16.5), (16.7) is a saddle, and $(\theta_-, 0)$ is a stable node.
- 16.2. (*) Generate a figure similar to Fig. 16.4 with $z_{\max} = 0.05$, $\tau_z = 100$.
- 16.3. (*) Generate an analogue of Fig. 16.4 for the smooth self-exciting theta neuron given by (16.9) and (16.10), demonstrating numerically that it is of bifurcation type 3.

Chapter 17

Frequency-Current Curves

In this chapter, we study the periodic firing frequency, f , of a model neuron as a function of input current density, I . The graph of f as a function of I is commonly called the *frequency-current curve*, or *f-I curve*, of the model neuron. The *f-I* curve summarizes important features of the dynamics of a neuron in a single picture.

17.1 Computation of f-I-Curves

When plotting *f-I* curves, we disregard *unstable* fixed points and unstable periodic orbits. Nonetheless it is not always true that for a given I , there is only one possible (stable) frequency f . We saw this in Chapter 14, where we found an interval of values of I in which both rest and periodic firing are possible and stable. The “*f-I* curve” of those model neurons has two branches; nonetheless we still use the phrase “*f-I* curve” for it.

For simple models such as the LIF and theta neuron, the *f-I* curve can easily be computed by hand. For Hodgkin-Huxley-like model neurons, it can only be computed numerically. We will begin by describing the numerical procedure that we use to do this.

Given a value of I , and a starting point in phase space, one of two things happens for all models considered here: The solution of the differential equations of the model neuron converges to a stable fixed point, or to a stable limit cycle. Of course, neither of these two would happen if the starting point were *precisely* an unstable fixed point, or belonged to an unstable periodic orbit; but in simulations this is never seen because of numerical and round-off errors.

In practice, we say that a steady state has been reached when none of the phase space variables changes by more than a small relative amount (we often use

Electronic supplementary material: The online version of this chapter (doi: [10.1007/978-3-319-51171-9_17](https://doi.org/10.1007/978-3-319-51171-9_17)) contains supplementary material, which is available to authorized users.

0.01%) over a substantial time period (we often use 1000 ms). When there is periodic spiking, we compute the frequency by first computing the times of the action potentials. Strictly speaking, of course, action potentials are events of positive duration, so the *time of the action potential* is not well-defined. We make an arbitrary convention, which we use throughout this book: We call the time at which v crosses -20 mV *from above* the *spike time* or the *time of the action potential*. Exercise 1 describes how we compute spike times numerically. In this chapter, we are interested in firing *periods*, not in absolute spike times, and therefore the arbitrariness of this convention has no impact. Our convention is a bit unusual, but it has some advantages. In particular, it avoids minor artifacts that arise in the *phase response curves* of Chapter 25 if the spike times are defined, more conventionally, as the times at which v crosses 0 from below. When there is an infinite sequence of action potentials, we denote the spike times by t_1, t_2, t_3, \dots .

Given a value of I and a starting position in phase space, we compute until either a steady state is reached or four spikes occur. If a steady state is reached, we set $f = 0$, otherwise $f = 1000/(t_4 - t_3)$. The numerator of 1000 is needed here because we measure time in ms but frequency in Hz=s⁻¹; see the discussion preceding eq. (7.10). We use t_3 and t_4 (not t_1 and t_2) to reduce initial transient effects.

For each model neuron, we calculate the f - I curve for $I_L \leq I \leq I_R$, where I_L is chosen so low that for $I = I_L$, there is a globally attracting fixed point. For all models considered here, numerical experiments indicate that there is a globally attracting fixed point when I is low enough (see exercise 2 for the proof of a weaker statement). We discretize the interval $[I_L, I_R]$, performing simulations for $I = I_j = I_L + j\Delta I = (I_R - I_L)/N$, where N is a large integer.

To capture the multi-valued nature of the f - I relation when the transition from rest to firing involves a subcritical Hopf bifurcation, we sweep through the values $I = I_j$ twice, first upwards, in the order of increasing j , then downwards, in the order of decreasing j . On the upward sweep, we start the simulation for $I = I_j$ in the point in phase space in which the simulation for $I = I_{j-1}$ ended, $j = 1, 2, \dots, N$. Note that it does not matter where in phase space we start the simulation for $I = I_0 = I_L$ — the result will always be convergence to the globally attracting fixed point, so $f = 0$. On the downward sweep, we start the simulation for $I = I_j$ in the point in phase space where the simulation for $I = I_{j+1}$ ended, $j = N-1, N-2, \dots, 0$. (For $I = I_N = I_R$, only one simulation is carried out, which we consider to be part of both sweeps.) In the interval of values of I for which there is bistability, the upward sweep captures the stable fixed point, and the downward one captures the stable limit cycle.

As a first example, we show in Fig. 17.1 the f - I curve of the classical Hodgkin-Huxley neuron. The dots indicate the results of the upward sweep, and the circles the results of the downward sweep. Thus in the range of bistability, dots reflect stable fixed points, and circles reflect stable limit cycles. There are two branches of the f - I curve, one indicated with dots and the other with circles; we call them the *lower branch* and the *upper branch* of the f - I curve, respectively. Outside the region of bistability, the lower and upper branches of the f - I curve coincide. The lower branch is discontinuous at $I = I_c \approx 9.7$, where the Hopf bifurcation occurs. The

upper branch is discontinuous at $I = I_* \approx 6.1$, where the saddle-node bifurcation of cycles occurs.

Because of the discontinuities in the lower and upper branches of the f - I curve, the classical Hodgkin-Huxley neuron has *discontinuous firing onset* as I rises above I_c , and *discontinuous firing offset* as I falls below I_* . The distinction be-

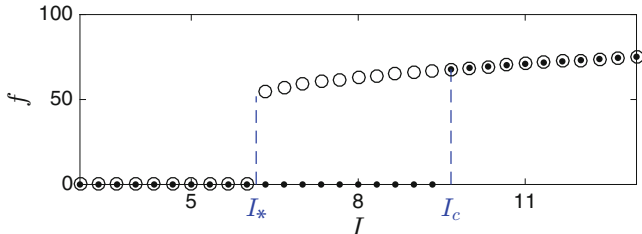


Figure 17.1. f - I curve of the classical Hodgkin-Huxley neuron. Dots refer to the upward sweep, and circles to the downward sweep. [HH_F_I_CURVE]

tween continuous and discontinuous onset was first described, based on experimental observations, in 1948 by Alan Hodgkin [75], who called neurons with continuous onset *class 1*, and neurons with discontinuous onset *class 2* neurons.

17.2 Examples of Continuous, Single-Valued f-I Curves

LIF Neuron

For the normalized LIF neuron, given by eqs. (7.6) and (7.7), eqs. (7.9) and (7.10) imply

$$f = \begin{cases} \frac{1000}{\tau_m \ln(\tau_m I / (\tau_m I - 1))} & \text{if } I > 1/\tau_m, \\ 0 & \text{otherwise} \end{cases} \quad (17.1)$$

For $\tau_m = 10$, Fig. 17.2 shows f as a function of I . For large I , the dependence of f

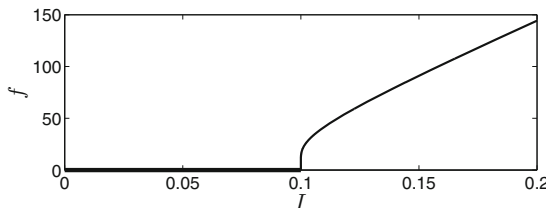


Figure 17.2. f - I curve of normalized LIF neuron with $\tau_m = 10$. [LIF_F_I_CURVE]

on I is almost linear: In the limit as $I \rightarrow \infty$,

$$f \sim 1000I, \quad (17.2)$$

and more precisely (see exercise 5)

$$\lim_{I \rightarrow \infty} (f - 1000I) = -\frac{500}{\tau_m}. \quad (17.3)$$

Near firing onset, the f - I curve is “steep to infinite order,” in the sense that its inverse is flat to infinite order. To see this, solve (17.1) for I , assuming $I \geq I_c = 1/\tau_m$:

$$I = \begin{cases} \frac{1}{\tau_m} \frac{1}{1 - e^{-1000/(\tau_m f)}} & \text{if } f > 0, \\ \frac{1}{\tau_m} & \text{if } f = 0. \end{cases} \quad (17.4)$$

(This is the inverse function of $f = f(I)$, $I \geq I_c$.) At $f = 0$, all derivatives of I with respect to f are zero; see exercise 6.

Theta Neuron

For the theta neuron, eq. (8.11) implies

$$f = \frac{1000\sqrt{4\tau_m I - 1}}{2\pi\tau_m}.$$

Using the notation

$$I_c = \frac{1}{4\tau_m}$$

for the threshold drive, we re-write the formula for f as

$$f = \frac{1000}{\pi\sqrt{\tau_m}} \sqrt{I - I_c}. \quad (17.5)$$

For $\tau_m = 1/2$ (the value used by Ermentrout and Kopell [49]), the f - I curve is shown in Fig. 17.3.

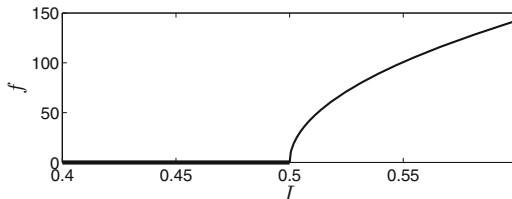


Figure 17.3. f - I curve of the theta neuron with $\tau_m = 1/2$. [\[THETA_F_I_CURVE\]](#)

According to eq. (17.5), the f - I relation of the theta neuron is of the form

$$f = C\sqrt{I - I_c} \quad \text{for } I \geq I_c, \quad (17.6)$$

with $C > 0$. The theta neuron is of bifurcation type 1. In fact, for *any* neuronal model of bifurcation type 1,

$$f \asymp \sqrt{I - I_c} \quad (17.7)$$

as $I \searrow I_c$. (See Section 1.2 for the meaning of “ \searrow ”.) The calculation at the end of Chapter 11 explains why: The period is dominated by the time it takes to move past the “ghost” of the two fixed points annihilated in the saddle-node collision, and this time is $\asymp 1/\sqrt{I - I_c}$, therefore the frequency is $\asymp \sqrt{I - I_c}$.

From (17.7), it follows that the f - I curve of a model neuron of bifurcation type 1 has a (right-sided) infinite slope at $I = I_c$. However, it is still much less steep than the f - I curve of the LIF neuron. To understand in which sense this is true, think of I as a function of $f \geq 0$. Solving (17.6), we obtain

$$I - I_c = \frac{f^2}{C^2},$$

so $I - I_c$ vanishes to second order at $f = 0$ for the theta neuron, and, more generally, for a model neuron of bifurcation type 1. For the LIF neuron, we showed that $I - I_c$, as a function of f , vanishes to infinite order at $f = 0$.

RTM Neuron

For the RTM model neuron, we calculate the f - I curve numerically, as described in Section 17.1. The upward and downward sweeps yield the same result; for each I , there is only one possible (stable) f ; the dots and circles coincide — see Fig. 17.4. The dependence of f on I is continuous. For $I > I_c$ but $I \approx I_c$, the form of the f - I curve is approximately $f = C\sqrt{I - I_c}$, where $C > 0$ is a constant. Figure 17.5 shows computed frequencies for I near I_c , together with the graph of a function of the form $f = C\sqrt{I - I_c}$, where the values of C and I_c are chosen to make the fit with the computed data good: $I_c \approx 0.11935$, $C \approx 54$. (We omit a description of how these parameters were estimated; the interested reader can take a look at the code that generates Fig. 17.5.)

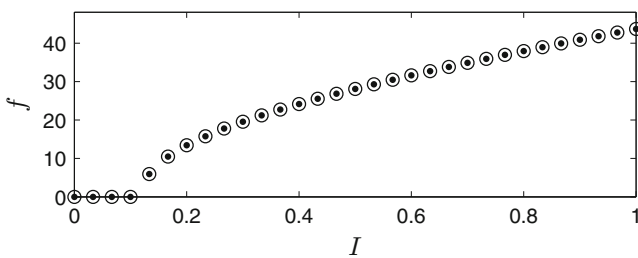


Figure 17.4. f - I curve of the RTM neuron. [RTM_F_I_CURVE]

WB Neuron

The f - I curve of the WB neuron looks closer to linear than that of the RTM neuron, but is otherwise similar; see Fig. 17.6. A close-up confirms that f is again of the form $C\sqrt{I - I_c}$ for $I \geq I_c$, $I \approx I_c$; see Fig. 17.7.

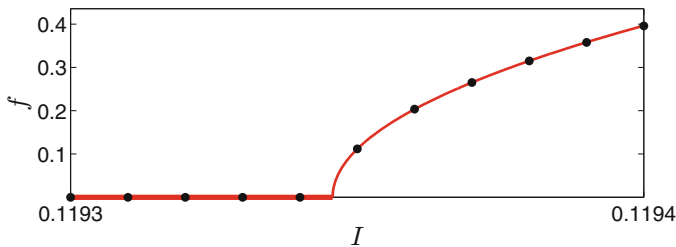


Figure 17.5. f - I curve of the RTM neuron, near the onset. The red curve is of the form $f = C\sqrt{I - I_c}$ for $I > I_c$, $f = 0$ for $I \leq I_c$. [RTM_F_I_CURVE_AT_ONSET]

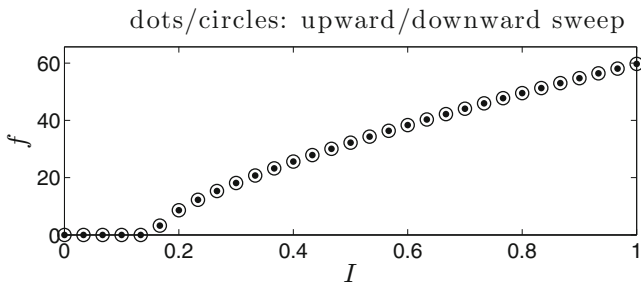


Figure 17.6. f - I curve of the WB neuron. [WB_F_I_CURVE]

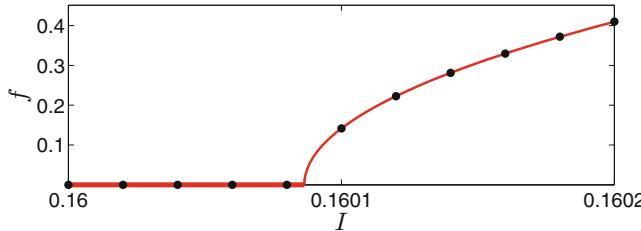


Figure 17.7. f - I curve of the WB neuron, close-up near onset. The red curve is of the form $f = C\sqrt{I - I_c}$ for $I \geq I_c$. [WB_F_I_CURVE_AT_ONSET]

17.3 Examples of f-I Curves with Discontinuities and an Interval of Bistability

Classical Hodgkin-Huxley Neuron

The f - I curve of the classical Hodgkin-Huxley model was shown in Fig. 17.1 already. Stable periodic firing is possible if I is greater than I_* (but not too large), and stable rest is possible if I is less than I_c . There is an interval of bistability between I_* and I_c , in which both rest and periodic firing are stable. We will now discuss several other model neurons with similar f - I curves, always using the notation I_* and I_c for the two critical values of I .

Hodgkin-Huxley Neuron, Reduced to Two Dimensions

As before, we reduce the Hodgkin-Huxley model to two dimensions by setting $m = m_\infty(v)$ and $h = 0.83 - n$. Figure 17.8 shows the f - I curve for this model. The reduced model fires more rapidly and more easily than the original one: For a given I for which both fire, f is greater for the reduced model, and both I_* and I_c are smaller for the reduced model.

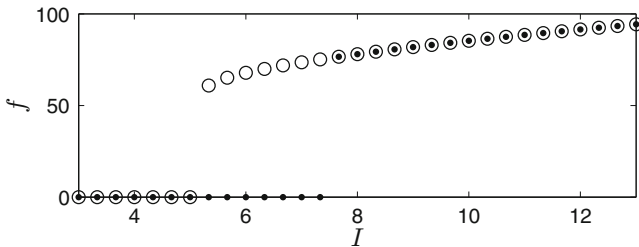


Figure 17.8. Same as Fig. 17.1, but with the reduction to two dependent variables ($m = m_\infty(v)$, $h = 0.83 - n$). [HH_REDUCED_F_I_CURVE]

Erisir Neuron

For the Erisir model, the range of values of I for which there is bistability is much smaller than for the Hodgkin-Huxley model; see Fig. 17.9.

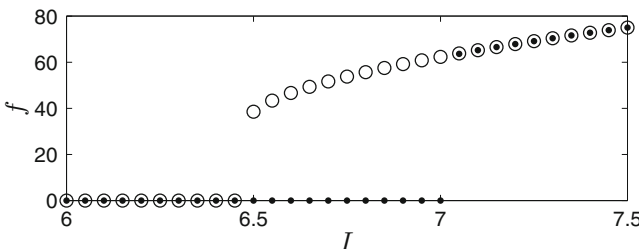


Figure 17.9. f - I curve of the Erisir neuron. [ERISIR_F_I_CURVE]

RTM Neuron with M-Current

We add to the RTM model the M-current given by eqs. (9.1)–(9.4), with $\bar{g}_M = 0.2 \text{ mS/cm}^2$. Surprisingly, the model is now of bifurcation type 2; see exercise 3. The f - I curve has qualitative features similar to that of the classical Hodgkin-Huxley

and Erisir neurons; see Fig. 17.10. Notice, however, that the interval of bistability in Fig. 17.10 is very short, and firing onset and offset are only weakly discontinuous.

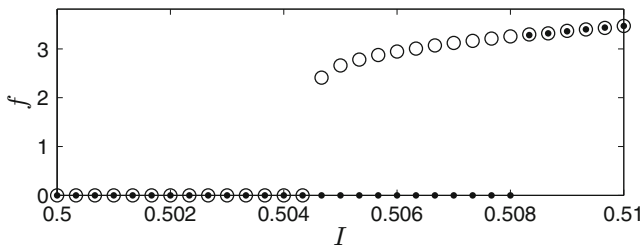


Figure 17.10. f - I curve of the RTM neuron with M-current.
[RTM_WITH_M_CURRENT_F_I]

Izhikevich's $I_{Na,p}$ - I_K Model

Figure 17.11 shows the f - I curve of the $I_{Na,p}$ - I_K model. Notice the very high firing frequencies. Although this f - I curve looks qualitatively similar to those of the other examples in this section, the bifurcations in the $I_{Na,p}$ - I_K model are different, as discussed in Section 16.1. The possibility of stable reset is lost as I rises above I_c as a result of a saddle-node collision, not a Hopf bifurcation. The possibility of stable periodic firing is lost as I falls below I_* as a result of a saddle-cycle collision, a homoclinic bifurcation.

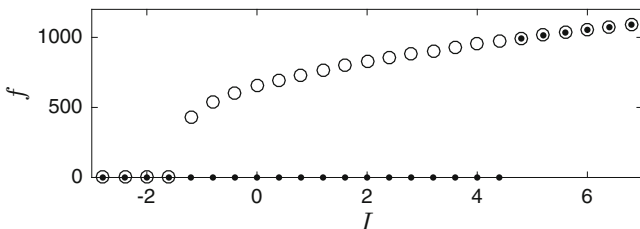


Figure 17.11. f - I curve of the $I_{Na,p}$ - I_K model. [INAPIK_F_I_CURVE]

When $I > I_*$ but $I \approx I_*$, the saddle is close to the limit cycle, and it takes a long time to traverse the cycle, since the motion in phase space is slow near a fixed point. Thus the firing period is long, i.e., the firing frequency is small. As the distance between the saddle and the limit cycle approaches zero, the frequency approaches zero; that is, the upper branch of the f - I curve is continuous at I_* in this example.

To better understand the shape of the upper branch of the f - I curve at $I = I_*$, we investigate first how fast the distance between the saddle and the limit cycle tends

to zero in this limit. Figure 17.12 shows the distance, d , between the saddle and the limit cycle as a function of I . The figure shows that $d \asymp I - I_*$ in the limit as $I \searrow I_*$.

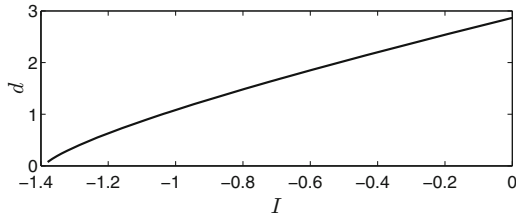


Figure 17.12. Distance, d , between saddle and limit cycle as a function of I . [INAPIK_SADDLE_CYCLE_DISTANCE]

To pass a saddle point at a small distance $d > 0$ requires time $\asymp \ln(1/d)$; see exercise 9. Therefore the period of the $I_{\text{Na,p}} - I_K$ model is $\asymp \ln(1/(I - I_*))$ in the limit $I \searrow I_*$. For the frequency f , we conclude

$$f \asymp \frac{1}{\ln \frac{1}{I - I_*}}. \quad (17.8)$$

(If you are wondering whether a constant is missing in the argument of \ln in this formula, or if you think I made the terrible mistake of taking the logarithm of a dimensional quantity in eq. (17.8), see exercise 10.) As $I \searrow I_*$, the right-hand side of (17.8) tends to zero. The graph of f as a function of I is extremely steep at I_* , just like the f - I curve of the LIF neuron near the firing onset; see also exercise 11.

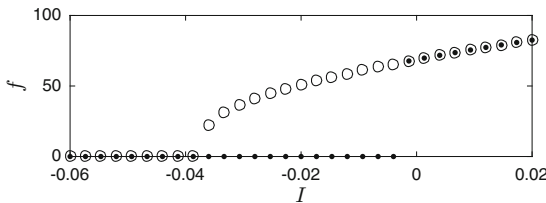


Figure 17.13. The f - I curve of the smooth self-exciting theta neuron given by eqs. (16.9) and (16.10), with $\tau_z = 100$ and $z_{\max} = 0.05$. [SETN_F_I]

Smooth Self-Exciting Theta Neuron

Figure 17.13 shows the f - I curve of the self-exciting theta neuron with smooth reset of z , given by eqs. (16.9) and (16.10). As for the $I_{\text{Na,p}} - I_K$ model, there is a saddle-node collision as I rises above I_c , and a saddle-cycle collision (homoclinic bifurcation) as I drops below I_* ; see Section 16.2, and in particular exercise 16.3. As a result, the f - I curve in Fig. 17.13 has the same characteristics as that of the

$I_{\text{Na,p}}-I_K$ model. The lower branch is discontinuous at I_c . The upper branch is continuous at I_* , but gets steep to infinite order as $I \searrow I_*$, in the sense that we explained when discussing the f - I curve of the $I_{\text{Na,p}}-I_K$ model, as $I \searrow I_*$.

Exercises

- 17.1. Suppose that we simulate a neuron using a numerical method, such as the midpoint method, computing approximations of the membrane potential v at times $k\Delta t$, $k = 0, 1, 2, \dots$ We denote these approximations by v_k , $k = 0, 1, 2, \dots$ (Unfortunately we must code v_0 as $v(1)$ in Matlab, and consequently v_k as $v(k+1)$, because Matlab requires positive indices.) We will think here about how to compute *spike times*, which we (somewhat arbitrarily but consistently) define to be times at which the membrane potential crosses -20mV from above. Suppose that $v_{k-1} \geq -20\text{mV}$ and $v_k < -20\text{mV}$. We approximate the spike time as the time, t_* , at which the straight line in the (t, v) -plane through the points $((k-1)\Delta t, v_{k-1})$ and $(k\Delta t, v_k)$ crosses the horizontal line $v = -20$. Find a formula for t_* .
- 17.2. (\dagger) Show that the classical Hodgkin-Huxley neuron has a single fixed point when I is sufficiently low.
- 17.3. (*) Demonstrate numerically that the RTM neuron with M-current, modeled as in Section 9.1 with $\bar{g}_M = 0.2\text{ mS/cm}^2$ and $v_K = -100\text{ mV}$, undergoes a Hopf bifurcation as I crosses I_c . You may find it useful to start with, for instance, the code that generated Fig. 16.1, but note that the model is very different here, and there are four dependent variables (v , h , n , and w), so the Jacobi matrices will be 4×4 .
- 17.4. (a) (*) Demonstrate that the RTM neuron with calcium-dependent AHP current, modeled as in Section 9.2 with $\bar{g}_{\text{AHP}} = 0.2\text{ mS/cm}^2$ and $v_K = -100\text{ mV}$, is of bifurcation type 1. You may find it useful to start with, for instance, the code that generated Fig. 16.1, but note that the model is very different here, and there are four dependent variables (v , h , n , and $[\text{Ca}^{2+}]_{\text{in}}$), so the Jacobi matrices will be 4×4 . (b) Explain why (a) is not surprising.
- 17.5. (a) Prove (17.3). (b) Show that (17.3) implies (17.2).
- 17.6. Show that all right-sided derivatives of the function $I = I(f)$, $f \geq 0$, defined by (17.4) are zero.
- 17.7. The functions in (16.3) are both of the form

$$x_\infty(v) = \frac{1}{1 + \exp((v_{1/2} - v)/k)}. \quad (17.9)$$

Show: (a) x_∞ is an increasing function of v . (b) $\lim_{v \rightarrow -\infty} x_\infty(v) = 0$ and $\lim_{v \rightarrow \infty} x_\infty(v) = 1$. (c) $x_\infty(v_{1/2}) = 1/2$. (d) k measures how steep x_∞ is at $v = v_{1/2}$, in the sense that

$$\frac{dx_\infty}{dv}(v_{1/2}) = \frac{1}{4k}.$$

- 17.8. (*) Izhikevich, in [82], refers to the potassium current in the $I_{\text{Na,p}}-I_K$ model, in the form described in Section 16.1, as a *high-threshold potassium current*. In general, a high-threshold potassium current I_K is one that is only activated when v is high. Currents of this sort are found in many fast-firing neurons, and are believed to help neurons fire rapidly by shortening the spike afterhyperpolarization [45].

One way of quantifying the phrase *high-threshold* would be to consider the value, $v_{1/2}$, of v at which I_K would have half its maximal strength in the steady state if the membrane potential were fixed (“clamped”). For Izhikevich’s high-threshold potassium current, this value is clearly $v_{1/2} = -25 \text{ mV}$. For the classical Hodgkin-Huxley, RTM, and WB neurons, $v_{1/2}$ would be the solution of $(n_\infty(v))^4 = 1/2$. For the Erisir neuron, it would be the solution of $(n_\infty(v))^2 = 1/2$. Compute $v_{1/2}$ for the potassium currents in the classical Hodgkin-Huxley, RTM, WB, and Erisir models, rounded to the nearest mV.

- 17.9. Consider the system

$$\frac{dx}{dt} = x, \quad \frac{dy}{dt} = -y. \quad (17.10)$$

The origin $(x, y) = (0, 0)$ is a saddle point here. Let d be a positive number smaller than 1; think of d as small. (a) Find an $\epsilon > 0$ (depending, of course, on d) with the property that for the solution of (17.10) with $x(0) = \epsilon$ and $y(0) = 1$,

$$\min_{t \geq 0} \sqrt{x^2(t) + y^2(t)} = d.$$

(b) Show that for the solution in part (a), there is a $T > 0$ with $x(T) = 1$, $y(T) = \epsilon$. We say that T is the *time at which it takes to pass the saddle at distance d* . Compute T as a function of d .

- 17.10. (a) Following the reasoning at the end of the section, you might think that a constant is missing in the argument of the logarithm in (17.8): We said that $d \asymp I - I_*$, so $d \sim C(I - I_*)$ for some $C > 0$, and $f \asymp 1/\ln(1/d)$, so you might think that

$$f \asymp \frac{1}{\ln \frac{1}{C(I - I_*)}}. \quad (17.11)$$

Show that (17.11) and (17.8) are equivalent. (b) You might think that eq. (17.8) is dimensionally nonsensical, since the logarithm of a dimensional quantity appears on the right-hand side. Explain why there is no dimensional problem with (17.8). (Hint: It has to do with part (a) of this exercise.)

- 17.11. Suppose that

$$f = \begin{cases} \frac{C}{\ln(1/(I - I_*))} & \text{if } I > I_*, \\ 0 & \text{if } I = I_*, \end{cases}$$

with $C > 0$. (Compare eq. (17.8).) Express $I \geq I_*$ as a function of $f \geq 0$. Show that all derivatives of I at $f = 0$ are zero. (See also exercise 6.)

Chapter 18

Bistability Resulting from Rebound Firing

We have seen that some model neurons have continuous, single-valued f - I curves. With the exception of the LIF neuron, all of these model neurons transition from rest to firing via a SNIC. Other model neurons have discontinuous f - I curves with an interval of *bistability*, in which both rest and periodic firing are possible. The examples we have seen transition from rest to firing either via a subcritical Hopf bifurcation, or via a saddle-node bifurcation *off* an invariant cycle. The distinction between continuous and discontinuous f - I curves closely resembles the distinction between “class 1” and “class 2” neurons made by Hodgkin in 1948 [75].

The discussion in the preceding chapters is not quite satisfactory, however, because it does not address the *physical* difference between the two classes. In this chapter, we will ask what it is about the classical Hodgkin-Huxley neuron, the Erisir neuron, and the RTM neuron with an M-current, that causes bistability in a range of values of I .

We have no rigorous answer to this question. However, in all three cases, we will give numerical results indicating that bistability is attributable to *rebound firing*. By this we mean that the hyperpolarization following an action potential invokes a depolarizing mechanism that results in another action potential, and thus in a periodic sequence of action potentials. The hyperpolarization-induced depolarizing mechanism responsible for rebound firing is associated with one of the gating variables for each of the three models, but the mechanism is different for different models. For the classical Hodgkin-Huxley neuron, it is de-activation of the delayed rectifier potassium current (reduced n). For the Erisir neuron, it is de-inactivations of the sodium current (raised h). For the RTM neuron with M-current, it is de-activation of the M-current (reduced w).

Electronic supplementary material: The online version of this chapter (doi: [10.1007/978-3-319-51171-9_18](https://doi.org/10.1007/978-3-319-51171-9_18)) contains supplementary material, which is available to authorized users.

In this chapter, we also introduce the *h-current*, a non-specific inward *cation* (positive ion) current induced by hyperpolarization (hence the letter “h”); see [107] for a review. H-currents are found in numerous places in the brain, for instance, in the dendrites of pyramidal cells, and are often associated with rebound firing. One would expect, based on the discussion in the preceding paragraph, that addition of an h-current to the RTM model could result in bistability for a certain range of drives I , and in discontinuous onset. We confirm this in Section 18.4, although the range of values of I for which there is bistability is narrow, and the discontinuity is weak.

We will not examine the $I_{\text{Na,p}}-I_K$ model in detail in this chapter, but note that it differs from the models discussed above: In the range of bistability, firing is sustained not by hyperpolarization-induced dynamics, but by a depolarization-induced current, the persistent sodium current.

18.1 Classical Hodgkin-Huxley Model

For $I = 8 \mu\text{A}/\text{cm}^2$, the classical Hodgkin-Huxley neuron can either rest, or fire periodically; see Fig. 18.1, and compare also Fig. 17.1. We denote the stable fixed point by (v_*, m_*, h_*, n_*) . In particular, v_* is the value of v seen in the upper panel of Fig. 18.1.

Following an action potential induced, for instance, by choosing an initial value of v significantly above v_* , v drops to levels far below v_* . This causes m to become small. However, it also raises h , i.e., it de-inactivates the spike-generating sodium current. Finally it brings down n , the activation variable of the delayed rectifier potassium current. The three panels in Fig. 18.2 show m , h , and n as functions of time, for the simulation in the bottom panel of Fig. 18.1. We have added to these plots the equilibrium values m_* , h_* , and n_* (red horizontal lines), and also the values $m_\infty(v)$, $h_\infty(v)$, and $n_\infty(v)$ that m , h , and n are tracking (blue dashed curves). We see that m tracks $m_\infty(v)$ nearly perfectly. We note that there could be no rebound spike if all gating variables x tracked $x_\infty(v)$ perfectly as v approaches v_* (exercise 1). However, h and n do not track $h_\infty(v)$ and $n_\infty(v)$ tightly; the reason, of course, is that τ_h and τ_n are much larger than τ_m . During time intervals indicated by magenta bars in the figure, h rises above h_* , and n falls below n_* . During a large portion of these time intervals, v is still below v_* . (One can see this from Fig. 18.2: The blue dashed curves intersect the red lines when $v = v_*$.)

It turns out to that the drop in n below n_* is responsible for the rebound spike here, even though n only drops very slightly below n_* . In fact, if we replace n by $\max(n, n_*)$ in each time step of the simulation, there is no rebound spike; see Fig. 18.3. Even though the amount by which h exceed h_* is greater than the amount by which n falls below n_* (compare the middle and bottom panels of Fig. 18.2), replacing h by $\min(h, h_*)$ in each time step of the simulation does not prevent the rebound spike; see exercise 2.

18.2 Erisir Model

For $I = 6.9 \mu\text{A}/\text{cm}^2$, both rest and periodic firing are stable for the Erisir neuron; see Figs. 18.4 and 17.9. To examine the mechanisms at work here, we plot in Fig. 18.5 the gating variables $m = m_\infty(v)$, h , and n as functions of t , for the simulation in the lower panel of Fig. 18.4. One sees that n is very close to zero except during an action potential and the brief refractory period following it. While it is true that following an action potential, n falls below n_* , this has little effect because n and n_* are so small; see exercise 3. On the other hand, the inactivation variable h is

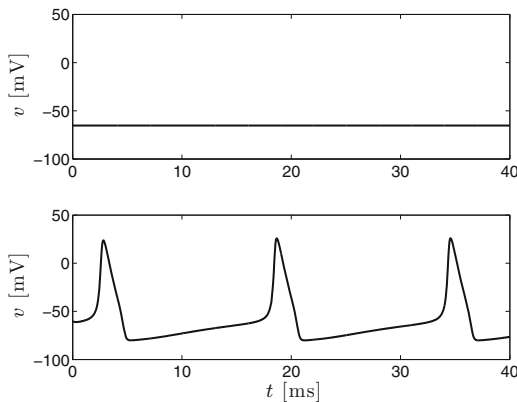


Figure 18.1. Two possible voltage traces of the classical Hodgkin-Huxley neuron for $I = 8 \mu\text{A}/\text{cm}^2$. [HH_BISTABLE]

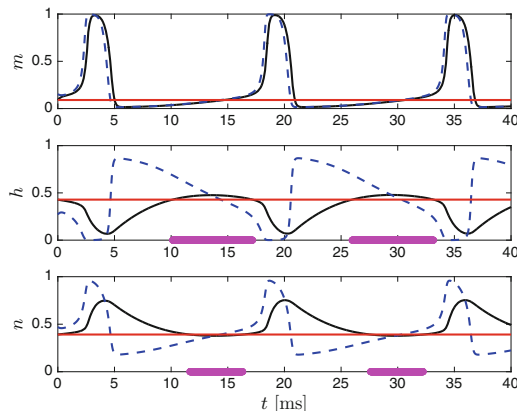


Figure 18.2. The gating variables in the simulation in the lower panel of Fig. 18.1. Black solid curves are the computed gating variables. Blue dashed curves indicate $m_\infty(v)$, $h_\infty(v)$, and $n_\infty(v)$, the “moving targets” tracked by the gating variables. Red horizontal lines indicate the equilibrium values of the gating variables, m_* , h_* , and n_* . The magenta bars on the t -axis indicate time intervals during which h exceeds h_* , or n drops below n_* . [HH_BISTABLE_GATES]

very much smaller than 1 even in equilibrium, so inactivation of the sodium current plays a significant role in maintaining the equilibrium. Once an action potential is triggered, the hyperpolarization following it causes h to rise above h_* for a prolonged time. This is why a rebound spike is generated. In fact, if we replace, in each time step, h by $\min(h, h_*)$, the rebound spike is abolished; see Fig. 18.6.

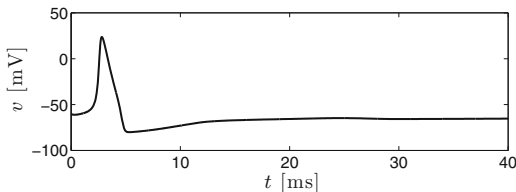


Figure 18.3. Same as lower panel in Fig. 18.1, but with n replaced by $\max(n, n_*)$ in each time step of the simulation. [HH_BISTABLE_LIMITED_N]

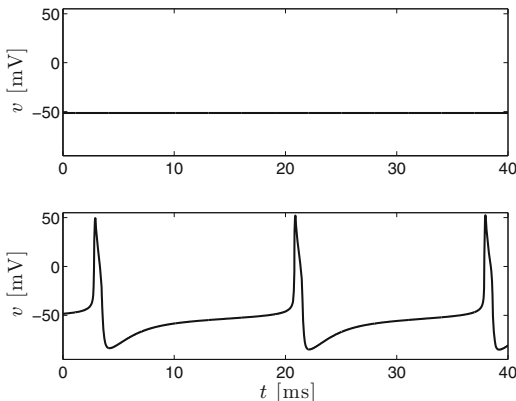


Figure 18.4. Two possible voltage traces of the Erisir neuron with $I = 6.9 \mu\text{A}/\text{cm}^2$. [ERISIR_BISTABLE]

18.3 RTM Model with an M-Current

When we add to the RTM model an M-current with $\bar{g}_M = 0.2 \text{ mS/cm}^2$, rest and periodic firing are both stable for $I = 0.506 \mu\text{A}/\text{cm}^2$; see Figs. 18.7 and 17.10. We denote the stable fixed point by (v_*, h_*, n_*, w_*) ; w is the gating variable of the M-current. For the simulation in the lower panel of Fig. 18.7, we plot in Fig. 18.8 the functions n , h , and w as functions of t . We see that h and n follow h_∞ and n_∞ closely. By contrast, w follows w_∞ only very loosely and with a long delay, except during an action potential; the reason, of course, is that $\tau_w(v)$ is large except for high v — see Fig. 9.2. For extended time intervals, indicated in magenta in Fig. 18.8, w drops below w_* , albeit by a small amount. This is what causes the rebound spike. When we replace, in each time step, w by $\max(w, w_*)$, there is no rebound spike; see Fig. 18.9.

18.4 RTM Neuron with an h-Current

In [157], the following model h-current was proposed:

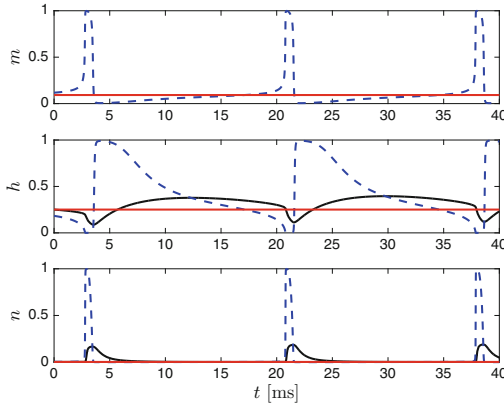


Figure 18.5. Analogous to Fig. 18.2, for the simulation of the lower panel of Fig. 18.4. In the Erisir model, $m = m_\infty$. This is why there is no solid black curve in the top panel; it would be identical with the dashed blue curve.

[ERISIR_BISTABLE_GATES]

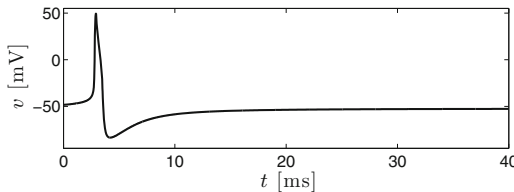


Figure 18.6. Same as lower panel in Fig. 18.4, but with h replaced by $\min(h, h_*)$ in each time step of the simulation. [ERISIR_BISTABLE_LIMITED_H]

$$I_h = \bar{g}_h r(v_h - v) \quad (18.1)$$

with $v_h = -32.9$ mV and

$$\frac{dr}{dt} = \frac{r_\infty(v) - r}{\tau_r(v)}, \quad (18.2)$$

$$r_\infty(v) = \frac{1}{1 + e^{(v+84)/10.2}}, \quad \tau_r(v) = \frac{1}{e^{-14.59 - 0.086v} + e^{-1.87 + 0.0701v}}. \quad (18.3)$$

Fig. 18.10 shows the graphs of these functions. For low v , $r_\infty(v)$ is close to 1 and $\tau_r(v)$ is large; thus the current builds up gradually when the neuron is hyperpolarized. For high v , r_∞ is close to 0, and $\tau_r(v)$ is small; thus the current shuts off when the neuron fires.

The h-current is also called the *sag current*. The reason is illustrated by Fig. 18.11. When the neuron receives a hyperpolarizing input, the membrane potential first drops, but then the rise in the h-current causes v to rise again, giving

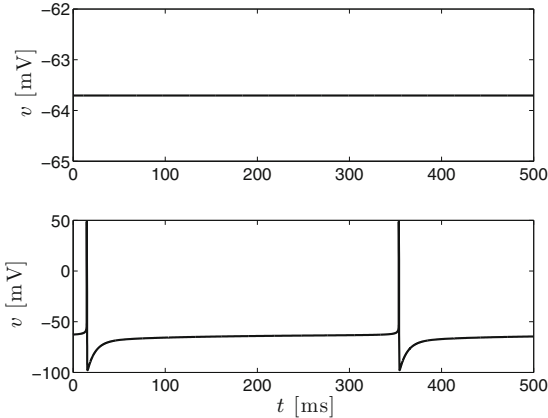


Figure 18.7. Two possible voltage traces of the RTM model with an M-current with $\bar{g}_M = 0.2 \text{ mS/cm}^2$, for $I = 0.506 \mu\text{A/cm}^2$. [\[RTM_WITH_I_M_BISTABLE\]](#)

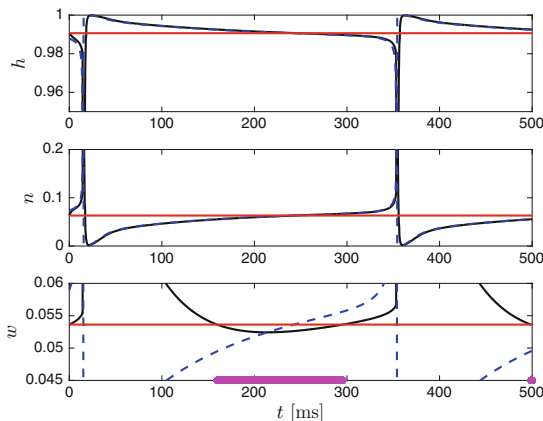


Figure 18.8. Analogous to Fig. 18.2, for the simulation of the lower panel of Fig. 18.7. The gating variables shown here are h , n , and w .

[\[RTM_WITH_I_M_BISTABLE_GATES\]](#)

the graph of v a “sagging” appearance. Fig. 18.11 also demonstrates that a neuron with an h-current can fire a rebound spike following a time of hyperpolarization.

The h-current seems to do precisely what we have identified as the source of bistability in the classical Hodgkin-Huxley and Erisir neurons, and in the RTM neuron with M-current: It responds to hyperpolarization with a depolarizing current that is not rapidly turned down as v rises again. We might therefore expect

that for the RTM neuron with an h-current, there should be an interval of bistability. We investigate now whether this is indeed the case, by means of numerical experiments with $\bar{g}_h = 1 \text{ mS/cm}^2$.

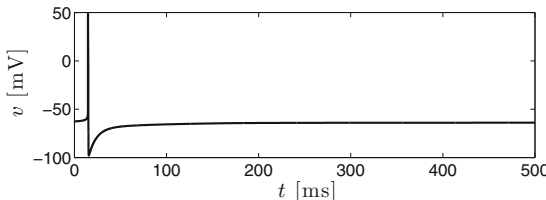


Figure 18.9. Same as lower panel in Fig. 18.7, but with w replaced by $\max(w, w_*)$ in each time step of the simulation. [RTM_WITH_I_M_LIMITED_W]

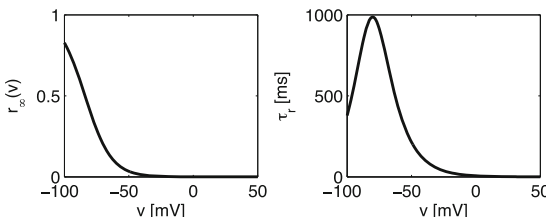


Figure 18.10. The steady state and time constant of the gating variable in the model h-current of [157]. [H_CURRENT]

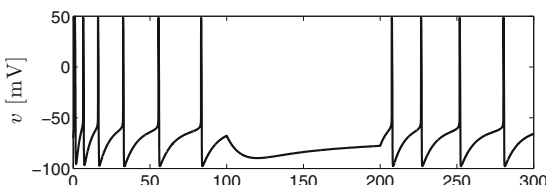


Figure 18.11. RTM neuron with h-current ($I = 0 \mu\text{A}/\text{cm}^2$, $\bar{g}_h = 1 \text{ mS/cm}^2$). Between times 100 and 200 ms, a hyperpolarizing current is injected ($I = -4 \mu\text{A}/\text{cm}^2$). Notice the “sag” in the membrane potential: It is first lowered greatly, but then rises again because of the h-current. Notice also the rebound spike fired almost immediately after the hyperpolarizing current is removed at $t = 200 \text{ ms}$. [RTM_VOLTAGE_TRACE_WITH_I_H]

Figure 18.12 shows the f - I curve of the RTM neuron with the model h-current added, with $\bar{g}_h = 1 \text{ mS/cm}^2$. There is indeed bistability for I between two critical values, I_* and I_c , but the two critical values are extremely close to each other. The smallest positive firing frequency is quite low, just slightly greater than 1 Hz.

To understand this example better, we consider specifically the value $I = -3.19 \mu\text{A/cm}^2$, for which rest and slow firing are both possible and stable; see Fig. 18.13. We denote the stable fixed point by (v_*, h_*, n_*, r_*) . In the upper panel of the figure, we deliberately started at a small distance from this fixed point, to show the oscillatory convergence to the fixed point. For the simulation in the lower

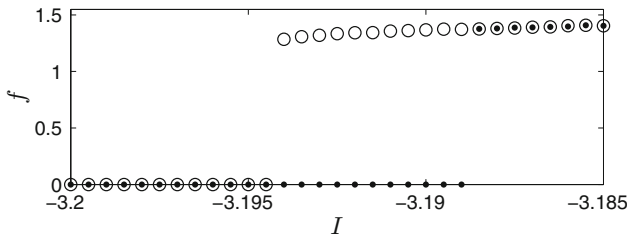


Figure 18.12. f - I curve of the RTM neuron with h -current with $\bar{g}_h = 1 \text{ mS/cm}^2$. As is typical for neurons of bifurcation type 2, there are two branches, a lower (dots) and an upper one (circles); see Chapter 17 for a description of how these two branches are computed. [RTM_F_I_CURVE_WITH_I_H]

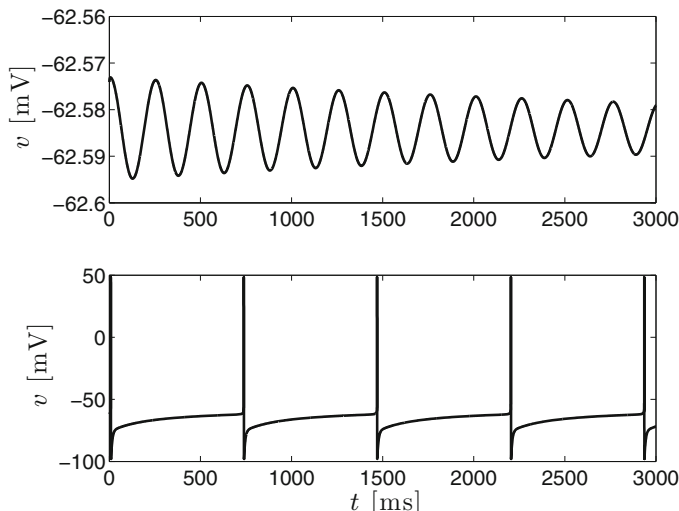


Figure 18.13. Bistability of the RTM neuron with h -current, with $\bar{g}_h = 1 \text{ mS/cm}^2$, $I = 3.19 \mu\text{A/cm}^2$. [RTM_WITH_I_H_BISTABLE]

panel of Fig. 18.13, we show in Fig. 18.14 the gating variables h , n , and r . During the inter-spike intervals, h and n follow $h_\infty(v)$ and $n_\infty(v)$ tightly, while r follows $r_\infty(v)$ sluggishly. Within each inter-spike interval, there is a time interval during which r rises very slightly above its equilibrium value r_* ; the effect is so slight that it isn't even clearly visible in the bottom panel of Fig. 18.14, but the time intervals during which $r > r_*$ are indicated in magenta. In spite of being so small, this effect causes the rebound firing: If we replace, in each time step, r by $\min(r, r_*)$, the rebound spike is prevented; see Fig. 18.15.

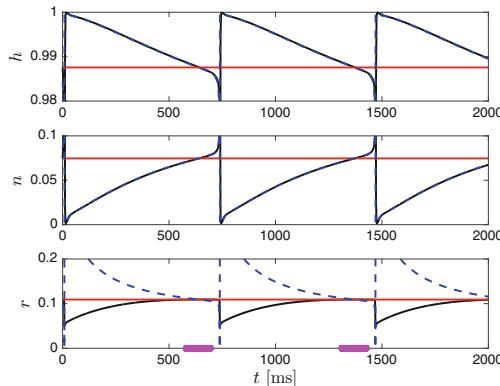


Figure 18.14. Analogous to Fig. 18.2, for the simulation of the lower panel of Fig. 18.13. [RTM_WITH_I_H_BISTABLE_GATES]

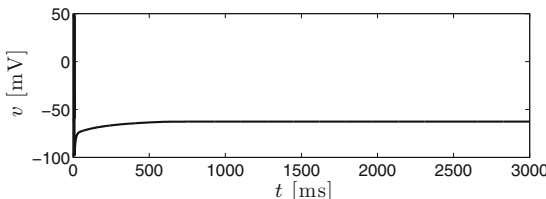


Figure 18.15. When r is not allowed to exceed r_* , the rebound spiking in the lower panel of Fig. 18.13 is abolished. [RTM_WITH_I_H_LIMITED_R]

Exercises

- 18.1. Explain: For all the model neurons discussed in this chapter, if between spikes, each gating variable x satisfied $x \equiv x_\infty(v)$, there would be no bistability.
- 18.2. (*) Verify that in the simulation of the lower panel of Fig. 18.1, replacing h by $\min(h, h_*)$ in each time step does not abolish the rebound firing.

- 18.3. (*) Verify that in the simulation of the lower panel of Fig. 18.4, replacing n by $\max(n, n_*)$ in each time step does not abolish the rebound firing.
- 18.4. (*) The reasoning in this chapter suggests that the interval of bistability for the RTM neuron with h-current should become larger if $\tau_r(v)$ were reduced for very low v , while remaining unchanged for all other v : The gating variable r would then respond to deep hyperpolarization with a quicker and more pronounced rise, while it would still only sluggishly approach r_* as v approaches v_* . To test this, we replace τ_r by $q\tau_r$, with

$$q(v) = \begin{cases} (v/20 + 5)^2 & \text{if } -100 \leq v \leq -80, \\ 1 & \text{otherwise.} \end{cases} \quad (18.4)$$

Note that $q(-100) = 0$ and $q(-80) = 1$. The graphs of τ_r and $q\tau_r$ are plotted in Fig. 18.16. The motivation for this modification is not biological; the goal here is merely to put our understanding of the mechanism underlying bistability to a test.

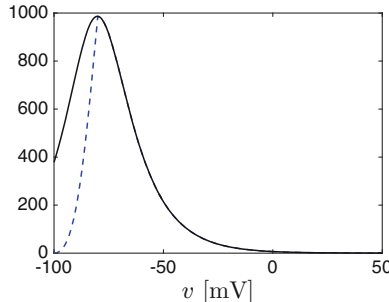


Figure 18.16. Black, solid: time constant τ_r in the model of the h-current, and the modification. Blue, dashes: $q\tau_r$, with q defined in (18.4). The maximum of τ_r occurs approximately at $v = -80$, and for $v > -80$, τ_r and $q\tau_r$ are the same.
[PLOT_MODIFIED_TAU_R]

Using the code generating Fig. 18.12 as a starting point, plot the f - I curve of the model with τ_r replaced by $q\tau_r$, for $-4 \leq I \leq -3$. See whether introducing the factor of q changes the f - I curve in the expected way.

This exercise won't take you much time, but the computation will take the computer a fairly long time, so you'll need to be a little patient.

Chapter 19

Bursting

Bursting is a very common behavior of neurons in the brain. A bursting neuron fires groups of action potentials in quick succession, separated by pauses which we will call the *inter-burst intervals*. Figure 19.1 shows an experimentally recorded voltage trace illustrating bursting. Figure 19.2 shows a simulation discussed in detail later in this chapter.



Figure 19.1. Voltage trace from Fig. 6F of [138], showing an in vitro recording from a neuron in layer III of ferret piriform cortex (a cortical region that processes smells). Reproduced with publisher's permission.

19.1 Hysteresis-Loop Bursting

Consider a model neuron with an interval of bistability of the sort discussed in Section 17.3: A stable fixed point and a limit cycle co-exist in an interval (I_*, I_c) . The stable fixed point becomes unstable, or disappears altogether, as I rises above I_c , and the limit cycle disappears as I falls below I_* . From such a model, we can

Electronic supplementary material: The online version of this chapter (doi: [10.1007/978-3-319-51171-9_19](https://doi.org/10.1007/978-3-319-51171-9_19)) contains supplementary material, which is available to authorized users.

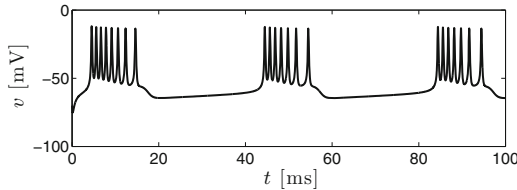


Figure 19.2. Simulation of bursting. The underlying model is discussed later in this chapter. [[INAPIK_PLUS_SLOW_I_K](#)]

obtain a model of bursting by adding a spike frequency adaptation current, that is, a hyperpolarizing current that is gradually strengthened by firing, and slowly decays in the absence of firing. An alternative possibility is to add a depolarizing current that is weakened by firing, and slowly recovers in the absence of firing.

As before, we use the notation I for the drive to the model neuron. We also use the notation I_{eff} for the “effective drive,” the sum of I and the added slow current controlling the bursting. For the purposes of the present discussion, we assume that I_{eff} is reduced with each action potential, and returns to its original value gradually in the absence of firing. Suppose that initially, $I_{\text{eff}} > I_c$, and the neuron fires rapidly. With each action potential, I_{eff} is reduced. If it drops below I_* , the firing stops. Now I_{eff} gradually recovers. As soon as it rises above I_c , firing resumes, and the cycle repeats. The time intervals of rapid firing, during which I_{eff} is gradually reduced, are the bursts; the times during which I_{eff} slowly recovers are the inter-burst intervals. Figure 19.3 shows a schematic illustration of the mechanism.

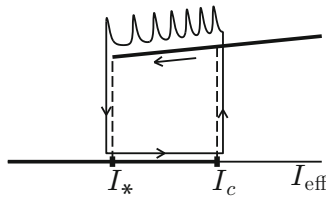


Figure 19.3. Schematic illustration of the bursting mechanism. The bold lines represent the frequency-current relation. The system moves in a hysteresis loop: As the neuron fires, the effective drive, I_{eff} , gradually decreases to I_* . Then the neuron rests, and I_{eff} gradually returns to I_c . Then firing resumes and the cycle repeats.

The kind of bursting described above is called *hysteresis-loop bursting*. In general, the word *hysteresis* denotes the dependence of the output of a system not

only on present inputs, but also on past inputs that affected an unobserved variable, and thereby altered the state of the system.¹⁵

The M- and calcium-dependent AHP currents discussed in Chapter 9 are examples of depolarization- or firing-induced hyperpolarizing currents that decay slowly in the absence of firing. The h-current, introduced in Chapter 18, is an example of a depolarizing current that inactivates as a result of firing, and slowly de-inactivates in the absence of firing. Another example is the *T-current*, an inward (depolarizing) calcium current inactivated by firing [77]. Each of these currents has been found to be involved in controlling bursts in experiments; see, for instance, [27, 77, 115], and [116].

In patients with schizophrenia, bursting in the prefrontal cortex has been found to be reduced [83]; a resulting loss of efficacy in signal transmission is hypothesized in [83] to be a cause for cognitive deficits associated with schizophrenia.

19.2 A Concrete Example

The specific model of bursting that I will describe here, and that underlies Fig. 19.2, was proposed by Izhikevich in [82]. It is based on the $I_{\text{Na,p}} - I_K$ model described in Section 16.1 (eqs. (16.1), (16.2)). The spiking-activated hyperpolarizing current is assumed to be of the form

$$I_{K,\text{slow}} = \bar{g}_{K,\text{slow}} n_{\text{slow}} (v_K - v), \quad (19.1)$$

with

$$\frac{dn_{\text{slow}}}{dt} = \frac{n_{\text{slow},\infty} - n_{\text{slow}}}{\tau_{n,\text{slow}}}, \quad n_{\text{slow},\infty}(v) = \frac{1}{1 + \exp((-20 - v)/5)}, \quad (19.2)$$

and

$$\bar{g}_{K,\text{slow}} = 5 \text{ mS/cm}^2, \quad \tau_{n,\text{slow}} = 20 \text{ ms}. \quad (19.3)$$

This current is added to the right-hand side of the equation governing v , eq. (16.1). Figure 19.2 shows $v(t)$ for a solution of the resulting system with $I = 7 \mu\text{A}/\text{cm}^2$. The solution converges to an attracting limit cycle, shown in the three-dimensional phase space of the model in Fig. 19.4. The turns are rapid, and correspond to firing. The descent to lower values of n_{slow} is slow, and corresponds to the inter-burst interval. Notice that in Fig. 19.2, the inter-spike interval within a burst increases. This reflects the fact that in a homoclinic bifurcation, the frequency decreases as the saddle approaches the cycle; this was discussed in Section 17.3.

Whether or not the model described above produces periodic bursting depends on the value of $\bar{g}_{K,\text{slow}}$. If $\bar{g}_{K,\text{slow}}$ is slightly reduced, the slow potassium current is no longer strong enough to terminate bursts, and very high-frequency periodic

¹⁵A thermostat is a familiar example. Whether or not your heat is on depends not only on the current temperature in your room, but also on its history. The thermostat might turn the heat on when the temperature drops below 66°F, and turn it off when the temperature rises above 70°F. If it is currently 68°F, the heat may be on or off, depending on which part of the cycle the thermostat is in. Without the hysteresis effect, the heat would turn on and off very frequently.

firing results; see Fig. 19.5. On the other hand, a four-fold increase in $\bar{g}_{K,\text{slow}}$ results in lower-frequency periodic firing; see Fig. 19.6.

The kind of bursting studied in this section, involving a saddle-node bifurcation at I_c and a homoclinic bifurcation at I_* , is called *square-wave bursting*. The name can be understood by removing the spikes in Fig. 19.2, and plotting what remains; see the red curve in Fig. 19.7. (To be precise, we numerically estimated dv/dt , left out all values of v where the absolute value of the estimate of dv/dt was greater than 1, and filled the gaps by linear interpolation.) The bursts ride on plateaus of elevated v . The reason for this behavior can be seen from Fig. 16.2:

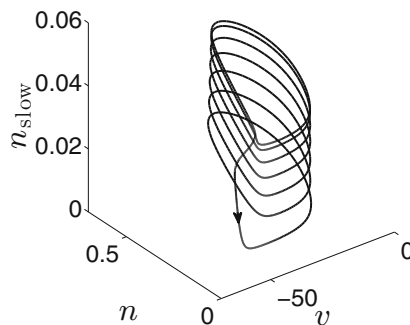


Figure 19.4. Attracting limit cycle corresponding to periodic bursting.
[INAPIK_PLUS_SLOW_I_K_3D]

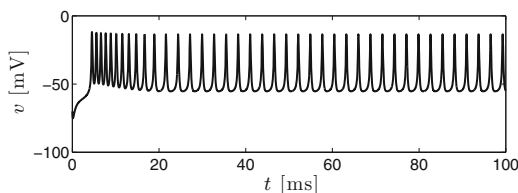


Figure 19.5. Same as Fig. 19.2, with $\bar{g}_{K,\text{slow}}$ reduced from 5 to 4 mS/cm^2 .
[INAPIK_PLUS_WEAK_SLOW_I_K]

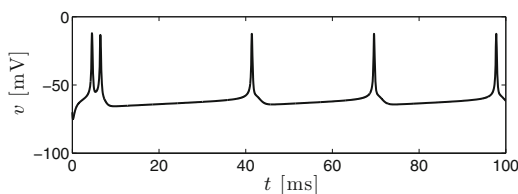


Figure 19.6. Same as Fig. 19.2, with $\bar{g}_{K,\text{slow}}$ increased from 5 to 20 mS/cm^2 . [INAPIK_PLUS_STRONG_SLOW_I_K]

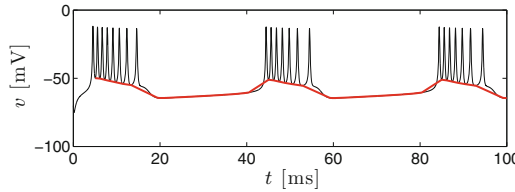


Figure 19.7. Voltage trace of Fig. 19.2, and (in red) the same voltage trace but without the spikes. This picture explains, to a viewer who isn't fussy, what square-wave bursting has to do with square waves. [SQUARE_WAVES]

The entire limit cycle lies to the right of the saddle and the node in the (v, n) -plane. Thus throughout the bursts, v is higher than during the inter-burst intervals. For much more about square-wave bursting, see [51, Section 5.2].

19.3 Analysis in an Idealized Setting

In this section, the letter I appears with various different subscripts. To help avoid confusion, I will list all the different subscripts here. The reader should refer back to this list when losing track.

I_{eff} = time-varying effective drive (sum of external drive and a current that is reduced rapidly by firing and builds up slowly between spikes)

I_c = drive value above which rest becomes unstable

I_* = drive value below which periodic firing becomes impossible ($I_* < I_c$)

I_k = value of I_{eff} just prior to the k -th action potential of a burst,

$k = 0, 1, 2, 3, \dots$ ($I_0 > I_c$ but $I_0 \approx I_c$)

$I_\infty = \lim_{k \rightarrow \infty} I_k$ (if the burst continued indefinitely)

We will analyze an idealized version of hysteresis-loop bursting. We assume that a burst starts with an action potential at time $t = 0$, and that the subsequent action potentials occur at times $\delta, 2\delta, 3\delta, \dots$, with $\delta > 0$. We assume further that the value of the effective drive, I_{eff} , just prior to the first action potential of the burst at time 0 is $I_0 > I_c$, $I_0 \approx I_c$. We assume that each action potential reduces I_{eff} by $\epsilon > 0$, and that I_{eff} moves back towards I_0 during inter-spike intervals, following the differential equation

$$\frac{dI_{\text{eff}}}{dt} = \frac{I_0 - I_{\text{eff}}}{\tau_{\text{slow}}}. \quad (19.4)$$

We denote by I_k the value of I_{eff} just prior to the action potential at time $k\delta$, $k = 1, 2, 3, \dots$. Then

$$I_k = (I_{k-1} - \epsilon)e^{-\delta/\tau_{\text{slow}}} + I_0 \left(1 - e^{-\delta/\tau_{\text{slow}}}\right), \quad k = 1, 2, 3, \dots \quad (19.5)$$

(See exercise 1.) We write (19.5) as

$$I_k = \alpha I_{k-1} + \beta, \quad (19.6)$$

with

$$\alpha = e^{-\delta/\tau_{\text{slow}}}, \quad \beta = -\epsilon e^{-\delta/\tau_{\text{slow}}} + I_0 \left(1 - e^{-\delta/\tau_{\text{slow}}}\right).$$

If I_k has a limit, I_∞ , as $k \rightarrow \infty$, then (19.6) implies

$$I_\infty = \alpha I_\infty + \beta. \quad (19.7)$$

Using (19.7), we can re-write (19.6) as

$$I_\infty - I_k = \alpha (I_\infty - I_{k-1}). \quad (19.8)$$

(See exercise 2.) By mathematical induction, we conclude

$$I_\infty - I_k = \alpha^k (I_\infty - I_0). \quad (19.9)$$

Since $0 < \alpha < 1$, this implies that in fact $I_k \rightarrow I_\infty$ as $k \rightarrow \infty$. We can compute I_∞ from eq. (19.7):

$$I_\infty = \frac{\beta}{1 - \alpha} = I_0 - \epsilon \frac{e^{-\delta/\tau_{\text{slow}}}}{1 - e^{-\delta/\tau_{\text{slow}}}}. \quad (19.10)$$

We will assume now that $\delta \ll \tau_{\text{slow}}$. This amounts to assuming that the inter-spike interval within bursts is much shorter than the inter-burst interval; without this assumption, it would hardly make sense to refer to ‘‘bursts’’ of action potentials. We can then simplify the formulas for α and I_∞ , using a local linear approximation valid for $\delta/\tau_{\text{slow}} \ll 1$:

$$I_\infty \approx I_0 - \epsilon \frac{\tau_{\text{slow}}}{\delta}. \quad (19.11)$$

(See exercise 3). We re-write (19.9) as

$$I_k = I_\infty + \alpha^k (I_0 - I_\infty). \quad (19.12)$$

We assume that the burst is terminated when I_k reaches or falls below I_* . For this to happen eventually, we need $I_\infty < I_*$. Using (19.11), and with the approximation $I_0 \approx I_c$, this condition becomes

$$\frac{\tau_{\text{slow}}}{\delta} > \frac{I_c - I_*}{\epsilon}. \quad (19.13)$$

When $\delta \ll \tau_{\text{slow}}$, the recovery of I_{eff} between spikes is negligible, and therefore the right-hand side of inequality (19.13) is approximately the number of action potentials in a burst. The duration of the burst is therefore

$$\delta \frac{I_c - I_*}{\epsilon},$$

and inequality (19.13) expresses that the time constant τ_{slow} associated with the slow current should be greater than the burst duration.

19.4 Comparison of the Idealized Analysis with Biophysical Models

For the model in Section 19.2, Fig. 19.8 shows I_{eff} as a function of time. In contrast with our idealized analysis, the action potentials do not just make I_{eff} drop slightly. Instead, they make I_{eff} drop substantially, then recover rapidly, but only to a local maximum slightly below the previous one. Except for this difference, the analysis in Section 19.3 qualitatively describes the bursting mechanism in this example reasonably well. The burst duration is approximately 12 ms here, well below $\tau_{n,\text{slow}} = 20$ ms.

Notice that in Fig. 19.10, firing ceases long after I_{eff} drops below I_* for the first time, and it resumes approximately 10 ms after I_{eff} rises above I_c . What explains these delays? Shouldn't the burst end immediately when I_{eff} drops below I_* for the first time, and shouldn't the next burst start immediately when I_{eff} rises above I_c ? Concerning the end of the burst, we observe that towards the end of the burst, and in fact throughout much of the burst, I_{eff} oscillates between values below I_* , and values above I_* . Persistent firing is not possible with a constant drive below I_* , but this does not imply that it isn't possible with a drive oscillating rapidly between values below and above I_* . Concerning the resumption of firing, the essential point to note is that a neuron with a gradually rising drive $I(t)$ generally does not start firing as soon as I rises above I_c . When I rises above I_c , the stable fixed point disappears in a saddle-node collision (for type 1 and type 3 models), or becomes unstable (for type 2 models). However, it still takes some time to leave the vicinity of the “ghost” left behind by the saddle-node collision, or the vicinity of the fixed point that has become unstable, and for the first action potential to build up. For an illustration of this point, see exercise 6.

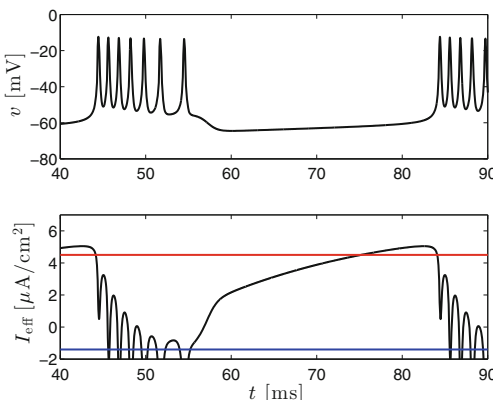


Figure 19.8. Upper panel: A segment of 19.2. Lower panel: $I_{\text{eff}} = I + I_{K,\text{slow}}$, where I denotes the drive in the simulation of Fig. 19.2 ($I = 7 \mu\text{A}/\text{cm}^2$). The red line approximately indicates I_c , and the blue line I_* , for the $I_{\text{Na,p}}-I_K$ model. [INAPIK_SHOW_SLOW_I_K]

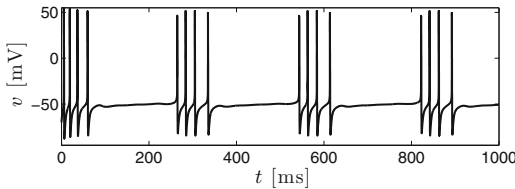


Figure 19.9. The Erisir neuron, turned into a burster by adding a slow potassium current that is strengthened by firing. [ERISIR_PLUS_SLOW_I_K]

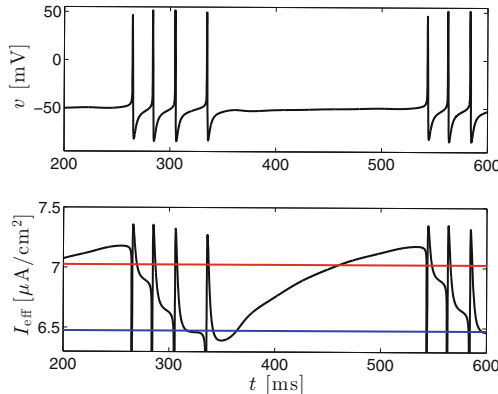


Figure 19.10. Upper panel: A segment of Fig. 19.9. Lower panel: $I_{\text{eff}} = I + I_{K,\text{slow}}$ (here $I = 7.5 \mu\text{A}/\text{cm}^2$). The red line approximately indicates I_c , and the blue line I_* . [ERISIR_SHOW_SLOW_I_K]

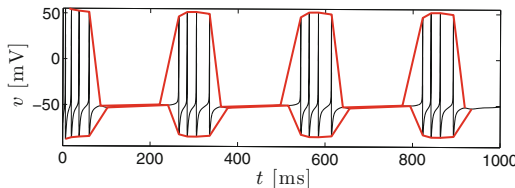


Figure 19.11. Upper panel: Voltage trace of Fig. 19.9, and (in red) the envelope of the spikes. This picture explains, at least to a lenient reader, what elliptic bursting has to do with ellipses. [ELLIPSES]

As another example, we add the slow potassium current of Section 19.2 to the Erisir model with $I = 7.5 \mu\text{A}/\text{cm}^2$. The Erisir neuron, throughout its range of bistability, fires at approximately 40–60 Hz only, i.e., with an inter-spike interval of approximately 16 to 25 ms; see Fig. 17.9. To obtain bursts of several spikes, $\tau_{n,\text{slow}}$ should therefore, by the analysis of Section 19.3, be near 100 ms. We choose $\tau_{n,\text{slow}} = 100$ ms, then adjust $\bar{g}_{K,\text{slow}}$ so that bursts of a few spikes occur: $\bar{g}_{K,\text{slow}} = 1.5 \text{ mS}/\text{cm}^2$. Figure 19.9 shows a voltage trace of the resulting model,

demonstrating that in fact the addition of the slow potassium current leads to burst firing. Figure 19.10 shows a segment of Fig. 19.9 again, together with the effective current I_{eff} . Again the details are different from those in our idealized analysis in Section 19.3, but qualitatively, the analysis captures what happens. In particular, the burst duration is about 80 ms, smaller than $\tau_{n,\text{slow}} = 100$ ms.

In Fig. 19.10, as in Fig. 19.8, we see that the instant when I_{eff} falls below I_* is not the instant when the burst ends (in fact, I_{eff} briefly falls below I_* with the very first action potential of the burst), and there is a considerable delay between the instant when I_{eff} rises above I_c and the burst onset. The reason for this delay was discussed earlier already.

The kind of bursting seen in Fig. 19.9, involving a subcritical Hopf bifurcation at I_c and a saddle-node collision of cycles at I_* , is called *elliptic bursting*. The name can be understood from Fig. 19.11, which shows the voltage trace of Fig. 19.9, together with the envelope of the spikes. (To be precise, we marked the local maximum and local minimum points of v in red, and connected them piecewise linearly.) It is typical of elliptic bursters that the spike amplitude waxes as the trajectory spirals out from the fixed point to the stable limit cycle, after the fixed point loses its stability in a subcritical Hopf bifurcation, and wanes as the slow hyperpolarizing current strengthens. This effect, a trace of which is visible in Fig. 19.11, gives the envelope during a burst an “elliptical” shape. For more about elliptic bursting, see [51, Section 5.3].

Exercises

- 19.1. Derive eq. (19.5).
- 19.2. Derive eq. (19.8).
- 19.3. Derive (19.11).
- 19.4. (*) Suppose that in the model of Section 19.2, you lowered $\bar{g}_{K,\text{slow}}$ from 5 to 4.6 mS/cm². Would the bursts get longer or shorter? Would the inter-bursts intervals get longer or shorter? What would happen if you increased $\bar{g}_{K,\text{slow}}$ to 10 mS/cm²?

Try to guess the answer using the analysis in Section 19.3, and only then check numerically whether you guessed correctly, using the program that generates Fig. 19.2 as a starting point.

- 19.5. (*) Repeat problem 4, but this time modifying $\tau_{n,\text{slow}}$, not $\bar{g}_{K,\text{slow}}$. Think about lowering $\tau_{n,\text{slow}}$ from 20 to 15 ms, or raising it to 25 ms. Again, try to guess the answers first, then find them by numerical simulation.
- 19.6. (*) This exercise is motived by the discussion surrounding Fig. 19.8.

For the $I_{\text{Na,p}}-I_K$ model, $I_* \approx -1.4$ and $I_c \approx 4.5$. (You can get these values from the code generating Fig. 17.11. In that code, the I -axis was discretized crudely, since that makes the resulting plot easier to read. To obtain I_* and I_c with good accuracy, you would want to refine the discretization of I .)

Starting with the code that generates Fig. 17.11, plot $v(t)$ as a function of t , $0 \leq t \leq 500$, starting with $I = -4$ at time $t = 0$, and letting I rise linearly to 8 at time $t = 500$. Does firing start as soon as I rises above I_c ? You will have to plot a narrower time window, containing the time when I rises above I_c and the time when firing starts, to clearly see the answer to this question.

Part III

Modeling Neuronal Communication

Chapter 20

Chemical Synapses

We now think about neuronal communication via (chemical) synapses; see Section 1.1 for a brief general explanation of what this means. In this chapter, we describe how to model chemical synapses in the context of differential equations models of neuronal networks.



Figure 20.1. Image of a synapse between a starburst amacrine cell (yellow) and a ganglion cell (blue) in the retina. Image: Alex Norton, EyeWire. Reproduced with permission.

Electronic supplementary material: The online version of this chapter (doi: [10.1007/978-3-319-51171-9_20](https://doi.org/10.1007/978-3-319-51171-9_20)) contains supplementary material, which is available to authorized users.

20.1 Nearly Instantaneous Rise

We consider two synaptically connected neurons. The *pre-synaptic* neuron gives input to the *post-synaptic* one. We denote the two membrane potentials by v_{pre} and v_{post} , respectively, but will usually drop the subscript “pre,” simply denoting the pre-synaptic membrane potential by v .

We assume that the effect of the pre-synaptic neuron on the post-synaptic neuron can be represented by a term of the form

$$I_{\text{syn}} = g_{\text{syn}}(t)(v_{\text{rev}} - v_{\text{post}}) \quad (20.1)$$

on the right-hand side of the equation governing v_{post} . Here $g_{\text{syn}}(t)$ is a conductance density; it rises in response to pre-synaptic action potentials, and decays to zero otherwise. The potential v_{rev} is called the *reversal potential* of the synapse. (The name is explained by the fact that $v_{\text{rev}} - v_{\text{post}}$ changes its sign when v_{post} crosses v_{rev} .) The term I_{syn} will tend to drive v_{post} towards v_{rev} .

For instance, if the synapse is GABA_A receptor-mediated, v_{rev} should be v_{Cl} , the Nernst potential of chloride, since GABA_A receptors are chloride channels. If the synapse is GABA_B receptor-mediated, v_{rev} should be v_K , since activation of GABA_B receptors opens, via a second messenger cascade, potassium channels. It is less clear what v_{rev} should be for AMPA and NMDA receptor-mediated synapses, since AMPA and NMDA receptors are non-specific cation channels, and different cations (positively charged ions) have different Nernst potentials. The overall effect of AMPA and NMDA receptor activation turns out to be excitatory, and we will use the value $v_{\text{rev}} = 0\text{ mV}$ for AMPA or NMDA receptor-mediated synapses. Notice that 0 mV is “high,” namely higher than the membrane potential at rest, which is negative. Note that both excitatory and inhibitory synaptic currents have the form (20.1). For inhibitory synaptic currents, no minus sign appears in front of $g_{\text{syn}}(t)$; instead, v_{rev} is low.

We write

$$g_{\text{syn}}(t) = \bar{g}_{\text{syn}} s(t),$$

where the conductance density \bar{g}_{syn} is an upper bound on the possible values of $g_{\text{syn}}(t)$, and $s(t) \in [0, 1]$ rises in response to pre-synaptic action potentials, and decays to zero otherwise. We call s the *synaptic gating variable*. One can think of it as the fraction of post-synaptic receptors that are activated.

It is possible for two neurons to make contact in several locations. However, since we always make the idealizing assumption that neurons have no spatial extent, we will disregard this possibility.

Since s should rise when the pre-synaptic neuron spikes, but decay to zero otherwise, we let s be governed by an equation of the form

$$\frac{ds}{dt} = \frac{1 + \tanh(v/10)}{2} \frac{1 - s}{\tau_r} - \frac{s}{\tau_d}, \quad (20.2)$$

where $\tau_r > 0$ and $\tau_d > 0$ are time constants discussed below. Note that the factor $(1 + \tanh(v/10))/2$ on the right-hand side of eq. (20.2) varies between 0 and 1, and is close to 0 when $v \ll 0$, and close to 1 when $v \gg 0$. For instance, when $v < -20$,

this factor is less than 0.02, and when $v > 20$, it is greater than 0.98. When $(1 + \tanh(v/10))/2 \approx 0$, (20.2) is approximately equivalent to

$$\frac{ds}{dt} = -\frac{s}{\tau_d},$$

which describes exponential decay to zero, with time constant τ_d . This explains the subscript d in “ τ_d ”: τ_d is the decay time constant of s when the pre-synaptic neuron is silent. We call τ_d the *synaptic decay time constant*. When $(1 + \tanh(v/10))/2 \approx 1$, the term

$$\frac{1 + \tanh(v/10)}{2} \frac{1 - s}{\tau_r} \approx \frac{1 - s}{\tau_r}$$

on the right-hand side of eq. (20.2) drives s towards 1 with time constant approximately equal to τ_r . This explains the subscript r in “ τ_r ”. We call τ_r the *synaptic rise time constant*.

The function $(1 + \tanh(v/10))/2$ appearing on the right-hand side of eq. (20.2) could be replaced, without any significant effect, by many other increasing functions of v that are close to 0 when $v \ll 0$ and close to 1 when $v \gg 0$. For instance, $(1 + \tanh(v/4))/2$ has been used by some authors; see, for instance, [17, 50]. Many other choices would work equally well; see exercise 1.

The decay time constants of AMPA receptor-mediated synapses are short; $\tau_d = 2\text{ms}$ is not unreasonable [91]. For GABA_A receptor-mediated synapses, various different decay time constants have been reported in the literature, often between 4 and 10 ms or so [69, 137]. For GABA_A receptor-mediated inhibition among basket cells in the hippocampus, much shorter decay time constants, on the order of 2 to 3 ms or even less, have also been measured [6, 97]. On the other hand, much longer decay time constants of GABA_A receptor-mediated inhibition targeting the dendrites of hippocampal pyramidal cells, on the order of tens of ms, have also been reported and used in modeling studies [58, 133, 179].

Decay time constants for GABA_B receptor-mediated synapses are much longer. For instance, in [125], the time of decay to half amplitude of the *post-synaptic potential* (the change in post-synaptic membrane potential) due to GABA_B receptor activation is reported to be slightly above 200 ms, corresponding to $\tau_d \approx 300\text{ ms}$ (exercise 2). Decay time constants for NMDA receptor-mediated synapses are of a similar order of magnitude [187]. The exact values depend on what kind of cell the post-synaptic neuron is, and in fact it is reported in [187] that the decay is best described by the sum of two exponentials, with two different decay rates; the *longer* of the two decay time constants is on the order of 200–300 ms, approximately.

When modeling a network of N synaptically connected neurons, we denote the membrane potentials by v_i , $i = 1, 2, \dots, N$. Let the i -th neuron be the pre-synaptic one, and the j -th the post-synaptic. The gating variable s and the parameters \bar{g}_{syn} , v_{rev} , τ_r , and τ_d may now all depend on i and j , and we indicate this dependence with the double index “ ij ”. The synaptic input from neuron i into neuron j is then

$$I_{\text{syn},ij} = \bar{g}_{\text{syn},ij} s_{ij}(t) (v_{\text{rev},ij} - v_j), \quad (20.3)$$

and

$$\frac{ds_{ij}}{dt} = \frac{1 + \tanh(v_i/10)}{2} \frac{1 - s_{ij}}{\tau_{r,ij}} - \frac{s_{ij}}{\tau_{d,ij}}. \quad (20.4)$$

In an all-to-all connected network, i.e., one with $\bar{g}_{\text{syn},ij} > 0$ for all i and j , each neuron receives N synaptic inputs. (We do allow $i = j$. Synapses of a neuron onto itself are called *autapses*, and they exist in the brain [154].) The number of dependent variables in such a simulation is exactly $O(N^2)$, because there are N^2 synaptic gating variables s_{ij} . (See Section 1.2 for the meaning of “exactly $O(N^2)$ ”.) If one wants to simulate large networks, this is a potential reason for concern.

However, with certain simplifying assumptions, one can reduce the number of dependent variables. We will always assume that $\tau_{r,ij}$, $\tau_{d,ij}$, and $s_{ij}(0)$ do not depend on j :

$$\tau_{r,ij} = \tau_{r,i}, \quad \tau_{d,ij} = \tau_{d,i}, \quad \text{and} \quad s_{ij}(0) = s_i(0). \quad (20.5)$$

Equation (20.4) then implies that $s_{ij}(t)$ is independent of j for all t , and this reduces the number of dependent variables from $O(N^2)$ to $O(N)$: There is now only one synaptic gating variable, $s_i = s_i(t)$, per neuron, not one per pair of neurons.

Unfortunately, this simplification is less important than it might first seem: Although there are no longer $O(N^2)$ dependent variables, there are still $O(N^2)$ terms on the right-hand side of the equations governing the v_i , and as a result the number of arithmetic operations per time step is still $O(N^2)$. To reduce this number to $O(N)$ in an all-to-all connected network requires far more restrictive and less realistic assumptions. For instance, if the $v_{\text{rev},ij}$ and $\bar{g}_{\text{syn},ij}$ depend neither on i nor on j , then the complexity per time step can be reduced from $O(N^2)$ to $O(N)$; see exercise 3. Notice that a network in which all synaptic reversal potentials are the same consists of excitatory cells only or of inhibitory cells only. The reduction to $O(N)$ arithmetic operations per time step is in fact also possible for networks including both excitatory and inhibitory neurons. However, in any case an unrealistic degree of uniformity of synaptic strengths has to be assumed for this reduction.

We do assume (20.5) now, so synaptic gating variables can be thought of as being associated with the pre-synaptic neuron. For the remainder of this section, we drop the subscripts i and j again, as we did at the beginning of the section, and denote the pre- and post-synaptic membrane potentials by v and v_{post} . Associated with the pre-synaptic neuron is the synaptic gating variable s , satisfying eq. (20.2). For the reduced Traub-Miles neuron with $I = 1 \mu\text{A}/\text{cm}^2$, we show in Fig. 20.2 graphs of v (upper panel), and s with $\tau_d = 2 \text{ ms}$, $\tau_r = 0.2 \text{ ms}$ (middle panel), and $\tau_r = 1 \text{ ms}$ (lower panel). The graphs show that one does not actually change the kinetics of s in a meaningful way by changing τ_r . Larger values of τ_r simply translate into smaller peak values of s , so increasing τ_r is very nearly equivalent to lowering \bar{g}_{syn} , i.e., to weakening the synapses. Regardless of the value of τ_r , the rise of s is limited by the duration of the action potential, and therefore very brief. An increase in τ_r simply makes s less responsive to the action potential.

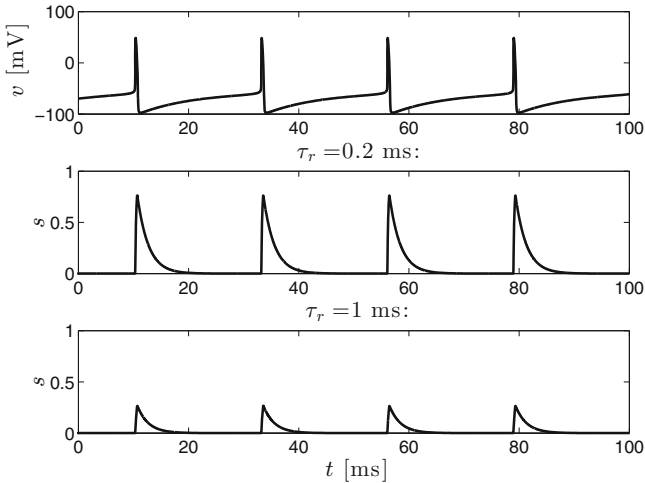


Figure 20.2. Voltage trace of RTM neuron with $I = 1 \mu\text{A}/\text{cm}^2$ (upper panel), and associated synaptic gating variable following (20.2) with $\tau_d = 2 \text{ ms}$ and $\tau_r = 0.2 \text{ ms}$ (middle panel), $\tau_r = 1 \text{ ms}$ (lower panel). [RTM_PLOT_S]

20.2 Gradual Rise

It is not always acceptable to assume that synaptic currents rise nearly instantaneously. The rise time of GABA_B receptor-mediated post-synaptic potentials was reported in [125] to be about 100 ms. For NMDA receptor-mediated synapses, rise times of approximately 5–15 ms are reported in [187]. We now describe a modification of the model of Section 20.1 that does allow a gradual rise of the synaptic gating variable. Up to details, the model described here is that proposed in [172].

We introduce a new dependent variable, q , which one might think of as a dimensionless measure of the amount of neurotransmitter in the synaptic cleft. Like the synaptic gating variable s , the variable q is associated with the pre-synaptic neuron. It satisfies an equation of the form

$$\frac{dq}{dt} = \frac{1 + \tanh(v/10)}{2} \frac{1 - q}{\tau_{r,q}} - \frac{q}{\tau_{d,q}}, \quad (20.6)$$

with $\tau_{r,q} > 0$ and $\tau_{d,q} > 0$. This is eq. (20.2), with s replaced by q , and τ_r , τ_d replaced by $\tau_{r,q}$, $\tau_{d,q}$. The term $\tanh(v/10)$ in eq. (20.6) could be replaced by many others without consequence; compare exercise 20.1.

The synaptic gating variable s is then governed by

$$\frac{ds}{dt} = q \frac{1 - s}{\tau_r} - \frac{s}{\tau_d}, \quad (20.7)$$

with $\tau_r > 0$ and $\tau_d > 0$. As long as q is close to 1, the term

$$q \frac{1 - s}{\tau_r}$$

drives s towards 1 with a time constant of τ_r . When q is close to 0, s decays to 0 with time constant τ_d .

We will discuss the choice of the time constants now. The rise time constant of q simply determines the peak value of q . Regardless of this choice, q will rise very rapidly in response to an action potential, but for larger $\tau_{r,q}$, its peak value will be smaller; see the discussion of τ_r in Section 20.1. We always choose $\tau_{r,q} = 0.1$ ms. This ensures that q reaches peak values fairly close to 1; see Fig. 20.3, which is very similar to Fig. 20.2. You might wonder why we don't make $\tau_{r,q}$ even smaller. The answer is that very small values of $\tau_{r,q}$ cause numerical stability problems, forcing us to use very small time steps Δt ; see exercise 4.1. The rapid rise of v already forces us to use small Δt , typically on the order of 0.01 ms [15]; we choose $\tau_{r,q}$ significantly larger than 0.01 ms in order to avoid having to reduce Δt even further.

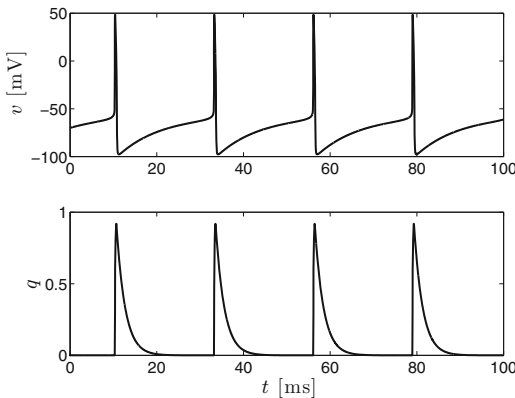


Figure 20.3. Voltage trace of RTM neuron with $I = 1 \mu\text{A}/\text{cm}^2$ (upper panel), and associated variable q following (20.6) with $\tau_d = 2$ ms and $\tau_r = 0.1$ ms (lower panel). [RTM_PLOT_Q]

In summary, our model is given by the following equations:

$$I_{\text{syn}} = \bar{g}_{\text{syn}} s(t)(v_{\text{rev}} - v_{\text{post}}), \quad (20.8)$$

$$\frac{dq}{dt} = \frac{1 + \tanh(v/10)}{2} \frac{1 - q}{0.1} - \frac{q}{\tau_{d,q}}, \quad (20.9)$$

$$\frac{ds}{dt} = q \frac{1 - s}{\tau_r} - \frac{s}{\tau_d}. \quad (20.10)$$

The current density I_{syn} is added to the right-hand side of the equation governing v_{post} . The intuitive meaning of τ_d and τ_r is easy to understand: τ_d measures how fast s decays, and τ_r measures how fast it rises *initially*; note that for $s = 0$ and $q = 1$, $ds/dt = 1/\tau_r$. The decay time constant $\tau_{d,q}$ is less intuitive; roughly, it measures how long q stays elevated following a pre-synaptic action potential, and it therefore governs how long s rises.

Figure 20.4 shows s for an RTM neuron, using rise time constants τ_r reminiscent of NMDA receptor-mediated synapses ($\tau_r = 10$ ms) and GABA_B receptor-mediated synapses ($\tau_r = 100$ ms).

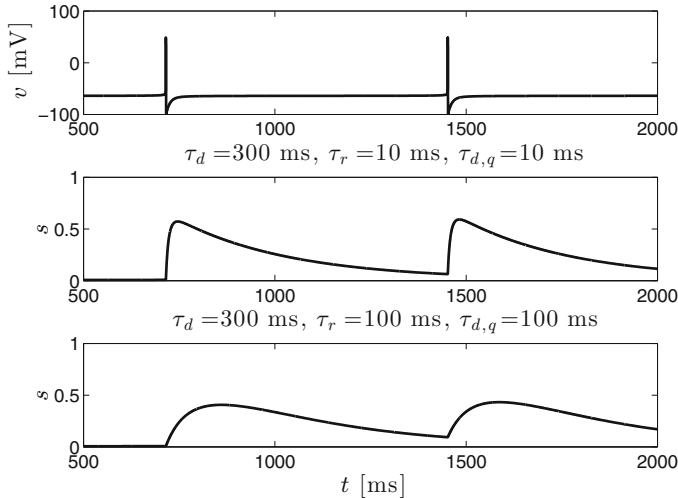


Figure 20.4. Top: Voltage trace of RTM neuron with $I = 0.12 \mu\text{A}/\text{cm}^2$. Middle: Trace of synaptic gating variable s , computed using eqs. (20.9) and (20.10), with $\tau_d = 300$ ms, $\tau_r = \tau_{d,q} = 10$ ms. Bottom: Same with $\tau_d = 300$ ms and $\tau_r = \tau_{d,q} = 100$ ms. [RTM_PLOT_S_TWO_VARIABLES]

The time course of s depends, to a small extent, on the shape of the pre-synaptic action potential. However, a pre-synaptic action potential approximately makes q jump to 1. If there is an action potential at time $t = 0$, then approximately s satisfies

$$\frac{ds}{dt} = e^{-t/\tau_{d,q}} \frac{1-s}{\tau_r} - \frac{s}{\tau_d} \quad (20.11)$$

for $t > 0$. We think about the solution of this equation with

$$s(0) = 0. \quad (20.12)$$

The term $e^{-t/\tau_{d,q}}(1-s)/\tau_r$ initially drives s up. However, as $e^{-t/\tau_{d,q}}$ decays, the term $-s/\tau_d$ takes over. As a result, s first rises, then decays. The time-to-peak τ_{peak} , i.e., the time at which the solution of (20.11), (20.12) reaches its maximum, depends continuously on $\tau_{d,q}$. (This is so because solutions of differential equations in general depend continuously on parameters in the differential equations.) The greater $\tau_{d,q}$, the slower is the decay of $e^{-t/\tau_{d,q}}$, and as a result the larger is τ_{peak} . Furthermore, τ_{peak} is very small when $\tau_{d,q}$ is very small, since then the term $e^{-t/\tau_{d,q}}(1-s)/\tau_r$ in (20.11) quickly becomes negligible. On the other hand, τ_{peak} is very large when $\tau_{d,q}$ is very large, since then (20.12) is, for a long time, approximately

$$\frac{ds}{dt} = \frac{1}{\tau_r} - \left(\frac{1}{\tau_r} + \frac{1}{\tau_d} \right) s, \quad (20.13)$$

and the solution of (20.13) with $s(0) = 0$ is monotonically increasing for all times. In summary, we have derived, not entirely rigorously but hopefully entirely convincingly, the following proposition.

Proposition 20.1. Denote by τ_{peak} the time at which the solution of (20.11), (20.12) reaches its maximum. For fixed $\tau_d > 0$ and $\tau_r > 0$, τ_{peak} is a continuous and strictly increasing function of $\tau_{d,q}$ with

$$\lim_{\tau_{d,q} \searrow 0} \tau_{\text{peak}} = 0 \quad \text{and} \quad \lim_{\tau_{d,q} \rightarrow \infty} \tau_{\text{peak}} = \infty.$$

Given $\tau_d > 0$ and $\tau_r > 0$, Proposition 20.1 implies that for any prescribed value $\hat{\tau} > 0$, there is exactly one $\tau_{d,q} > 0$ for which $\tau_{\text{peak}} = \hat{\tau}$. Furthermore, this value $\tau_{d,q}$ is easy to compute using the bisection method (see Appendix A). We therefore will from here on think of τ_{peak} , not $\tau_{d,q}$, as the given model parameter. The value of $\tau_{d,q}$ is computed from τ_{peak} , using the simplified equation (20.11), but then used in the full model given by eqs. (20.8)–(20.10); see Fig. 20.5.

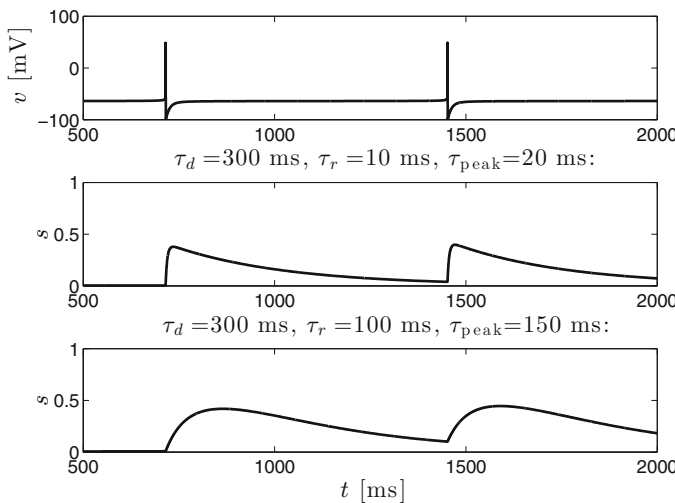


Figure 20.5. Similar to Fig. 20.4, but with τ_{peak} prescribed and $\tau_{d,q}$ calculated from it. [RTM_PLOT_S_PRESCRIBE_TAU_PEAK]

Both the model in Section 20.1, and the modified model in the present section, are not, of course, derived from first principles. For a more fundamental discussion of the modeling of synapses, see [36].

20.3 The Self-Exciting RTM Neuron

The motivation for the model discussed here was given in Section 16.2. Figure 20.6 shows the f - I curve for an RTM neuron with an *autapse*, i.e., a synapse from the neuron onto itself, modeled as described in Section 20.2, with $v_{\text{rev}} = 0 \text{ mV}$, $\bar{g}_{\text{syn}} = 0.1 \text{ mS/cm}^2$, $\tau_d = 5 \text{ ms}$, $\tau_r = 0.2 \text{ ms}$, $\tau_{\text{peak}} = 0.6 \text{ ms}$. We see bistability between

two critical values of I , which we call, as before, I_* and I_c . This is not surprising: For I strong enough, but not so strong that stable rest is no longer possible, one would expect that the excitatory autapse could perpetuate firing once it begins. A more detailed investigation shows that there are a saddle-node bifurcation at I_c (exercise 4), and a homoclinic bifurcation at I_* , so we have here another example of a model of bifurcation type 3.

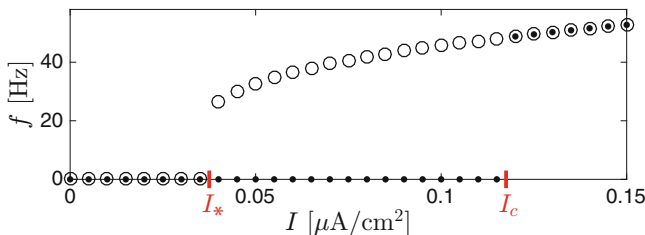


Figure 20.6. f - I curve of the RTM neuron with an excitatory autapse, modeled as in Section 20.2, with $\tau_d = 5 \text{ ms}$, $\tau_r = 0.2 \text{ ms}$, $\tau_{\text{peak}} = 0.6 \text{ ms}$.
[RTM_WITH_AUTAPSE_F_I_CURVE]

The parameters in Fig. 20.6 may not be so realistic (too slow for AMPA receptor-mediated synapses, too fast for NMDA receptor-mediated ones), but see exercise 5.

20.4 The Jahr-Stevens Model of NMDA Receptor-Mediated Synapses

For NMDA receptor-mediated synapses, there is a complication that ought to be reflected by the model synapse: The receptors can be blocked by magnesium. This effect is stronger when the post-synaptic neuron is more strongly hyperpolarized; depolarization removes the magnesium block. The simplest and most common model of this effect is due to Jahr and Stevens [84]: Instead of the usual formula

$$I_{\text{syn}} = \bar{g}_{\text{syn}} s(t)(v_{\text{rev}} - v_{\text{post}}),$$

one uses

$$I_{\text{syn}} = \bar{g}_{\text{syn}} s(t)B(v_{\text{post}})(v_{\text{rev}} - v_{\text{post}}), \quad (20.14)$$

with

$$B(v_{\text{post}}) = \frac{1}{1 + \frac{[\text{Mg}]_{\text{ex}}}{3.57} \exp(-0.062v_{\text{post}})}$$

where $[\text{Mg}]_{\text{ex}}$ denotes the magnesium concentration in the extracellular fluid, measured in mM (*millimolar*). By definition, mM stands for 10^{-3}M , and M (*molar*) stands for moles per liter. A *mole* of a substance consists of N_A molecules, where N_A denotes *Avogadro's number*, $N_A \approx 6 \times 10^{23}$. A typical value of $[\text{Mg}]_{\text{ex}}$ is 1 mM.

This is the value that we will use in this book, so we will write

$$B(v_{\text{post}}) = \frac{1}{1 + \frac{\exp(-0.062v_{\text{post}})}{3.57}}. \quad (20.15)$$

Figure 20.7 shows B as a function of v_{post} .

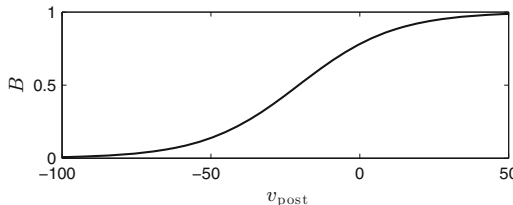


Figure 20.7. The function B defined in eq. (20.15). [B_JAHR_STEVENS]

20.5 Buildup of the Synaptic Gating Variable over Multiple Action Potentials

Figure 20.8 shows the voltage trace of an RTM neuron with $I = 0.2$, and the synaptic gating variable s of the model in Section 20.2, with the parameter values indicated in the caption, and with $s(0) = 0$. We see s build up over several action potentials. Figure 20.9 shows another example, in which the build up lasts over a much greater number of action potentials.

In view of these figures, it seems plausible that the buildup of s will be gradual if two conditions are met: First, the decay in s between two action potentials is small, and second, the rise in s caused by a single action potential is small. In terms of the parameters of our model, the first of these conditions translates into $\tau_d \gg T$, where T is the firing period. To understand what the second condition means for the parameters of our model, notice that from eq. (20.10), for $s \approx 0$, $ds/dt \approx 1/\tau_r$ soon after an action potential. (Recall that in response to an action potential, q jumps to a value near 1 nearly instantaneously.) This suggests that the condition under which the rise in s remains much smaller than 1 should be $\tau_{d,q} \ll \tau_r$ — that is, the rise of s is cut short by the removal of neurotransmitter from the synaptic cleft.

In summary, we obtain graduate buildup of s over many action potentials if the inactivation of the synaptic receptors is slow, and the removal of neurotransmitter from the synaptic cleft is fast:

$$\tau_d \gg T \quad \text{and} \quad \tau_{q,d} \ll \tau_r. \quad (20.16)$$

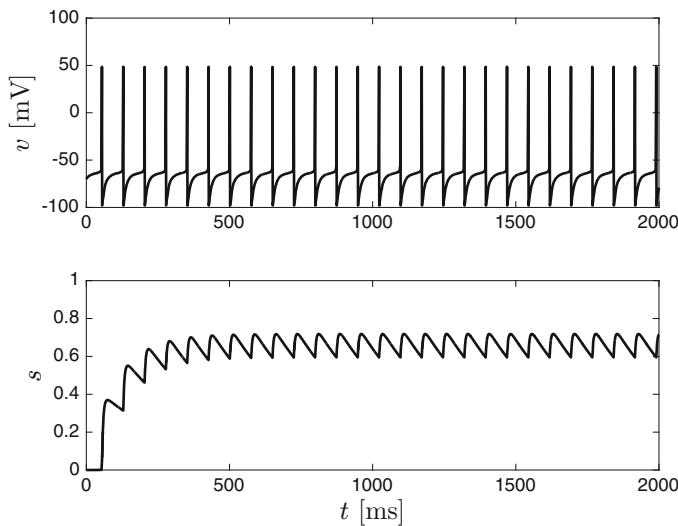


Figure 20.8. Buildup of the synaptic gating variable s over several action potentials. The upper panel shows the voltage trace of an RTM neuron firing with period $T \approx 74.5$. The lower panel shows the time evolution of s , with $\tau_r = 10$, $\tau_{d,q} = 5$, $\tau_d = 300$. [S_BUILDUP]

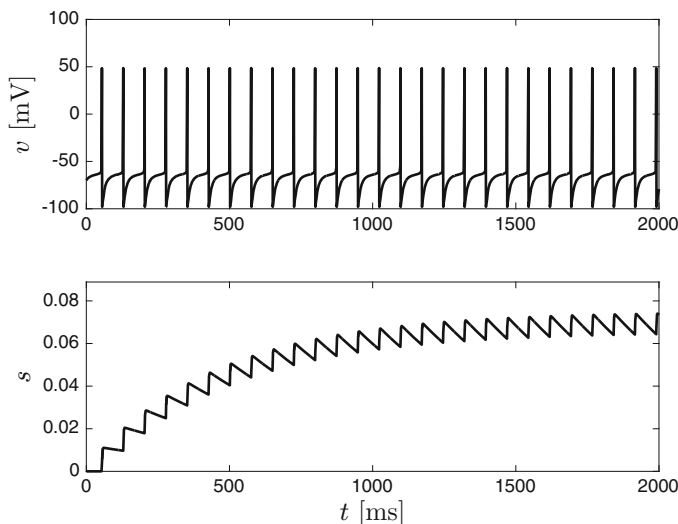


Figure 20.9. Analogous to Fig. 20.8, but with $\tau_r = 100$, $\tau_{d,q} = 1$, $\tau_d = 500$. [S_SLOW_BUILDUP]

Exercises

- 20.1. (a) Suppose that $g = g(v)$ is an increasing function with the properties $\lim_{v \rightarrow -\infty} g(v) = 0$, $\lim_{v \rightarrow \infty} g(v) = 1$, and $g(0) = 1/2$. Show that for any $\Delta > 0$, the function $g(v/\Delta)$ has these properties as well. Does the function get steeper, or less steep, near $v = 0$ as Δ increases? (b) Show that the functions $g(v) = (1 + \tanh(v))/2$, $\arctan(v)/\pi + 1/2$, and $(v/\sqrt{1 + v^2} + 1)/2$ have the properties listed in part (a). (c) (*) On the right-hand side of eq. (20.2), you could replace $(1 + \tanh(v/10))/2$ by many other functions of the form $g(v/\Delta)$, where g has the properties listed in part (a), and $\Delta > 0$. Re-compute the middle panel of Fig. 20.2 using the three choices of g in part (b), and using $\Delta = 1, 5$, and 10 . You will get 9 different plots. One of them, the one with $g(v) = (1 + \tanh(v))/2$ and $\Delta = 10$, will be the middle panel of Fig. 20.2. How do the others differ from it? Can you explain the differences you see?
- 20.2. In [125], the time it takes for GABA_B receptor-mediated inhibition to decay to half amplitude is reported to be about 200 ms. Assuming that the amplitude decays proportionally to e^{-t/τ_d} , what is τ_d ?
- 20.3. Consider a network of N model neurons, synaptically connected as described in Section 20.1. Make the assumptions given by eq. (20.5), and in addition assume

$$v_{\text{rev},ij} = v_{\text{rev},j} \quad \text{and} \quad \bar{g}_{\text{syn},ij} = \bar{g}_{\text{syn},i}. \quad (20.17)$$

Explain why now the number of operations needed in each time step can be reduced from $O(N^2)$ to $O(N)$.

The first of the two assumptions in (20.17) would be satisfied, for instance, if all synaptic reversal potentials were the same. All synapses would then be inhibitory, or all would be excitatory. There are contexts in which this is not unreasonable: For instance, the *lateral septum* is a brain structure mostly comprised of inhibitory cells [142]. Furthermore, the assumption $v_{\text{rev},ij} = v_{\text{rev},j}$ can be relaxed a bit, allowing both excitatory and inhibitory synapses.

The most problematic assumption in (20.17) is the second one. It is a *homogeneity* assumption: All synapses in which neuron i is the pre-synaptic cell have to have the same strength. This is not usually the case in real networks, and heterogeneity (non-uniformity) of synaptic strengths in networks has significant consequences.

- 20.4. (*) (†) Demonstrate numerically that the self-exciting RTM neuron with $\bar{g}_{\text{syn}} = 0.1 \text{ mS/cm}^2$, $v_{\text{rev}} = 0 \text{ mV}$, $\tau_d = 5 \text{ ms}$, $\tau_r = 0.2 \text{ ms}$, $\tau_{\text{peak}} = 0.6 \text{ ms}$ (see Fig. 20.6) has a saddle-node bifurcation at I_c .
- 20.5. (*) Compute the f - I curve of the self-exciting RTM neuron with $\bar{g}_{\text{syn}} = 0.02 \text{ mS/cm}^2$, $v_{\text{rev}} = 0 \text{ mV}$, and time constants reminiscent of NMDA receptor-mediated synapses: $\tau_d = 300 \text{ ms}$, $\tau_r = 10 \text{ ms}$, $\tau_{\text{peak}} = 20 \text{ ms}$. Include the Jahr-Stevens model of the magnesium block.

Chapter 21

Gap Junctions

In addition to *chemical synapses* involving neurotransmitters, there are also *electrical synapses* at sites known as *gap junctions*. A gap junction is a location where two neuronal membranes come very close to each other, with holes in both membranes allowing direct passage of charged particles from one cell into the other. We will always assume that there is no preferred direction for the flow of ions [29]; in this regard, most gap-junctional coupling is very different from chemical synaptic coupling, where communication is asymmetric. In invertebrates, however, there do exist gap junctions that allow the passage of charged particles in only one direction; they are called *rectifying* [111].

Signaling via gap junctions is very fast. In fact the earliest examples of gap junctions found in vertebrates involve cells mediating escape maneuvers of crayfish and gold fish [42, 95], where of course speed can be important for survival. Gap-junctional coupling also plays an important role in the synchronization of neuronal activity [29]; see Proposition 21.1 below.

We assume that the gap-junctional coupling of two neurons with membrane potentials v_i and v_j causes the flow of a current

$$I_{i \rightarrow j} = g_{\text{gap},ij}(v_i - v_j)$$

into neuron j . More precisely, $I_{i \rightarrow j}$ should be thought of as a current *density*, and it appears as an extra summand on the right-hand side of the equation governing v_j . The parameter $g_{\text{gap},ij}$ is a conductance density. At the same time, an extra current density

$$I_{j \rightarrow i} = g_{\text{gap},ji}(v_j - v_i)$$

Electronic supplementary material: The online version of this chapter (doi: [10.1007/978-3-319-51171-9_21](https://doi.org/10.1007/978-3-319-51171-9_21)) contains supplementary material, which is available to authorized users.

appears on the right-hand side of the equation for v_i . The symmetry of the gap junction is reflected by the relation

$$g_{\text{gap},ji} = g_{\text{gap},ij}, \quad (21.1)$$

which implies that

$$I_{j \rightarrow i} = -I_{i \rightarrow j}.$$

In fact, $I_{j \rightarrow i}$ and $I_{i \rightarrow j}$ represent the same current: A positive current from neuron i into neuron j , for instance, can also be interpreted as a negative current of the same magnitude from neuron j into neuron i . Notice that $I_{j \rightarrow j} = 0$. We might as well assume that

$$g_{\text{gap},jj} = 0 \quad \text{for all } j,$$

and we will make this assumption from here on.

In a network of N neurons with all-to-all gap-junctional coupling, the equation for v_j includes the term

$$I_{\text{gap},j} = \sum_{i=1}^N g_{\text{gap},ij}(v_i - v_j) \quad (21.2)$$

on the right-hand side. In reality, gap-junctional coupling is usually quite sparse, so many of the $g_{\text{gap},ij}$ are zero. We will use the notation

$$\mathbf{v} = \begin{bmatrix} v_1 \\ v_2 \\ \vdots \\ v_N \end{bmatrix}, \quad G = [g_{\text{gap},ij}]_{1 \leq i,j \leq N}.$$

\mathbf{v} is a vector in \mathbb{R}^N , and G a real $N \times N$ -matrix. Equation (21.1) states that G is symmetric, i.e., it equals its transpose: $G^T = G$. The expression in (21.2) can then be written as

$$I_{\text{gap},j} = [G^T \mathbf{v}]_j - c_j v_j = [G \mathbf{v}]_j - c_j v_j, \quad (21.3)$$

where $[\cdot]_j$ denotes the j -th component of the vector in the brackets, and

$$c_j = \sum_{i=1}^N g_{\text{gap},ij} \quad (21.4)$$

is the sum of the entries of the j -th column of G , briefly called the j -th *column sum* of G . Because G is symmetric, c_j is also the j -th *row sum* of G , i.e., the sum of the entries in the j -th row of G . To write (21.2) in the form (21.3) is useful because it suggests arranging the computation in a cost-saving way, as follows. Let us (unrealistically) assume that the N neurons are gap-junctionally coupled with all-to-all connectivity, i.e., that the $g_{\text{gap},ij}$ are all positive, or (more realistically) that the fact that many of them are zero is ignored in the computation for convenience. Then the computation of the c_j takes $O(N^2)$ operations, but can be done once

and for all before the computation starts, and need not be repeated in each time step. The matrix-vector multiplication $G\mathbf{v}$ is then the only piece of the computation of (21.2) that requires $O(N^2)$ operations per time step.

If (21.2) were the entire right-hand side of the j -th equation, the system of differential equations would be

$$C \frac{dv_j}{dt} = \sum_{i=1}^N g_{\text{gap},ij}(v_i - v_j), \quad j = 1, 2, \dots, N. \quad (21.5)$$

One says that this system describes *discrete diffusion*: Voltage flows from the i -th neuron to the j -th at a rate proportional to $v_i - v_j$. The name “discrete diffusion” is especially justified if we assume that $g_{\text{gap},ij} > 0$ only when neurons i and j are neighbors — as, of course, is the case in the brain.

If the connectivity is “dense enough” (see below), discrete diffusion tends to equilibrate the membrane potentials of all neurons in the network. Intuitively, this is not surprising: If $v_j < v_i$, there is a current from neuron i into neuron j , and vice versa. To explain what “dense enough” means, we symbolize the N neurons by N dots in the plane, and connect the i -th dot with the j -th if and only if $g_{\text{gap},ij} > 0$. This is called the *connectivity graph*; see Fig. 21.1. The dots are called the *nodes* of the graph. The connectivity is dense enough for the assertion made above to hold if the connectivity graph is *connected*, meaning that it is possible to walk from any node in the graph to any other node following edges.



Figure 21.1. Two examples of connectivity graphs of networks of $N = 5$ gap-junctionally connected neurons. The left one is connected, the right one is not.

We can now make a precise statement about discrete diffusion equilibrating the v_j . To prove the following proposition, with a sequence of hints, is exercise 1.

Proposition 21.1. Suppose that the connectivity graph is connected, and $v_j(t)$, $t \geq 0$, $1 \leq j \leq N$, satisfy (21.5). Then

$$\lim_{t \rightarrow \infty} v_j(t) = m_0 \quad \text{for all } j, \quad \text{with} \quad m_0 = \frac{1}{N} \sum_{j=1}^N v_j(0).$$

Things become more complicated, of course, when we bring the Hodgkin-Huxley currents back. We consider two WB neurons, connected by a gap junction of strength $g_{\text{gap}} = 0.01 \text{ mS/cm}^2$. The first neuron has drive $I = 1 \mu\text{A/cm}^2 > I_c$, so it fires periodically, while the second neuron has drive $I = 0 \mu\text{A/cm}^2$, so it does not fire intrinsically. We plot the membrane potentials, v_1 and v_2 . The results are

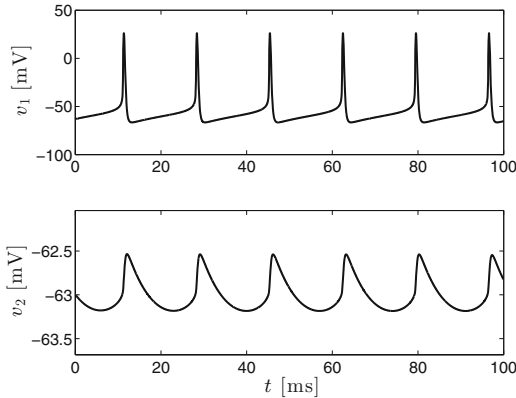


Figure 21.2. Two WB neurons, one driven above threshold and the other below threshold, with weak gap-junctional coupling ($g_{\text{gap}} = 0.01$). [WB_NETWORK_WITH_GJ]

shown in Fig. 21.2. The membrane potential v_2 oscillates in response to the periodic firing of the first neuron. Each time the first neuron fires, there is a sudden steep surge in v_2 by about 0.5 mV. This is comparable to the amplitudes of gap-junctional potentials reported in [152]. It is clear why there are sudden nearly instantaneous rises in v_2 in response to action potentials of the first neuron: The gap-junctional current (to be precise, current density) into the second neuron is

$$I_{\text{gap}} = g_{\text{gap}}(v_1 - v_2),$$

and when v_1 spikes, so does I_{gap} .

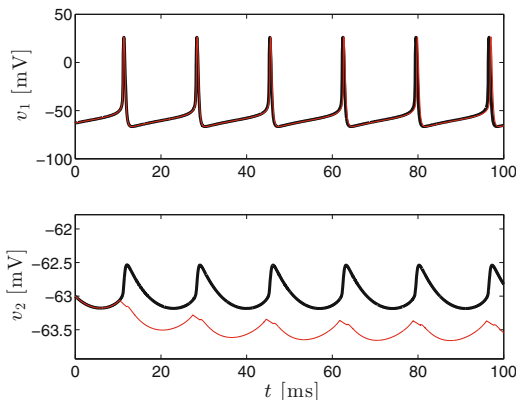


Figure 21.3. Black: Same as Fig. 21.2. Red: Results of a simulation in which the gap-junctional coupling is turned off whenever $v_1 > -50$ mV. [WB_NETWORK_WITH_GJ_SUBTHRESHOLD]

You might wonder whether the sudden surge in v_2 triggered when the first neuron fires is really important during inter-spike intervals. Figure 21.3 suggests that it is. The red curves in Fig. 21.3 show how Fig. 21.2 changes if we turn off the gap junctions whenever v_1 exceeds -50 mV, that is, during action potentials: v_1 remains nearly unchanged, but v_2 drops by 0.5 mV even during the inter-spike intervals of the first neuron.

This sounds like bad news for integrate-and-fire models, which do not attempt to reproduce the shape of the voltage spikes. However, this problem has the following simple solution, proposed in [103]. Suppose that v_1 and v_2 are the membrane potentials of two gap-junctionally coupled integrate-and-fire neurons. When v_1 reaches the firing threshold and is therefore reset, v_2 is raised by a small amount $\epsilon > 0$ to account for the effect that the spike in v_1 would have had on v_2 , had it been simulated. If adding ϵ raises v_2 above the firing threshold, then we reset it as well.

Two gap-junctionally coupled LIF neurons, with the normalizations in eqs. 7.6 and 7.7, are therefore governed by the following equations.

$$\frac{dv_1}{dt} = -\frac{v_1}{\tau_m} + I_1 + g_{\text{gap}}(v_2 - v_1) \quad \text{if } v_1 < 1 \text{ and } v_2 < 1, \quad (21.6)$$

$$\frac{dv_2}{dt} = -\frac{v_2}{\tau_m} + I_2 + g_{\text{gap}}(v_1 - v_2) \quad \text{if } v_1 < 1 \text{ and } v_2 < 1, \quad (21.7)$$

$$v_1(t+0) = 0 \quad \text{and}$$

$$v_2(t+0) = \begin{cases} v_2(t-0) + \epsilon & \text{if } v_2(t-0) + \epsilon < 1, \\ 0 & \text{if } v_2(t-0) + \epsilon \geq 1, \end{cases} \quad \text{if } v_1(t-0) = 1, \quad (21.8)$$

$$v_2(t+0) = 0 \quad \text{and}$$

$$v_1(t+0) = \begin{cases} v_1(t-0) + \epsilon & \text{if } v_1(t-0) + \epsilon < 1, \\ 0 & \text{if } v_1(t-0) + \epsilon \geq 1, \end{cases} \quad \text{if } v_2(t-0) = 1. \quad (21.9)$$

(For simplicity, we have taken the membrane time constant, τ_m , to be the same for both neurons; of course one could think about the case of two different membrane time constants as well.) The two parameters $g_{\text{gap}} > 0$ and $\epsilon > 0$ are not unrelated. As pointed out in [103], ϵ should be taken to be proportional to g_{gap} :

$$\epsilon = \beta g_{\text{gap}},$$

where $\beta > 0$. We will do a rough calculation to see what a sensible choice of β might be. In Fig. 5.3, the membrane potential of a periodically firing WB neuron approximately resets to -67 mV in each spike, then rises to approximately -52 mV, and then an action potential occurs; this is demonstrated by Fig. 21.4, where we have indicated the horizontal lines $v \equiv -67$ mV and $v \equiv -52$ mV in blue. Since in a normalized LIF neuron, v rises by 1 unit between reset and threshold, we should approximately identify a rise of the membrane potential of the WB neuron by 0.5 mV with a rise of the normalized v of the LIF neuron by $\epsilon = 0.5/15 = 1/30$. Since in Fig. 21.2, $g_{\text{gap}} = 0.01$ and there is a rise in v_2 by approximately 0.5 mV each time the first neuron fires, it is not unreasonable to set β so that $1/30 \approx 0.01\beta$. We will therefore use

$$\beta = 3.$$

(With $g_{\text{gap}} = 0.01$, this yields $\epsilon = 0.03$, comparable to the value of 0.04 in [103, Fig. 2]. Note, however, that $g_{\text{gap}} = 0.2$ in [103, Fig. 2].) Using $\beta = 3$, we reproduce Fig. 21.3 using two LIF neurons; this is shown in Fig. 21.5. The figures are qualitatively quite similar. Again, omitting the impact of spikes in v_1 on v_2 would lead to a significant decrease in v_2 even between spikes.

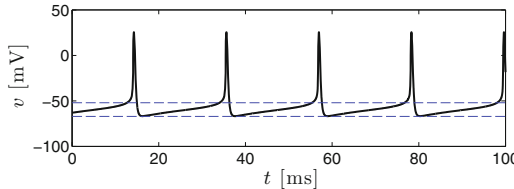


Figure 21.4. Like Fig. 5.3, with the lines $v \equiv -67 \text{ mV}$ and $v \equiv -52 \text{ mV}$ indicated as dashed blue lines, to demonstrate that the WB neuron resets at approximately -67 mV , and its firing threshold is at approximately -52 mV . [RESET_THRESHOLD]

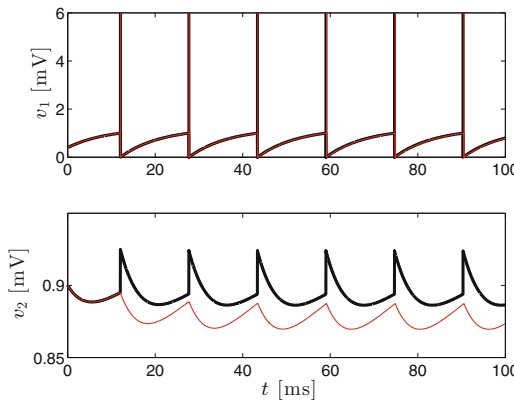


Figure 21.5. Two LIF neurons, with $\tau_m = 10$ and $I_1 = 0.125$ (above the spiking threshold $I_c = 1/\tau_m = 0.1$), $I_2 = 0.09$ (below the spiking threshold), gap-junctionally connected with $g_{\text{gap}} = 0.01$, $\epsilon = \beta g_{\text{gap}}$, $\beta = 3$ (black) and $\epsilon = 0$ (red). We have indicated voltage spikes with vertical lines in the graph of v_1 . This figure should be compared with Fig. 21.3. [LIF_NETWORK_WITH_GJ]

In general, when modeling gap-junctional coupling, models or numerical methods that do not reproduce accurate spike shapes are problematic. For example, it is not clear how to properly include gap-junctional coupling when using theta neurons. Another example is the numerical method that we proposed in [15], which

sacrifices resolution during action potentials to gain overall computational speed; it is not clear how one can accurately reproduce the effects of gap-junctional coupling when using this method.

Exercises

- 21.1. (†) The aim of this exercise is to prove Proposition 21.1. Let $\mathbf{v}_0 \in \mathbb{R}^N$, and supplement (21.5) with the initial condition

$$\mathbf{v}(0) = \mathbf{v}_0. \quad (21.10)$$

Denote by m_0 the average of the entries in \mathbf{v}_0 . You will prove that the solution of (21.5), (21.10) converges to $m_0 \mathbf{e}$, where

$$\mathbf{e} = \begin{bmatrix} 1 \\ \vdots \\ 1 \end{bmatrix}.$$

In other words, all v_j converge to m_0 as $t \rightarrow \infty$. We write (21.5) in matrix-vector form:

$$C \frac{d\mathbf{v}}{dt} = (G - D)\mathbf{v}, \quad (21.11)$$

where D denotes the diagonal $N \times N$ -matrix that has in its main diagonal the column sums (or, equivalently, the row sums) of G , i.e., the c_j defined in eq. (21.4). The matrix $G - D$ is symmetric. Using a theorem from Linear Algebra, we conclude that there is an orthogonal basis of \mathbb{R}^N consisting of eigenvectors of $G - D$, associated with real eigenvalues. We call the basis vectors $\mathbf{b}_1, \mathbf{b}_2, \dots, \mathbf{b}_N$, and the associated eigenvalues $\lambda_1, \lambda_2, \dots, \lambda_N$, so

$$(G - D)\mathbf{b}_k = \lambda_k \mathbf{b}_k, \quad k = 1, 2, \dots, N.$$

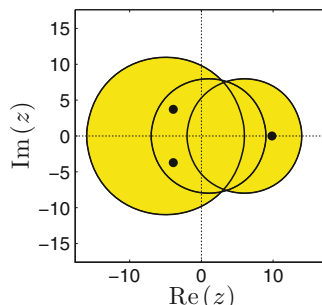


Figure 21.6. Gershgorin disks (yellow) and eigenvalues (black dots) of a real 3×3 -matrix.

(a) Your first task is to prove that the eigenvalues must be ≤ 0 . You can do this using *Gershgorin's Theorem*, which states that for any complex $N \times N$ -matrix

$$A = [a_{ij}]_{1 \leq i,j \leq N},$$

any eigenvalue, λ , lies in one of the *Gershgorin disks*. The Gershgorin disks are the disks

$$\{z \in \mathbb{C} : |z - a_{jj}| \leq \sum_{i \neq j} |a_{ij}|\}, \quad 1 \leq j \leq N,$$

in the complex plane. For instance, take

$$A = \begin{bmatrix} -5 & 3 & 0 \\ -7 & 6 & -8 \\ -4 & -5 & 1 \end{bmatrix}.$$

Figure 21.6 shows the Gershgorin disks and eigenvalues of A .

- (b) Show that $(G - D)\mathbf{e} = \mathbf{0}$, so 0 is an eigenvalue with eigenvector \mathbf{e} .
 - (c) Let $\mathbf{v} \in \mathbb{R}^N$ with $(G - D)\mathbf{v} = \mathbf{0}$. Prove that \mathbf{v} has the *discrete mean value property*, that is: For each j , v_j is a weighted average of those v_i that have the property that nodes i and j are connected in the connectivity matrix, in other words $g_{\text{gap},ij} > 0$.
 - (d) Prove: If $(G - D)\mathbf{v} = \mathbf{0}$, then \mathbf{v} is a constant multiple of \mathbf{e} , that is, all the v_j are the same. Hint: Think first about a j with $v_j = \max_{1 \leq k \leq N} v_k$. Prove that for all i with $g_{\text{gap},ij} > 0$, $v_i = v_j$. Then use the connectedness of the connectivity graph.
 - (e) Complete the proof of the proposition by expanding \mathbf{v} with respect to the eigenvectors $\mathbf{b}_1, \dots, \mathbf{b}_N$.
- 21.2. (*) In the simulation of Fig. 21.2, how large would g_{gap} have to be to make the second neuron fire?
- 21.3. (*) In the program that generated Fig. 21.2, set the drive, I_2 , to the second neuron to a value slightly below 1. The drive to the first neuron, I_1 , should be 1, as in Fig. 21.2. Then explore whether the gap-junctional connection, using $g_{\text{gap}} = 0.01$ as in Fig. 21.2, will cause the two neurons to fire at the exactly same frequency after a while.
- Here is a suggested way of doing this. Simulate the two neurons for a long time, say for 2000 ms. Record their spike times. (Refer to exercise 17.1.) Let's denote the spike times by

$$t_{1,1} < t_{1,2} < \dots < t_{1,n_1} \quad \text{and} \quad t_{2,1} < t_{2,2} < \dots < t_{2,n_2}.$$

The inter-spike intervals are then of durations

$$t_{1,2} - t_{1,1}, \dots, t_{1,n_1} - t_{1,n_1-1} \quad \text{and} \quad t_{2,2} - t_{2,1}, \dots, t_{2,n_2} - t_{2,n_2-1}.$$

In a single figure, plot i vs. $t_{1,i} - t_{1,i-1}$, $i = 2, \dots, n_1$ and, in a different color, i vs. $t_{2,i} - t_{2,i-1}$, $i = 2, \dots, n_2$.

One says that the two neurons are *phase-locked* when their periods (that is, their frequencies) are equal. Note that this does not mean that they fire at the same times, only that the first neuron always fires at the same phase in the cycle of the second and vice versa. We will distinguish *phase-locking* from *synchronization*, which we will define to mean that the neurons fire at the same times. So synchronization is a special kind of phase-locking.

Chapter 22

A Wilson-Cowan Model of an Oscillatory E-I Network

There is a large literature on neuronal network models attempting to model neuronal population activity without modeling individual neurons. It is useful to develop such models because the number of neurons that one must deal with to understand the brain is so overwhelmingly large. One of the earliest and most influential such models is the *Wilson-Cowan model*, first introduced in 1972 [185].

Models of this kind are not the focus of this book, but we will discuss a simple example here, a Wilson-Cowan model describing the dynamics of a network of neurons consisting of excitatory and inhibitory neurons (*E-cells* and *I-cells*). We call such a network an *E-I network*. In general, in an E-I network, the E-cells excite each other and the I-cells, and the I-cells inhibit each other and the E-cells. In addition, both the E- and the I-cells receive external drives, which we will denote by I_E and I_I . Figure 22.1 shows a symbolic depiction of an E-I network. In the figure, arrows indicate excitation, and solid circles indicate inhibition. This convention will be used frequently throughout the remainder of this book.

A Wilson-Cowan model of an E-I network describes the time evolution of the mean firing rates, $E = E(t)$ and $I = I(t)$, of the E- and I-cells, respectively. To explain the phrase *mean firing rate*, suppose that there is a very large number, N_E , of excitatory neurons. Assume also that $\Delta t > 0$ is small. Then the number of excitatory neurons that fire between times $t - \Delta t$ and t is approximately $E(t)\Delta t N_E$. The interpretation of $I(t)$ is analogous. We think of E and I as frequencies measured in Hz, and, as previously, of time as measured in ms, and will usually not specify the units explicitly.

The general Wilson-Cowan model is given by two differential-integral equations relating the derivatives dE/dt and dI/dt to present and past values of E and I . We will focus on a simplification of the model, called *time coarse-grained* in [185], in

Electronic supplementary material: The online version of this chapter (doi: [10.1007/978-3-319-51171-9_22](https://doi.org/10.1007/978-3-319-51171-9_22)) contains supplementary material, which is available to authorized users.

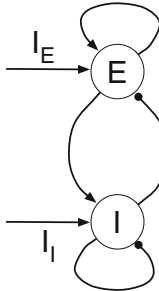


Figure 22.1. Symbolic depiction of an E-I network. Arrows indicate excitation, and solid circles inhibition.

which dE/dt and dI/dt depend on present values of E and I only. Thus the model is a system of ODEs. It is of the general form

$$\frac{dE}{dt} = \frac{f(w_{EE}E - w_{IE}I + I_E) - E}{\tau_E}, \quad \frac{dI}{dt} = \frac{g(w_{EI}E - w_{II}I + I_I) - I}{\tau_I}. \quad (22.1)$$

(In writing the system in this form, I also assumed that refractoriness is unimportant; see [185] for the small corrections to the equations needed to account for refractoriness.) We will next discuss the physical dimensions and meaning of the parameters and the functions f and g appearing in eqs. (22.1).

The weights $w_{EE} \geq 0$, $w_{IE} \geq 0$, $w_{EI} \geq 0$, and $w_{II} \geq 0$ are dimensionless. They represent coupling strengths: w_{EE} measures how strongly E-cells excite each other, w_{EI} measures how strongly E-cells excite I-cells, and so on. The parameters I_E and I_I , which should be thought of as normalized input drives to the E- and I-cells, respectively, are frequencies, and so are the values of the functions f and g . We assume that f and g are increasing, and will say more about them shortly. If f and g were constant, say $f \equiv f_0$ and $g \equiv g_0$, then eqs. (22.1) would drive E and I towards f_0 and g_0 , respectively, exponentially fast with time constants τ_E and τ_I .

We will assume that neuronal frequencies vary between 0 and 100 Hz. (Although there are examples of faster firing in the brain, it isn't common.) It is therefore natural to assume that f and g have values between 0 and 100 Hz. With this assumption, if $E(0)$ and $I(0)$ lie between 0 and 100 Hz, then $E(t)$ and $I(t)$ lie between 0 and 100 Hz for all $t \geq 0$ (exercise 1). We also typically assume that f and g are differentiable, increasing, and have exactly one inflection point. We call a function of a single real variable that is bounded, differentiable, increasing, and has exactly one inflection point *sigmoidal*.

We now consider an example of specific choices for the parameters in (22.1), and for the functions f and g . Our example is almost precisely taken from [184]. First, we set

$$w_{EE} = 1.5, \quad w_{IE} = 1, \quad w_{EI} = 1, \quad w_{II} = 0. \quad (22.2)$$

Thus we omit self-inhibition of the inhibitory population, but not *recurrent excitation*, i.e., self-excitation of the excitatory population. Next, we set

$$\tau_E = 5, \quad \tau_I = 10. \quad (22.3)$$

Neuronal activity does not follow excitation instantly, but with a delay, since synapses don't act instantaneously and there are delays in the conduction of neuronal signals. We think of the interactions in our network as mediated by AMPA and GABA_A receptors. Since AMPA receptor-mediated excitation is typically somewhat faster than GABA_A receptor-mediated inhibition, it is reasonable to make τ_I greater than τ_E .

We set

$$f(x) = \begin{cases} \frac{100x^2}{30^2 + x^2} & \text{if } x \geq 0, \\ 0 & \text{otherwise,} \end{cases} \quad (22.4)$$

and

$$g(x) = \begin{cases} \frac{100x^2}{20^2 + x^2} & \text{if } x \geq 0, \\ 0 & \text{otherwise,} \end{cases} \quad (22.5)$$

Notice the significance of the terms 30^2 and 20^2 appearing in these definitions: $f(30) = 50$ and $g(20) = 50$. For all x , $f(x) \leq g(x)$; that is, the I-cells are assumed to be activated more easily than the E-cells.

Finally, we set

$$I_E = 20, \quad I_I = 0. \quad (22.6)$$

Thus we assume that the E-cells are driven harder than the I-cells.

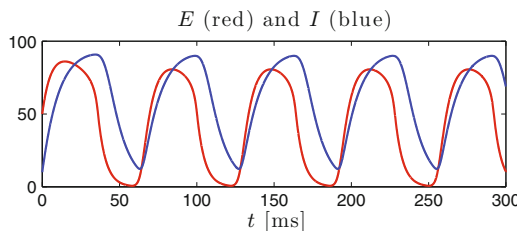


Figure 22.2. A solution of the Wilson-Cowan model of an E-I network given by eqs. (22.1)–(22.6). [WILSON_COWAN_E_AND_I]

A solution is shown in Fig. 22.2. Figure 22.3 depicts the same solution in the phase plane. There is an attracting limit cycle, an oscillatory solution, with surges in E always promptly followed by surges in I .

Remembering that E and I denote mean firing frequencies of large populations of neurons, we can visualize the solution of eqs. (22.1)–(22.6) depicted in Figs. 22.2 and 22.3 in yet another way; see Fig. 22.4. This figure indicates firing times of $N_E = 80$ E-cells and $N_I = 20$ I-cells. (We will explain shortly how those firing times are derived from the computed mean frequencies E and I .) The horizontal axis in Fig. 22.4 indicates time in ms. The vertical axis indicates neuronal index;

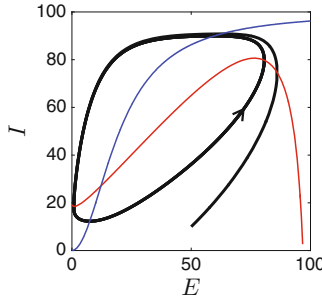


Figure 22.3. Depiction of the solution of Fig. 22.2 in the (E, I) -plane (black). The red and blue curves are the E - and I -nullclines, respectively; compare this with Fig. 10.3. [WILSON_COWAN_PHASE_PLANE]

the i -th E-cell has index $i + N_I$, and the j -th I-cell has index j . A dot in the location (t, m) indicates that the m -th neuron fires at time t ; spikes of E-cells are indicated by red dots, and spikes of I-cells by blue ones. A plot of the sort shown in Fig. 22.4 is called a *spike rastergram*. We chose the ratio $N_E : N_I$ to be 4 : 1 here because this is often said to be the approximate ratio of glutamatergic to GABAergic neurons in the brain [136].

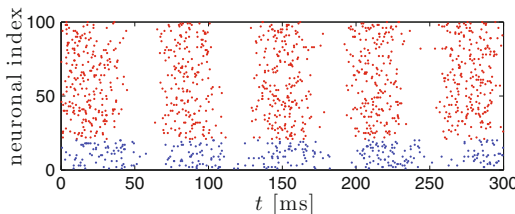


Figure 22.4. Spike rastergram derived from the solution shown in Fig. 22.2. Red and blue dots indicate firing times of E- and I-cells, respectively. [WILSON_COWAN_RASTERGRAM]

We will now explain how the spike times in Fig. 22.4 were derived from the functions E and I . We assume that in a time interval $[k\Delta t, (k+1)\Delta t]$, neuron m fires with probability

$$p_{m,k} = \begin{cases} \frac{1}{1000} \frac{E_k + E_{k+1}}{2} \Delta t & \text{if neuron } m \text{ is an E-cell,} \\ \frac{1}{1000} \frac{I_k + I_{k+1}}{2} \Delta t & \text{if neuron } m \text{ is an I-cell,} \end{cases} \quad (22.7)$$

where $E_k, E_{k+1}, I_k, I_{k+1}$ are the computed approximations for $E(k\Delta t), E((k+1)\Delta t), I(k\Delta t), I((k+1)\Delta t)$. Here Δt denotes the time step size used for solving the differential equations (22.1). (To generate our figures in this chapter, we used

$\Delta t = 0.01$ ms.) The denominators of 1000 in (22.7) are needed because we measure time in ms, but frequency in Hz. In the k -th time step, we have the computer draw uniformly distributed (pseudo-)random numbers $U_{m,k} \in (0, 1)$, $m = 1, 2, \dots, N_E + N_I$, and say that neuron m fires if and only if $U_{m,k} \leq p_{m,k}$. The $U_{m,k}$ are independent of each other.

Readers unfamiliar with the basic notions in probability theory used in the preceding discussion can learn about those notions in Appendix C, or, more thoroughly, in any elementary book on probability theory.

Figure 22.4 shows what Fig. 22.2 really means: Bursts of activity of the E-cells bring on bursts of activity of the I-cells, which in turn bring on a pause. Then the cycle repeats.

It is interesting to modify model parameters and see what happens. For a particularly interesting example, suppose that we reduce w_{EE} . Figure 22.5 shows that the limit cycle shrinks. In fact, when w_{EE} drops below approximately 0.85, the limit cycle disappears. There is a bifurcation here in which a limit cycle shrinks and eventually collapses into a stable fixed point, or — if we let w_{EE} increase rather than decrease — a bifurcation in which a limit cycle is born at zero amplitude out of a stable fixed point, then grows. You might expect it to be a supercritical Hopf bifurcation, and indeed it is; see exercise 2.

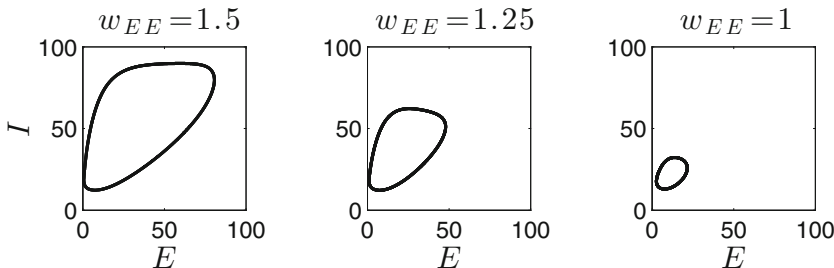


Figure 22.5. As w_{EE} is reduced, the limit cycle shrinks.

[WILSON_COWAN_LOWER_W_EE]

In fact, one can easily prove in much greater generality that time coarse-grained Wilson-Cowan models without recurrent excitation do not allow periodic solutions; see exercise 4. Unfortunately, however, this conclusion is misleading. It suggests that recurrent excitation is needed to get oscillatory behavior in E-I networks. This is most definitely not the case; see Chapter 30. A new interesting question therefore arises: What exactly is it about the Wilson-Cowan model that leads to this incorrect conclusion? We will leave this question unanswered here.

Exercises

- 22.1. Assume that $f = f(x)$ and $g = g(x)$ are continuously differentiable functions, defined for $x \in \mathbb{R}$, with $f(x) \in [0, 100]$ and $g(x) \in [0, 100]$ for all $x \in \mathbb{R}$. Assume that E and I satisfy eqs. (22.1), and $0 \leq E(0), I(0) \leq 100$. Prove that $0 \leq E(t), I(t) \leq 100$ for all $t \geq 0$.
- 22.2. (*) Verify that the system defined by eqs. (22.1) with $w_{IE} = w_{II} = 1$, $I_E = 20$, $I_I = 0$, $\tau_E = 5$, $\tau_I = 10$, and f and g defined as in eqs. (22.4) and (22.5), undergoes a Hopf bifurcation at a critical value $w_{EE,c} \approx 0.85$. Hint: Compute the fixed points and the eigenvalues of the Jacobi matrix at those points. Show: As w_{EE} drops below $w_{EE,c}$, an unstable spiral becomes stable.
- 22.3. Assume that $f = f(x)$ and $g = g(x)$ are continuously differentiable, strictly increasing functions, defined for $x \in [0, 100]$, with values in $[0, 100]$. Consider the Wilson-Cowan system

$$\frac{dE}{dt} = \frac{f(-w_{IE}I + I_E) - E}{\tau_E}, \quad \frac{dI}{dt} = \frac{g(w_{EI}E + I_I) - I}{\tau_I}, \quad (22.8)$$

with $w_{IE} > 0$ and $w_{EI} > 0$. This models an E-I network without recurrent excitation and without inhibition of I-cells by each other. Prove: This system has exactly one fixed point, and the fixed point is stable.

- 22.4. (†) Assume that $f = f(x)$ and $g = g(x)$ are continuously differentiable functions defined for $x \in [0, 100]$, with $f(x) \in [0, 100]$ and $g(x) \in [0, 100]$ for all $x \in [0, 100]$. Assume that g is increasing. (Although this assumption would be natural for f as well, we don't need it.) Consider the Wilson-Cowan system

$$\frac{dE}{dt} = \frac{f(-w_{IE}I + I_E) - E}{\tau_E}, \quad \frac{dI}{dt} = \frac{g(w_{EI}E - w_{II}I + I_I) - I}{\tau_I}, \quad (22.9)$$

with $w_{IE} \geq 0$, $w_{EI} \geq 0$, and $w_{II} \geq 0$. This models an E-I network without recurrent excitation. Show that (22.9) has no periodic solutions. Hint: Suppose there were a periodic solution $(E(t), I(t))$. Let D denote the region in the (E, I) -plane enclosed by $(E(t), I(t))$. Derive a contradiction by applying the divergence theorem to the vector field

$$\begin{bmatrix} (f(-w_{IE}I + I_E) - E)/\tau_E \\ (g(w_{EI}E - w_{II}I + I_I) - I)/\tau_I \end{bmatrix}$$

in D . This argument is known as *Dulac's criterion* [149].

The reasoning sketched here, and more about the bifurcation analysis of Wilson-Cowan models of E-I networks, can be found, for instance, in [51, Section 11.3.3].

Part IV

Entrainment, Synchronization, and Oscillations

Chapter 23

Entrainment by Excitatory Input Pulses

Part IV of the book is about synchronization in populations of nerve cells. Rhythmic synchronization is the simplest form of cooperative behavior of nerve cells seen in the brain, and is typically reflected in *oscillations* or *rhythms* in large-scale measures of electrical activity in the brain, such as *EEG traces*. The abbreviation *EEG* stands for *electroencephalography*, and denotes the measurement of fluctuations in electrical potentials on the scalp surface. An example of oscillating EEG traces measured on the scalp of an anesthetized rat is shown in Fig. 23.1. Oscillations are also seen in *local field potentials (LFPs)*, which are electrical potentials in the extracellular fluid measured by an electrode inserted into the brain, reflecting the summed neuronal activity in a small volume of tissue; for an example, see Fig. 23.2. Different EEG or LFP rhythms are correlated with different cognitive states, and pathologies in rhythms are associated with brain disease; see, for instance, [162].

Electronic supplementary material: The online version of this chapter (doi: [10.1007/978-3-319-51171-9_23](https://doi.org/10.1007/978-3-319-51171-9_23)) contains supplementary material, which is available to authorized users.

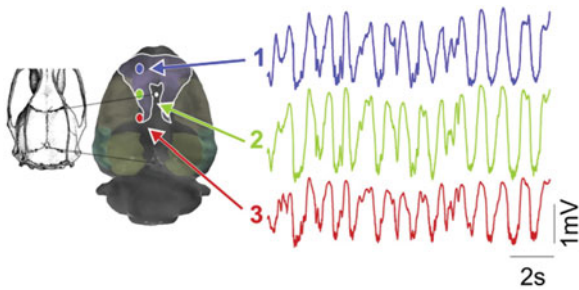


Figure 23.1. Figures 1A and 1B of [65]. The oscillatory traces are EEG traces measured from three different locations on the scalp of an anesthetized rat. Reproduced with publisher's permission.

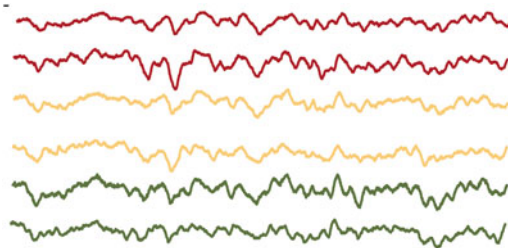


Figure 23.2. From Fig. 1 of [23]. LFP traces recorded from human amygdala and hippocampus. Reproduced with publisher's permission.

The simplest way in which synchronous, rhythmic spiking can occur in a population of neurons is via a *pacemaker*, a source of periodic excitatory input pulses received equally and simultaneously by all cells of a population. In this section, we study whether such a sequence of pulses will indeed *entrain* its targets, making them phase-lock to the input pulses. In other words, this section is about the question when an oscillation arising in one part of the brain can be imposed on another part of the brain via excitatory projections.

23.1 Simulations for a WB Neuron

We begin with a WB neuron, with $I = 0$ (significantly below the firing threshold). The neuron receives excitatory synaptic input pulses at times kT , $k = 1, 2, 3, \dots$. These pulses are modeled as described in Section 20.2:

$$I_{\text{syn}} = -\bar{g}_{\text{syn}} s(t)v, \quad \frac{ds}{dt} = q \frac{1-s}{\tau_r} - \frac{s}{\tau_d},$$

where I_{syn} is the synaptic input current density, v denotes the membrane potential of the WB neuron, and q rises to 1 abruptly at times kT , $k = 1, 2, 3, \dots$, and decays exponentially with a time constant $\tau_{d,q}$ otherwise. We use $\tau_r = 0.5 \text{ ms}$, $\tau_d = 2 \text{ ms}$,

and set $\tau_{d,q}$ so that τ_{peak} , the time it takes s to reach its maximum, starting from $q = 1$ and $s = 0$, becomes equal to τ_r ; see Section 20.2.

For $T = 50$ ms and two different values of \bar{g}_{syn} , the responses of the WB neuron to the input pulse sequence are shown in Fig. 23.3. The figure shows v , and indicates the times kT , $k = 1, 2, 3, \dots$ (red dotted lines). For $\bar{g}_{\text{syn}} = 0.195$, it also shows (left lower panel) the time δ between each voltage spike and the most recent previous input pulse. Phase-locking means convergence of δ . For $\bar{g}_{\text{syn}} = 0.195$, there is *1:1 entrainment*: The target neuron settles into regular firing with period T . For $\bar{g}_{\text{syn}} = 0.14$, the target responds to the input with subthreshold oscillations, but does not fire. In fact, 1:1 entrainment is obtained for \bar{g}_{syn} between approximately 0.19 and 0.9. (More complicated response patterns, with one input pulse triggering more spikes than one, can arise when \bar{g}_{syn} is greater than 0.9.) No firing is triggered for $\bar{g}_{\text{syn}} < 0.14$.

We find numerically that more generally, also for other choices of T , τ_r , τ_{peak} , τ_d , and $I < I_c$, there are values $A > 0$ and $B > A$ so that there is 1:1 entrainment when \bar{g}_{syn} is greater than B , but not too large, and no firing at all when \bar{g}_{syn}

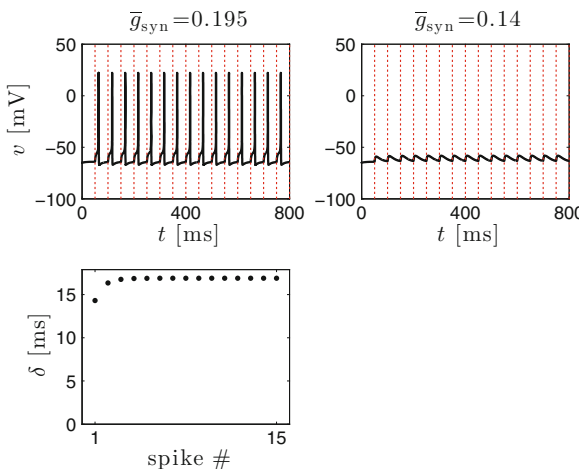


Figure 23.3. WB neuron receiving a periodic sequence of excitatory input pulses. Left upper panel: 1:1 entrainment. Left lower panel: The time, δ , between input arrival and spike. Right panel: no firing response. The dotted vertical red lines indicate the times of input pulse arrivals. [WB_NEURON_ENTRAINED]

is less than A . In the example discussed here, $A \approx 0.14$ and $B \approx 0.19$. For \bar{g}_{syn} between A and B , the target neuron responds to the inputs by firing, but at a frequency slower than the input frequency. We will refer to this as *sparse entrainment*. Figure 23.4 shows examples of *n:1 entrainment* with $n > 1$; that is, the target neuron fires periodically with period nT . Figure 23.5 shows examples of sparse entrainment where there is not *n:1 entrainment* for any integer n ; we will use the phrase *irregular entrainment* for these cases (but see exercise 1). We use the ratio B/A as a measure of how robustly sparse entrainment is possible. For the

example that we discussed here, $B/A \approx 0.19/0.14 \approx 1.36$. This means that within the window of sparse entrainment, input strengths differ by about 36%.

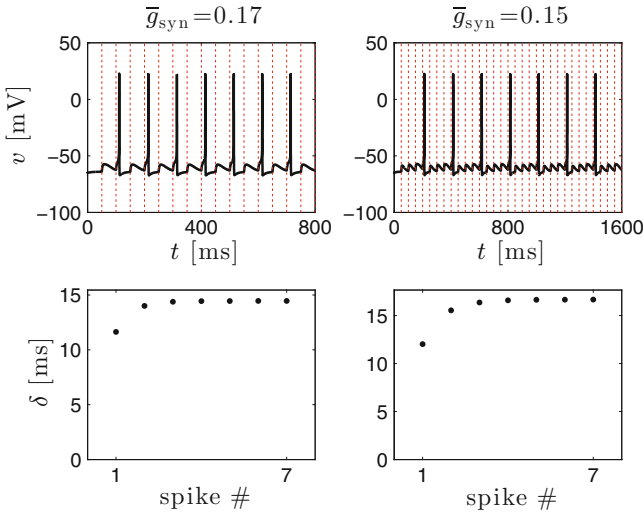


Figure 23.4. WB neuron receiving a periodic sequence of excitatory input pulses, with strengths that result in $n:1$ entrainment with $n > 1$. Left: 2:1 entrainment. Right: 4:1 entrainment. [WB_NEURON_N_TO_ONE]

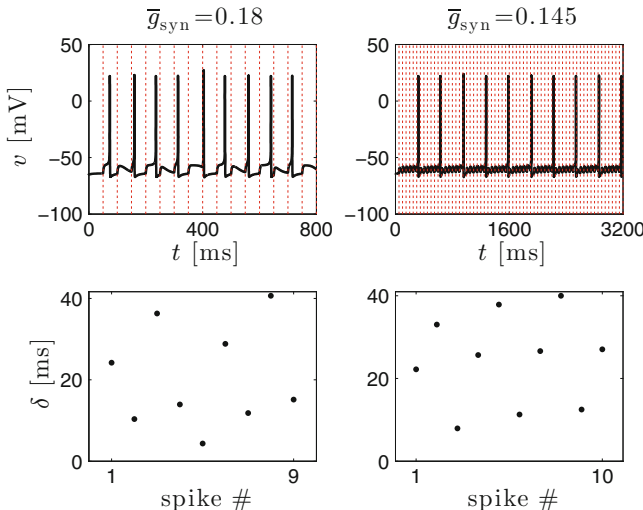


Figure 23.5. Similar to Figs. 23.3 and 23.4, but with choices of \bar{g}_{syn} that do not lead to $n:1$ entrainment for any n . [WB_NEURON_IRREGULAR]

Figure 23.6 shows n (computed as explained in the caption of the figure) as a function of $\bar{g}_{\text{syn}} \in [0.14, 0.19]$. The figure shows that only a fairly small fraction

of the interval of sparse entrainment consists of subintervals in which there is $n:1$ entrainment; those subintervals are separated by intervals of irregular entrainment. For an interesting consequence of this observation, see exercises 2 and 3.

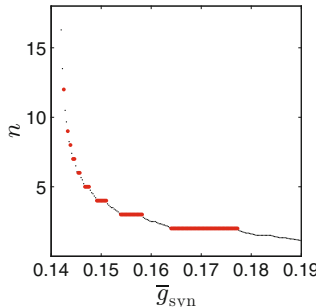


Figure 23.6. Structure of the interval of sparse entrainment for our model. Here n is defined as the average firing period between $t = 5,000$ and $t = 10,000$, divided by T . Integer values of n are indicated in red. [WB_ENTRAINMENT_INTERVALS]

Looking closely at the graph in Fig. 23.6, one sees much more structure than we have discussed. There are plateaus other than the ones indicated in red. For example, there is a fairly pronounced plateau to the right of $\bar{g}_{\text{syn}} = 0.18$, where $n \equiv 1.5$, corresponding to 3:2 entrainment. Another plateau that you may be able to make out, just barely, in the figure is near $\bar{g}_{\text{syn}} = 0.16$, where $n \equiv 5/2$, corresponding to 5:2 entrainment.¹⁶

23.2 Analysis for a LIF Neuron

What determines whether there is 1:1 entrainment, sparse entrainment, or no firing response at all? In this section, we will analyze this question for a very simple model. For this model, it will turn out that irregular entrainment is impossible, and the interval of input strengths for which there is sparse entrainment is of length $e^{-T/\tau}$, where τ is the membrane time constant of the model. Thus if $T \gg \tau$ (slow input and/or a leaky target), sparse entrainment is all but impossible — the input strength would have to be tuned exquisitely finely to achieve it.

We consider an integrate-and-fire neuron, governed by

$$\frac{dv}{dt} = -\frac{v}{\tau}$$

in the absence of input. Now we suppose that the neuron receives instantaneous charge injections at times $T, 2T, 3T, \dots$, where $T > 0$ is fixed. An instantaneous charge injection raises the membrane potential v by a positive amount. Let's say that v jumps up by $\epsilon > 0$ every time a charge injection occurs. If this brings v to or above 1, then we say that a spike has occurred, and v is reset to 0.

¹⁶In fact, the graph in Fig. 23.6 resembles the *Cantor function*, also called the *devil's staircase*. The Cantor function is a standard example of a function that is differentiable with derivative zero everywhere except on a set with measure zero, but not constant. We won't pursue this connection here, though.

If $\epsilon \geq 1$, every input pulse will trigger a spike, so there is 1:1 entrainment. Suppose that $\epsilon < 1$. After a spike, the neuron will reset to $v = 0$, and until the next input pulse arrives, it will stay there. When the next input pulse arrives, v will jump to ϵ , but since $\epsilon < 1$, this will not trigger a spike. So for $\epsilon < 1$, 1:1 entrainment is not possible; it occurs if and only if $\epsilon \geq 1$.

Assume $0 < \epsilon < 1$ now. The key here is to watch v at the right moments in time. The convenient times to focus on are the times just before the inputs (the charge injections) arrive. If $v(kT - 0) = \alpha_k$, with $0 \leq \alpha_k \leq 1$, then

$$v((k+1)T - 0) = \alpha_{k+1} = \begin{cases} (\alpha_k + \epsilon)e^{-T/\tau} & \text{if } \alpha_k + \epsilon < 1, \\ 0 & \text{if } \alpha_k + \epsilon \geq 1. \end{cases}$$

So if we write

$$F(\alpha) = \begin{cases} (\alpha + \epsilon)e^{-T/\tau} & \text{if } \alpha + \epsilon < 1, \\ 0 & \text{if } \alpha + \epsilon \geq 1, \end{cases} \quad (23.1)$$

then

$$\alpha_{k+1} = F(\alpha_k). \quad (23.2)$$

The behavior of the α_k as $k \rightarrow \infty$ can be understood geometrically, by thinking about the graph of F ; see Appendix B. The graph of the function F defined by eq. (23.1) is shown, for one choice of parameters, in Fig. 23.7. For this particular case, one can easily see from the graph that $\alpha_k \rightarrow \alpha_*$ (the fixed point of F) as $k \rightarrow \infty$ (exercise 4). Depending on the initial value of v , the first input pulse can trigger a spike, but after that, there will be no spikes in response to the inputs any more (exercise 5).

The discontinuity in Fig. 23.7 occurs at $\alpha = 1 - \epsilon$. The figure looks qualitatively similar, and the conclusions are the same, as long as

$$\lim_{\alpha \nearrow 1-\epsilon} F(\alpha) < 1 - \epsilon. \quad (23.3)$$

From eq. (23.1), it is clear that

$$\lim_{\alpha \nearrow 1-\epsilon} F(\alpha) = e^{-T/\tau}, \quad (23.4)$$

and therefore we conclude, combining (23.3) and (23.4), that the target does not respond to the input pulses by firing as long as $e^{-T/\tau} < 1 - \epsilon$, or equivalently,

$$\epsilon < 1 - e^{-T/\tau}.$$

It is not hard to convince yourself that even when $\epsilon = 1 - e^{-T/\tau}$ precisely, there can be at most one spike in response to the input sequence (exercise 6). So the precise condition under which there is no firing response to the input sequence (with the possible exception of a single initial spike, depending on the initial value of v) is

$$\epsilon \leq 1 - e^{-T/\tau}. \quad (23.5)$$

Now let us assume

$$1 - e^{-T/\tau} < \epsilon < 1.$$

So the inputs are strong enough to make the target respond by firing, but not strong enough to entrain the target 1:1. Figure 23.8 shows the example $T = 25$, $\tau = 50$, $\epsilon = 0.6$. The figure also indicates the iteration $\alpha_{k+1} = F(\alpha_k)$, starting with $\alpha_1 = 0$. As the figure shows, the sequence $\{\alpha_k\}$ will be periodic with period three: $\alpha_1, \alpha_2, \alpha_3, \alpha_1, \alpha_2, \alpha_3, \alpha_1, \dots$ The LIF neuron will therefore be entrained to the input pulses 3:1 — it will fire on every third input pulse.

In general, suppose that $\alpha_1 = 0$; that is, the target is at rest until the first input arrives at time T . Let us compute formulas for $\alpha_2, \alpha_3, \alpha_4, \dots$, assuming that they are all smaller than $1 - \epsilon$:

$$\begin{aligned}\alpha_2 &= \epsilon e^{-T/\tau}, \\ \alpha_3 &= (\alpha_2 + \epsilon)e^{-T/\tau} = \epsilon e^{-T/\tau} (e^{-T/\tau} + 1), \\ \alpha_4 &= (\alpha_3 + \epsilon)e^{-T/\tau} = \epsilon e^{-T/\tau} (e^{-2T/\tau} + e^{-T/\tau} + 1),\end{aligned}$$

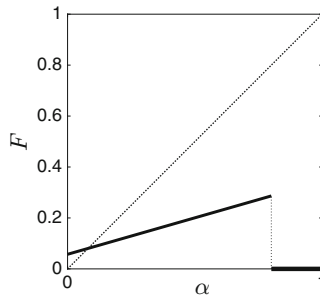


Figure 23.7. Graph of F for $T = 25$, $\tau = 20$, $\epsilon = 0.2$. [PLOT_F_ENTRAINMENT]

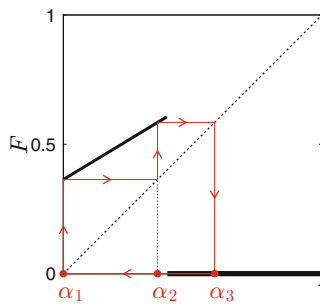


Figure 23.8. Graph of F for $T = 25$, $\tau = 50$, $\epsilon = 0.6$. [PLOT_F_ENTRAINMENT_2]

and so on. The general formula is

$$\alpha_k = \epsilon e^{-T/\tau} \sum_{j=1}^{k-2} e^{-jT/\tau} = \epsilon e^{-T/\tau} \frac{1 - e^{-(k-1)T/\tau}}{1 - e^{-T/\tau}}. \quad (23.6)$$

(We used the formula for a *geometric sum* in the last step.) There will be $n:1$ entrainment if and only if

$$\alpha_{n-1} < 1 - \epsilon, \quad \text{but} \quad \alpha_n \geq 1 - \epsilon, \quad (23.7)$$

for in that case $\alpha_{n+1} = 0$, so the sequence $\{\alpha_k\}$ is periodic with period n ; compare also Fig. 23.8. Using (23.6), (23.7) becomes

$$\epsilon e^{-T/\tau} \frac{1 - e^{-(n-2)T/\tau}}{1 - e^{-T/\tau}} < 1 - \epsilon \quad \text{and} \quad \epsilon e^{-T/\tau} \frac{1 - e^{-(n-1)T/\tau}}{1 - e^{-T/\tau}} \geq 1 - \epsilon.$$

Solving these inequalities for ϵ , we find

$$\epsilon \in \left[\frac{1 - e^{-T/\tau}}{1 - e^{-nT/\tau}}, \frac{1 - e^{-T/\tau}}{1 - e^{-(n-1)T/\tau}} \right). \quad (23.8)$$

We write $r = e^{-T/\tau}$. Then the length of the interval on the right side of (23.8) is

$$\frac{1 - r}{1 - r^{n-1}} - \frac{1 - r}{1 - r^n} = \frac{(1 - r^n)(1 - r) - (1 - r^{n-1})(1 - r)}{(1 - r^{n-1})(1 - r^n)} \sim r^{n-1} \quad (23.9)$$

as $r \rightarrow 0$ (see exercise 7).

We summarize our conclusion in the following proposition:

Proposition 23.1. *For the model studied in this section, the behavior of the target neuron depends on the pulse strength ϵ as follows:*

$\epsilon \geq 1$: ‘1:1 entrainment.’

$$\frac{1 - e^{-T/\tau}}{1 - e^{-nT/\tau}} \leq \epsilon < \frac{1 - e^{-T/\tau}}{1 - e^{-(n-1)T/\tau}}, \quad n \geq 2: \quad \text{‘n:1 entrainment.’}$$

$\epsilon \leq 1 - e^{-T/\tau}$: No firing response. (At most one action potential in response to the inputs.)

The interval of sparse entrainment is $(1 - e^{-T/\tau}, 1)$, so it is of length $e^{-T/\tau}$. The interval of $n:1$ entrainment is of length $\sim e^{-nT/\tau}$ in the limit as $T/\tau \rightarrow \infty$.

This result suggests that $n:1$ entrainment with $n > 1$ is an important phenomenon only if the input pulses arrive at high frequency (T small) or the target neuron is not very leaky (τ not very small). This is what one should expect: When T/τ is large, the neuron has nearly ‘forgotten’ the previous input pulse when the next one arrives, and therefore 1:1 entrainment or no entrainment at all should essentially be the only possibilities.

We conclude with an example of 10:1 entrainment. Suppose that $T = 20$ ms, $\tau = 30$ ms, and $n = 10$. The interval of 10 : 1 entrainment is then

$$\left[\frac{1 - e^{-T/\tau}}{1 - e^{-nT/\tau}}, \frac{1 - e^{-T/\tau}}{1 - e^{-(n-1)T/\tau}} \right) = [0.48720\dots, 0.48779\dots).$$

Figure 23.9 shows a simulation with $\epsilon = 0.48750$.

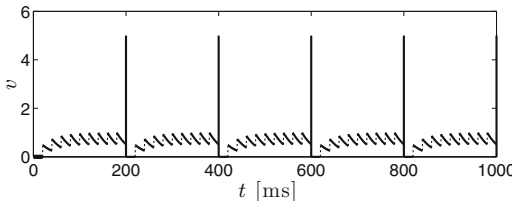


Figure 23.9. An example of 10:1 entrainment of a LIF neuron by excitatory input pulses. Spikes are indicated by tall vertical lines. [[LIF_ENTRAINMENT](#)]

Exercises

- 23.1. (*) Run the two examples of Fig. 23.5 for much longer times, to show that there is in fact a considerable degree of regularity in the behavior.
- 23.2. (*) Starting with the program generating Fig. 23.3, generate a code that simulates 100 independent WB neurons, driven by input pulses as in Section 23.1, with the i -th neuron driven at a strength $\bar{g}_{\text{syn}} = \bar{g}_{\text{syn},i}$, chosen at random with uniform distribution in the interval $[0.14, 0.19]$ (approximately the interval of sparse entrainment).¹⁷ Choose the $\bar{g}_{\text{syn},i}$ independently of each other, but for a given i , fix the value for all times. Note that many of the values $\bar{g}_{\text{syn},i}$ will result in irregular entrainment, not $n:1$ entrainment with an integer n .
After seeing the result, you may be tempted to conclude that clean entrainment of a population by a sequence of input pulses at 20 Hz ($T = 50$ ms) is unlikely unless many neurons in the target population receive pulses strong enough for 1:1 entrainment.¹⁸
- 23.3. (*) In Section 23.1, it is interesting to think about broader input pulses. They might model a large network of neurons in approximate (but not tight) synchrony delivering input to a target neuron. We will study whether sparse and irregular entrainment are more or less common with broad input pulses than with narrow ones.
 - (a) Start with the code that generates Fig. 23.3. Change the kinetics of the input pulses as follows: $\tau_r = \tau_{\text{peak}} = \tau_d = 3$ ms. By trial and error, approximate A and B for this case. Is B/A larger or smaller than for the example discussed in Section 23.1?
 - (b) Start with the code generating Fig. 23.6, and generate the analogous figure for $\tau_r = \tau_{\text{peak}} = \tau_d = 3$ ms. (Note: You must do (a) first, so that you know which interval to vary \bar{g}_{syn} in.) Is irregular entrainment more or less common when the input pulses are broader?

¹⁷Matlab command for generating a column vector of 100 independent, uniformly distributed random numbers between 0.14 and 0.19: `g=0.14+rand(100,1)*0.05;`

¹⁸One should be a bit skeptical of this conclusion. It is based on one very simple model only.

- 23.4. Explain why for the function shown in Fig. 23.7, $\alpha_k \rightarrow \alpha_*$ as $k \rightarrow \infty$, where α_* denotes the fixed point of F .
- 23.5. Explain why in the case of Fig. 23.7, there can be no voltage spike in response to the inputs at times $2T$, $3T$, $4T$, etc. (There could be one in response to the input at time T , depending on initialization.)
- 23.6. Assume $\epsilon = e^{-T/\tau}$ in the model of Section 23.2. Show that the target neuron can fire at most once in response to the input sequence.
- 23.7. Explain the asymptotic statement in (23.9).

Chapter 24

Synchronization by Fast Recurrent Excitation

In this chapter, we begin our study of synchronization via mutual synaptic interactions. The simplest example is a population of N identical neurons, driven so strongly that by themselves they would fire periodically, coupled to each other by excitatory synapses. For simplicity, we assume for now that all neurons receive the same drive, all synaptic strengths are equal, and the coupling is *all to all*, i.e., any two neurons are synaptically coupled with each other. (We do not include autapses here.) We ask whether the neurons will *synchronize* their firing, i.e., whether they will all fire at (nearly) the same times after a while.

We think about this question intuitively first. Suppose that the neurons are already in approximate, but imperfect synchrony. The neurons that are ahead fire earlier, and accelerate the ones that are behind. This promotes synchronization. On the other hand, the neurons that are behind, when they fire, accelerate the ones that are ahead, and that opposes synchronization. Whether or not there will be synchronization is therefore not at all intuitively obvious.

24.1 Asynchronous Initialization

In this chapter and in later ones, we will describe network simulations in which we start the neurons in asynchrony, then see whether synchrony (or approximate synchrony) develops over time. It is not entirely clear what it means to start the neurons “in asynchrony,” though. We explain what we mean by it here.

We begin by defining the notion of *phase* first. Think about an isolated neuron, i.e., a neuron that receives no input from other neurons, and assume that it fires periodically with period T . If the time that has elapsed since the most recent action

Electronic supplementary material: The online version of this chapter (doi: [10.1007/978-3-319-51171-9_24](https://doi.org/10.1007/978-3-319-51171-9_24)) contains supplementary material, which is available to authorized users.

potential is φT , with $0 \leq \varphi < 1$, we call φ the current *phase* of the neuron. Thus if there is an action potential at time t_0 , then

$$\varphi = \frac{t - t_0}{T} \bmod 1.$$

(In general, “ $x \bmod 1$ ” means the number in the interval $[0, 1)$ that differs from x by an integer.)

Figure 24.1 is a spike rastergram illustrating one possible notion of *asynchrony*. Here $N = 30$ RTM neurons, not connected to each other, all with $I = 0.3$ and therefore all firing at the same period T , have been initialized so that the i th neuron fires at times

$$\frac{i - 1/2}{N} T + kT, \quad k = 0, 1, 2, \dots, \quad i = 1, 2, \dots, N.$$

One says that the neurons fire in a *splay state*. At any time, the phases of the N neurons occupy a grid of points in the interval $[0, 1)$ with spacing $1/N$ between the grid points. The splay state is the extreme opposite of the synchronous state, obtained in Fig. 24.2 by initializing all 30 neurons in the same way.

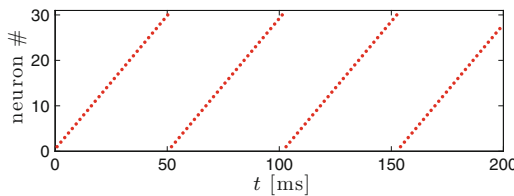


Figure 24.1. Thirty RTM neurons firing in splay state. [RTM_SPLAY]

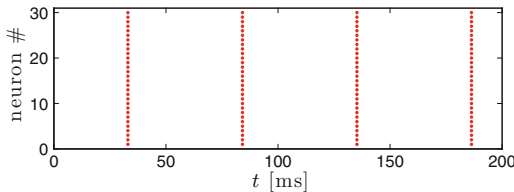


Figure 24.2. Thirty RTM neurons firing in synchrony. [RTM_SYNC]

In most of our simulations, we don’t initialize in splay state. The reason is that the notion of splay state has clear meaning only when all neurons fire at the same period, not when they don’t. Suppose, for instance, that the external drives are *heterogeneous*. The word *heterogeneous* simply means that different neurons receive different external drives. We denote the *intrinsic period* of the i -th neuron (the period with which the neuron fires if it receives no inputs from other neurons) by T_i . By *asynchronous initialization*, we will mean that we initialize the i -th neuron

at a point on its limit cycle with a random, uniformly distributed phase in $[0, 1)$. Our notion of asynchronous initialization disregards synaptic connections; we think of them as being turned on *after* the neurons have been initialized.

Only intrinsically firing model neurons can be asynchronously initialized in the sense that we have described. Neurons with subthreshold drives will typically be initialized at or near their stable equilibrium in our simulations.

24.2 Simulations

We begin by initializing 30 RTM neurons in splay state, then couple them by excitatory synapses from time $t = 0$ on. The model synapses are defined as in Section 20.2, with $v_{\text{rev}} = 0$, $\tau_r = \tau_{\text{peak}} = 0.5 \text{ ms}$, $\tau_d = 2 \text{ ms}$; thus the model synapses are reminiscent of AMPA receptor-mediated synapses. For each synapse, we use $\bar{g}_{\text{syn}} = 0.0075$; we will discuss this choice below. Figure 24.3 shows the result of a simulation of this network.

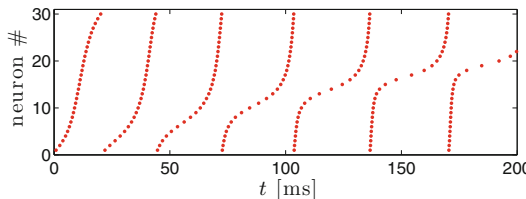


Figure 24.3. Spike rastergram of the thirty RTM neurons of Fig. 24.1, initialized as in Fig. 24.1, but now coupled with excitatory synapses. [RTM_E_TO_E_NETWORK_1]

The frequency with which each neuron fires is about 20 Hz when there is no synaptic coupling (Fig. 24.1), and nearly 30 Hz with the coupling (Fig. 24.3). Somewhat greater values of \bar{g}_{syn} yield much greater and perhaps biologically unrealistic frequencies; $\bar{g}_{\text{syn}} = 0.015$, for instance, yields 103 Hz already.

Note that the neurons are in fact much closer to synchrony towards the end of the simulation of Fig. 24.3 than at the beginning; see also exercise 1. One might suspect that perfect synchrony will eventually be reached. However, Fig. 24.4 shows results of the last 200 ms of a 10,000 ms simulation; even after such a large amount of simulated time, tight synchrony has not been reached.

We repeat similar experiments with just $N = 2$ neurons, to see whether in this simple case at least, tight synchrony is reached when the neurons are close to it already, i.e., whether synchrony is stable. In the preceding simulations, each neuron received 29 inputs with $\bar{g}_{\text{syn}} = 0.0075$. Now, since $N = 2$, each neuron receives only one input; we therefore define $\bar{g}_{\text{syn}} = 29 \times 0.0075 = 0.2175$. The drive to each of the two neurons is $I = 0.3$, as before. We first let the two neurons fire five times in synchrony. At the time of the fifth spike, we introduce a very slight perturbation (see the caption of the figure). In Fig. 24.5, we show the difference between the spike times of the second neuron and the spike times of the first, as a function of spike number. Once synchrony is perturbed, the two neurons do not return to it,

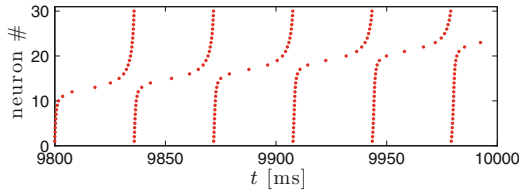


Figure 24.4. Simulation of Fig. 24.3, continued for a much longer amount of time. Only the last 200 ms of simulated time are shown. [RTM_E_TO_E_NETWORK_2]

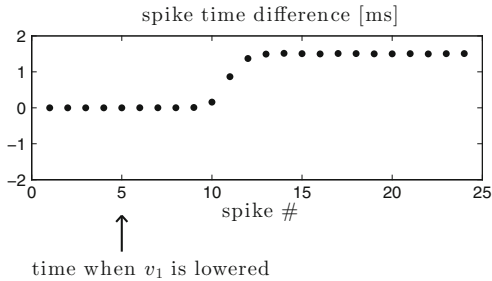


Figure 24.5. Difference between spike times of two RTM neurons, coupled with AMPA-like synapses. The first five spikes are simultaneous because the two neurons are identical, and have been initialized identically. At the time of the fifth spike, the membrane potential of the first neuron is lowered by 10^{-5} mV. This causes the two neurons to lock at a small but non-zero phase difference. [RTM_TWO_CELL_NETWORK]

but instead phase-lock at a non-zero phase difference; synchrony is unstable here. This result is in agreement with our earlier results for larger networks: The eventual state of the two cells is not tightly synchronous, but it is not very far from it either.

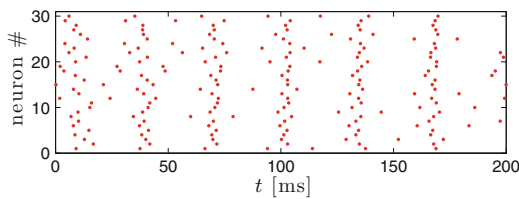


Figure 24.6. Similar to Fig. 24.3, but with heterogeneity in drives and synaptic strengths, and random asynchronous initialization.

[RTM_E_TO_E_HETEROGENEOUS]

The networks that we have considered so far ought to be ideal for synchronization: All neurons receive the same drive, and all synapses are of the same strength. For more biological realism, and to test the robustness of the approximate synchronization that we see in Figs. 24.3 and 24.4, we now consider heterogeneous external

drives. We denote the drive to the i -th neuron by I_i , and let it be random, uniformly distributed between 0.25 and 0.35. Further, we assume that the strength of the synapse from neuron i to neuron j is a random number $\bar{g}_{\text{syn},ij}$, uniformly distributed between 0.00625 and 0.00875, so the synaptic strengths are heterogeneous, too. All of these random quantities, the I_i and the $\bar{g}_{\text{syn},ij}$, are taken to be independent of each other. They are chosen once and for all, before the simulation begins; they don't vary with time. The “noise” that we have introduced by making the I_i and $\bar{g}_{\text{syn},ij}$ random is therefore sometimes called *frozen noise*.

Figure 24.6 shows the transition from asynchronous initialization, in the sense explained in Section 24.1, to approximate synchrony resulting from the synaptic coupling. (Roughly the same degree of synchrony seen at time $t = 200$ in Fig. 24.6 is still seen at time $t = 10,000$.)

In general, synaptic *inhibition* is thought to create neuronal synchrony more effectively than *excitation* [167]. In later chapters, we will discuss results supporting this idea. However, the results presented here, and those in Chapters 26 and 27, confirm that excitatory synaptic connections can reasonably robustly create approximate synchrony as well. In fact, oscillations in rat neocortex that arise when blocking inhibition and rely on AMPA receptor-mediated synaptic excitation were reported in [26].

Exercises

- 24.1. (*) Sometimes the average, \bar{v} , of all computed membrane potentials is taken to be a (probably poor) computational analogue of the LFP. Plot \bar{v} as a function of time, for a network of 30 RTM neurons that are uncoupled and in splay state for the first 100 ms of simulated time, then connected as in Fig. 24.3 for the remaining 200 ms of time. (Use the code generating Fig. 24.3 as a starting point.)

The plot that you will obtain demonstrates resoundingly that the synaptic interaction creates a network oscillation.

- 24.2. (*) Reproduce Fig. 24.3 with the i -th neuron initialized at phase $\varphi_i \in [0, 1)$, where the φ_i are random, uniformly distributed, and independent of each other.
- 24.3. (*) Reproduce Fig. 24.3 with $\bar{g}_{\text{syn}} = 0.015$ (twice the value used in Fig. 24.3). You will see that there is no synchronization any more. Run the simulation to $t = 10,000$ (as in Fig. 24.4, but with $\bar{g}_{\text{syn}} = 0.015$) and see whether synchronization arises after a long time.
- 24.4. (*) The AMPA receptor-dependent oscillations in [26] were at 10 Hz. In the code generating Fig. 24.3, can you reduce I to a point where the oscillations that emerge are at 10 Hz?
- 24.5. (*) If you use $\tau_r = \tau_{\text{peak}} = 10\text{ms}$, $\tau_d = 200\text{ms}$ (values approximately appropriate for NMDA receptor-mediated synapses) in the code generating Fig. 24.3, do you still get approximate synchronization? You will need to reduce \bar{g}_{syn} by a lot, to avoid very high-frequency, unrealistic-looking activity.

Chapter 25

Phase Response Curves (PRCs)

Phase response curves (PRCs) describe how neurons respond to brief, transient input pulses. They are of fundamental importance in the theory of neuronal synchronization, and can also be measured experimentally.

25.1 Input Pulses of Positive Strength and Duration

Suppose a neuron fires periodically with period T , and receives, at some time t , a brief input pulse, for instance, a brief synaptic input. The effect will be a shift in the timing of the next action potential. The magnitude of this shift, and sometimes even its sign, depends on the phase, $\varphi \in [0, 1]$, of the neuron at time t . The PRC captures this dependence.

Note that in the absence of the input pulse, the next action potential would have occurred at time $t + (1 - \varphi)T$. In the presence of the input, the next action potential occurs at some different time t_* . The amount by which the time of the next action potential is advanced by the input is therefore

$$t + (1 - \varphi)T - t_*.$$

The next action potential is delayed if this quantity is negative. Since phase is time divided by T , the phase is advanced by

$$g(\varphi) = 1 - \varphi - \frac{t_* - t}{T}.$$

Electronic supplementary material: The online version of this chapter (doi: [10.1007/978-3-319-51171-9_25](https://doi.org/10.1007/978-3-319-51171-9_25)) contains supplementary material, which is available to authorized users.

We call g the *phase response function*. From the definition, it follows that

$$g(\varphi) \leq 1 - \varphi \quad (25.1)$$

for all $\varphi \in [0, 1]$, with strict inequality unless the input causes a spike *instantaneously*. The graph of g is called the *phase response curve* (PRC).

Figure 25.1 illustrates the phase shifts caused by input pulses. The input arrival time is indicated by a vertical thin dashed line in each of the two panels. In the upper panel, the input comes early in the cycle, and advances the subsequent spikes only slightly. In the lower panel, the input comes in the middle of the cycle, and advances the subsequent spikes much more.

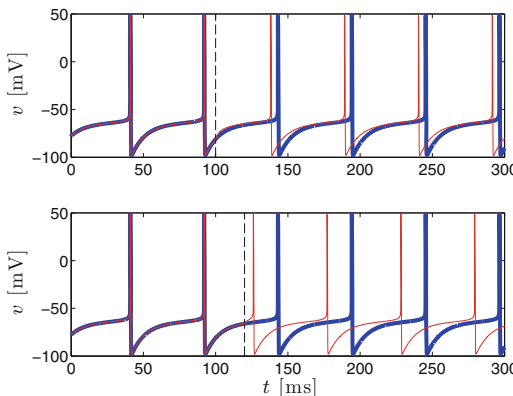


Figure 25.1. Blue: Voltage trace of a periodically firing RTM neuron. Red: Perturbed voltage trace obtained when there is a brief excitatory synaptic input pulse, arriving at the time indicated by the dashed vertical line. [PHASE_SHIFT]

By definition, the phase response function tells us nothing about the timing of later action potentials, following the one at time t_* . In applications of the PRC, however, it is typically assumed that those action potentials occur at times $t_* + kT$, $k = 1, 2, 3, \dots$. This is often close to the truth, provided that the input pulse is brief, and the phase φ of the neuron at the input arrival time is not too close to 1; see exercises 1 and 2, and also Fig. 25.1.

A first example of a PRC is shown in Fig. 25.2; see the figure caption for details. The figure tells us that the phase of an RTM neuron is always advanced by the input pulse, but more so if the input pulse comes in the middle of the cycle ($\varphi \approx 0.5$) than when it comes at the beginning or end of the cycle ($\varphi \approx 0$ or $\varphi \approx 1$).

A feature of the curve in Fig. 25.2 that may seem surprising at first sight is that $g(0) \neq g(1)$. “Phase 0” means the same as “phase 1” — both refer to the time at which the neuron fires. So why is $g(0)$ not the same as $g(1)$? An input pulse that arrives at phase 0 or at phase 1 arrives at the time when the neuron spikes, i.e., crosses -20 mV from above. However, when computing $g(0)$, we consider how the *next* spike is affected, whereas when computing $g(1)$, we consider how the spike that occurs at the time of input arrival is affected. Clearly, that spike cannot be affected at all, so we must always have $g(1) = 0$.

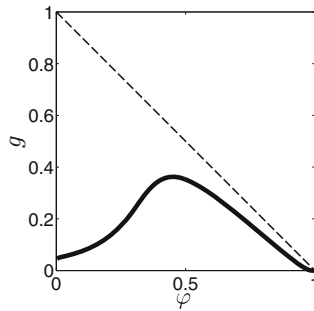


Figure 25.2. *PRC of the RTM neuron with $I = 0.3$, in response to an excitatory synaptic pulse with $\tau_r = 0.5$, $\tau_{\text{peak}} = 0.5$, $\tau_d = 2$, $\bar{g}_{\text{syn}} = 0.1$, $v_{\text{rev}} = 0 \text{ mV}$. (For the notation, see Section 20.2. The input pulse is triggered by setting $q = 1$). Dashed straight line: $g \equiv 1 - \varphi$. The PRC must stay below this line; see (25.1).*

[RTM_PRC]

PRCs can be measured experimentally. As an example, panel A of Fig. 25.3 reproduces Fig. 1C of [52]; it shows a measured PRC of a neuron in the *subthalamic nucleus (STN)* of a rat. The STN is a brain structure that is part of the *basal ganglia* system. Stimulation of the STN (*deep brain stimulation*) is used to relieve the motor symptoms of Parkinson's disease.

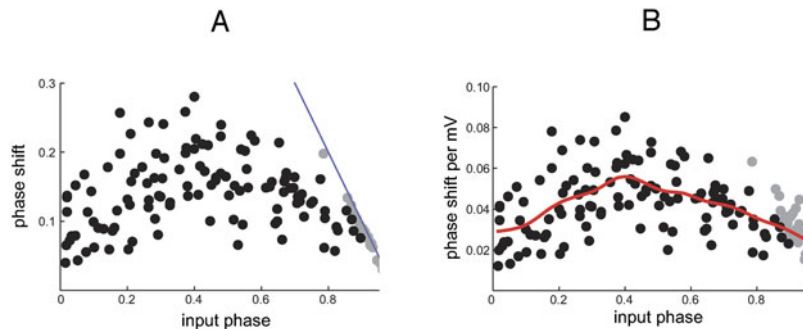


Figure 25.3. Panel A: Figure 1C of [52], showing the measured PRC of a rat STN neuron. Grey dots indicate trials on which a spike occurred while the input was still ongoing. The thin blue line is the same as the dashed line in Fig. 25.2. Panel B: Figure 1E of the same reference, showing an approximate infinitesimal PRC derived from the figure in panel A. Reproduced with publisher's permission.

In some places in later section, it is convenient to use the notation

$$f(\varphi) = \varphi + g(\varphi). \quad (25.2)$$

So $f(\varphi)$ is the phase that the neuron is reset to if the input finds it at phase φ . I will call f the *interaction function*, since it describes the outcome of synaptic interactions.

The graph of the interaction function corresponding to the PRC in Fig. 25.2 is shown in Fig. 25.4.¹⁹ Equation (25.1) is equivalent to

$$f(\varphi) \leq 1. \quad (25.3)$$

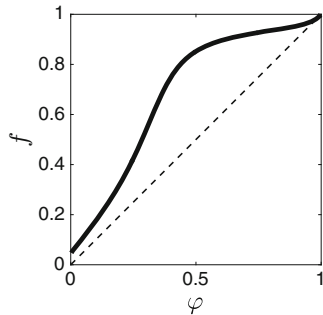


Figure 25.4. Interaction function $f = f(\varphi) = \varphi + g(\varphi)$ derived from Fig. 25.2. The dashed line is $f \equiv \varphi$. [RTM_INTERACTION_FUNCTION]

25.2 Input Pulses That Are Infinitesimally Weak, Infinitesimally Brief, or Both

For analysis, it is often useful to consider *infinitesimal* phase response curves. Two different quantities can be taken to be “infinitesimal” here: The *strength* and the *duration* of the input pulse. We will discuss these two possibilities separately first, then in combination.

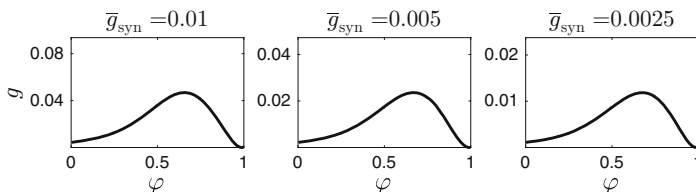


Figure 25.5. Three PRCs similar to that in Fig. 25.2, but with much weaker inputs. Notice that the scaling of the vertical axis is not the same in the three plots, and in none of these three plots is it the same as in Fig. 25.2. [RTM_PRC_THREE_WEAK_ONES]

Figure 25.5 shows three PRCs similar to the one in Fig. 25.2, but with smaller values of \bar{g}_{syn} . The three panels of Fig. 25.5 all look very similar to Fig. 25.2, except for the scaling of the vertical axis. The figure suggests that the phase response

¹⁹The graph of f is often called the *phase transition curve*. I don’t use this terminology to avoid confusion with the phase response curve.

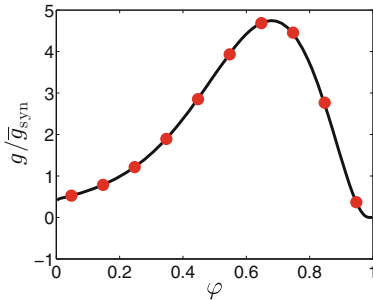


Figure 25.6. Phase response of RTM neuron with $I = 0.3$, subject to a synaptics input pulse as in Fig. 25.2, but with strengths $\bar{g}_{\text{syn}} = 0.001$ (black curve) and $\bar{g}_{\text{syn}} = 0.0001$ (red dots). The graph of $g(\varphi)/\bar{g}_{\text{syn}}$ is shown, which is an excellent approximation of the PRC with infinitesimal input strength. [RTM_PRCE_WEAK]

function is, for small \bar{g}_{syn} , proportional to \bar{g}_{syn} . Writing $g = g(\varphi, \bar{g}_{\text{syn}})$ to remind ourselves of the fact that g depends on \bar{g}_{syn} , it appears that

$$\lim_{\bar{g}_{\text{syn}} \rightarrow 0} \frac{g(\varphi, \bar{g}_{\text{syn}})}{\bar{g}_{\text{syn}}} \quad (25.4)$$

exists. In Fig. 25.6, we plot approximations of this limit, as a function of φ , obtained by setting $\bar{g}_{\text{syn}} = 0.001$ (black curve), and then again by setting $\bar{g}_{\text{syn}} = 0.0001$ (red dots). The figure convincingly demonstrates that $g(\varphi, 0.001)/0.001$ is an excellent approximation of the limit. We note that $g(\varphi, 0) = 0$ — an input of zero strength doesn't do anything. This implies that eq. (25.4) can also be written as

$$\tilde{g}(\varphi) = \left. \frac{\partial g(\varphi, \bar{g}_{\text{syn}})}{\partial \bar{g}_{\text{syn}}} \right|_{\bar{g}_{\text{syn}}=0}. \quad (25.5)$$

We call this limit the *PRC with infinitesimal input strength*.

It is also common to consider PRCs with infinitesimal input *duration*. By this we mean that we replace the synaptic input pulse by an instantaneous charge injection, that is, a sudden jump in v by some positive amount Δv . We denote the resulting PRC by g as well. Figure 25.7 shows an example.

To stress the Δv -dependence of the phase response function with infinitesimal input duration, we also write $g = g(\varphi, \Delta v)$. We define

$$\hat{g}(\varphi) = \lim_{\Delta v \rightarrow 0} \frac{g(\varphi, \Delta v)}{\Delta v} = \left. \frac{\partial g(\varphi, \Delta v)}{\partial \Delta v} \right|_{\Delta v=0}.$$

The graph of \hat{g} is commonly called the *infinitesimal PRC*, although perhaps it should really be called the *doubly infinitesimal PRC* — both the input strength and the input duration are infinitesimal now. Figure 25.8 shows an example.

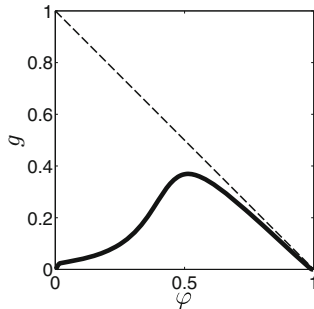


Figure 25.7. PRC of the RTM neuron with $I = 0.3$, responding to an instantaneous charge injection that causes v to rise by $\Delta v = 4 \text{ mV}$. The value of Δv is chosen to make the maximum value similar to that in Fig. 25.2. Dashed line: $g \equiv 1 - \varphi$. [RTM_PRC_SHORT]

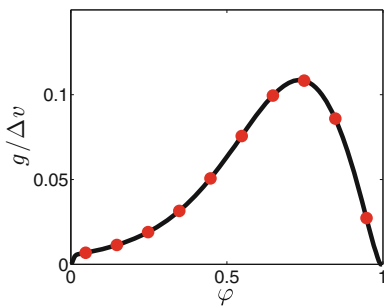


Figure 25.8. The infinitesimal PRC of the RTM neuron with $I = 0.3$, approximated using $\Delta v = 0.01$ (solid black curve) and $\Delta v = 0.001$ (red dots). [RTM_PRC_SHORT_AND_WEAK]

Panel B of Fig. 25.3 is a reproduction of [52, Fig. 1E], which shows an approximate *infinitesimal* PRC derived from [52, Fig. 1C] (reproduced in panel A of Fig. 25.3).

25.3 Type 1 vs. Type 2 Phase Response

Fig. 25.9 shows PRCs for the WB, classical Hodgkin-Huxley, and Erisir neurons; for the details, see the figure caption. The classical Hodgkin-Huxley neuron has a phase response function with negative values, even though the input pulse is excitatory ($v_{\text{rev}} = 0 \text{ mV}$). Thus an “excitatory” input pulse can delay the next spike of the classical Hodgkin-Huxley neuron. A phase response function is called of *type 2* if it has both positive and negative values, and of *type 1* otherwise. This classification of PRCs goes back to [71]. There is a different classification of PRCs into “types” based on *winding numbers* [186], but we won’t discuss that classification here.

The PRCs of the RTM neuron shown in the preceding section are of type 1, and so are the PRC of the WB neuron in the left panel of Fig. 25.9, and that of the Erisir neuron in the right panel. As stated earlier, the PRC of the classical Hodgkin-Huxley neuron shown in the middle panel of Fig. 25.9 is of type 2. It is often the case that neurons of bifurcation type 1 have PRCs of type 1, and neurons of bifurcation type 2 have PRCs of type 2.

The PRC of the Erisir neuron in the right panel of Fig. 25.9 is an exception: The neuron is of bifurcation type 2, but the PRC in the right panel of Fig. 25.9 is positive. However, for different input pulses, the Erisir neuron does have type 2 PRCs; see [17]. For an example of a model of bifurcation type 1 with a type 2 PRC is described, see [48].

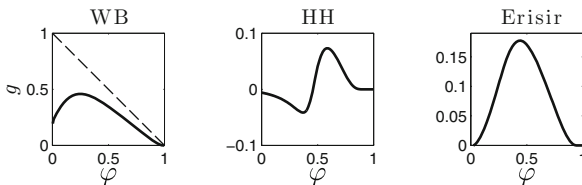


Figure 25.9. Phase response curves of the WB, classical Hodgkin-Huxley (HH), and Erisir neurons. The drives are $I = 0.3$ for the WB neuron, 10.0 for the HH neuron, 7.1 for the Erisir neuron. In each case, the input is an excitatory synaptic pulse with $\tau_r = \tau_{\text{peak}} = 0.5$, $\tau_d = 2$, $\bar{g}_{\text{syn}} = 0.1$, and $v_{\text{rev}} = 0$ mV. Notice that the scaling of the vertical axis is different in the three different plots. [MISC_PRC]

It is not hard to understand why for a neuron with a Hopf bifurcation at I_c , it might be possible for an excitatory pulse to delay firing: When $I \approx I_c$, such a neuron has a fixed point, which is stable or unstable, depending on the sign of $I - I_c$. Even when $I > I_c$ and the fixed point is unstable, an excitatory pulse can move the trajectory into the vicinity of the fixed point, and it can take a long time to move on from there; see exercise 4 and reference [14].

In all examples of PRCs given so far, the input pulse was excitatory. In Fig. 25.10, we show the PRC of the WB neuron with $I = 1$ responding to a brief pulse of synaptic inhibition: $\tau_r = \tau_{\text{peak}} = 0.5$, $\tau_d = 2$, $\bar{g}_{\text{syn}} = 0.5$, and $v_{\text{rev}} = -70$ mV.

25.4 The PRC of a Theta Neuron with an Infinitesimally Brief Input

Very few PRCs can be computed explicitly. One example is the PRC of a theta neuron when the input is an instantaneous charge injection. We do this calculation in this section. We will need a few formulas from Chapter 8, and for convenience we review them first, numbering them as they were numbered in Chapter 8.

The differential equation of the theta neuron is

$$\frac{d\theta}{dt} = -\frac{\cos \theta}{\tau_m} + 2I(1 + \cos \theta). \quad (8.8)$$

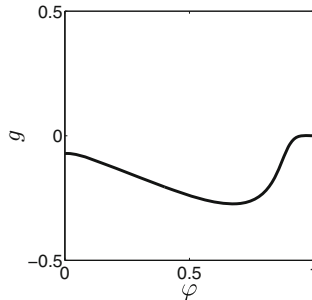


Figure 25.10. PRC of the WB neuron for a brief inhibitory input pulse:
 $I = 1$, $\tau_r = \tau_{\text{peak}} = 0.5$, $\tau_d = 2$, $\bar{g}_{\text{syn}} = 0.5$, $v_{\text{rev}} = -70$ mV.
[WB_PRC_INHIBITORY_PULSE]

This is equivalent to

$$\frac{dv}{dt} = -\frac{v(1-v)}{\tau_m} + I, \quad (8.1)$$

with

$$v = \frac{1}{2} + \frac{1}{2} \tan \frac{\theta}{2}. \quad (8.7)$$

For later use, we solve (8.7) for θ :

$$\theta = 2 \arctan(2v - 1). \quad (25.6)$$

We assume that the external drive is above the firing threshold:

$$I > \frac{1}{4\tau_m}. \quad (8.3)$$

The period of the theta neuron, namely the time that it takes for v to move from $-\infty$ to $+\infty$ (or, equivalently, the time it takes for θ to move from $-\pi$ to $+\pi$) is then

$$T = \frac{\pi\tau_m}{\sqrt{\tau_m I - 1/4}}. \quad (8.11)$$

The solution of (8.1) with an initial condition $v(0) = v_0 \in \mathbb{R}$ is given by eq. (8.4), which we re-write, using (8.11), as follows:

$$v(t) = \frac{1}{2} + \frac{\pi\tau_m}{T} \tan \left(\frac{\pi}{T} t + \arctan \frac{(v_0 - 1/2)T}{\pi\tau_m} \right). \quad (25.7)$$

The special case $v_0 = -\infty$ of this formula is

$$v = \frac{1}{2} + \frac{\pi\tau_m}{T} \tan \left(\pi\varphi - \frac{\pi}{2} \right), \quad (25.8)$$

where $\varphi = t/T$ is the phase. For later use, we solve this equation for φ :

$$\varphi = \frac{1}{\pi} \arctan \left(\frac{T}{\pi \tau_m} (v - 1/2) \right) + \frac{1}{2}. \quad (25.9)$$

We now assume that at some time t_* , an “instantaneous charge injection” occurs, i.e., if $v(t_* - 0) = v_0$, then $v(t_* + 0) = v_0 + \Delta v$ with $\Delta v > 0$. We will work out what this means in terms of θ . When $v = v_0$, then

$$\theta = \theta_0 = 2 \arctan(2v_0 - 1)$$

by (25.6). When v jumps from v_0 to $v_0 + \Delta v$, then θ jumps from θ_0 to

$$\theta_0 + \Delta\theta = 2 \arctan(2(v_0 + \Delta v) - 1) = 2 \arctan \left(\tan \frac{\theta_0}{2} + 2\Delta v \right).$$

(The second of these two equations follows from eq. (8.7).) Thus

$$\theta(t_* + 0) = 2 \arctan \left(\tan \frac{\theta(t_* - 0)}{2} + 2\Delta v \right). \quad (25.10)$$

This is what “instantaneous charge injection” means for the theta neuron.

Next we work out what the instantaneous charge injection means in terms of φ . First, $v = v_0$ means, by eq. (25.9),

$$\varphi = \varphi_0 = \frac{1}{\pi} \arctan \left(\frac{T}{\pi \tau_m} (v_0 - 1/2) \right) + \frac{1}{2}. \quad (25.11)$$

When v_0 is raised to $v_0 + \Delta v$, the phase is raised to

$$\varphi_0 + \Delta\varphi = \frac{1}{\pi} \arctan \left(\frac{T}{\pi \tau_m} (v_0 + \Delta v - 1/2) \right) + \frac{1}{2}, \quad (25.12)$$

so

$$\Delta\varphi = \frac{1}{\pi} \arctan \left(\frac{T}{\pi \tau_m} (v_0 + \Delta v - 1/2) \right) + \frac{1}{2} - \varphi_0.$$

Using eqs. (25.8) and (8.11), we find $\Delta\varphi = g(\varphi_0)$ with

$$g(\varphi) = \frac{1}{\pi} \arctan \left(\tan \left(\pi\varphi - \frac{\pi}{2} \right) + \frac{\Delta v}{\sqrt{\tau_m I - 1/4}} \right) + \frac{1}{2} - \varphi. \quad (25.13)$$

This is the phase response function for the theta neuron when the input is an instantaneous charge injection. It does not depend on the parameters Δv , τ_m , and I individually, but only on

$$\epsilon = \frac{\Delta v}{\sqrt{\tau_m I - 1/4}}. \quad (25.14)$$

Figure 25.11 shows an example for which $\epsilon = 1$.

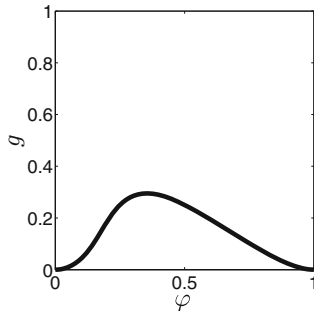


Figure 25.11. PRC of theta neuron with $\tau_m = 2$, $I = 0.13$, $\Delta v = 0.1$.
[THETA_PRC]

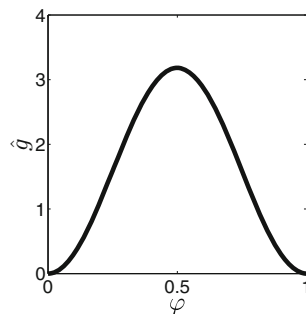


Figure 25.12. Infinitesimal PRC of theta neuron with $\tau_m = 2$, $I = 0.13$.
[THETA_PRC_SHORT_WEAK]

From eq. (25.13), we obtain a formula for the infinitesimal PRC, which is the partial derivative of g with respect to Δv , at $\Delta v = 0$:

$$\hat{g}(\varphi) = \frac{1}{\pi\sqrt{\tau_m I - 1/4}} \frac{1}{1 + \tan^2(\pi(\varphi - 1/2))}. \quad (25.15)$$

The infinitesimal PRC is symmetric with respect to $\varphi = 1/2$, whereas the non-infinitesimal PRC reaches its maximum to the left of $\varphi = 1/2$; see Fig. 25.12.

The PRC given by eq. (25.13), graphed in Fig. 25.11, has a hidden symmetry property, which becomes apparent when plotting the graph of the interaction function f ; see Fig. 25.13. The figure suggests that the graph of f becomes the graph of an even function if it is rotated by 45° in the clockwise direction, then shifted horizontally to make the origin coincide with the center point of the dashed line in Fig. 25.13. I will call this property *diagonal symmetry*. In Section 26.4, we will prove that this property implies that for two theta neurons, coupled via instantaneous charge injections, any phase difference is neutrally stable.

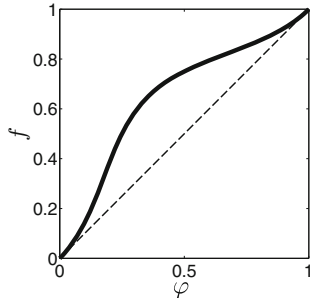


Figure 25.13. Interaction function corresponding to the PRC in Fig. 25.11. [THETA_F]

Proposition 25.1. The interaction function f associated with instantaneous charge injection into a theta neuron is diagonally symmetric.

Proof. Let s label locations along the dashed diagonal in Fig. 25.13, with $s = 0$ corresponding to the center of the diagonal (that is, the center of the square), and $s = \pm 1/\sqrt{2}$ corresponding to the vertices $(0,0)$ and $(1,1)$ of the square. Thus points (φ, φ) on the diagonal can be parametrized either by $\varphi \in [0, 1]$, or by $s \in [-1/\sqrt{2}, 1/\sqrt{2}]$. The relation between the two coordinates is

$$\varphi = s/\sqrt{2} + 1/2. \quad (25.16)$$

To convince yourself, just check the cases $s = -1/\sqrt{2}$ and $s = 1/\sqrt{2}$, and note that the relation between φ and s is linear. For later use, we solve eq. (25.16) for s :

$$s = \sqrt{2}(\varphi - 1/2). \quad (25.17)$$

For $s \in [-1/\sqrt{2}, 1/\sqrt{2}]$, we define $\tilde{f}(s)$ as in Fig. 25.14. See exercise 7 for the proof that the picture looks qualitatively similar to that in Fig. 25.14 for all values of $\epsilon > 0$, and therefore \tilde{f} is well-defined. Our claim is that \tilde{f} is an even function of s .

Let $\varphi \in [0, 1]$, and consider the point (φ, φ) on the diagonal. To compute $\tilde{f}(s)$ (with s given by eq. (25.17)), we must compute how far we have to move in the direction perpendicular to the diagonal to get to the graph of f , starting at (φ, φ) . In other words, we should find $u \geq 0$ so that the point $(\varphi - u, \varphi + u)$ lies on the graph of f , i.e., so that

$$\varphi + u = f(\varphi - u). \quad (25.18)$$

$\tilde{f}(s)$ is the length of the red line segment in Fig. 25.14, which is $\sqrt{2}u$:

$$\tilde{f}(s) = \sqrt{2}u. \quad (25.19)$$

Before continuing, we summarize what we have proved, combining (25.16), (25.18), and (25.19):

$$\tilde{f}(s) = \sqrt{2}u \Leftrightarrow \frac{s}{\sqrt{2}} + \frac{1}{2} + u = f\left(\frac{s}{\sqrt{2}} + \frac{1}{2} - u\right). \quad (25.20)$$

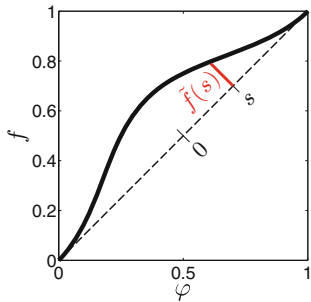


Figure 25.14. Definition of the function $\tilde{f} = \tilde{f}(s)$. [THETA_F_TILDE]

We use $f(\varphi) = \varphi + g(\varphi)$ and eq. (25.13) to write eq. (25.18) as

$$\varphi + u = \frac{1}{\pi} \arctan \left(\tan \left(\pi(\varphi - u) - \frac{\pi}{2} \right) + \epsilon \right) + \frac{1}{2}.$$

Now we use $\varphi = s/\sqrt{2} + 1/2$, and simplify a bit:

$$\frac{s}{\sqrt{2}} + u = \frac{1}{\pi} \arctan \left(\tan \left(\pi \left(\frac{s}{\sqrt{2}} - u \right) \right) + \epsilon \right).$$

We multiply by π , and take the tangent on both sides:

$$\tan \left(\pi \left(\frac{s}{\sqrt{2}} + u \right) \right) = \tan \left(\pi \left(\frac{s}{\sqrt{2}} - u \right) \right) + \epsilon. \quad (25.21)$$

If we replace s by $-s$ in this equation, we obtain

$$\tan \left(\pi \left(-\frac{s}{\sqrt{2}} + u \right) \right) = \tan \left(\pi \left(-\frac{s}{\sqrt{2}} - u \right) \right) + \epsilon. \quad (25.22)$$

We denote the solutions u of (25.21) and (25.22) by u_+ and u_- , respectively. From our earlier discussion, $\tilde{f}(s) = \sqrt{2}u_+$, and $\tilde{f}(-s) = \sqrt{2}u_-$. However, because \tan is an odd function, eqs. (25.21) and (25.22) are equivalent, so $u_+ = u_-$. This implies $\tilde{f}(s) = \tilde{f}(-s)$, so indeed \tilde{f} is even. \square

Surprisingly the infinitesimal PRC, given by eq. (25.15), does *not* have the same hidden symmetry property; see Proposition 26.6.

Exercises

- 25.1. (*) As mentioned in Section 25.1, we will assume in future chapters that following the arrival of the input pulse, there is a first spike at a time t_* significantly affected by the input pulse, but perfectly periodic firing with

τ_r	τ_{peak}	τ_d	\bar{g}_{syn}	φ_0	E_1	E_2
0.5	0.5	2	0.05	0.1		
0.5	0.5	2	0.05	0.5		
0.5	0.5	2	0.05	0.9		
0.5	0.5	2	0.1	0.1		
0.5	0.5	2	0.1	0.5		
0.5	0.5	2	0.1	0.9		
0.5	0.5	2	0.2	0.1		
0.5	0.5	2	0.2	0.5		
0.5	0.5	2	0.2	0.9		
1.0	1.0	5	0.05	0.1		
1.0	1.0	5	0.05	0.9		
1.0	1.0	5	0.1	0.1		
1.0	1.0	5	0.1	0.9		

Table 25.1. Results for exercise 1.

inter-spike interval T resumes immediately after that spike, so that the subsequent spikes occur at $t_* + T$, $t_* + 2T$, ... In other words, we will assume that there is no memory of the input lasting past time t_* .

To test the validity of this assumption, we initialize an RTM neuron with $I = 1$ at a phase $\varphi_0 \in [0, 1)$, and give it an excitatory synaptic input pulse at time 0 (that is, we set $q(0) = 1$). The pulse is characterized by four parameters: τ_r , τ_{peak} , τ_d , and \bar{g}_{syn} , which we will vary. (We always take v_{rev} to be zero here.) Denoting the spike times by $t_* = t_1, t_2, t_3, \dots$, we set $T_k = t_{k+1} - t_k$. If our assumption is valid, the T_k should all be very close to T . In any case, T_{10} is very close to T . (You can check this numerically if you want.) We therefore compute the relative differences

$$\frac{T_{10} - T_1}{T_{10}} \quad \text{and} \quad \frac{T_{10} - T_2}{T_{10}},$$

hoping that they will be close to zero. Multiplying these numbers by 100%, we get percentage errors:

$$E_1 = \frac{T_{10} - T_1}{T_{10}} \times 100\%, \quad E_2 = \frac{T_{10} - T_2}{T_{10}} \times 100\%.$$

Fill in Table 25.1. Round the answers to the nearest one-hundredth of a percent. Also check other parameter combinations that you find interesting.

- 25.2. If you repeat exercise 1, but for a theta neuron (driven above the firing threshold), with an instantaneous charge injection modeling the input pulse, what are E_1 and E_2 ?
- 25.3. Explain why (25.4) and (25.5) are the same.

- 25.4. Recall Fig. 14.3. For $I > I_c$, but I not too large, the stable limit cycle would still be present, and it would still encircle a fixed point, but that fixed point would be unstable. (You may take this for granted, or you could show it numerically. It is not shown in Fig. 14.3.)

Explain: For the classical Hodgkin-Huxley neuron, reduced to two dimensions, when $I > I_c$ but I is not too large, there is a value of $\Delta v > 0$ for which the minimum of the phase response function g , for an input that causes v to rise by Δv instantaneously, equals $-\infty$.

- 25.5. Show that for the theta neuron, $g(\varphi)$, given by eq. (25.13), converges to $1 - \varphi$ as $\Delta v \rightarrow \infty$.
- 25.6. $(*)$ (\dagger) Plot a picture like that in the middle panel of Fig. 25.9, but with $\bar{g}_{\text{syn}} = 0.30$. What you will see will probably surprise you. Can you understand the picture? Plotting $(v(t), n(t))$ for selected values of φ is suggestive.
- 25.7. Let f be the interaction function of the theta neuron subject to an instantaneous charge injection. (a) Show that f is strictly increasing. (b) Show that $f(\varphi) \geq \varphi$ for all $\varphi \in [0, 1]$, with strict inequality for $\varphi \in (0, 1)$. (c) Explain why Fig. 25.14 defines \tilde{f} uniquely.

Chapter 26

Synchronization of Two Pulse-Coupled Oscillators

There is a vast literature on the question when firing-triggered pulsatile signaling among neurons will lead to synchrony. In this chapter, we analyze the simplest formalization of this question. Perhaps the main worthwhile conclusion from the analysis presented here is that there is no general statement of the form “excitatory interactions synchronize” or “inhibitory interactions synchronize.” Whether or not pulse-coupling synchronizes depends on the detailed nature of the responses of the neurons to signals they receive; see Proposition 26.2. Approximately speaking, excitatory pulse-coupling synchronizes if the phase response is of type 2, or if there is strong refractoriness; this will be made precise in inequality (26.12).

The analysis in this chapter uses ideas due to Peskin [123], who analyzed the case of two pulse-coupled LIF neurons. Peskin’s analysis was later extended to arbitrary numbers of neurons by Mirollo and Strogatz [119].

26.1 The Model

Consider two identical neurons A and B. We will not specify what kind of neurons they are, but simply assume that without interaction, both would fire periodically with a period T . We call T the *intrinsic firing period*.

A neuron is at *phase* $\varphi \in [0, 1]$ if in the absence of any interactions, the time to the next spike of the neuron would be $(1 - \varphi)T$. We denote the phases of A and B by φ_A and φ_B , respectively. Suppose that A fires at some time t_* . Then $\varphi_A(t_* + 0) = 0$, and we assume that

$$\varphi_B(t_* + 0) = \varphi_B(t_* - 0) + g(\varphi_B(t_* - 0)),$$

Electronic supplementary material: The online version of this chapter (doi: [10.1007/978-3-319-51171-9_26](https://doi.org/10.1007/978-3-319-51171-9_26)) contains supplementary material, which is available to authorized users.

where g is the phase response function. Similarly, if B fires at time t_* , we assume that

$$\varphi_A(t_* + 0) = \varphi_A(t_* - 0) + g(\varphi_A(t_* - 0)).$$

We will assume that g is defined and differentiable on the closed interval $[0, 1]$, with

$$g(0) = g(1) = 0. \quad (26.1)$$

This eliminates possible ambiguity about what happens when both neurons fire at the same time — they don't influence each other at all in that case. We also assume

$$g'(\varphi) \geq -1 \quad \text{for } \varphi \in [0, 1], \quad \text{and } g'(\varphi) > -1 \text{ for } \varphi \in (0, 1). \quad (26.2)$$

Assumptions (26.1) and (26.2), taken together, imply (see exercise 1)

$$-\varphi \leq g(\varphi) \leq 1 - \varphi \quad \text{for } \varphi \in [0, 1], \quad \text{and } -\varphi < g(\varphi) < 1 - \varphi \text{ for } \varphi \in (0, 1). \quad (26.3)$$

For the *interaction function* $f = f(\varphi) = \varphi + g(\varphi)$, (26.1) and (26.2) imply (see exercise 1)

$$f(0) = 0, \quad f(1) = 1, \quad f'(\varphi) \geq 0 \quad \text{for } \varphi \in [0, 1], \quad f'(\varphi) > 0 \quad \text{for } \varphi \in (0, 1). \quad (26.4)$$

In particular, the interaction function is strictly increasing.

A pair of theta neurons interacting through instantaneous charge injection (see Section 25.4) strictly falls into the framework described here. However, in general, this framework describes the interaction of two neurons only approximately, and only if the synaptic interactions are brief and relatively weak; compare, for instance, exercises 25.1 and 25.6.

We will analyze the question whether the two neurons phase-lock, and if so, at which phase difference. Two important examples of phase-locking are *synchrony* (A and B eventually fire at the same times), and *anti-synchrony* (A fires exactly in the middle of the inter-spike intervals of B , and vice versa.)

26.2 Abstract PRCs

The examples of PRCs given here are called “abstract” in the section title because they are not derived from neuronal models. Five examples are shown in Figs. 26.1–26.5. In each case, we plot the graph of g . In Figs. 26.1 and 26.4, we also plot the graph of the interaction function f defined by $f(\varphi) = \varphi + g(\varphi)$. In addition, we plot other related functions called F and G , but at this point, the reader should simply ignore those panels. The functions F and G will be introduced, and their significance explained, in Section 26.3.

In Fig. 26.1, $g(\varphi) \geq 0$ for all φ , so the pulses are excitatory. For $\varphi \approx 0$, $g(\varphi)$ is small. One might refer to this as *refractoriness* — inputs that reach a target neuron soon after the target fires have little effect. The PRC has some qualitative resemblance with the PRCs of the RTM neuron in Fig. 25.5. In Fig. 26.2, $g(\varphi)$ rises fairly quickly near $\varphi = 0$, so refractoriness is not pronounced. The PRC has some qualitative resemblance with the PRC of the WB neuron in Fig. 25.9. In Fig. 26.3,

the PRC looks somewhat similar to that of the classical Hodgkin-Huxley neuron in Fig. 25.9. A type 2 PRC for an excitatory input pulse usually looks qualitatively similar to that in Fig. 26.3. Figure 26.4 shows one example of a family of phase response functions, parametrized by $\epsilon \in (0, 1]$, and given by the rather bizarre formula

$$g(\varphi) = 2(1 - \varphi) - \frac{1 + \epsilon - \sqrt{(1 + \epsilon)^2 - 4\epsilon(1 - \varphi)}}{\epsilon}. \quad (26.5)$$

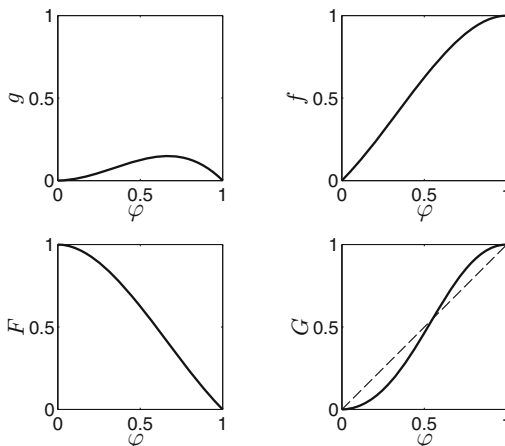


Figure 26.1. Graphs of the functions g , f , F , and G , where $g(\varphi) = \varphi^2(1 - \varphi)$. [ABSTRACT_PULSE_COUPLING_1]

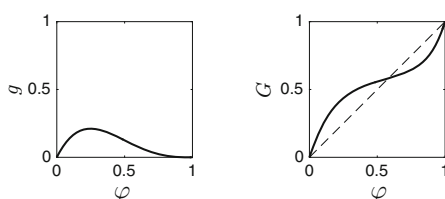


Figure 26.2. Graphs of g and G , where $g(\varphi) = 2\varphi(1 - \varphi)^3$. [ABSTRACT_PULSE_COUPLING_2]

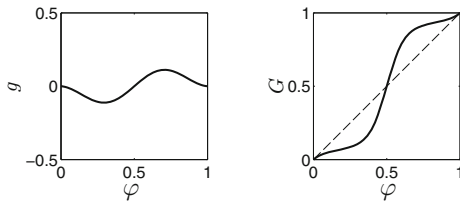


Figure 26.3. Graphs of g and G , where $g(\varphi) = -\sin(2\pi\varphi)(\varphi(1 - \varphi) + 0.05)/2$. [ABSTRACT_PULSE_COUPLING_3]

What is natural about this formula will be explained in exercise 3. The PRC has qualitative resemblance with the PRC of the WB neuron in Fig. 25.9. In Fig. 26.4, we also show the interaction function f . We observe that it is *diagonally symmetric*. This term was defined in Section 25.4; its significance will be explained in Section 26.4. In Fig. 26.5, $g(\varphi) \leq 0$ for all $\varphi \in [0, 1]$. This is a model

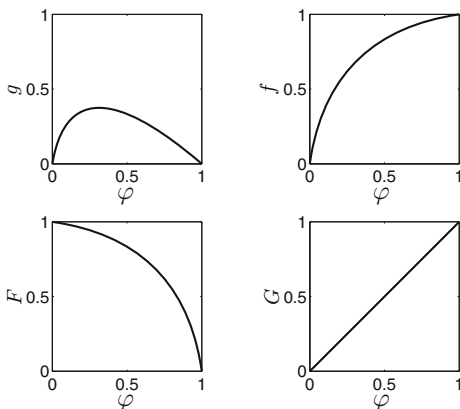


Figure 26.4. Graphs of the functions g , f , F , and G , where g is given by eq. (26.5) with $\epsilon = 0.75$. [ABSTRACT_PULSE_COUPLING_4]

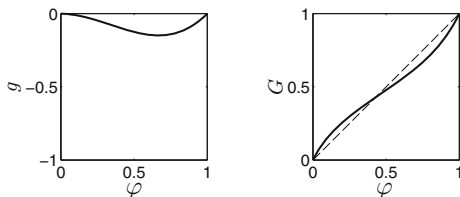


Figure 26.5. Graphs of g and G , where $g(\varphi) = -\varphi^2(1 - \varphi)$. [ABSTRACT_PULSE_COUPLING_5]

of interaction by brief *inhibitory* synaptic pulses.

26.3 Analysis

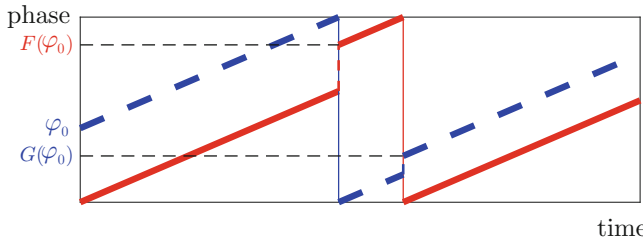


Figure 26.6. Diagram illustrating the reasoning in Section 26.3. “A” is red and solid, “B” is blue and dashed.

As you read this section, it may help to look at the diagram in Fig. 26.6. Suppose that at time 0, neuron A has just fired, and is therefore now at phase $\varphi_A = 0$, and neuron B has just received the signal from neuron A, and is now at some phase $\varphi_B = \varphi_0 \in [0, 1)$. The next event of interest is a spike of B at time $(1 - \varphi_0)T$. This spike will reset φ_B to 0, while raising φ_A to $f(1 - \varphi_0)$. We define

$$F(\varphi) = f(1 - \varphi), \quad (26.6)$$

Thus the spike of B at time $(1 - \varphi_0)T$ raises φ_A to $F(\varphi_0)$. We are then back to the situation that we started with: One neuron has just fired, and the other has just responded to the resulting signal. However, A and B have swapped places, but we can continue our reasoning: When A fires next, the phase of B is advanced to $F(F(\varphi_0))$. We define

$$G(\varphi) = F(F(\varphi)), \quad (26.7)$$

and write

$$\varphi_1 = G(\varphi_0), \quad \varphi_2 = G(\varphi_1), \quad \dots$$

So φ_k is the phase of B immediately after the k -th spike of A. (The initial spike of A is considered the 0-th spike here.) This is the fixed point iteration for G . Fixed points of G are closely linked with phase-locking of the two neurons A and B.

Thus the function G will be central to our analysis. For all examples of phase response functions g in Figs. 26.1–26.5, we also plotted G , although we asked the reader to disregard those plots earlier. In some cases (Figs. 26.1 and 26.4), we also plotted f and F . Before continuing our discussion, we note some simple properties of F and G , derived using eq. (26.4):

$$F(0) = 1, \quad F(1) = 0, \quad G(0) = 0, \quad G(1) = 1, \quad G'(0) = G'(1) \geq 0, \quad (26.8)$$

$$F \text{ is strictly decreasing, } G \text{ is strictly increasing.} \quad (26.9)$$

We now analyze the fixed point of F and G , and their connection with phase-locking of A and B.

Proposition 26.1. (a) $\varphi_* \in [0, 1]$ is a fixed point of G if and only if it is possible for the two neurons to fire in a phase-locked state with B at phase φ_* immediately after a spike of A , and A at phase $F(\varphi_*)$ immediately after a spike of B .

(b) If φ_* is a fixed point of G , so is $F(\varphi_*)$, so fixed points of G come in pairs.

(c) If φ_* is a fixed point of G , the period of the corresponding phase-locked firing pattern of A and B equals $(2 - \varphi_* - F(\varphi_*))T$.

(d) $\varphi_* = 0$ is always a fixed point of G , and therefore so is $\varphi_* = 1$, since $F(0) = 1$. This pair of fixed points, 0 and 1, corresponds to synchronization, i.e., phase-locking with zero phase difference.

(e) There is exactly one fixed point φ_* of G that is also a fixed point of F . It corresponds to precise anti-synchrony, that is, neuron B fires precisely at the midpoints of the inter-spike intervals of neuron A , and vice versa.

Proof. (a) This is a direct consequence of the definitions of F and G . (b) Suppose $G(\varphi_*) = \varphi_*$. This means $F(F(\varphi_*)) = \varphi_*$. We apply F to both sides of this equation: $F(F(F(\varphi_*))) = F(\varphi_*)$. But this can be re-written as $G(F(\varphi_*)) = F(\varphi_*)$. (c) Suppose A has just fired, and has had its effect on B , and now B is at phase φ_* . After time $(1 - \varphi_*)T$, B fires, and sends a signal to A . This signal finds A at phase $1 - \varphi_*$, and moves it to phase $f(1 - \varphi_*) = F(\varphi_*)$. After time $(1 - F(\varphi_*))T$, A fires again, and the resulting signal moves B to phase φ_* again. One full cycle is now complete, and the time that it took is

$$(1 - \varphi_*)T + (1 - F(\varphi_*))T = (2 - \varphi_* - F(\varphi_*))T.$$

(d) $G(0) = F(F(0)) = F(1) = 0$ and $G(1) = F(F(1)) = F(0) = 1$. The fixed point 0 corresponds to a phase-locked pattern where B is at phase 0 when A has just fired and has had its effect on A — so when A has just fired, B has just fired. The fixed point $1 = F(0)$ corresponds to the same phase-locked firing pattern. (e) That there is such a fixed point follows from $F(0) = 1$ and $F(1) = 0$, using the intermediate value theorem. That there is only one such fixed point follows from the fact that F is strictly decreasing. By part (c), the period of the corresponding phase-locked firing pattern is $2(1 - \varphi_*)T$, and the time between a spike of A and the next spike of B is $(1 - \varphi_*)T$, exactly half the period of the phase-locked firing pattern. \square

The fixed point φ_* corresponding to anti-synchrony (see part (e) of Proposition 26.1) is not usually $1/2$, contrary to what you might think. To understand this, denote the period of the anti-synchronous solution by T_a , and note that T_a is not in general T . We pointed out in the proof of Proposition 26.1 that the period of the anti-synchronous solution is $2(1 - \varphi_*)T$, so $2(1 - \varphi_*)T = T_a$, or

$$\varphi_* = 1 - \frac{1}{2} \frac{T_a}{T}.$$

If, for instance, the interactions are strictly excitatory, i.e., $g(\varphi) > 0$ for all $\varphi \in (0, 1)$, then $T_a < T$, and therefore $\varphi_* > 1/2$.

In Figs. 26.1–26.3 and 26.5, there are exactly three fixed points of G : 0, 1, and a fixed point φ_* with $0 < \varphi_* < 1$. By Proposition 26.1, parts (d) and (e), these fixed points must correspond to synchrony (0 and 1) and precise anti-synchrony

$(\varphi_* \in (0, 1))$. In Fig. 26.4, all $\varphi \in [0, 1]$ are fixed point of G . This implies that the initial phase difference between A and B is simply conserved for all times.

Using the ideas explained in Appendix B, we see immediately that synchrony is stable, and anti-synchrony is unstable, in the examples of Figs. 26.1 and 26.3. In the examples of Figs. 26.2 and 26.5, synchrony is unstable and anti-synchrony is stable. (When we say “synchrony is stable,” we mean that 0 and 1 are stable fixed points of G , and when we say “anti-synchrony is stable,” we mean that the fixed point $\varphi_* \in (0, 1)$ of G that corresponds to anti-synchrony is stable.) Comparing Figs. 26.1 and 26.2, we see that synchrony can be stable or unstable when the pulse-coupling is excitatory and the PRC is of type 1 ($g(\varphi) \geq 0$ for all φ). The details of the PRC matter. Figures 26.7 and 26.8 illustrate convergence to synchrony or anti-synchrony, respectively.

It is easy to describe in general when synchrony is stable, using part (e) of Proposition 26.1:

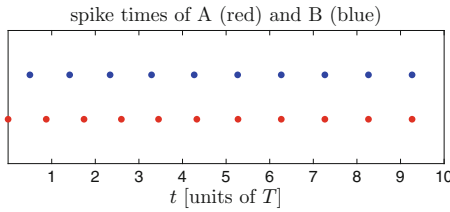


Figure 26.7. Two oscillators, pulse-coupled with the phase response function $g(\varphi) = \varphi^2(1 - \varphi)$, synchronize. [TWO_PULSE_COUPLED_OSC]

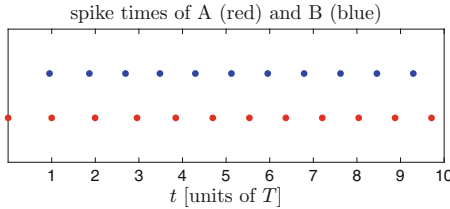


Figure 26.8. Two oscillators, pulse-coupled with the phase response function $g(\varphi) = 2\varphi(1 - \varphi)^3$, anti-synchronize. [TWO_PULSE_COUPLED_OSC_2]

Proposition 26.2. Suppose that $g = g(\varphi)$ is differentiable on the interval $[0, 1]$ and satisfies (26.1) and (26.2). Synchrony is locally attracting, i.e., 0 and 1 are locally attracting fixed points of G , if

$$(1 + g'(0))(1 + g'(1)) < 1. \quad (26.10)$$

It is repelling, i.e., 0 and 1 are repelling fixed points of G , if

$$(1 + g'(0))(1 + g'(1)) > 1. \quad (26.11)$$

Proof. The left-hand side of inequalities (26.10) and (26.11) equals $G'(0)$:

$$G'(0) = F'(F(0))F'(0) = F'(1)F'(0) = (-f'(0))(-f'(1)) =$$

$$f'(0)f'(1) = (1 + g'(0))(1 + g'(1)) = (1 + g'(0))(1 + g'(1)).$$

This implies the assertion because $G'(0) = G'(1) \geq 0$. \square

Corollary 26.3. *If $g'(1) \leq 0$, as is the case for the PRCs shown in Figs. 26.1–26.4, synchrony is attracting if $g'(0)$ is small enough, namely*

$$g'(0) < \frac{|g'(1)|}{1 + g'(1)}, \quad (26.12)$$

and repelling if

$$g'(0) > \frac{|g'(1)|}{1 + g'(1)}.$$

Proof. Condition (26.10) is equivalent to

$$g'(0) < \frac{1}{1 + g'(1)} - 1 = \frac{-g'(1)}{1 + g'(1)} = \frac{|g'(1)|}{1 + g'(1)}.$$

(The last equation holds because we assume $g'(1) \leq 0$). \square

If g has the usual “type 2” shape, i.e., $g(\varphi) < 0$ for small φ , and $g(\varphi) > 0$ for large φ , then (26.12) holds, so synchrony is stable. If $g'(0) \geq 0$ and $g'(1) \leq 0$, as would be the case for a type 1 PRC in response to an excitatory pulse, then synchrony is stable only if $g'(0)$ is small enough, i.e., refractoriness is pronounced enough.

26.4 Diagonally Symmetric PRCs

The next proposition explains the significance of diagonal symmetry of the interaction function, the symmetry property of the theta neuron responding to instantaneous charge injection that we found in Section 25.4. The proposition states that this property is equivalent to $G(\varphi) = \varphi$ for all φ — so the initial phase difference between A and B is conserved for all times. It seems like a peculiar accident that the theta neuron responding to instantaneous charge injection has this property. This implies that two theta neurons, coupled via instantaneous charge injections, constitute a poor model of two neurons, coupled with brief excitatory synapses; see, for instance, Fig. 24.5, where phase-locking at a specific phase difference, different from the initial phase difference, clearly does occur.

Proposition 26.4. *The interaction function f is diagonally symmetric if and only if $G(\varphi) = \varphi$ for all $\varphi \in [0, 1]$.*

Proof. We want to prove the equivalence of the following two statements:

- (i) f is diagonally symmetric.
- (ii) $G(\varphi) = \varphi$ for all $\varphi \in [0, 1]$.

Refer to the proof of Proposition 25.1. From (25.20), we see that (i) can be re-stated as follows:

- (i) For all $s \in [-1/\sqrt{2}, 1/\sqrt{2}]$,

$$\frac{s}{\sqrt{2}} + \frac{1}{2} + u = f\left(\frac{s}{\sqrt{2}} + \frac{1}{2} - u\right) \Rightarrow -\frac{s}{\sqrt{2}} + \frac{1}{2} + u = f\left(-\frac{s}{\sqrt{2}} + \frac{1}{2} - u\right).$$

From the definitions, (ii) means $f(1 - f(1 - \varphi)) = \varphi$ for all $\varphi \in [0, 1]$, or equivalently:

- (ii) $f(1 - f(\varphi)) = 1 - \varphi$ for all $\varphi \in [0, 1]$.

We will prove that (i) implies (ii), and vice versa.

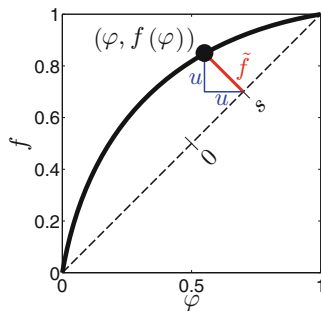


Figure 26.9. Illustration of the notation used in the proof of Proposition 26.4. [F_TILDE]

(i) \Rightarrow (ii): Figure 26.9 will help in following the argument that we are about to give. Let $\varphi \in [0, 1]$. Consider the point $(\varphi, f(\varphi))$ on the graph of f . Draw a line segment that starts in this point, ends on the diagonal of the unit square indicated as a dashed line in Fig. 26.9, and is perpendicular to that diagonal. This line segment is indicated in red in Fig. 26.9. The point on the diagonal in which the line segment ends has a coordinate $s \in [-1/\sqrt{2}, 1/\sqrt{2}]$. The red line segment has length $\tilde{f}(s)$, in the notation used in the proof of Proposition 25.1. If the graph of f were on the other side of the diagonal, then $\tilde{f}(s)$ would be negative, and the length of the red segment would be $|\tilde{f}(s)|$; this possibility is allowed here. The two segments indicated in blue in Fig. 26.9, together with the red segment, form an isosceles right triangle. The blue segments are of length $u = |\tilde{f}(s)|/\sqrt{2}$. If $\tilde{f}(s)$ were negative, we would still define u to be $|\tilde{f}(s)|/\sqrt{2}$, but the blue segments would then be of length $|u|$.

We now note that

$$\varphi = \frac{s}{\sqrt{2}} + \frac{1}{2} - u \quad \text{and} \quad f(\varphi) = \frac{s}{\sqrt{2}} + \frac{1}{2} + u. \quad (26.13)$$

Because we assume (i), we conclude that

$$-\frac{s}{\sqrt{2}} + \frac{1}{2} + u = f\left(-\frac{s}{\sqrt{2}} + \frac{1}{2} - u\right). \quad (26.14)$$

Now we can prove (ii):

$$f(1 - f(\varphi)) = f\left(-\frac{s}{\sqrt{2}} + \frac{1}{2} - u\right) = -\frac{s}{\sqrt{2}} + \frac{1}{2} + u = 1 - \varphi.$$

We used eq.(26.13) for the first of these equations, eq.(26.14) for the second, and (26.13) again for the third. The proof of (i) \Rightarrow (ii) is thereby complete.

(ii) \Rightarrow (i): Let $s \in [-1/\sqrt{2}, 1/\sqrt{2}]$, and let u be the solution of

$$\frac{s}{\sqrt{2}} + \frac{1}{2} + u = f\left(\frac{s}{\sqrt{2}} + \frac{1}{2} - u\right). \quad (26.15)$$

Define

$$\varphi = \frac{s}{\sqrt{2}} + \frac{1}{2} - u. \quad (26.16)$$

Then (26.15) becomes

$$f(\varphi) = \frac{s}{\sqrt{2}} + \frac{1}{2} + u. \quad (26.17)$$

But we also assume (ii) now, so

$$f(1 - f(\varphi)) = 1 - \varphi,$$

and inserting (26.16) and (26.17), we find

$$f\left(-\frac{s}{\sqrt{2}} + \frac{1}{2} - u\right) = -\frac{s}{\sqrt{2}} + \frac{1}{2} + u.$$

Therefore (ii) \Rightarrow (i) is proved. \square

We summarize in Section 26.5 what our discussion of diagonal symmetry implies for two theta neurons interacting via instantaneous positive charge injections.

26.5 A Borderline Case in Which the Infinitesimal PRC Leads to a False Conclusion

Propositions 25.1 and 26.4 imply the following result:

Proposition 26.5. *For two identical theta neurons coupled via instantaneous charge injection as described in Section 25.4, the initial phase difference is preserved for all time.*

We will show that one would come to a different conclusion if one analyzed the situation using the infinitesimal PRC, no matter how weak the interactions are. In fact, the following proposition holds:

Proposition 26.6. *For two identical theta neurons coupled via instantaneous charge injection as described in Section 25.4, if the phase response function is replaced by $\Delta v \hat{g}(\varphi)$, where \hat{g} is the infinitesimal phase response function, then synchrony is locally attracting for all sufficiently small $\Delta v > 0$.*

Proof. From eqs. (25.14) and (25.15),

$$\Delta v \hat{g}(\varphi) = \frac{\epsilon}{1 + \tan^2(\pi(\varphi - 1/2))}. \quad (26.18)$$

We assume that Δv , and therefore ϵ (see eq. (25.14)), is fixed, and is so small that the assumptions in (26.2) hold. For simplicity, we denote the interaction function associated with (26.18) by \hat{f} , not indicating in the notation the dependence on Δv :

$$\hat{f}(\varphi) = \varphi + \frac{\epsilon}{1 + \tan^2(\pi(\varphi - 1/2))}.$$

The function “ F ” derived from this interaction function (see eq. (26.6)) will be denoted by \hat{F} :

$$\begin{aligned} \hat{F}(\varphi) &= \hat{f}(1 - \varphi) = 1 - \varphi + \frac{\epsilon}{1 + \tan^2(\pi(1/2 - \varphi))} = \\ &1 - \varphi + \epsilon \cos^2(\pi(1/2 - \varphi)) = 1 - \varphi + \epsilon \sin^2(\pi\varphi). \end{aligned}$$

Differentiating once, we obtain (see exercise 5)

$$\hat{F}'(\varphi) = -1 + \epsilon \pi \sin(2\pi\varphi). \quad (26.19)$$

We want to prove now that 0 is a locally attracting fixed point of $\hat{G}(\varphi) = \hat{F}(\hat{F}(\varphi))$. Using our formulas for \hat{F} and \hat{F}' , one easily finds (see exercise 6)

$$\hat{G}(0) = 0, \quad \hat{G}'(0) = 1, \quad \hat{G}''(0) = 0, \quad \hat{G}'''(0) = -12\epsilon^2\pi^4. \quad (26.20)$$

By Taylor’s theorem, then $\hat{G}(\varphi) < \varphi$ if $\varphi > 0$ is close enough to 0, and therefore our assertion follows using the ideas of Appendix B. \blacksquare

One might accuse the infinitesimal PRC of being misleading in this example: It predicts that synchrony is attracting, when in fact it is not, regardless of how small $\Delta v > 0$ may be. However, the accusation isn’t entirely fair: Notice that the analysis based on the infinitesimal PRC predicts that synchrony is “just barely” attracting, in the sense that $\hat{G}'(0)$ is in fact equal to 1. In cases that are not borderline, the predictions derived using the infinitesimal PRC are right for small $\Delta v > 0$; see exercise 7 for a way of making this precise.²⁰

²⁰This is reminiscent of the *Hartman-Grobman Theorem* for ordinary differential equations [149]: Linearization can mislead only in borderline cases.

26.6 Pulse-Coupled RTM Neurons

The framework of this chapter is an idealization, and Hodgkin-Huxley-like neurons with synaptic interactions don't quite fit into it. In particular, the phase response functions g that we computed in Chapter 25 for Hodgkin-Huxley-like models such as the RTM and WB neurons, with synaptic pulses as inputs, do not quite satisfy the assumption $g(0) = 0$; see, for instance, Fig. 25.2.

However, as long as

$$f(\varphi) = \varphi + g(\varphi) \in [0, 1]$$

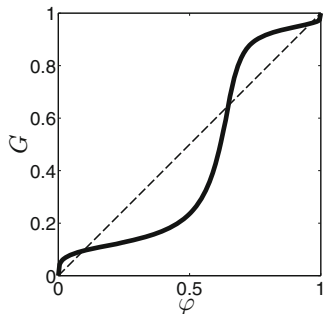


Figure 26.10. The function G derived from the PRC in Fig. 25.2. [RTM_PLOT_G]

for all $\varphi \in [0, 1]$, we can still compute the function $G = G(\varphi) = F(F(\varphi))$, with $F(\varphi) = f(1 - \varphi)$, and plot its graph. It seems plausible that this can still give valid indications about synchronization behavior. Doing this for the PRC of Fig. 25.2, we obtain Fig. 26.10. This plot suggests that for two RTM neurons, coupled with the kind of synaptic pulses used in the computation of Fig. 25.2, there is a stable phase-locked state that is nearly, but not precisely synchronous.

One must be somewhat skeptical of this reasoning. The analysis assumes that an input pulse only affects the duration of the inter-spike period during which it arrives, not the durations of the subsequent inter-spike periods, and this is especially inaccurate when the pulse arrives shortly before the end of the period (see exercise 25.1), so conclusions about near-synchronous phase-locked states deserve special skepticism. However, Fig. 24.5 shows that our conclusion is, in fact, correct. It is also in line with the result from Chapter 24 that fast excitatory synapses in a network of RTM neurons produce sloppy, but not precise synchronization.

Exercises

- 26.1. Prove that (26.1) and (26.2) imply (26.3) and (26.4).
- 26.2. Verify the properties of F and G listed in (26.8) and (26.9).
- 26.3. (†) We will use the notation introduced in Section 25.4 here. As explained there, the diagonal connecting the points $(0, 0)$ and $(1, 1)$ in the unit square

will be parametrized either by $\varphi \in [0, 1]$, or by $s \in [-1/\sqrt{2}, 1/\sqrt{2}]$. From any strictly increasing function $f = f(\varphi)$ with $f(0) = 0$ and $f(1) = 1$, we can derive a function $\tilde{f} = \tilde{f}(s)$, as indicated in Fig. 26.9. Recall that we call f diagonally symmetric if f is an even function of s . The end point conditions $f(0) = 0$, $f(1) = 1$ translate into $\tilde{f}(-1/\sqrt{2}) = \tilde{f}(1/\sqrt{2}) = 0$.

The simplest even functions $\tilde{f} = \tilde{f}(s)$ with $\tilde{f}(-1/\sqrt{2}) = \tilde{f}(1/\sqrt{2}) = 0$ are the quadratics

$$\tilde{f}(s) = c \left(-s^2 + \frac{1}{2} \right).$$

We assume the constant c to be positive.

(a) Explain why \tilde{f} corresponds to a strictly increasing function f if $c \in (0, 1/\sqrt{2}]$, but not if $c > 1/\sqrt{2}$. (Refer to Fig. 26.9.)

(b) Write $c = \epsilon/\sqrt{2}$, $\epsilon \in (0, 1]$, so

$$\tilde{f}(s) = \frac{\epsilon}{\sqrt{2}} \left(-s^2 + \frac{1}{2} \right). \quad (26.21)$$

Compute the function $f = f(\varphi)$ corresponding to this function \tilde{f} . (Refer to Fig. 26.9.) Show that $g(\varphi) = f(\varphi) - \varphi$ is precisely the function defined by eq. (26.5).

26.4. We concluded that assuming $g'(1) \leq 0$, synchrony is attracting if $g'(0)$ is small enough (Corollary 26.3). Explain intuitively why that's what you would expect.

26.5. Verify eq. (26.19).

26.6. Verify the equations in (26.20).

26.7. (†) The goal of this exercise is to prove that the curious situation of Section 26.5, where the infinitesimal PRC suggests a result that is false for arbitrarily small $\Delta v > 0$, is possible only in borderline cases, in a sense that we will make precise.

Assume that $g = g(\varphi, \Delta v)$ is the phase response function of a model neuron responding to instantaneous charge injections. As before, $\varphi \in [0, 1]$ is phase, and $\Delta v \geq 0$ is the rise in v caused by a charge injection. Assume that g is twice differentiable with respect to φ and Δv , and that $g(\varphi, 0) = 0$ for all $\varphi \in [0, 1]$. The infinitesimal phase response function is defined by

$$\hat{g}(\varphi) = \left. \frac{\partial g}{\partial \Delta v}(\varphi, \Delta v) \right|_{\Delta v=0}.$$

Fix $\Delta v > 0$, and let $G(\varphi)$ denote the function G derived, as described in Section 26.2, from the phase response function $g(\varphi, \Delta v)$, and $\hat{G}(\varphi)$ the function G derived from the phase response function $\Delta v \hat{g}(\varphi)$. (Of course, G and \hat{G} depend on Δv , but we don't indicate that in the notation here.)

Show:

- (a) $\hat{G}'(0) = 1 + C\Delta v + D\Delta v^2$ for constants C and D independent of Δv .
- (b) If $C < 0$, then $G'(0) < 1$ for sufficiently small Δv .
- (c) In Section 26.5, $C = D = 0$.

26.8. For the PRC shown in Fig. 25.10, the function G is not well-defined. Why not?

Chapter 27

Oscillators Coupled by Delayed Pulses

Action potentials in the brain travel at a finite speed. The conduction delays between different brain areas can be on the order of 10 ms or more [151, Table 1]. Nonetheless, precise synchronization between oscillations in different parts of the brain has been reported numerous times [166]. This may sound surprising at first. However, there is a large body of theoretical work proposing mechanisms that could lead to synchronization in the presence of conductance delays. In this chapter, we discuss what is arguably the simplest result of this sort. We consider two identical oscillators, called A and B, pulse-coupled as in Chapter 26, but with a conduction delay.

27.1 Two Abstract Oscillators

We will not think of the “oscillators” as neurons in this section. Each oscillator might more typically be an oscillating neuronal network. When it reaches the phase $\varphi = 1$, it is assumed to send a signal to the other oscillator. This signal travels for a time δT , where $\delta > 0$, and T denotes, as in Chapter 26, the intrinsic period of the two oscillators. We will assume

$$\delta < 1. \quad (27.1)$$

Biologically, this assumption, which will soon prove convenient, is reasonable: One might think, for instance, of a delay of 10ms and an intrinsic frequency below 100Hz, corresponding to an intrinsic period greater than 10 ms. When the signal reaches the other oscillator, it shifts the phase of that oscillator from φ to $f(\varphi) = \varphi + g(\varphi)$, as in Chapter 26.

Electronic supplementary material: The online version of this chapter (doi: [10.1007/978-3-319-51171-9_27](https://doi.org/10.1007/978-3-319-51171-9_27)) contains supplementary material, which is available to authorized users.

We will analyze the *local stability* of synchrony: If A and B already start out near synchrony, will they become synchronous? We assume that at time $t = 0$, A reaches phase 1, and its phase is reset to $\varphi_A = 0$. We assume that B is slightly behind, at phase $\varphi_B = 1 - \alpha$, with $\alpha > 0$ small enough; it will become clear during the course of our discussion what “small enough” should mean here. We also assume that no signal is traveling in either direction just prior to time 0.

We will track *events*. We say that an “event occurs” if one of the oscillators reaches phase 1 and is therefore reset to phase 0 and sets in motion a signal traveling towards the other oscillator, or when a traveling signal reaches its target. For each event, we record the following data:

- the time at which the event occurs,
- the phases φ_A and φ_B of the two oscillators immediately *after* the event, and
- the upcoming events, and for each of them the time that would have to pass before its occurrence if no other event occurred earlier.

Event 1: A reaches phase 1. (It is reset to phase 0.)

This event occurs, by assumption, at time 0. The event is described by the following data:

- $t = 0$
- $\varphi_A = 0, \varphi_B = 1 - \alpha$
- upcoming events:
 - A reaches phase 1 within time T
 - B reaches phase 1 within time αT
 - signal from A to B reaches B within time δT

We assume

$$\alpha < \delta. \quad (27.2)$$

(Inequality (27.2) is the first of several conditions that a “small enough” α must satisfy.) This inequality implies that the second event of interest is the event that B reaches phase 1.

Event 2: B reaches phase 1. (It is reset to phase 0.)

- $t = \alpha T$
- $\varphi_A = \alpha, \varphi_B = 0$
- upcoming events:
 - A reaches phase 1 within time $(1 - \alpha)T$
 - B reaches phase 1 within time T

- signal from A to B reaches B within time $(\delta - \alpha)T$
- signal from B to A reaches A within time δT

Since we assume $\delta < 1$ (see eq. (27.1)), the next event is that the signal traveling from A to B reaches B.

Event 3: Signal traveling from A to B reaches B. (It resets φ_B .)

- $t = \delta T$
- $\varphi_A = \delta$, $\varphi_B = f(\delta - \alpha)$
- upcoming events:
 - A reaches phase 1 within time $(1 - \delta)T$
 - B reaches phase 1 within time $(1 - f(\delta - \alpha))T$
 - signal from B to A reaches A within time αT

(Recall that the phases recorded here are phases immediately *after* the event. Immediately prior to the arrival of the signal, B is at phase $\delta - \alpha$. The arrival of the signal changes this phase to $f(\delta - \alpha)$.) We assume now that

$$\alpha < 1 - \delta. \quad (27.3)$$

This inequality implies that the signal from B to A reaches A before A reaches phase 1. We will show that it also reaches A before B reaches phase 1. That is, we will show (for small enough α) that

$$\alpha < 1 - f(\delta - \alpha).$$

We assume that the phase response function g is defined and differentiable on the closed interval $[0, 1]$, and satisfies (26.1) and (26.2). This implies that f is strictly increasing; see Section 26.1. Therefore a sufficient condition for $\alpha < 1 - f(\delta - \alpha)$ is

$$\alpha < 1 - f(\delta). \quad (27.4)$$

We assume now that this holds. (This is simply one of the conditions defining a “small enough” α .) Note that the right-hand side of (27.4) is positive, since $f(\delta) < 1$. The next event of interest is then the arrival of the signal at A.

Event 4: Signal traveling from B to A reaches A. (It resets φ_A .)

- $t = (\alpha + \delta)T$
- $\varphi_A = f(\alpha + \delta)$, $\varphi_B = \alpha + f(\delta - \alpha)$
- upcoming events:

- A reaches phase 1 within time $(1 - f(\alpha + \delta))T$
- B reaches phase 1 within time $(1 - \alpha - f(\delta - \alpha))T$

The next event of interest is either the event that A reaches phase 1, or that B reaches phase 1. We will make an assumption that insures that A reaches phase 1 first:

$$1 - f(\alpha + \delta) < 1 - \alpha - f(\delta - \alpha),$$

or, equivalently,

$$\frac{f(\delta + \alpha) - f(\delta - \alpha)}{2\alpha} > \frac{1}{2}.$$

Using $f(\varphi) = \varphi + g(\varphi)$, we see that this means

$$\frac{g(\delta + \alpha) - g(\delta - \alpha)}{2\alpha} > -\frac{1}{2}. \quad (27.5)$$

The left-hand side of this inequality is a *central difference approximation* for $g'(\delta)$; see exercise 2. Therefore (27.5) holds for sufficiently small $\alpha > 0$, provided that

$$g'(\delta) > -\frac{1}{2}. \quad (27.6)$$

We will assume (27.6) to hold from here on, and we assume that α is so small that (27.5) holds as well. One might think of (27.6) as reflecting an assumption that interactions are not too strong; g — or, to be more precise, g' — should not be too far from 0. The next event of interest is then the event that A reaches phase 1:

Event 5: A reaches phase 1. (It is reset to phase 0.)

- $t = (\alpha + \delta + 1 - f(\delta + \alpha))T$
- $\varphi_A = 0, \varphi_B = \alpha + f(\delta - \alpha) + 1 - f(\delta + \alpha)$
- upcoming events:
 - A reaches phase 1 within time T
 - B reaches phase 1 within time $(f(\delta + \alpha) - f(\delta - \alpha) - \alpha)T$
 - signal from A to B reaches B within time δT

We have now returned to a situation precisely analogous to that at time $t = 0$ (Event 1). However, φ_B is not $1 - \alpha$, as it was in Event 1, but

$$\begin{aligned} \alpha + f(\delta - \alpha) + 1 - f(\delta + \alpha) &= 1 - \alpha + g(\delta - \alpha) - g(\delta + \alpha) = \\ 1 - \alpha - 2\alpha \frac{g(\delta + \alpha) - g(\delta - \alpha)}{2\alpha} &= 1 - \alpha(1 + 2g'(\delta)) + o(\alpha). \end{aligned}$$

(See exercise 2 for the justification of the last equation.) Recall that we have assumed $g'(\delta) > -1/2$, so $1 + 2g'(\delta) > 0$. For small α , the two oscillators are closer to synchrony after Event 5 than after Event 1 if $1 + 2g'(\delta) < 1$, i.e., $g'(\delta) < 0$. In this

case, synchrony is locally attracting. They are further away from synchrony, again assuming small enough α , if $1 + 2g'(\delta) > 1$, i.e., $g'(\delta) > 0$. In this case, synchrony is locally repelling. We summarize our conclusion in the following proposition:

Proposition 27.1. *Consider the model of Chapter 26, with g differentiable on $[0, 1]$, $g(0) = g(1) = 0$, and $g'(\varphi) > -1/2$ for all $\varphi \in (0, 1)$, modified by the assumption that the effect of one oscillator that reaches phase 1 on the other oscillator occurs with a delay of magnitude δT , where $\delta \in (0, 1)$. Synchrony of the two oscillators is locally attracting if $g'(\delta) < 0$, and locally repelling if $g'(\delta) > 0$.*

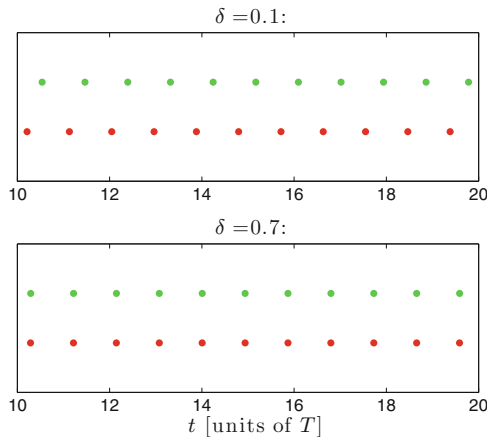


Figure 27.1. Two oscillators, pulse-coupled with delays, with the phase response function $g(\varphi) = \varphi(1 - \varphi)/3$, starting out near synchrony ($\varphi_A = 0$, $\varphi_B = 0.9$). The red and green dots indicate the times when A and B reach phase 1, respectively, and are reset to phase 0. Only the second half of the simulation is shown. Synchrony is repelling when the conduction delay is shorter (upper panel), but attracting when it is longer (lower panel). [[TWO_DELAYED_PULSE_COUPLED_OSC](#)]

A surprising consequence of this proposition is that for phase response functions g satisfying the assumptions of Proposition 27.1 and $g(\varphi) > 0$ for $\varphi \in (0, 1)$, synchrony is repelling when $\delta > 0$, $\delta \approx 0$, but attracting when $\delta < 1$, $\delta \approx 1$. As an example, consider

$$g(\varphi) = \frac{\varphi(1 - \varphi)}{3}.$$

Note that $g'(\varphi) \geq -1/3 > -1/2$ for all $\varphi \in [0, 1]$. Here Proposition 27.1 implies that synchrony is stable if $\delta > 1/2$, unstable if $\delta < 1/2$; Fig. 27.1 illustrates this.

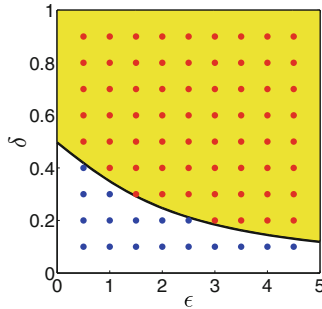


Figure 27.2. Yellow: Points (ϵ, δ) , with $\epsilon = \Delta v / \sqrt{\tau_m I} - 0.25$ and $\delta = \text{conduction delay}/T$, for which synchrony of two pulse-coupled theta neurons is stable, according to inequality (27.8). The dots show results of numerical simulations of two pulse-coupled theta neurons; red and blue dots indicate stable and unstable synchrony, respectively. The figure demonstrates that the conduction delay must be large enough for synchrony to be stable. [TWO_THETA_NEURONS]

27.2 Two Theta Neurons

For two theta neurons interacting via instantaneous charge injections without conduction delays, synchrony is not attracting. In fact, the initial phase difference remains unchanged for all times; see Section 26.4. On the other hand, conduction delays can make synchrony attracting. To analyze under which circumstances synchrony becomes attracting for two theta neurons interacting via instantaneous charge injections with conduction delays, recall eq. (25.13):

$$g(\varphi) = \frac{1}{\pi} \arctan \left(\tan \left(\pi \left(\varphi - \frac{1}{2} \right) \right) + \epsilon \right) + \frac{1}{2} - \varphi, \quad (27.7)$$

with

$$\epsilon = \frac{\Delta v}{\sqrt{\tau_m I - 1/4}}.$$

Synchrony is locally attracting, by Proposition 27.1, if

$$g'(\delta) < 0 \Leftrightarrow \frac{1}{1 + (\tan(\pi(\delta - 1/2)) + \epsilon)^2} \frac{1}{\cos^2(\pi(\delta - 1/2))} - 1 < 0.$$

Before we continue the calculation, we introduce the notation

$$\psi = \pi \left(\delta - \frac{1}{2} \right).$$

Since we assume $\delta \in (0, 1)$, we have $\psi \in (-\pi/2, \pi/2)$. The condition $g'(\delta) < 0$ is then equivalent to

$$\left(1 + (\tan \psi + \epsilon)^2 \right) \cos^2 \psi > 1.$$

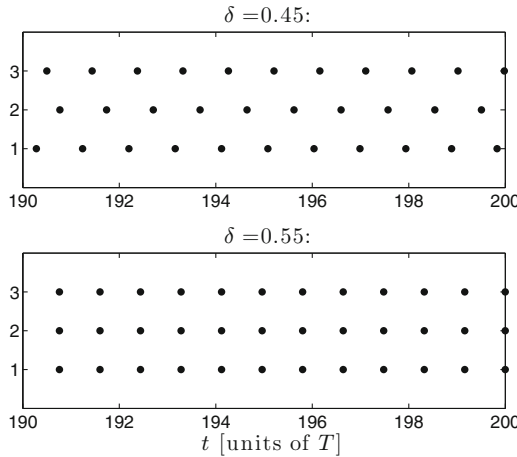


Figure 27.3. Three identical abstract oscillators with initialization near synchrony. The dots indicate the times at which the oscillators reach phase 1, and are reset to phase 0. When an oscillator reaches phase 1, it sends a signal to each of the other two oscillators. This signal travels for time δT . When it arrives, it resets the phase of its target from φ to $f(\varphi) = \varphi + g(\varphi)$, with $g(\varphi) = \varphi(1 - \varphi)/3$. Only the last 10 time units of a longer simulation are shown here.
`[THREE_DELAYED_PULSE_COUPLED_OSC]`

We expand this:

$$\cos^2 \psi + \cos^2 \psi (\tan^2 \psi + 2\epsilon \tan \psi + \epsilon^2) > 1.$$

Using $\tan \psi = \sin \psi / \cos \psi$ and $\cos^2 \psi + \sin^2 \psi = 1$:

$$2\epsilon \sin \psi \cos \psi + \epsilon^2 \cos^2 \psi > 0.$$

Since $\epsilon > 0$ and $\psi \in (-\pi/2, \pi/2)$, $\epsilon \cos^2 \psi$ is not zero, and we can divide by $\epsilon \cos^2 \psi$:

$$2 \tan \psi + \epsilon > 0,$$

or

$$\psi > -\arctan \frac{\epsilon}{2}.$$

Using the definition of ψ , we conclude that synchrony is locally attracting if

$$\delta > \frac{1}{2} - \frac{1}{\pi} \arctan \frac{\epsilon}{2} \tag{27.8}$$

(recall that we always assume $\delta < 1$ here), and locally repelling if

$$\delta < \frac{1}{2} - \frac{1}{\pi} \arctan \frac{\epsilon}{2}.$$

Longer delays stabilize synchrony, shorter ones do not. Regardless of the value of $\epsilon > 0$, synchrony is locally attracting if $\delta \in [1/2, 1)$. Figure 27.2 shows the region in the (ϵ, δ) -plane where synchrony is locally attracting according to (27.8), and also shows numerical results confirming our analysis.

27.3 Larger Networks of Abstract Oscillators

We present two numerical experiments for three oscillators in Figure 27.3. Again shorter delays do not allow synchronization, whereas longer ones do. Heterogeneous conduction delays (that is, conduction delays of different durations for different pairs of oscillators) do perturb synchrony, though, even when the delays are long; see exercise 3.

Exercises

- 27.1. Can you explain in words why *longer* delays may make synchrony locally attracting when *shorter* delays don't?
- 27.2. Assume that g is differentiable. Explain why for any $\delta \in (0, 1)$,

$$\lim_{\alpha \rightarrow 0} \frac{g(\delta + \alpha) - g(\delta - \alpha)}{2\alpha} = g'(\delta).$$

This shows that the left-hand side of eq. (27.5) approximates $g'(\delta)$ for small α .

- 27.3. (*) Modify the code that generates the lower panel of Fig. 27.3 so that the conduction delays between oscillators 1 and 2 are $0.55T$ (in both directions, from 1 to 2 and from 2 to 1), those between oscillators 1 and 3 are $0.6T$, and those between oscillators 2 and 3 are $0.65T$. Thus the conduction delays are now *heterogeneous*. What does the plot look like now?

Chapter 28

Weakly Coupled Oscillators

When coupling is weak, the equations of pulse-coupled oscillators can be simplified, in a way that is mathematically attractive and facilitates analysis, by *averaging* the effects of several discrete pulses over time.²¹ Even though weak coupling is not our focus in this book, we describe two simple examples here.

In Section 28.1 we show that the time evolution of the phase difference between two pulse-coupled identical oscillators is governed by a differential equation when the interactions are weak. Numerical experiments demonstrate that the coupling does not in fact have to be *very* weak for this description to be fairly accurate.

In Section 28.2 we apply similar ideas to the case of two *non-identical* pulse-coupled oscillators, assuming that the intrinsic periods are not equal to each other. We show that the two oscillators phase-lock if the difference in intrinsic periods is below a threshold, which can, for infinitesimally weak coupling, be determined easily using the differential equation governing the phase difference.

28.1 Two Weakly Pulse-Coupled Identical Oscillators

Consider two pulse-coupled oscillators, A and B, as in Chapter 26. We make the assumptions about the phase response function stated in Section 26.1. We assume also that the coupling is weak, that is, that the phase response function is small. To express this, we write $g = \epsilon g_0$, and think of the limit $\epsilon \searrow 0$ with $g_0 = g_0(\varphi)$

Electronic supplementary material: The online version of this chapter (doi: [10.1007/978-3-319-51171-9_28](https://doi.org/10.1007/978-3-319-51171-9_28)) contains supplementary material, which is available to authorized users.

²¹ *Averaging methods* are common in much greater generality in the study of dynamical systems arising in scientific applications [139].

fixed. In the absence of interactions, the phases φ_A and φ_B rise by 1 in time T . We could, of course, describe this by the differential equations

$$\frac{d\varphi_A}{dt} = \frac{1}{T}, \quad \frac{d\varphi_B}{dt} = \frac{1}{T}.$$

Contrary to Chapter 26, we will not assume any more that φ_A and φ_B are reset to 0 when they reach 1. A pulse is emitted by A and received by B when φ_A passes an integer, and of course the same is true with the roles of A and B reversed. We now think of $g = g(\varphi)$ as a function defined for $\varphi \in \mathbb{R}$, not just for φ between 0 and 1, but with $g(\varphi + 1) = g(\varphi)$ for all φ , or equivalently, $g_0(\varphi + 1) = g_0(\varphi)$.

When φ_B passes an integer, then φ_A is raised slightly, by

$$\epsilon g_0(\varphi_A) = \epsilon g_0(\varphi_A - \varphi_B).$$

(The equation holds because φ_B is an integer when the increase in φ_A occurs, and g_0 is periodic with period 1.) This increase in φ_A happens approximately once in time T . Thus the time rate at which φ_A is advanced by B is

$$\frac{\epsilon g_0(\varphi_A - \varphi_B)}{T}.$$

We therefore modify the equation for φ_A as follows:

$$\frac{d\varphi_A}{dt} = \frac{1}{T} + \frac{\epsilon}{T} g_0(\varphi_A - \varphi_B). \quad (28.1)$$

(If you are skeptical, please keep reading until you have read the next paragraph, where your objections may be addressed.) Similarly, of course, we modify the equation for φ_B :

$$\frac{d\varphi_B}{dt} = \frac{1}{T} + \frac{\epsilon}{T} g_0(\varphi_B - \varphi_A). \quad (28.2)$$

You may see inconsistencies in the reasoning of the preceding paragraph. First, if (28.2) is the equation for φ_B , then the frequency with which B sends pulses to A is no longer $1/T$, yet in writing down (28.1), we appear to assume that $1/T$ is the frequency with which A receives inputs from B. This is indeed an inaccuracy, but its effect is of *higher order in ϵ* and therefore negligible. In fact, the actual frequency differs from $1/T$ only by a term on the order of ϵ , and is multiplied by another factor of ϵ in (28.1), so altogether this effect is quadratic in ϵ . Second, after φ_B has passed an integer value once, and therefore φ_A has been increased by $\epsilon g_0(\varphi_A - \varphi_B)$, the phase difference $\varphi_A - \varphi_B$ is no longer what it was before, and yet the argument leading to (28.1) seems to assume that the phase difference remains constant over multiple input pulses. Again the error caused by this inaccuracy is quadratic in ϵ , since the shift in φ_A caused by the signal from B is only of order ϵ .

We define now $\psi = \varphi_B - \varphi_A$. Subtracting eq. (28.1) from (28.2), and using the fact that $g_0(-\psi) = g_0(1 - \psi)$ because g_0 is periodic with period 1, we find

$$\frac{d\psi}{dt} = H(\psi), \quad (28.3)$$

with

$$H(\psi) = \frac{\epsilon}{T} (g_0(\psi) - g_0(1 - \psi)). \quad (28.4)$$

We will test numerically whether this equation in fact describes the time evolution of the phase difference between the two oscillators accurately for weak interactions.

Example 1: $g_0(\varphi) = \varphi^2(1 - \varphi)$. Using Proposition 26.2, one can easily show that synchrony is attracting for any $\epsilon \in (0, 1]$ here. For two different values of ϵ , Fig. 28.1 shows the actual phase difference between the two oscillators as a function of time (black), and the time evolution of ψ obtained from eq. (28.3) (red). For small ϵ , there is close agreement. In fact, ϵ need not be extremely small: Note that in the upper panel of Fig. 28.1, where eq. (28.3) is already a fairly good approximation, the coupling is still so strong that the transition from near-anti-synchrony to near-synchrony occurs in no more than about 10 periods.

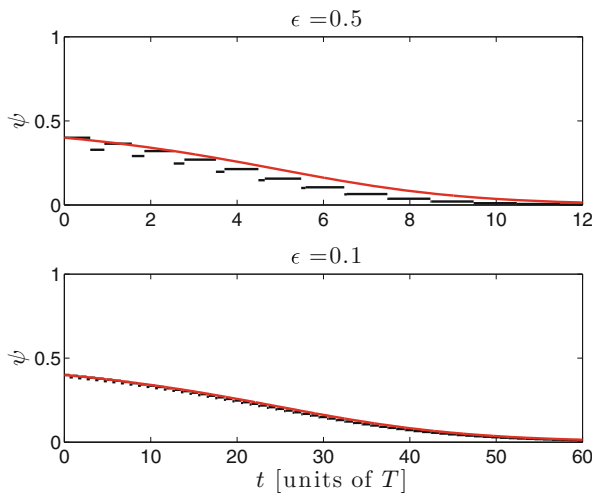


Figure 28.1. The exact phase difference between A and B obtained by simulation of the two oscillators (black), and predictions of the phase difference derived from eq. (28.3) (red), for the phase response function $g(\varphi) = \epsilon\varphi^2(1 - \varphi)$, with two different values of ϵ . Note that the phase difference $\psi = \varphi_B - \varphi_A$ jumps when φ_A or φ_B passes through an integer, and is constant otherwise. This is the reason why the black curve is piecewise constant with jump discontinuities. [WEAKLY_COUPLED_1]

Example 2: $g_0(\varphi) = \varphi(1 - \varphi)^3$. We assume $\epsilon \in (0, 4]$ here to satisfy assumption (26.2). Using Proposition 26.2, one can easily show that synchrony is repelling for all $\epsilon \in (0, 4]$. Anti-synchrony is attracting; for $\epsilon = 2$, this is demonstrated by Fig. 26.2. (For other values of $\epsilon \in (0, 4]$, it can be demonstrated using a modification of the code that generates Fig. 26.2. It can also be proved analytically, but that is not the main point of this example.) Figure 28.2 shows again that eq. (28.3) predicts the time evolution of ψ well, even when ϵ is not extremely small.

The assumptions from Section 26.1, which we adopt here, included $g(0) = g(1) = 0$. Using the notation $g = \epsilon g_0$ that we use here and recalling that $\epsilon > 0$, this means the same as $g_0(0) = g_0(1) = 0$, and it implies $H(0) = 0$. Thus $\psi_* = 0$ is a fixed point of eq. (28.3). We will ask when this fixed point is attracting or repelling, i.e., when eq. (28.3) predicts that synchrony of the two oscillators is attracting or repelling. This is a matter of analyzing the sign of $H'(0)$. First we must ask whether H is even differentiable.

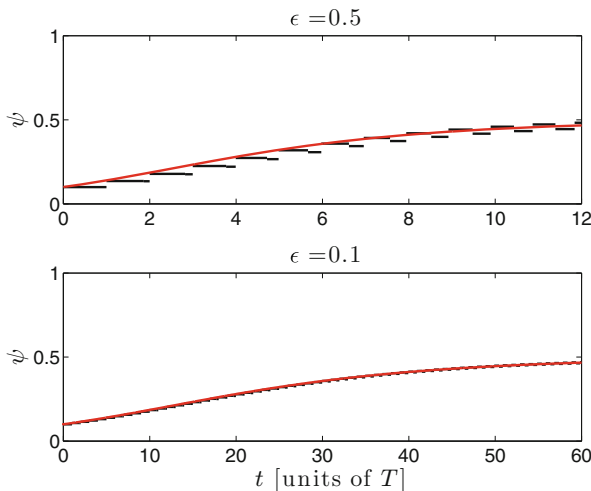


Figure 28.2. Like Fig. 28.1, but with phase response function $\epsilon\varphi(1 - \varphi)^3$. Synchrony is unstable here. [WEAKLY_COUPLED_2]

Because $g_0(0) = g_0(1) = 0$, the extension of g_0 to the whole real axis with period 1 is continuous. In Section 26.1, we also assumed that g was continuously differentiable on the interval $[0, 1]$, and here that means the same as to say that g_0 is continuously differentiable on $[0, 1]$. Therefore the extension of g_0 to the entire real axis is continuously differentiable everywhere, except possibly at integer values of φ . The “ $g'(0)$ ” of Section 26.1 is the right-sided derivative of the extension at 0; we will still denote it by $g'(0)$, though. Similarly, $g'_0(0)$ denotes the right-side derivative of g_0 at 0, and $g'_0(1)$ the left-sided derivative of g_0 at 1, or, equivalently, the left-sided derivative of the extension of g_0 at 0. We did not assume in Section 26.1 that $g'(0) = g'(1)$, and don’t assume $g'_0(0) = g'_0(1)$ here. In fact, in Examples 1 and 2 above, $g'_0(0) \neq g'_0(1)$. Therefore the periodic extension of g_0 is not in general differentiable at integer values of φ .

Because the periodic extension of g_0 is continuous with period 1, so is H . We will now show that even though (the extension of) g_0 need not be differentiable at integer arguments φ , it is always true that $H = H(\psi)$ is differentiable at integer arguments ψ . We note first that the right-sided derivative of H at $\psi = 0$ exists, because the one-sided derivatives of g_0 at 0 and at 1 exist. Further, H is an odd function (exercise 1). For an odd function, if the right-sided derivative at 0 exists,

so does the left-sided derivative, and it is equal to the right-sided derivative; see exercise 2. We conclude that $H'(0)$ exists, and from (28.4),

$$H'(0) = \frac{\epsilon}{T}(g'_0(0) + g'_0(1)).$$

Therefore $\psi_* = 0$ is a stable fixed point of eq. (28.3) if

$$g'_0(0) + g'_0(1) < 0, \quad (28.5)$$

and an unstable fixed point if $g'_0(0) + g'_0(1) > 0$. The value of ϵ plays no role.

In Section 26.1, we found a different condition for synchrony to be attracting, namely inequality (26.10). Replacing g by ϵg_0 in that condition, it becomes

$$(1 + \epsilon g'_0(0))(1 + \epsilon g'_0(1)) < 1,$$

or after a small amount of algebra,

$$g'_0(0) + g'_0(1) < -\epsilon g'_0(0)g'_0(1). \quad (28.6)$$

As $\epsilon \rightarrow 0$, (28.6) becomes (28.5); thus eq. (28.3) correctly answers the question whether synchrony is attracting or repelling in the limit as $\epsilon \rightarrow 0$.

28.2 Two Weakly Pulse-Coupled Non-identical Oscillators

Suppose now that the two oscillators have two somewhat different intrinsic periods. We did not discuss this case in Chapter 26, but will include it here as another example of interesting things that can be done using the assumption of weak coupling and the method of averaging. We call the two periods T_A and T_B . If T_A and T_B are very different from each other, then weak coupling cannot result in phase-locking. We will assume that

$$T_B = (1 + c\epsilon)T_A, \quad (28.7)$$

where $c > 0$ is fixed. Of course, the assumption that T_B is greater than T_A is no restriction of generality — we can reverse the roles of A and B if that is not the case. Even though $\epsilon > 0$ is already assumed to be small, we will find that c also has to be small for phase-locking. We assume that the phase response function, ϵg_0 , is still the same in both directions, from A to B and from B to A. Equations (28.1) and (28.2) now become

$$\frac{d\varphi_A}{dt} = \frac{1}{T_A} + \frac{\epsilon}{T_B}g_0(\varphi_A - \varphi_B) \quad (28.8)$$

and

$$\frac{d\varphi_B}{dt} = \frac{1}{T_B} + \frac{\epsilon}{T_A}g_0(\varphi_B - \varphi_A). \quad (28.9)$$

Again you may see an inconsistency: The phase difference $\varphi_A - \varphi_B$ has another reason to drift now, since $1/T_A$ is not the same as $1/T_B$. Why is this not reflected

in eqs. (28.8) and (28.9)? The answer is similar to the answers to similar objections in Section 28.1: In a fixed amount of time, the drift in the phase difference is of order ϵ , and will therefore only cause a correction proportional to ϵ^2 in eqs. (28.8) and (28.9). We neglect quantities that are quadratic in ϵ .

Subtracting (28.8) from (28.9), and using the fact that g is periodic with period 1, we get the following equation for the phase difference $\psi = \varphi_B - \varphi_A$:

$$\frac{d\psi}{dt} = \frac{1}{T_B} - \frac{1}{T_A} + \frac{\epsilon}{T_A} g_0(\psi) - \frac{\epsilon}{T_B} g_0(1 - \psi).$$

We use eq. (28.7) now, and drop terms that are of higher order in ϵ (exercise 3):

$$\frac{d\psi}{dt} = H(\psi), \quad (28.10)$$

with

$$H(\psi) = \frac{\epsilon}{T_A} (-c + g_0(\psi) - g_0(1 - \psi)). \quad (28.11)$$

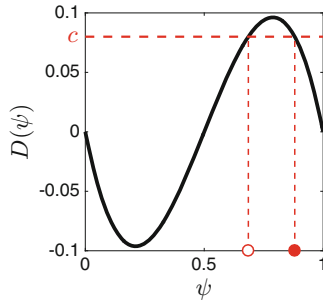


Figure 28.3. Graph of the function D defined by eq. (28.14), together with the two fixed points of eq. (28.10) for $c = 0.08$. The stable fixed point is indicated by a solid circle, and the unstable one by an open circle. [PLOT_D_TWO_FIXED_POINTS]

Fixed points of eq. (28.10) are phase differences at which the two oscillators can lock. However, eq. (28.10) need not have any fixed point at all. The equation has a fixed point if and only if there is a solution of $H(\psi) = 0$, that is, if and only if there is a solution of

$$D(\psi) = c, \quad (28.12)$$

where

$$D(\psi) = g_0(\psi) - g_0(1 - \psi). \quad (28.13)$$

For $g_0(\varphi) = \varphi^2(1 - \varphi)$, the example of Fig. 26.1,

$$D(\psi) = 2\psi(1 - \psi) \left(\psi - \frac{1}{2} \right). \quad (28.14)$$

The black curve in Fig. 28.3 shows the graph of D . The maximal value of D is $\sqrt{3}/18 \approx 0.096$ (exercise 5). So for $0 \leq c \leq \sqrt{3}/18$, eq. (28.10) has a fixed point,

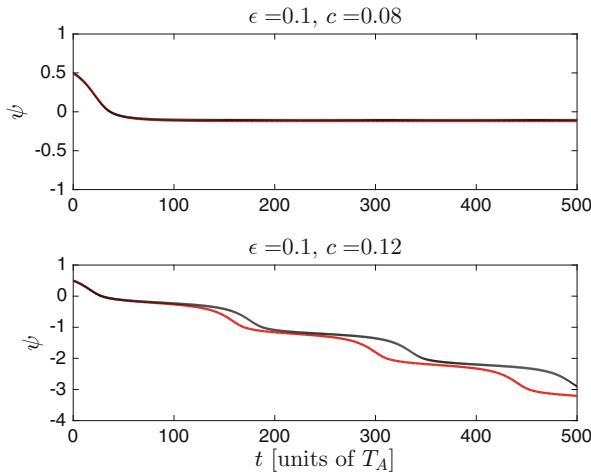


Figure 28.4. Two oscillators, one with intrinsic period $T_A = 1$ and the other with intrinsic period $T_B = (1 + c\epsilon)T_A$, pulse-coupled with phase response function $\epsilon g_0(\varphi) = \epsilon\varphi^2(1 - \varphi)$. Top panel: $c = 0.08 < \sqrt{3}/18$ yields phase-locking for small ϵ : The black curve shows the real value of $\psi = \varphi_B - \varphi_A$ as a function of time, computed by simulating the two oscillators. Equation (28.10) predicts this outcome; the solution ψ of (28.10) was plotted in red, but is entirely covered by the black curve in the upper panel. Bottom panel: $c = 0.12 > \sqrt{3}/18$ yields phase walkthrough for small ϵ (black). Again eq. (28.10) predicts this outcome (red), although the prediction becomes quantitatively inaccurate after some time.

[WEAKLY_COUPLED_HETEROGENEOUS_1]

whereas for $c > \sqrt{3}/18$ it does not. Furthermore, for $0 \leq c < \sqrt{3}/18$, there are two fixed points of eq. (28.10), a stable one and an unstable one, as illustrated in Fig. 28.3.

We simulate the two oscillators for $c = 0.08 < \sqrt{3}/18$ and for $c = 0.12 > \sqrt{3}/18$, and compare with the predictions derived from the differential equation (28.10). The results are shown in Fig. 28.4, and confirm that (28.10) correctly predicts the behavior for small ϵ .

Exercises

- 28.1. Explain why the function H defined by eq. (28.4) is odd.
- 28.2. Show: For any odd function $H = H(\psi)$, if the right-sided derivative of H at 0 exists, then the left-sided derivative of H at 0 exists as well, and is equal to the right-sided derivative.
- 28.3. Explain how (28.10), (28.11) come about.
- 28.4. Derive eq. (28.14).

- 28.5. Show that the maximal value of the function D defined by eq. (28.14) is $\sqrt{3}/18$.
- 28.6. Think about two identical oscillators A and B, with intrinsic period T. Assume that the phase response function is $\epsilon\varphi(1 - \varphi)$ with $0 < \epsilon < 1$. (a) What is the right-hand side $H(\psi)$ of eq. (28.3) in this case? Is the fixed point $\psi_* = 0$ attracting? (b) Using the analysis of Chapter 26, determine whether or not synchrony is attracting here.
- 28.7. Think about two oscillators, A and B, with intrinsic periods $T_A > 0$ and $T_B = (1+c\epsilon)T_A$, where $c > 0$, and $\epsilon > 0$ is small. Assume that the two oscillators are pulse-coupled with phase response function $\epsilon g_0(\varphi)$, where $g_0(\varphi) = \varphi(1 - \varphi)^3$. (a) Use eq. (28.10) to analyze for which values of c there will be stable phase-locking. (b) (*) Check your answer numerically, using a modification of the code that generates Fig. 28.4.
- 28.8. Think about two oscillators A and B with intrinsic periods T_A and $T_B = (1+c\epsilon)T_A$, with $c > 0$ and $\epsilon > 0$. Assume that the phase response function is $\epsilon\varphi(1 - \varphi)$ with $0 < \epsilon < 1$. (a) Explain why eq. (28.10) now predicts that there is no phase-locking for any $c > 0$. (b) (*) Check the conclusion from part (a) by generating a plot like those in Fig. 28.4 with $c = 0.005$ and $\epsilon = 0.02$, computing up to time 50,000. This will take some computing time, but it isn't prohibitive.
- 28.9. (a) Figure 28.3 shows that D is an odd function with respect to $\psi = 1/2$. That is,

$$D\left(\frac{1}{2} - s\right) = -D\left(\frac{1}{2} + s\right) \quad (28.15)$$

for all s . Show that this is the case for all g_0 , not just for the specific g_0 used in Fig. 28.3. (b) Assume that $g_0(\varphi) \not\equiv g_0(1 - \varphi)$. Show that there is a value $M > 0$ so that eq. (28.10) (with H defined by eq. (28.11)) has a fixed point if $c \in [0, M]$, but not if $c > M$. (c) Again assume that $g_0(\varphi) \not\equiv g_0(1 - \varphi)$. Assume, as we did throughout this section, that $g_0 = g_0(\varphi)$ is defined and continuous for all $\varphi \in \mathbb{R}$, with $g_0(\varphi) + 1 \equiv g_0(\varphi)$. Let $c \in (0, M)$, with M defined as in part (b). Show that eq. (28.10) has a *stable* fixed point.

Chapter 29

Approximate Synchronization by a Single Inhibitory Pulse

A simple way of synchronizing a population of neurons is to subject all neurons to the same inhibitory synaptic input pulse. This mechanism is thought to be fundamental to the origins of synchronized rhythmic activity in the brain in many cases. We will study examples in later chapters. Here we think about the (approximate) synchronization of a population of neurons by a single inhibitory pulse.

29.1 Simulations for Normalized LIF Neurons

We begin with a population of N normalized LIF neurons. Each of the neurons is assumed to be governed by eqs. (7.6) and (7.7):

$$\begin{aligned}\frac{dv_i}{dt} &= -\frac{v_i}{\tau_m} + I, \\ v_i(t+0) &= 0 \quad \text{if } v_i(t-0) = 1,\end{aligned}\tag{29.1}$$

with $\tau_m > 0$ and $I > 1/\tau_m$, where v_i denotes the membrane potential of the i -th LIF neuron, for $1 \leq i \leq N$. In Chapter 7, we showed (see eq. (7.9)) that each of the LIF neurons will then, as long as I is the only input, fire periodically with period

$$T = \tau_m \ln \frac{\tau_m I}{\tau_m I - 1}.\tag{29.2}$$

We choose $v_i(0)$ in such a way that the i -th LIF neuron would, if I were the only input, fire at time iT/N , for $1 \leq i \leq N$:

$$v_i(0) = \left(1 - e^{-(N-i)T/(N\tau_m)}\right) \tau_m I.\tag{29.3}$$

Electronic supplementary material: The online version of this chapter (doi: [10.1007/978-3-319-51171-9_29](https://doi.org/10.1007/978-3-319-51171-9_29)) contains supplementary material, which is available to authorized users.

(See exercise 1.) Thus we initialize the neurons in a *splay state*. At time 0, we give the neurons an inhibitory pulse, modeled by adding the term

$$-\bar{g}_{\text{syn}} e^{-t/\tau_I} v_i \quad (29.4)$$

to the right-hand side of eq. (29.1), where $\bar{g}_{\text{syn}} > 0$ is the maximal “conductance” of the inhibitory term (because we non-dimensionalize most variables, but not time, \bar{g}_{syn} is actually a reciprocal time in this model), and $\tau_I > 0$ is the decay time constant. The added term (29.4) is inhibitory because it drives v_i towards 0. Thus the differential equation for v_i is now

$$\frac{dv_i}{dt} = -\frac{v_i}{\tau_m} + I - \bar{g}_{\text{syn}} e^{-t/\tau_I} v_i.$$

Figure 29.1 shows results of simulations with $N = 10$, and $\bar{g}_{\text{syn}} = 0$ (no inhibitory pulse, top panel), a “weak and long” inhibitory pulse (middle panel), and “strong and brief” inhibitory pulse (bottom panel). The definitions of “weak and long” and “strong and brief” are of course a bit subjective here; see discussion below. Dotted vertical lines in Fig. 29.1 indicate times at which a membrane potential reaches the threshold value 1, resulting in a reset to zero. The simulation of the i -th neuron is halted as soon as v_i is reset.

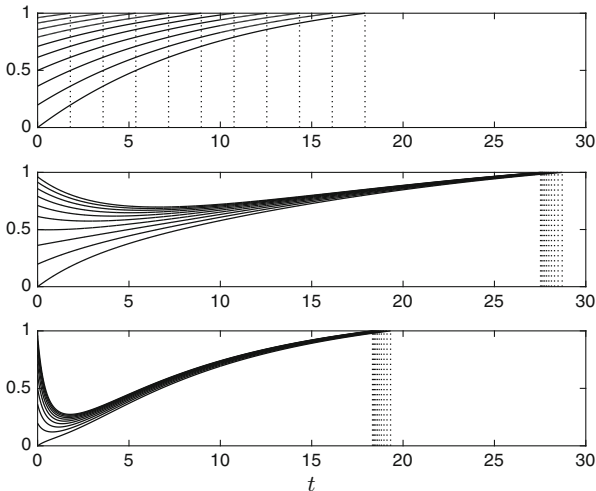


Figure 29.1. A population of ten normalized LIF neurons with $\tau_m = 10$ and $I = 0.12$, initialized in splay state (see upper panel, where there is no inhibitory pulse), subject to a weak long-lasting inhibitory pulse ($\bar{g}_{\text{syn}} = 0.15$, $\tau_I = 9$ middle panel), or to a strong brief one ($\bar{g}_{\text{syn}} = 2$, $\tau_I = 1$, bottom panel).

[LIF_WITH_INHIBITORY_PULSE]

We always (even in the normalized LIF model) think of time as measured in ms. The parameter choices $\tau_I = 9$ and $\tau_I = 1$ are motivated by the fact that for

GABA_A receptor-mediated synapses, decay time constants on the order of 9 ms [69, 137], but also much shorter decay time constants [6, 97] have been reported. Given τ_I , we chose values of \bar{g}_{syn} for Fig. 29.1 that result in fairly tight synchronization. Smaller τ_I require larger \bar{g}_{syn} for the same degree of synchronization.

The inhibitory pulse that begins at time 0 causes a time of silence, i.e., a time during which none of the v_i reaches the threshold value 1. When firing resumes, it is nearly synchronous. Figure 29.1 demonstrates that both longer-lasting, weaker inhibitory input pulses, and briefer, stronger ones can have the synchronizing effect. There is, however, a striking difference: When the input pulse is brief but strong, as in the bottom panel of the figure, synchronization occurs rapidly, and the time that it takes for the population to resume firing, now in near-synchrony, is only slightly greater than T . When the input pulse is weaker but longer-lasting, synchronization develops more gradually, and firing resumes at a time significantly greater than T .

As simple as this model of synchronization by inhibition may seem, it is not easy to understand completely. There are four parameters: τ_m , I , \bar{g}_{syn} , and τ_I . They have biological meaning: They measure the leakiness and drive of the neurons, and the strength and duration of the inhibitory input pulse, respectively. The two quantities of greatest interest are the time at which firing resumes, following the arrival of the inhibitory pulse at time 0, and the degree of synchrony created by the inhibitory pulse. More precise definitions are needed here: We must say what we mean by “time at which firing resumes,” since firing does not resume in perfect synchrony, and we must say what we mean by “degree of synchrony.”

For this purpose, we let v_0 be the solution of

$$\frac{dv}{dt} = -\frac{v}{\tau_m} + I - \bar{g}_{\text{syn}}e^{-t/\tau_I}v, \quad v(0) = 0,$$

and v_1 the solution of

$$\frac{dv}{dt} = -\frac{v}{\tau_m} + I - \bar{g}_{\text{syn}}e^{-t/\tau_I}v, \quad v(0) = 1,$$

It is not possible to write v_0 and v_1 explicitly as functions of the parameters; see exercise 2. We let P_0 be the time at which v_0 reaches the threshold value 1, and P_1 the *positive* time at which v_1 reaches 1, with $P_1 = 0$ if $dv_1/dt(0) \geq 0$. See Fig. 29.2 for an illustration. For any $v_* \in (0, 1)$, the solution of

$$\frac{dv}{dt} = -\frac{v}{\tau_m} + I - \bar{g}_{\text{syn}}e^{-t/\tau_I}v, \quad v(0) = v_*,$$

lies between v_0 and v_1 .

We define

$$P = \frac{P_0 + P_1}{2}, \quad S = \frac{P_0 - P_1}{P}. \quad (29.5)$$

We refer to P as the *time at which firing resumes*, and S as the *relative duration of the spike volley* following the inhibitory input pulse (*relative* because we measure it in units of P). Both P and S are functions of the four parameters τ_m , I , \bar{g}_{syn} , τ_I , with $\tau_m > 0$, $I > 1/\tau_m$, $\bar{g}_{\text{syn}} > 0$, and $\tau_I > 0$.

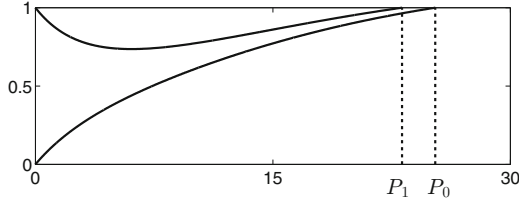


Figure 29.2. Illustration of definitions of P_0 and P_1 . (The parameters used here are $\tau_m = 10$, $I = 0.12$, $\bar{g}_{\text{syn}} = 0.15$, $\tau_I = 7$.) [ILLUSTRATE_P0_AND_P1]

In this section, we will not use $I > 1/\tau_m$ but $J = I - 1/\tau_m > 0$, the *drive above firing threshold*, as the parameter measuring the strength of the external drive. Either I or J could be used, of course. The choice makes a difference when studying the sensitivity of the dependence of T , P , and S on external drive; this point will be explained in the last paragraph of this section.

To fully understand the synchronization of a population of normalized LIF neurons by an inhibitory pulse would mean to fully understand how P and S depend on the four parameters τ_m , J , \bar{g}_{syn} , and τ_I . I have no clear-cut and complete description of this dependence, but will give a few relevant numerical results. In Fig. 29.3, we perturb the parameters around $\tau_m = 10$, $J = 0.02$, $\bar{g}_{\text{syn}} = 0.15$, and $\tau_I = 9$. These are the parameters of the middle panel of Fig. 29.1 — synchronization by a long, weak inhibitory pulse. We vary τ_I (left two panels of Fig. 29.3), \bar{g}_{syn} (middle two panels), or J (right two panels), and find that P depends significantly on all three of these parameters.

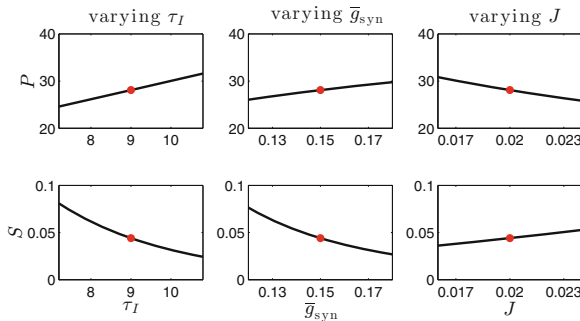


Figure 29.3. P and S , as defined in (29.5), as functions of τ_I , \bar{g}_{syn} , and $J = I - 1/\tau_m$. Parameters are perturbed around the baseline point $\tau_m = 10$, $J = 0.02$, $\bar{g}_{\text{syn}} = 0.15$, $\tau_I = 9$ (indicated as a red dot in each figure), varying one of the three parameters τ_I , \bar{g}_{syn} , and J while holding the others fixed. [LIF_P_AND_S]

We also quantify the sensitivity of P to parameter perturbations in a different way. Using again $\tau_m = 10$, and starting with the baseline values $J = 0.02$, $\bar{g}_{\text{syn}} = 0.15$, and $\tau_I = 9$, we lower J by 1%, or raise τ_I or \bar{g}_{syn} by 1%, computing in each case

the resulting percentage increase in P . The results are displayed in the upper row of Table 29.1. We see that P is a bit more sensitive to changes in τ_I than to changes in \bar{g}_{syn} and J , but it has some (moderate) dependence on all three parameters. In the lower row of Table 29.1, we show similar results, now perturbing from the reference values $J = 0.02$, $\bar{g}_{\text{syn}} = 2$, and $\tau_I = 1$, corresponding to the bottom row of Fig. 29.1 — a strong, brief inhibitory pulse. Here P is much less dependent on τ_I and \bar{g}_{syn} , but still as strongly dependent on J as before. The reduced dependence on τ_I and \bar{g}_{syn} is not surprising: When τ_I is much shorter than T , then during most of the time that it takes the membrane potential to reach the threshold value 1, inhibition is small, regardless of what the precise values of \bar{g}_{syn} and τ_I are, and P is in any case not much greater than T .

	$J \rightarrow 0.99J$	$\bar{g}_{\text{syn}} \rightarrow 1.01\bar{g}_{\text{syn}}$	$\tau_I \rightarrow 1.01\tau_I$
increase in P (weak, long-lasting pulse):	0.44%	0.33%	0.62%
increase in P (strong, brief pulse):	0.44%	0.11%	0.19%

Table 29.1. Parameter sensitivity of $P =$ delay between the arrival of an inhibitory pulse acting on a population of ten LIF neurons in splay state, and the approximately synchronous resumption of firing. (See text for precise definition of P .) Here $\tau_m = 10$, and the baseline parameter values are $\tau_I = 9$, $\bar{g}_{\text{syn}} = 0.15$, $J = I - 1/\tau_m = 0.02$ (upper row) and $\tau_I = 1$, $\bar{g}_{\text{syn}} = 2$, $J = 0.02$ (lower row). [LIF_CONDITION_NUMBERS]

The entries in the first column of Table 29.1 would become larger if we replaced I by $0.99I$, rather than J by $0.99J$. This follows from the fact that

$$J = I - \frac{1}{\tau_m} < I.$$

A once percent reduction in I is a smaller percentage reduction in J . In fact, with our standard value $\tau_m = 10$, the firing frequency becomes unrealistically high unless

$$J \ll I.$$

To see this, suppose that J were even as large as $I/2$. Then eq. (29.2) would imply

$$T = \tau_m \ln \frac{\tau_m I}{\tau_m I - 1} = \tau_m \ln \frac{I}{J} = \tau_m \ln 2.$$

With $\tau_m = 10$, this would translate into the very high frequency of about 144Hz already. Larger values of J translate into even greater frequencies. As a consequence, in fact the entries in the first column of Table 29.1 would be *much* larger if they were based on reducing I , not J , by 1%.

29.2 Simulations for RTM Neurons

Synchronization by inhibitory pulses works in much the same way for RTM neurons as for LIF neurons; see Fig. 29.4. We add the term

$$\bar{g}_{\text{syn}} e^{-t/\tau_I} (-75 - v_i)$$

to the right-hand side of the equation for the i -th RTM neuron in the population, where v_i denotes the membrane potential of the i -th neuron. Again the synchronizing inhibitory pulse can be long and weak, or short and strong. Again, the time P that it takes for the population to recover from the inhibition, and resume firing in near-synchrony, is much greater when the pulse is long and weak than when it is brief and strong.

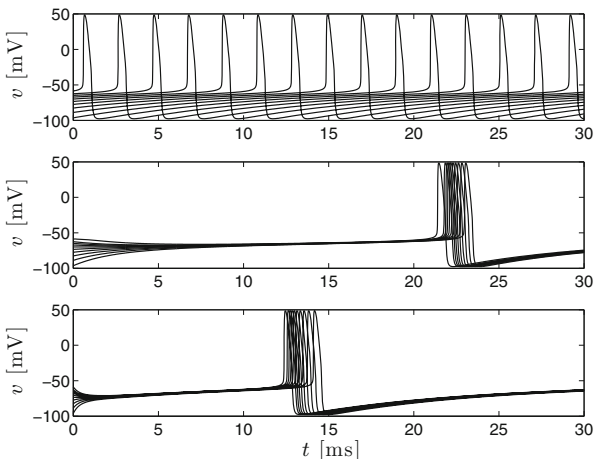


Figure 29.4. A population of ten RTM neurons with $I = 1.2$, initialized in splay state (upper panel, where there is no inhibitory pulse), subject to a weak long-lasting inhibitory pulse ($\bar{g}_{\text{syn}} = 0.3 \text{ mS/cm}^2$, $\tau_I = 9 \text{ ms}$, middle panel), or to a strong brief one ($\bar{g}_{\text{syn}} = 2.25 \text{ mS/cm}^2$, $\tau_I = 1 \text{ ms}$, bottom panel). In both the middle and bottom panels, the reversal potential of inhibition is taken to be -75 mV . [\[RTM_WITH_INHIBITORY_PULSE\]](#)

As before, we denote by P the time between the arrival of the inhibitory pulse and the resumption of firing in approximate synchrony. Precisely, P is taken to be the average first spike time of the ten RTM neurons, where for each neuron its “spike time” is, as earlier, taken to be the time at which the membrane potential crosses -20 mV from above.

The intrinsic period of the RTM neurons in Fig. 29.4, which have external drive $I = 1.2$, is $T \approx 20.4 \text{ ms}$. In the middle panel of Fig. 29.4, P is slightly greater than T , but in the bottom panel, it is significantly smaller than P . This seems surprising: Why should an *inhibitory* pulse make some cells fire *sooner* than they would have fired otherwise? The answer is that the reversal potential of the inhibitory pulse, which is taken to be -75 mV in Fig. 29.4, lies significantly above

the membrane potential to which an RTM neuron resets after firing. Those cells that are initialized near the reset potential are therefore initially *accelerated* by the inhibitory pulse.

The sensitivity of P to small parameter changes is explored in Table 29.2, which is fairly similar to the analogous table for LIF neurons, Table 29.1. Note that P depends on none of the three parameters very sensitively (a 1% perturbation in one of the parameters results in a perturbation smaller than 1% in P). It is most sensitive to perturbations in I , and least sensitive to perturbations in \bar{g}_{syn} .

	$I \rightarrow 0.99I$	$\bar{g}_{\text{syn}} \rightarrow 1.01\bar{g}_{\text{syn}}$	$\tau_I \rightarrow 1.01\tau_I$
increase in P (weak, long-lasting pulse):	0.75%	0.39%	0.57%
increase in P (strong, brief pulse):	0.72%	0.08%	0.20%

Table 29.2. Analogous to Table 29.1, but for ten RTM neurons (see text for the precise definition of P in the present context), with synaptic reversal potential -75 mV, and baseline parameter values $I = 1.2$, $\bar{g}_{\text{syn}} = 0.3$, $\tau_I = 9$, (upper row) and $I = 1.2$, $\bar{g}_{\text{syn}} = 2.25$, $\tau_I = 1$, (lower row). [RTM_CONDITION_NUMBERS]

29.3 The River Picture for Theta Neurons

Synchronization by long and weak inhibitory pulses can be understood more clearly using a picture suggested in [12]. We think about a population of N theta neurons, with the i -th theta neuron governed by

$$\frac{d\theta_i}{dt} = -\frac{\cos \theta_i}{\tau_m} + 2I(1 + \cos \theta_i),$$

$1 \leq i \leq N$. We assume that at time 0, an inhibitory synaptic pulse affects all N of the theta neurons equally, and ask whether and why this will synchronize the next spike of the theta neurons.

First, we must think about how to model synaptic input into a theta neuron. We drop the subscript i to simplify our notation:

$$\frac{d\theta}{dt} = -\frac{\cos \theta}{\tau_m} + 2I(1 + \cos \theta), \quad (29.6)$$

Recall from Chapter 8 that this equation is equivalent to the equation of a normalized QIF neuron,

$$\frac{dv}{dt} = -\frac{v(1-v)}{\tau_m} + I, \quad (29.7)$$

with the relation between θ and the membrane potential v given by

$$v = \frac{1}{2} + \frac{1}{2} \tan \frac{\theta}{2}. \quad (29.8)$$

We now add a synaptic input term to (29.7):

$$\frac{dv}{dt} = -\frac{v(1-v)}{\tau_m} + I + g_{\text{syn}}(t)(v_{\text{rev}} - v), \quad (29.9)$$

and write this equation in terms of θ again:

$$\frac{1}{4} \sec^2 \frac{\theta}{2} \frac{d\theta}{dt} = -\frac{1}{4\tau_m} \left(1 - \tan^2 \frac{\theta}{2} \right) + I + g_{\text{syn}}(t) \left(v_{\text{rev}} - \frac{1}{2} - \frac{1}{2} \tan \frac{\theta}{2} \right).$$

We multiply both sides by $4 \cos^2(\theta/2)$ to get an equation for $d\theta/dt$:

$$\begin{aligned} \frac{d\theta}{dt} &= -\frac{1}{\tau_m} \left(\cos^2 \frac{\theta}{2} - \sin^2 \frac{\theta}{2} \right) + 4I \cos^2 \frac{\theta}{2} + \\ &\quad 2g_{\text{syn}}(t) \left(2v_{\text{rev}} \cos^2 \frac{\theta}{2} - \cos^2 \frac{\theta}{2} - \sin \frac{\theta}{2} \cos \frac{\theta}{2} \right) = \\ &\quad -\frac{\cos \theta}{\tau_m} + 2I(1 + \cos \theta) + 2g_{\text{syn}}(t) \left(v_{\text{rev}} - \frac{1}{2} \right) (1 + \cos \theta) - g_{\text{syn}}(t) \sin \theta. \end{aligned}$$

(We used trigonometric addition formulas in the last step.) In summary,

$$\frac{d\theta}{dt} = -\frac{\cos \theta}{\tau_m} + 2 \left(I + g_{\text{syn}}(t) \left(v_{\text{rev}} - \frac{1}{2} \right) \right) (1 + \cos \theta) - g_{\text{syn}}(t) \sin \theta. \quad (29.10)$$

Equation (29.10) describes how synaptic input to a theta neuron should be modeled.

We now consider a theta neuron subject to an inhibitory pulse with

$$g_{\text{syn}}(t) = \bar{g}_{\text{syn}} e^{-t/\tau_I},$$

or equivalently

$$\frac{dg_{\text{syn}}}{dt} = -\frac{g_{\text{syn}}}{\tau_I} \quad (29.11)$$

and $g_{\text{syn}}(0) = \bar{g}_{\text{syn}}$. We think of (29.10) and (29.11) as a system of two differential equations in the two unknowns θ and g_{syn} . With $v_{\text{rev}} = 0$, this system reads as follows:

$$\frac{d\theta}{dt} = -\frac{\cos \theta}{\tau_m} + (2I - g_{\text{syn}})(1 + \cos \theta) - g_{\text{syn}} \sin \theta, \quad (29.12)$$

$$\frac{dg_{\text{syn}}}{dt} = -\frac{g_{\text{syn}}}{\tau_I}. \quad (29.13)$$

Notice that $g_{\text{syn}}(0) = \bar{g}_{\text{syn}}$.

Figure 29.5 shows solutions of eqs. (29.12), (29.13) in the (θ, g_{syn}) -plane. The picture should be thought of as 2π -periodic: When a solution exits through the right edge, i.e., reaches $\theta = \pi$, it re-enters through the left edge, with the same value of g_{syn} with which it exited. Recall that reaching $\theta = \pi$ means firing for a theta neuron; this is why the exit of a solution through the right edge of the rectangle shown in Fig. 29.5 is of special interest.

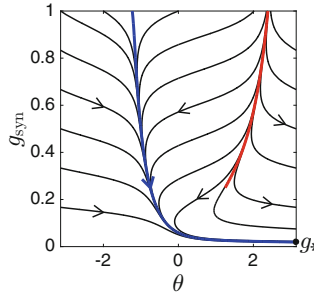


Figure 29.5. Solutions of eqs. (29.12) and (29.13), with $\tau_m = 1$, $I = 0.3$, $\tau_I = 9$. Notice that g_{syn} is a dependent variable here, not a parameter, and the parameter \bar{g}_{syn} does not appear in eqs. (29.12) and (29.13). Instead, \bar{g}_{syn} should be thought of as the value of g_{syn} at time zero. The rectangle shown is $[-\pi, \pi] \times [0, 1]$. The blue trajectory, the “stable river” (see text), exits the rectangle at $\theta = \pi$, $g_{\text{syn}} = g_*$. [RIVER]

There is a special solution, indicated in blue in the figure, with the property that most solutions come very close to it before exiting through the right edge. This solution is *exponentially attracting* (the convergence of other solutions to it is exponentially fast). Such solutions are common in systems of ODEs. They are called *rivers*, and have been the subject of extensive study [37, 38]. We also indicate another special curve in Fig. 29.5, in red. Solutions approach it in *backward time*, that is, when the arrows indicating the direction of motion are reversed. We won’t give it a precise definition, but nonetheless we will give it a name: We call it the *unstable river*, and for clarity we also call the river the *stable river*.²²

We denote the point at which the stable river reaches $\theta = \pi$ and therefore exits the rectangle by (π, g_*) , with $g_* > 0$. Consider now a solution $(\theta(t), g_{\text{syn}}(t))$ that starts, at time 0, at $(\theta_0, \bar{g}_{\text{syn}})$. If it comes very close to the stable river before reaching $\theta = \pi$, then it exits the rectangle, to very close approximation, at (π, g_*) . This means that the time, P , at which it exits the rectangle satisfies $e^{-P/\tau_I} \bar{g}_{\text{syn}} = g_*$, or

$$P = \tau_I \ln \frac{\bar{g}_{\text{syn}}}{g_*}, \quad (29.14)$$

and is, in particular, independent of θ_0 . The neurons of a population, initialized with different values of θ_0 , will all reach π at nearly the same time, namely the time P given by (29.14). Thus the population will synchronize.

Trajectories that start out to the right of the unstable river exit through the right edge, re-enter through the left edge, then approach the stable river, and exit near (π, g_*) again, that is, reach $\theta = \pi$ at approximately the time P given by eq. (29.14). This means that a theta neuron that is close to firing at time 0, the

²²The stable river is a well-defined trajectory of the system (29.12),(29.13): It is the only solution of (29.12), (29.13) with $\theta(t) \in (-\pi, \pi)$ for all t , $\theta(t) \rightarrow -\pi/2$ as $t \rightarrow -\infty$. By contrast, the “unstable river” is not a well-defined trajectory here.

onset time of the inhibitory pulse, will fire once soon after onset of the inhibitory pulse, but then again at approximately time P .

There is an interesting conclusion from formula (29.14). Note that g_* is independent of \bar{g}_{syn} . In fact, the whole picture in Fig. 29.5 does not depend on one particular \bar{g}_{syn} ; instead, \bar{g}_{syn} should be thought of as the value of g_{syn} at time zero. Therefore (29.14) implies

$$P = \tau_I \ln \bar{g}_{\text{syn}} + C, \quad (29.15)$$

with C independent of \bar{g}_{syn} (but dependent, of course, on τ_I , τ_m , and I). Thus the dependence of P on \bar{g}_{syn} is logarithmic. Since we don't non-dimensionalize time, not even for the theta neuron, we must strictly speaking think of \bar{g}_{syn} as a reciprocal time. Consequently, there is a dimensional problem with (29.15): The logarithm of a quantity that is physically a reciprocal time is taken. However, this could easily be fixed by multiplying the argument of \ln in (29.15) by a reference time not dependent on \bar{g}_{syn} — for instance, τ_m .

One might be tempted to conclude from eq. (29.14) that P is proportional to τ_I . However, this is not the case, since g_* depends on τ_I ; see exercise 7.

Exercises

- 29.1. Explain why eq. (29.3) describes initialization in *splay state*.
- 29.2. Explain why the functions v_0 and v_1 in Section 29.1 cannot be written explicitly as functions of the parameters. Hints: (i) If it cannot be done using the method of integrating factors, it cannot be done. (ii) The integral $\int (e^{-u}/u) du$ cannot be done explicitly. Both of these statements are provably correct, but you may take both of them for granted.
- 29.3. Using the notation of eq. (29.5), show: $S \leq 1/2$, and $S < 1/2$ if and only if

$$\bar{g}_{\text{syn}} > I - \frac{1}{\tau_m}.$$

- 29.4. Let us think about *very* strong and *very* brief inhibitory pulses synchronizing a population of LIF neurons. We consider the initial-value problem

$$\frac{dv}{dt} = -\frac{v}{\tau_m} + I - \bar{g}_{\text{syn}} e^{-t/\tau_I} v, \quad v(0) = v_*,$$

with $v_* > 0$. We now take a limit in which $\bar{g}_{\text{syn}} \rightarrow \infty$, $\tau_I \rightarrow 0$, and $\bar{g}_{\text{syn}} \tau_I$ remains constant — call that constant value γ .

- (a) (†) Explain: In the limit, v converges to the solution of

$$\frac{dv}{dt} = -\frac{v}{\tau_m} + I, \quad v(0) = v_* e^{-\gamma}.$$

You are allowed to be a bit non-rigorous. In particular, because we are interested in a limit in which $\bar{g}_{\text{syn}} \rightarrow \infty$, you may assume that the only term

on the right-hand side of the differential equation that matters initially is $-\bar{g}_{\text{syn}}e^{-t/\tau_I}v$, and therefore drop $-v/\tau_m + I$ at first. Think about the time interval on which that is valid, though.

(b) (*) Write a program that verifies the statement in (a). (You will have to make your time step, Δt , small as τ_I gets small, to avoid the sort of instability discussed in exercise 4.1. Use $\Delta t = \tau_I/100$, for instance.)

The conclusion is that a strong, brief pulse of inhibition results in tight synchronization of a population of normalized LIF neurons if and only if $\bar{g}_{\text{syn}}\tau_I$ is large. In that case, all membrane potentials of the population are reset to a value near 0 by the pulse.

(c) Verify that $\bar{g}_{\text{syn}}\tau_I$ can be interpreted as the *total amount of inhibition* delivered by the pulse, in the sense that

$$\int_0^{\infty} \bar{g}_{\text{syn}}e^{-t/\tau_I} dt = \bar{g}_{\text{syn}}\tau_I.$$

- 29.5. (*) Re-compute Table 29.2 perturbing the three parameters I , \bar{g}_{syn} , and τ_I by 10% instead of 1%, and discuss how the resulting table does or does not differ from Table 29.2.
- 29.6. (*) If you look at eq. (29.10), you will see that synaptic input into a theta neuron has two effects: First, the *drive* I is changed. I is replaced by

$$I + g_{\text{syn}}(t) \left(v_{\text{rev}} - \frac{1}{2} \right).$$

But second, there is the extra term $-g_{\text{syn}}(t) \sin \theta$, which by itself would drive θ towards 0. For a theta neuron, synaptic inputs differ from current inputs by the presence of the term $-g_{\text{syn}}(t) \sin \theta$.

Note that for a Hodgkin-Huxley-like model neuron, a synaptic input is, similarly, of the form

$$g_{\text{syn}}(t)(v_{\text{rev}} - v) = g_{\text{syn}}(t)(v_{\text{rev}} - v_{\text{rest}}) + g_{\text{syn}}(t)(v_{\text{rest}} - v),$$

where v_{rest} is a “rest” potential”; its exact definition is immaterial to the above calculation. The term $g_{\text{syn}}(t)(v_{\text{rev}} - v_{\text{rest}})$ can be thought of as a transient current input. The term $g_{\text{syn}}(t)(v_{\text{rest}} - v)$ is what makes a synaptic input different from a current input, and its analogue for the theta neuron is $-g_{\text{syn}}(t) \sin \theta$.

Does the synchronizing effect of inhibition depend on the presence of this term?²³ To find out, re-compute the river picture, Fig. 29.5, omitting the term $-g_{\text{syn}}(t) \sin \theta$.

- 29.7. (*) (†) Plot the quantity g_* from Section 29.3 as a function of τ_I , for $\tau_m = 1$ and $I = 0.3$ (the parameters of Fig. 29.5). You can do this by solving

²³I certainly hope it doesn’t, since we omitted this term in [11]. We did include it in the later paper [12].

eqs. (29.12), (29.13) with initial condition $\theta(0) = 0$, say, and some large $g_{\text{syn}}(0)$. The approximation for g_* is the value of g_{syn} at the time when θ reaches π . The initial value $g_{\text{syn}}(0)$ ought to be thought of here as a numerical parameter — the larger it is, the greater is the accuracy with which g_* is calculated. Choose it so large that there is no change in your plot visible to the eye when you halve it.

- 29.8. (*) The river picture, Fig. 29.5, shows that for theta neurons, firing resumes, following a pulse of inhibition, as soon as the time-dependent inhibitory conductance, $\bar{g}_{\text{syn}}e^{-t/\tau_I}$, has fallen to some value that is approximately independent of \bar{g}_{syn} and $\theta(0)$, although it depends on other parameters. Is this true for RTM neurons? To see, do the following numerical experiment.

Consider a single RTM neuron, subject to an inhibitory pulse, with parameters as in Fig. 29.4, middle panel, except for \bar{g}_{syn} , which will be varied here. Initialize the neuron at phase $\varphi_0 = 0.3$, say. Record the time P at which it fires. The inhibitory conductance at the time of spiking is then $\bar{g}_{\text{syn}}e^{-P/\tau_I}$. (You ought to realize that this quantity depends on \bar{g}_{syn} in a more complicated way than meets the eye, since P depends on \bar{g}_{syn} .) Plot $\bar{g}_{\text{syn}}e^{-P/\tau_I}$ as a function of $\bar{g}_{\text{syn}} \in [0.25, 1]$. Then repeat for $\varphi_0 = 0.7$. Does $\bar{g}_{\text{syn}}e^{-P/\tau_I}$ appear to be approximately independent of φ_0 and of \bar{g}_{syn} ?

Chapter 30

The PING Model of Gamma Rhythms

When populations of excitatory and inhibitory neurons are synaptically connected, oscillations often emerge. The reason is apparent: Activity of the excitatory neurons (which we will call *E-cells* from here on, as we did in Chapter 22) generates activity of the inhibitory neurons (*I-cells*). The activity of the I-cells causes the activity of the E-cells to cease transiently, and when it resumes, the E-cell population is closer to synchrony, as discussed in Chapter 29.²⁴ The oscillations in Chapter 22 are of a similar nature, although there individual cells were not modeled. Figure 30.1 (nearly identical with Fig. 22.1) represents the interaction of E- and I-cells symbolically.

Electronic supplementary material: The online version of this chapter (doi: [10.1007/978-3-319-51171-9_30](https://doi.org/10.1007/978-3-319-51171-9_30)) contains supplementary material, which is available to authorized users.

²⁴This requires that input from the I-cells in fact delays and synchronizes E-cell firing. For example, an h-current in the E-cells can undermine the mechanism, since hyperpolarization turns on the h-current, which is depolarizing. However, in this chapter, we will take the E-cells to be RTM neurons, for which no such complications arise.

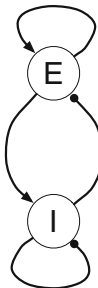


Figure 30.1. Symbolic depiction of a network of E- and I-cells. The large circles labeled “E” and “I” represent populations of cells. Lines ending in arrows indicate excitation, and lines ending in solid circles indicate inhibition.

In particular, brain oscillations with frequencies of about 30–80 Hz are thought to arise in this way in many instances. Oscillations in the 30–80 Hz frequency range are called *gamma oscillations* or *gamma rhythms*. They are seen in EEG traces and in local field potentials, and are correlated with perception, attention, and memory; for a review, see, for instance, [18]. A connection between meditation and gamma rhythms has been documented several times; see, for instance, [108]. Pathologies in gamma rhythms are associated with schizophrenia [63, 126, 146]. Notwithstanding these observed correlations, it is not universally agreed upon that gamma rhythms (or rhythms in any frequency band) play an important role in coding or information processing in the brain; see, for instance, [128]. Here we will focus on how gamma rhythms may arise, and make no claims about their function. Results potentially pertinent for their function will be presented in Chapters 35–38.

The E- and I-cells believed to generate gamma rhythms are pyramidal neurons and fast-firing PV+ interneurons. Rhythms of this kind are therefore referred to as *pyramidal-interneuronal network gamma (PING)* rhythms. The acronym PING goes back at least to Traub *et al.* [163]; the observation that gamma rhythms can be generated in this way goes back further; see, for instance, [43, 85, 94, 159].

A natural question arises here: What is special about the gamma frequency? Why can’t the interaction of E- and I-cells generate oscillations at any frequency? In fact it can. For instance, [175] describes oscillations in a model network at frequencies around 10 Hz arising from the interaction of excitatory and inhibitory cell populations. These oscillations model *sleep spindles*, oscillations that appear in the EEG during *stage 2 sleep*. The frequency of an oscillation in an *E-I-network* (a network of excitatory and inhibitory neurons) depends in general on the strength and duration of the inhibitory synaptic currents that impose the breaks between population spike volleys, as well as on the external drive. In the network of [175], for instance, there are slow, GABA_B-receptor-mediated inhibitory synapses. The decay time constant of GABA_A receptor-mediated inhibitory synapses has been reported in some places to be on the order of 10 ms [69, 137], and the gamma period (approximately 12 to 33 ms) is a small multiple of this value; this may suggest that GABA_A receptor-mediated inhibition will tend to generate oscillations in the gamma

frequency range. However, the strength of the inhibitory synapses and especially the external drive contribute significantly to setting the frequency; see Table 29.2, and also Table 30.1.

Experimental evidence supports the idea that the PING mechanism often underlies gamma rhythms. One of many examples is reproduced in Fig. 30.2, which shows recordings from the CA1 area of rat hippocampus. (Areas CA1, CA2, and CA3 are subdivisions of the hippocampus. “CA” stands for “cornu Ammonis,” the horn of the ancient Egyptian god Amun. *Cornu ammonis* is an 18th-century term for a part of the hippocampal formation.) The figure demonstrates that during gamma rhythms triggered by *tetanic stimulation* (stimulation by a high-frequency train of electrical pulses) in CA1, both pyramidal cells and inhibitory interneurons fire at approximately gamma frequency.

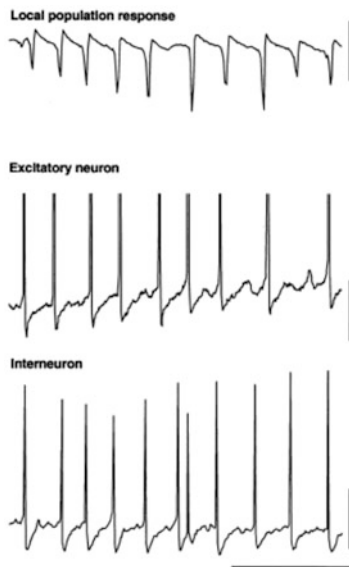


Figure 30.2. Figure 5 of [183], reproduced with publisher's permission. These are recordings from the CA1 region of rat hippocampus. Gamma oscillations are triggered by tetanic stimulation, i.e., by a high-frequency train of stimulating electrical pulses. Tetanic stimulation leads to the depolarization of both pyramidal neurons and inhibitory interneurons, as a result of metabotropic glutamate receptor activation [180]. The figure shows a local field potential (top trace), and membrane potentials of a pyramidal cell and an inhibitory interneuron (middle and bottom traces). The three traces were not recorded concurrently. The horizontal scale bar indicates 100 ms. The vertical scale bars indicate 1 mV (top trace), 4 mV (middle trace), and 20 mV (bottom trace).

30.1 Two-Cell PING

To build intuition, we begin with a two-cell network, consisting of a single E- and a single I-cell, with E-to-I and I-to-E (but not E-to-E or I-to-I) connectivity. The E-cell is an RTM neuron, and the I-cell a WB neuron. Voltage traces resulting from a simulation of such a two-cell network are shown in Fig. 30.3; the parameter values are specified in the caption of the figure. (Note that we use the notation $\tau_{d,E}$ for the decay time constant of the excitatory synapse, and $\tau_{d,I}$ for that of the inhibitory synapse.) Each time the E-cell fires, the I-cell promptly responds.

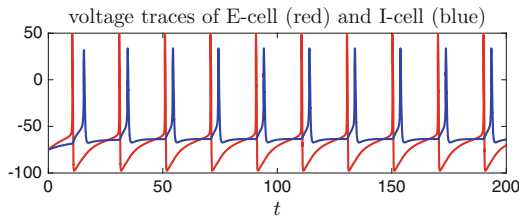


Figure 30.3. Voltage traces of the two neurons of a network consisting of one RTM and one WB neuron. The external drives are $I_E = 1.4$ and $I_I = 0$. The parameters characterizing the E-to-I and I-to-E synapses are $\bar{g}_{EI} = \bar{g}_{IE} = 0.25$, $\tau_r = \tau_{peak} = 0.5$ for both synapses, $\tau_d = \tau_{d,E} = 3$ for the E-to-I synapse, and $\tau_d = \tau_{d,I} = 9$ for the I-to-E synapse. There are no E-to-E or I-to-I synapses. [2_CELL_PING]

We denote the period at which each of the two cells in Fig. 30.3 fires by P , and explore the parameter dependence of P . In analogy with Tables 29.1 and 29.2, we compute the percentage change in P resulting from a 1% reduction in I_E , a 1% increase in \bar{g}_{IE} , and a 1% increase in $\tau_{d,I}$. By this measure, the period of the rhythm depends far more sensitively on external drive than on the strength or decay time constant of inhibition.

	$I_E \rightarrow 0.99I_E$	$\bar{g}_{IE} \rightarrow 1.01\bar{g}_{IE}$	$\tau_{d,I} \rightarrow 1.01\tau_{d,I}$
increase in P :	0.66%	0.10%	0.14%

Table 30.1. Parameter dependence of the period P of the rhythm of Fig. 30.3. [2_CELL_PING_CONDITION_NUMBERS]

30.2 Basic Network Simulations

In this section, we study numerical results obtained with a network code similar to the one that we used in [92], but using the synaptic model of Section 20.2. (In [92], we used the model of Section 20.1.) The code simulates a network of N_E RTM neurons (E-cells), and N_I WB neurons (I-cells). The numbers N_E and N_I are parameters specified by the user of the code. We usually take N_E to be four times

bigger than N_I , since this is often said to be the approximate ratio of glutamatergic to GABAergic neurons in the brain [136]. However, the ratio N_E/N_I is not of great importance for the properties of PING rhythms if the synaptic strengths are scaled as described below.

For each neuron in the network, we define a constant drive I . Different neurons are allowed to have different drives. For any pair of neurons, A and B, in the network, we define parameters associated with a synapse from A to B (compare Section 20.2):

$$\bar{g}_{\text{syn}}, \quad v_{\text{rev}}, \quad \tau_r, \quad \tau_{\text{peak}}, \quad \tau_d.$$

The maximal conductance \bar{g}_{syn} is allowed to be zero, so not all possible connections are necessarily present. For simplicity, we do not allow the possibility of two different synapses from A to B, for instance, a faster and a slower one, here.

In the examples of this section, the parameters are chosen as follows. The i -th E-cell receives input drive

$$I_{E,i} = \bar{I}_E(1 + \sigma_E X_i), \quad (30.1)$$

where \bar{I}_E and $\sigma_E \geq 0$ are fixed numbers, and the X_i are independent standard Gaussian random variables (see Appendix C). Similarly, the j -th I-cell receives input drive

$$I_{I,j} = \bar{I}_I(1 + \sigma_I Y_j), \quad (30.2)$$

where the Y_j are independent standard Gaussians. To set the strengths (maximal conductances) of the synaptic connections from E-cells to I-cells, the *E-to-I connections*, we choose two parameters, $\hat{g}_{EI} \geq 0$ and $p_{EI} \in (0, 1]$. The maximal conductance associated with the i -th E-cell and the j -th I-cell is then

$$\bar{g}_{EI,ij} = \frac{\hat{g}_{EI} Z_{EI,ij}}{p_{EI} N_E}, \quad (30.3)$$

where the $Z_{EI,ij}$ are independent random numbers with

$$Z_{EI,ij} = \begin{cases} 1 & \text{with probability } p_{EI}, \\ 0 & \text{otherwise.} \end{cases}$$

The total number of excitatory synaptic inputs to the j -th I-cell is

$$\sum_{i=1}^{N_E} Z_{EI,ij}. \quad (30.4)$$

The expected value of this number is $p_{EI} N_E$ (exercise 2), the denominator in (30.3). Consequently \hat{g}_{EI} is the expected value of the sum of all maximal conductances associated with excitatory synaptic inputs into a given I-cell (exercise 3). Similarly, the strength of the synaptic connection from the j -th I-cell to the i -th E-cell is

$$\bar{g}_{\text{syn},IE,ji} = \frac{\hat{g}_{IE} Z_{IE,ji}}{p_{IE} N_I}, \quad (30.5)$$

with

$$Z_{IE,ji} = \begin{cases} 1 & \text{with probability } p_{IE}, \\ 0 & \text{otherwise.} \end{cases}$$

The strengths of the E-to-E and I-to-I synapses are set similarly.

We use the same values of τ_r , τ_{peak} , τ_d , and v_{rev} for all excitatory synapses. We denote these values by $\tau_{r,E}$, $\tau_{\text{peak},E}$, $\tau_{d,E}$, and $v_{\text{rev},E}$. Similarly, all inhibitory synapses are characterized by parameters $\tau_{r,I}$, $\tau_{\text{peak},I}$, $\tau_{d,I}$, and $v_{\text{rev},I}$.

Figure 30.4 shows the result of a typical network simulation. Starting with E-cell initialized asynchronously, as described in Section 24.1, oscillations at approximately 45Hz develop rapidly, within about 50ms. Human reaction times are about 200 to 250ms, so if gamma rhythms are important for stimulus processing [18], then it must be possible to generate these oscillations in a time much shorter than 200ms, as indeed seen in Fig. 30.4. In fact, we gave an argument in [16] suggesting that in

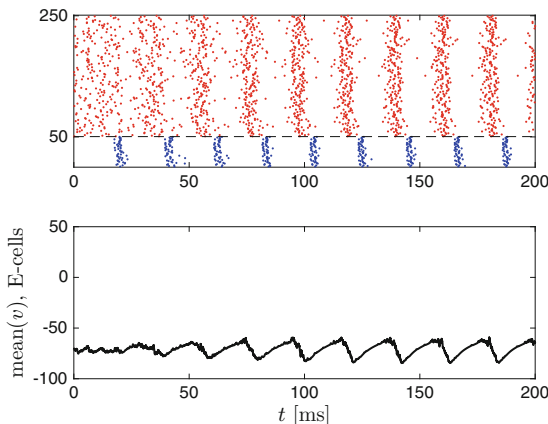


Figure 30.4. Spike rastergram of a PING network (top), and mean membrane potential of the E-cells (bottom). Spike times of E-cells are indicated in red, and spike times of I-cells in blue. The parameters are $N_E = 200$, $N_I = 50$, $\bar{I}_E = 1.4$, $\sigma_E = 0.05$, $\bar{I}_I = 0$, $\hat{g}_{EE} = 0$, $\hat{g}_{EI} = 0.25$, $\hat{g}_{IE} = 0.25$, $\hat{g}_{II} = 0.25$, $p_{EI} = 0.5$, $p_{IE} = 0.5$, $p_{II} = 0.5$, $\tau_{r,E} = 0.5$, $\tau_{\text{peak},E} = 0.5$, $\tau_{d,E} = 3$, $v_{\text{rev},E} = 0$, $\tau_{r,I} = 0.5$, $\tau_{\text{peak},I} = 0.5$, $\tau_{d,I} = 9$, $v_{\text{rev},I} = -75$. [PING_1]

networks with *drive heterogeneity* (different neurons receive different drives), PING oscillations must be created rapidly, within a small number of gamma cycles, if they are to be created at all.

Properties of activity in E-I-networks have been studied extensively; for example, see [11, 12, 61, 155, 156, 168, 183]. In the following sections, we will consider only a few of many interesting aspects of PING rhythms.

30.3 Sparse and Random Connectivity

Neither of the two-cell populations (E and I) synchronizes tightly in Fig. 30.4; this is an effect of heterogeneity in the external drives, and of randomness in the synaptic connectivity. To illustrate this point, Fig. 30.5 shows the same simulation as that of Fig. 30.4, but with all heterogeneity removed. Synchronization now becomes perfect in the limit as $t \rightarrow \infty$. This is, of course, not a biologically realistic picture.

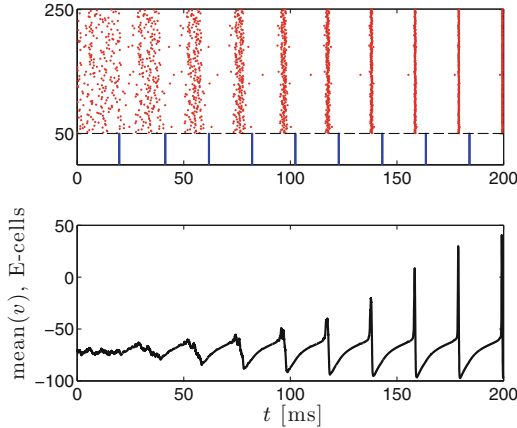


Figure 30.5. As Fig. 30.4, but with all network heterogeneity removed: $\sigma_E = 0$, $p_{EI} = p_{IE} = p_{II} = 1$. [PING_2]

Let us ask just how small p_{EI} , p_{IE} , and p_{II} can be before the oscillation is lost. (Note that p_{EE} plays no role yet because we are setting $\hat{g}_{EE} = 0$ for now.) For instance, if we set $p_{EI} = p_{IE} = p_{II} = 0.05$ in the simulation of Fig. 30.4, we obtain Fig. 30.6 — there is only a very faint indication of an oscillation left. However, if we keep the values of p_{EI} , p_{IE} , and p_{II} as in Fig. 30.6, but multiply N_E and N_I by 4 (recall that the strengths of individual synapses are then reduced by 4, see eq. (30.3)), rhythmicity returns; see Fig. 30.7.

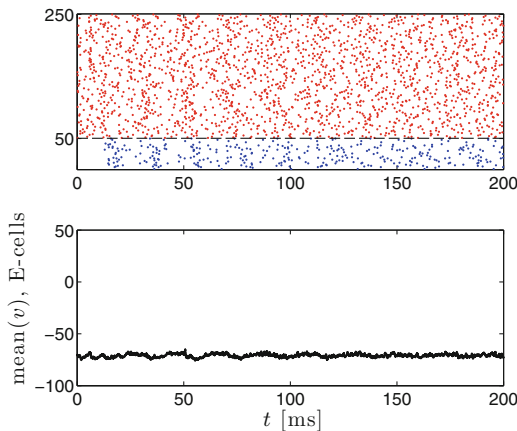


Figure 30.6. As Fig. 30.4, but with much greater sparseness of the connectivity: $p_{EI} = p_{IE} = p_{II} = 0.05$. [PING_3]

For the ability of the network to synchronize and form a rhythm, p_{EE} , p_{EI} , p_{IE} , and p_{II} are not as important as $p_{EE}N_E$, $p_{EI}N_E$, $p_{IE}N_I$, and $p_{II}N_I$, the

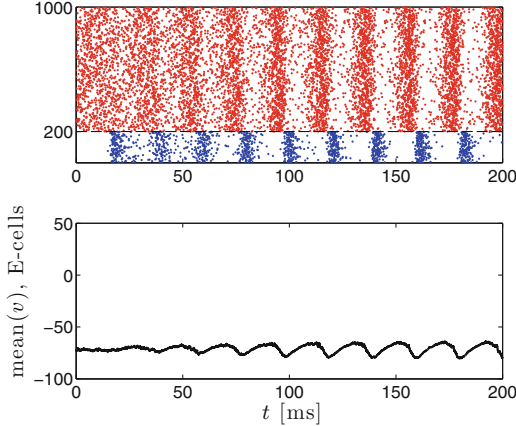


Figure 30.7. As Fig. 30.6, but for a four times larger network. [PING_4]

expected numbers of (excitatory or inhibitory) inputs per cell. In fact, $p_{EE}N_E$, $p_{EI}N_E$, $p_{IE}N_I$, and $p_{II}N_I$ largely determine the size of random fluctuations in the input strengths per cell. To show this, consider, for instance, the sum of all maximal conductances of inhibitory synapses into the i -th E-cell. We denote this sum by \bar{g}_{Ii} :

$$\bar{g}_{Ii} = \bar{g}_{IE} \sum_{j=1}^{N_I} Z_{IE,ji}. \quad (30.6)$$

Taking expectations on both sides, we obtain

$$E(\bar{g}_{Ii}) = \bar{g}_{IE} \sum_{j=1}^{N_I} E(Z_{IE,ji}) = \bar{g}_{IE} p_{IE} N_I. \quad (30.7)$$

Since the $Z_{IE,ji}$ are independent of each other, their variances sum (see Appendix C):

$$\text{var}(\bar{g}_{Ii}) = (\bar{g}_{IE})^2 \sum_{j=1}^{N_I} \text{var}(Z_{IE,ji}) = (\bar{g}_{IE})^2 \sum_{j=1}^{N_I} \left(E(Z_{IE,ji}^2) - (E(Z_{IE,ji}))^2 \right).$$

Since the only possible values of $Z_{IE,ji}$ are 0 and 1, $Z_{IE,ji}^2 = Z_{IE,ji}$, and therefore

$$\begin{aligned} & (\bar{g}_{IE})^2 \sum_{j=1}^{N_I} \left(E(Z_{IE,ji}^2) - (E(Z_{IE,ji}))^2 \right) = \\ & (\bar{g}_{IE})^2 \sum_{j=1}^{N_I} \left(E(Z_{IE,ji}) - (E(Z_{IE,ji}))^2 \right) = (\bar{g}_{IE})^2 N_I (p_{IE} - p_{IE}^2). \end{aligned}$$

Taking square roots, we obtain the standard deviation:

$$\text{std}(\bar{g}_{Ii}) = \bar{g}_{IE} \sqrt{N_I p_{IE} (1 - p_{IE})}. \quad (30.8)$$

From (30.7) and (30.8), we obtain the *coefficient of variation* of \bar{g}_{Ii} :

$$\text{cv}(\bar{g}_{Ii}) = \frac{\text{std}(\bar{g}_{Ii})}{E(\bar{g}_{Ii})} = \sqrt{\frac{1 - p_{IE}}{p_{IE}N_I}}.$$

For $p_{IE} \ll 1$, therefore,

$$\text{cv}(\bar{g}_{Ii}) \approx \sqrt{\frac{1}{p_{IE}N_I}}.$$

Analogous calculations are possible, of course, for the E-to-I, E-to-E, and I-to-I synaptic connections. This completes our argument showing that $p_{EE}N_E$, $p_{EI}N_E$, $p_{IE}N_I$, and $p_{II}N_I$ determine, in a sparse network, the size of variations in synaptic input strengths per cell.

One might summarize the conclusion by saying that it is not the *sparseness* of connectivity that hinders synchronization, but its *randomness*. In fact, what really matters is one particular aspect of that randomness, namely the variability in the numbers of excitatory and inhibitory inputs per cell. This point is illustrated by Fig. 30.8. The middle panel of the figure shows results of a simulation in which connectivity is so sparse that the *mean* number of excitatory and inhibitory inputs per cell is 1. Not surprisingly, synchronization is lost. The bottom panel of the figure shows results of a simulation of a very similar network, in which, however, the *exact* number of excitatory and inhibitory inputs per cell equals 1. The E- and I-cells from which these inputs originate are still chosen at random, but the fluctuations in the numbers of inputs per cell have been eliminated. Pronounced rhythmicity is recovered. The point is made again, more strikingly, by Fig. 30.9, which shows results of the same simulations, but continued over a long time interval. (Only the last 200 ms of simulated time are shown.) Synchronization eventually becomes perfect with just one single excitatory and inhibitory input per cell!

30.4 Strengths of External Drives and the Suppression Boundary

For the PING mechanism to work, the I-cells should not fire without being prompted by an E-cell spike volley. In the notation used earlier, this roughly means that \bar{I}_E must be large enough, or \bar{I}_I small enough. If \bar{I}_E is fixed, rhythmicity is lost as \bar{I}_I rises. Similarly, if \bar{I}_I is fixed, rhythmicity is lost as \bar{I}_E falls. In idealized circumstances, there is a sharply defined boundary in parameter space, with the property that PING is possible on one side of the boundary, but not on the other [12]. We called this the *suppression boundary* in [12], and hypothesized in [10] that it might play a role in brain function because it allows toggling between non-rhythmic and rhythmic states with only small changes in parameters. In less idealized circumstances, with heterogeneity in external drives and randomness in synaptic connectivity, the “suppression boundary” is not sharply defined. There is a more gradual, but often still fairly abrupt transition from rhythmic to non-rhythmic states as the I-cells become more excited, or as the E-cells become less excited. Figures 30.10 and 30.11 illustrate the fairly abrupt loss of rhythmicity as \bar{I}_I is raised. Note that

Fig. 30.10 looks quite similar to Fig. 30.4 — the fact that the I-cells have more drive than in Fig. 30.4 is of little consequence. However, as \bar{I}_I rises from 0.7 (Fig. 30.10) to 0.9 (Fig. 30.11), rhythmicity is largely lost.

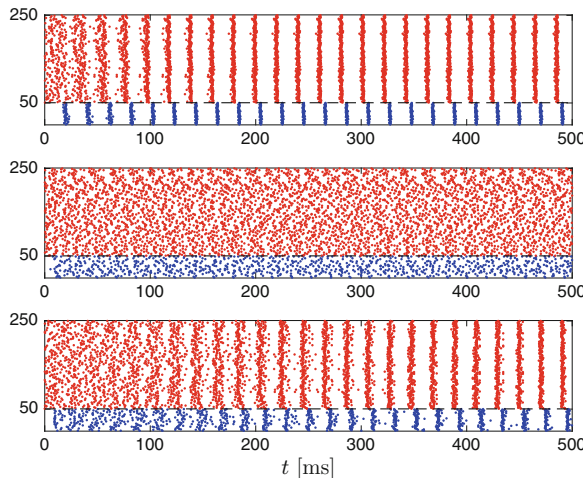


Figure 30.8. Top panel: As in Fig. 30.4 (a longer time interval is simulated here), but with heterogeneity in the drive to the E-cells removed, i.e., $\sigma_E = 0$. The failure to reach perfect synchrony is now exclusively due to the randomness of the synaptic connections. Middle panel: A similar simulation, but with $p_{EI} = 1/200$, $p_{IE} = 1/50$, and $p_{II} = 1/50$, so the expected numbers of excitatory and inhibitory inputs per cell are 1. Bottom panel: Same as middle panel, but now the actual numbers of excitatory and inhibitory inputs per cell are 1. Note that there is very little, if any, rhythmicity in the middle panel, while pronounced rhythmicity emerges in the bottom panel. [PING_5]

30.5 Recurrent Inhibition

By *recurrent inhibition*, we mean I-to-I synapses here. When \hat{g}_{II} is set to zero in the simulation of Fig. 30.4, i.e., when recurrent inhibition is eliminated, the result is largely unchanged; the frequency rises slightly (exercise 4). On the other hand, by tripling \hat{g}_{II} one can restore rhythmicity in Fig. 30.11 (exercise 5). Thus I-to-I connectivity can play the role of “calming” the I-cells and thereby allowing the PING mechanism to work when the external drive to the I-cells would otherwise be too strong, but it is not needed for the emergence of a PING rhythm when the drive to the I-cells is weak enough.

30.6 Recurrent Excitation

Up to this point, we have set $\hat{g}_{EE} = 0$ in this chapter, so there have not been any E-to-E synaptic connections. When we add weak E-to-E connections, with

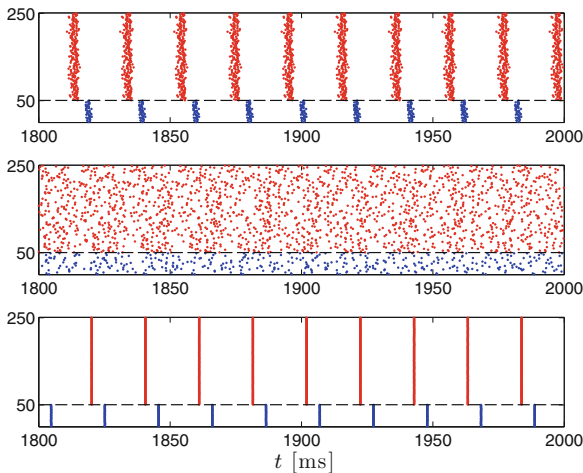


Figure 30.9. Same as Fig. 30.8, but with simulations continued up to time 2000. Only the last 200 ms of simulated time are shown. [PING_6]

the same time constants as for the E-to-I connections ($\tau_{r,E} = \tau_{\text{peak},E} = 0.5$ ms, $\tau_{d,E} = 3$ ms), the PING rhythm is barely affected. Stronger E-to-E connections destroy the rhythm; see Fig. 30.12. This is in contrast with the Wilson-Cowan model of Chapter 22, which *requires* recurrent excitation for oscillations.

Exercises

- 30.1. Vary the baseline parameters perturbed in Table 30.1, and see how the results change.
- 30.2. Explain why the expectation of (30.4) is $p_{EI}N_E$.
- 30.3. Explain why \hat{g}_{EI} is the expected value of the sum of all maximal conductances associated with excitatory synaptic inputs into a given I-cell.
- 30.4. (*) Verify that the rhythm in Fig. 30.4 is largely unchanged when \hat{g}_{II} is set to zero.
- 30.5. (*) Verify that the rhythm in Fig. 30.11 is restored when \hat{g}_{II} is tripled.
- 30.6. Explain why one would *expect* that short recurrent excitatory synapses would not affect PING rhythms much.
- 30.7. (*) (†) PING rhythms in our model networks have very regular population frequencies; that is, the times between population spike volleys are nearly constant. Experimentally recorded gamma rhythms are much less regular; see, for instance, the top trace of Fig. 30.2.

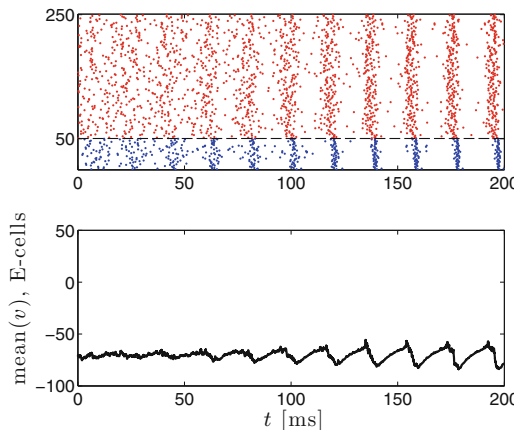


Figure 30.10. Same as Fig. 30.4, but with $\bar{I}_I = 0.7$, $\sigma_I = 0.05$. [PING_7]

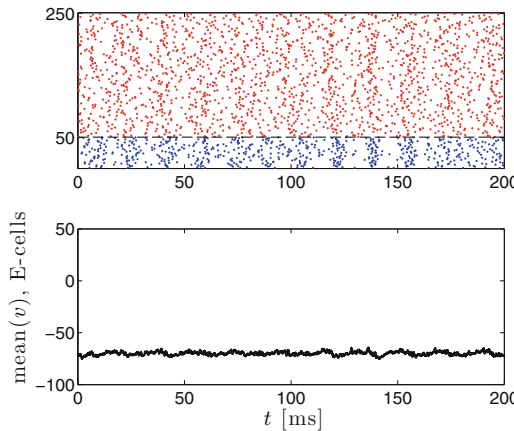


Figure 30.11. Same as Fig. 30.4, but with $\bar{I}_I = 0.9$, $\sigma_I = 0.05$. [PING_8]

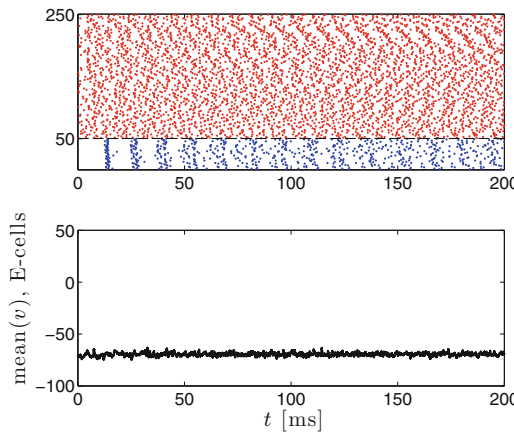


Figure 30.12. Same as Fig. 30.4, but with $\hat{g}_{EE} = 0.25$, $p_{EE} = 0.5$. [PING_9]

One can try to introduce more variability by adding to the drives $I_{E,i}$ a single discrete Ornstein-Uhlenbeck process $S(t)$ (independent of i), as defined by eqs. (C.20)–(C.22) in Appendix C.6. This would model global fluctuations in the excitability of E-cells. In a living brain, such fluctuations could result from *neuromodulation*. (In general, the word *neuromodulation* denotes the regulation of a whole population of neurons by a diffusely released neurotransmitter.)

Explore computationally whether you can set the parameters of the discrete Ornstein-Uhlenbeck process so that the PING rhythm is not destroyed, but its frequency becomes significantly more variable.

- 30.8. (*) What happens if you make the inhibitory synapses in the simulation of Fig. 30.4 much stronger, but also much faster, say $\tau_{r,I} = \tau_{\text{peak},I} = 0.5$ ms, $\tau_{d,I} = 3$ ms? Can you still get a gamma rhythm?

Chapter 31

ING Rhythms

Gamma rhythms can also be generated by the interaction of I-cells alone, without any involvement of E-cells. For example, in brain slices, gamma rhythms can be evoked even in the presence of drugs blocking AMPA and NMDA receptors. See Fig. 31.1 for an example, recorded from rat CA1.

Assuming strong external drive to the I-cells, the mechanism seems, at first sight, similar to PING: Activity of the I-cells creates inhibition, which silences the entire population temporarily, and when firing resumes, it is in greater synchrony, as described in Chapter 29.²⁵ Gamma rhythms created in this way were called *Interneuronal Network Gamma (ING) rhythms* in [183]; earlier studies of such rhythms include [174] and [182].

To construct model networks of inhibitory cells, we simply omit the E-cells from the networks of Chapter 30 and strengthen the external drive to the I-cells. The resulting networks are capable of generating gamma rhythms, but only under idealized circumstances, namely with little heterogeneity in external drives (σ_I small) and very little randomness in synaptic connectivity (p_{II} very close to 1); see Sections 31.1 and 31.2 for examples.

The fast-firing interneurons involved in generating gamma rhythms are well known to be connected by gap junctions [57]. When gap-junctional coupling is added to the model networks, ING rhythms become much more robust; this is demonstrated with examples in Section 31.3. It is in line with many experimental and modeling studies that have found gap junctions to drive neurons towards

Electronic supplementary material: The online version of this chapter (doi: [10.1007/978-3-319-51171-9_31](https://doi.org/10.1007/978-3-319-51171-9_31)) contains supplementary material, which is available to authorized users.

²⁵This requires that inhibitory input in fact delays and synchronizes I-cell firing. For example, an h-current in the I-cells may undermine the mechanism, just as an h-current in the E-cells can undermine PING. However, in this chapter, we will take the I-cells to be WB neurons, for which there are no such complications.

synchrony (see, for instance, [93, 153, 160]), and is expected because of the equilibrating effect of discrete diffusion (see Chapter 21).²⁶

Even in the absence of any heterogeneity, ING networks without gap junctions can generate *clustering*, with individual cells firing only on a fraction (most typically

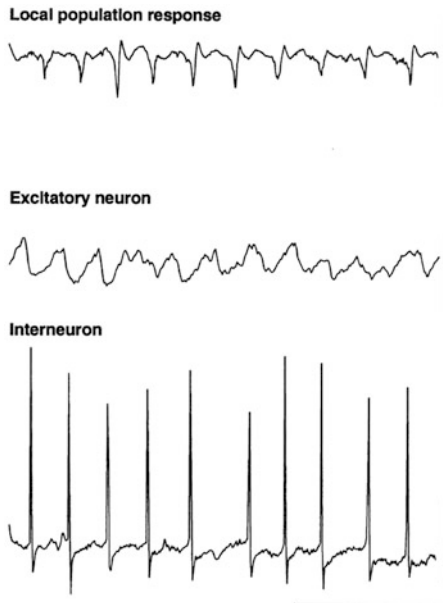


Figure 31.1. Figure 3 of [183], reproduced with publisher's permission. These are in vitro recordings from rat CA1. AMPA and NMDA receptors were blocked by drugs, and the inhibitory interneurons were excited using a technique called pressure ejection of glutamate. The figure shows a local field potential (top trace), and membrane potentials of a pyramidal cell and an inhibitory interneuron (middle and bottom traces). The three traces were not recorded concurrently. The horizontal scale bar indicates 100 ms. The vertical scale bars indicate 1 mV (top trace), 4 mV (middle trace), and 20 mV (bottom trace).

one half) of the population spike volleys. This was shown in [174] (and also, for purely inhibition-based rhythms at lower frequencies, earlier in [62]). We show examples in Section 31.4.

In summary, synchrony in networks of inhibitory cells without gap-junctional coupling seems fairly fragile. In Section 31.5, we illustrate this point in yet another way, using the example of a pair of abstract oscillators coupled by inhibitory pulses.

²⁶It is not, however, *obvious* that the equilibrating effect of discrete diffusion carries over to the case of spiking neurons, and in fact it is not always true; see [28, Fig. 8].

31.1 Single-Cell ING

To build intuition, we begin with a single WB neuron with an inhibitory autapse. A voltage trace resulting from a simulation of such a single-cell “network” model is shown in Fig. 31.2; the parameter values are specified in the caption of the figure. Not surprisingly, the voltage trace does not look much different from that of a WB neuron without the autapse.

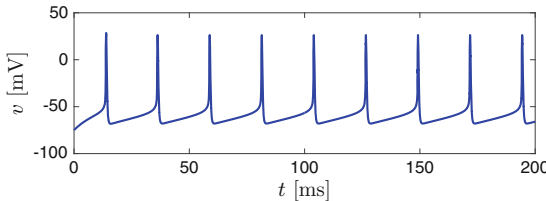


Figure 31.2. Voltage trace of a WB neuron with an inhibitory autapse. The external drive is $I = 1.5$. The parameters characterizing the autapse are $\bar{g}_{\text{syn}} = 0.5$, $\tau_r = \tau_{\text{peak}} = 0.5$, $\tau_d = 9$, and $v_{\text{rev}} = -75$. [\[1_CELL_ING\]](#)

We denote the period at which the cell in Fig. 31.2 fires by P , and explore the parameter dependence of P . In analogy with Table 30.1, we compute the percentage change in P resulting from a 1% reduction in I , a 1% increase in \bar{g}_{syn} , and a 1% increase in τ_d . Again we find that the period depends more sensitively on external drive than on the strength or decay time constant of the autapse.

	$I \rightarrow 0.99I$	$\bar{g}_{\text{syn}} \rightarrow 1.01\bar{g}_{\text{syn}}$	$\tau_d \rightarrow 1.01\tau_d$
increase in P :	0.77	0.35	0.47

Table 31.1. Parameter dependence of the period P of the rhythm of Fig. 31.2. [\[1_CELL_ING_CONDITION_NUMBERS\]](#)

31.2 Basic Network Simulations

Figure 31.3 shows an ING rhythm generated by 100 WB neurons coupled with inhibitory synapses. Note that it takes longer to reach synchrony than in, for instance, the PING network of Fig. 30.4. In Fig. 31.3, conditions for synchronization are ideal: There is no heterogeneity in external drives, synaptic connectivity is all-to-all, and all synapses have the same strength. This is why *perfect* synchrony is reached in the limit as $t \rightarrow \infty$. With a modest level of drive heterogeneity ($\sigma_I = 0.03$), it takes even longer to reach (approximate) synchrony; see Fig. 31.4. A similar effect is seen when 15% of the synaptic connections in Fig. 31.3 are omitted at random ($p_{II} = 0.85$), and the remaining ones strengthened by the factor 100/85; see Fig. 31.5. As in Chapter 30, this is not primarily an effect of sparseness and randomness *per se*, but of variations in the total amount of synaptic input per cell; see Fig. 31.6. With greater heterogeneity, the rhythm disappears; see Fig. 31.7, and also exercise 3. For an analysis of the sensitivity of ING rhythms to heterogeneity, see [178].

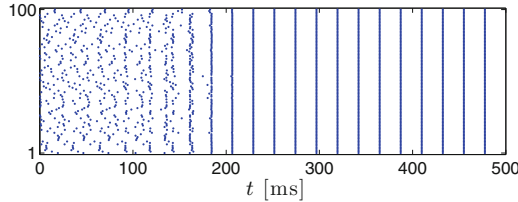


Figure 31.3. Spike rastergram of 100 synaptically coupled WB neurons. Spike times of I -cells (which are the only cells in the network) are indicated in blue. The parameters, using the notation of Chapter 30, are $N_I = 100$, $\bar{I}_I = 1.5$, $\hat{g}_{II} = 0.5$, $p_{II} = 1$, $\tau_{r,I} = 0.5$, $\tau_{\text{peak},I} = 0.5$, $\tau_{d,I} = 9$, $v_{\text{rev},I} = -75$. There is no heterogeneity of any kind in the network. Initialization is, as in Chapter 30, asynchronous, in the sense explained in Section 24.1. [ING_1]

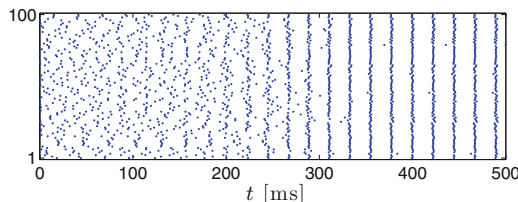


Figure 31.4. Same as Fig. 31.3, but with heterogeneous external drive (different neurons receive different, temporally constant drives): $\sigma_I = 0.03$. [ING_2]

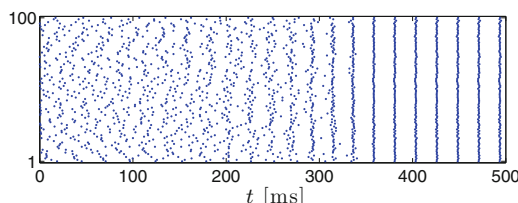


Figure 31.5. Same as Fig. 31.3, but with 15% of synaptic connections omitted at random ($p_{II} = 0.85$), and the remaining ones strengthened by the factor 100/85. [ING_3]

Several studies have suggested, based on both experiments and simulations, that parameter choices such as those in Figs. 31.3–31.7 might be far from realistic, and that the inhibitory synapses should be briefer, stronger, and shunting rather than hyperpolarizing; see in particular [7] and [169]. We will not discuss this point further here, and leave it to the reader to investigate ING rhythms with briefer, stronger, shunting inhibition; see exercise 12.

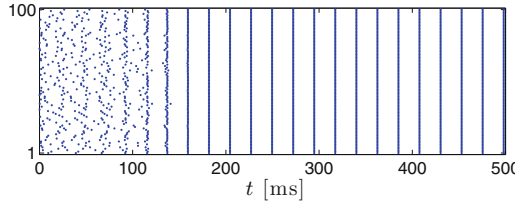


Figure 31.6. Same as Fig. 31.5, but now each cell receives inputs from exactly 85 cells, instead of receiving input from a random number of cells with mean 85. [ING_4]

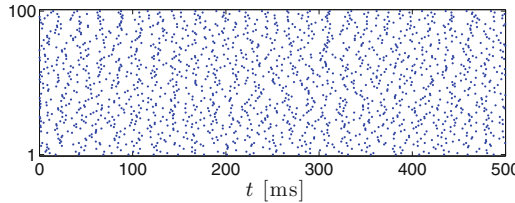


Figure 31.7. As in Fig. 31.3, but with $\sigma_I = 0.05$ and $p_{II} = 0.5$ [ING_5]

31.3 Adding Gap Junctions

We model gap junctions as described in Chapter 21. In our code, the strength of the connection between neurons i and j is taken to be

$$g_{\text{gap},ij} = \begin{cases} \hat{g}_{\text{gap}} / (p_{\text{gap}}(N_I - 1)) & \text{with probability } p_{\text{gap}}, \\ 0 & \text{with probability } 1 - p_{\text{gap}}, \end{cases}$$

for $i > j$, $g_{\text{gap},ij} = g_{\text{gap},ji}$ for $i < j$, and $g_{\text{gap},ii} = 0$. The parameter p_{gap} determines the density of gap-junctional connections, and \hat{g}_{gap} determines their strength. We scale by $p_{\text{gap}}(N_I - 1)$ to make the expected value of the total gap-junctional conductance affecting a cell independent of p_{gap} and N_I ; compare the discussion in Section 30.2. (Note that a cell can receive gap-junctional input only from *other* cells, not from itself. This is why we scale by $p_{\text{gap}}(N_I - 1)$ here, not by $p_{\text{gap}}N_I$.) In the simulations presented here, we use $N_I = 100$ and $p_{\text{gap}} = 0.05$, so the expected number of gap-junctional contacts per cell is $99 \times 0.05 = 4.95 \approx 5$, and $\hat{g}_{\text{gap}} = 0.1$, so the strength of each gap-junctional connection is $g_{\text{gap},ij} \approx 0.02$. With this gap-junctional coupling added, (approximate) synchrony is reached extremely rapidly, within two gamma cycles, in the simulations of Figs. 31.4 and 31.5 (exercise 2), and even a much greater degree of heterogeneity does not destroy the rhythm; see Fig. 31.8.

31.4 Clustering

Even in purely inhibitory networks without any heterogeneity, synchronization is somewhat fragile in the absence of gap junctions. There are parameter choices for

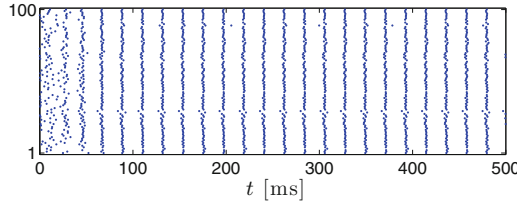


Figure 31.8. As in Fig. 31.7, but with $\hat{g}_{\text{gap}} = 0.1$ and $p_{\text{gap}} = 0.05$. [ING_6]

which one sees a breakup of the cells into $n > 1$ clusters (usually $n = 2$, but see exercise 7), with each cluster firing on every n -th population cycle. However, the clustering behavior is fragile as well: A moderate amount of drive heterogeneity destroys it, and gap-junctional coupling does *not* restore it, but instead results in complete synchronization, even for parameters for which there is clustering in the absence of heterogeneity. For these reasons, it seems unclear whether clustering in ING networks could have biological relevance. Nonetheless we will briefly discuss it here, as another illustration of the fragility of ING rhythms in the absence of gap junctions.

Wang and Buzsáki [174] demonstrated numerically that in networks without heterogeneity, clustering is seen when the hyperpolarization following firing is pronounced [174, Fig. 3], especially when the synaptic reversal potential is relatively high. The hyperpolarization following firing can be made pronounced by slowing down the variables h and n , which play central roles in ending the action potential; see [174], and also Exercise 5.6. If we multiply the functions α_h , β_h , α_n , and β_n by 1/2 (this amounts to doubling τ_h and τ_n , or to reducing the scaling factor ϕ of [174] from 5 to 2.5), Fig. 31.3 turns into 31.9. The red rectangle in Fig. 31.9 is shown once more, enlarged, in Fig. 31.10. There are two clusters firing alternately.²⁷

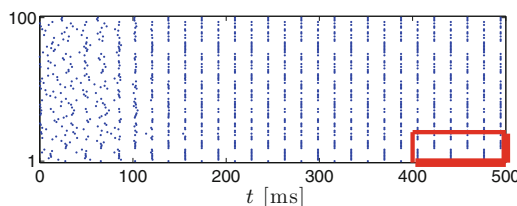


Figure 31.9. As in Fig. 31.3, but with α_h , β_h , α_n , and β_n reduced by a factor of 2. The red rectangle indicates the window that is enlarged in Fig. 31.9. [ING_7]

Heuristically, one can see why strong spike afterhyperpolarization and a relatively high synaptic reversal potential might counteract synchronization: Inhibition soon after firing is then *depolarizing*, since the membrane potential after firing will

²⁷If you conclude, after looking at Fig. 31.10, that something must be wrong with my code, download and examine the code, or do exercise 5, or both.

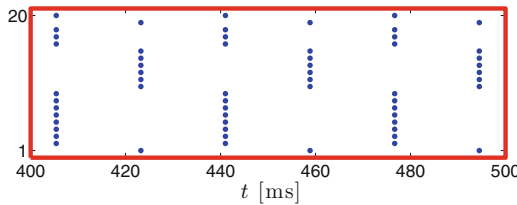


Figure 31.10. Red window in Fig. 31.9, enlarged. [ING_8]

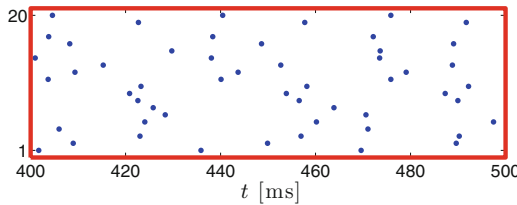


Figure 31.11. Like Fig. 31.10, but with $\sigma_I = 0.05$. [ING_9]

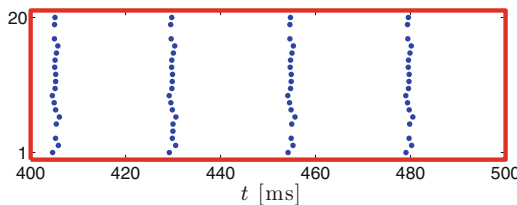


Figure 31.12. Like Fig. 31.11, but with weak, sparse gap junctions: $\hat{g}_{\text{gap}} = 0.04$, $p_{\text{gap}} = 0.05$. [ING_10]

be below the synaptic reversal potential, whereas inhibition arriving soon before firing will of course be *hyperpolarizing*. Consequently, the cells that fire first in an approximately (but not perfectly) synchronous spike volley accelerate each other by their inhibitory interactions, while slowing down the cells that are behind and receive the inhibition before firing.

When we introduce heterogeneity in drive ($\sigma_I = 0.05$) in the simulation of Fig. 31.9, the firing becomes asynchronous; see Fig. 31.11. When we add gap junctions, even quite weak and sparse ones, clustering does not return, but instead the entire population synchronizes; see Fig. 31.12.

You might wonder whether in a PING rhythm, clustering of the E-cells couldn't happen for the precisely same reason for which it happens in ING. In fact it can; see Chapter 32. For PING rhythms, clustering occurs easily when the E-cells express²⁸ adaptation currents. It is possible even without adaptation currents, but requires very rapid, and probably unrealistically rapid, inhibitory feedback; see Section 32.3.

²⁸The word “express,” used in this way, is useful neuroscience jargon. A cell in which a certain current is present is briefly said to “express” that current.

31.5 Two Abstract Oscillators Coupled by Inhibitory Pulses

Figure 25.10 shows a PRC of a WB neuron responding to a brief inhibitory pulse. We now consider a pair of abstract oscillators of the sort analyzed in Chapter 26, with a phase response function qualitatively resembling the function shown in Fig. 25.10. We define the phase response function by

$$g(\varphi) = -\mathcal{H}\left(\frac{\varphi - 0.1}{0.1}\right) \left(\mathcal{H}\left(\frac{0.8 - \varphi}{0.05}\right) - \mathcal{H}(-4) \right) \frac{\varphi}{2} \quad (31.1)$$

with

$$\mathcal{H}(s) = \frac{1 + \tanh(s)}{2}. \quad (31.2)$$

See exercise 8 for the motivation for this definition. Figure 31.13 shows the graph of g , and the graph of the function G derived from it as described in Section 26. Note that there is qualitative similarity between the graph of g and Fig. 25.10, but there is also a significant difference: In Fig. 25.10, $g(0) < 0$ (even an inhibitory pulse that arrives right at the moment at which the membrane potential crosses -20 mV from above will retard the next spike), whereas in the framework of Chapter 26, $g(0) = g(1) = 0$. The graph of G shows that synchrony is weakly attracting (in fact, $G'(0) \approx 0.9467$, see exercise 9), but anti-synchrony is attracting as well. This is reminiscent of the network of Figs. 31.9 and 31.10, where clustering is a stable state, but so is synchrony (see exercise 6b). For further discussion of this example, see exercise 10.

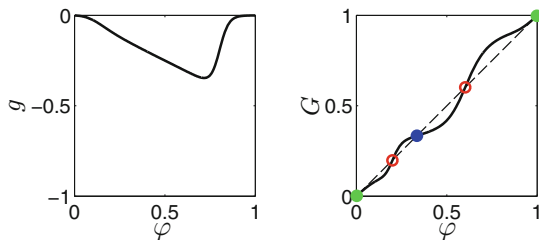


Figure 31.13. The function g defined by eqs. (31.1) and (31.2), and the function G derived from it as described in Section 26. Fixed points of G correspond to possible phase-locked states of the two oscillators. Synchrony (solid green points) and anti-synchrony (solid blue point) are stable. There is another possible, but unstable phase-locked state (red circles). [ABSTRACT_PULSE_COUPLING_INH]

Note that the value of φ corresponding to anti-synchrony in Fig. 31.13 is clearly not $1/2$, contrary to what you might have expected. This is explained in the paragraph following the proof of Proposition 26.1.

31.6 Entrainment of Excitatory Cells by ING Rhythms

What happens when an ING network gives input to a population of other neurons, say a population of pyramidal cells? Is the rhythmicity projected into the target population? We can experiment by adding, for instance, to the network of Fig. 31.8, a population of E-cells, with $\hat{g}_{IE} > 0$ but $\hat{g}_{EI} = 0$, so that the E-cells are affected by, but do not affect the I-cells. If the E-cells receive too little external drive, then of course they will simply be suppressed by the inhibitory input. But given external drive sufficient to make them fire, will they fire rhythmically, phase-locked with the I-cells?

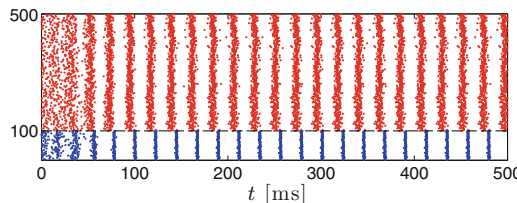


Figure 31.14. The ING network of Fig. 31.8 entraining a population of $N_E = 400$ E-cells. Here $\hat{g}_{EE} = \hat{g}_{EI} = 0$, but $\hat{g}_{IE} = 0.5$, $p_{EI} = 0.5$, $\bar{I}_E = 1.5$, and $\sigma_E = 0.1$. [ING_ENTRAINING_E_CELLS]

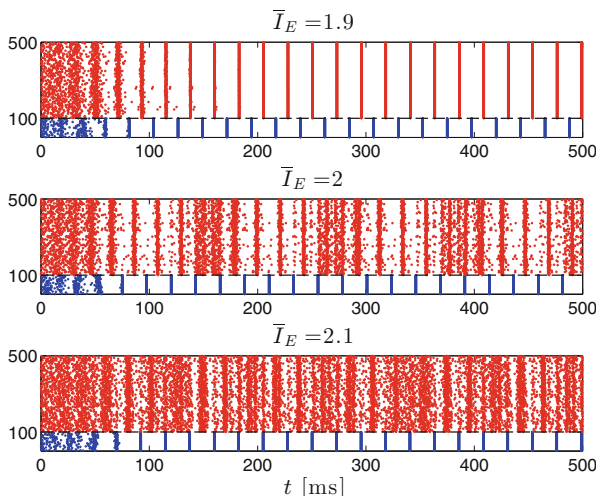


Figure 31.15. Same network as in Fig. 31.14, with all heterogeneity in drives and randomness in connectivity removed ($\sigma_E = \sigma_I = 0$, $p_{II} = p_{IE} = 1$). As \bar{I}_E crosses a threshold, phase-locking of the E-cell population with the I-cell population is lost. [ING_ENTRAINING_E_CELLS_2]

Figure 31.14 shows a case in which the answer to the above question is “yes.” Note that the firing looks very similar to that in a PING network, in spite of the fact that there is no E-to-I coupling. There is a broad range of drives to the E-cells for which similar patterns are obtained. As the drive to the E-cells gets stronger, the phase relation between E- and I-cells changes, with the E-cells firing earlier in the cycle of the I-cells; see upper panel of Fig. 31.15.

Then, as a threshold value is crossed, there is an abrupt transition from phase-locking of the E-cells with the I-cell to a “phase walkthrough” pattern, shown in the middle panel of Fig. 31.15. The E-cells fire earlier and earlier in the I-cell cycle, until they fire twice in one cycle, then return to firing later in the cycle, and the gradual shift to earlier phases resumes. For yet stronger drive, there is greater irregularity; see bottom panel of Fig. 31.15. To separate the effect of a strong drive to the E-cells from the effects of heterogeneity in drives and randomness in connectivity, drive heterogeneity and randomness of connectivity were omitted in Fig. 31.15.

Exercises

- 31.1. (*) Compute tables similar to Table 31.1 for other parameter values. Also investigate how sensitively P depends on other parameters, for instance, on \bar{g}_L .
- 31.2. (*) Add gap junctions with $\hat{g}_{\text{gap}} = 0.1$ and $p_{\text{gap}} = 0.05$ to the codes generating Figs. 31.4 and 31.5, and see what you get. (Hint: This is already programmed in the codes generating Figs. 31.4 and 31.5, all you need to do is make \hat{g}_{gap} non-zero!)
- 31.3. (*) In the code that generates Fig. 31.7, change the initialization so that each neuron is initialized at a random phase uniformly distributed not in $[0, 1]$, but in $[0, 0.02]$. Thus the population is nearly synchronous at the beginning. How does the rastergram change? Does (approximate) synchrony appear to be stable?
- 31.4. (*) To which extent does the rhythm in Fig. 31.8 depend on the chemical synapses? Would the neurons similarly synchronize, because of the gap junctions, even if \hat{g}_{II} were zero?
- 31.5. (*) When you look at Figs. 31.9 and 31.10, do you think something must be wrong? I did, when I first saw these figures. There are strangely long sequences of neurons with consecutive indices that belong to the same cluster. It looks as though neurons with nearby indices were correlated. But membership in clusters should really be random here, shouldn’t it? There should be no correlation between the cluster that neuron i belongs to, and the cluster that neuron $i + 1$ belongs to.

To reassure yourself that nothing is alarming about Fig. 31.9, define

$$f(i) = \begin{cases} 1 & \text{with probability } 1/2, \\ 2 & \text{with probability } 1/2, \end{cases} \quad i = 1, 2, \dots, 20,$$

and plot $f(i)$ as a function of i . Compute several realizations of f , of course using different random number generator seeds each time. (All you need to do in Matlab to get different realizations of f is not reset the seed before computing a new realization.) Do you see plateaus that seem surprisingly long, suggesting a correlation between $f(i)$ and $f(i + 1)$?

The phenomenon that you see here is well-known in sports: Fairly long “winning streaks” and “losing streaks” are more likely to emerge by pure chance than most of us would expect [59].

- 31.6. (*) (a) Does the clustering shown in Fig. 31.10 persist for a much longer time? Run the simulation for 2000 ms, and see whether you still observe the same clusters as in Fig. 31.10 in the last 100 ms of simulated time. (b) Repeat the simulation of Fig. 31.10 with initial conditions close to synchrony. (For instance, start all neurons at phases selected with uniform distribution from the interval $[0, 0.1]$.) Do you get clustering, as in Fig. 31.10?
- 31.7. (*) In the code that generates Fig. 31.10, use the parameters $\tau_{r,I} = 0.2$, $\tau_{peak,I} = 0.2$, $\tau_{d,I} = 1$. (These values are admittedly implausible biologically.) Show that you get three clusters.
- 31.8. (a) Plot the function \mathcal{H} defined in eq. (31.2). (b) Explain what motivates the definition (31.1).
- 31.9. (*) Use the code that generates Fig. 31.13 to verify that $G'(0) \approx 0.9467$.

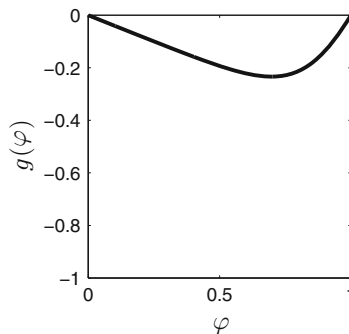


Figure 31.16. A simplification of the function g in Fig. 31.13.
[ABSTRACT_PULSE_COUPLING_INH_2]

- 31.10. (†) Figure 31.16 shows a phase response function qualitatively similar to that in Fig. 31.13, but with simpler behavior near $\varphi = 0$ and 1. The behavior of g near 0 and 1 determines the stability of synchrony; see (26.10). The stability of non-synchronous phase-locked states, on the other hand, is determined by the behavior away from the edges. So by analyzing non-synchronous phase-locked states for the PRC shown in 31.16, we can understand non-synchronous phase-locked states for the PRC in Fig. 31.13.

Assume that $g(\varphi) = \epsilon g_0(\varphi)$, where $\epsilon \in (0, 1]$, and $g_0 = g_0(\varphi)$, $\varphi \in [0, 1]$, is a continuously differentiable function with $g_0(0) = g_0(1) = 0$, $g_0(\varphi) < 0$ for $\varphi \in (0, 1)$, and $|g'(0)| < g'(1)$.

- (a) Show that synchrony is unstable for sufficiently small $\epsilon \in (0, 1]$.
 - (b) Assume that the function G , derived from g as in Chapter 26, has finitely many fixed points only. Show that there is a stable non-synchronous phase-locked state.
- 31.11. (*) Test what happens when one makes \bar{T}_E much smaller in the simulations of Fig. 31.15. Find various possible entrainment patterns by varying \bar{T}_E .
- 31.12. (*) Investigate ING rhythms with briefer, stronger, shunting inhibition, and compare their properties with those of the ING rhythms studied in this chapter, using variations on the codes generating the figures in this chapter.

Chapter 32

Weak PING Rhythms

In the PING model of Chapter 30, each E-cell and each I-cell fires once on each cycle of the oscillation. This is not what is usually seen experimentally in gamma rhythms. Much more typically, each participating pyramidal cells fires on some, but not all population cycles. The same is true for the participating inhibitory interneurons, although they usually participate on a larger proportion of population cycles. Figure 32.1 reproduces a small part of [34, Fig. 1] to illustrate this point. In the experiment underlying [34, Fig. 1], the gamma oscillations were induced by application of *kainate*, which activates glutamate receptors called the *kainate receptors*. This sort of oscillations can persist for very long times in the *in vitro* preparation (on the order of hours), and are therefore called *persistent gamma oscillations* [21, 33].

We call PING-like models in which the E-cells participate “sparsely,” i.e., on a fraction of the population cycles only, *weak PING* models. By contrast, we will refer to the models of Chapter 30 as *strong PING* models. One way of obtaining weak PING oscillations is to make the drive to the E-cells stochastic [10]. In such a model, each individual E-cell participates only on those population cycles on which it happens to have sufficient drive. We refer to this as *stochastic weak PING*. A far more detailed stochastic model of gamma rhythms with sparse participation of the E-cells is due to Roger Traub; see, for instance, [158]. In Traub’s model, individual model neurons have multiple compartments. The gamma rhythm is driven by stochastic activity originating in the pyramidal cell axons and amplified by axo-axonal gap junctions. One can think of the stochastic weak PING model studied here as a very much simplified caricature of Traub’s model.

An alternative way of obtaining sparse participation of E-cells is to add adaptation currents to the E-cell model, which can prevent individual E-cells from firing at or even near gamma frequency [89, 98, 110]. We call this *adaptation-based*

Electronic supplementary material: The online version of this chapter (doi: [10.1007/978-3-319-51171-9_32](https://doi.org/10.1007/978-3-319-51171-9_32)) contains supplementary material, which is available to authorized users.

weak PING. We illustrate the stochastic and adaptation-based weak PING mechanisms with numerical examples in Sections 32.1 and 32.2, and discuss differences in their properties.

LeMasson and Kopell [94] proposed an *h-current-based weak PING* mechanism.



Figure 32.1. Two voltage traces from Fig. 1 of [34]. These are recordings from a slice of rat auditory cortex. Gamma oscillations are induced by applying kainate. Fast-firing interneurons fire on almost every gamma cycle (bottom trace), while pyramidal cells fire sparsely (top trace). Scale bars: 200 ms and 25 mV. Copyright (2004) National Academy of Sciences, USA. Reproduced with permission.

In their model, each E-cell has an h-current that builds up as the cell is hyperpolarized by the activity of the I-cells, until it reaches a level that forces a spike of the E-cell. Abstractly, adaptation-based and h-current-based weak PING are similar. In the former, a hyperpolarizing current is activated by firing, then gradually decays in the absence of firing; in the latter, a depolarizing current is inactivated by firing, then gradually recovers in the absence of firing.

32.1 Stochastic Weak PING

We begin with the code generating Fig. 30.4. We reduce the mean external drive \bar{I}_E , but instead each E-cell now receives a sequence of brief excitatory synaptic input pulses, modeled as in Section 20.2, with parameters $\tau_{r,E}$, $\tau_{\text{peak},E}$, $\tau_{d,E}$, and $v_{\text{rev},E}$ as in Section 30.2. These pulses arrive on a Poisson schedule with mean frequency f_{stoch} . The Poisson schedules for different E-cells are independent of each other, and are discretized as described in Appendix C.11, with the time step Δt used to integrate the differential equations.

We will describe explicitly what this means. Focus on a single E-cell. Associated with this cell, there is a variable q_{stoch} . In each time step, this variable decays according to the differential equation

$$\frac{dq_{\text{stoch}}}{dt} = -\frac{q_{\text{stoch}}}{\tau_{d,q,E}}, \quad (32.1)$$

where $\tau_{d,q,E}$ is set so that $\tau_{\text{peak},E}$ has the desired value (we always use $\tau_{\text{peak},E} = 0.5 \text{ ms}$, as in Chapter 30). We discretize all differential equations using the midpoint method, even eq. (32.1), which we could of course also solve analytically. At the end of the time step, q_{stoch} jumps to 1 with probability (see eq. (C.30))

$$\frac{f_{\text{stoch}}}{1000} \Delta t.$$

The jumps in the variables q_{stoch} associated with different E-cells are independent of each other. A second variable associated with each E-cell is the synaptic gating variable s_{stoch} . It satisfies (see eq. (20.7))

$$\frac{ds_{\text{stoch}}}{dt} = q_{\text{stoch}} \frac{1 - s_{\text{stoch}}}{\tau_{r,E}} - \frac{s_{\text{stoch}}}{\tau_{d,E}}.$$

The stochastic input to the E-cell is then (see eq. (20.8))

$$I_{\text{stoch}} = \bar{g}_{\text{stoch}} s_{\text{stoch}} (v_{\text{rev},E} - v),$$

where $\bar{g}_{\text{stoch}} > 0$.

One other detail of the simulations deserves mention: As discussed in Section 24.1, we initialize each E-cell at a random phase, uniformly distributed between 0 and 1, on its limit cycle. The initialization takes into account the deterministic external drive, but *not* the stochastic external drive.

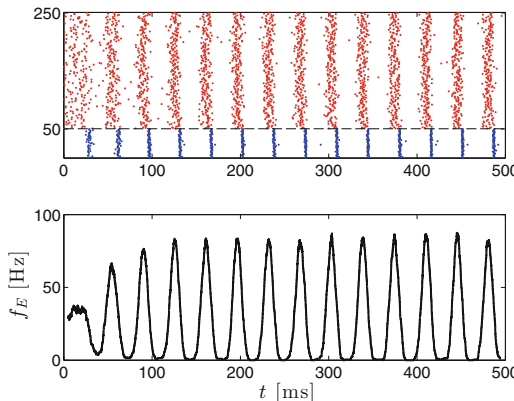


Figure 32.2. Upper panel: Like upper panel of Fig. 30.4, but \bar{I}_E has been reduced from 1.4 to 0.5, and instead the E-cells are driven by Poisson sequences of excitatory synaptic input pulses. The parameters characterizing the stochastic input are $f_{\text{stoch}} = 60$, $\bar{g}_{\text{stoch}} = 0.03$. Lower panel: Time-dependent mean firing frequency of E-cells, as defined in eq. (32.2). The overall mean firing frequencies of the E- and I-cells (see eq. (32.3)) are $\hat{f}_E \approx 27.4 \text{ Hz}$ and $\hat{f}_I \approx 27.0 \text{ Hz}$. [POISSON_PING_1]

Our goal is to set parameters so that participation of the E-cells is sparse — the mean firing frequency of an E-cell should be much below that of an I-cell.

At any given time, most E-cells will be near rest. Therefore plotting the average membrane potential of the E-cells, as we did in most of the figures of Chapter 30, is not the best way of displaying the rhythmicity that emerges in the network here. We plot instead the *time-varying mean firing frequency*, $f_E = f_E(t)$, of the E-cells, which we define as follows:

$$f_E(t) = 1000 \times \frac{\text{number of spikes of E-cells in interval } [t - 5, t + 5]}{10N_E}. \quad (32.2)$$

For t within less than 5 ms of the start or the end of the simulation, we leave $f_E(t)$ undefined. The factor of 1000 in eq. (32.2) is needed because we measure time in ms, but frequency in Hz. Finally, we also define the *overall mean firing frequencies*, \hat{f}_E and \hat{f}_I , of the E- and I-cells. The definition of \hat{f}_E is

$$\hat{f}_E = 1000 \times \frac{\text{number of spikes of E-cells overall}}{\text{time simulated (in ms)} \times N_E}, \quad (32.3)$$

and the definition of \hat{f}_I is analogous. We want to set parameters so that the E-cells have mean firing frequencies far below those of the I-cells, so $\hat{f}_E \ll \hat{f}_I$.

Figure 32.2 shows results of a first network simulation. There is a very clean oscillation visible in Fig. 32.2, but it is a bit slow for a gamma oscillation (below 30Hz), and the E- and I-cells fire at approximately equal mean frequencies, once per population cycle. To reduce the E-cell participation rate, we raise the excitability of the I-cells, by increasing \bar{I}_I from 0 to 0.8. This should cause the I-cell spike volleys to be triggered more quickly, aborting some of the E-cell spiking activity. Indeed that is precisely what happens; see Fig. 32.3, where the E-cells participate on fewer than every second population cycle, on the average: $\hat{f}_E \approx 16.3$ Hz, $\hat{f}_I \approx 39.6$ Hz. (\hat{f}_I is approximately the frequency of the population rhythm.)

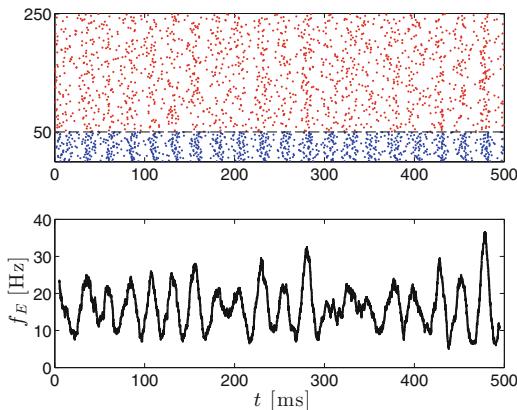


Figure 32.3. Like Fig. 32.2, but with $\bar{I}_I = 0.8$, $\sigma_I = 0.05$. Now the overall mean firing frequencies are $\hat{f}_E \approx 16.3$ Hz, $\hat{f}_I \approx 39.6$ Hz. [POISSON_PING_2]

How changes in the network parameters affect stochastic weak PING is not satisfactorily understood at the present time. However, not surprisingly, sparseness

of E-cell firing is promoted by factors that make inhibitory feedback faster and more effective. Such factors include large \bar{I}_I (but not too large, so that the I-cells still fire only in response to E-cell activity), large \hat{g}_{EI} and \hat{g}_{IE} , and small \hat{g}_{II} (yet still large enough to keep the I-cells from firing without being prompted by the E-cells). Figure 32.4 shows an example in which I deliberately chose parameters to make E-cell firing sparse. I left out all network heterogeneity in this example, to make sure that \hat{f}_E is not affected by *suppression* of E-cells with low external drive, but only by *cycle skipping* resulting from random lulls in the Poisson sequence of excitatory input pulses. Individual E-cells participate on approximately every fifth population cycle on the average in Fig. 32.4.

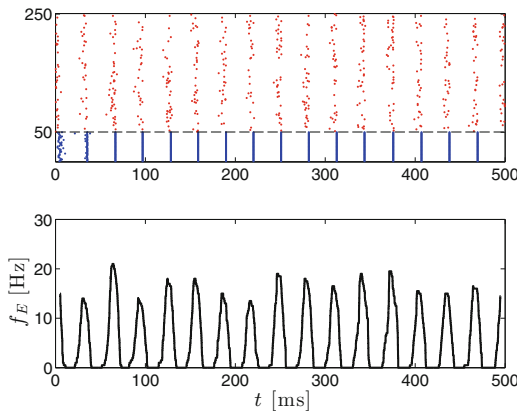


Figure 32.4. Spike rastergram of a stochastically driven weak PING network (top), and time-dependent mean firing frequency of the E-cells (bottom). The parameters are $N_E = 200$, $N_I = 50$, $\bar{I}_E = 0.6$, $\sigma_E = 0$, $\bar{I}_I = 0.6$, $\sigma_I = 0$, $\hat{g}_{EE} = 0$, $\hat{g}_{EI} = 1.25$, $\hat{g}_{IE} = 1.25$, $\hat{g}_{II} = 0.4$, $p_{EI} = 1$, $p_{IE} = 1$, $p_{II} = 1$, $\tau_{r,E} = 0.3$, $\tau_{\text{peak},E} = 0.3$, $\tau_{d,E} = 3$, $v_{\text{rev},E} = 0$, $\tau_{r,I} = 0.3$, $\tau_{\text{peak},I} = 0.3$, $\tau_{d,I} = 9$, $v_{\text{rev},I} = -75$, $f_{\text{stoch}} = 40$, $g_{\text{stoch}} = 0.1$. Here the overall mean frequency of the E-cells is $\hat{f}_E \approx 5.7$ Hz, and that of the I-cells is $\hat{f}_I \approx 31.7$ Hz. [POISSON_PING_3]

It is interesting to plot a single E-cell voltage trace; see Fig. 32.5. (I intentionally picked one that fires four spikes in the simulated time interval; most fire fewer than four.) When comparing with the upper trace of Fig. 32.1, you will see significant differences. In particular, the firing of the pyramidal cell in Fig. 32.1 is fairly regular, while in Fig. 32.5, the inter-spike intervals vary greatly. Also, the pyramidal cell in Fig. 32.1 has a rising membrane potential between spikes (with fluctuations superimposed), whereas the voltage trace in Fig. 32.5 shows oscillations around a roughly constant mean between spikes. Both of these discrepancies could be explained by an adaptation current, brought up by firing and gradually decaying between spikes. We will next consider networks in which there is such an adaptation current in the E-cells.

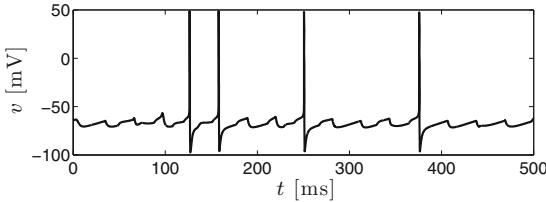


Figure 32.5. Voltage trace of one of the E-cells in Fig. 32.4. [POISSON_PING_3_VOLTAGE_TRACE]

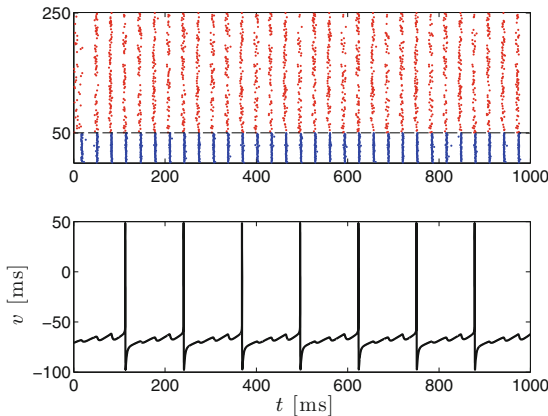


Figure 32.6. Spike rastergram of a PING network with an M-current in the E-cells (top), and voltage trace of one of the E-cells (bottom). The parameters are $N_E = 200$, $N_I = 50$, $\bar{I}_E = 3.0$, $\sigma_E = 0.05$, $\bar{I}_I = 0.7$, $\sigma_I = 0.05$, $\hat{g}_{EE} = 0$, $\hat{g}_{EI} = 0.5$, $\hat{g}_{IE} = 0.5$, $\hat{g}_{II} = 0.5$, $p_{EI} = 0.5$, $p_{IE} = 0.5$, $p_{II} = 0.5$, $\tau_{r,E} = 0.5$, $\tau_{peak,E} = 0.5$, $\tau_{d,E} = 3$, $v_{rev,E} = 0$, $\tau_{r,I} = 0.5$, $\tau_{peak,I} = 0.5$, $\tau_{d,I} = 9$, $v_{rev,I} = -75$, $\bar{g}_M = 1.0$. The overall mean frequency of E-cells is $\hat{f}_E \approx 10$ Hz, and that of the I-cells is $\hat{f}_I \approx 29$ Hz. [M_CURRENT_PING_1]

32.2 Adaptation-Based, Deterministic Weak PING

Again we begin with the code generating Fig. 30.4. We add to the E-cells the model M-current of Section 9.1. We take the maximum conductance \bar{g}_M to be the same for all E-cells. We initialize each E-cell at a random phase, uniformly distributed between 0 and 1, on its limit cycle. The M-current is considered part of the neuronal model, so it is turned on during the preliminary calculation that initializes the E-cells. Because the M-current is active even in the absence of firing (see Section 9.1), we must raise the drive to the E-cells to maintain a gamma frequency rhythm. As in Section 32.1, sparseness of E-cell firing is promoted by making the inhibitory feedback loop more responsive and more effective: We take \bar{I}_I to be larger than in Fig. 30.4, and we double \hat{g}_{EI} and \hat{g}_{IE} , in comparison with the simulation of Fig. 30.4. We also double \hat{g}_{II} , but for a different reason: With

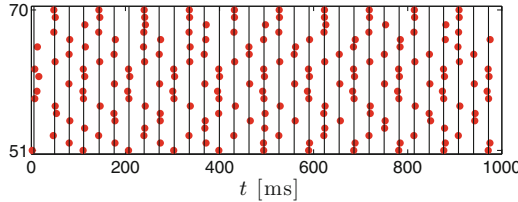


Figure 32.7. Close-up of the rastergram in Fig. 32.6, showing only the spike times of the first 20 E-cells. The vertical lines indicate “local maxima of the overall E-cell firing rate.” (For the precise definition of that, consult the Matlab code that generates the figure.) [M_CURRENT_PING_1_CLOSEUP]

our parameter choices as described so far, some I-cells fire without being prompted by an E-cell spike volley. Raising \hat{g}_{II} prevents this. Figure 32.6 shows a simulation with these parameter choices. In two regards, there appears to be a better match with Fig. 32.1 in Fig. 32.6 than in Fig. 32.5: There is now an upward trend between spikes (although a slight one), and the firing of the E-cell is regular, just much slower than the population rhythm.

A closer look at the rastergram reveals — not surprisingly, considering the regularity of the voltage trace in Fig. 32.6 — approximate *clustering* of the E-cell action potentials. Figure 32.7 is a close-up of Fig. 32.6, and demonstrates the clustering. The spiking pattern is shown for 20 E-cells in Fig. 32.7, cells 51 through 70 in the network. (Cells 1 through 50 are I-cells.) Some E-cells fire on one out of three population cycles, others on one out of four, and some cells toggle between these two patterns.

Shortening the decay time constant of inhibition in Fig. 32.6, while leaving all other parameters unchanged, results in a higher population frequency, but in similar E-cell firing rates, and therefore sparser E-cell participation, i.e., more clusters; see Fig. 32.8. Shortening the decay time constant of adaptation (here, of the M-current), while leaving all other parameters unchanged, results in a slight increase in the population frequency, but in a substantial increase in the E-cell firing rate, and therefore less sparse E-cell participation, i.e., fewer clusters; see Fig. 32.9. The population fires another volley as soon as inhibition falls to a sufficiently low level, while an individual cell fires another action potential as soon as its adaptation (M-current) falls to a sufficiently low level. For detailed analyses of the parameter dependence of the number of clusters and the population frequency in adaptation-based weak PING, see [89] and [98].

For the parameters of Fig. 32.6, the clustered solution shown in the figure is not the only possible clustered solution. In particular, if all cells are initialized approximately equally, there will be one dominating cluster, much larger than the others. To demonstrate this, assume that for $-200 \leq t \leq 0$, the drive \bar{I}_E and \bar{I}_I are zero, with all other parameters as in Fig. 32.6. By time $t = 0$, all cells then come to rest to very good approximation, regardless of how they are initialized at

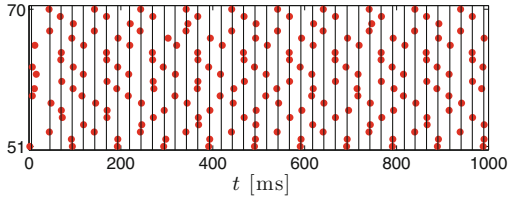


Figure 32.8. Same as Fig. 32.7, but with $\tau_{d,I} = 4.5$. The overall mean frequency of E-cells is $\hat{f}_E \approx 10$ Hz, and that of the I-cells is $\hat{f}_I \approx 38$ Hz. [M_CURRENT_PING_2_CLOSEUP]

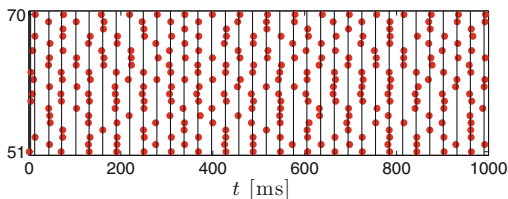


Figure 32.9. Same as Fig. 32.7, but with the decay time constant of the M-current halved. The overall mean frequency of E-cells is $\hat{f}_E \approx 15$ Hz, and that of the I-cells is $\hat{f}_I \approx 33$ Hz. [M_CURRENT_PING_3_CLOSEUP]

time $t = -200$. Assume that at time $t = 0$, \bar{I}_E is raised to 3.0, and \bar{I}_I to 0.7, the values of Fig. 32.6. The result is shown in Fig. 32.10. There are three clusters — two smaller ones, and a dominating one of approximately twice the size of the two smaller ones.

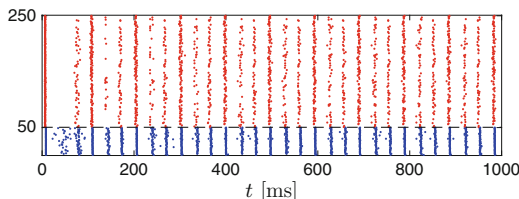


Figure 32.10. Simulation as in Fig. 32.6, but with all cells starting at time 0 from the equilibrium positions corresponding to $\bar{I}_E = \bar{I}_I = 0$. [M_CURRENT_PING_1_FROM_REST]

32.3 Deterministic Weak PING Without Any Special Currents

We saw that in ING clustering is possible (although fragile) with just the spike-generating sodium and delayed rectifier potassium currents; see Section 31.4. Is the same true in PING? The answer is yes. An example is shown in Fig. 32.11. However, the parameters here seem unlikely to be biologically realistic; the E-to-I synapses are extremely strong in fast, in order to generate very rapid inhibitory feedback. I have not been able to find a similar example with biologically more plausible parameters.

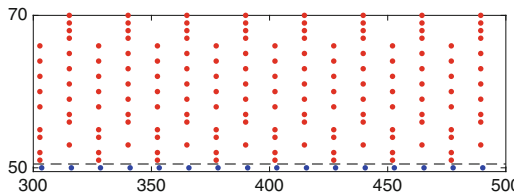


Figure 32.11. Spike rastergram of a PING network with $N_E = 200$, $N_I = 50$, $\bar{I}_E = 1.4$, $\sigma_E = 0$, $\bar{I}_I = 0.2$, $\sigma_I = 0$, $\hat{g}_{EE} = 0$, $\hat{g}_{EI} = 5$, $\hat{g}_{IE} = 0.25$, $\hat{g}_{II} = 0.75$, $p_{EI} = 1$, $p_{IE} = 1$, $p_{II} = 1$, $\tau_{r,E} = 0.05$, $\tau_{peak,E} = 0.05$, $\tau_{d,E} = 1$, $v_{rev,E} = 0$, $\tau_{r,I} = 0.1$, $\tau_{peak,I} = 0.1$, $\tau_{d,I} = 9$, $v_{rev,I} = -75$. Only the last 200 ms of a 500 ms simulation and only spike times of one of the I-cells and 20 of the E-cells are shown. [PING_CLUSTERS]

We will discuss clustering in PING networks without adaptation in a more theoretical way using what is arguably the simplest possible PING-like network: Two identical LIF neurons, with membrane potentials v_1 and v_2 , governed by

$$\frac{dv_1}{dt} = -\frac{v_1}{\tau_m} + I - g_{IS}(t)v_1 \quad \text{for } v_1 < 1, \quad (32.4)$$

$$\frac{dv_2}{dt} = -\frac{v_2}{\tau_m} + I - g_{IS}(t)v_2 \quad \text{for } v_2 < 1, \quad (32.5)$$

$$\frac{ds}{dt} = -\frac{s}{\tau_I} \quad \text{for } v_1 < 1 \text{ and } v_2 < 1, \quad (32.6)$$

$$v_1(t+0) = 0 \quad \text{if } v_1(t-0) = 1, \quad (32.7)$$

$$v_2(t+0) = 0 \quad \text{if } v_2(t-0) = 1, \quad (32.8)$$

$$s(t+0) = 1 \quad \text{if } v_1(t-0) = 1 \text{ or } v_2(t-0) = 1. \quad (32.9)$$

We assume drive above the firing threshold: $\tau_m I > 1$. We refer to the two LIF neurons as the *E-cells*. The firing of one E-cell is assumed to trigger an inhibitory response. There are no I-cells explicitly included in this model, but the effect of the inhibitory population is represented by the gating variable s , assumed to be raised to its maximum value 1 in response to firing of one of the two E-cells.

We note that our model system differs from a system of two LIF neurons coupled by inhibitory synapses: Here there is only one single gating variable s ,

affecting both neurons equally. In a network of two LIF neurons with inhibitory coupling, there would be two different gating variables, s_1 and s_2 .

We refer to a solution of (32.4)–(32.9) as a *cluster solution* if the firing of the two E-cells alternates. We call a cluster solution *anti-synchronous* if the firing of the first E-cell always occurs exactly in the middle of the inter-spike interval of the second E-cell, and vice versa.

To study phase-locking in our system, we assume that the first E-cell fires at time 0, so $v_1(0+0) = 0$ and $s(0+0) = 1$. We use the letter x to denote $v_2(0+0)$, and assume $0 < x < 1$. We denote by T_1 the smallest positive time with $v_2(T_1 - 0) = 1$, and define $\psi(x) = v_1(T_1)$. We record some simple properties of the function ψ in the following proposition; compare Fig. 32.12.

Proposition 32.1. (a) *The function $\psi = \psi(x)$, $0 < x < 1$, is strictly decreasing and continuous, with $0 < \psi(x) < 1$ and $\lim_{x \searrow 0} \psi(x) = 1$. (b) The limit $\lim_{x \nearrow 1} \psi(x)$ equals 0 if $0 \leq g_I \leq I - 1/\tau_m$, and lies strictly between 0 and 1 if $g_I > I - 1/\tau_m$.*

Proof. Exercise 4. □

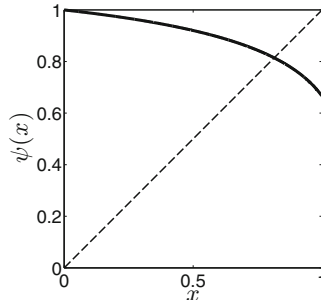


Figure 32.12. The function ψ defined in this section, for $\tau_m = 10$, $I = 0.12$, $g_I = 0.05$, $\tau_I = 5$. [PLOT_PSI]

We denote by T_2 the smallest positive time with $v_1(T_2 - 0) = 1$, and define $\phi(x) = v_2(T_2)$. For all $x \in (0, 1)$,

$$\phi(x) = \psi(\psi(x)) \tag{32.10}$$

(see exercise 5). For the parameters of Fig. 32.12, the graph of ϕ is shown in Fig. 32.13. In words, if the first E-cell fires, and the second E-cell is at membrane potential $x \in (0, 1)$, then the next time when the first E-cell fires, the second E-cell will be at membrane potential $\phi(x) \in (0, 1)$.

The limits of ψ and ϕ as $x \searrow 0$ or $x \nearrow 1$ exist by Proposition 32.1. We denote them by $\psi(0)$, $\psi(1)$, $\phi(0)$, and $\phi(1)$. There is a possible point of confusion here, which we will address next. Note that in Fig. 32.13, $\phi(0)$ is not zero. In fact, Proposition 32.1 implies that $\phi(0) = 0$ if and only if $g_I \leq I - 1/\tau_m$, and

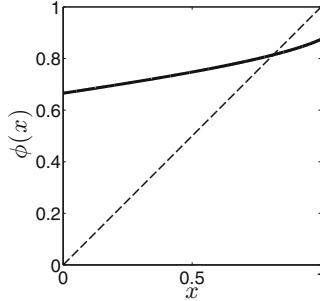


Figure 32.13. The function ϕ defined in this section, for $\tau_m = 10$, $I = 0.12$, $g_I = 0.05$, $\tau_I = 5$. [PLOT_PHI]

in Fig. 32.13, $g_I = 0.05 > I = 1/\tau_m = 0.02$. You might think that this should imply that perfect synchrony of the two E-cells is not a possibility. This is not correct. Perfect synchrony is always a possibility in this model. If the two E-cells fire at exactly the same time once, the feedback inhibition will affect them in exactly the same way, and they will therefore always fire in synchrony in the future. However, if they fire only in *approximate* synchrony, the one that fires earlier can very substantially delay the one that fires later. So $\phi(0) > 0$ does not imply that synchrony is impossible, but it does imply that synchrony is unstable.

The solution of (32.4)–(32.9) is a cluster solution if and only if $x = v_2(0 + 0)$ is a fixed point of ϕ , and an anti-synchronous solution if and only if x is a fixed point of ψ . The fixed point x_* in Fig. 32.13 is stable because $|\phi'(x_*)| < 1$; see Appendix B. It is the same as the fixed point in Fig. 32.12. It corresponds to the anti-synchronous solution, which is stable here.

In Figs. 32.12 and 32.13, one would have to choose $g_I \leq 0.02$ for $\psi(1)$ to become 0, and therefore $\phi(0)$ to become 0 and $\phi(1)$ to become 1. In Fig. 32.14, we show ψ and ϕ for the same parameters as in Figs. 32.12 and 32.13, but with g_I lowered to 0.015. Now $\phi(0) = 0$, but $\phi'(0) > 1$, and this implies that synchrony of the two E-cells is still unstable. The anti-synchronous solution is still stable.

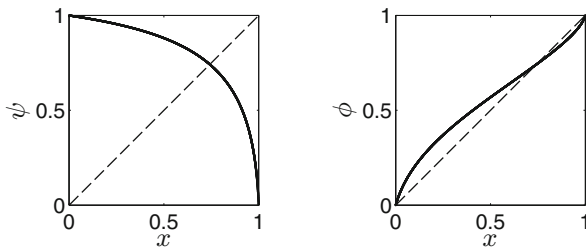


Figure 32.14. The functions ψ and ϕ defined in this section, for $\tau_m = 10$, $I = 0.12$, $g_I = 0.015$, $\tau_I = 5$. Here g_I is so small that $\psi(1) = 0$, and therefore $\phi(0) = 0$ and $\phi(1) = 1$. Synchrony of the two E-cells is still unstable. [PLOT_PSI_PHI]

This discussion suggests that in an E-I network with a very rapid inhibitory response, the E-cells will cluster, not synchronize. PING rhythms are possible only because the inhibitory response is *not* instantaneous. For instance, if a small delay between the firing of an E-cell and the inhibitory response (the reset of s to 1) is added to our model, synchrony becomes stable; see exercise 6.

Adaptation currents amplify the tendency towards clustering by holding back cells that are behind, since those cells have a stronger active adaptation current.

Exercises

- 32.1. (*) In the simulation of Fig. 32.4, what happens if you double (a) f_{stoch} , or (b) g_{stoch} ? How are \hat{f}_E and \hat{f}_I affected?
- 32.2. (*) (†) Produce a figure similar to Fig. 32.4, but now using independent discrete Ornstein-Uhlenbeck processes (see eqs. (C.20)–(C.22) in Appendix C.6) in place of the independent Poisson sequences of excitatory input pulses used in Section 32.1. Note that this is different from what you did in exercise 30.7. There the same Ornstein-Uhlenbeck process was used for all neurons. Here the Ornstein-Uhlenbeck processes used for different neurons are independent of each other. Unlike the *global stochastic drive* in exercise 30.7, this sort of *cell-specific stochastic drive* cannot produce strongly varying population frequencies, but it can produce sparse participation of the E-cells.
- 32.3. (*) How does Fig. 32.7 change (a) when \hat{g}_{IE} is doubled, (b) when \bar{g}_M is doubled?
- 32.4. (†) Prove Proposition 32.1.
- 32.5. Explain eq. (32.10).
- 32.6. (*) In the code that generates Fig. 32.14, add a delay of 2ms between the firing of an E-cell and the inhibitory response. Show that this renders synchrony of the two E-cells stable, although anti-synchronous clustering remains stable.
- 32.7. (*) (†) Generalize the model given by (32.4)–(32.9) to $N > 2$ LIF neurons, again with common feedback inhibition triggered immediately when just one of the LIF neurons fires. Initializing at random, does one typically obtain clustering, splay state solutions, or what else?

Chapter 33

Beta Rhythms

Oscillations at frequencies of approximately 12–30 Hz — roughly half the gamma frequency — are called *beta oscillations* or *beta rhythms* in neuroscience. Many experimental studies have linked beta oscillations to motor function. They are, in particular, more pronounced during holding periods, and attenuated during voluntary movement. Engel and Fries [44] have hypothesized that more generally, beta oscillations may signal the expectation or intent of maintaining a sensorimotor or cognitive *status quo*. (The *sensorimotor* areas of the brain are those that combine sensory and motor functions.) This fits with the observation that in patients suffering from Parkinson’s disease and the associated slowed movement (*bradykinesia*), power and coherence of beta oscillations in the *basal ganglia* are abnormally high, and are attenuated by *levodopa*, a drug commonly used to treat Parkinson’s disease [20].

Many mechanisms that can produce beta oscillations have been proposed, and it is thought that beta-band oscillations in different parts of the brain originate in different ways. Here we study just a few of the many possible mechanisms.

33.1 PING-Like Beta Rhythms

The interaction of E- and I-cells, as in PING, can produce oscillations at frequencies below the gamma range. We have already mentioned reference [175] as an example. In [175], oscillations in a model network at frequencies around 10 Hz arise from the interaction of excitatory and inhibitory cell populations. The inhibitory synapses in [175] are GABA_B receptor-mediated, and therefore much slower than GABA_A receptor-mediated ones.

A PING rhythm can in principle be slowed down from gamma frequency to beta frequency in several ways. For instance, we can (1) make inhibition

Electronic supplementary material: The online version of this chapter (doi: [10.1007/978-3-319-51171-9_33](https://doi.org/10.1007/978-3-319-51171-9_33)) contains supplementary material, which is available to authorized users.

longer-lasting, or (2) make inhibition stronger, or (3) lower the external drive to the E-cells. These three possibilities are illustrated by Figs. 33.1–33.3.

One must make the decay time constant of the I-to-E synapses very much longer (from 9 ms to 90 ms) to turn the gamma rhythm of Fig. 30.4 into the beta

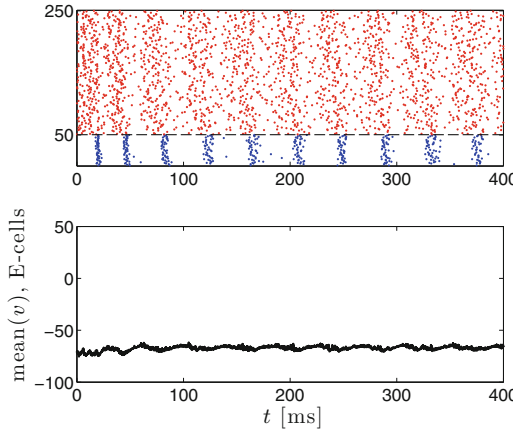


Figure 33.1. Spike rastergram of an E-I network (top), and mean membrane potential of the E-cells (bottom). All parameters as in Fig. 30.4, except the decay time constant of I-to-E synapses is 90 ms here, while it was 9 ms in Fig. 30.4. (The decay time constant of I-to-I synapses is still 9 ms, as in Fig. 30.4.) Note that the simulated time interval is twice longer than in Fig. 30.4. [PINB_1]

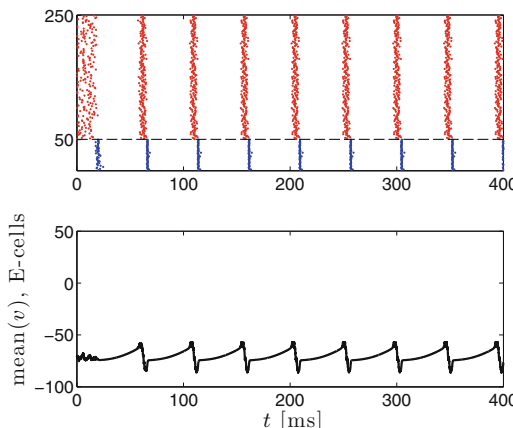


Figure 33.2. Spike rastergram of an E-I network (top), and mean membrane potential of the E-cells (bottom). All parameters as in Fig. 30.4, except $\hat{g}_{IE} = 10$ here, while $\hat{g}_{IE} = 0.25$ in Fig. 30.4. [PINB_2]

rhythm of Fig. 33.1. Also notice that the synchrony of the E-cells is fairly poor in Fig. 33.1. This is an effect of heterogeneity in external drives to the E-cells, and

heterogeneity in the number of inhibitory synaptic inputs per E-cell. The same level of heterogeneity has little effect in Fig. 33.2 (compare exercise 1). However, to turn the gamma rhythm of Fig. 30.4 into the beta rhythm of Fig. 33.2, one must strengthen I-to-E inhibition by a very large factor.

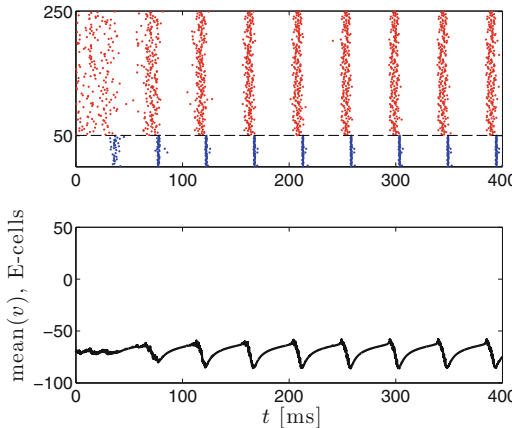


Figure 33.3. Spike rastergram of an E-I network (top), and mean membrane potential of the E-cells (bottom). All parameters as in Fig. 30.4, except $\bar{I}_E = 0.4$ here, while $\bar{I}_E = 1.4$ in Fig. 30.4. [PINB_3]

33.2 A Period-Skipping Beta Rhythm, and Cell Assemblies

In this section we describe a model introduced in [181], and simplified and studied in greater detail in [122]. The model explains experimental results presented in [181] and [122]. In these experiments, tetanic stimulation of a hippocampal slice generates a gamma oscillation, which after less than a second slows down and transitions into a beta oscillation.

From a more general point of view, these studies are about *cell assemblies*. The concept of a cell assembly was proposed in 1949 by the neuropsychologist Donald Hebb [73], and has been greatly influential in neuroscience. Hebb suggested that the brain represents information in the form of ensembles of neurons, which he called cell assemblies, firing together, with the information encoded in membership in the assembly.

Hebb's ideas about cell assemblies are closely linked to his hypotheses about *plasticity*, i.e., the modification of synaptic strengths as a result of experience, or learning. He suggested that if neuron A participates in making neuron B fire, then the excitatory synaptic connection from A to B will be strengthened [73]. This is often summarized by saying: “Neurons that fire together wire together.” The slogan is memorable, but does not precisely reflect Hebb's hypothesis, as “together” suggests symmetry between A and B, whereas in Hebb's hypothesis, A and B clearly do not play the same role.

For an extension of Hebb's idea, referred to as *spike timing-dependent plasticity (STDP)*, experimental evidence was presented in [68]: The connection from A to B (pyramidal cells in layer V of rat neocortex) was shown to be strengthened when A fires just before B (*Hebbian learning*), and weakened when B fires just before A (*anti-Hebbian learning*). We will study a mathematical model of STDP in the last two chapters of this book.

For now, we return to [181] and [122]. The firing during the gamma oscillation activates an AHP current in the participating pyramidal cells [181], modeled as an M-current in [122]. This is one central ingredient for explaining the slow-down. It is, however, not the only ingredient. The introduction of an adaptation current by itself would simply generate a *clustered* gamma oscillation, i.e., it would lead to a reduction in the mean firing frequency of individual pyramidal cells, without bringing the population frequency into the beta range; see Section 32.2, and also Fig. 33.4.

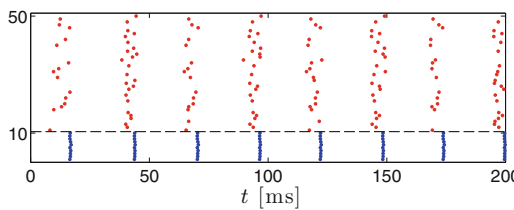


Figure 33.4. Clustered PING rhythm similar to that in Fig. 32.6. The strength of the M-current is chosen deliberately here to create two clusters: $\bar{g}_M = 0.5$. To make the details of the clustering easier to see, the number of neurons in the network is reduced: $N_E = 40$, $N_I = 10$. To obtain a network comparable to the larger one, the reduction in N_E and N_I must be accompanied by an increase in the connection probabilities p_{EI} , p_{IE} , p_{II} (see Section 30.3). Since sparseness and randomness of connectivity is not the main focus here, we simply use all-to-all connectivity. All other parameters are as in Fig. 32.6. The population frequency is slightly below 40 Hz. [M_CURRENT_PING_4]

The second central ingredient in the model of [181] and [122] is plasticity. The gamma oscillation was shown in [181] to lead to a strengthening of excitatory synaptic connections among the pyramidal cells participating in the oscillation. The effect is that pyramidal cells that participate in the gamma oscillation don't cluster; they (approximately) synchronize during the later phase of the experiment; see Fig. 33.5. Note that the transition from Fig. 33.4 to Fig. 33.5 illustrates that recurrent excitation can *lower* the network frequency.

The E-to-E connectivity introduced here is symmetric: The connection from B to A is strengthened just as much as the connection from A to B. As pointed out earlier, this is not quite in line with the original Hebbian hypothesis, and certainly not with STDP as described in [68], but it is in line with yet another variation on the Hebbian hypothesis, formulated, for instance, in [32]: (a) Temporal correlation of pre- and post-synaptic activity will lead to synaptic strengthening, and (b) lack of correlation will lead to synaptic weakening.

In both the experiments and the model of [181] and [122], some E-cells participated in the gamma oscillation, while others did not. Following [122], we call the two groups the E_P -cells and the E_S -cells (with P standing for *participating*, and S for

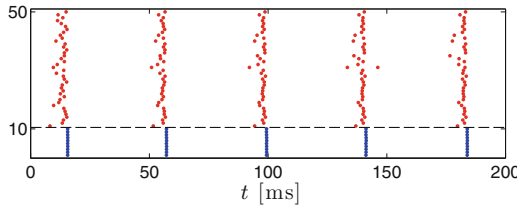


Figure 33.5. Effect of introducing E-E connections ($\hat{g}_{EE} = 0.35$) in Fig. 33.4. There is now a beta rhythm with a frequency slightly under 25 Hz. [M_CURRENT_PING_5]

suppressed). Experimentally, the separation into E_P - and E_S -cells was accomplished by treating some of the pyramidal cells with potassium-free artificial cerebrospinal fluid (ACSF), which lowers their excitability. In the model, different E-cells received different external drives. This can result in sharp *thresholding*: The most strongly driven E-cells participate on each cycle of the gamma oscillation, while (most of) the others do not participate at all; see Chapter 37.

The division of the E-cells into E_P - and E_S -cells makes the plasticity of the E-to-E connections selective: Only connections among E_P -cells are strengthened (or, in our model, created). Figure 33.6 shows what happens when in Fig. 33.5, only half the E-cells, the ones with neuronal indices 31 through 50, are connected synaptically.

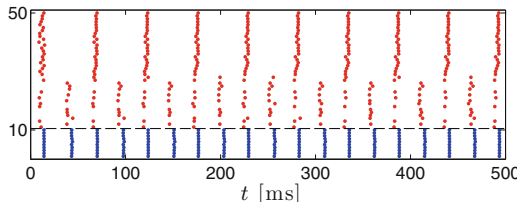


Figure 33.6. Effect of introducing E-to-E connections only among cells 31 through 50 (half of all E-cells) in Fig. 33.4. There is a population gamma rhythm with two clusters. Those E-cells that are synaptically connected all belong to the same cluster, and therefore fire at half the gamma frequency, slightly below 20 Hz here. [M_CURRENT_PING_6]

In [122], it was demonstrated, both experimentally and in the simulations, that (nearly) all E_S -cells fired on precisely those gamma cycles on which the E_P -cells did not fire. In other words, the two E-cell clusters were the E_P -cells and the E_S -cells. This *temporal separation* of E_P - and E_S -cells is not seen in Fig. 33.6, but can be reproduced in simulations when one includes other plastic changes likely

caused by the gamma oscillation. In [122], it was assumed that the E_S -to-I synapses are weakened during the gamma oscillation, when the E_S -cells are silent and the I-cells are active. Indeed, if we halve the strength of the E_S -to-I synapses in Fig. 33.6, fairly clean temporal separation of E_P -cells and E_S -cells results; see Fig. 33.7.

It is easy to see why weakening the E_S -to-I synapses will tend to promote temporal separation of E_P - and E_S -cells. Let us call the gamma cycles on which the E_P -cells fire the *on-beats*, and the gamma cycles on which they don't fire the *off-beats*. Weakening the E_S -to-I synapses causes the I-cell spike volleys on the off-beats to occur slightly later, and thereby allows more E_S -cells to fire on the off-beats. This falls short of explaining why the separation should become as clean as in Fig. 33.7, but in fact it is *not* always as clean; see exercise 2.

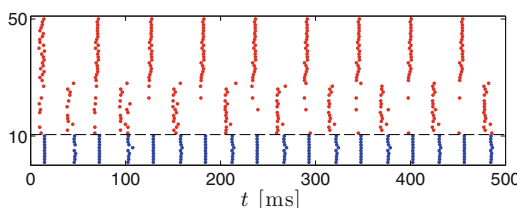


Figure 33.7. Like Fig. 33.6, with the strengths of the synapses from E -cells 11 through 30 (the E_S -cells) cut in half. [M_CURRENT_PING_7]

The reasoning of the preceding paragraph suggests another way of separating E_P - and E_S -cells into two nearly disjoint clusters: We can make the on-beats occur slightly earlier, for instance, by slightly raising external drive to the E_P -cells (but not to the E_S -cells). The E_P -cells participated in the gamma oscillation because they were more strongly driven, or perhaps because they were intrinsically more easily excitable, than the others. So greater external drive to the E_P -cells during the beta oscillation could be seen as a model of greater intrinsic excitability. Alternatively, the increased drive to the E_P -cells might also be thought of as reflecting slow recurrent excitation among the E_P -cells. Figure 33.8 shows that raising the drive to the E_P -cells can lead to the temporal separation of E_P - and E_S -cells even without altering the E_S -to-I synapses. The increased drive makes it easier for the E_P -cells to silence the E_S -cells on the on-beats.

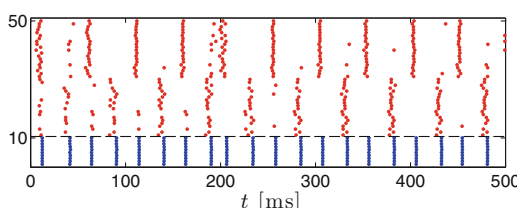


Figure 33.8. Like Fig. 33.6, with the external drive to the E_P -cells (but not the E_S -cells) raised by 20%. [M_CURRENT_PING_8]

We think of the EP-cells as forming a Hebbian cell assembly. From this point of view, what is interesting about Figs. 33.7 and 33.8 is that plastic changes help the cell assembly, which started out firing at gamma frequency, survive the gamma-beta transition caused by the rising M-current.

33.3 A Non-synaptic Beta Rhythm

In [130], a beta rhythm in layer V of rat neocortical slices was examined experimentally and via computer simulations. An interesting feature of this rhythm is that it survives disruption of AMPA- and GABA_A receptor-mediated synaptic transmission. It does depend on gap junctions and M-currents.

The model in [130] is quite complex. Most of the model neurons, the ones that are primarily responsible for generating the rhythm, represent *intrinsically bursting* (IB) cells, a class of pyramidal cells in neocortex. (The RTM model, by contrast, represents *regular spiking* (RS) pyramidal cells.) The neuronal models have many compartments, and the gap junctions are assumed axo-axonal. The drive that gives rise to the rhythm is stochastic.

We will not re-implement this complex model here, but merely show in Fig. 33.9 that the combination of M-currents and gap junctions can, in a network of RTM neurons, generate a beta frequency oscillation. We model gap junctions as described in Chapter 21, with

$$g_{\text{gap},ij} = \begin{cases} \hat{g}_{\text{gap}} / (p_{\text{gap}}(N - 1)) & \text{with probability } p_{\text{gap}}, \\ 0 & \text{with probability } 1 - p_{\text{gap}}, \end{cases}$$

where N denotes the number of neurons in the network; $N = 200$ in Fig. 33.9. The cells in Fig. 33.9 fire in (loosely defined) clusters; see exercise 4.

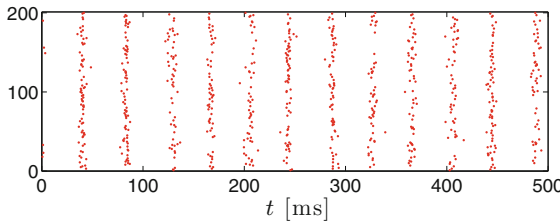


Figure 33.9. A network of 200 RTM neurons, with M-currents ($\bar{g}_M = 1$) and gap junctions ($p_{\text{gap}} = 0.1$, $\hat{g}_{\text{gap}} = 0.2$) but no synaptic connections. Other parameters here are $I_E = 3$ and $\sigma_E = 0.05$. [\[M_CURRENT_BETA_WITH_GJ\]](#)

Exercises

- 33.1. (*) A PING rhythm can be slowed down to beta frequency by increasing τ_I , the decay time constant of inhibition (Fig. 33.1), or by raising \hat{g}_{IE} , the parameter determining the strength of I-to-E synapses (Fig. 33.2). Comparison

of the two figures shows that the effects of drive heterogeneity become large when τ_I is raised, not when \hat{g}_{IE} is raised. We won't give a rigorous explanation of this observation. However, plot $0.25e^{-t/90}$ and $10e^{-t/9}$ as functions of $t \in [0, 50]$ in a single figure, and explain why what you see yields at least a heuristic explanation.

- 33.2. (*) The nearly strict temporal separation of E_P - and E_S -cells seen in Fig. 33.7 is not a completely robust effect. To see this, halve the strength of the E_S -to-I synapses in Fig. 33.7 once more. You will see that the temporal separation of E_P - and E_S -cells becomes a bit less clean.
- 33.3. (*) What happens if in Fig. 33.6, you halve the strengths of the E_S -to-I synapses *and* raise the drive to the E_P -cells by 20%?
- 33.4. (*) Demonstrate numerically that the cells in Fig. 33.9 fire in (loosely defined) clusters.

Chapter 34

Nested Gamma-Theta Rhythms

In many brain structures, in particular in the hippocampus, gamma oscillations appear near the crests of much slower, 4–11 Hz oscillations, called *theta oscillations* or *theta rhythms*. For an example, see Fig. 34.1.

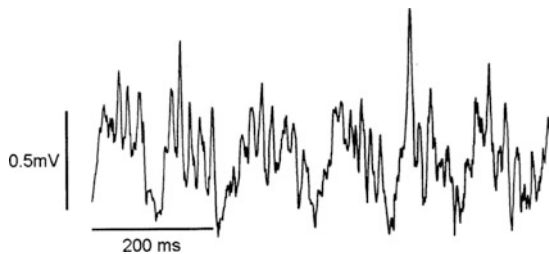


Figure 34.1. Figure 4A of [24], showing gamma oscillations riding (primarily) on the crests of theta oscillations in an in vivo local field potential recording from the CA1 region of mouse hippocampus. Reproduced with publisher's permission.

In rodents, theta oscillations have been linked to exploratory behavior [22], and to learning and memory [72]. Furthermore, gamma oscillations nested in theta oscillations have been hypothesized to serve the purpose of “representing multiple items in an ordered way” [106], with different gamma sub-cycles of the theta cycle corresponding to different items. Note that the number of gamma cycles that fit into a theta cycle is about seven: 20 ms and 140 ms are typical durations of gamma and theta cycles, respectively. Lisman and Idiart [105] have suggested that this may be the reason why the maximal number of items that humans can typically hold in

Electronic supplementary material: The online version of this chapter (doi: [10.1007/978-3-319-51171-9_34](https://doi.org/10.1007/978-3-319-51171-9_34)) contains supplementary material, which is available to authorized users.

brief, transient memory (*working memory*) is on the order of seven (plus or minus two) [118]. Most of us can briefly hold a seven-digit phone number in memory, while we are looking for the phone, but few of us could do the same with a fourteen-digit phone number.

Computationally, one can obtain a gamma oscillation riding on the crests of a theta oscillation simply by driving the E-cells in a PING network at theta frequency; see Section 34.1. Qualitatively, this might model a theta rhythm that is “externally imposed,” projected into the network that we are studying from another brain structure, somewhat reminiscent of a suggestion in [25] that inhibitory “supernetworks” rhythmically entrain large populations of pyramidal cells throughout the brain.

A model network that *intrinsically* generates both the theta rhythm and the gamma rhythm nested in it can be obtained by adding to a PING network a second class of inhibitory cells intrinsically firing at theta frequency. We will call this new class of inhibitory cells the *O-cells*, a terminology that will be motivated shortly. If the O-cells received no input from the PING network, and if they synchronized, then this would not be very different from the PING networks driven at theta frequency discussed in Section 34.1. However, a mechanism by which the O-cells can synchronize is needed. One natural such mechanism would be common input from the PING network. For nested gamma-theta oscillations to result, the O-cells must allow several gamma cycles between any two of their population spike volleys. This can be accomplished in a robust way if the O-cells express a slowly building depolarizing current that is rapidly reduced by firing, such as an h-current, or a slowly decaying hyperpolarizing current that is rapidly raised by firing, such as a firing-induced slow potassium current. Several model networks generating nested gamma-theta rhythms following these ideas have been proposed; examples can be found in [157] and [173].

In Sections 34.2 and 34.3, we describe (in essence) the model from [157], in which the second class of inhibitory cells represent the so-called *oriens lacunosum-moleculare (O-LM) interneurons* [90] of the hippocampus; this is the reason for the name *O-cells*.

34.1 Gamma Rhythms Riding on Externally Imposed Theta Rhythms

Figures 34.2 and 34.3 show examples of PING networks with external input to the E-cells oscillating at theta frequency (8 Hz). In Fig. 34.2, the oscillatory input is a sinusoidal injected *current*, whereas in Fig. 34.3, it is (a bit more in line with [25]) *synaptic inhibition* with an oscillating synaptic gating variable. In both figures, we see bursts of gamma frequency oscillations, occurring in theta frequency packets.

Note that the local field potential in Fig. 34.1 looks quite different from the mean membrane potentials of the E-cells depicted in the middle panels of Figs. 34.2 and 34.3, and from the mean E-cell gating variables depicted in the lower panels of Figs. 34.2 and 34.3. However, this by itself does not necessarily imply that the nested gamma-theta rhythm of Fig. 34.1 has to be fundamentally different from a PING network driven at theta frequency; we don’t know what is a good analogue of

the LFP in our model networks, and neither the mean membrane potential of the E-cells, nor the mean gating variable of the E-cells, are likely to be good analogues.

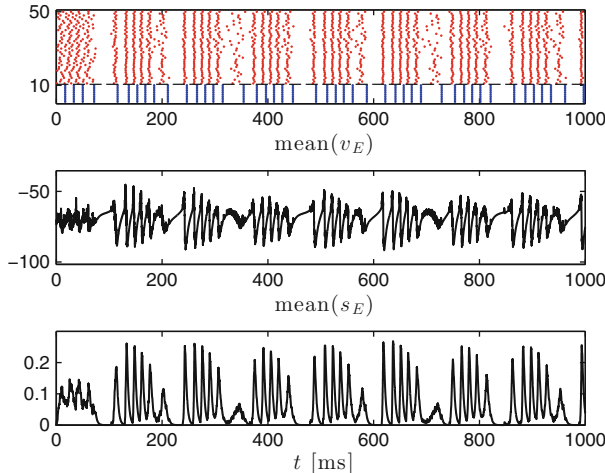


Figure 34.2. A PING network with external drive to the E-cells oscillating at theta frequency. Spike rastergram (top panel), mean of membrane potentials of E-cells (middle panel), mean of gating variables of E-cells (bottom panel). The parameters of the PING network are $N_E = 40$, $N_I = 10$, $\bar{I}_E = 1.4$, $\sigma_E = 0.05$, $\bar{I}_I = 0$, $\hat{g}_{EE} = 0$, $\hat{g}_{EI} = 0.25$, $\hat{g}_{IE} = 0.25$, $\hat{g}_{II} = 0.25$, $p_{EI} = 1$, $p_{IE} = 1$, $p_{II} = 1$, $\tau_{r,E} = 0.5$, $\tau_{peak,E} = 0.5$, $\tau_{d,E} = 3$, $v_{rev,E} = 0$, $\tau_{r,I} = 0.5$, $\tau_{peak,I} = 0.5$, $\tau_{d,I} = 9$, $v_{rev,I} = -75$. The actual drive to the i -th E-cell, however, is not $I_{E,i} = \bar{I}_E(1 + \sigma_E X_i)$, but $(1 + 0.8 \sin(2\pi t/125)) I_{E,i}$, i.e., it oscillates with period 125 ms, or frequency 8 Hz. [\[PING_WITH_THETA_DRIVE\]](#)

34.2 A Model O-LM Cell

The cell bodies of the hippocampal *orientis lacunosum-moleculare* (*O-LM*) interneurons [90] lie in a deep layer of the hippocampus called the *stratum oriens*. Their axonal arbors lie in a superficial layer called the *stratum lacunosum-moleculare*. This explains their name.

O-LM cells are *somatostatin-positive* (SOM+), i.e., they contain the hormone somatostatin. They inhibit *distal dendrites* (dendrites far from the cell body) of pyramidal cells. This is in contrast with the fast-firing basket cells instrumental in generating gamma oscillations, which are *parvalbumin-positive* (PV+) and inhibit pyramidal cells *perisomatically*, i.e., near the cell body. Since we use single-compartment model neurons, the difference between inhibition of distal dendrites and perisomatic inhibition is not represented in our models. However, following [157], we will assume that the inhibitory input to pyramidal cells from O-LM cells rises and decays more slowly than that from fast-firing basket cells. This assumption is in line with experimental evidence; see [69].

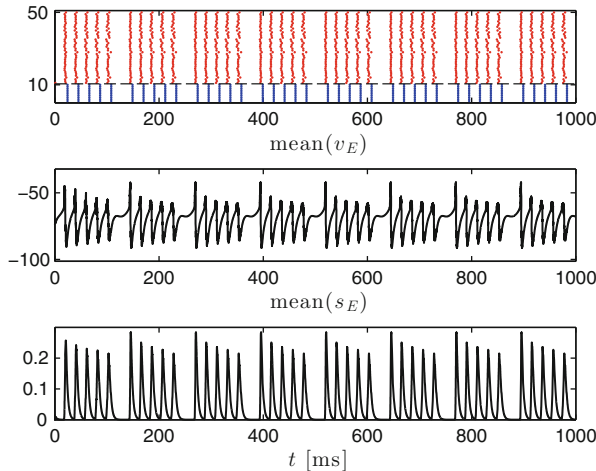


Figure 34.3. Same as Fig. 34.2, but the external current inputs are constant in time ($I_{E,i} = \bar{I}_E(1 + \sigma_E X_i)$), and instead the pulsatile synaptic input $0.2e^{-10\sin^2(\pi t/125)}(v_{rev,I} - v)$ is added to each E-cell. [PING_WITH_THETA_INHIBITION]

In Section 34.3, the O-LM cells will play the role of pacing the theta oscillation. As discussed in the introduction to this chapter, for them to be able to do that robustly, they should express a slowly building depolarizing current that is rapidly reduced by firing, or a slowly decaying hyperpolarizing current that is rapidly raised by firing. In the model of [157], they are assumed to express an h-current, which is rapidly reduced by firing and slowly builds up between action potentials; this is in agreement with experimental evidence [109]. The model O-LM cells of [157] also express a transient (inactivating) hyperpolarizing potassium current called an A-current, again in agreement with experimental evidence [189]. This current will be discussed in detail later.

In [157], the h- and A-currents were added to a single-compartment model with the standard Hodgkin-Huxley currents, that is, the spike-generating sodium, delayed rectifier potassium, and leak currents. That model was of the same form as the RTM and WB models from Sections 5.1 and 5.2, except for the assumption $m = m_\infty(v)$, which was made in Sections 5.1 and 5.2, but not in [157]. We modify the model of [157] in that regard, i.e., we do set $m = m_\infty(v)$. Thus the form of our O-LM cell model, without the h- and A-currents, is precisely the same as that of the RTM and WB models. The constants are

$$C = 1.3 \mu\text{F}/\text{cm}^2, \quad v_{\text{Na}} = 90 \text{ mV}, \quad v_K = -100 \text{ mV}, \quad v_L = -70 \text{ mV}, \\ \bar{g}_{\text{Na}} = 30 \text{ mS}/\text{cm}^2, \quad \bar{g}_K = 23 \text{ mS}/\text{cm}^2, \quad \bar{g}_L = 0.05 \text{ mS}/\text{cm}^2.$$

The functions α_x and β_x , $x = m, h, n$, are

$$\alpha_m(v) = \frac{0.1(v + 38)}{1 - \exp(-(v + 38)/10)}, \quad \beta_m(v) = 4 \exp(-(v + 65)/18),$$

$$\alpha_h(v) = 0.07 \exp(-(v + 63)/20), \quad \beta_h(v) = \frac{1}{1 + \exp(-(v + 33)/10)},$$

$$\alpha_n(v) = \frac{0.018(v - 25)}{1 - \exp(-(v - 25)/25)}, \quad \beta_n(v) = \frac{0.0036(35 - v)}{1 - \exp(-(35 - v)/12)}.$$

Figure 34.4 shows the graphs of x_∞ and τ_x , $x = m, h$, and n . A comparison with the blue, dash-dotted curves in Fig. 5.1 shows that the most striking difference between this model and the WB model is that the inactivation variable, h , of the spike-generating sodium current is much slower here. This results in fairly broad action potentials; see Fig. 34.5, and compare with Fig. 5.3.

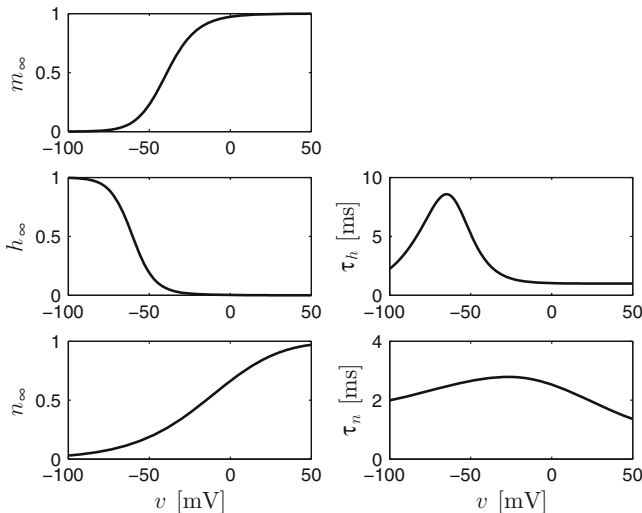


Figure 34.4. The functions x_∞ and τ_x in the O-LM cell model of [157], but without the h - and A -currents. We left out τ_m because we set $m = m_\infty(v)$.
[PRE_OLM_X_INF_TAU_X]

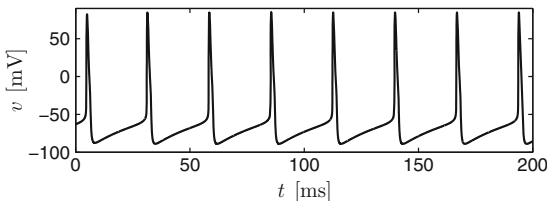


Figure 34.5. Voltage trace of the O-LM cell model of [157], but without the h - and A -currents, and with $m = m_\infty(v)$. In this simulation, $I = 1.5 \mu\text{A}/\text{cm}^2$.
[PRE_OLM_VOLTAGE_TRACE]

We now add the h -current defined by eqs. (18.1)–(18.3) to this model. Following [157], we use $\bar{g}_h = 12 \text{ mS}/\text{cm}^2$. The resulting voltage trace is shown in

Fig. 34.6, upper panel. The graph of r (lower panel of Fig. 34.6) shows that indeed the h-current plummets to near zero in response to an action potential, then rises more gradually. Note that addition of the h-current significantly accelerates the neuron: Compare Fig. 34.5 with Fig. 34.6. The reason is that $v_h = -32.9 \text{ mV}$ is far above rest.

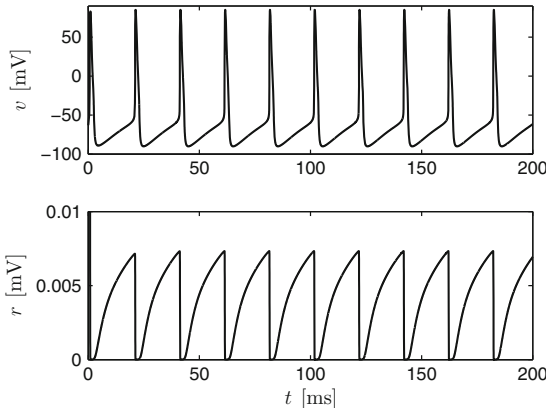


Figure 34.6. Upper panel: Same as Fig. 34.5, but with h-current defined by eqs. (18.1)–(18.3), with $\bar{g}_h = 12 \text{ mS/cm}^2$, and with $I = 0 \mu\text{A/cm}^2$. Lower panel: Gating variable, r , of the h-current (see eqs. (18.1)–(18.3)). [OLM_WITH_H_CURRENT]

Finally, we consider the model *A-current* of [157]. An A-current is a slowly decaying hyperpolarizing potassium current, rapidly raised by firing. This description makes it sound very similar to adaptation of the kind we discussed in Chapter 9. What is special about the A-current, however, is that it is *transient*, i.e., it has an *inactivation gate*.

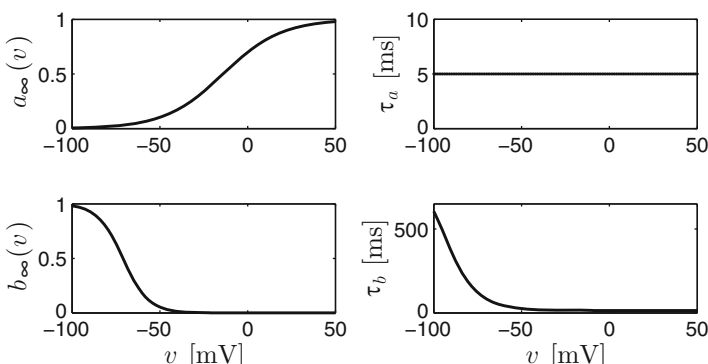


Figure 34.7. The steady states and time constants of the gating variables in the model A-current of [157]. [A_CURRENT]

The model A-current in [157] is given by

$$I_A = \bar{g}_A ab(-90 - v), \quad (34.1)$$

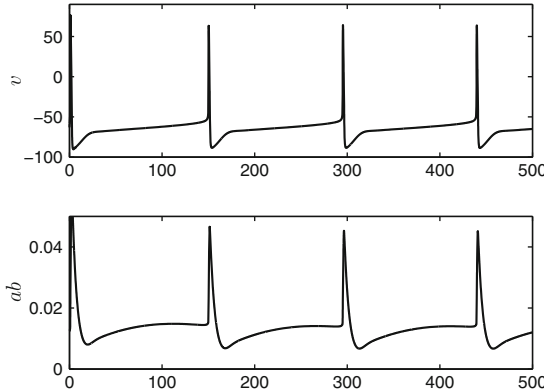


Figure 34.8. Upper panel: Same as Fig. 34.6, but with A-current defined by eqs. (34.1)–(34.4), with $\bar{g}_A = 22 \text{ mS/cm}^2$. Lower panel: The product, ab , of the two gating variables of the A-current (see eqs. (34.1)–(34.4)).
[OLM_WITH_H_AND_A_CURRENTS]

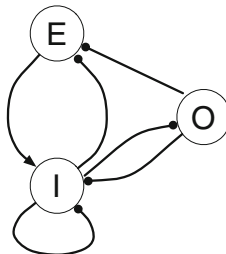


Figure 34.9. Symbolic depiction of the network of Fig. 34.10. The large circles labeled “E,” “I,” and “O” represent populations of cells. Lines ending in arrows indicate excitation, and lines ending in solid circles indicate inhibition.

with

$$\frac{dx}{dt} = \frac{x_\infty(v) - x}{\tau_x(v)} \quad \text{for } x = a, b,$$

$$a_\infty(v) = \frac{1}{1 + \exp(-(v + 14)/16.6)}, \quad \tau_a(v) = 5, \quad (34.2)$$

$$b_\infty(v) = \frac{1}{1 + \exp((v + 71)/7.3)}, \quad (34.3)$$

$$\tau_b(v) = \frac{1}{\frac{0.000009}{\exp((v - 26)/28.5)} + \frac{0.014}{0.2 + \exp((v + 70)/11)}}. \quad (34.4)$$

Note that $a_\infty(v)$ and $b_\infty(v)$ are increasing and decreasing functions of v , respectively. This is why a is called an *activation variable*, and b an *inactivation*

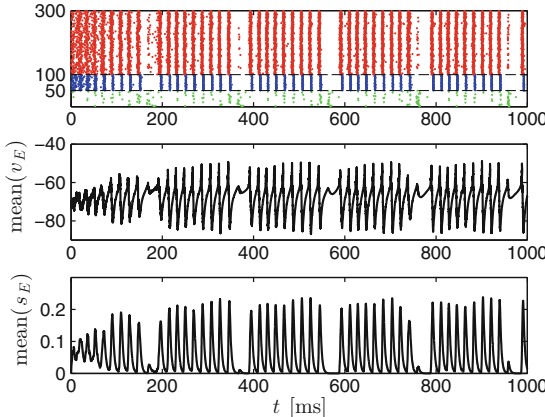


Figure 34.10. Upper panel: Spike rastergram of a network of 50 O-cells (green), 50 I-cells (blue), and 200 E-cells (red). The parameters are $\bar{I}_E = 1.8$, $\sigma_E = 0.05$, $\bar{I}_I = 1$, $\sigma_I = 0.1$, $\bar{I}_O = -2$, $\sigma_O = 0.05$, $\hat{g}_{EE} = 0$, $\hat{g}_{EI} = 0.25$, $\hat{g}_{EO} = 0$, $\hat{g}_{IE} = 0.25$, $\hat{g}_{II} = 0.25$, $\hat{g}_{IO} = 0.5$, $\hat{g}_{OE} = 1$, $\hat{g}_{OI} = 0.5$, $\hat{g}_{OO} = 0$, $p_{UV} = 1$ for all $U, V \in \{E, I, O\}$ (all-to-all connectivity). For all synapses, the rise times are 0.5 ms, the times-to-peak are 0.5 ms as well, and the decay times are $\tau_{d,E} = 3$, $\tau_{d,I} = 9$, and $\tau_{d,O} = 20$ ms. The synaptic reversal potentials are 0 mV for excitatory synapses, and -75 mV for all inhibitory synapses. Middle and bottom panels: Means of E-cell voltages and E-cell synaptic gating variables, respectively.

[EIO_1]

variable (see Section 3.2). From Fig. 34.7, you see that *inactivation* is fast, but *de-inactivation* is slow: τ_b is small for large v , but large for v below threshold. As a result, the total conductance density $\bar{g}_A ab$ behaves very differently from the total conductance density of an adaptation current: When the neuron fires, $\bar{g}_A ab$ very briefly rises. However, when the membrane potential falls, $\bar{g}_A ab$ rapidly follows it, because a follows v with a short time constant. (In fact, in [135] the activation gate of the A-current was taken to be an instantaneous function of v .) The inactivation gate, which also drops during the action potential, takes some time to recover. This is why there is a prolonged dip in ab following an action potential; see Fig. 34.8. Throughout the remainder of this chapter, we use $\bar{g}_A = 22 \text{ mS/cm}^2$.

The values of ab between two action potentials only vary by about a factor of 2 in Fig. 34.8. So to reasonably good approximation, the A-current adds *tonic inhibition* (namely, inhibition with a constant conductance) to the cell. The question whether the time dependence of ab actually matters to the model of nested gamma-theta oscillations in Section 34.3 will be the subject of exercise 3.

34.3 An E-I-O Network Generating Nested Gamma-Theta Rhythms

Following [157], we add a population of O-cells (model O-LM cells as described in Section 34.2) to a PING network; see Fig. 34.9. In analogy with eqs. (30.1) and (30.2), we take the drive to the k -the O-cell to be

$$I_{O,k} = \bar{I}_O (1 + \sigma_O Z_k), \quad (34.5)$$

where \bar{I}_O and $\sigma_O \geq 0$ are fixed numbers, and the Z_k are independent standard Gaussians. The resulting network can indeed generate nested gamma-theta oscillations; see Fig. 34.10 for an example. As in previous simulations, each cell of the network was initialized at a random phase with uniform distribution on its limit cycle.

Note that in Fig. 34.10, there are no E-to-O synapses. In [92, Fig. 3], nested gamma-theta oscillations were shown for an E-I-O network with positive, albeit very weak, E-to-O conductance. For more on this issue, see exercise 1.

Exercises

- 34.1. (*) In Fig. 34.10, there is no feedback from E-cells to O-cells, as indicated in Fig. 34.9. In [92, Fig. 3], there is such feedback, but it is quite weak. It is known, however, that there are projections from CA1 pyramidal cells to CA1 O-LM cells [150].
- (a) What happens if we add E-to-O synapses, say with $\hat{g}_{EO} = 0.1$, in the simulation of Fig. 34.10? Try it out. You will see that the O-cells don't reach near-synchrony now. Some fire on each cycle of the gamma oscillation. As a result, there is no nested gamma-theta rhythm, just an ongoing gamma rhythm slowed down by the O-cells.
 - (b) Suppose there is some initial mechanism that roughly synchronizes the O-cells, maybe some excitatory signal that makes many of them fire. To model this, suppose that the initial phases of the O-cells are chosen at random not between 0 and 1, but between 0 and 0.1. Is there then a nested gamma-theta rhythm even when $\hat{g}_{EO} = 0.1$?
- 34.2. (*) When the I-to-O connections are cut in Fig. 34.10, there is nothing to synchronize the O-cells any more, and the nested gamma-theta rhythm is lost. (Try it!) But now suppose that as in exercise 1b, we approximately synchronize the O-cells at the start of the simulation, by choosing their initial phases randomly between 0 and 0.1, not between 0 and 1. Does this restore the nested gamma-theta oscillations for a significant amount of time?²⁹

²⁹It couldn't restore them forever: There is nothing to enforce synchrony of the O-cells now, other than the initialization, and because of the heterogeneity of the external drives to the O-cells, their synchrony must disintegrate eventually, and with it the nested gamma-theta oscillation.

- 34.3. (*) In the simulation of Fig. 34.10, replace ab by 0.013, which is approximately its average subthreshold value in Fig. 34.8 (lower panel). This means replacing the A-current by *tonic inhibition* (inhibition with constant conductance). How does the figure change?

Part V

Functional Significance of Synchrony and Oscillations

Chapter 35

Rhythmic vs. Tonic Inhibition

In experiments described in [143], fast-firing inhibitory interneurons in the *barrel cortex* of mice, the part of the mouse brain that processes input from the whiskers, were driven to synchronize at 40 Hz, using optogenetic techniques. (In general, *optogenetic* techniques involve genetically sensitizing neurons to light, then using light to control them.) Figure 35.1 is a reproduction of Fig. 3A of [143]. The figure shows LFP recordings from barrel cortex during 40 Hz optogenetic stimulation of the fast-firing inhibitory interneurons. The central finding of [143] was that making the activity of fast-firing inhibitory interneurons rhythmic at 40 Hz improved the ability of the mice to perceive certain whisker deflections.

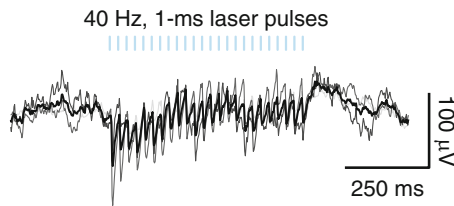


Figure 35.1. Figure 3A of [143]. The figure shows an LFP in mouse barrel cortex during activation of fast-firing inhibitory interneurons with 40 Hz light pulses. Thin lines refer to individual mice, and the solid line is the average over three mice. The blue bars indicate the light pulses. Reproduced with publisher's permission.

This result points towards one possible general function of rhythmicity: Making inhibition rhythmic might enhance input sensitivity. One can immediately see

Electronic supplementary material: The online version of this chapter (doi: [10.1007/978-3-319-51171-9_35](https://doi.org/10.1007/978-3-319-51171-9_35)) contains supplementary material, which is available to authorized users.

a heuristic reason why that might be true: When inhibition waxes and wanes, the waning phase offers a window of opportunity to weak inputs.

It is, however, not entirely clear that this reasoning is correct. We will compare the effects of tonic inhibition, with a constant conductance \bar{g} , and rhythmic inhibition, with an oscillating conductance $g(t)$ with temporal average \bar{g} , and ask: Is the rhythmic inhibition, in some precise sense, less powerful than the tonic inhibition? It is true that the input will be more effective while inhibition is down, but it will also be less effective while inhibition is up, and therefore what happens on balance is not so obvious.

Even if it is correct that rhythmic inhibition is less powerful than tonic inhibition, the question arises how significant an effect that is. For example, in [143], the rhythmic stimulation of the fast-firing inhibitory interneurons might make their firing rhythmic, but at the same time recruit a larger number of them. How easily would that erase the effect of making inhibition rhythmic?

In this chapter, we think about precise versions of these questions. For a target LIF neuron, we study the comparison between oscillatory and tonic inhibition by means of a combination of analysis and computing. We then also present simulations for a target RTM neuron.

35.1 Periodic Pulse Trains

In this and later chapters, we will describe computational experiments involving oscillatory synaptic conductances, or oscillatory drive. We will use oscillatory functions of the general form

$$g(t) = A \frac{e^{\alpha \cos^2(\pi t/T)} - 1}{\frac{1}{T} \int_0^T (e^{\alpha \cos^2(\pi s/T)} - 1) ds},$$

where $T > 0$ is the period, $A \geq 0$ is the time average, and $\alpha > 0$ governs the “peakedness” or “coherence” of the pulses; the greater α , the narrower are the pulses. We note that the denominator in the definition of $g(t)$ is independent of T (substitute $u = s/T$ to see this), so

$$g(t) = A \frac{e^{\alpha \cos^2(\pi t/T)} - 1}{\int_0^1 (e^{\alpha \cos^2(\pi s)} - 1) ds}. \quad (35.1)$$

The integral cannot be evaluated analytically, but it is easy to evaluate it numerically with great accuracy.³⁰ In the limit as $\alpha \searrow 0$, $g(t)$ becomes (using the local linear approximation $e^x - 1 \sim x$, and using the double-angle formula for the cosine)

$$A \frac{\cos^2(\pi t/T)}{\int_0^1 \cos^2(\pi s) ds} = A \left(1 + \cos \frac{2\pi t}{T} \right).$$

As α increases, g becomes increasingly “peaked.” As $\alpha \rightarrow \infty$, $g(t) \rightarrow A \sum_{k \in \mathbb{Z}} \delta(t - kT)$, where δ denotes the *Dirac delta function*. (This is not important for our

³⁰Because the integrand is smooth and periodic, and the integral extends over one period, the trapezoid method for evaluating integrals is of infinite order of accuracy here [78].

discussion here, so if you don't know what it means, that won't be a problem.) Figure 35.2 shows examples with $A = 1$, $T = 1$, and various different values of α .

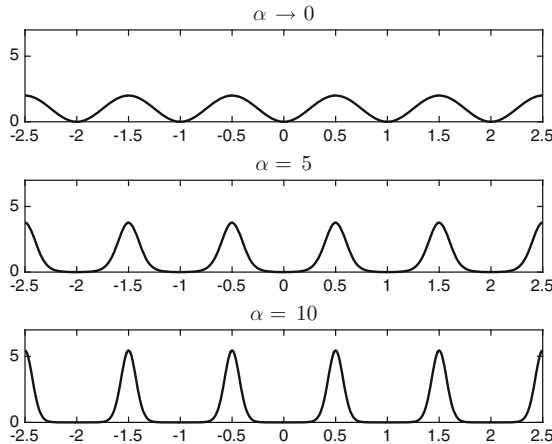


Figure 35.2. The function g defined by eq. (35.1), with $A = 1$, $T = 1$, and different values of α . [OSCILLATIONS]

35.2 LIF Neuron Subject to Synaptic Inhibition

We now consider a single LIF neuron subject to inhibition, and assume that the inhibitory conductance oscillates with a period $T > 0$. The membrane potential v is governed by

$$\frac{dv}{dt} = -\frac{v}{\tau_m} + I + g(t)(v_{\text{rev}} - v), \quad t \geq 0, \quad (35.2)$$

$$v(0) = 0, \quad (35.3)$$

$$v(t+0) = 0 \quad \text{if } v(t-0) = 1. \quad (35.4)$$

Here $\tau_m > 0$, $I \in \mathbb{R}$, $v_{\text{rev}} \in \mathbb{R}$, and

$$g(t) \geq 0 \quad \text{for all } t \geq 0, \quad g(t+T) = g(t) \quad \text{for all } t \geq 0.$$

We think of the synaptic reversal potential v_{rev} as “low” here, for instance, $v_{\text{rev}} = 0$, but in our argument, we don't make any assumption on the value of v_{rev} . We compare this LIF neuron with one subject to *tonic inhibition* with a conductance equal to the temporal average of g ,

$$\bar{g} = \frac{1}{T} \int_0^T g(t) dt.$$

We denote the membrane potential of the LIF neuron with tonic inhibition by \bar{v} :

$$\frac{d\bar{v}}{dt} = -\frac{\bar{v}}{\tau_m} + I + \bar{g} (v_{\text{rev}} - \bar{v}), \quad t \geq 0 \quad (35.5)$$

$$\bar{v}(0) = 0, \quad (35.6)$$

$$\bar{v}(t+0) = 0 \text{ if } \bar{v}(t-0) = 1. \quad (35.7)$$

The following proposition is Theorem 2 in [12, Appendix A].

Proposition 35.1. *Under the assumptions stated above, $\sup_{t \geq 0} \bar{v}(t) \leq \sup_{t \geq 0} v(t)$.*³¹

Thus the tonic inhibition is at least as effective at keeping the membrane potential down as the oscillatory inhibition, and in particular, if \bar{v} ever reaches the firing threshold 1, so does v .

Proof. We set

$$\hat{v} = \sup_{t \geq 0} v(t).$$

So we want to prove

$$\bar{v}(t) \leq \hat{v} \text{ for all } t \geq 0.$$

Note that $\hat{v} \geq 0$. If $\hat{v} = \infty$, there is nothing to be proved. Assume therefore that $\hat{v} < \infty$ now. Equation (35.2) implies

$$\frac{dv}{dt} \geq -\frac{\hat{v}}{\tau_m} + I + g(t)(v_{\text{rev}} - \hat{v}). \quad (35.8)$$

The right-hand side of (35.8) is periodic with period T . For any integer $k \geq 0$,

$$v((k+1)T) - v(kT) = \int_{kT}^{(k+1)T} \frac{dv}{dt} dt \geq T \left(-\frac{\hat{v}}{\tau_m} + I + \bar{g}(v_{\text{rev}} - \hat{v}) \right). \quad (35.9)$$

If the right-most expression in (35.9) were positive, the sequence $\{v(kT)\}_{k=0,1,2,\dots}$ would grow beyond all bounds, contradicting our assumption $\hat{v} < \infty$. Therefore we conclude that this expression is ≤ 0 , i.e.,

$$-\left(\frac{1}{\tau_m} + \bar{g}\right)\hat{v} + I + \bar{g}v_{\text{rev}} \leq 0.$$

At any time at which $\bar{v}(t) > \hat{v}$, we would have

$$\begin{aligned} \frac{d\bar{v}}{dt} &= -\frac{\bar{v}}{\tau_m} + I + \bar{g}(v_{\text{rev}} - \bar{v}) = -\left(\frac{1}{\tau_m} + \bar{g}\right)\bar{v} + I + \bar{g}v_{\text{rev}} < \\ &\quad -\left(\frac{1}{\tau_m} + \bar{g}\right)\hat{v} + I + \bar{g}v_{\text{rev}} \leq 0. \end{aligned}$$

This implies that \bar{v} cannot become greater than \hat{v} ,³² so our assertion is proved. \square

³¹For any function $f = f(t)$, $t \geq 0$, the notation “ $\sup_{t \geq 0} f(t)$ ” denotes the supremum of $f(t)$ over $t \geq 0$, i.e., the lowest upper bound, the smallest $A \in (-\infty, \infty]$ such that $f(t) \leq A$ for all $t \geq 0$.

³²Here is a completely precise way of reasoning. Suppose $\bar{v}(t_0) > \hat{v}$. Since \bar{v} is continuous, there is an $\epsilon > 0$ with $\bar{v}(t) > \hat{v}$ for all $t \in (t_0 - \epsilon, t_0)$. We choose the largest possible such ϵ . Therefore $\bar{v}(t_0 - \epsilon) = \hat{v}$. The mean value theorem now implies that there is a time t strictly between $t_0 - \epsilon$ and t_0 at which $d\bar{v}/dt > 0$. This is a contradiction because at this time, $\bar{v} > \hat{v}$, and we showed that $\bar{v} > \hat{v}$ implies $d\bar{v}/dt < 0$.

Figure 35.3 illustrates this result. Inhibition with a constant conductance \bar{g} prevents the neuron from firing, while inhibition with an oscillating conductance $g(t)$ with time average \bar{g} allows firing in each of the “windows of opportunity” when $g(t)$ is low. With greater drive, there may be several action potentials in each window of opportunity; see bottom panel of Fig. 35.3.

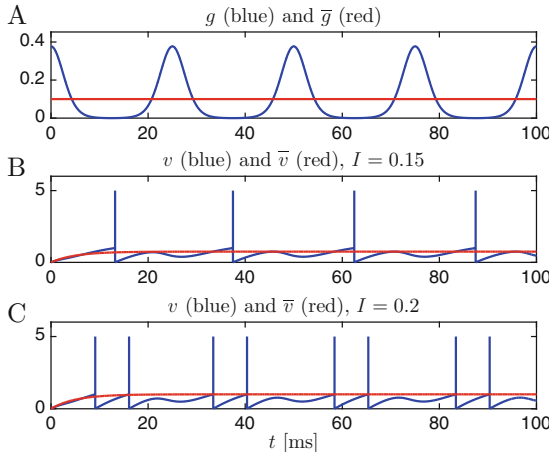


Figure 35.3. *A*, blue curve: oscillating inhibitory conductance $g(t) = \varphi(t)$ defined as in eq. (35.1), with $A = \bar{g} = 0.1$, $\alpha = 5$, $T = 25$. *A*, red line: $\bar{g} = 0.1$, the time average of g . *B*, blue curve: solution v of eqs. (35.2) and (35.4), with vertical lines inserted in the plot to indicate spike times, i.e., times at which the threshold $v = 1$ is reached, resulting in a reset. *B*, red curve: solution \bar{v} of eqs. (35.5) and (35.6). In these simulations, $v_{\text{rev}} = 0$, $\tau_m = 10$, and $I = 0.15$. The tonic inhibition prevents firing, while the oscillatory inhibition opens windows of opportunity at a frequency of 40 Hz, resulting in 40 Hz firing. *C*: Same as *B*, with I raised to 0.2.

[PERIODIC_INHIBITION]

To see the effect of oscillations in the inhibitory conductance more clearly, we plot f - I curves for (35.5)–(35.7), and for (35.2)–(35.4), using the same pulsatile g as in Fig. 35.3. For eqs. (35.5)–(35.7), the f - I curve can easily be computed analytically, replacing τ_m in (7.9) by $1/(1/\tau_m + \bar{g}) = \tau_m/(1 + \tau_m \bar{g})$, and I by $I + \bar{g}v_{\text{rev}}$. The frequency of the LIF neuron described by eqs. (35.5)–(35.7) is

$$f = \begin{cases} 0 & \text{if } I \leq 1/\tau_m + \bar{g}(1 - v_{\text{rev}}), \\ \frac{1000(1 + \tau_m \bar{g})}{\tau_m(I + \bar{g}v_{\text{rev}})} & \text{if } I > 1/\tau_m + \bar{g}(1 - v_{\text{rev}}). \end{cases} \quad (35.10)$$

We estimate the frequency of the LIF neuron given by (35.2)–(35.4) based on 2000 ms simulations. The result, for $\tau_m = 10$ and $v_{\text{rev}} = 0$, is in Fig. 35.4. Note that the f - I curve for eqs. (35.2)–(35.4) is (nearly) piecewise constant — the frequency is an integer multiple of 40 Hz for most values of I . There is a broad range of values

of I for which the LIF neuron with oscillating inhibition fires, but the LIF neuron with tonic inhibition does not fire. Thus rhythmicity of the inhibition makes the target neuron more input sensitive for a broad range of drives. However, for very strong drives, the effect can be the reverse: Firing can be faster with tonic than with rhythmic inhibition; see also exercise 3.

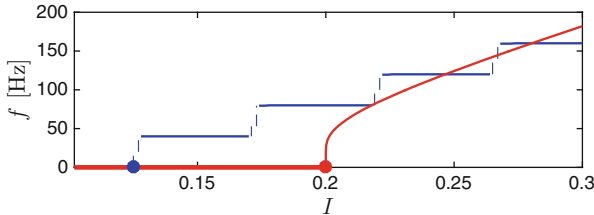


Figure 35.4. f - I curves of (35.2)–(35.4) (blue) and (35.5)–(35.7) (red), with parameters as in Fig. 35.3. The content of Proposition 35.1 is that the red dot does not lie to the left of the blue dot. [PERIODIC_INHIBITION_F_I_CURVE]

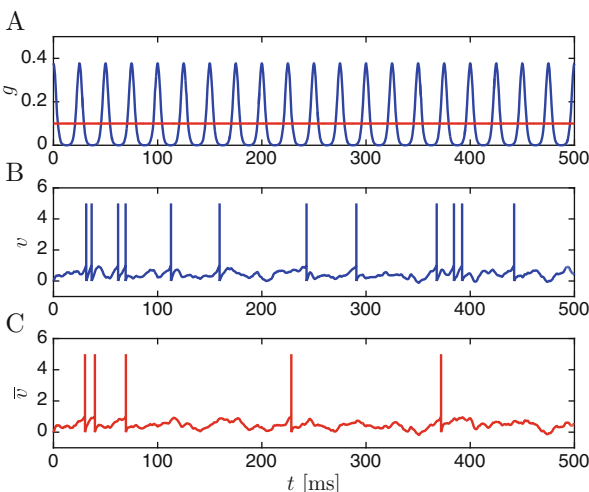


Figure 35.5. A: oscillating inhibitory conductance as in Fig. 35.3 (blue), and tonic inhibitory conductance $\bar{g} = 0.1$, the time average of g (red). B: solution v of eqs. (35.2)–(35.4), with vertical lines inserted in the plot to indicate spike times. C: solution \bar{v} of eqs. (35.5)–(35.7). In these simulations, $\tau_m = 10$ and $I = 0.1 + S$, where S is a discrete Ornstein-Uhlenbeck process with mean zero, $\tau_{\text{noise}} = 3 \text{ ms}$, and $\sigma_{\text{noise}} = 0.08$; see Appendix C.6. With oscillating inhibition, there are 12 action potentials in 500 ms, while with tonic inhibition there are only 5. [PERIODIC_INHIBITION_2]

A far less regular and therefore far more realistic-looking figure is obtained by reducing the constant drive I in Fig. 35.3, and adding instead a discrete Ornstein-Uhlenbeck process (see Appendix C.6); see Fig. 35.5.

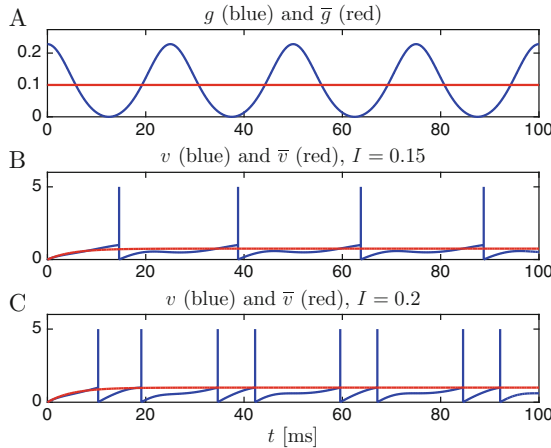


Figure 35.6. Same as Fig. 35.3, but with $\alpha = 1$. [PERIODIC_INHIBITION_3]

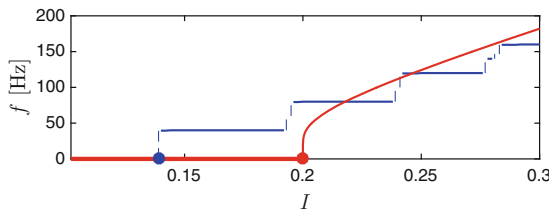


Figure 35.7. Like Fig. 35.4, but with a lower-amplitude oscillation in the inhibitory conductance ($\alpha = 1$). [PERIODIC_INHIBITION_F_I_CURVE_2]

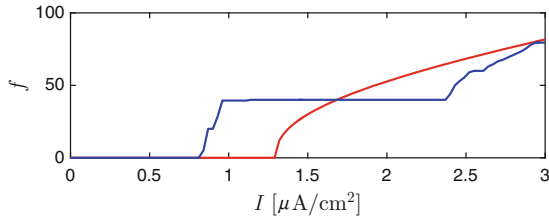


Figure 35.8. f - I curves of RTM neuron subject to inhibition with the constant synaptic conductance $\bar{g} = 0.1 \text{ mS/cm}^2$ (red), and with the same rhythmic conductance as in Fig. 35.3 (blue). The reversal potential of inhibition is -75 mV . [RTM_F_I_CURVE_WITH_INHIBITION]

In Figs. 35.3–35.5, the oscillations in the inhibitory conductance are pronounced, with peak values exceeding the average by nearly a factor of 4. Even with less pronounced oscillations (that is, smaller α), the cell responds to some signals to which it would not respond if the inhibition were tonic; see Fig. 35.6 for an example. This is not a surprise — after all, Proposition 35.1 contains no

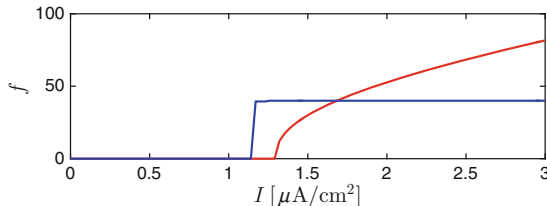


Figure 35.9. Same as Fig. 35.8, but with the rhythmic inhibition (not the tonic inhibition) amplified by a factor of 2. [RTM_F_I_CURVE_WITH_INHIBITION_2]

assumption about the amplitude of oscillations. Qualitatively, nothing changes about the frequency-current relation either; see Fig. 35.7. However, the range of values of I for which rhythmicity of the inhibitory conductance enhances the response is now a bit narrower than before.

35.3 RTM Neuron Subject to Synaptic Inhibition

Figure 35.8 shows the f - I curve of an RTM neuron subject to inhibition with a constant synaptic conductance $\bar{g} = 0.1 \text{ mS}/\text{cm}^2$ (red), and subject to rhythmic inhibition with temporal average \bar{g} (blue). Again one sees that making inhibition rhythmic amplifies the response to weak stimuli, but can weaken the response to stronger stimuli.

It seems reasonable to speculate that with the light stimulation in [143], there may be more fast-firing inhibitory interneurons activated on each gamma cycle than in the natural state; see Fig. 3A of [143], reproduced in Fig. 35.1, which indeed shows very strong gamma oscillations in the LFP during light stimulation. Remarkably, however, the enhancement of sensitivity to weak inputs shown in Fig. 35.8 persists even if the strength of the rhythmic inhibition (but not the tonic inhibition) in Fig. 35.8 is doubled; see Fig. 35.9.

Exercises

- 35.1. Derive eq. (35.10).
- 35.2. Assume that $I > 1/\tau_m$ and $v_{\text{rev}} < 1$. Let f denote the firing frequency of the LIF neuron defined by eqs. (35.5)–(35.7). We write $f = f(\bar{g})$. Of course f also depends on the parameters I , τ_m , and v_{rev} , but those are taken to be fixed here. (a) Show that there is a critical value \bar{g}_c such that $f(\bar{g}) = 0$ for $\bar{g} \geq \bar{g}_c$ and $f(\bar{g}) > 0$ for $\bar{g} < \bar{g}_c$. (b) (*) For $\bar{g} < \bar{g}_c$, $f''(\bar{g}) < 0$. This will be used in exercise 3b. I am not asking you to prove it analytically here, that is an unpleasant calculation that yields no insight. However, plot f as a function of $\bar{g} < \bar{g}_c$ for some sample parameter choices, and convince yourself that indeed the graph is concave-down.

35.3. (a) (*) Plot the analogue of Fig. 35.4 for

$$g(t) = \begin{cases} 0.3 & \text{if } 0 \leq t < 12.5, \\ 0.1 & \text{if } 12.5 \leq t < 25, \end{cases} \quad (35.11)$$

and $g(t + 25) = g(t)$ for all t . (b) Explain why for large I , the oscillatory inhibitory conductance (35.11) will yield a lower mean firing frequency than the constant inhibitory conductance $\bar{g} = 0.2$. (Hint: Use exercise 2b.)

Chapter 36

Rhythmic vs. Tonic Excitation

In Chapter 35, we showed that inhibition can become less powerful when it is made rhythmic. More precisely, a *weak* signal can elicit a response more easily when the inhibition in the receiving network oscillates. The opposite effect is seen for a *strong* signal. Here we will argue that excitation can become more powerful when it is made rhythmic. More precisely, *weak* signals benefit from being made rhythmic, while *strong* ones become less effective when made rhythmic.

We will model the excitatory signals as *currents* here, not as *synaptic inputs*. You may wonder why I was careful to use *synaptic inputs*, including the reversal term $v_{\text{rev}} - v$, in Chapter 35, but not here. Using input currents instead of synaptic inputs amounts to approximating the reversal term $v_{\text{rev}} - v$ by a constant. This is much more reasonable when $v_{\text{rev}} \gg v$ most of the time, as is the case for excitatory synaptic inputs, than when $v_{\text{rev}} \approx v$ most of the time, as is the case for inhibitory input. So it is in fact more justifiable to model *excitatory* synaptic inputs as currents than it is to do the same for *inhibitory* synaptic inputs.

36.1 Analysis in an Idealized Setting

Consider a neuron with a continuous, single-valued f - I relation, with $f(I) = 0$ for $I \leq I_c$ and $f(I) > 0$ for $I > I_c$; think, for instance, of the LIF, theta, RTM, or WB neurons. Assume that $f''(I) < 0$ for $I > I_c$, as is the case for all four of the examples we have mentioned. Figure 36.1 illustrates the form of the f - I curve that we assume. Suppose now that the neuron receives a sequence of input pulses with period $T > 0$, in the idealized form

Electronic supplementary material: The online version of this chapter (doi: [10.1007/978-3-319-51171-9_36](https://doi.org/10.1007/978-3-319-51171-9_36)) contains supplementary material, which is available to authorized users.

$$I_p = I_p(t) = \begin{cases} I_H & t - kT \in [0, \epsilon] \text{ for some integer } k, \\ I_L & \text{otherwise,} \end{cases} \quad (36.1)$$

with $I_L < I_H$, $0 < \epsilon < T$; see Fig. 36.2. We will compare the effect of this sequence of input pulses with the effect of a constant input equal to the time average of the pulsed input,

$$\bar{I} = \frac{\epsilon}{T} I_H + \left(1 - \frac{\epsilon}{T}\right) I_L.$$

We write

$$\bar{f} = f(\bar{I}).$$

We make one more idealizing assumption: We assume that the mean frequency at which the target neuron fires when it receives the pulsed input equals

$$f_p = \frac{\epsilon}{T} f(I_H) + \left(1 - \frac{\epsilon}{T}\right) f(I_L).$$

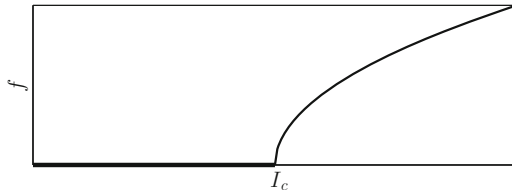


Figure 36.1. Idealized f - I curve assumed in Proposition 36.1.
[IDEALIZED_F_I_CURVE]

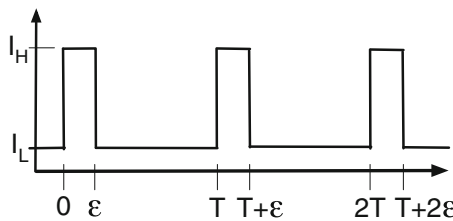


Figure 36.2. Idealized pulsed input I_p defined in eq. (36.1). [SQUARE_PULSES]

Proposition 36.1. Under the assumptions stated above, (a) sufficiently strong pulsing enables weak inputs to have an effect:

$$I_H > I_c \Rightarrow f_p > 0,$$

(b) pulsing makes strong inputs less effective:

$$f_p < \bar{f} \text{ for sufficiently large } \bar{I}$$

(all other parameters fixed), and (c) pulsing makes strong inputs less effective also in the following sense:

$$f_p < \bar{f} \quad \text{if } I_L \geq I_c.$$

Proof. Exercise 1. \square

Weak signals benefit from being made rhythmic because of the *leakiness* of the target: When a constant input current is delivered, the charge entering the cell has time to leak back out before triggering an action potential, while the same charge injected as a brief pulse is capable of making the target fire. However, the fact that strong signals elicit a *lower* mean firing frequency in the target when they are made rhythmic is a consequence of leakiness as well, reflected in the condition $f''(I) < 0$ for $I > I_c$; see exercise 2.

36.2 Frequency-Current Curve of the RTM Neuron with Pulsed Input

Figure 36.3 shows f - I curves for the RTM neuron assuming that the input current is constant (red), or that it is pulsed at gamma frequency (blue).

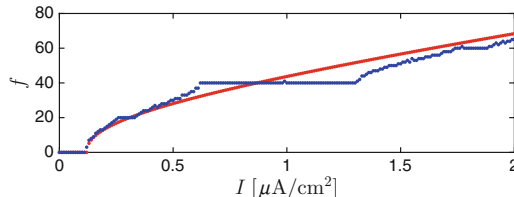


Figure 36.3. f - I curve of RTM neuron with constant input current (red), and with input current pulsed at 40 Hz (blue). For a given I , the pulsed input current has time average I , but is proportional to $e^{\alpha \cos^2(\pi t/25)} - 1$, with $\alpha = 1$. [RTM_F_I_CURVE_PULSED_EXCITATION]

The figure shows that pulsing the input enhances the downstream impact, measured by mean firing frequency of the target RTM neuron, only in a narrow range of values of I . This is, however, a matter of leakiness; doubling the leak conductance makes the efficacy-enhancing effect of pulsing more pronounced; see Fig. 36.4.

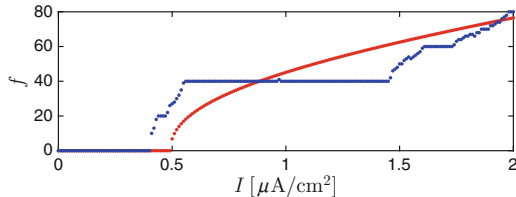


Figure 36.4. Like Fig. 36.3, but with \bar{g}_L doubled: $\bar{g}_L = 0.2 \text{ mS/cm}^2$.
[RTM_F_I_CURVE_PULSED_EXCITATION_2]

Exercises

- 36.1. Prove Proposition 36.1. (Compare also with exercise 35.3.)
- 36.2. (a) For the non-leaky LIF neuron ($\tau_m = \infty$), explain why $f''(I) = 0$ for $I > I_c$. (b) For the non-leaky LIF neuron, under the assumptions made in Section 36.1 and also assuming $I_L \geq 0$, show that pulsing an excitatory input current never has any effect.
- 36.3. (*) (†) Draw a curve similar to that in Fig. 36.3 for the Erisir neuron. The point, of course, is to see whether for a type 2 neuron, the curve looks similar.

Hints: Start with the code that generates Fig. 36.3, and replace the RTM neuron by the Erisir neuron. Explore $I \in [2, 8]$. The simulation will be a bit costly. To reduce the cost, you might divide the interval $[2, 8]$ into 100 subintervals, not 200 as in the code that generates Fig. 36.3.

Chapter 37

Gamma Rhythms and Cell Assemblies

In Section 33.2, we mentioned Hebb’s idea of *cell assemblies*. The hypothesis is that information is carried by membership in neuronal ensembles that (temporarily) fire together. One attractive aspect of this idea is that it would give a brain with 10^{11} neurons an unfathomably large storage capacity, since the number of subsets of a large set is huge.

For Hebbian cell assemblies to play a central role in brain function, there would have to be a mechanism defining membership in an assembly, keeping non-members from firing while the assembly is active. Olufsen *et al.* [122] pointed out that the PING mechanism could serve this purpose: On a given gamma cycle, the participating, most strongly excited E-cells fire, thereby rapidly creating feedback inhibition that keeps nearby, less strongly excited E-cells from firing.

37.1 An Example

Figure 37.1 shows an example of thresholding, similar to examples in [122]. E-cells 1 through 73 (neurons 51 through 123 in the spike rastergram, as neurons 1 through 50 are I-cells) are fully suppressed. E-cells 77 through 200 participate on every gamma cycle. Only three E-cells, namely E-cells 74, 75, and 76, participate sparsely, i.e., on some but not all cycles of the gamma oscillation. E-cell 76 skips every third gamma cycle, and E-cells 74 and 75 skip every second; see Fig. 37.2.

Electronic supplementary material: The online version of this chapter (doi: [10.1007/978-3-319-51171-9_37](https://doi.org/10.1007/978-3-319-51171-9_37)) contains supplementary material, which is available to authorized users.

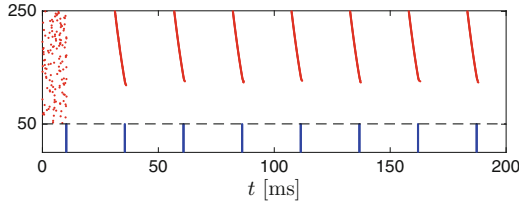


Figure 37.1. Spike rastergram of a PING network with $N_E = 200$ E-cells and $N_I = 50$ I-cells. The external drive to the i -th E-cell is $1.2 + 0.8i/200$, $1 \leq i \leq 200$, so E-cells with higher indices are driven more strongly. This is why they fire earlier in the gamma cycle. Other parameters, using the notation of Chapter 30, are $\bar{I}_I = 0.5$, $\sigma_I = 0$, $\hat{g}_{EE} = 0$, $\hat{g}_{EI} = 0.5$, $\hat{g}_{IE} = 1.5$, $\hat{g}_{II} = 0.25$, $p_{EI} = 1$, $p_{IE} = 1$, $p_{II} = 1$, $\tau_{r,E} = 0.5$, $\tau_{peak,E} = 0.5$, $\tau_{d,E} = 3$, $v_{rev,E} = 0$, $\tau_{r,I} = 0.5$, $\tau_{peak,I} = 0.5$, $\tau_{d,I} = 9$, $v_{rev,I} = -75$. [PING_THR_1]

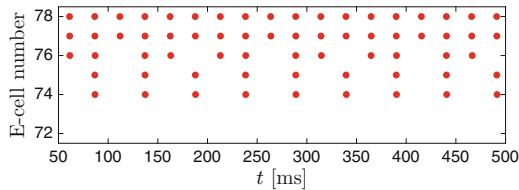


Figure 37.2. Simulation of Fig. 37.1, carried on for a longer time, now showing only spike times of E-cells 72 through 78 (cells 122 through 128 in Fig. 37.1). We have omitted the first 50 ms of simulated time to eliminate initialization effects. [PING_THR_1_ZOOM]

Note that \hat{g}_{IE} is six times stronger in Fig. 37.1 than it was in Fig. 30.4. To obtain a picture like that in Fig. 37.1, one needs strong inhibition: E-cells 70 and 80, say, have very similar external drives (1.48 and 1.52), and nonetheless one is completely suppressed, the other fires at gamma frequency. On each gamma cycle, E-cell 70 comes close to firing; the inhibition must be strong enough to pull it back.

37.2 The Exponential Sharpness of Thresholding

Figures 35.8 and 35.9 already reflected the sharpness of thresholding and its dependence on the strength of inhibition. Those figures showed that a neuron subject to pulsed inhibition, for a wide range of constant external drives I , fires either once on each cycle of the oscillatory inhibition, or not at all. There is only a narrow range of values of I in which the neuron fires on some, but not all cycles. Comparison of Figs. 35.8 and 35.9 suggests that this range narrows as the strength of inhibition increases.

We denote by T the period with which the inhibitory input pulses arrive ($T = 25$ ms in Figs. 35.8 and 35.9), by I_L the largest value of I with $f(I) = 0$, by I_H the smallest value of I with $f(I) = 1000/T$, and we define $w = I_H - I_L$.

Thus w is the width of the transition from $f = 0$ to $f = 1000/T$. The value of w depends on \bar{g} (the notation here is as in Chapter 35), and we will write $w = w(\bar{g})$. In Fig. 35.9, $\bar{g} = 0.2$ and $w \approx 0.0129$, so $w(0.2) \approx 0.0129$. Table 37.1 shows $w(\bar{g})$ for $\bar{g} = 0.15 + 0.05k$, $k = 0, 1, 2, 3, 4$, and the ratios $w(\bar{g})/w(\bar{g} + 0.05)$. The table indicates that

$$\frac{w(\bar{g})}{w(\bar{g} + 0.5)} \approx 2.8$$

independently of \bar{g} , suggesting $w \sim e^{-\ln(2.8)\bar{g}/0.05}$, which is approximately $e^{-20\bar{g}}$. As \bar{g} rises, w tends to zero exponentially fast.

\bar{g}	0.15	0.2	0.25	0.3	0.35
$w = w(\bar{g})$	0.036	0.013	0.0046	0.0016	0.00059
$w(\bar{g})/w(\bar{g} + 0.05)$	2.8	2.8	2.8	2.8	—

Table 37.1. The length $w = I_H - I_L$ of the interval $[I_L, I_H]$ of values of I with $0 < f < 40$, obtained from simulations similar to those of Fig. 35.9, but with various different values of \bar{g} , and the ratios $w(\bar{g})/w(\bar{g} + 0.05)$. All entries shown were rounded to two significant digits, but the ratios were computed before the values of w were rounded. [THRESHOLDING]

37.3 Analysis in an Idealized Setting

Here we will study the f - I curve of a LIF neuron subject to inhibitory pulses that arrive with a period $T > 0$ and last for a time $\epsilon \in (0, T)$. Normalizing the LIF neuron as we usually do, we take the governing equation to be

$$\frac{dv}{dt} = \begin{cases} -v/\tau_m + I - (T/\epsilon)\bar{g}v & \text{if } t \in [kT, kT + \epsilon] \text{ for some integer } k, \\ -v/\tau_m + I & \text{otherwise} \end{cases} \quad (37.1)$$

as long as $v < 1$, with $\tau_m > 0$, $\bar{g} > 0$, $I \geq 0$. To facilitate our analysis, we are assuming here that the inhibitory conductance does not decay exponentially, but stays constant for a fixed time $\epsilon > 0$, then drops to zero abruptly. The factor of T/ϵ appears in eq. (37.1) to make \bar{g} the mean inhibitory conductance, as it was in Chapter 35. As usual, the reset condition is

$$v(t+0) = 0 \quad \text{if} \quad v(t-0) = 1. \quad (37.2)$$

For illustration, Fig. 37.3 shows a solution of eq. (37.1) with $v(0) = 1$. In this example, $v(t) < 1$ for $t > 0$, so the model neuron is permanently suppressed by the inhibitory pulses.

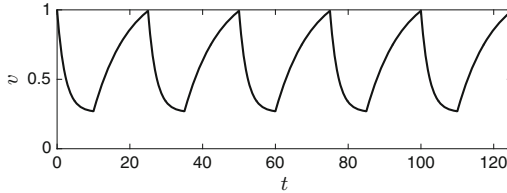


Figure 37.3. The solution of eq. (37.1), with $\tau_m = 10$, $I = 0.12$, $\bar{g} = 1/7$, $T = 35$, $\epsilon = 10$, $v(0) = 1$. [NO_RESET]

Proposition 37.1. Let $\tau_m > 0$, $T > 0$, $\epsilon > 0$, and $\bar{g} > 0$ be given.

- (a) For sufficiently large I , the model neuron defined by eqs. (37.1) and (37.2) will fire (that is, v will be reset) at least once in each period $[kT, (k+1)T)$, $k = 0, 1, 2, \dots$, regardless of the value of $v(0) \in [0, 1]$.
- (b) For sufficiently small positive I , the model neuron will not fire at all, regardless of the value of $v(0) \in [0, 1]$.
- (c) Denote by I_H the smallest number so that for $I > I_H$, there will be at least one reset per period, regardless of the value of $v(0) \in [0, 1]$. Similarly denote by I_L the largest number so that for $I < I_L$, there will be no reset, regardless of the value of the value of $v(0) \in [0, 1]$. Then

$$I_H - I_L \asymp e^{-T\bar{g}}$$

as $\bar{g} \rightarrow \infty$.

This proposition confirms again, for the very simple model problem considered here, that thresholding by inhibitory pulses is exponentially sharp as the strength of inhibition grows.

Proof. (a) There is at least one reset in each period $[kT, (k+1)T)$ if the solution of

$$\frac{dv}{dt} = -\frac{v}{\tau_m} + I, \quad v(0) = 0 \tag{37.3}$$

reaches 1 before time $T - \epsilon$, that is, if

$$\tau_m \ln \frac{\tau_m I}{\tau_m I - 1} < T - \epsilon. \tag{37.4}$$

This inequality holds for sufficiently large I . This proves (a).

(b) The model neuron does not fire if $I \leq 1/\tau_m$, since then it would not even fire in the absence of the inhibitory pulses.

(c) For the solutions of eqs. (37.1), (37.2) there is at least one reset in each period, regardless of the value of $v(0) \in [0, 1]$, if and only if there is a reset in $[0, T)$

for the solution with $v(0) = 0$. If $v(0) = 0$, then $v(\epsilon) = v_{\epsilon,0}$ with

$$v_{\epsilon,0} = \left(1 - e^{-\epsilon(1/\tau_m + (T/\epsilon)\bar{g})}\right) \frac{I}{1/\tau_m + (T/\epsilon)\bar{g}}, \quad (37.5)$$

and

$$v(T) = v_{\epsilon,0}e^{-(T-\epsilon)/\tau_m} + \tau_m I \left(1 - e^{-(T-\epsilon)/\tau_m}\right), \quad (37.6)$$

We conclude that I_H satisfies the equation

$$v_{\epsilon,0}e^{-(T-\epsilon)/\tau_m} + \tau_m I_H \left(1 - e^{-(T-\epsilon)/\tau_m}\right) = 1. \quad (37.7)$$

We will similarly derive an equation for I_L . For the solutions of eqs. (37.1), (37.2) there is no reset at all, regardless of the value of $v(0) \in [0, 1]$, if the solution with $v(0) = 1$ does not reach 1 in the time interval $(0, T]$. The calculation is precisely as before, except that $v_{\epsilon,0}$ is replaced by

$$v_{\epsilon,1} = e^{-\epsilon(1/\tau_m + (T/\epsilon)\bar{g})} + v_{\epsilon,0}.$$

In particular,

$$v_{\epsilon,1}e^{-(T-\epsilon)/\tau_m} + \tau_m I_L \left(1 - e^{-(T-\epsilon)/\tau_m}\right) = 1. \quad (37.8)$$

Note that $v_{\epsilon,1}$ differs from $v_{\epsilon,0}$ only by a term that is $\asymp e^{-T\bar{g}}$. (The limit that this asymptotic statement refers to is the limit as $\bar{g} \rightarrow \infty$.) From eqs. (37.7) and (37.8), we then conclude that I_H and I_L only differ by a term that is $\asymp e^{-T\bar{g}}$. \square

The preceding analysis gives at least a heuristic explanation of the sharpness of the transition in the blue curve of Fig. 35.9 from approximately 40 Hz to 0 Hz. This transition becomes narrower exponentially fast as the strength of inhibition increases because the inhibition causes an exponentially strong compression of the voltage traces.

The question why in Fig. 37.1, the transition from participation on each cycle to complete suppression is so narrow, with only three cells falling into an intermediate regime of sparse participation, is clearly related, although it is not the same. The difference is that in Fig. 37.1, the E-cell firing triggers the I-cell firing, while the analysis in this section refers to externally imposed inhibitory pulses. For further numerical exploration, see exercise 1.

Exercises

- 37.1. (*) Repeat the simulation of Fig. 37.1 with 500 E-cells instead of 200 E-cells (still 50 I-cells), and carry it out up to time 500. For each E-cell, estimate its firing frequency by determining how often it fires between $t = 50$ and $t = 500$, then scaling appropriately to get an estimate of the frequency in Hz. Determine how many E-cells with sparse participation (neither firing on each cycle, nor altogether suppressed) there are. In Fig. 37.1, we used $\hat{g}_{IE} = 1.5$. Repeat the experiment with $\hat{g}_{IE} = 1.3, 1.7$, and 1.9. Explain why what you see is evidence that the number of E-cells that are partially, but not completely suppressed drops exponentially as \hat{g}_{IE} increases.

- 37.2. (*) (†) A flaw of the analysis in this chapter is that the excitatory drive to the target is assumed to be constant in time. Investigate the case when the target neuron is subject to strong deterministic pulses of synaptic inhibition, and weak excitatory current pulses arriving on a Poisson schedule. (See the discussion at the start of Chapter 36 for a justification of using *current* pulses for the excitation, while using *synaptic* pulses for the inhibition.) Plot the mean firing frequency of the target as a function of the mean frequency of excitatory inputs, or as a function of the strengths of the excitatory input pulses. Do you find thresholding?

Chapter 38

Gamma Rhythms and Communication

38.1 Gamma Phase-Dependent Communication

During a PING oscillation, the pyramidal cells are subject to inhibition of oscillating strength. Inputs to the pyramidal cells should be more effective at times when inhibition is weak than when it is strong. Pascal Fries [56] has suggested that the brain may make use of this fact, making neuronal communication more or less effective by shifting the phase differences between rhythmic senders and oscillating receivers. This hypothesis, called the *communication through coherence (CTC) hypothesis*, has attracted considerable interest in the neuroscience literature.

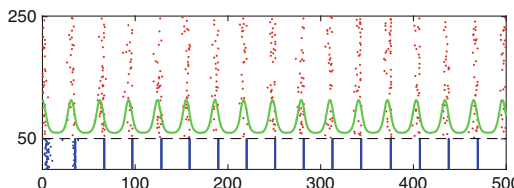


Figure 38.1. Figure 32.4, with an oscillation with period exactly equal to 31 ms superimposed in green. The period in Fig. 32.4 is so close to 31 ms that a perfectly periodic signal with period 31 ms is very close to phase-locked with the network throughout the simulated 500 ms interval. [POISSON_PING_3_PLUS_GREEN]

To examine the CTC hypothesis computationally, we consider a stochastic weak PING network, say that of Fig. 32.4. The oscillations in Fig. 32.4 are nearly, but not perfectly regular. (Real gamma oscillations are far less regular.) Therefore a periodic sequence of input pulses with just the right period will be very close

Electronic supplementary material: The online version of this chapter (doi: [10.1007/978-3-319-51171-9_38](https://doi.org/10.1007/978-3-319-51171-9_38)) contains supplementary material, which is available to authorized users.

to phase-locked with the network. Figure 38.1 shows that indeed a periodic signal with period 31 ms is very close to phase-locked with the network throughout the simulated 500 ms interval.

We now subject the first 5 E-cells in Fig. 38.1 to an additional pulsatile excitatory input with period 31 ms. We expect that the cells receiving the added input will be affected, but the overall network oscillation will remain largely unchanged, since the input is received by such a small number of E-cells only. We will examine how the effect of the input pulses depends on their phase relative to the network oscillation. We add to the first 5 E-cells in Fig. 38.1 the pulsatile excitatory drive

$$I_p(t) = 0.1 \frac{e^{\alpha \cos^2(\pi t/T - \varphi)} - 1}{\int_0^1 (e^{\alpha \cos^2(\pi s)} - 1) ds}. \quad (38.1)$$

with $T = 31$, $\alpha = 4$, $\varphi \in [0, 1]$; compare eq. (35.1). I_p oscillates with period T and has temporal average 0.1. The parameter φ is a phase shift. Up to shifting and scaling, the green curve in Fig. 38.1 is I_p with $\varphi = 0$.

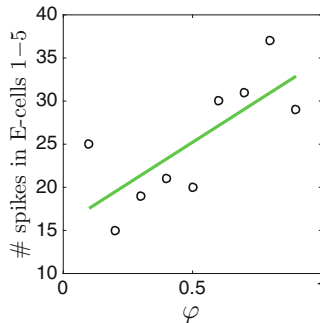


Figure 38.2. Phase dependence of response of E-cells 1 through 5 to an added pulsatile drive. The network is as in Fig. 30.6, but E-cells 1 through 5 receive additional pulsatile drive, define as in eq. (38.1), with $T = 31$, $\alpha = 4$. The total number of action potentials in E-cells 1–5 over the simulated time interval of 500 ms is recorded. The green line segment is the linear least squares fit.

[POISSON_PING_3_PLUS_PULSES]

Figure 38.2 shows the total number of action potentials fired by E-cells 1 through 5 in 500 ms, as a function of φ . The results are noisy, and that is not surprising, since the rhythm is noise-driven. However, the dependence on φ is clear and pronounced.

Not surprisingly, this effect is dependent on a precise match between the frequency of the sender and that of the receiver. When the period of the sender is reduced by 2 ms, the effect gets much weaker; see Fig. 38.3. “Communication through coherence,” in the sense in which we have interpreted it here, requires the frequencies of sender and receiver to be closely matched. For real gamma rhythms, which will likely not be as regular as the model rhythms considered here, this match may be difficult to achieve.

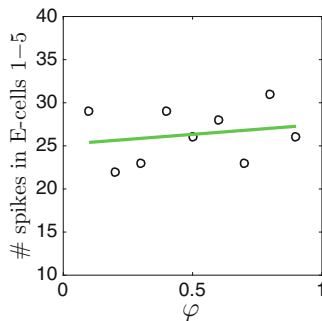


Figure 38.3. Like Fig. 38.2, but with slightly mismatched periods: The input has period 29 ms here. [POISSON_PING_3_MISMATCHED_PULSES]

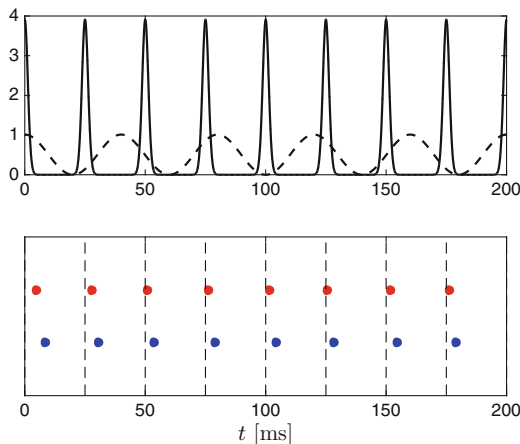


Figure 38.4. Top: A sharply peaked input (solid), and a nearly sinusoidal one (dashes) with the same temporal mean. Using the notation of eq. (35.1), and writing $T = 1000/f$, the parameters are $A = 0.5$ for both inputs, and $f = 40$ Hz, $\alpha = 20$ for the more sharply peaked input, $f = 25$ Hz, $\alpha = 0.1$ for the less sharply peaked one. Bottom: Response of an E-I pair consisting of one RTM neuron (E-cell) and one WB neuron (I-cell) to the sum of the two inputs. The pulsatile inputs drive the E-cell. Spike times of the E-cell are indicated in red, and spike times of the I-cell in blue. The times at which the more sharply peaked input reaches its maximum are indicated by vertical dashed lines in the bottom panel. The constant external drive to both cells is zero. Other parameters are $\hat{g}_{EI} = 0.35$, $\hat{g}_{IE} = 0.5$, $\hat{g}_{EE} = 0$, $\hat{g}_{II} = 0.15$, $\tau_{r,E} = 0.5$, $\tau_{\text{peak},E} = 0.5$, $\tau_{d,E} = 3$, $v_{\text{rev},E} = 0$, $\tau_{r,I} = 0.5$, $\tau_{\text{peak},I} = 0.5$, $\tau_{d,I} = 9$, $v_{\text{rev},I} = -75$. [GAMMA_COHERENCE_1]

38.2 Gamma Coherence-Dependent Communication

Here we will discuss a different interpretation of the phrase *communication through coherence*: Among two pulsatile inputs competing for control of an E-I network, the one that is *more coherent*, namely more sharply peaked, often wins, in the sense that it entrains the target network [13]. The pulsatile inputs should be thought of as resulting from the approximately synchronous, rhythmic firing of neurons in

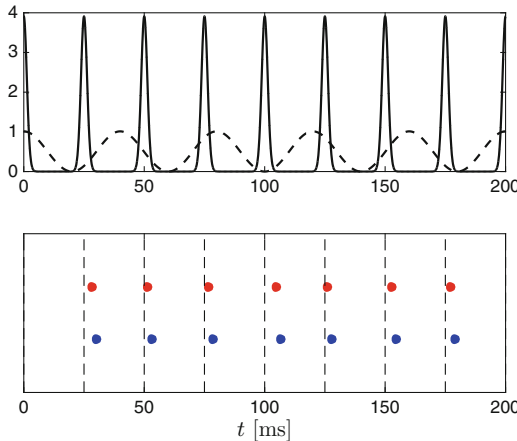


Figure 38.5. Like Fig. 38.4, but with the inhibitory conductance affecting the E-cell replaced by the time average of the inhibitory conductance affecting the E-cell in Fig. 38.4. [GAMMA_COHERENCE_2]

other networks, which we will refer to as the *upstream networks*, to distinguish them from the *target network* receiving the inputs. The tighter the synchrony in an upstream network, the more sharply peaked are the input pulses received by the target network. This is why we use the phrase *coherent* for *sharply peaked*.

We present here variations on the numerical experiments of [13]. Figure 38.4 shows an example. Our target network is a PING network consisting, for simplicity, of just a single RTM neuron (E-cell) and a single WB neuron (I-cell). The E-cell is driven by a superposition of two pulsatile inputs that take the form of the right-hand side of (35.1), with different values of α . For the more coherent input, $\alpha = 20$, whereas for the less coherent one, $\alpha = 0.1$. We will call the more coherent input the *primary input*, and less coherent one the *distractor*. The primary input, i.e., the one with greater α , entrains the target. There is barely any response to the distractor.

We clear up two potential misunderstandings about Fig. 38.4. First, one might think that the *faster* input wins, not the more coherent one. This is incorrect; see exercise 4. Second, one might think that the effect is a matter of *timing* primarily. One could argue as follows. Suppose that one of the primary input pulses triggers a spike in the E-cell, which triggers a spike in the I-cell. The resulting inhibition temporarily prevents any distracting pulses from having effects. From then on, the

primary input will always be timed in a way that is advantageous to it, with the pulses arriving when inhibition is at its weakest, while the pulses of the distractor come at different phases, usually when inhibition is stronger. There are in fact examples in which this argument is correct, and timing does decide which of the two competing inputs entrains the network. This is the case in particular if the distractor is just as coherent as the primary input. In many other cases, and in particular in Fig. 38.4, however, *coherence* matters much more than *timing*. To illustrate this, Fig. 38.5 shows the simulation of Fig. 38.4, but with the inhibitory conductance affecting the E-cell constant in time, equal to the temporal average of what it was in Fig. 38.4.

While the inhibitory conductance itself is important for coherence-dependent communication, as it raises leakiness in the target, its *time dependence* is much less important; see [13] for further discussion of this point.

Exercises

- 38.1. (*) Replace the factor 0.1 in eq. (38.1) by 0.3, then re-compute Fig. 38.2 to see whether the phase dependence is more or less pronounced when the oscillatory input is stronger.
- 38.2. (*) Compute Fig. 38.2 with E-cells 1 through 50 (instead of 5) receiving the periodic drive I_p . Plot the total number of action potentials in E-cells 1 through 50 as a function of φ .
- 38.3. (*) The computational experiments in Section 38.1 started with the stochastic weak PING rhythm of Fig. 32.4. What happens if you start with the deterministic weak PING rhythm of Fig. 32.6 instead? Can you obtain similar results?
- 38.4. (*) Show that Fig. 38.4 does not qualitatively change when the distractor frequency is raised from 25 Hz to 55 Hz.

Part VI

Synaptic Plasticity

Chapter 39

Short-Term Depression and Facilitation

At many synapses, repeated firing of the pre-synaptic neuron can lead to a transient decrease in the strengths of post-synaptic currents, for instance, because of neurotransmitter depletion [53]. This is called *short-term depression*. A phenomenological model of short-term depression was proposed by Tsodyks and Markram [165]. We describe it in Section 39.1.

The first few action potentials after a longer pause in firing can lead to the opposite of short-term depression, *short-term facilitation* [87]. To sketch the hypothesized physical mechanisms of short-term facilitation, we first briefly sketch the mechanism of neurotransmitter release at chemical synapses in general. Neurotransmitter is held in the pre-synaptic cell in small packets called *synaptic vesicles*. A pre-synaptic action potential leads to the opening of voltage-dependent calcium channels in the axon terminal. This results in the influx of calcium into the axon terminal. The calcium interacts with the vesicles in complex ways [4], causing synaptic vesicles to fuse with the cell membrane and release their neurotransmitter into the synaptic cleft. Short-term facilitation may be the result of residual calcium left-over in the axon terminal from preceding action potentials [53, 87]. Repeated firing of the pre-synaptic cell may also enhance the calcium influx into the axon terminal [79]. Tsodyks and Markram extended their model to include this possibility in [164]. Their model of facilitation is described in Section 39.2.

In the models of [164] and [165], dependent variables such as the amount of neurotransmitter present in the synaptic cleft are assumed to jump discontinuously in response to an action potential. In Section 39.3, we replace continuous jumps by rapid transitions, returning to a model that is a system of ODEs. This is convenient because one can then use standard methods for ODEs to solve the equations of

Electronic supplementary material: The online version of this chapter (doi: [10.1007/978-3-319-51171-9_39](https://doi.org/10.1007/978-3-319-51171-9_39)) contains supplementary material, which is available to authorized users.

the model. It may also be more realistic — discontinuous jumps are, after all, idealizations of rapid transitions.

39.1 The Tsodyks-Markram Model of Short-Term Depression

In addition to the dependent variable q of Chapter 20, there are two further dependent variables in the Tsodyks-Markram model of [165], which we will call p and r . All three of these variables lie between 0 and 1, and their sum equals 1. The variable p represents the fraction of neurotransmitter that is available for release, q is, as in Chapter 20, the fraction that is active in the synaptic cleft, and r is the fraction that is “inactive,” i.e., has been removed from the synaptic cleft, and is in the process of being transported back to the pre-synaptic terminal.

When the pre-synaptic neuron fires, q is assumed to be raised by Up , where $U \in (0, 1)$ is a model parameter measuring how effectively the available neurotransmitter is utilized. Simultaneously p drops by Up , so $r = 1 - p - q$ remains unaffected. Between pre-synaptic action potentials, q decreases exponentially, as in Chapter 20:

$$\frac{dq}{dt} = -\frac{q}{\tau_{d,q}}.$$

The time constant $\tau_{d,q}$ was taken to be 3 ms in [165]. At the same time, “inactive” neurotransmitter gradually becomes available for release again:

$$\frac{dp}{dt} = \frac{r}{\tau_{\text{rec}}} = \frac{1 - p - q}{\tau_{\text{rec}}}. \quad (39.1)$$

The time constant τ_{rec} is long; 450 ms and 800 ms are values used in [165]. The subscript “rec” in “ τ_{rec} ” stands for “recovery.” We use the variable q in precisely the same way as in Chapter 20, so the time evolution of the synaptic gating variable s is governed by eq. (20.7), which we re-state here for the reader’s convenience:

$$\frac{ds}{dt} = q \frac{1 - s}{\tau_r} - \frac{s}{\tau_d}. \quad (20.7)$$

This constitutes a model of short-term *depression* because the variable p , measuring the amount of neurotransmitter available for release, drops with each pre-synaptic action potential, and therefore the rise in q caused by a pre-synaptic action potential becomes smaller.

39.2 The Tsodyks-Markram Model of Short-Term Facilitation

Tsodyks and Markram extended their model to include the possibility of facilitation by making U a function of time, letting U rise by a fixed fraction of $1 - U$ in response to each pre-synaptic spike. We call this fraction μ , and assume $0 < \mu \leq 1$. Thus

$$U(t_0 + 0) = U(t_0 - 0) + \mu(1 - U(t_0 - 0)), \quad (39.2)$$

where t_0 denotes the time of an action potential; see eq. (2.2) of [164].

Since U jumps instantaneously in response to a pre-synaptic action potential in this model, the question arises whether the old (pre-jump) value of U , or the new (post-jump) one is to be used in determining the amounts by which q rises and p falls. We will not answer this question for now. When we replace discontinuous jumps by rapid transitions governed by ODEs in Section 39.3, the question will disappear; see the last paragraph of Section 39.3.

Between pre-synaptic action potentials, U is assumed to decay exponentially with a time constant τ_{facil} ; again compare eq. (2.2) of [164]. In [164], U is assumed to decay to zero in the absence of firing. This implies that the first action potential after a long pause in firing causes no synaptic current at all. I will instead assume that U decays to a value $U_0 \in [0, 1]$, and allow the possibility $U_0 > 0$; thus U_0 is another parameter of the model.

39.3 Replacing Jumps by Transitions Governed by ODEs

We now replace the discontinuous changes in the variables p and q of the model of Section 39.1 by rapid but continuous changes, governed by differential equations. Let t_0 be the time of an action potential. The changes in p and q resulting from the action potential are, according to Tsodyks and Markram,

$$q(t_0 + 0) = q(t_0 - 0) + Up(t_0 - 0), \quad (39.3)$$

$$p(t_0 + 0) = p(t_0 - 0) - Up(t_0 - 0). \quad (39.4)$$

(For now, $U \in (0, 1)$ is a constant, as in Section 39.1.) We focus first on eq. (39.4), which we re-write as

$$p(t_0 + 0) = (1 - U)p(t_0 - 0).$$

Taking logarithms on both sides, we find that the pre-synaptic action potential causes $\ln p$ to jump by $\ln(1 - U) = -\ln(1/(1 - U))$:

$$\ln p(t_0 + 0) = \ln p(t_0 - 0) - \ln \frac{1}{1 - U}.$$

(Note that $\ln(1/(1 - U)) > 0$.) Suppose now that $\gamma = \gamma(t)$ is a smooth function that is positive on a small interval surrounding t_0 , but zero everywhere else, with $\int_{-\infty}^{\infty} \gamma(t)dt = 1$.³³ If $p = p(t) > 0$ solves

$$\frac{d}{dt} \ln p = -\gamma \ln \frac{1}{1 - U} \quad (39.5)$$

then $\ln p$ decreases rapidly (but continuously) by $\ln(1/(1 - U))$ as t rises above t_0 , and is otherwise constant. Using the chain rule, we re-write eq. (39.5) as

$$\frac{dp}{dt} = -p\gamma \ln \frac{1}{1 - U}. \quad (39.6)$$

³³If you know the definition of the *Dirac delta function* δ , then you will realize that γ is a smooth approximation of δ . However, I am presenting this derivation without assuming that you know what the delta function is.

By adding the right-hand side of (39.6) to the right-hand side of (39.1), we obtain an equation that makes p fall rapidly by the correct amount as t rises above t_0 , and preserves eq. (39.1) otherwise:

$$\frac{dp}{dt} = \frac{1-p-q}{\tau_{\text{rec}}} - p\gamma \ln \frac{1}{1-U}. \quad (39.7)$$

The term that we just subtracted from the equation for dp/dt reflects the release of available neurotransmitter as a result of the action potential. The same term should be *added* to the equation for dq/dt , since $p+q$ should not change as a result of the action potential:

$$\frac{dq}{dt} = -\frac{q}{\tau_{d,q}} + p\gamma \ln \frac{1}{1-U}. \quad (39.8)$$

We now have to specify the pulse γ used in eq. (39.7). I have no entirely satisfactory choice of γ , but will make γ proportional to $1 + \tanh(v/10)$, since $1 + \tanh(v/10) \approx 2$ during voltage spikes, and $1 + \tanh(v/10) \approx 0$ otherwise.³⁴ Figure 39.1 demonstrates this point.

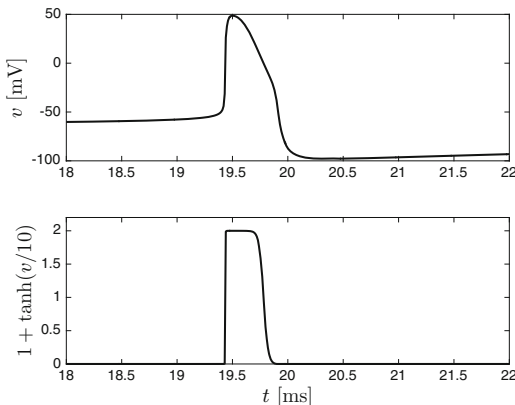


Figure 39.1. An action potential of an RTM neuron, and the function $(1 + \tanh(v/10))$ (as a function of t). [PULSES]

To make the area under the pulse in the lower panel of Fig. 39.1 equal to 1, one must multiply the function $1 + \tanh(v/10)$ by a scaling factor C . The choice of C is what is not entirely satisfactory about our definition of γ . Its value should depend on the shape of the voltage trace during an action potential, and in particular on the duration of the action potential. However, since the action potential shape is largely independent of external or synaptic input to the neuron, it is not unreasonable to choose a single value of C for the RTM neuron; see also exercise 1. The area under the pulse in the lower panel of Fig. 39.1 is about 0.69, and $1/0.69 \approx 1.45$, so $C = 1.45$ will be our choice.

³⁴The function $1 + \tanh(v/10)$ is a fairly arbitrary choice here; compare exercise 20.1.

With these modifications, the Tsodyks-Markram model of short-term depression is very similar to the model of Chapter 20, with the dependent variable p added. The equations governing p , q , and s are

$$\frac{dp}{dt} = \frac{1-p-q}{\tau_{\text{rec}}} - 1.45 \left(1 + \tanh \frac{v}{10}\right) p \ln \frac{1}{1-U}, \quad (39.9)$$

$$\frac{dq}{dt} = -\frac{q}{\tau_{d,q}} + 1.45 \left(1 + \tanh \frac{v}{10}\right) p \ln \frac{1}{1-U}, \quad (39.10)$$

$$\frac{ds}{dt} = q \frac{1-s}{\tau_r} - \frac{s}{\tau_d}. \quad (39.11)$$

Figure 39.2 shows the voltage trace of a periodically firing RTM neuron, and the associated synaptic gating variables p , q , and s derived from eqs. (39.9)–(39.11). The most important panel is the right lower one, which shows the depressing gating variable s .

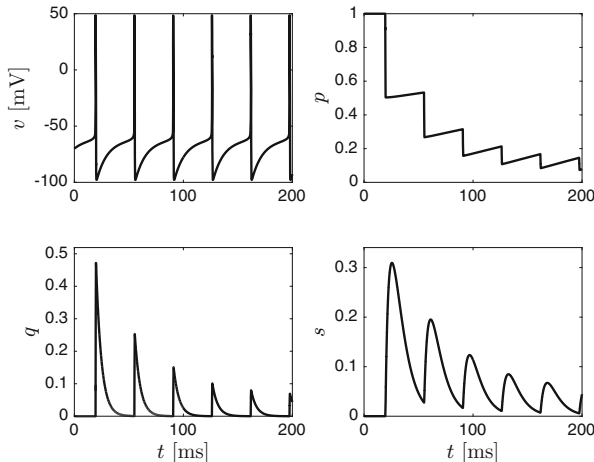


Figure 39.2. Voltage trace of a periodically firing RTM neuron ($I = 0.5$), and the solutions p , q , and s of eqs. (39.9)–(39.11). The parameters are $\tau_{\text{rec}} = 500$, $U = 0.5$, $\tau_{d,q} = 5$, $\tau_r = 0.5$, $\tau_d = 3$. [RTM_WITH_DEPRESSING_S]

It is easy to show that the model of Section 20.2, with $\tau_{r,q} = 0.1$, is the limiting case of infinitely fast recovery ($\tau_{\text{rec}} \rightarrow 0$) of the model in the present section, with almost perfect efficiency: $U = 1 - e^{-1/0.29} \approx 0.968$ (exercise 2).

For the WB neuron, the choice of C that makes the area under the pulses in $C(1 + \tanh(v/10))$ equal to 1 is approximately 1.25. Figure 39.3 shows the analogue of Fig. 39.2 with the RTM neuron replaced by the WB neuron, and with $C = 1.25$ instead of $C = 1.45$.

We now turn to the model of Section 39.2, and again turn discontinuous jumps into rapid transitions governed by ordinary differential equations. We rewrite eq. (39.2) as

$$1 - U(t_0 + 0) = (1 - \mu)(1 - U(t_0 - 0)). \quad (39.12)$$

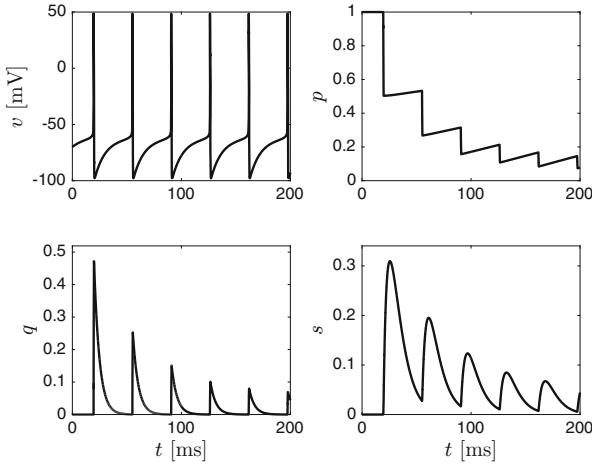


Figure 39.3. Like Fig. 39.2, but with the RTM neuron replaced by the WB neuron, and with $C = 1.25$ instead of $C = 1.45$. [WB_WITH_DEPRESSING_S]

Taking logarithms and multiplying by -1 , we find

$$\ln \frac{1}{1 - U(t_0 + 0)} = \ln \frac{1}{1 - U(t_0 - 0)} + \ln \frac{1}{1 - \mu}. \quad (39.13)$$

With the notation

$$W = \ln \frac{1}{1 - U} \quad (39.14)$$

eq. (39.13) becomes

$$W(t_0 + 0) = W(t_0 - 0) + \ln \frac{1}{1 - \mu}. \quad (39.15)$$

A smoothed version of this reset condition is

$$\frac{dW}{dt} = \gamma \ln \frac{1}{1 - \mu} \quad (39.16)$$

where $\gamma = \gamma(t)$ is the pulse defined earlier. A short calculation (exercise 3) shows that the equation

$$\frac{dU}{dt} = \frac{U_0 - U}{\tau_{\text{facil}}}, \quad (39.17)$$

which describes the decay of U between pre-synaptic spikes, translates into

$$\frac{dW}{dt} = -\frac{(1 - U_0)e^W - 1}{\tau_{\text{facil}}}. \quad (39.18)$$

Combining eq. (39.16) and (39.18), we find

$$\frac{dW}{dt} = -\frac{(1 - U_0)e^W - 1}{\tau_{\text{facil}}} + \gamma \ln \frac{1}{1 - \mu}. \quad (39.19)$$

We write $W_0 = \ln(1/(1 - U_0))$ and $\nu = \ln(1/(1 - \mu))$. Then the preceding equation becomes (exercise 4)

$$\frac{dW}{dt} = -\frac{e^{W-W_0} - 1}{\tau_{\text{facil}}} + \gamma\nu. \quad (39.20)$$

This equation is now added to (39.9)–(39.11). Remembering $W = \ln(1/(1 - U))$, we obtain the final form of our smoothed version of the Tsodyks-Markram model:

$$\frac{dp}{dt} = \frac{1-p-q}{\tau_{\text{rec}}} - C \left(1 + \tanh \frac{v}{10} \right) pW, \quad (39.21)$$

$$\frac{dq}{dt} = -\frac{q}{\tau_{d,q}} + C \left(1 + \tanh \frac{v}{10} \right) pW, \quad (39.22)$$

$$\frac{ds}{dt} = q \frac{1-s}{\tau_r} - \frac{s}{\tau_d}, \quad (39.23)$$

$$\frac{dW}{dt} = -\frac{e^{W-W_0} - 1}{\tau_{\text{facil}}} + C\nu \left(1 + \tanh \frac{v}{10} \right), \quad (39.24)$$

$$W_0 = \frac{1}{1-U_0}, \quad \nu = \ln \frac{1}{1-\mu}.$$

We use $C = 1.45$ for the RTM model, and $C = 1.25$ for the WB model. Figure 39.4 shows a solution of these equations, for the RTM model with $I = 0.5$. The crucial panel in the figure is the middle one in the bottom row: s first facilitates, then depresses.

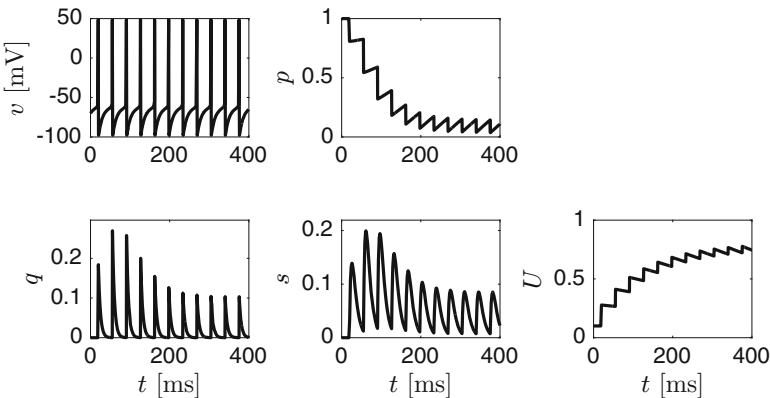


Figure 39.4. Voltage trace of a periodically firing RTM neuron ($I = 0.5$), and the functions p , q , s , and $U = 1 - e^{-W}$ obtained from eqs. (39.21)–(39.24). The parameters are $\tau_{\text{rec}} = 300$, $\tau_{\text{facil}} = 500$, $U_0 = 0.1$, $\mu = 0.2$, $\tau_{d,q} = 5$, $\tau_r = 0.5$, $\tau_d = 3$, $C = 1.45$. [RTM_WITH_DEPRESSING_AND_FACILITATING_S]

In Section 39.2, the question arose whether one should use the pre-jump or post-jump value of U to compute the jumps in p and q . Turning the model into a system of differential equations has made the question disappear: p , q , and U (or, equivalently, W) change simultaneously and smoothly.

As pointed out earlier, the choice of C is a somewhat unsatisfactory aspect of the approach described here. Strictly, C should depend on external and synaptic drives to a small degree. We have ignored this dependence, but chosen different values of C for different neuronal models. It would not seem unreasonable, however, to simply set $C = 1$ (or $C = 1.25$) in all cases. For instance, if one re-computes Fig. 39.4 with $C = 1$, the result does not look very different from Fig. 39.4.

Exercises

- 39.1. (*) In this chapter, we used the assumption that the differential equation

$$\frac{dw}{dt} = C \left(1 + \tanh \frac{v}{10} \right), \quad (39.25)$$

with v = membrane potential of an RTM neuron and $C = 1.45$, raises w by 1 each time the RTM neuron fires. Of course this can't be *precisely* correct, for example, because the spike shape depends at least slightly on parameters such as the external drive. To get a sense for how close to correct this assumption is, do the following experiment. Start an RTM neuron with a drive I above threshold at $v = -70$ mV, $m = m_\infty(v)$, $h = h_\infty(v)$, $n = n_\infty(v)$. Simulate until 3 ms past the third action potential. At the same time, solve eq. (39.25), with $C = 1.45$, starting at $w = 0$. Plot the final value of w , divided by 3, as a function of I . The final value of w , divided by 3, ought to be close to 1, since each of the three action potentials should raise w by about 1.

Start with the code that generates Fig. 5.2. You might want to consider $I \geq 0.15$ only, avoiding values of I for which the firing period is so long that the simulation will take a long time.

- 39.2. Show that the model of Section 20.2, with $\tau_{r,q} = 0.1$, is the special case of (39.9)–(39.11) when $\tau_{\text{rec}} \rightarrow 0$ and $U = 1 - e^{-1/0.29}$.
- 39.3. Derive eq. (39.18).
- 39.4. Explain how eq. (39.19) becomes eq. (39.20).

Chapter 40

Spike Timing-Dependent Plasticity (STDP)

We mentioned spike timing-dependent plasticity (STDP) in Section 33.2 already. Experimental evidence for STDP was presented in [68]: The connection from cell A to cell B was shown to be strengthened when A fired just before B (*Hebbian learning*), and weakened when B fired just before A (*anti-Hebbian learning*). To model STDP at a synapse, we make the maximum conductance \bar{g}_{syn} associated with the synapse (see eq. (20.8)) time-dependent. In analogy with Sections 39.1 and 39.2, we first describe a model in which the value of \bar{g}_{syn} jumps discontinuously, and then turn it into a differential equations model in which the change is rapid but continuous.

40.1 The Song-Abbott Model

Following Song and Abbott [145], we assume that the results of STDP can be described as follows. Suppose that in a network, neuron j fires at a time t_j . Let $t_{i,0} < t_j$ be the most recent spike time of neuron i . Denote the maximum conductance associated with the synaptic input from neuron i into neuron j by \bar{g}_{ij} , and define \bar{g}_{ji} analogously. At time t_j , we strengthen \bar{g}_{ij} and weaken \bar{g}_{ji} :

$$\bar{g}_{ij} \rightarrow \bar{g}_{ij} + K_+ e^{-(t_j - t_{i,0})/\tau_+}, \quad (40.1)$$

$$\bar{g}_{ji} \rightarrow \bar{g}_{ji} - K_- e^{-(t_j - t_{i,0})/\tau_-}, \quad (40.2)$$

where K_+ , K_- , τ_+ , and τ_- are positive constants. They may depend on i and j , but we don't indicate this dependence in our notation for simplicity. The values of K_+ and K_- determine how much the strengths of synapses change as a result of plasticity, and τ_+ and τ_- determine how soon one spike must follow another for

Electronic supplementary material: The online version of this chapter (doi: [10.1007/978-3-319-51171-9_40](https://doi.org/10.1007/978-3-319-51171-9_40)) contains supplementary material, which is available to authorized users.

there to be significant plasticity. For experimental evidence that this is at least in some instances a reasonable caricature of reality, see Fig. 5 of [190], reproduced in Fig. 40.1.

As written, the model has a discontinuity: If neuron j fires very soon after neuron i , then \bar{g}_{ij} is significantly strengthened, and \bar{g}_{ji} is significantly weakened.

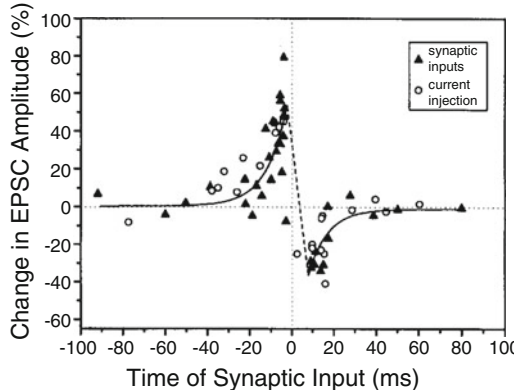


Figure 40.1. Part of Fig. 5 of [190], reproduced with publisher's permission. The figure shows results of experiments on nerve cells in tadpole tectum (a brain structure important for visual reflexes). In each experiment, the tectal cell received a series of 100 input pairs, arriving at a frequency of 1 Hz. Each input pair consisted of an input A strong enough to trigger firing, and an input B that only triggered a transient surge in membrane potential, an excitatory post-synaptic potential (EPSP), but no action potential. Ten to thirty minutes after stimulation, the EPSP triggered by B was found to be strengthened if B had always arrived just before A, weakened if B had always arrived just after A. The plot shows the percentage change in the amplitude of the EPSP, as a function of the arrival time of B, with the convention that time 0 is the arrival time of A. Solid triangles and open circles refer to two different methods of stimulation, synaptic inputs and current injections.

However, if neuron i fires very soon after neuron j , the reverse happens. We remove this discontinuity by modifying eqs. (40.1) and (40.2) like this:

$$\bar{g}_{ij} \rightarrow \bar{g}_{ij} + K_+ e^{-(t_j - t_{i,0})/\tau_+} \left(1 - e^{-5(t_j - t_{i,0})/\tau_+} \right), \quad (40.3)$$

$$\bar{g}_{ji} \rightarrow \bar{g}_{ji} - K_- e^{-(t_j - t_{i,0})/\tau_-} \left(1 - e^{-5(t_j - t_{i,0})/\tau_-} \right). \quad (40.4)$$

To put it without using the subscripts i and j , if the pre-synaptic neuron fires at time t_{pre} , the post-synaptic neuron fires at time t_{post} , and $z = t_{\text{post}} - t_{\text{pre}}$, then the change in the synaptic strength from the pre-synaptic to the post-synaptic neuron is $F_0(z)$ according to (40.1) and (40.2), and $F(z)$ according to the smoothed model (40.3), (40.4), with

$$F_0(z) = \begin{cases} K_+ e^{-z/\tau_+} & \text{if } z > 0, \\ -K_- e^{z/\tau_-} & \text{if } z < 0, \end{cases} \quad (40.5)$$

and

$$F(z) = \begin{cases} K_+ e^{-z/\tau_+} (1 - e^{-5z/\tau_+}) & \text{if } z > 0, \\ -K_- e^{z/\tau_-} (1 - e^{5z/\tau_-}) & \text{if } z < 0. \end{cases} \quad (40.6)$$

Figure 40.2 shows the graphs of F_0 (black) and F (red) for one particular choice of parameters.

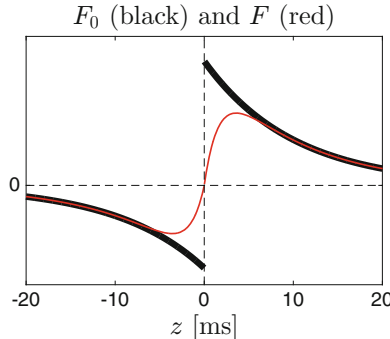


Figure 40.2. Graphs of functions of the forms (40.5) and (40.6). The analogue of the horizontal coordinate in Fig. 40.1 is $-z$, not z . [ABBOTT_SONG]

The function F is not in general differentiable at $z = 0$ (exercise 1). However, this will not make the right-hand side of the differential equations model in Section 40.2 non-smooth. The reason is that the two formulas in (40.6) apply to two different conductances. The upper formula is relevant for the synaptic input from the earlier-firing neuron to the later-firing one. The lower formula is relevant for the reverse direction.

The reset described by (40.3) can make \bar{g}_{ij} arbitrarily large, and similarly (40.4) can result in negative \bar{g}_{ji} . These observations suggest replacing (40.3) and (40.4) by

$$\bar{g}_{ij} \rightarrow \min\left(B, \bar{g}_{ij} + K_+ e^{-(t_j - t_{i,0})/\tau_+} \left(1 - e^{-5(t_j - t_{i,0})/\tau_+}\right)\right), \quad (40.7)$$

$$\bar{g}_{ji} \rightarrow \max\left(0, \bar{g}_{ji} - K_- e^{-(t_j - t_{i,0})/\tau_-} \left(1 - e^{-5(t_j - t_{i,0})/\tau_-}\right)\right), \quad (40.8)$$

where $B > 0$ is an upper bound imposed on \bar{g}_{ij} . However, this would have the effect of making the right-hand side of our differential equations in Section 40.2 non-smooth, since $\min(B, x)$ and $\max(0, x)$ are not differentiable functions of x . We therefore use the smooth approximations \min_δ and \max_δ for \min and \max defined in eqs. (D.4) and (D.6), using a smoothing parameter $\delta > 0$ yet to be chosen. (We typically take it to be a fraction of the initial value of \bar{g}_{syn} .) Therefore (40.7) and (40.8) now turn into

$$\bar{g}_{ij} \rightarrow \min_\delta\left(B, \bar{g}_{ij} + K_+ e^{-(t_j - t_{i,0})/\tau_+} \left(1 - e^{-5(t_j - t_{i,0})/\tau_+}\right)\right), \quad (40.9)$$

$$\bar{g}_{ji} \rightarrow \max_\delta\left(0, \bar{g}_{ji} - K_- e^{-(t_j - t_{i,0})/\tau_-} \left(1 - e^{-5(t_j - t_{i,0})/\tau_-}\right)\right). \quad (40.10)$$

We re-write (40.10) with the roles of i and j reversed: When neuron i fires soon after neuron j , then \bar{g}_{ij} is weakened:

$$\bar{g}_{ij} \rightarrow \max_{\delta} \left(0, \bar{g}_{ij} - K_- e^{-(t_i - t_{j,0})/\tau_-} \left(1 - e^{-5(t_i - t_{j,0})/\tau_-} \right) \right). \quad (40.11)$$

(40.11) describes how \bar{g}_{ij} is weakened when neuron i fires soon after neuron j , while (40.9) describes how \bar{g}_{ij} is strengthened when neuron j fires soon after neuron i .

40.2 Replacing Jumps by Transitions Governed by ODEs

Equations (40.9) and (40.11) describe discontinuous resets. We would like to replace them by differential equations describing rapid but smooth transitions. To this end, we first associate with each neuron a variable that we will call $a = a(t)$; approximately, it will be the time elapsed since the most recent spike. Between spikes, a should therefore simply satisfy

$$\frac{da}{dt} = 1. \quad (40.12)$$

However, a spike should cause a to be reset to 0, approximately. It is easier to reset a to a small fraction of its pre-spike value. We choose the fraction to be 1/100. If t_0 is the time of a spike, then we will try to accomplish, approximately,

$$a(t_0 + 0) = \frac{a(t_0 - 0)}{100}.$$

Taking logarithms on both sides, we obtain

$$\ln a(t_0 + 0) = \ln(a(t_0 - 0)) - \ln(100).$$

A smooth approximation of this equation is

$$\frac{d}{dt} (\ln(a(t))) = -C \ln(100) \left(1 + \tanh \frac{v}{10} \right),$$

with C defined as in Section 39.1: $C = 1.45$ for the RTM model, and $C = 1.25$ for the WB model. Thus

$$\frac{da}{dt} = -Ca \ln(100) \left(1 + \tanh \frac{v}{10} \right).$$

Note that we made the fairly arbitrary choice of (approximately) resetting a to the fraction 1/100 of its pre-spike value when the neuron fires. Therefore the factor $\ln(100) \approx 4.61$ in the differential equation is somewhat arbitrary. We will replace $C \ln(100)$ by 5, for both the RTM and WB neurons:

$$\frac{da}{dt} = -5a \left(1 + \tanh \frac{v}{10} \right). \quad (40.13)$$

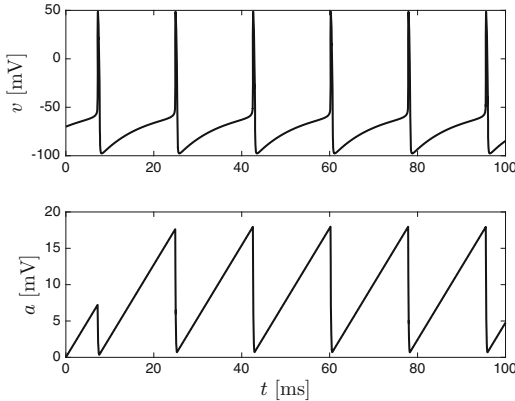


Figure 40.3. Voltage trace of the RTM neuron with $I = 1.5$, and the function a satisfying (40.14) with $a(0) = 0$. [RTM_VOLTAGE_TRACE_WITH_A]

Combining eqs. (40.12) and (40.13), we obtain

$$\frac{da}{dt} = 1 - 5a \left(1 + \tanh \frac{v}{10} \right). \quad (40.14)$$

Figure 40.3 confirms that a keeps track of the time elapsed since the last spike.

In a network, each neuron is associated with its own variable a . We denote the variable a associated with the i -th neuron by a_i . The reset conditions (40.9) and (40.11) are replaced by

$$\begin{aligned} \frac{d\bar{g}_{ij}}{dt} &= C \left(1 + \tanh \frac{v_j}{10} \right) \left[\min_{\delta} \left(B, \bar{g}_{ij} + K_+ e^{-a_i/\tau_+} \left(1 - e^{-5a_i/\tau_+} \right) \right) - \bar{g}_{ij} \right] \\ &\quad + C \left(1 + \tanh \frac{v_i}{10} \right) \left[\max_{\delta} \left(0, \bar{g}_{ij} - K_- e^{-a_j/\tau_-} \left(1 - e^{-5a_j/\tau_-} \right) \right) - \bar{g}_{ij} \right], \end{aligned}$$

again with C defined as in Section 39.1: $C = 1.45$ for the RTM model, and $C = 1.25$ for the WB model.

This completes the statement of our smoothed version of the STDP model of Song and Abbott [145], except for parameter choices: K_+ , K_- , τ_+ , τ_- , B , and δ are yet to be chosen. We will describe now how these parameters are set in the numerical experiments of Chapter 40. We do not claim biological accuracy here, but we do strive to make our choices of K_+ , K_- , τ_+ , and τ_- roughly compatible with Fig. 5 of [190] (reproduced in Fig. 40.1). First, for each pair of neurons, say neurons i and j , we choose an initial value of \bar{g}_{ij} . These values are set as in Section 30.2, and we will use the notation $\bar{g}_{ij}^{(0)}$ to indicate that they are only the *initial* values of the \bar{g}_{ij} , which evolve according to differential equations now. The values K_+ and K_- associated with the synaptic connection from the i -th neuron to the j -th are then

$$K_{+,ij} = \frac{\bar{g}_{ij}^{(0)}}{2}, \quad K_{-,ij} = \frac{\bar{g}_{ij}^{(0)}}{3}.$$

Thus if neuron i fires just before neuron j , the connection from i to j strengthens by about $\bar{g}_{ij}^{(0)}/2$, but with the constraint that the strength cannot rise above $B = B_{ij}$. If neuron i fires just after neuron j , the connection from i to j weakens by about $\bar{g}_{ij}^{(0)}/3$, but with the constraint that the strength cannot fall below 0. The equation $K_- = 2K_+/3$ is in rough agreement with Fig. 5 of [190] (see Fig. 40.1). We always use

$$\tau_+ = \tau_- = 10 \text{ ms}.$$

This is compatible with Fig. 5 of [190]. Thus two action potentials separated by several tens of ms will have very little effect on synaptic strengths. The value of \bar{g}_{ij} is bounded by five times its initial value:

$$B_{ij} = 5\bar{g}_{ij}^{(0)}.$$

We generally set the value of the smoothing parameter δ to

$$\delta_{ij} = \frac{\bar{g}_{ij}^{(0)}}{2}.$$

40.3 STDP in Three-Cell Networks

Heuristically, one might think that recurrent excitation would tend to synchronize neurons effectively: The neurons that fire help the ones that are behind. We saw in Chapter 24 that recurrent excitation can in fact create approximate synchrony, but the mechanism is more brittle than one might expect. Excitation-based synchrony is less robust than inhibition-based synchrony.

Here we take up this issue one more time, but with two twists. First, we now study PING networks instead of purely excitatory ones. The I-cells take over the primary responsibility for creating synchrony, but we ask whether recurrent excitation can support synchronization when there is heterogeneity in network parameters such as external drives. Often the answer is yes: Fast recurrent excitation can tighten synchrony in PING networks. Not surprisingly, it also accelerates the rhythm. Furthermore, with strong recurrent excitation, there can be *runaway firing*; we will not define precisely what we mean by that, but will give examples shortly. If one starts with weak recurrent excitation, then adds STDP to allow recurrent excitatory connections to strengthen or weaken selectively, one can obtain the tightening effect with very little acceleration of the rhythm, and remove the possibility of runaway firing. This is what we will demonstrate in this and the next section.

We begin with a network of two E-cells and one I-cell, in which the two E-cells receive very different external drives; see Fig. 40.4. The heterogeneity in the drive to the E-cells prevents the formation of a PING rhythm. The I-cell fires at about 23 Hz. The E-cells don't synchronize.

We now add recurrent excitation: The first E-cell excites the second, and vice versa. Both directions are characterized by a maximal conductance \bar{g}_{EE} . There are no excitatory autapses. Even with weak recurrent excitation, a PING rhythm forms; see Fig. 40.5, upper panel. The period is now about 32ms, corresponding to a

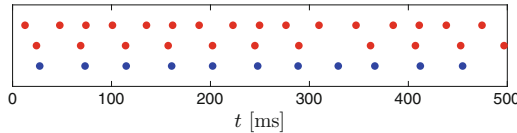


Figure 40.4. Spike rastergram for a network of two E-cells and one I-cell. The E-cells receive external drives 0.4 and 0.8, respectively. All possible synapses are present, except for E-to-E connections. The maximal conductances associated with the synapses are $\bar{g}_{EI} = 0.125$, $\bar{g}_{IE} = 0.25$, and $\bar{g}_{II} = 0.25$. The time constants and reversal potentials associated with the synapses are $\tau_{r,E} = 0.5$, $\tau_{\text{peak},E} = 0.5$, $\tau_{d,E} = 3$, $v_{\text{rev},E} = 0$, $\tau_{r,I} = 0.5$, $\tau_{\text{peak},I} = 0.5$, $\tau_{d,I} = 9$, $v_{\text{rev},I} = -75$. [[THREE_CELL_PING_1](#)]

frequency of about 31 Hz, considerably faster than the I-cell frequency in Fig. 40.4. For very strong recurrent excitation, there can be *runaway firing*; see Fig. 40.5, lower panel.

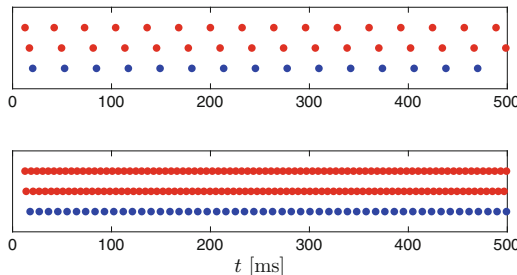


Figure 40.5. Same as Fig. 40.4, but the E-cells now excite each other, with maximum conductance $\bar{g}_{EE} = 0.05$ (upper panel) or $\bar{g}_{EE} = 0.4$ (lower panel). They do not self-excite. [[THREE_CELL_PING_2](#)]

The two E-cells in the upper panel of Fig. 40.5 are tightly phase-locked, but their phase difference is substantial, with the first E-cell lagging behind the second. The phase difference can be reduced by raising the strength of recurrent excitation. We use

$$\Delta = \text{average delay between spike of E-cell 2 and next spike of E-cell 1} \quad (40.15)$$

as a measure of E-cell synchronization, and plot it as a function of \bar{g}_{EE} ; see the left panel of Fig. 40.6. In the right panel of the same figure, we show the frequency of the second (more strongly driven) E-cell as a function of \bar{g}_{EE} . (“Frequency” is defined here as the reciprocal of the mean inter-spike interval, times 1000.) The synchronization of the two E-cells becomes tighter with increasing \bar{g}_{EE} , until \bar{g}_{EE} reaches a threshold value of about 0.23. As \bar{g}_{EE} crosses this threshold, the drive to the second E-cell becomes so strong that there is phase walkthrough, and as a result Δ rises again; see exercise 5.

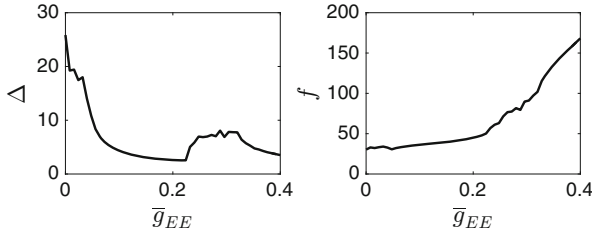


Figure 40.6. Network as in Fig. 40.5, but with varying values of \bar{g}_{EE} . Left: Synchrony measure Δ defined in eq. (40.15), as a function of \bar{g}_{EE} . Right: Frequency of the second E-cell, as a function of \bar{g}_{EE} . [THREE_CELL_PING_3]

Since the second E-cell is driven much more strongly than the first, all we really need to bring their spike times together is a strong excitatory connection from the second E-cell to the first. Figure 40.7 shows the same results as Fig. 40.6, but with an excitatory connection only from the second E-cell to the first, not the other way around. As the connection is strengthened, the frequency now stays constant, while synchrony improves.

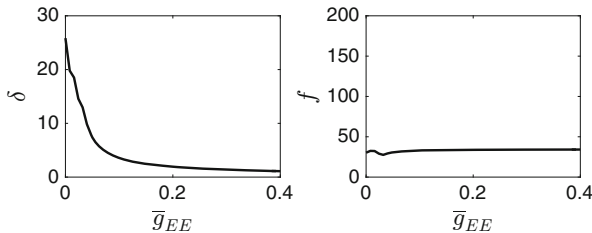


Figure 40.7. Like Fig. 40.6, but with the synaptic connection from E-cell 1 to E-cell 2 removed. [THREE_CELL_PING_4]

The asymmetric connectivity used in Fig. 40.7 is precisely what STDP produces automatically. This is demonstrated by Fig. 40.8.

40.4 STDP in Larger PING Networks

Figure 40.9 shows a PING simulation with recurrent excitation and STDP. Notice the gradual tightening of the E-cell spike volleys, analogous to that seen in Fig. 40.8. In Fig. 40.9, approximately 130 E-cells participate in the spike volleys, with approximately 120 permanently suppressed.

In Fig. 40.10, we show the distribution of synaptic strengths in the network of Fig. 40.8, at time $t = 500$.³⁵ The plot shows that STDP creates a bimodal

³⁵To be precise, what is shown in Fig. 40.10 is

$$\rho(\bar{g}_{EE}) = \frac{1}{N_E(N_E - 1)} \sum_{i=1}^{N_E} \sum_{j \neq i} \frac{e^{-(\bar{g}_{EE,ij} - \bar{g}_{EE})^2 / (2\sigma^2)}}{\sqrt{2\pi\sigma^2}}$$

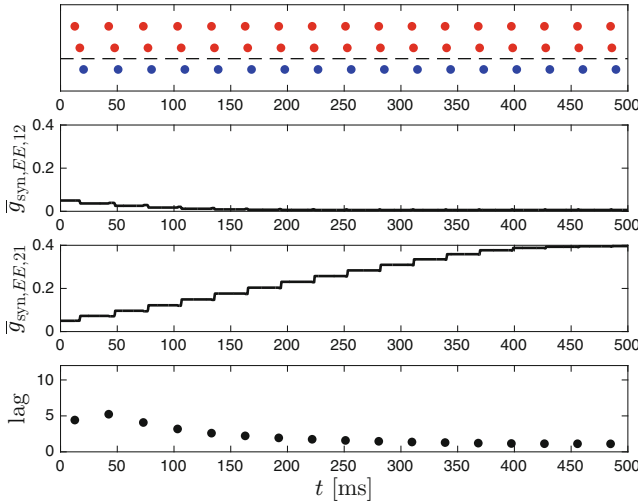


Figure 40.8. Network as in Figs. 40.4 and 40.5, but now with plastic \bar{g}_{EE} , with STDP modeled as in Chapter 40. The values \bar{g}_{EE} start out at 0.05 for the excitatory connections from E-cell 2 to E-cell 1, and vice versa. The parameters associated with the STDP model are $K_+ = 0.05/2$, $K_- = 0.05/3$, $\tau_+ = \tau_- = 10$, $B = 0.4$, and $\delta = 0.05/2$. [THREE_CELL_PING_5]

distribution of E-to-E strengths — some strong ones, and many weak ones. This is why STDP creates recurrent excitation that sharpens synchrony without creating runaway activity: The strongly driven E-cells accelerate the weakly driven ones, but there is no indiscriminate all-to-all excitation among the E-cells.

Exercises

- 40.1. Show that the function $F(z)$ in eq. (40.6) is continuous, but not in general differentiable at $z = 0$.
- 40.2. How large does $z > 0$ have to be for $F(z)$ to differ from $F_0(z)$ by no more than 2%?
- 40.3. Suppose that there is an autapse from neuron i to itself. What happens to \bar{g}_{II} when neuron i fires, according to our smoothed version of the Song-Abbott model?
- 40.4. Let $\delta > 0$, and $M_\delta(x) = \max_\delta(0, x)$ for all $x \in \mathbb{R}$. (See eq. (D.6) for the definition of \max_δ .) (a) Prove that M_δ is an infinitely often differentiable

with $\sigma = 10^{-4}$. Note that the function $\frac{e^{-(\bar{g}_{EE,ij} - \bar{g}_{EE})^2 / (2\sigma^2)}}{\sqrt{2\pi\sigma^2}}$ is a Gaussian density in the variable \bar{g}_{EE} with standard deviation σ centered at $\bar{g}_{EE,ij}$; see eq. (C.12). Its integral with respect to \bar{g}_{EE} is 1. Therefore the integral of the function ρ is 1 as well.

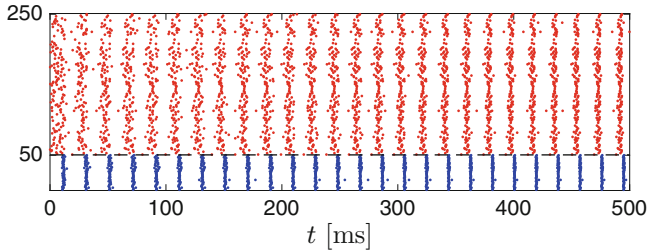


Figure 40.9. Spike rastergram of a PING network with a large degree of heterogeneity in external drives to the E-cells, and with recurrent excitation with STDP. The drives $I_{E,i}$, $1 \leq i \leq N_E$, to the E-cells are independent, uniformly distributed random numbers between 0.2 and 2.0 (chosen once and for all at the start of the simulation, i.e., independent of time). Notice the gradual tightening of the E-cell spike volleys (red). Other parameters, in the notation of Chapter 30, are $N_E = 200$, $N_I = 50$, $\bar{I}_I = 0.25$, $\sigma_I = 0$, $\hat{g}_{EI} = 0.5$, $\hat{g}_{IE} = 0.5$, $\hat{g}_{II} = 0.25$, $p_{EI} = 0.5$, $p_{IE} = 0.5$, $p_{II} = 0.5$, $\tau_{r,E} = 0.5$, $\tau_{\text{peak},E} = 0.5$, $\tau_{d,E} = 3$, $v_{\text{rev},E} = 0$, $\tau_{r,I} = 0.5$, $\tau_{\text{peak},I} = 0.5$, $\tau_{d,I} = 9$, $v_{\text{rev},I} = -75$. Between any two E-cells i and j with $i \neq j$, there is initially an excitatory synaptic connection with maximal conductance 0.05/199. The parameters associated with the STDP model are $K_+ = 0.05/199$, $K_- = (2/3) \times 0.05/199$, $\tau_+ = \tau_- = 10$, $B = 0.4/199$, and $\delta = 0.025/199$.

[PING_WITH_STDP, figure 1]

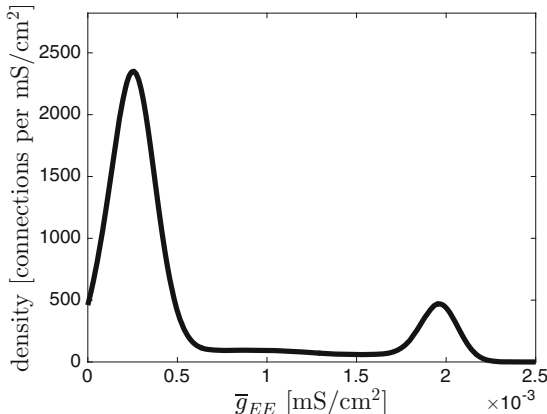


Figure 40.10. Density of recurrent excitation strengths in Fig. 40.9, smoothed as explained in footnote 35, at time $t = 500$.

[PING_WITH_STDP, figure 2]

function. (b) Prove that M_δ is strictly increasing. (c) Plot $M_\delta(x)$ for $\delta = 0.1$, $-1 \leq x \leq 1$.

- 40.5. (*) Why does Δ in the left panel of Fig. 40.6 suddenly rise again as \bar{g}_{EE} exceeds a threshold value of about 0.23?

- 40.6. Without STDP, there are $O(N_E + N_I)$ dependent variables in a PING network model, and each equation has $O(N_E + N_I)$ terms on the right-hand side. With recurrent excitation with STDP, there are $O(N_E^2 + N_I)$ dependent variables, since now the synaptic strengths become dependent variables. Each equation governing one of the E-to-E synaptic strengths has $O(N_E^k)$ terms on the right-hand side. What is k ?
- 40.7. (*) For Fig. 40.9, plot the standard deviation of the spike times in the n -th spike volley of the E-cells as a function of n .
- 40.8. (*) Can you generate a simulation similar to that of Fig. 40.9, but with *stochastic* drive to the E-cells?

Appendix A

The Bisection Method

In several places in this book, we use the *bisection method*. It is the simplest method for solving nonlinear equations. If f is a continuous function of a single real variable, say $f = f(x)$ with $x \in \mathbb{R}$, and if a and b are real numbers with $a < b$ and $f(a)f(b) \leq 0$ (that is, $f(a)$ and $f(b)$ have opposite signs), then there is a solution of the equation

$$f(x) = 0$$

in the interval $[a, b]$, by the intermediate value theorem. The bisection method for finding a solution up to an error of, say, 10^{-12} , is defined in pseudo code as follows:

```
while  $b - a > 2 \times 10^{-12}$ ,  
     $c = (a + b)/2;$   
    if  $f(a)f(c) \leq 0$ ,  
         $a = c;$   
    else  
         $b = c;$   
    end if;  
end while;  
 $x = (a + b)/2;$ 
```

When the while loop stops, the interval $[a, b]$ is of length $\leq 2 \times 10^{-12}$, and $f(a)f(b) \leq 0$, so the interval $[a, b]$ still contains a solution. The midpoint, x , of the interval $[a, b]$ is therefore no further than 10^{-12} from a solution.

Advantages of the bisection method are that it is simple and guaranteed to work provided that an initial interval $[a, b]$ with $f(a)f(b) \leq 0$ is given, and that a bound on the error can be guaranteed. The main disadvantage is that, at least in the simple form given above, it is only applicable to one equation in one unknown.

Appendix B

Fixed Point Iteration

We consider a sequence of real numbers satisfying a recursion relation of the form

$$x_{k+1} = F(x_k), \quad k = 0, 1, 2, \dots . \quad (\text{B.1})$$

Think of x as a time-dependent quantity, and of x_k as the value of x after k time units. Time ticks discretely here, instead of flowing continuously. Equation (B.1) expresses that the future of x depends on the present value of x , and on nothing else. It is the simplest example of *time-discrete dynamics*. To compute all values of x_k , we must be given x_0 . We can then compute $x_1 = F(x_0)$, and from it $x_2 = F(x_1)$, etc. This procedure for generating the sequence $\{x_k\}_{k=0,1,2,\dots}$ is called *fixed point iteration*.

We will usually assume that F is continuous. If that is so, and if the sequence $\{x_k\}_{k=0,1,2,\dots}$ has a limit $x_* \in \mathbb{R}$, then

$$x_* = F(x_*). \quad (\text{B.2})$$

You can see that by taking the limit as $k \rightarrow \infty$ on both sides of eq. (B.1), and noticing that the limit as $k \rightarrow \infty$ is the limit as $k + 1 \rightarrow \infty$. A number x_* satisfying (B.2) is called a *fixed point* of F . The graph of F crosses the 45° -line in the point (x_*, x_*) . So if F is continuous, and if fixed point iteration generates a convergent sequence, the limit is a fixed point of F . This explains the name *fixed point iteration*. The iteration has a simple geometric interpretation, illustrated in Fig. B.1.

For the remainder of this appendix, we will assume that there are lower and upper bounds on the quantity x , which we call a and b . So $F(x)$ is defined for $x \in [a, b]$, and we also assume that $F(x) \in [a, b]$. If F is continuous, this guarantees that there is a fixed point:

Proposition B.1. *If $F = F(x)$, $x \in [a, b]$ (with $a < b$) is a continuous function and $F(x) \in [a, b]$ for all $x \in [a, b]$, then F has at least one fixed point in $[a, b]$.*

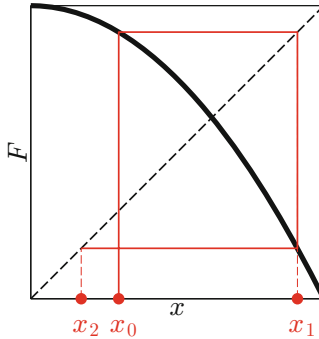


Figure B.1. Geometric construction of the x_k .

Proof. Let $G(x) = x - F(x)$. Then G is continuous, $G(a) \leq 0$ and $G(b) \geq 0$. By the intermediate value theorem, $G(x_*) = 0$ for some $x_* \in [a, b]$, so $x_* = F(x_*)$. \square

Proposition B.1 is a very simple special case of a far more profound result called the *Brouwer fixed point theorem*.

Suppose now that x_* is a fixed point of F . Suppose that x_0 is near x_* . Will the sequence $\{x_k\}_{k=0,1,2,\dots}$ converge to x_* ? The answer depends on the derivative $F'(x_*)$; let's assume that that derivative exists now. If $-1 < F'(x_*) < 1$, then indeed $x_k \rightarrow x_*$ as $k \rightarrow \infty$. We say that x_* is an *attracting* fixed point in this case. If $|F'(x_*)| > 1$, then x_* is *repelling*. We will state and prove a proposition making these statements precise shortly, but first we illustrate them in Fig. B.2.

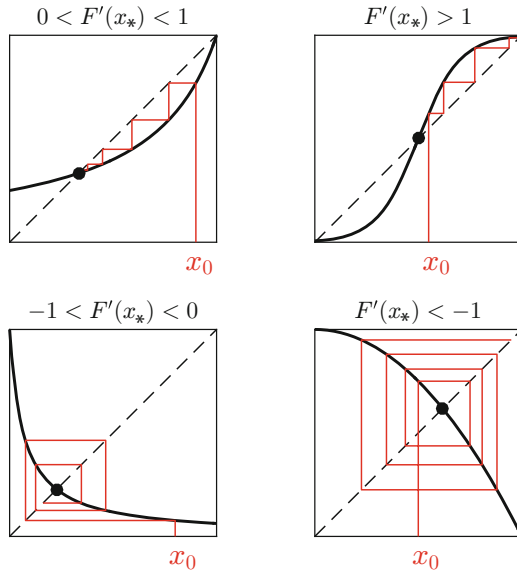


Figure B.2. Typical examples of fixed point iteration. The left panels show examples of attracting fixed points, and the right panels show examples of repelling fixed points.

The following proposition is one way of making precise that small $|F'|$ results in convergence of the fixed point iteration:

Proposition B.2. *If $F = F(x)$, $x \in [a, b]$, is a continuously differentiable function, $F(x) \in [a, b]$ for all $x \in [a, b]$, and $|F'(x)| < 1$ for all $x \in [a, b]$, then there exists exactly one fixed point $x_* \in [a, b]$ of F , and $\lim_{k \rightarrow \infty} x_k = x_*$ regardless of the value of x_0 .*

Proof. There exists a fixed point by Proposition B.1. Because F' is a continuous function (this is what *continuously differentiable* means), and $|F'(x)| < 1$ for all $x \in [a, b]$, there is a number L with $L < 1$ so that $|F'(x)| \leq L$ for all $x \in [a, b]$. Suppose that there were two fixed points, $x_{*,1}$ and $x_{*,2}$. Then

$$|x_{*,1} - x_{*,2}| = |F(x_{*,1}) - F(x_{*,2})| = |F'(c)(x_{*,1} - x_{*,2})|$$

for some c between $x_{*,1}$ and $x_{*,2}$, by the mean value theorem. Further,

$$|F'(c)(x_{*,1} - x_{*,2})| \leq L |x_{*,1} - x_{*,2}|,$$

so we conclude

$$|x_{*,1} - x_{*,2}| \leq L |x_{*,1} - x_{*,2}|.$$

Since $L < 1$, this implies $x_{*,1} = x_{*,2}$. This proves that there cannot be two different fixed points.

Let $x_* \in [a, b]$ denote the unique fixed point of F . Then for any $k \geq 1$,

$$|x_* - x_k| = |F(x_*) - F(x_{k-1})| = |F'(c_{k-1})(x_* - x_{k-1})|$$

for some number c_{k-1} between x_{k-1} and x_* , by the mean value theorem. Further,

$$|F'(c_{k-1})(x_* - x_{k-1})| \leq L |x_* - x_{k-1}|,$$

so we conclude

$$|x_* - x_k| \leq L |x_* - x_{k-1}|.$$

By induction, this implies

$$|x_* - x_k| \leq L^k |x_* - x_0|$$

for all k , and since $L < 1$, this implies $|x_* - x_k| \rightarrow 0$ as $k \rightarrow \infty$. \square

Proposition B.2 is a special case of a more general result called the *Banach fixed point theorem*. It is a result about *global convergence* — that is, convergence irrespective of the starting point x_0 . There is a similar result about *local convergence*, which we state next.

Proposition B.3. *Assume that $F = F(x)$, $x \in \mathbb{R}$, is continuously differentiable. Suppose that x_* is a fixed point of F . (a) If $|F'(x_*)| < 1$, then x_* is locally attracting, that is, there exists a number $\epsilon > 0$ so that*

$$x_0 \in [x_* - \epsilon, x_* + \epsilon] \Rightarrow \lim_{k \rightarrow \infty} x_k = x_*.$$

(b) If $|F'(x_*)| > 1$, then x_* is repelling, that is, there exists a number $\epsilon > 0$ so that

$$x_0 \in [x_* - \epsilon, x_* + \epsilon] \quad \text{and} \quad x_0 \neq x_* \quad \Rightarrow \quad |x_* - x_1| > |x_* - x_0|.$$

Proof. (a) Because F' is continuous and $|F'(x_*)| < 1$, we can choose $\epsilon > 0$ so that the assumptions of Proposition B.2 are satisfied with $[a, b] = [x_* - \epsilon, x_* + \epsilon]$. This implies the assertion. (b) Because F' is continuous and $|F'(x_*)| > 1$, there is an $\epsilon > 0$ so that $|F'(x)| > 1$ for $x \in [x_* - \epsilon, x_* + \epsilon]$. If $x_0 \in [x_* - \epsilon, x_* + \epsilon]$, $x_0 \neq x_*$, then $|x_* - x_1| = |F(x_*) - F(x_0)| = |F'(c)(x_* - x_0)|$ for some c between x_0 and x_* , and $|F'(c)(x_* - x_0)| > |x_* - x_0|$. \square

Appendix C

Elementary Probability Theory

The presentation in this appendix is quick and informal. It is intended to refresh your memory, or introduce you to the ideas presented here very briefly, focusing exclusively on material that is useful somewhere in this book. You can learn all of this much more thoroughly from any elementary textbook on probability theory.

C.1 Basic Vocabulary and Facts

The *probability of an event A* is denoted by $P(A)$. It is a number between 0 and 1. The event is sure to occur if $P(A) = 1$, and sure not to occur if $P(A) = 0$.³⁶ If A and B are events, the *conditional probability of A, given B* is

$$P(A|B) = \frac{P(A \text{ and } B)}{P(B)}. \quad (\text{C.1})$$

In probability theory, one thinks of events as subsets of the set of all possible outcomes of a random experiment. (So strictly speaking, it's not the “event A ,” but the “event that the outcome lies in A .”) Therefore one can write (C.1) using set notation:

$$P(A|B) = \frac{P(A \cap B)}{P(B)}.$$

However, we won't be formal here, and will continue writing our formulas as in (C.1). Because we divide by $P(B)$ in (C.1), we must assume $P(B) > 0$.

One of the most fundamental notions in probability theory is the concept of *random number*, also called *random variable*. We will usually (not always) denote

The online version of chapter 1 (doi: [10.1007/978-3-319-51171-9_1](https://doi.org/10.1007/978-3-319-51171-9_1)) contains supplementary material of this appendix, which is available to authorized users.

³⁶If you have learned probability theory, you will know that I should, strictly speaking, have written “almost sure,” not “sure.”

random numbers by capital letters, for instance, X . We will not rigorously define what we mean by a random real number.³⁷ You should simply think of a random number as an oracle: If you ask the oracle for the value of X once, it might answer 0.734957, but if you ask it a second time, it might answer something different, maybe 0.174023.

For a random real number X , there is often a *probability density function* (*p.d.f.*), that is, a function ρ with the property that for any a and b with $-\infty \leq a < b \leq \infty$,

$$P(X \in [a, b]) = \int_a^b \rho(x) dx.$$

If X is a random real number, its *mean value* or *expected value* or *expectation* is the value that the oracle gives *on the average* — ask it very many times, and average. It is denoted by $E(X)$. It is easy to calculate $E(X)$ if the only possible values of X are the members of a (finite or infinite) *sequence* $\{x_i\}$. Suppose that $P(X = x_i) = p_i$, with $p_i \in [0, 1]$. Since the x_i are assumed to be the only possible values of X , $\sum_i p_i = 1$. Then

$$E(X) = \sum_i p_i x_i. \quad (\text{C.2})$$

The oracle says “ x_i ” a fraction p_i of times, this is why x_i is weighed by p_i in computing the expectation. If X is a random real number with density ρ , then we can approximate X by choosing a small $h > 0$ and setting

$$\tilde{X} = ih \quad \text{if } X \in [(i-1)h, ih], \quad i \text{ integer.}$$

The smaller h , the better is the approximation. Note that the possible values of \tilde{X} are the members of the (two-sided infinite) sequence $\{ih\}$. Then

$$P(\tilde{X} = ih) = p_i = P(X \in [(i-1)h, ih]) = \int_{(i-1)h}^{ih} \rho(x) dx.$$

We can compute $E(\tilde{X})$ using eq. (C.2), and find

$$E(\tilde{X}) = \sum_{i=-\infty}^{\infty} \left(\int_{(i-1)h}^{ih} \rho(x) dx \right) ih = \sum_{i=-\infty}^{\infty} \left(\int_{(i-1)h}^{ih} ih \rho(x) dx \right).$$

As $h \rightarrow 0$, this becomes

$$\sum_{i=-\infty}^{\infty} \int_{(i-1)h}^{ih} x \rho(x) dx = \int_{-\infty}^{\infty} x \rho(x) dx.$$

This is the expectation of X :

$$E(X) = \int_{-\infty}^{\infty} x \rho(x) dx. \quad (\text{C.3})$$

³⁷The correct rigorous formalization requires knowing measure theory.

Similarly, if $f = f(x)$ is a function,

$$E(f(X)) = \int_{-\infty}^{\infty} f(x)\rho(x)dx. \quad (\text{C.4})$$

Expectation is linear. That is, if X and Y are random real numbers, and c and d are (non-random) real numbers, then

$$E(cX + dY) = cE(X) + dE(Y).$$

This is easy to understand if you think of X and Y as oracles, as discussed earlier.

Independence of random variables is among the most important notions in probability theory. Loosely speaking, random variables are independent if knowing some of their values does not improve your chances of correctly guessing the value of another. If X and Y are random real numbers, then independence means more precisely that for any choices of a , b , c , and d with $-\infty \leq a < b \leq \infty$ and $-\infty \leq c < d \leq \infty$,

$$P(X \in [a, b] | Y \in [c, d]) = P(X \in [a, b]), \quad (\text{C.5})$$

and

$$P(Y \in [c, d] | X \in [a, b]) = P(Y \in [c, d]). \quad (\text{C.6})$$

Using the definition of conditional probability, (C.5) and (C.6) can be seen to be equivalent, and can be re-written as

$$P(X \in [a, b] \text{ and } Y \in [c, d]) = P(X \in [a, b]) \cdot P(Y \in [c, d]).$$

This way of writing it also avoids having to state that $P(Y \in [c, d]) \neq 0$ (which we should have assumed when writing down (C.5)) or $P(X \in [a, b]) \neq 0$ (which we should have assumed when writing down (C.6)). Similarly, n random real numbers, X_1, X_2, \dots, X_n , are independent if and only if for any real intervals I_j , $1 \leq j \leq n$,

$$P(X_j \in I_j \text{ for } 1 \leq j \leq n) = P(X_1 \in I_1) \cdot P(X_2 \in I_2) \cdot \dots \cdot P(X_n \in I_n).$$

By definition, infinitely many random variables are independent if and only if any finite subsets of them are independent.

The *variance* of a random number X is

$$\text{var}(X) = E((X - E(X))^2). \quad (\text{C.7})$$

So the variance measures how big $(X - E(X))^2$ is on the average.³⁸ The *standard deviation* is

$$\text{std}(X) = \sqrt{\text{var}(X)}.$$

³⁸You might first think that the average of $X - E(X)$ would also be an interesting quantity, but it isn't: It is always zero. The average of $|X - E(X)|$ is an interesting quantity, but the average of $(X - E(X))^2$ is easier to deal with, in essence because x^2 is differentiable everywhere, while $|x|$ is not differentiable at $x = 0$.

If X is a physical quantity, $\text{std}(X)$ has the same physical dimension as X . Deviations from the expected value by many standard deviations are highly unlikely. A simple way of making this precise is *Chebyshev's inequality*,

$$P(|X - E(X)| \geq k \text{std}(X)) \leq \frac{1}{k^2}.$$

A relative (or, in physical terms, non-dimensional) measure of the size of the “typical” deviations of X from its mean is the *coefficient of variation*,

$$\text{cv}(X) = \frac{\text{std}(X)}{E(X)}. \quad (\text{C.8})$$

Using the linearity of the expectation, we can re-write eq. (C.7) as follows:

$$\begin{aligned} \text{var}(X) &= E((X - E(X))^2) = E(X^2 - 2XE(X) + (E(X))^2) = \\ &= E(X^2) - 2E(X)E(X) + (E(X))^2 = E(X^2) - (E(X))^2. \end{aligned}$$

We summarize this result:

$$\text{var}(X) = E(X^2) - (E(X))^2. \quad (\text{C.9})$$

This implies immediately that

$$\text{var}(cX) = c^2 \text{var}(X)$$

if c is a (non-random) real number, and therefore

$$\text{std}(cX) = |c| \text{std}(X).$$

Variance is not *additive*, that is, $\text{var}(X + Y)$ is not $\text{var}(X) + \text{var}(Y)$ in general. However, we can calculate exactly what $\text{var}(X + Y)$ really is, using (C.9):

$$\begin{aligned} \text{var}(X + Y) &= E((X + Y)^2) - (E(X + Y))^2 = \\ &= E(X^2 + 2XY + Y^2) - (E(X) + E(Y))^2 = \\ &= E(X^2) - (E(X))^2 + E(Y^2) - (E(Y))^2 + 2E(XY) - 2E(X)E(Y) = \\ &= \text{var}(X) + \text{var}(Y) + 2(E(XY) - E(X)E(Y)). \end{aligned}$$

So we see that the variance is additive if and only if the expectation is *multiplicative*:

$$E(XY) = E(X)E(Y).$$

This is not generally the case. Expectation is additive ($E(X + Y) = E(X) + E(Y)$) and in fact, more generally, it is linear ($E(cX + dY) = cE(X) + dE(Y)$), but it is not in general multiplicative. We say that X and Y are *uncorrelated* if the expectation does happen to be multiplicative: $E(XY) = E(X)E(Y)$. So X and

X and Y are uncorrelated if and only if for X and Y , expectation is multiplicative and variance is additive. An easy calculation verifies that

$$E(XY) - E(X)E(Y) = E((X - E(X))(Y - E(Y))). \quad (\text{C.10})$$

The expression

$$\text{cov}(X, Y) = E((X - E(X))(Y - E(Y)))$$

that appears on the right-hand side of eq. (C.10) is called the *covariance* of X and Y . So X and Y are uncorrelated if and only if their covariance is zero.

One can show (but we will omit the argument) that X and Y are uncorrelated if they are independent. However, the reverse implication does not hold: X and Y can be dependent, yet still uncorrelated. As an example, suppose that X is a random real number with mean 0, and

$$Y = \begin{cases} X & \text{with probability } 1/2, \\ -X & \text{with probability } 1/2. \end{cases}$$

Then

$$XY = \begin{cases} X^2 & \text{with probability } 1/2, \\ -X^2 & \text{with probability } 1/2. \end{cases}$$

It is clear that $E(XY) = 0$, and $E(X)E(Y) = 0$ as well, so X and Y are uncorrelated. They are not, of course, independent: Knowing X helps us guess Y , in fact once we know X , we know Y up to sign! So uncorrelatedness is a weaker property than independence.

C.2 Uniform Distributions

A random number X in an interval $[a, b]$, with $-\infty < a < b < \infty$, is called *uniformly distributed* if its p.d.f. is

$$\rho(x) = \begin{cases} 1/(b-a) & \text{if } x \in [a, b], \\ 0 & \text{otherwise.} \end{cases}$$

Intuitively, this means that X is “equally likely to be anywhere in $[a, b]$.”

C.3 Uniform Distributions in Matlab

Matlab's function `rand` generates pseudo-random uniformly distributed random numbers between 0 and 1. If you type `rand` into the Matlab command window many times, you get as many different answers, always numbers between 0 and 1. The computer makes it look as if it generated these numbers at random, uniformly distributed in $[0, 1]$, independently of each other. Of course, one must say “makes it look as if,” since in reality nothing truly random happens in the computer. This is why `rand` is called a *pseudo-random number* generator. The syntax is

```
X= rand(1,1)
```

for a single pseudo-random number X , and

$$X = \text{rand}(N, 1)$$

for a column vector of N (seemingly) independent ones. To generate N (seemingly) independent pseudo-random numbers that are (seemingly) uniformly distributed in $[a, b]$, one can use the following command:

$$X = a + \text{rand}(N, 1) * (b - a)$$

Now that I have stressed often enough that computer-generated “random” numbers are merely pseudo-random, and only seemingly have the desired distribution, I will drop “pseudo” and “seemingly” in similar contexts from here on.

C.4 Gaussian Distributions

Arguably the most important p.d.f. is

$$\rho(x) = \frac{1}{\sqrt{2\pi}} e^{-x^2/2}.$$

The graph of ρ is shown in Fig. C.1. One ought to convince oneself that this is indeed a valid p.d.f., that is, that

$$\int_{-\infty}^{\infty} \frac{1}{\sqrt{2\pi}} e^{-x^2/2} dx = 1. \quad (\text{C.11})$$

The calculation that accomplishes this is a popular example in multivariate calculus courses. A random variable X with this p.d.f. is called a *standard Gaussian*. Its graph is shown in Fig. C.1. It is called *standard* because its mean is 0 and its variance is 1. This can be proved using eqs. (C.4), (C.7), and (C.11).

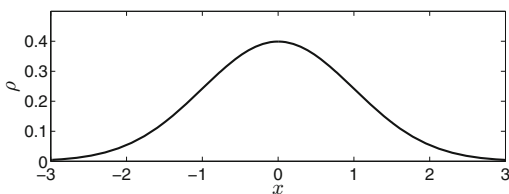


Figure C.1. Standard Gaussian p.d.f. [PLOT_GAUSSIAN]

If X is a standard Gaussian, and if $\mu \in \mathbb{R}$ and $\sigma > 0$, then

$$Y = \mu + \sigma X$$

has mean μ and standard deviation σ , and its p.d.f. can easily be shown to be

$$\rho_Y(y) = \frac{1}{\sqrt{2\pi\sigma^2}} e^{-(y-\mu)^2/(2\sigma^2)}. \quad (\text{C.12})$$

One calls Y a *Gaussian with mean μ and standard deviation σ* .

C.5 Gaussian Distributions in Matlab

Matlab has a built-in function called `randn` which computes standard Gaussians. The command

$$X = \text{randn}(N, 1)$$

defines X to be a column vector of N independent standard Gaussians.

C.6 Discrete Ornstein-Uhlenbeck Processes

In several places in this book, we use external drive to model neurons in the form

$$I(t) = \bar{I} + \text{stochastically fluctuating drive}, S(t),$$

where \bar{I} is a constant. Here we describe how we define $S(t)$, the stochastically fluctuating component of the drive.

Let $\Delta t > 0$ denote the time step used in the numerical integration of the differential equations that define the model neuron. Preliminarily, we define $S(t)$ by the following equations:

$$S(0) = 0, \tag{C.13}$$

$$\frac{dS}{dt} = -\frac{S}{\tau_{\text{noise}}} \quad \text{for } (k-1)\Delta t < t < k\Delta t, k = 1, 2, 3, \dots, \tag{C.14}$$

$$S(k\Delta t + 0) = S(k\Delta t - 0) + \gamma G_k \quad k = 1, 2, 3, \dots, \tag{C.15}$$

where $\tau_{\text{noise}} > 0$, $\gamma > 0$, and the G_k are independent standard Gaussians. (These equations will be modified later.)

To understand eqs. (C.13)–(C.15) better, we define

$$S_k = S(k\Delta t + 0), \quad k = 0, 1, 2, \dots .$$

Then $S_0 = 0$, and

$$S_k = S_{k-1} e^{-\Delta t / \tau_{\text{noise}}} + \gamma G_k, \quad k = 1, 2, 3, \dots . \tag{C.16}$$

Taking expectations on both sides of this equation, we find $E(S_k) = E(S_{k-1})$, and therefore, since $E(S_0) = 0$, $E(S_k) = 0$ for all k . Taking variances on both sides of (C.16), we obtain

$$\text{var}(S_k) = e^{-2\Delta t / \tau_{\text{noise}}} \text{var}(S_{k-1}) + \gamma^2. \tag{C.17}$$

We used here that G_k is independent of S_{k-1} (since S_{k-1} depends only on G_1, G_2, \dots, G_{k-1}), and that therefore the variances of the two summands on the right-hand side of (C.16) can simply be added.

Equation (C.17) is a fixed point iteration, and using Appendix (B), we see that the iteration converges as $k \rightarrow \infty$. So $\lim_{k \rightarrow \infty} \text{var}(S_k) = v_\infty$ with

$$v_\infty = e^{-2\Delta t / \tau_{\text{noise}}} v_\infty + \gamma^2,$$

so

$$v_\infty = \frac{\gamma^2}{1 - e^{-2\Delta t/\tau_{\text{noise}}}}. \quad (\text{C.18})$$

We are primarily interested in small Δt , since Δt is the time step used in solving the differential equations of the model. However, for small Δt , the denominator in (C.18) is small. Therefore γ^2 ought to be small as well, to keep v_∞ from tending to ∞ as $\Delta t \rightarrow 0$. We define

$$\gamma = \sigma_{\text{noise}} \sqrt{1 - e^{-2\Delta t/\tau_{\text{noise}}}}, \quad (\text{C.19})$$

where $\sigma_{\text{noise}} > 0$ is independent of Δt . Using (C.19) in (C.18), we find

$$v_\infty = \sigma_{\text{noise}}^2.$$

With this definition of γ , the variance of the S_k converges to σ_{noise}^2 . However, if we had taken $S(0) = S_0$ to be not 0, but a Gaussian with mean 0 and variance σ_{noise}^2 , then it is clear from the calculations presented above that all S_k would have been Gaussian with mean 0 and variance σ_{noise}^2 . We therefore modify eqs. (C.13)–(C.15) as follows:

$$S(0) = \sigma_{\text{noise}} G_0, \quad (\text{C.20})$$

$$\frac{dS}{dt} = -\frac{S}{\tau_{\text{noise}}} \quad \text{for } (k-1)\Delta t < t < k\Delta t, \quad k = 1, 2, 3, \dots, \quad (\text{C.21})$$

$$S(k\Delta t + 0) = S(k\Delta t - 0) + \sigma_{\text{noise}} \sqrt{1 - e^{-2\Delta t/\tau_{\text{noise}}}} G_k \quad k = 1, 2, 3, \dots, \quad (\text{C.22})$$

where G_0, G_1, G_2, \dots are independent standard Gaussians.

Equations (C.20)–(C.22) describe how we generate noisy drive in our codes. Figure C.2 shows a typical example.

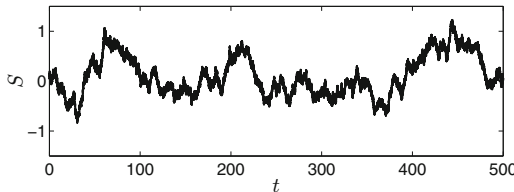


Figure C.2. Plot of $S(t)$, defined by (C.20)–(C.22), with $\sigma_{\text{noise}} = 0.5$, $\tau_{\text{noise}} = 50$, $\Delta t = 0.01$. [DISCRETE_OU]

The last paragraph of this appendix is not comprehensible without background that I am not providing here, and it is not needed to follow what we do in this book. However, it justifies the title of this appendix.

Figure C.2 would look very similar for smaller values of Δt . (This means that the *statistics* would be similar, not of course the exact shape of the graph, which is random.) One can make rigorous sense of the notion of passing to the limit $\Delta t \rightarrow 0$ in eqs. (C.21) and (C.22). This results in the *stochastic differential equation (SDE)*

$$dS = -\frac{S}{\tau_{\text{noise}}} dt + \sigma_{\text{noise}} \sqrt{\frac{2}{\tau_{\text{noise}}}} dW, \quad (\text{C.23})$$

where dW denotes the infinitesimal increment of the *Wiener process*. Solutions of (C.23) are *Ornstein-Uhlenbeck processes*. Equations (C.20)–(C.22) therefore define a *discrete Ornstein-Uhlenbeck process*.

C.7 Exponential Distributions and Lack of Memory

Let $T > 0$ be a random number. We think of T as a random time — the time between bus arrivals, for instance, or the life span of a person. We say that T is *exponentially distributed* if it has a p.d.f. of the form

$$\rho(t) = \begin{cases} \frac{e^{-t/\bar{T}}}{\bar{T}} & \text{if } t > 0, \\ 0 & \text{otherwise,} \end{cases} \quad (\text{C.24})$$

for some constant $\bar{T} > 0$. Then

$$P(T > t) = \int_t^\infty \rho(s)ds = e^{-t/\bar{T}}$$

for all $t > 0$. The equation

$$P(T > t) = e^{-t/\bar{T}} \quad (\text{C.25})$$

can also be taken to be the definition of *exponentially distributed* — it is equivalent to saying that (C.24) is the p.d.f.

Exponentially distributed random variables *lack memory*:

$$P(T > t|T > s) = P(T > t - s) \quad (\text{C.26})$$

for all $s > 0$ and $t > s$. I will first explain why (C.26) expresses lack of memory, and then explain why it follows from (C.25).

If you think of T as the life span of a person measured in years, for instance, the equation says that the probability that you become t years old, given that you are already s years old, is the same as the probability that you reach $t - s$ years of age from the time of your birth. Clearly, the life span of a person does *not* have this property — the likelihood of living for another 40 years is much greater for a newborn than for a 70-year-old. When estimating how much time you have left to live, your age matters. On the other hand, the time between two incoming cell phone calls in the afternoon may approximately lack memory — the fact that you got two calls in the past ten minutes probably does not make it much more or much less likely that you will get another in the next ten minutes.³⁹ One could say that T is “completely random” when it lacks memory — the past does not help you predict it.

³⁹You might object “If you got two phone calls in the past ten minutes, you seem to be getting phone calls at a high rate, so that makes it more likely that you’ll get another one in the next ten minutes.” However, we assume here that we already know the *mean* rate at which phone calls come in, and don’t need to try to estimate it by observing the rate at which phone calls have come in recently.

I will now explain the link between exponential distribution and lack of memory. Equation (C.26) means, by the definition of conditional probability,

$$\frac{P(T > t \text{ and } T > s)}{P(T > s)} = P(T > t - s),$$

and since $t \geq s$, this means

$$\frac{P(T > t)}{P(T > s)} = P(T > t - s),$$

or

$$P(T > t) = P(T > s)P(T > t - s). \quad (\text{C.27})$$

By eq. (C.25), this simply means

$$e^{-t/\bar{T}} = e^{-s/\bar{T}} e^{-(t-s)/\bar{T}},$$

so it follows from the law by which exponentials are multiplied. This shows that exponentially distributed random numbers lack memory. The implication in fact works the other way around as well: If $T > 0$ is a random number and $P(T > t)$ depends on $t > 0$ continuously and T lacks memory, then T is exponentially distributed. This is a consequence of the fact that a continuous function $f = f(t)$ of $t > 0$ with $f(a+b) = f(a)f(b)$ for all $a > 0$ and $b > 0$ is an exponential.

The parameter \bar{T} in eq. (C.25) is the expected value of T . You can verify this easily using eq. (C.3).

C.8 Exponentially Distributed Random Numbers in Matlab

If $U \in (0, 1)$ is uniformly distributed, then $T = -\bar{T} \ln(U)$ is exponentially distributed with expected value \bar{T} . The reason is that

$$P(T > t) = P(-\bar{T} \ln U > t) = P(\bar{T} \ln U < -t) = P\left(U < e^{-t/\bar{T}}\right) = e^{-t/\bar{T}}.$$

Thus to generate N independent random numbers with exponential distribution with expectation $\bar{T} > 0$, we use the following command:

```
T=-T_bar*log(rand(N,1))
```

(In Matlab, `log` is the natural logarithm.)

C.9 Discrete Approximation of Exponential Distributions

In our simulations, we discretize time, and it is often useful to “discretize” the exponential distribution as well, replacing an exponentially distributed random number $T > 0$ by an approximation $\tilde{T} = k\Delta t$, $k > 0$ integer, where Δt is the time step used in our numerical simulations. We define \tilde{T} as follows. Let

$$p = 1 - e^{-\Delta t/\bar{T}}. \quad (\text{C.28})$$

From eq. (C.25), it follows that this is $P(T \leq \Delta t)$. Let U_1, U_2, U_3, \dots be independent random variables, uniformly distributed in $(0, 1)$. Let k be the smallest integer with $U_k \leq p$. We set $\tilde{T} = k\Delta t$. In Matlab, this is implemented as follows:

```
p=1-exp(-Delta_t/T_bar);
k=1; U=rand; while U>p, k=k+1; U=rand; end;
T_tilde=k*dt;
```

If $t = k\Delta t$, then $P(\tilde{T} > t)$ is the probability that \tilde{T} is *not* $\Delta t, 2\Delta t, \dots, k\Delta t$, which is

$$(1 - p) \cdot (1 - p) \cdot \dots \cdot (1 - p) \quad (k \text{ factors}) = (1 - p)^k = e^{-k\Delta t/\bar{T}} = e^{-t/\bar{T}}.$$

In summary,

$$P(\tilde{T} > t) = e^{-t/\bar{T}} \quad \text{if } t \text{ is an integer multiple of } \Delta t.$$

This shows in which sense \tilde{T} is an approximation to a random number T satisfying (C.25).

C.10 Poisson Schedules

We consider a sequence of random times t_1, t_2, t_3, \dots with

$$0 < t_1 < t_2 < t_3 < \dots$$

Think of t_j as the time at which the j -th bus comes to a bus stop, or the time at which the j -th input reaches a neuron. We will refer to the t_j as the *arrival times*. We set

$$T_1 = t_1,$$

and

$$T_j = t_j - t_{j-1} \quad \text{for } j = 2, 3, \dots$$

The T_j are called the *inter-arrival times*. If the T_j are exponentially distributed, all with the same mean $\bar{T} > 0$, and independent of each other, we call t_1, t_2, t_3, \dots a *Poisson schedule*. The associated *Poisson process* is the random function

$$N(t) = \text{number of } j \text{ with } t_j \leq t.$$

This function has jump discontinuities at the arrival times t_j .

The Poisson schedule is a formalization of what one might mean by a “perfectly random” schedule. Because of the lack of memory of exponentially distributed random variables, knowing the past arrival times does not help predict the time of the next arrival.

C.11 Discrete Approximation of Poisson Schedules

When simulating neurons or neuronal networks with a time step Δt , with inputs arriving on Poisson schedules, it is convenient to discretize the Poisson schedules as well.

To discretize a Poisson schedule with expected inter-arrival time \bar{T} , we draw, following Section C.9, a sequence of independent, uniformly distributed random numbers in $(0, 1)$, U_1, U_2, U_3, \dots , and let $k\Delta t$ ($k > 0$) be an arrival time if and only if $U_k \leq p$, where p is defined by eq. (C.28). The arrival times $0 < t_1 < t_2 < \dots$ constructed in this way will closely resemble a Poisson schedule, but will be integer multiples of Δt .

Because $\Delta t \ll \bar{T}$ typically, we usually approximate (C.28) by

$$p = \frac{\Delta t}{\bar{T}}. \quad (\text{C.29})$$

(Recall that $e^x \approx 1+x$ for $x \approx 0$. This is the linear approximation of the exponential function at 0.) We call

$$f = \frac{1000}{\bar{T}}$$

the mean frequency of the Poisson schedule. As usual, the numerator of 1000 is needed because we think of time as measured in ms, but frequency as measured in Hz. With this notation, (C.29) becomes

$$p = \frac{f}{1000} \Delta t. \quad (\text{C.30})$$

Appendix D

Smooth Approximations of Non-smooth Functions

In several places in this book, functions with discontinuities, or with discontinuous derivatives, are approximated by smooth, i.e., infinitely often differentiable ones. In this appendix, we describe how we generally construct such approximations. Our smooth approximations always depend on a positive *smoothing parameter*, which we call δ here. Smaller values of δ yield approximations that are closer to the non-smooth function being approximated.

D.1 Jump Discontinuities

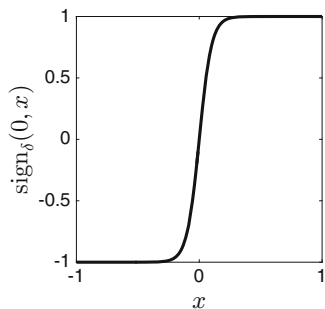


Figure D.1. The graph of $\text{sign}_\delta(0, x)$, as defined in eq. (D.1), for $\delta = 0.1$.
[SIGN_DELTA]

The online version of chapter 1 (doi: [10.1007/978-3-319-51171-9_1](https://doi.org/10.1007/978-3-319-51171-9_1)) contains supplementary material of this appendix, which is available to authorized users.

For the function

$$\text{sign}(x) = \begin{cases} 1 & \text{if } x > 0, \\ 0 & \text{if } x = 0, \\ -1 & \text{if } x < 0, \end{cases}$$

we use the approximation

$$\text{sign}_\delta(x) = \tanh \frac{x}{\delta}. \quad (\text{D.1})$$

The graph of the function sign_δ for $\delta = 0.1$ is shown in Fig. D.1.

More generally, for

$$f(x) = \begin{cases} a & \text{if } x < x_0 \\ (a+b)/2 & \text{if } x = x_0 \\ b & \text{if } x > x_0 \end{cases} = \frac{a+b}{2} + \frac{b-a}{2} \text{sign}(x - x_0),$$

we use the approximation

$$f_\delta(x) = \frac{a+b}{2} + \frac{b-a}{2} \tanh \frac{x - x_0}{\delta}.$$

D.2 Absolute Values

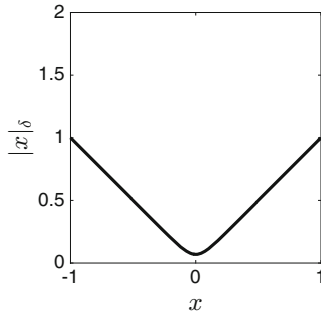


Figure D.2. The graph of $|x|_\delta$, as defined in eq. (D.3), for $\delta = 0.1$. [ABS_DELTA]

Integrating (D.1) once, we obtain a smooth approximation for $|x|$, which we will denote by $|x|_\delta$:

$$|x|_\delta = \delta \ln \left(2 \cosh \frac{x}{\delta} \right).$$

The factor of 2 in front of \cosh adds a constant, i.e., a quantity independent of x , to the right-hand side, and is needed for the expression to be an approximation for $|x|$. Using the definition of \cosh ,

$$|x|_\delta = \delta \ln \left(e^{x/\delta} + e^{-x/\delta} \right). \quad (\text{D.2})$$

We re-write this formula a bit as follows:

$$\begin{aligned}|x|_\delta &= \delta \ln \left(e^{x/\delta} + e^{-x/\delta} \right) \\&= \delta \ln \left(e^{|x|/\delta} + e^{-|x|/\delta} \right) \\&= \delta \ln \left(e^{|x|/\delta} \left(1 + e^{-2|x|/\delta} \right) \right) \\&= \delta \left(\ln e^{|x|/\delta} + \ln \left(1 + e^{-2|x|/\delta} \right) \right) \\&= |x| + \delta \ln \left(1 + e^{-2|x|/\delta} \right)\end{aligned}$$

In summary,

$$|x|_\delta = |x| + \delta \ln \left(1 + e^{-2|x|/\delta} \right). \quad (\text{D.3})$$

Although (D.2) and (D.3) are equivalent, (D.3) is preferable because it avoids evaluation of exponentials of very large numbers and numerical issues potentially associated with that. Figure D.2 shows the graph of $|x|_\delta$ for $\delta = 0.1$.

D.3 Maxima and Minima

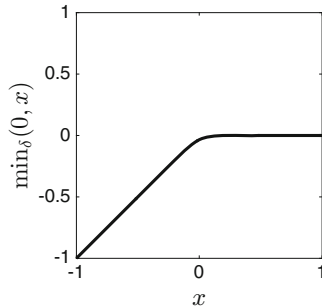


Figure D.3. The graph of $\min_\delta(0, x)$, as defined in eq. (D.4), for $\delta = 0.1$.
[MIN_DELTA]

For a fixed real number a , we approximate the function $\min(a, x)$ like this:

$$\min(a, x) = \frac{a+x}{2} - \frac{|a-x|}{2} \approx \min_\delta(a, x) = \frac{a+x}{2} - \frac{|a-x|_\delta}{2}.$$

Using our definition (D.3) this means

$$\min_\delta(a, x) = \min(a, x) - \frac{\delta}{2} \ln \left(1 + e^{-2|x-a|/\delta} \right). \quad (\text{D.4})$$

To estimate the difference between $\min(a, x)$ and its smooth approximation $\min_\delta(a, x)$, we use the inequality $\ln z \leq z - 1$, which holds for all $z > 0$ because $z - 1$ is the tangent approximation to $\ln z$ at $z = 1$, and the graph of $\ln z$ is

concave-down. Using this inequality in the definition (D.4), we find

$$0 < \min(a, x) - \min_\delta(a, x) \leq \frac{\delta}{2} e^{-2|x-a|/\delta}. \quad (\text{D.5})$$

The right-most expression in (D.5) is extremely small for $|x - a| \gg \delta$, and in any case less than or equal to $\delta/2$. Figure D.3 shows the graph of the function $\min_\delta(0, x)$ for $\delta = 0.1$.

In analogy with eq. (D.4), we define a smooth approximation to the function $\max(a, x)$ by

$$\max_\delta(a, x) = \max(a, x) + \frac{\delta}{2} \ln \left(1 + e^{-2|x-a|/\delta} \right). \quad (\text{D.6})$$

Appendix E

Solutions to Selected Homework Problems

2.5. When the gas fills a spherical container of radius R , it occupies the volume

$$V = \frac{4}{3}\pi R^3,$$

and the pressure P that it exerts on the container walls is therefore

$$P = \frac{kNT}{4\pi R^3/3},$$

where N denotes the number of gas molecules, and T the temperature. We compress the spherical container by gradually reducing its radius to $R' < R$, thereby reducing the volume to

$$V' = \frac{4}{3}\pi R'^3$$

and increasing the number density from

$$[X] = \frac{N}{4\pi R^3/3}$$

to

$$[X]' = \frac{N}{4\pi R'^3/3},$$

while keeping T constant. In general, reduction of the radius of the spherical container from some value $r > 0$ to $r - \Delta r$, where $\Delta r > 0$ is small, requires work

$$\text{pressure} \times \text{surface area of sphere} \times \Delta r = \frac{kNT}{4\pi r^3/3} \times 4\pi r^2 \times \Delta r = \frac{3kNT}{r} \Delta r.$$

The online version of chapter 1 (doi: [10.1007/978-3-319-51171-9_1](https://doi.org/10.1007/978-3-319-51171-9_1)) contains supplementary material of this appendix, which is available to authorized users.

Therefore the work required to reduce the radius from R to R' is

$$\int_{R'}^R \frac{3kNT}{r} dr = 3kNT \ln \frac{R}{R'} = kNT \ln \left(\left(\frac{R}{R'} \right)^3 \right) =$$

$$kNT \ln \frac{R^3}{R'^3} = kNT \ln \frac{V}{V'} = kNT \ln \frac{[X]'}{[X]}.$$

The work W per gas molecule is obtained by dividing by N , which yields (2.8).

4.5. We will show: If $x = m$, h , or n ever were to reach 0, then dx/dt would have to be positive; this implies that x cannot, in fact, reach 0. To see this, note that if $x = 0$, then

$$\frac{dx}{dt} = \frac{x_\infty - x}{\tau_x} = \frac{x_\infty}{\tau_x} > 0.$$

Similarly, if x were to reach 1, then dx/dt would have to be negative, and therefore x cannot reach 1. If v were to reach A , then

$$C \frac{dv}{dt} = \bar{g}_{\text{Na}} m^3 h (v_{\text{Na}} - A) + \bar{g}_{\text{K}} n^4 (v_{\text{K}} - A) + \bar{g}_{\text{L}} (v_{\text{L}} - A) + I >$$

$$\bar{g}_{\text{L}} (v_{\text{L}} - A) + I \geq \bar{g}_{\text{L}} \left(v_{\text{L}} - v_{\text{L}} - \frac{I}{\bar{g}_{\text{L}}} \right) + I = 0,$$

so v cannot, in fact, reach A , and similarly, if v were to reach B , then dv/dt would have to be negative, and therefore v cannot reach B .

5.2. The plot is shown in Fig. E.1.

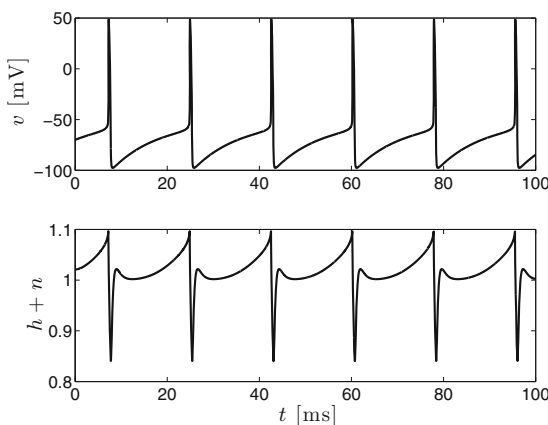


Figure E.1. A voltage trace of the RTM neuron (upper panel), and the sum $h + n$ (lower panel). [RTM_H_PLUS_N]

5.3. The plot is shown in Fig. E.2.

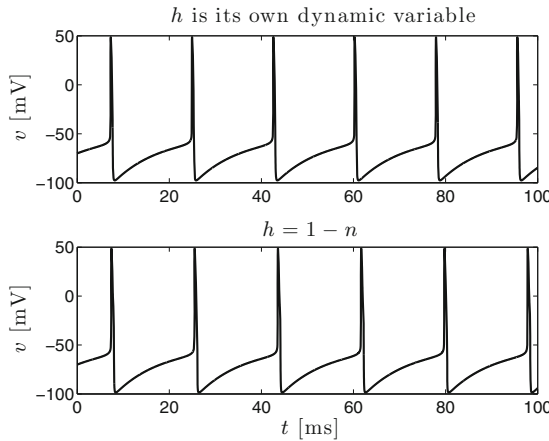


Figure E.2. A voltage trace of the RTM neuron (upper panel), and the voltage trace obtained if h is simply set to $1 - n$ (lower panel). [RTM_2D]

5.4. A voltage spike has a rising phase, and a falling phase. Thus there are pairs of times, t_1 and t_2 , such that

$$v(t_1) = v(t_2), \quad \text{but} \quad \frac{dv}{dt}(t_1) > 0, \quad \frac{dv}{dt}(t_2) < 0.$$

However, if

$$\frac{dv}{dt} = F(v), \tag{E.1}$$

regardless of what F is,

$$v(t_1) = v(t_2) \Rightarrow \frac{dv}{dt}(t_1) = \frac{dv}{dt}(t_2).$$

This argument proves that any solution of an ODE of the form (E.1) is either monotonically increasing, or monotonically decreasing.

5.5. The plot is shown in Fig. E.3.

5.7. The plots are shown in Figs. E.4–E.6.

6.4. Suppose that $\Delta z > 0$ is small, and let us focus on the small piece of axon between $z - \Delta z/2$ and $z + \Delta z/2$. The surface area of this piece of axon is approximately

$$2\pi a(z)\sqrt{1 + a'(z)^2}\Delta z,$$

where a' denotes the derivative of a with respect to z . The current entering this piece through the cell membrane is therefore approximately

$$I_m = 2\pi a(z)\sqrt{1 + a'(z)^2}\Delta z \left[\bar{g}_{\text{Na}} m(z, t)^3 h(z, t) (v_{\text{Na}} - v(z, t)) + \bar{g}_{\text{K}} n(z, t)^4 (v_{\text{K}} - v(z, t)) + \bar{g}_{\text{L}} (v_{\text{L}} - v(z, t)) + I(z, t) \right]. \tag{E.2}$$

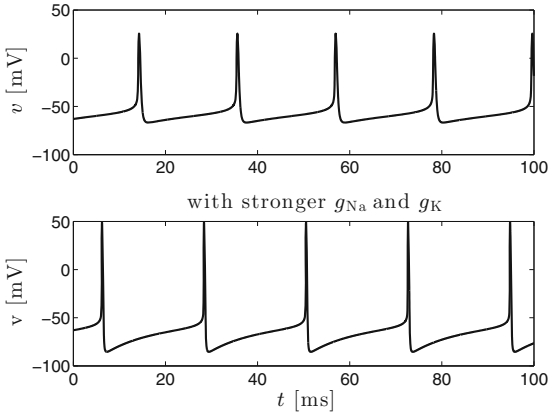


Figure E.3. A voltage trace of the WB neuron (upper panel), and the voltage trace obtained if with strengthened \bar{g}_{Na} and \bar{g}_{K} (lower panel). [WB_MODIFIED]

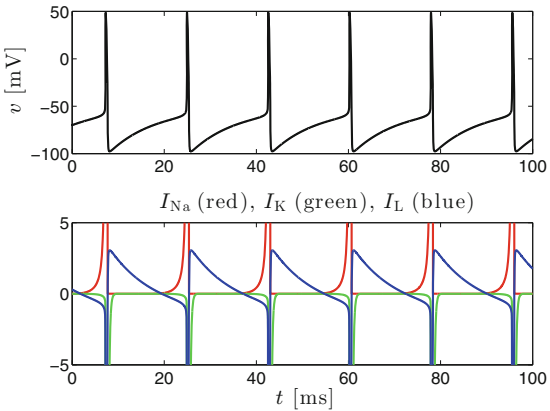


Figure E.4. A voltage trace of the RTM neuron (upper panel), and the sodium, potassium, and leak currents (lower panel). [RTM_CURRENTS]

As before, \bar{g}_{Na} , \bar{g}_{Na} , and \bar{g}_{L} denote conductances per unit membrane area, and I denotes external input current per unit membrane area. The voltage difference between locations z and $z - \Delta z$ gives rise to a current into the piece of axon between $z - \Delta z/2$ and $z + \Delta z/2$ as well. The current entering from the left is approximately

$$I_l = \frac{\pi(a(z - \Delta z/2))^2}{R_i \Delta z} (v(z - \Delta z, t) - v(z, t)). \quad (\text{E.3})$$

Here we used the relation (6.7) between resistance of the cell interior per unit length and resistivity. Similarly, the current entering from the right is approximately

$$I_r = \frac{\pi(a(z + \Delta z/2))^2}{R_i \Delta z} (v(z + \Delta z, t) - v(z, t)). \quad (\text{E.4})$$

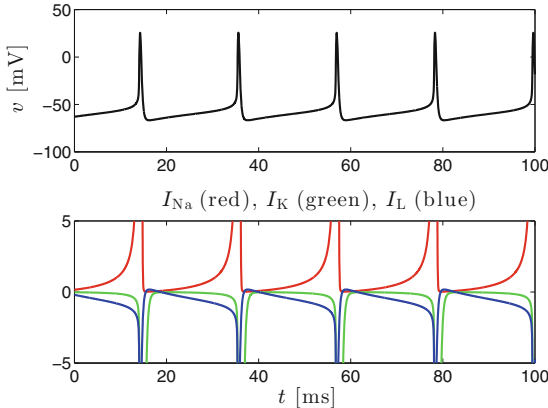


Figure E.5. A voltage trace of the WB neuron (upper panel), and the sodium, potassium, and leak currents (lower panel).[\[WB_CURRENTS\]](#)

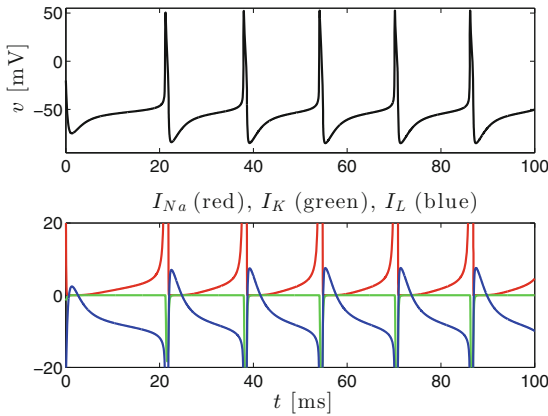


Figure E.6. A voltage trace of the Erisir neuron (upper panel), and the sodium, potassium, and leak currents (lower panel).[\[ERISIR_CURRENTS\]](#)

The equation governing $v(z, t)$ is

$$2\pi a(z)\sqrt{1+a'(z)^2}\Delta z C \frac{\partial v}{\partial t}(z, t) = I_m + I_l + I_r, \quad (\text{E.5})$$

where C denotes capacitance density as before. Using eqs. (E.2), (E.3), and (E.4), and dividing (E.5) by $2\pi a(z)\sqrt{1+a'(z)^2}\Delta z$, we find:

$$C \frac{\partial v}{\partial t}(z, t) = \frac{1}{2R_i a(z)\sqrt{1+a'(z)^2}\Delta z} \left[\frac{(a(z + \Delta z/2))^2(v(z + \Delta z, t) - v(z, t))}{\Delta z} - \frac{(a(z - \Delta z/2))^2(v(z) - v(z - \Delta z, t))}{\Delta z} \right] +$$

$$\bar{g}_{\text{Na}} m(z, t)^3 h(z, t) (v_{\text{Na}} - v(z, t)) + \bar{g}_{\text{K}} n(z, t)^4 (v_{\text{K}} - v(z, t)) + \bar{g}_{\text{L}} (v_{\text{L}} - v(z, t)) + I(z, t). \quad (\text{E.6})$$

Passing to the limit as $\Delta z \rightarrow 0$, we find:

$$Cv_t = \frac{(a^2 v_z)_z}{2R_i a \sqrt{1 + (a')^2}} + \bar{g}_{\text{Na}} m^3 h (v_{\text{Na}} - v) + \bar{g}_{\text{K}} n^4 (v_{\text{K}} - v) + \bar{g}_{\text{L}} (v_{\text{L}} - v) + I. \quad (\text{E.7})$$

This result can be found, for instance, in Appendix A of [100]. Note that in [100], the “external input current density” is taken to be a current per unit length in the z -direction (called the x -direction in [100]), not per unit membrane area. This accounts for the very slight difference between the equation in [100] and (E.7).

7.4. The period T is the solution of $\tau_m I (1 - e^{-T/\tau_m}) = 1$, so

$$\frac{1}{\tau_m I} = 1 - e^{-T/\tau_m}.$$

Similarly, \tilde{T} is the solution of $\tau_m I (1 - e^{-\tilde{T}/\tau_m}) = 0.95$, and solving for \tilde{T} we find

$$\tilde{T} = \tau_m \ln \frac{\tau_m I}{\tau_m I - 0.95}.$$

This implies

$$\frac{\tilde{T}}{\tau_m} = \ln \frac{\tau_m I}{\tau_m I - 0.95} = \ln \frac{1}{1 - 0.95(1 - e^{-T/\tau_m})}.$$

Therefore

$$\frac{T - \tilde{T}}{T} = \frac{T/\tau_m - \tilde{T}/\tau_m}{T/\tau_m} = 1 - \frac{1}{T/\tau_m} \ln \frac{1}{1 - 0.95(1 - e^{-T/\tau_m})}.$$

Figure E.7 shows the graph of $(T - \tilde{T})/T$ as a function of T/τ_m . The greater T/τ_m , the larger is the proportion of the inter-spike interval spent close to threshold, namely between $v = 0.95$ and $v = 1$. As discussed in the chapter, this results in high noise-sensitivity when T/τ_m is large.

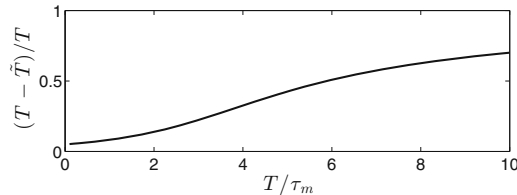


Figure E.7. $(T - \tilde{T})/T$ as a function of T/τ_m . [LIF_SENSITIVITY]

7.5. The plot is shown in Fig. E.8.

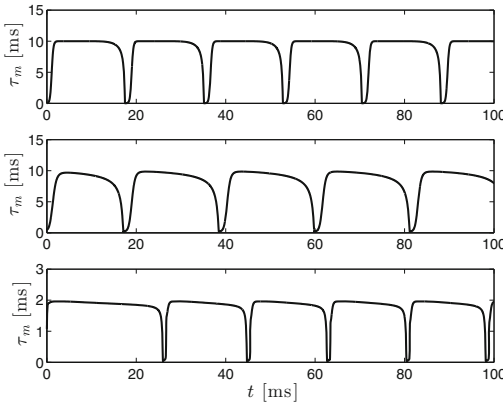


Figure E.8. Membrane time constants, as functions of time, for RTM (top), WB (middle), and Erisir (bottom) models. [MEMBRANE_TIME_CONSTANTS]

8.4. Figure E.9 shows the voltage trace of a normalized QIF neuron with $\tau_m = 1/2$ and $I = 0.5018$. During a large fraction of the period, v is now near $1/2$, not near 1. If during this time a small random input arrives, firing in response to that input will not be immediate. For small τ_m , the QIF neuron is not as noise sensitive as the LIF neuron.

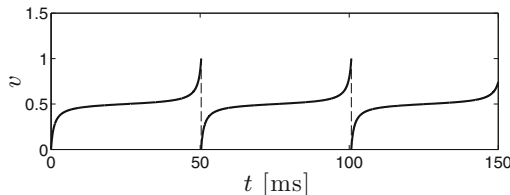


Figure E.9. The voltage trace of a QIF neuron with $\tau_m = 1/2$, firing at 20 Hz. [QIF_VOLTAGE_TRACE_SMALL_TAU_M]

8.5. For the LIF neuron,

$$T = \tau_m \ln \frac{\tau_m I}{\tau_m I - 1}.$$

Thus

$$\begin{aligned} \kappa &= \left| \frac{dT}{dI} \frac{I}{T} \right| = \left| \left(\frac{\tau_m}{I} - \frac{\tau_m^2}{\tau_m I - 1} \right) \frac{I}{T} \right| = \left| \frac{1}{T/\tau_m} - \frac{\tau_m I}{\tau_m I - 1} \frac{1}{T/\tau_m} \right| = \\ &\quad \left| \frac{1}{T/\tau_m} - \frac{e^{T/\tau_m}}{T/\tau_m} \right| = \frac{e^{T/\tau_m} - 1}{T/\tau_m}. \end{aligned}$$

For the theta neuron,

$$T = \frac{2\pi\tau_m}{\sqrt{4\tau_m I - 1}}.$$

Therefore

$$\begin{aligned}\kappa &= \left| \frac{dT}{dI} \frac{I}{T} \right| = \left| 4\pi\tau_m^2 (4\tau_m I - 1)^{-3/2} \frac{I}{T} \right| = \left| 4\pi\tau_m^2 \left(\frac{T}{2\pi\tau_m} \right)^3 \frac{I}{T} \right| = \\ &\left| \frac{1}{2\pi^2} \frac{T^2}{\tau_m^2} \tau_m I \right| = \left| \frac{1}{2\pi^2} \frac{T^2}{\tau_m^2} \left(\left(\frac{\pi\tau_m}{T} \right)^2 + \frac{1}{4} \right) \right| = \frac{1}{2} + \frac{(T/\tau_m)^2}{8\pi^2}.\end{aligned}$$

9.5. We start with eq. (9.12):

$$\frac{dv}{dt} = -\frac{v}{\tau_m} + I - w_k e^{-(t-t_k)/\tau_w} v. \quad (9.12)$$

We move all terms involving v to the left side:

$$\frac{dv}{dt} + g(t)v = I, \quad \text{with } g(t) = \frac{1}{\tau_m} + w_k e^{-(t-t_k)/\tau_w}.$$

Let

$$G(t) = \frac{t}{\tau_m} - w_k \tau_w e^{-(t-t_k)/\tau_w}. \quad (\text{E.8})$$

(Note that G is an anti-derivative of g .) Multiply both sides of the differential equation by $e^{G(t)}$:

$$e^{G(t)} \frac{dv}{dt} + e^{G(t)} g(t)v = I e^{G(t)}.$$

This is equivalent to

$$\frac{d}{dt} (e^{G(t)} v(t)) = I e^{G(t)},$$

so (using that $v(t_k + 0) = 0$)

$$e^{G(t)} v(t) = I \int_{t_k}^t e^{G(s)} ds \quad \Rightarrow \quad v(t) = I \int_{t_k}^t e^{G(s)-G(t)} ds.$$

Now insert (E.8). Using the notation $\exp(z) = e^z$,

$$v(t) = I \int_{t_k}^t \exp \left(-\frac{t-s}{\tau_m} - w_k \tau_w (e^{-(s-t_k)/\tau_w} - e^{-(t-t_k)/\tau_w}) \right) ds,$$

as claimed.

9.6. (a) Figure E.10 shows the two plots.

(b) In the proof of Lemma 9.4, we showed that

$$\phi(z) \leq I - \frac{1}{\tau_m} + \epsilon.$$

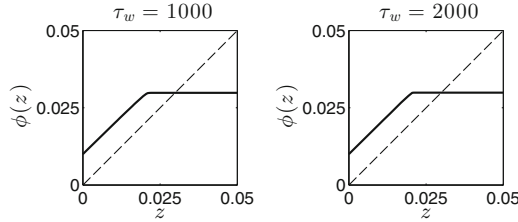


Figure E.10. The map ϕ , with $\tau_m = 10$, $I = 0.12$, $\epsilon = 0.01$, and for two different large values of τ_w : $\tau_w = 1000$ (left) and $\tau_w = 2000$ (right). [SLOW_ADAPT]

For large τ_w and large z , ϕ is nearly constant. It seems natural to guess that the approximate value of ϕ for large τ_w and large z is just this upper bound,

$$I - \frac{1}{\tau_m} + \epsilon.$$

If this is so, then

$$z_c = I - \frac{1}{\tau_m}.$$

Figure E.11 confirms this guess. The figure shows, for $\tau_w = 2000$ and for three different choices of the parameters τ_m , I , and ϵ , the graph of ϕ (black solid), and the graph of the function

$$\begin{cases} z + \epsilon & \text{for } 0 \leq z \leq I - \frac{1}{\tau_m}, \\ I - \frac{1}{\tau_m} + \epsilon & \text{for } z > I - \frac{1}{\tau_m} \end{cases} \quad (\text{E.9})$$

(red dots).

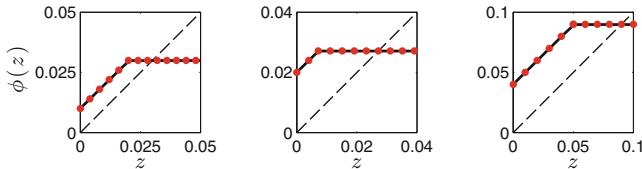


Figure E.11. The map ϕ , with $\tau_w = 2000$, and $\tau_m = 10$, $I = 0.12$, $\epsilon = 0.01$ (left panel), $\tau_m = 7$, $I = 0.15$, $\epsilon = 0.02$ (middle panel), $\tau_m = 10$, $I = 0.15$, $\epsilon = 0.04$ (right panel). The red dots show values of the function (E.9), confirming that this function is very close to ϕ . [LIMITING_FORM_OF_PHI]

(c) Since $\phi(z) = e^{-T(z)/\tau_w} z + \epsilon$, our assertion is equivalent to

$$\lim_{\tau_w \rightarrow \infty} \frac{T(z)}{\tau_w} = \begin{cases} 0 & \text{if } z < I - 1/\tau_m, \\ \ln(z/(I - 1/\tau_m)) & \text{if } z > I - 1/\tau_m. \end{cases}$$

We denote by $T_\infty(z) > 0$ the time at which the solution of

$$\frac{dv}{dt} = -\frac{v}{\tau_m} + I - zv, \quad v(0) = 0,$$

reaches $v = 1$; in other words, $T_\infty(z)$ is $T(z)$ with $\tau_w = \infty$, i.e., with no decay at all of the variable w . It is not surprising, and easy to prove, that $T(z) \leq T_\infty(z)$. The condition $z < I - 1/\tau_m$ is equivalent to $T_\infty(z) < \infty$. If this is the case, then

$$\lim_{\tau_w \rightarrow \infty} \frac{T_\infty(z)}{\tau_w} = 0$$

since $T_\infty(z)$ does not depend on τ_w . Therefore also

$$\lim_{\tau_w \rightarrow \infty} \frac{T(z)}{\tau_w} = 0$$

if $z < I - 1/\tau_m$.

Now assume that $z > I - 1/\tau_m$. Recall that $T(z)$ is the time at which the solution of

$$\frac{dv}{dt} = -\frac{v}{\tau_m} + I - ze^{-t/\tau_w}v, \quad v(0) = 0,$$

reaches 1. For v to reach 1, we must first wait until

$$\left[-\frac{v}{\tau_m} + I - ze^{-t/\tau_w}v \right] \Big|_{v=1} = -\frac{1}{\tau_m} + I - ze^{-t/\tau_w}, \quad (\text{E.10})$$

which starts out negative, becomes zero. The time that this takes is

$$\tau_w \ln \frac{z}{I - 1/\tau_m}, \quad (\text{E.11})$$

which is large when τ_w is large. After (E.10) becomes positive, the time it takes for v to reach 1 is negligible in comparison with (E.11) for large τ_w . (This is not difficult to make rigorous, but we won't.) Therefore

$$\lim_{\tau_w \rightarrow \infty} \frac{T(z)}{\tau_w} = \ln \frac{z}{I - 1/\tau_m}. \quad (\text{E.12})$$

(d) The question is how many iterations it takes for fixed point iteration for the function given by (E.9) and depicted in Fig. E.11 to reach the fixed point, starting at $z = 0$. Each iterate lies to the right of the previous iterate by ϵ , so the answer is approximately $(z_c + \epsilon)/\epsilon = (I - 1/\tau_m)/\epsilon + 1$.

(e) Fig. E.12 confirms that w saturates after approximately $(I - 1/\tau_m)/\epsilon + 1$ spikes, not only when τ_w is extremely large but even when $\tau_w = 100$.

10.2. We denote the left-hand side of eq. (10.5) by $g(n)$. If $v_K \leq v \leq v_{Na}$, then g is a strictly decreasing function of $n \geq 0$. This implies our assertion.

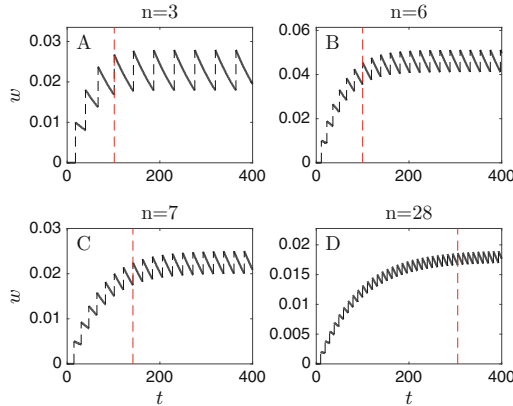


Figure E.12. The variable w as a function of time, for $\tau_w = 100$ and $(\tau_m, I, \epsilon) = (10, 0.12, 0.01)$ (A), $(10, 0.15, 0.01)$ (B), $(10, 0.13, 0.005)$ (C), $(8, 0.18, 0.002)$ (D). In each case the predicted number of spikes required before w saturates, $n = (I - 1/\tau_m)/\epsilon + 1$ (rounded to the nearest integer), is displayed, and the time of the $(n + 1)$ -st spike is indicated by a dashed red vertical line.

[ADAPTATION_SPEED]

10.6. (a) A fixed point (v_*, n_*) is a solution of the system

$$v - \frac{v^3}{3} - n + I = 0, \quad \frac{av - n}{\tau_n} = 0.$$

Thus $n_* = av_*$ and

$$v_* - \frac{v_*^3}{3} - av_* + I = 0,$$

i.e.,

$$(1 - a)v_* - \frac{v_*^3}{3} + I = 0. \quad (\text{E.13})$$

We denote the left-hand side of eq. (E.13) by $g(v_*)$, so

$$g(v) = (1 - a)v - \frac{v^3}{3} + I. \quad (\text{E.14})$$

For $a \geq 1$, the function g is strictly decreasing, and its limits as $v_* \rightarrow \mp\infty$ are $\pm\infty$. This implies that (E.13) has exactly one solution for $a \geq 1$, and therefore there is exactly one fixed point of the FitzHugh-Nagumo system.

(b) To analyze the stability of the fixed point, we must consider the Jacobi matrix

$$J_* = \begin{bmatrix} 1 - v_*^2 & -1 \\ a/\tau_n & -1/\tau_n \end{bmatrix}.$$

Its characteristic polynomial is

$$(1 - v_*^2 - \lambda) \left(-\frac{1}{\tau_n} - \lambda \right) + \frac{a}{\tau_n} = \lambda^2 + \left(v_*^2 - 1 + \frac{1}{\tau_n} \right) \lambda + \frac{1}{\tau_n} (a + v_*^2 - 1).$$

The eigenvalues are therefore

$$\lambda_{\pm} = \frac{-(v_*^2 - 1 + 1/\tau_n) \pm \sqrt{(v_*^2 - 1 + 1/\tau_n)^2 - 4(a + v_*^2 - 1)/\tau_n}}{2}.$$

If $I > a - 2/3$, then

$$g(1) = 1 - a - \frac{1}{3} + I = \frac{2}{3} - a + I > 0$$

(see eq. (E.14), therefore $v_* > 1$, and therefore

$$v_*^2 - 1 + 1/\tau_n > 0.$$

Furthermore, since $4(a + v_*^2 - 1)/\tau_n > 0$,

$$\sqrt{(v_*^2 - 1 + 1/\tau_n)^2 - 4(a + v_*^2 - 1)/\tau_n}$$

is either purely imaginary, or real and smaller than $|v_*^2 - 1 + 1/\tau_n|$. In either case, the eigenvalues λ_+ and λ_- both have negative real part, so the fixed point is stable.

11.2. There are fixed points only when $I \leq 0$, and in that case, the fixed points are $x_{*,\pm} = \pm\sqrt{-I}$. Figure E.13 shows $x_{*,\pm}$ as functions of I .

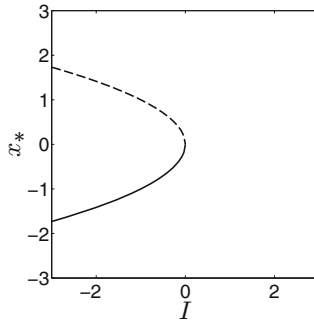


Figure E.13. The bifurcation diagram for $dx/dt = x^2 + I$. The solid curve indicates stable fixed points, and the dashed curve indicates unstable ones. [FORK]

11.3. The plots of $x(t)$ are in Fig. E.14. The long plateau during which x barely changes at all is the time during which the trajectory passes the “ghost” of the two fixed points annihilated in the saddle-node collision as I rises above 0.5. Table E.1 gives numerical results, confirming that $T\sqrt{I - I_c}$ is approximately independent of I when $I \approx I_c$, $I > I_c$.

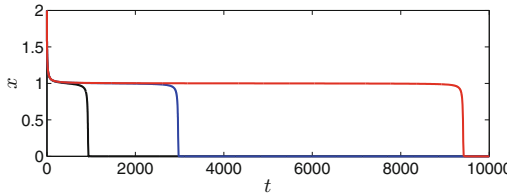


Figure E.14. $(x(t), y(t))$ solves (11.5), (11.6) with $x(0) = 1$, $y(0) = 0.5$, and $I = 0.5 + 10^{-4}$ (black), $0.5 + 10^{-5}$ (blue), and $0.5 + 10^{-6}$ (red). [GHOST]

I	T	$T\sqrt{I - I_c}$
$0.5 + 10^{-4}$	921	9.21
$0.5 + 10^{-5}$	2959	9.36
$0.5 + 10^{-6}$	9403	9.40

Table E.1. Results of the numerical experiments for problem 11.3. [GHOST]

A detail in the code that generates Fig. E.14 and Table E.1 deserves elaboration. The code generates approximations x_k for $x(k\Delta t)$, $k = 1, 2, \dots$. To approximate the time, t_* , at which x crosses 1.5, we first determine the largest k with $x_k > 1.5$. Note that then $x_{k+1} \leq 1.5$. We compute the straight line through the points $(k\Delta t, x_k)$ and $((k+1)\Delta t, x_{k+1})$, and define t_* to be the time at which this straight line intersects the horizontal line $x = 1.5$. Note that $t_* \in (k\Delta t, (k+1)\Delta t]$. The result of this calculation is easily seen to be

$$t_* = \frac{x_k - 1.5}{x_k - x_{k+1}} (k+1)\Delta t + \frac{1.5 - x_{k+1}}{x_k - x_{k+1}} k\Delta t. \quad (\text{E.15})$$

The time at which x crosses 0.5 is approximated analogously.

11.4. (a) The equation

$$|x| + I = 0$$

has two solutions, namely $x_{\pm} = \pm I$, when $I < 0$. The two solutions meet at 0 when $I = 0$, and there is no solution of the equation for $I > 0$. (b) Let $a > 0$. The time needed to move from $x = -a$ to $x = a$ is

$$\begin{aligned} \int_{-a}^a \frac{dt}{dx} dx &= \int_{-a}^a \frac{1}{|x| + I} dx = 2 \int_0^a \frac{1}{x + I} dx = 2 \ln(x + I)|_{x=0}^a = \\ &2(\ln(a + I) - \ln(I)) = 2 \left(\ln(a + I) + \ln \frac{1}{I} \right). \end{aligned}$$

This is $\sim 2 \ln(1/I)$ in the limit as $I \searrow 0$.

(c) This bifurcation does not behave like a typical saddle-node bifurcation because $|x| + I$ is not a differentiable function of x at $x = 0$, the site of the collision of the two fixed points.

12.2. (b) Figure 12.1 indicates three fixed points on, for instance, the vertical line $I = 0.05 \mu\text{A}/\text{cm}^2$. We will denote them by $(v_{*,L}, n_\infty(v_{*,L}))$, $(v_{*,M}, n_\infty(v_{*,M}))$, and $(v_{*,U}, n_\infty(v_{*,U}))$, with $v_{*,L} < v_{*,M} < v_{*,U}$. (Of course, L , M , and U stand for “lower,” “middle,” and “upper.”) Figure 12.1 shows that $(v_{*,L}, n_\infty(v_{*,L}))$ is a stable fixed point of (12.1), (12.2), whereas $(v_{*,M}, n_\infty(v_{*,M}))$ and $(v_{*,U}, n_\infty(v_{*,U}))$ are both unstable fixed points of (12.1), (12.2).

However, $v_{*,U}$ is a stable fixed point of (12.6). To see this, we denote the right-hand side of (12.6) by $F(v)$:

$$F(v) = \bar{g}_{\text{Na}} m_\infty(v)^3 (1 - n_\infty(v)) (v_{\text{Na}} - v) + \bar{g}_{\text{K}} n_\infty(v)^4 (v_{\text{K}} - v) + \bar{g}_{\text{L}} (v_{\text{L}} - v) + I.$$

For $I = 0.05 \mu\text{A}/\text{cm}^2$, the graph of F crosses the v -axis three times, in the points $v_{*,L}$, $v_{*,M}$, and $v_{*,U}$. Fixed points where F changes from positive to negative, as v increases, are stable, and fixed points where F undergoes the reverse change of signs are unstable. Thus drawing the graph of F will reveal whether $v_{*,U}$ is stable or unstable.

The graph of F is somewhat difficult to interpret because the values of F vary widely. We therefore plot not F , but $\tanh(5F)$, as a function of v . This function is zero if and only if $F = 0$. Since \tanh is strictly increasing, the graph of $\tanh(5F)$ reveals the stability of the fixed points just as the graph of F does. However, $\tanh(5F)$ only varies between -1 and 1 , and its graph crosses the v -axis 5 times more steeply than that of F , and as a result the crossings are more easily visible. Figure E.15 shows this plot, confirming that $v_{*,U}$ is a stable fixed point of (12.6).

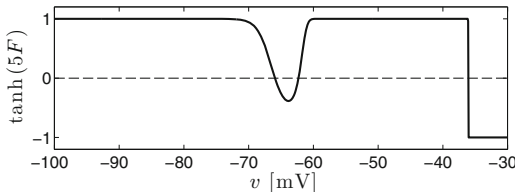


Figure E.15. $\tanh(5F)$ as a function of v , where $F = F(v)$ is the right-hand side of (12.6). [PLOT_F]

12.3. Figure E.16 shows the results.

12.4. Figure E.17 shows the result. The unstable node becomes stable at a critical value of I between 1000 and $1500 \mu\text{A}/\text{cm}^2$. This explains the difference in the two plots in exercise 12.3. In this plot, the saddle-node collision is barely visible, since it occurs for values of I that are very small in comparison with $2000 \mu\text{A}/\text{cm}^2$.

13.2.

$$\frac{dx}{dt} = (I \mp (x^2 + y^2)) x - y, \quad (\text{E.16})$$

$$\frac{dy}{dt} = (I \mp (x^2 + y^2)) y + x. \quad (\text{E.17})$$

(The minus signs are for part (a), and the plus signs for part (b).)

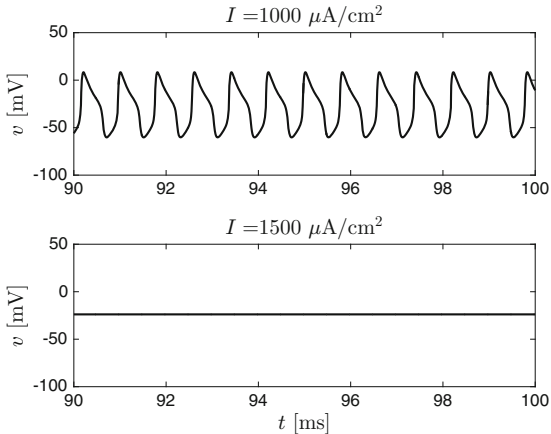


Figure E.16. Results for exercise 12.3, showing depolarization block for very large (and quite unrealistic) values of I . [DEPOLARIZATION_BLOCK]

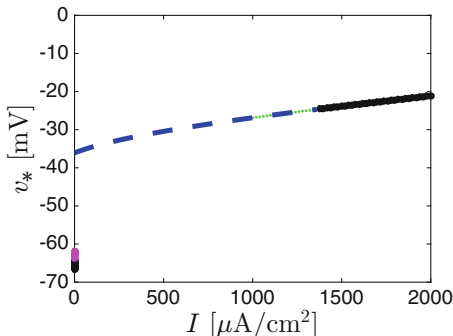


Figure E.17. Same as Fig. 12.1, but for a much larger range of drives, showing that the unstable node (blue, dashes) becomes stable (black, solid) for very large (and quite unrealistic) values of I . [RTM_2D_FP_LARGE_I]

13.4. (a)

$$\begin{aligned}\frac{dx}{dt} &= \left(I \mp \sqrt{x^2 + y^2} \right) x - y, \\ \frac{dy}{dt} &= \left(I \mp \sqrt{x^2 + y^2} \right) y + x.\end{aligned}$$

(b) $\sqrt{x^2 + y^2} x$ is obviously infinitely often differentiable as a function of (x, y) for $(x, y) \neq (0, 0)$. It is differentiable even at the origin. This is to say that there is a linear approximation of $\sqrt{x^2 + y^2} x$ near $(x, y) = (0, 0)$ which is accurate up to an error of size $o(\sqrt{x^2 + y^2})$ as $(x, y) \rightarrow (0, 0)$. (See Section 1.2 for the meaning of $o(\dots)$.) In fact, that linear approximation is zero:

$$\sqrt{x^2 + y^2} x = 0 + o(\sqrt{x^2 + y^2})$$

as $(x, y) \rightarrow (0, 0)$. Similarly, $\sqrt{x^2 + y^2} y$ is differentiable at $(0, 0)$ with zero derivative. However, $\sqrt{x^2 + y^2} x$ and $\sqrt{x^2 + y^2} y$ are not twice differentiable. If one of them were twice differentiable, the other would be as well by symmetry, and in that case

$$\sqrt{x^2 + y^2} x \cdot x + \sqrt{x^2 + y^2} y \cdot y = (x^2 + y^2)^{3/2} = r^{3/2}$$

would have to be twice differentiable; but it is not. On the other hand, the right-hand sides in (E.16) and (E.17) are clearly infinitely often differentiable.

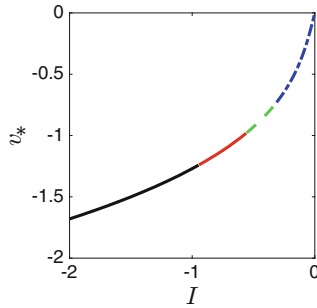


Figure E.18. v_* as a function of I for the FitzHugh-Nagumo equations with $a = 1.25$ and $\tau_n = 25$. Black, solid: stable node. Red, solid: stable spiral. Green, dashes: unstable spiral. Blue, dash-dots: unstable node. [FN_FP]

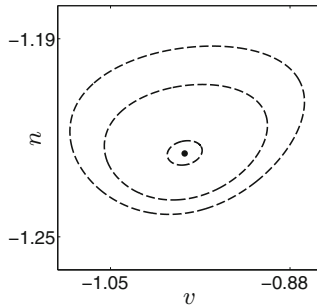


Figure E.19. Repelling limit cycles for the FitzHugh-Nagumo equations, for three values of I slightly smaller than I_c : $I = -0.5595$, -0.559 , and -0.5585 . The repelling limit cycle contracts to a single point as $I \nearrow I_c$. [FN_HOPF]

14.2. (a) Figure E.18 shows this curve. The code that generates this figure also determines where the transition from a stable spiral (indicated as a solid red line in the figure) to an unstable spiral (indicated as a dashed green line) occurs: The critical value of I is $I_c \approx -0.55848$. (b) The fact that there is a transition from a stable

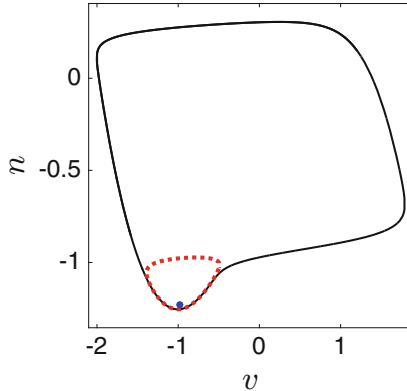


Figure E.20. Bistability for the FitzHugh-Nagumo equations: Stable limit cycle (black, solid), stable fixed point (blue), with a repelling limit cycle (red, dots) separating the basins of attraction. [FN_LIMIT_CYCLES]

to an unstable spiral is evidence for a Hopf bifurcation. To determine whether this Hopf bifurcation is subcritical or supercritical, we look for limit cycles for values of I close to I_c . We find that for $I < I_c$ but $I \approx I_c$, there is a repelling limit cycle surrounding the fixed point for $I = I_c$; see Fig. E.19. (As previously, we compute the repelling limit cycle using the fact that it becomes attracting when time is reversed.) This is strong evidence for a subcritical Hopf bifurcation. Figure E.20 shows, for $I = -0.563$ (very slightly below I_c), a stable limit cycle (black, solid), a repelling limit cycle (red, dots), and a stable fixed point (blue). The bistability seen here occurs only over a very small range of values of $I < I_c$. For instance, for $I = -0.565$, the fixed point appears to be globally attracting, judging by numerical experiments using the code that generates Fig. E.20.

15.2. We can think of n as a function of v for the curve shown in Fig. 15.7. Dividing eq. (10.7) by eq. (10.6), we find

$$\frac{dn}{dv} = \frac{1}{\tau_n} \frac{av - n}{v - v^3/3 - n + I}.$$

Note that the denominator $v - v^3/3 - n + I$ on the right-hand side is the vertical distance between the v -nullcline and the blue curve, and the numerator $av - n$ is the vertical distance between the n -nullcline and the blue curve. If $av - n$ is exactly $O(1)$ (bounded by positive constants from below and above), and dn/dv is exactly $O(1)$ (in the same sense), as it is in Fig. 15.7 between $v = -0.5$ and $v = 0.5$, for instance, then $v - v^3/3 - n + I$ must be exactly $O(1/\tau_n)$.

15.5. In this model, for there to be two action potentials in a row before the adaptation current is strong enough to prohibit firing, δ must be small. We set $\delta = 0.02$. Then τ_{adapt} must be lengthened to obtain subthreshold oscillations. $\tau_{\text{adapt}} = 200$ is enough, and yields the pattern shown in Fig. E.21.

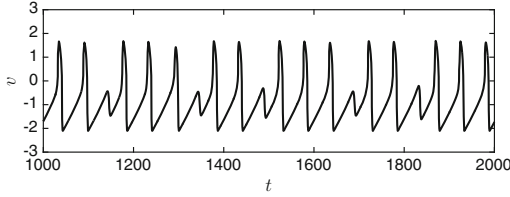


Figure E.21. Analogous to Fig. 15.5, but with a much smaller δ ($\delta = 0.02$ here), and a somewhat larger τ_{adapt} ($\tau_{\text{adapt}} = 200$). We continued the simulation to $t = 2000$, but show only times between 1000 and 2000, because there is an initial transition before a stable pattern emerges. [MMOS_2]

15.6. If I is slightly above I_* , a single spike may reduce effective drive to a point where periodic firing is no longer possible. The trajectory will then rapidly approach the attracting fixed points. As the effective drive recovers and rises above I_* again, the trajectory will stay in the vicinity of the attracting fixed point, and therefore there will be no second spike. If, on the other hand, I is slightly above I_c , a burst of spikes can bring the effective drive below I_* , thereby making firing cease. As soon as the recovering effective drive rises above I_c again, firing resumes. A resulting voltage trace is shown in Fig. E.22. One might call what is seen here “mixed-mode oscillations,” in the sense that there are subthreshold oscillations between the bursts, but they are of very small amplitude.

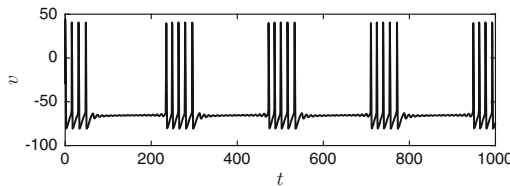


Figure E.22. Analogous to Fig. 15.5, but based on the model of Section 15.2, with $I = 8$, $\delta = 1.5$, and $\tau_{\text{adapt}} = 50$. [HH_MMOS]

16.2. See Fig. E.23.

17.1.

$$t_* = \frac{(k-1)\Delta t(-20 - v_k) + k\Delta t(v_{k-1} + 20)}{v_{k-1} - v_k}$$

17.2. We have to show that the equation $F(v) = 0$, with

$$F(v) = \bar{g}_{\text{Na}}(m_\infty(v))^3 h_\infty(v)(v_{\text{Na}} - v) + \bar{g}_K(n_\infty(v))^4 (v_K - v) + \bar{g}_L(v_L - v) + I,$$

has exactly one solution v_* . (The fixed point is then $(v_*, m_\infty(v_*), h_\infty(v_*), n_\infty(v_*))$.) From the definitions of m_∞ , h_∞ , and n_∞ , it is easy to verify that

$$\lim_{v \rightarrow \pm\infty} F(v) = \mp\infty, \quad (\text{E.18})$$

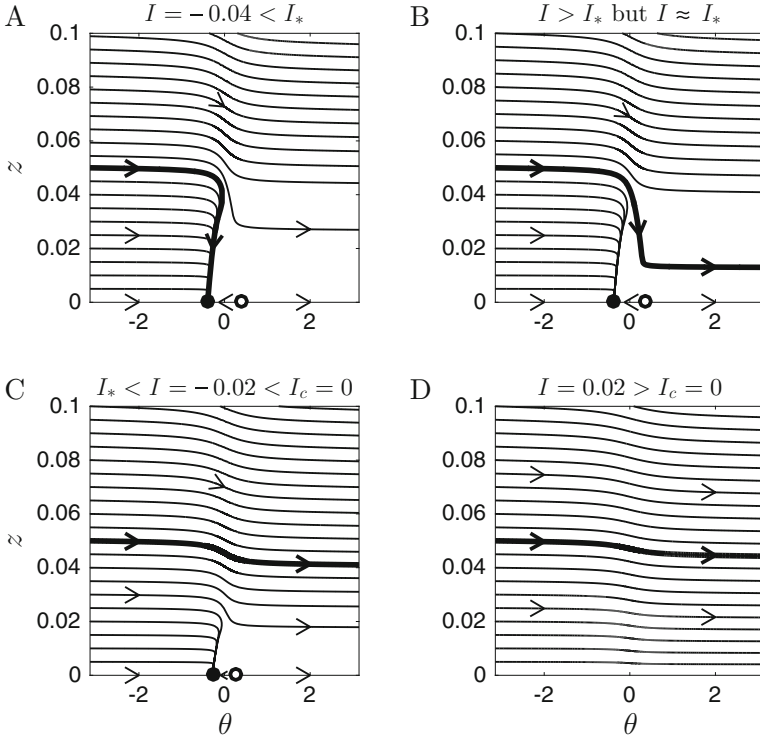


Figure E.23. Analogous to Fig. 16.4, but with $z_{\max} = 0.05$ and $\tau_z = 100$. For these parameter values, $I_* = -0.0364 \dots$ [SETN_PHASE_PLANE_SLOW]

and

$$\lim_{v \rightarrow -\infty} F'(v) = -\bar{g}_L. \quad (\text{E.19})$$

Equation (E.18) implies, by the intermediate value theorem, that $F(v) = 0$ has at least one solution $v = v_*$. Further, if v_* is a solution, then

$$\left(\bar{g}_{Na} (m_\infty(v_*))^3 h_\infty(v_*) + \bar{g}_K (n_\infty(v_*))^4 + \bar{g}_L \right) v_* =$$

$$\bar{g}_{Na} (m_\infty(v_*))^3 h_\infty(v_*) v_{Na} + \bar{g}_K (n_\infty(v_*))^4 v_K + \bar{g}_L v_L + I \leq \bar{g}_{Na} v_{Na} + \bar{g}_L v_L + I,$$

which implies

$$v_* \leq \frac{\bar{g}_{Na} v_{Na} + \bar{g}_L v_L + I}{\bar{g}_{Na} (m_\infty(v_*))^3 h_\infty(v_*) + \bar{g}_K (n_\infty(v_*))^4 + \bar{g}_L} \leq \frac{\bar{g}_{Na} v_{Na} + \bar{g}_L v_L + I}{\bar{g}_L}. \quad (\text{E.20})$$

By (E.19), we can choose a potential v_0 so that $F'(v) < 0$ for $v \in (-\infty, v_0]$. Inequality (E.20) implies that all solutions of $F(v) = 0$ lie in the interval $(-\infty, v_0]$ if I is sufficiently low. These two facts, taken together, imply that the solution of $F(v) = 0$ is unique for sufficiently low I .

17.3. We calculate and classify the fixed points for $0.5 \leq I \leq 0.51$. (This is the range in which the subcritical Hopf bifurcation appears to occur, see Fig. 17.10.) We find that a stable spiral turns into an unstable spiral as I rises above $I_c \approx 0.508$; see Fig. E.24. (There are other unstable fixed point in the same range of values of I , not shown in the figure.) We also find that the Jacobi matrix at this fixed point has a pair of complex-conjugate eigenvalues that passes through the imaginary axis from left to right as I rises above I_c ; see Fig. E.25.

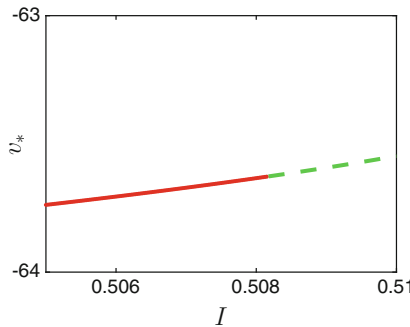


Figure E.24. For the RTM neuron with M -current, $\bar{g}_M = 0.2 \text{ mS/cm}^2$, $v_K = -100 \text{ mV}$, a stable spiral (red, solid) turns into an unstable spiral (green, dashes) as I rises above $I_c \approx 0.508$. [RTM_WITH_M_CURRENT_FP (figure 1)]

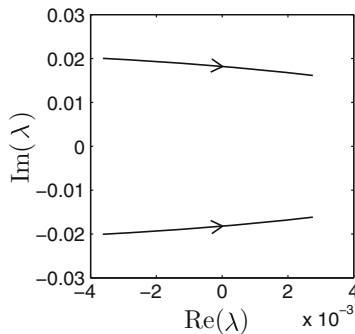


Figure E.25. As I rises above I_c in Fig. E.24, a complex-conjugate pair of eigenvalues of the Jacobi matrix passes through the imaginary axis from left to right. [RTM_WITH_M_CURRENT_FP (figure 2)]

17.4. (a) Figure E.26 shows the bifurcation diagram, and demonstrates that there is a saddle-node collision as I rises above I_c . (b) The calcium-activated AHP current is dormant as long as there is no firing. Therefore the mechanism by which the transition from rest to firing occurs cannot be affected by it.

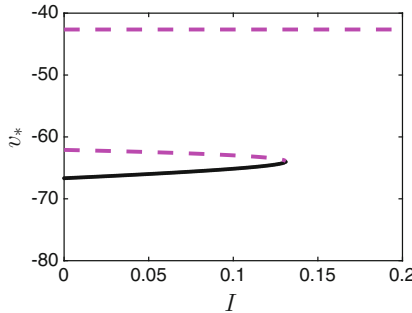


Figure E.26. For the RTM neuron with AHP-current, $g_{\text{AHP}} = 0.2 \text{ mS/cm}^2$, $v_K = -100 \text{ mV}$, a saddle (magenta, dashes) and a node (black, solid) collide and annihilate each other as I rises above I_c . [RTM_WITH_AHP_FP]

17.8. The results are shown in Table E.2. Among all the potassium currents considered here, in fact Izhikevich's has the *lowest* half-activation voltage.

model	$v_{1/2}$
classical Hodgkin-Huxley	-24 mV
RTM	-20 mV
WB	2 mV
Erisir	6 mV
$I_{\text{Na,p}}-I_K$ model	-25 mV

Table E.2. Half-activation voltage of the potassium current in mV, rounded to the nearest integer. [HALF_ACTIVATION_OF_POTASSIUM]

17.10. (a) Because

$$\ln \frac{1}{C(I - I_*)} = \ln \frac{1}{C} + \ln \frac{1}{I - I_*},$$

the right-hand sides of (17.11) and (17.8) are asymptotically the same as $I \searrow I_*$.

(b) A mathematical statement about a physical problem is “dimensionally correct” if a change of units results in an equivalent mathematical statement. This is indeed the case here: A change of units of current density simply causes $I - I_*$ on the right-hand side of (17.8) to be scaled by a constant. As explained in the solution to part (a), this does not have any impact on the asymptotic behavior as $I \searrow I_*$.

18.2. The result is shown in Fig. E.27.

18.3. The result is shown in Fig. E.28.

18.4. The result is in Fig. E.29. The range of values of I in which there is bistability is indeed enlarged significantly in comparison with Fig. 18.12.

19.1. The action potential at time $(k-1)\delta$ lowers the effective drive from I_{k-1} , its

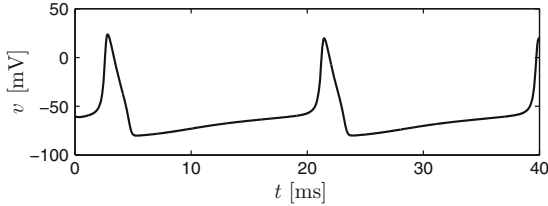


Figure E.27. Same as lower panel in Fig. 18.1, but with h replaced by $\min(h, h_*)$ in each time step of the simulation. [HH_BISTABLE_LIMITED_H]

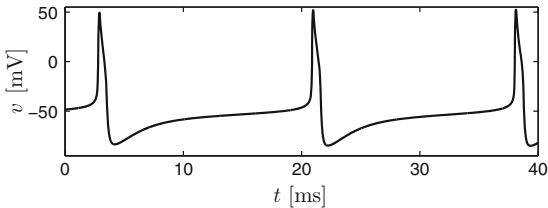


Figure E.28. Same as lower panel in Fig. 18.4, but with n replaced by $\max(n, n_*)$ in each time step of the simulation. [ERISIR_BISTABLE_LIMITED_N]

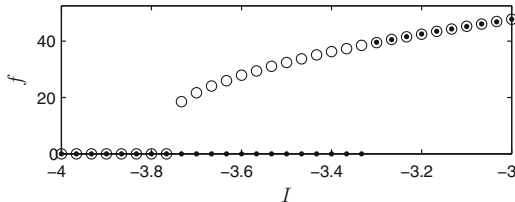


Figure E.29. f - I curve of the RTM neuron with h -current, modified as described in exercise 18.4. [RTM_F_I_CURVE_WITH_I_H_MODIFIED]

value just prior to the action potential, to $I_{k-1} - \epsilon$, its value just after the action potential. Between times $(k-1)\delta$ and $k\delta$, I_{eff} then evolves according to eq. (19.4); this implies eq. (19.5).

19.4. Raising $\bar{g}_{K,\text{slow}}$ should be akin to raising ϵ in the idealized analysis. Therefore the bursts should get shorter. Lowering $\bar{g}_{K,\text{slow}}$ should similarly make the bursts longer. There is no obvious reason why the value of $\bar{g}_{K,\text{slow}}$ should affect the inter-burst interval. Figure E.30 confirms these guesses quite strikingly.

19.5. Raising $\tau_{n,\text{slow}}$ should be akin to lowering ϵ and raising τ_{slow} in the idealized analysis. (The effect should be similar to lowering ϵ because with a larger $\tau_{n,\text{slow}}$, the response of the slow potassium current to firing should be more sluggish, and therefore weaker.) Therefore the bursts should get longer, and the inter-burst intervals should get longer as well, as $\tau_{n,\text{slow}}$ is raised. Figure E.31 confirms these guesses.

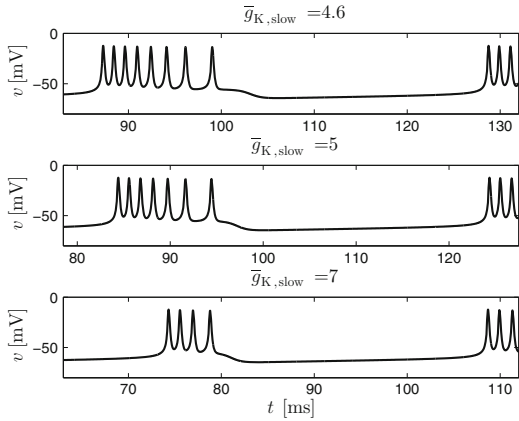


Figure E.30. Effects of varying $\bar{g}_{K,\text{slow}}$ in the model in Section 19.2. Although a different time interval is shown in each case, the length of the time interval, and hence the scaling of the horizontal axis, is the same in all three cases.
[INAPIK_SLOW_I_K_VARY_G]

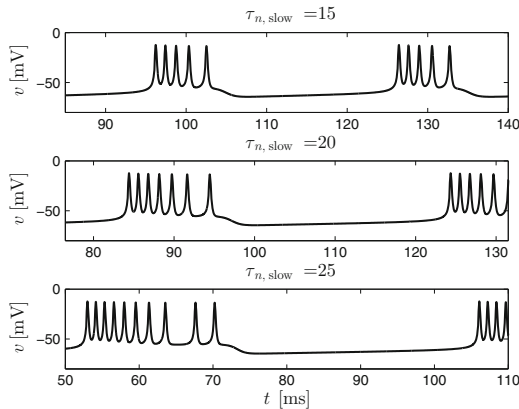


Figure E.31. Effects of varying $\tau_{n,\text{slow}}$ in the model in Section 19.2. Although a different time interval is shown in each case, the length of the time interval, and hence the scaling of the horizontal axis, is the same in all three cases.
[INAPIK_SLOW_I_K_VARY_TAU]

19.6. Figure E.32 shows the result. Note that there is a delay of a little over 10 ms between the instant when I rises above I_c and the onset of firing. This is consistent with Fig. 19.8.

20.1. (c) Figure E.33 shows the results. For s to be able to return to values very close to zero between spikes, we must choose g and Δ so that $g(v/\Delta)$ is close to zero for values of v near the resting membrane potential of a nerve cell. This means either to choose Δ small enough (compare, for instance, the left and middle panels

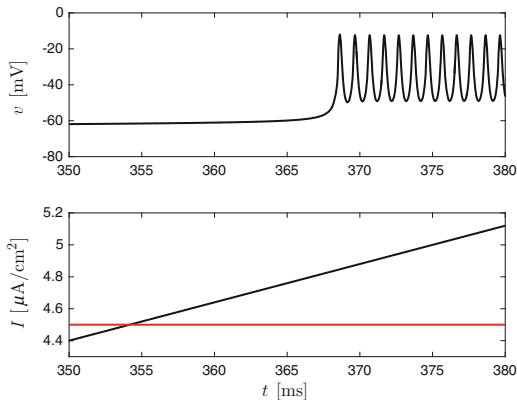


Figure E.32. Response of the $I_{\text{Na},\text{p}}-I_{\text{K}}$ model to external drive that ramps up gradually. The red horizontal line in the lower panel indicates I_c . There is a delay of more than 10 ms between the time when I rises above I_c and the onset of firing. [[INAPIK_RAMP](#)]

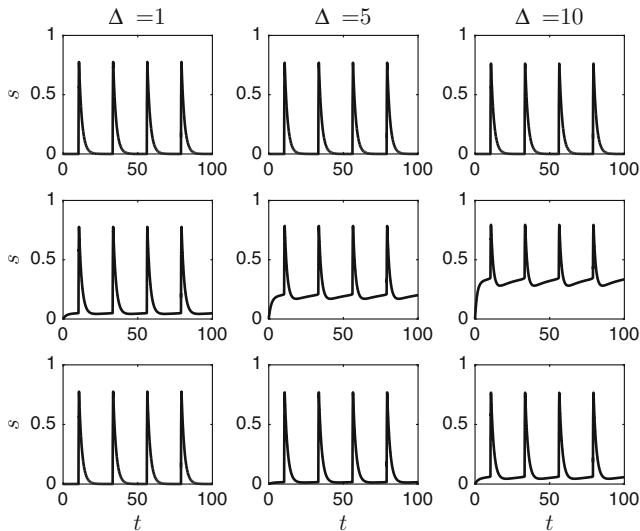


Figure E.33. Analogous to the middle panel of Fig. 20.2, but with the term $(1 + \tanh(v/10))/2$ on the right-hand side of eq. (20.2) replaced by $g(v/\Delta)$, with $g(v) = (1 + \tanh(v))/2$ (top row), $g(v) = \arctan(v)/\pi + 1/2$ (middle row), and $g(v) = (v/\sqrt{1+v^2} + 1)/2$ (bottom row), $\Delta = 1$ (left column), $\Delta = 5$ (middle column), and $\Delta = 10$ (right column). The panel in the right upper corner reproduces the middle panel of Fig. 20.2. [[DIFFERENT_SIGMOIDS](#)]

of the bottom row of Fig. E.33 with the right panel), or to choose g so that it converges to 0 as $v \rightarrow -\infty$ rapidly enough. Of the three choices of g tested here, $(1 + \tanh(v))/2$ converges to zero exponentially fast as $v \rightarrow -\infty$, while the others converge to zero much slower:

$$\frac{\arctan(v)}{\pi} + \frac{1}{2} \sim \frac{1}{\pi|v|} \quad \text{as } v \rightarrow -\infty, \quad (\text{E.21})$$

and

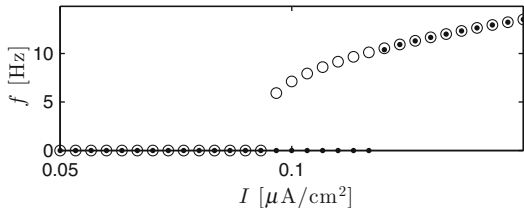
$$\frac{1}{2} \left(\frac{v}{\sqrt{1+v^2}} + 1 \right) \sim \frac{1}{4v^2} \quad \text{as } v \rightarrow -\infty. \quad (\text{E.22})$$

20.3. The synaptic input into the j -th neuron is now

$$\sum_{i=1}^N \bar{g}_{\text{syn},ij} s_{ij} (v_{\text{rev},ij} - v_j) = \left(\sum_{i=1}^N \bar{g}_{\text{syn},i} s_i \right) (v_{\text{rev},j} - v_j).$$

The sum in the parentheses only needs to be evaluated once, it is the same for all N neurons.

20.5. The result is shown in Fig. E.34.



(c) Suppose that $(G - D)\mathbf{v} = \mathbf{0}$. Because G is symmetric, this equation can also be written as $(G^T - D)\mathbf{v} = \mathbf{0}$. Take the j -entry of $(G^T - D)\mathbf{v}$:

$$\sum_{i=1}^N g_{\text{gap},ij} v_i - c_j v_j = 0. \quad (\text{E.23})$$

Solve eq. (E.23) for v_j :

$$v_j = \sum_{i=1}^N w_i v_i. \quad (\text{E.24})$$

with

$$w_i = \frac{g_{\text{gap},ij}}{c_j}.$$

(Of course w_i depends on j , but we don't indicate that in our notation here.) Note that $w_i > 0$ if $g_{\text{gap},ij} > 0$, $w_i = 0$ otherwise, and

$$\sum_{i=1}^N w_i = 1,$$

so the right-hand side of (E.24) is a weighted average over those v_i with $g_{\text{gap},ij} > 0$.

(d) We say that i is a *nearest neighbor* of j if $g_{\text{gap},ij} > 0$. In part (c), we concluded that v_j is a weighted average over v_i , taken over the nearest neighbors of j . Since $v_j \geq v_i$ for all i , this implies that $v_i = v_j$ if i is a nearest neighbor of j . We can then apply the same reasoning to the nearest neighbors of the nearest neighbors, and so on. Because the connectivity graph is connected, this eventually leads to the conclusion that $v_k = v_j$ for all k .

(e) We have concluded now that there is a one-dimensional eigenspace associated with the eigenvalue 0, spanned by \mathbf{e} . All other eigenvalues are strictly negative:

$$0 = \lambda_1 > \lambda_2 \geq \dots \geq \lambda_N,$$

and we may take \mathbf{b}_1 to be \mathbf{e} . We expand \mathbf{v}_0 in the form

$$\mathbf{v}_0 = c_1 \mathbf{e} + \sum_{k=2}^N c_k \mathbf{b}_k. \quad (\text{E.25})$$

Taking the dot product of both sides of (E.25) with \mathbf{e}/N , we conclude that c_1 is the mean of \mathbf{v}_0 , so $c_1 = m_0$. Further,

$$\mathbf{v}(t) = c_1 \mathbf{e} + \sum_{k=2}^N c_k \mathbf{b}_k e^{-\lambda_k t} \rightarrow c_1 \mathbf{e} = m_0 \mathbf{e}$$

as $t \rightarrow \infty$.

21.3. One finds that the two neurons phase-lock if I_1 and I_2 are close enough to each other, and not if not. Figure E.35 shows the examples $I_2 = 0.97 \mu\text{A}/\text{cm}^2$ (the two neurons phase-lock), and $I_2 = 0.96 \mu\text{A}/\text{cm}^2$ (they do not).

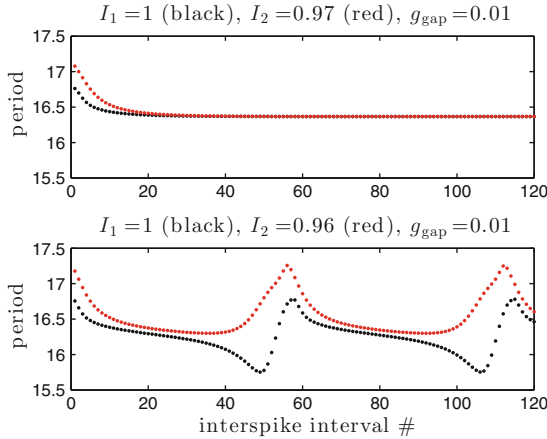


Figure E.35. Periods of two WB neurons coupled with $g_{\text{gap}} = 0.01 \text{ mS/cm}^2$, with I_2 close enough to $I_1 = 1 \mu\text{A}/\text{cm}^2$ for phase locking (upper trace), and I_2 too far from I_1 for phase-locking (lower trace). [WB_PHASE_LOCKING_BY_GJ]

22.1. Suppose that $E(t) < 0$ for some t . Let $t_0 \geq 0$ be the latest time prior to time t at which $E(t_0) = 0$. There is then, by the mean value theorem, some time $t_c \in (t_0, t)$ so that

$$\frac{dE}{dt}(t_c) = \frac{E(t) - E(t_0)}{t - t_0} < 0.$$

On the other hand,

$$\frac{dE}{dt}(t_c) = \frac{f(w_{EE}E(t_c) - w_{IE}I(t_c) + I_E) - E(t_c)}{\tau_E} \geq -\frac{E(t_c)}{\tau_E} > 0.$$

This contradiction proves that $E(t)$ cannot become negative. Similar arguments show that $E(t)$ cannot be greater than 100, and $I(t)$ cannot become negative or greater than 100.

22.2. Numerically, we find that there is only one fixed point (E_*, I_*) for $0 \leq w_{EE} \leq 1.5$. Figure E.36 shows E_* as a function of w_{EE} . The figure confirms that a stable spiral turns into an unstable spiral as w_{EE} rises above the critical value, i.e., a conjugate pair of complex eigenvalues crosses the imaginary axis.

I will not spell out all details of the calculation producing Fig. E.36, but refer the reader to the code generating the figure instead. However, I will explain how one finds all fixed points, for a given w_{EE} . A fixed point is a point (E_*, I_*) with $E_* = f(w_{EE}E_* - I_* + 20)$, $I_* = g(E_*)$. Inserting the second of these equations into the first, we find a single equation for E_* :

$$E_* = f(w_{EE}E_* - g(E_*) + 20). \quad (\text{E.26})$$

To find *all* solutions of this equation, we note that any solution must lie between 0 and 100, since values of f lie between 0 and 100. We discretize the interval

$[0, 100]$ into very short subintervals of length ΔE , evaluate the function $F(E) = f(w_{EE}E - g(E) + 20) - E$ at the boundary points of those subintervals, and look for subintervals on which F changes sign. In any such subinterval, we use the bisection method to find a solution up to a very small error.

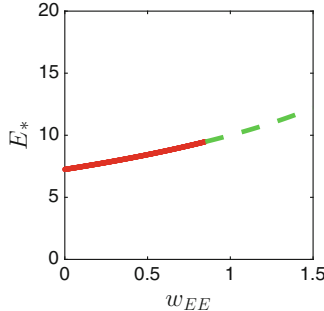


Figure E.36. Fixed point of the system given by eqs. (22.1)–(22.6), as a function of w_{EE} . A stable spiral (red, solid) becomes unstable (green, dashed) as w_{EE} rises above $w_{EE,c} \approx 0.85$. [WILSON_COWAN_BIF_DIAG]

22.3. A fixed point is a point (E_*, I_*) with

$$E_* = f(-w_{IE}I_* + I_E), \quad (\text{E.27})$$

$$I_* = g(w_{EI}E_* + I_I). \quad (\text{E.28})$$

We define

$$h(I_*) = f(-w_{IE}I_* + I_E),$$

and note that h is strictly decreasing. We denote the inverse function of h by $p = p(E_*)$. It is strictly decreasing as well. The right-hand side of eq. (E.28) is a strictly increasing function of E_* . We denote it by $q(E_*)$. So (E.27), (E.28) can be re-written as

$$I_* = p(E_*) = q(E_*). \quad (\text{E.29})$$

Define

$$r(E_*) = q(E_*) - p(E_*). \quad (\text{E.30})$$

Note that r is a strictly increasing function. To find a solution of (E.29), we must find a solution of $r(E_*) = 0$, then set $I_* = p(E_*)$ (or, equivalently, $I_* = q(E_*)$). Further, note that $h(0) = f(I_E)$, and $h(100) = f(I_E - 100w_{IE})$. So $p(f(I_E)) = 0 \leq q(f(I_E))$ and $p(f(I_E - 100w_{IE})) = 100 \geq q(f(I_E - 100w_{IE}))$, i.e., $r(f(I_E)) \geq 0$ and $r(f(I_E - 100w_{IE})) \leq 0$. By the intermediate value theorem, there is a solution of eq. (E.30) with $E_* \in [f(I_E - 100w_{IE}), f(I_E)]$. Furthermore, the solution is unique because r is strictly increasing.

This proves that there is exactly one fixed point. To prove that it is stable, we must consider the Jacobi matrix at the fixed point. It is given by the following

formula (look at (22.1) and remember that $w_{EE} = 0 = w_{II} = 0$):

$$J = \begin{bmatrix} -1/\tau_E & -f'(-w_{IE}I_* + I_E)w_{IE}/\tau_E \\ g'(w_{EI}E_* + I_I)w_{EI}/\tau_I & -1/\tau_I \end{bmatrix}.$$

The determinant of this matrix is positive, and its trace is negative. This implies that the fixed point is stable. (To understand why, either work out what positivity of the determinant and negativity of the trace imply for the eigenvalues, or read [149, Section 5.2].)

23.2. The result is in Fig. E.37. There is some degree of entrainment of the population activity by the rhythmic input, but it is not tight.

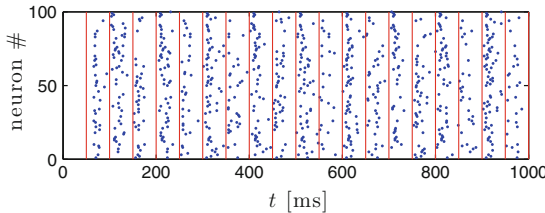


Figure E.37. 100 WB neurons driven by a sequence of input pulses at 20Hz, with pulse strengths uniformly distributed in the window of sparse entrainment (see Section 23.1 for modeling details). Blue dots indicate spike times, and red vertical lines indicate times of input pulse onset. [WB_NETWORK_ENTRAINED]

23.3. (a) I find $A \approx 0.037$ and $B \approx 0.053$. It is not surprising that A and B are smaller here than in Section 23.1: The input pulses are broader, so more current is injected altogether. Note, however, that $B/A \approx 1.43$ — only slightly different from the value in Section 23.1. See `WB_NEURON_BROAD_PULSES` for the Matlab program that I used to find these values. (b) Figure E.38 shows the result. The fraction of the interval of sparse entrainment that corresponds to irregular entrainment has grown somewhat.

24.1. The result is shown in Fig. E.39.

25.1. The results are in Table E.3. We have rounded all percentages to the nearest one-hundredth. Not surprisingly, the effect of the input on T_1 becomes stronger as the input becomes stronger or longer-lasting, or comes later in the cycle.

25.6. Figure E.40 shows the PRC, and Fig. E.41 shows a close-up. What is interesting here is the “staircase-like” appearance of the PRC. Three points on three different steps of the staircase are indicated in red in Fig. E.41. Their horizontal coordinates are $\varphi = 0.3995, 0.4245$, and 0.4395 , respectively. For the values of φ corresponding to these three points, Fig. E.42 shows the curves $(v(t), n(t))$, with $0 \leq t \leq T$, with $T = 20, 30$, and 40 , respectively. (For each of the three values of φ_0 , I chose T in such a way that the first passage of the trajectory through the window shown in the figure is visible, but the second passage is not.)

These results suggest that for φ approximately between 0.41 and 0.53, the input pulse sends the solution into the vicinity of a fixed point that is a weakly

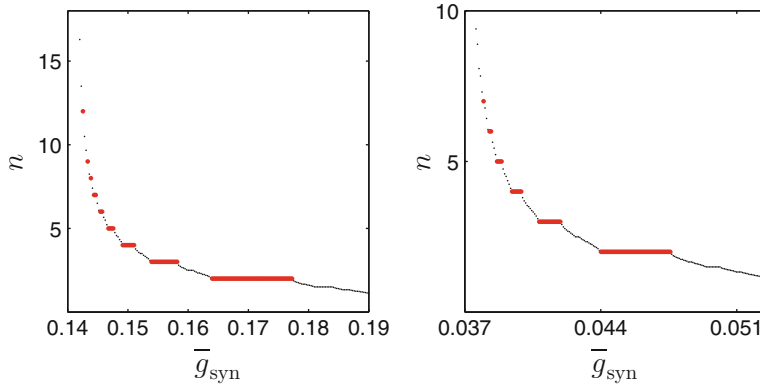


Figure E.38. Left: Fig. 23.6. Right: Same, but with broader input pulses.
[WB_INTERVALS_BROAD_PULSES]

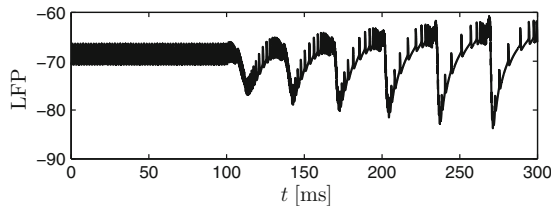


Figure E.39. The “LFP” (average of all computed membrane potentials) as a function of time, for a simulation of 30 RTM neurons firing in splay state for 100 ms, then synaptically connected as in Fig. 24.3 for the remaining 200 ms.
[RTM_LFP]

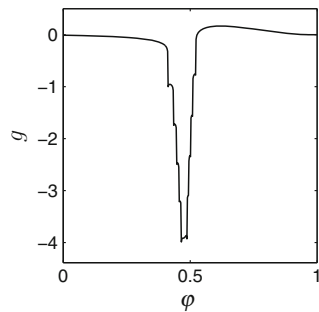


Figure E.40. Like middle panel of Fig. 25.9, but with $\bar{g}_{\text{syn}} = 0.30$. [HH_PRC]

repelling spiral. The different steps of the staircase correspond to different numbers of turns of the spiral that the trajectory must follow before leaving the vicinity of the fixed point.

τ_r	τ_{peak}	τ_d	\bar{g}_{syn}	φ_0	E_1	E_2
0.5	0.5	2	0.05	0.1	0.00%	0.00%
0.5	0.5	2	0.05	0.5	0.03%	0.00%
0.5	0.5	2	0.05	0.9	1.24%	0.00%
0.5	0.5	2	0.1	0.1	0.00%	0.00%
0.5	0.5	2	0.1	0.5	0.15%	0.00%
0.5	0.5	2	0.1	0.9	2.91%	0.00%
0.5	0.5	2	0.2	0.1	0.00%	0.00%
0.5	0.5	2	0.2	0.5	1.32%	0.00%
0.5	0.5	2	0.2	0.9	7.07%	0.00%
1.0	1.0	5	0.05	0.1	0.31%	0.00%
1.0	1.0	5	0.05	0.9	7.47%	0.10%
1.0	1.0	5	0.1	0.1	1.17%	0.01%
1.0	1.0	5	0.1	0.9	16.38%	0.33%

Table E.3. Results for exercise 25.1. Percentages are rounded to the nearest one-hundredth. [NO_MEMORY]

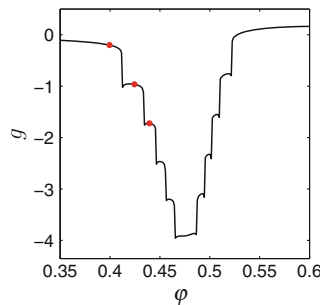


Figure E.41. Fig. E.40, close-up. [HH_PRC_ZOOM_IN, figure 1]

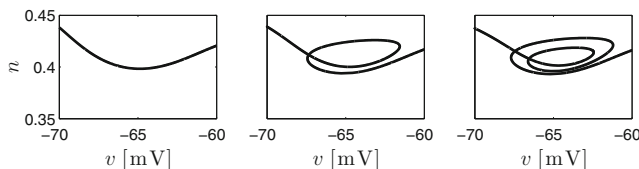


Figure E.42. $(v(t), n(t))$ corresponding to the three red dots in Fig. E.41. [HH_PRC_ZOOM_IN, figure 2]

25.7. (a) By eq. (25.13),

$$f(\varphi) = \varphi + g(\varphi) = \frac{1}{\pi} \arctan \left(\tan \left(\pi \varphi - \frac{\pi}{2} \right) + \frac{\Delta v}{\sqrt{\tau_m I - 1/4}} \right) + \frac{1}{2}. \quad (\text{E.31})$$

The assertion follows from the fact that \tan and \arctan are strictly increasing functions. (b) This follows from eq. (E.31), since $\arctan \psi \in (-\pi/2, \pi/2)$ for all $\psi \in \mathbb{R}$. (c) From part (b), the graph of f lies in the left upper half of the unit square. This implies (by the intermediate value theorem) that any line perpendicular to the diagonal must intersect the graph in some point within the left upper half of the unit square, and it can intersect the graph only once because f is increasing.

26.3. (a) From Fig. 26.9, we see that c has to be so small that the slope of \tilde{f} at $s = -1/\sqrt{2}$ is ≤ 1 , so $c\sqrt{2} \leq 1$ or $c \leq 1/\sqrt{2}$. (b) Let $s \in [-1/\sqrt{2}, 1/\sqrt{2}]$. The corresponding point on the diagonal line in the (φ, f) -plane is

$$(s/\sqrt{2} + 1/2, s/\sqrt{2} + 1/2).$$

Define $u = \tilde{f}(s)/\sqrt{2}$. Then the point

$$(s/\sqrt{2} + 1/2 - u, s/\sqrt{2} + 1/2 + u)$$

lies on the graph of f (see Fig. 26.9). So

$$f\left(\frac{s}{\sqrt{2}} + \frac{1}{2} - \frac{\tilde{f}(s)}{\sqrt{2}}\right) = \frac{s}{\sqrt{2}} + \frac{1}{2} + \frac{\tilde{f}(s)}{\sqrt{2}}.$$

Using (26.21), we find

$$f\left(\frac{s}{\sqrt{2}} + \frac{1}{2} - \frac{\epsilon}{2}\left(-s^2 + \frac{1}{2}\right)\right) = \frac{s}{\sqrt{2}} + \frac{1}{2} + \frac{\epsilon}{2}\left(-s^2 + \frac{1}{2}\right).$$

In other words, if

$$\varphi = \frac{s}{\sqrt{2}} + \frac{1}{2} - \frac{\epsilon}{2}\left(-s^2 + \frac{1}{2}\right), \quad (\text{E.32})$$

then

$$f(\varphi) = \frac{s}{\sqrt{2}} + \frac{1}{2} + \frac{\epsilon}{2}\left(-s^2 + \frac{1}{2}\right). \quad (\text{E.33})$$

Equation (E.32) is a quadratic equation in s . Solving it for s using the quadratic formula, we obtain

$$s = \frac{1}{\sqrt{2}\epsilon} \left(-1 \pm \sqrt{\epsilon^2 + 2\epsilon(2\varphi - 1) + 1} \right).$$

The square root in this formula lies between $1 - \epsilon$ (for $\varphi = 0$) and $1 + \epsilon$ (for $\varphi = 1$). Since $s \geq -1/\sqrt{2}$, only the positive square root is relevant:

$$s = \frac{1}{\sqrt{2}\epsilon} \left(-1 + \sqrt{\epsilon^2 + 2\epsilon(2\varphi - 1) + 1} \right). \quad (\text{E.34})$$

As φ ranges from 0 to 1, this expression ranges from $-1/\sqrt{2}$ to $1/\sqrt{2}$. Inserting eq. (E.34) into eq. (E.33), then simplifying, we obtain

$$f(\varphi) = -\varphi + 1 - \frac{1 - \sqrt{(1-\epsilon)^2 + 4\epsilon\varphi}}{\epsilon}.$$

Therefore

$$g(\varphi) = f(\varphi) - \varphi = -2\varphi + 1 - \frac{1 - \sqrt{(1-\epsilon)^2 + 4\epsilon\varphi}}{\epsilon} = \\ 2(1-\varphi) - \frac{1 + \epsilon - \sqrt{(1+\epsilon)^2 - 4\epsilon(1-\varphi)}}{\epsilon},$$

which is precisely (26.5).

26.7. From the proof of Proposition 26.2,

$$G'(0) = \left(1 + \frac{\partial g}{\partial \varphi}(0, \Delta v)\right) \left(1 + \frac{\partial g}{\partial \varphi}(1, \Delta v)\right) \quad (\text{E.35})$$

and

$$\hat{G}'(0) = \left(1 + \Delta v \frac{\partial^2 g}{\partial \varphi \partial \Delta v}(0, 0)\right) \left(1 + \Delta v \frac{\partial^2 g}{\partial \varphi \partial \Delta v}(1, 0)\right). \quad (\text{E.36})$$

Equation (E.36) immediately implies (a).

(b) Since $g(\varphi, 0) = 0$ for all $\varphi \in [0, 1]$, also $\frac{\partial g}{\partial \varphi}(\varphi, 0) = 0$ for all φ , and therefore $\Delta v \frac{\partial^2 g}{\partial \varphi \partial \Delta v}(0, 0)$ and $\Delta v \frac{\partial^2 g}{\partial \varphi \partial \Delta v}(1, 0)$ are local linear (in Δv) approximations of $\frac{\partial g}{\partial \varphi}(0, \Delta v)$ and $\frac{\partial g}{\partial \varphi}(1, \Delta v)$. Since g is assumed twice differentiable, we conclude that $G'(0)$ and $\hat{G}'(0)$ differ only by $o(\Delta v)$. Therefore $G'(0) = 1 + C\Delta v + o(\Delta v)$, so if $C < 0$, then $G'(0) < 1$ for sufficiently small Δv .

(c) $\hat{G}'(0) = 1$ for all Δv (see eq. (26.20)). This implies $C = D = 0$.

27.1. If A is slightly before B, the interaction should accelerate B more than A for synchrony to get tighter. Therefore the signals should arrive at a time of the cycle when the phase response function is decreasing. For a typical type 1 phase response function, that means they should arrive later, rather than earlier, in the cycle.

28.6. (a) $H(\psi) = 0$, therefore $\psi_* = 0$ is not an attracting fixed point. It is *neutrally stable* — any solution of eq. (28.3) is simply constant. (b) We use the notation of Section 26. When $g(\varphi) = \epsilon\varphi(1-\varphi)$ then $f(\varphi) = \varphi + \epsilon\varphi(1-\varphi)$, and $F(\varphi) = f(1-\varphi) = 1 - \varphi + \epsilon\varphi(1-\varphi)$. This implies that $G(\varphi) = F(F(\varphi)) = 1 - F(\varphi) + \epsilon F(\varphi)(1 - F(\varphi)) = 1 - (1 - \varphi + \epsilon\varphi(1-\varphi)) + \epsilon(1 - \varphi + \epsilon\varphi(1-\varphi))(1 - (1 - \varphi + \epsilon\varphi(1-\varphi))) = (1 - \epsilon^2)\varphi + \epsilon^2(3 - \epsilon)\varphi^2 - 2\epsilon^2(1 - \epsilon)\varphi^3 - \epsilon^3\varphi^4$. So

$$G'(0) = 1 - \epsilon^2,$$

so $G'(0) < 1$, and synchrony is attracting for all $\epsilon \in (0, 1)$.

Morale: When eq. (28.3) suggests that synchrony is *neutrally* stable, that conclusion cannot be trusted.

28.7. (a) We have to analyze the function

$$D(\psi) = g_0(\psi) - g_0(1 - \psi).$$

With a small amount of algebra, this turns out (by sheer coincidence) to be the negative of the function D shown in Fig. 28.3. Therefore, just as in the case of Fig. 28.3, there is a stable fixed point for $0 \leq c < \sqrt{3}/18$. (b) Figure E.43 shows the results.

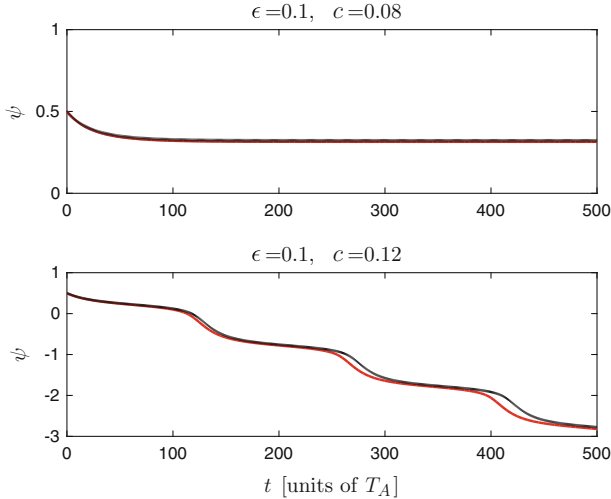


Figure E.43. Same as Fig. 28.4, but with $g_0(\varphi) = \varphi(1 - \varphi)^3$.
[WEAKLY_COUPLED_HETEROGENEOUS_2]

28.8. (a) Now $D(\psi) = 0$ for all ψ , and there is therefore no $c > 0$ for which eq. (28.10) has a fixed point. If ψ obeys eq. (28.10), it will simply decrease indefinitely. (b) Figure E.44 shows the result.

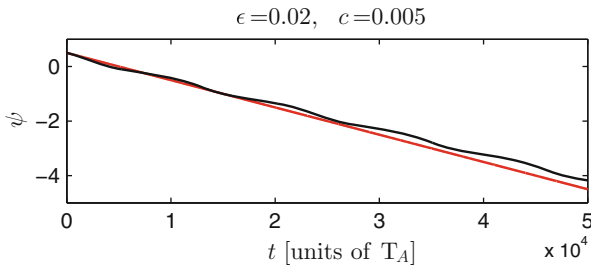


Figure E.44. Same as Fig. 28.4, but with $g_0(\varphi) = \varphi(1 - \varphi)$.
[WEAKLY_COUPLED_HETEROGENEOUS_3]

28.9. (a) Using the definition of D (eq. (28.13)),

$$D\left(\frac{1}{2} - s\right) = g_0\left(\frac{1}{2} - s\right) - g_0\left(\frac{1}{2} + s\right)$$

and

$$D\left(\frac{1}{2} + s\right) = g_0\left(\frac{1}{2} + s\right) - g_0\left(\frac{1}{2} - s\right).$$

This implies eq. (28.15). (b) The assumption $g_0(\varphi) \not\equiv g_0(1-\varphi)$ implies that $D(\psi) \not\equiv 0$. By part (a), D then has both positive and negative values. Furthermore, $D(1/2)$ is clearly 0. Let $M = \max_{\psi \in [0,1]} D(\psi)$. Then $D(\psi) = c$ has a solution ψ if $c \in [0, M]$ (by the intermediate value theorem), but not if $c > M$. (c) A stable fixed point of eq. (28.10) is a ψ where H falls from above to below 0, that is, where D falls from above to below c . Choose $\psi_{\max} \in \mathbb{R}$ with $D(\psi_{\max}) = M$, and $\psi_0 > \psi_{\max}$ with $D(\psi_0) = 0$. (It is possible to choose ψ_0 greater than ψ_{\max} because D is periodic with period 1.) Between ψ_{\max} and ψ_0 , there must be a value ψ where D falls from above to below c , since $0 < c < M$.

29.2. We apply the method of integrating factors. The equation

$$\frac{dv}{dt} = -\frac{v}{\tau_m} + I - \bar{g}_{\text{syn}} e^{-t/\tau_I} v$$

is equivalent to

$$\frac{d}{dt} \left(v(t) e^{t/\tau_m - \bar{g}_{\text{syn}} \tau_I e^{-t/\tau_I}} \right) = I e^{t/\tau_m - \bar{g}_{\text{syn}} \tau_I e^{-t/\tau_I}}.$$

To continue, we would have to integrate the right-hand side. Let's think about the special case $\tau_m = \bar{g}_{\text{syn}} = \tau_I = 1$. Can we explicitly integrate the function $e^{t-e^{-t}}$? Let's try:

$$\int e^{t-e^{-t}} dt = \int e^t e^{-e^{-t}} dt.$$

Substitute $u = e^{-t}$, so $du = -e^{-t} dt$, and therefore $dt = -du/u$:

$$\int e^t e^{-e^{-t}} dt = - \int \frac{1}{u^2} e^{-u} du.$$

Now integrate by parts:

$$- \int \frac{1}{u^2} e^{-u} du = \frac{e^{-u}}{u} + \int \frac{e^{-u}}{u} du$$

Finally, substitute $u = e^{-t}$ back:

$$\frac{e^{-u}}{u} + \int \frac{e^{-u}}{u} du = e^{t-e^{-t}} + \int \frac{e^{-u}}{u} du.$$

It is known that $\int (e^{-u}/u) du$ cannot be evaluated explicitly.⁴² In fact, $\int (e^{-u}/u) du$ can be shown to be $\text{Ei}(-u) + C$, where Ei denotes the *exponential integral*, which

⁴²You probably don't know how to prove such things, or what the statement even means precisely. However, a practical way of convincing yourself that the integral cannot be done is to try doing it with an online symbolic integrator.

is (provably) not an elementary function, i.e., cannot be expressed in simple terms. Using this notation, we conclude

$$\int e^{t-e^{-t}} dt = e^{t-e^{-t}} + \text{Ei}(-e^{-t}) + C,$$

and this is as explicit an expression for the integral as is possible.

29.4. (a) As long as $-v/\tau_m$ and I are negligible, the differential equation is

$$\begin{aligned} \frac{dv}{dt} &= -\bar{g}_{\text{syn}} e^{-t/\tau_I} v \\ \Leftrightarrow \quad \frac{1}{v} \frac{dv}{dt} &= -\bar{g}_{\text{syn}} e^{-t/\tau_I} \\ \Leftrightarrow \quad \frac{d}{dt} (\ln v) &= -\bar{g}_{\text{syn}} e^{-t/\tau_I} \\ \Leftrightarrow \quad \ln v &= \tau_I \bar{g}_{\text{syn}} \left(e^{-t/\tau_I} - 1 \right) + \ln v(0) \\ \Leftrightarrow \quad v &= v_* e^{\gamma(e^{-t/\tau_I} - 1)}. \end{aligned} \quad (\text{E.37})$$

If you don't pay attention, you might declare victory here: As $t \rightarrow \infty$, (E.37) tends to $v_* e^{-\gamma}$. The problem with that reasoning is that you have no right to let t tend to infinity — the above calculation relied on the assumption that $-v/\tau_m$ and I were negligible, and that assumption rapidly becomes invalid as t increases, since $\bar{g}_{\text{syn}} e^{-t/\tau_I}$ rapidly becomes small. The question is whether the calculation remains valid long enough for (E.37) to come close to $v_* e^{-\gamma}$.

The term that needs to be large for our analysis to be valid can be written like this:

$$\bar{g}_{\text{syn}} e^{-t/\tau_I} = \gamma \frac{e^{-t/\tau_I}}{\tau_I}. \quad (\text{E.38})$$

This term clearly decreases rapidly, and therefore our calculation becomes invalid rapidly, as t increases. We will now think about just how rapidly our calculation becomes invalid. The following time will play a critical role in our analysis, and is therefore denoted by t_c :⁴³

$$t_c = \tau_I \ln \frac{1}{\tau_I}. \quad (\text{E.39})$$

Note that $t_c \rightarrow 0$ as $\tau_I \rightarrow 0$. Inserting $t = \alpha t_c$ with $\alpha \in (0, 1)$ into (E.38), we get

$$\frac{\gamma}{\tau_I} e^{\alpha \ln \tau_I} = \frac{\gamma}{\tau_I^{1-\alpha}}. \quad (\text{E.40})$$

This tends to infinity as $\tau_I \rightarrow 0$, since $\alpha < 1$. So our calculation remains valid *asymptotically* (in the limit as $\tau_I \rightarrow 0$) up to time αt_c . If we insert $t = \alpha t_c$ into (E.37), we obtain

$$v_* e^{\gamma(e^{\alpha \ln \tau_I} - 1)} = v_* e^{\gamma(\tau_I^\alpha - 1)} \rightarrow v_* e^{-\gamma}$$

as $\tau_I \rightarrow 0$, since $\alpha > 0$. So within the short time αt_c , v moves from v_* to $v_* e^{-\gamma}$.

⁴³If you feel bothered by the fact that there is a logarithm of a reciprocal time in the definition of t_c — and you *should* feel bothered by that — you can replace $1/\tau_I$ by τ_m/τ_I in the logarithm. That will make no essential difference to the argument that follows, and will remove the dimensional issue. However, to keep the notation a little cleaner, I will not do that here.

On the other hand, now insert $t = \beta t_c$ with $\beta > 1$ into (E.38). The result is

$$\frac{\gamma}{\tau_I^{1-\beta}} = \gamma \tau_I^{\beta-1},$$

which tends to 0 as $\tau_I \rightarrow 0$, since $\beta > 1$. So for $t = \beta t_c$, the term (E.38) becomes irrelevant as $\tau_I \rightarrow 0$, and the differential equation becomes

$$\frac{dv}{dt} = -\frac{v}{\tau_m} + I.$$

This does not prove our assertion, but hopefully it makes it quite plausible. If you are not convinced yet, part (b) will probably do the trick.

(b) Figure E.45 shows a simulation that confirms the result of (a).

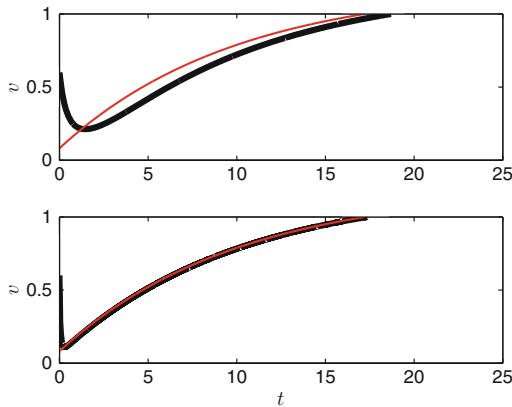


Figure E.45. Black: LIF neuron with a decaying inhibitory pulse, with $v(0) = v_* = 0.6$, $\tau_m = 10$, $I = 0.2$, $\tau_I = 1$ and $\bar{g}_{\text{syn}} = 2$ (upper panel), $\tau_I = 0.1$ and $\bar{g}_{\text{syn}} = 20$ (lower panel). Red: LIF neuron without inhibitory pulse, with $v(0) = v_* e^{-\gamma}$, where $\gamma = \bar{g}_{\text{syn}} \tau_I = 2$. [LIF_SHORT_STRONG_INHIBITION]

29.5. The results are in Table E.4. The ten times greater perturbations lead to approximately ten times greater changes in P .

	$I \rightarrow 0.9I$	$\bar{g}_{\text{syn}} \rightarrow 1.1\bar{g}_{\text{syn}}$	$\tau_I \rightarrow 1.1\tau_I$
increase in P (weak, long-lasting pulse):	8.0%	3.7%	5.7%
increase in P (strong, brief pulse):	7.8%	0.74%	2.0%

Table E.4. Analogous to Table 29.2, but with 10% perturbations of the parameters, instead of 1% perturbations. [RTM_CONDITION_NUMBERS_STRONG_PERT]

29.6. Figure E.46 shows what becomes of Fig. 29.5 when the sine term is dropped. There is still a stable river, so synchronization by an inhibitory pulse ought to work without the sine term. (In fact it does.)

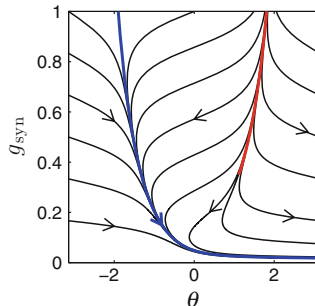


Figure E.46. Same as Fig. 29.5, but with the sine term omitted from the model; that is, the inhibitory pulse is now a current input, not a synaptic input. [RIVER_SIMPLIFIED]

29.7. The plot of g_* as a function of τ_I is shown in Fig. E.47.

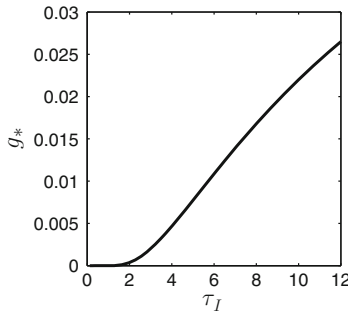


Figure E.47. The quantity g_* as a function of τ_I (see exercise 29.7).
[PLOT_G_STAR]

29.8. The plot is in Fig. E.48. It confirms that $\bar{g}_{\text{syn}} e^{-t/\tau_I}$ is largely independent of \bar{g}_{syn} and φ_0 , especially when \bar{g}_{syn} is large.

30.7. To make it easier to determine the inter-spike intervals, I simulated a network with only one I-cell. (This amounts to the assumption that the I-cells are perfectly synchronous.) Figures E.49 and E.50 show that a stochastic component of the drive to the E-cells, common to all E-cells of the network, can in fact cause substantial fluctuations in the PING frequency.

30.8. Yes, but it really requires much stronger inhibitory conductances; see Fig. E.51.

31.5. Figure E.52 shows a realization. You may suspect that I searched for a long time for a seed for the random number generator that would give me a very broad plateau — but no, the second seed I tried gave me Fig. E.52. (You might want to

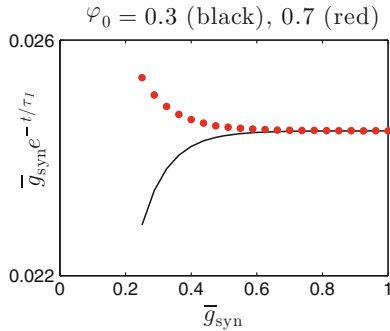


Figure E.48. Parameters as in the middle panel of Fig. 29.4. We now consider only a single RTM neuron, vary \bar{g}_{syn} , and record the time, P , that it takes the neuron to fire following the inhibitory input pulse. The figure shows $\bar{g}_{\text{syn}}e^{-P/\tau_I}$, the inhibitory conductance at the time of firing, as a function of \bar{g}_{syn} , for two different initial phases φ_0 . [RTM_WITH_INHIBITION_GSTAR]

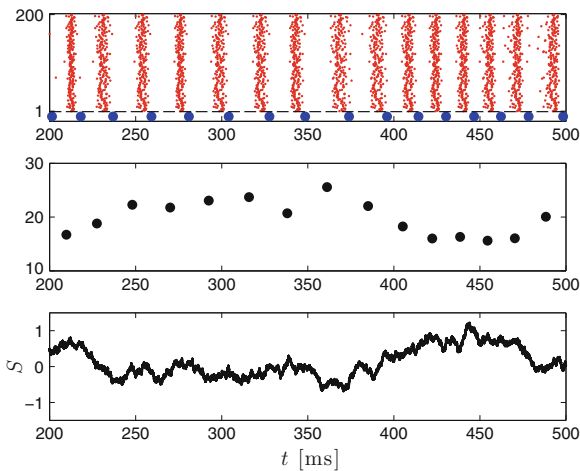


Figure E.49. Spike rastergram of a PING network with a single I-cell (top trace), intervals between spikes of I-cell (middle trace), and stochastic component of drive to E-cells (bottom trace). Spike times of E-cells are indicated in red, and spike times of I-cell in blue. The parameters are $N_E = 200$, $N_I = 1$, $\bar{I}_E = 1.4$, $\sigma_E = 0.05$, $\bar{I}_I = 0$, $\hat{g}_{EE} = 0$, $\hat{g}_{EI} = 0.25$, $\hat{g}_{IE} = 0.25$, $\hat{g}_{II} = 0.25$, $p_{EI} = 0.5$, $p_{IE} = 1$, $p_{II} = 1$, $\tau_{r,E} = 0.5$, $\tau_{\text{peak},E} = 0.5$, $\tau_{d,E} = 3$, $v_{\text{rev},E} = 0$, $\tau_{r,I} = 0.5$, $\tau_{\text{peak},I} = 0.5$, $\tau_{d,I} = 9$, $v_{\text{rev},I} = -75$. The stochastic component of the drive to the E-cells is an Ornstein-Uhlenbeck process with mean 0, as defined by eqs. (C.20)–(C.22), with $\tau_{\text{noise}} = 50$ and $\sigma_{\text{noise}} = 0.5$. Only the last 300 ms of a 500 ms simulation are shown, to avoid initialization effects. [PING_10]

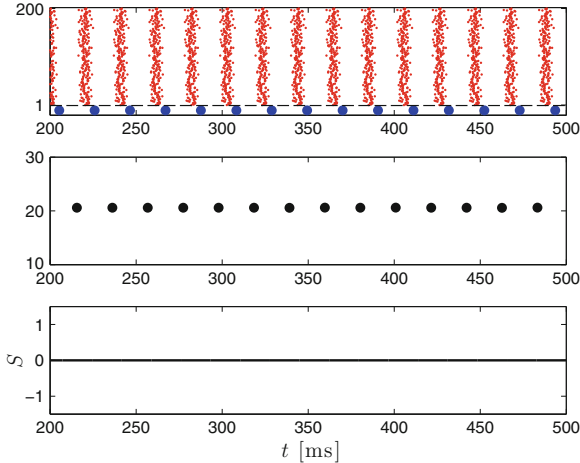


Figure E.50. For comparison, same as Fig. E.49 but with $\sigma_{\text{noise}} = 0$. [PING_11]

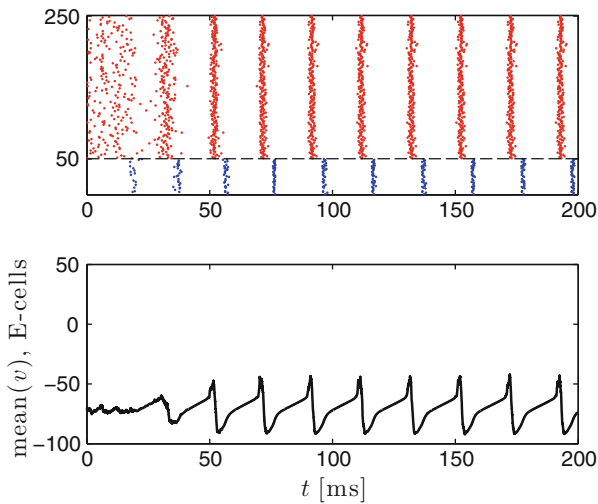


Figure E.51. Like Fig. 30.4, but with $\tau_{d,I} = 3$ ms, and with \hat{g}_{IE} and \hat{g}_{II} increased ten-fold (to 2.5) [PING_12]

try a few more seeds to convince yourself that “plateaus” are much more common than you might think.)

31.8. (a) Figure E.53 shows the graph. (b) To understand eq. (31.1), first omit the term $\mathcal{H}(-4)$, which is small, about 3.4×10^{-4} :

$$g(\varphi) \approx -\mathcal{H}\left(\frac{\varphi - 0.1}{0.1}\right) \mathcal{H}\left(\frac{0.8 - \varphi}{0.05}\right) \frac{\varphi}{2} \quad (\text{E.41})$$

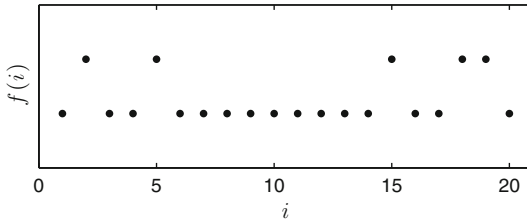


Figure E.52. A realization of the function f defined by $f(i) = 1$ with probability $1/2$, and $f(i) = 2$ otherwise, $i = 1, 2, \dots, 20$. [WINNING_STREAKS]

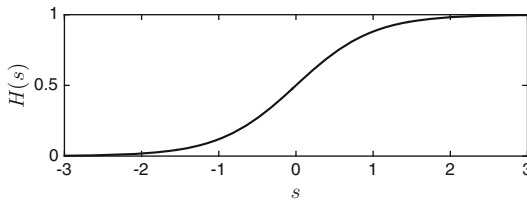


Figure E.53. Graph of the function \mathcal{H} defined by eq. (31.2). [CAL_H]

The function $\mathcal{H}(s)$ is a smooth approximation of the Heaviside function

$$\mathcal{H}(s) = \begin{cases} 1 & \text{if } s > 0, \\ 0 & \text{if } s < 0. \end{cases}$$

More generally, if $\epsilon > 0$, then $\mathcal{H}(s/\epsilon)$ is a smooth approximation of $H(s)$, and the approximation becomes better (the transition from values near 0 to values near 1 becomes steeper) as ϵ becomes smaller. Therefore the right-hand side of (E.41) is a smooth approximation of

$$\begin{cases} -\varphi/2 & \text{if } 0.1 < \varphi < 0.8, \\ 0 & \text{otherwise.} \end{cases}$$

Looking at Fig. 25.10, or at the left panel of Fig. 31.13, you will realize that this is what we want here. The right-hand side of (E.41) is zero at $\varphi = 0$, but at $\varphi = 1$, it is not zero, but $-\mathcal{H}(9)\mathcal{H}(-4)/2$. In (31.1), the factor

$$\mathcal{H}\left(\frac{0.8 - \varphi}{0.05}\right)$$

in (E.41) is replaced by

$$\mathcal{H}\left(\frac{0.8 - \varphi}{0.05}\right) - \mathcal{H}(-4)$$

to make it zero at $\varphi = 1$.

31.10. We first note that for sufficiently small ϵ , the function g defined by $g(\varphi) = \epsilon g_0(\varphi)$ satisfies

$$g'(\varphi) > -1 \quad \text{for } \varphi \in [0, 1].$$

Therefore the theory of Chapter 26 applies, and $G'(\varphi) > 0$ for $\varphi \in [0, 1]$. This will be used below.

(a) Synchrony is unstable if $G'(0)$, which is always the same as $G'(1)$, is greater than 1. We have (see the proof of Proposition 26.2)

$$\begin{aligned} G'(0) = G'(1) &= (1 + g'(0))(1 + g'(1)) = (1 + \epsilon g'_0(0))(1 + \epsilon g'_0(1)) = \\ &1 + \epsilon(g'_0(0) + g'_0(1)) + \epsilon^2 g'_0(0)g'_0(1). \end{aligned}$$

Our assumptions imply that $g'_0(0) \leq 0$ and $g'_0(1) > -g'_0(0)$, so $g'_0(0) + g'_0(1) > 0$, and therefore

$$1 + \epsilon(g'_0(0) + g'_0(1)) + \epsilon^2 g'_0(0)g'_0(1) > 1$$

for $\epsilon > 0$ small enough.

(b) Let $R(\varphi) = G(\varphi) - \varphi$. We have $R(0) = R(1) = 0$, and $R'(0) = R'(1) > 0$. Since G has finitely many fixed points, R is zero in finitely many points,

$$0 = \varphi_0 < \varphi_1 < \varphi_2 < \dots < \varphi_N = 1.$$

On each of the intervals $(\varphi_{j-1}, \varphi_j)$, $j = 1, 2, \dots, N$, the function R is either strictly positive or strictly negative. On the left-most interval, (φ_0, φ_1) , it is positive since $R'(0) > 0$, and on the right-most interval, $(\varphi_{N-1}, \varphi_N)$, it is negative since $R'(1) > 0$. This implies that there is some $j \in \{1, 2, \dots, N-1\}$ so that $R(\varphi) > 0$ for $\varphi \in (\varphi_{j-1}, \varphi_j)$ and $R(\varphi) < 0$ for $\varphi \in (\varphi_j, \varphi_{j+1})$. Then φ_j is a stable fixed point of G , corresponding to a stable non-synchronous phase-locked state.

31.11. Figure E.54 shows two interesting examples.

32.2. Figure E.55 shows an example.

32.4. I will only prove here that $\lim_{x \nearrow 1} \psi(x) > 0$ if $g_I > I - 1/\tau_m$. So we consider eqs. (32.4)–(32.6) with $v_1(0) = 0$, $v_2(0) = x \in (0, 1)$, and $s(0) = 1$, and assume that $g_I > I - 1/\tau_m > 0$. By eq. (32.5), v_2 cannot cross 1 until

$$-\frac{1}{\tau_m} + I - g_I e^{-t/\tau_I} \geq 0,$$

that is, until

$$t \geq T_* = \tau_I \ln \frac{g_I}{I - 1/\tau_m}. \quad (\text{E.42})$$

Denote by T the time at which v_2 reaches 1. Note that T depends on x , while T_* does not, and $T = T(x) \geq T_* > 0$. Choose $\delta > 0$ so that

$$\delta g_I < I - \frac{1}{\tau_m}.$$

As long as $v_1 \leq \delta$,

$$-\frac{v_1}{\tau_m} + I - g_I s(t)v_1 = -\frac{v_1}{\tau_m} + I - g_I e^{-t/\tau_I} v_1 > 0,$$

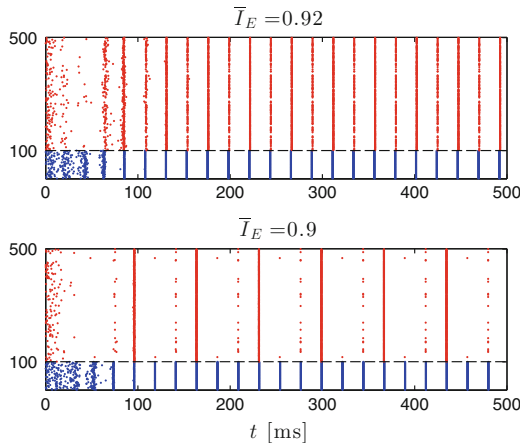


Figure E.54. Just like Fig. 31.15, but with smaller values of \bar{I}_E . A close-up look at the upper panel ($\bar{I}_E = 0.92$) reveals that each E-cell fires on every second inhibitory pulse. There are two clusters of E-cells firing in anti-synchrony. In the lower panel ($\bar{I}_E = 0.9$), each E-cell fires on every third inhibitory pulse. There are three clusters, a large one and two very much smaller ones. [[ING_ENTRAINING_E_CELLS_3](#)]

and therefore, by eq. (32.4), v_1 is strictly increasing as long as $v_1 \leq \delta$. Now $\psi(x) = v_1(T(x))$. If $v_1(t) \leq \delta$ for $t \leq T(x)$, then v_1 is strictly increasing for $t \leq T(x)$, and therefore $v_1(T(x)) \geq v_1(T_*)$. If $v_1(t)$ reaches δ at some time $t \leq T(x)$, it cannot fall back below δ and therefore $v(T(x)) \geq \delta$. Altogether:

$$\psi(x) \geq \min(v_1(T), \delta)$$

for all x . This implies $\lim_{x \nearrow 1} \psi(x) \geq \min(v_1(T), \delta) > 0$.

32.6. Figure E.56 shows the analogue of Fig. 32.14 with a 2 ms delay between the firing of an E-cell and the reset of s to 1. We now see that $0 < \phi'(0) < 1$, and therefore synchrony is stable. However, the fixed point x_* of ψ , which is also a fixed point of ϕ , also satisfies $0 < \phi'(x_*) < 1$, so anti-synchrony is stable as well.

32.7. Figure E.57 shows results of simulations with 3 neurons (upper panel), and with 20 neurons (lower panel). The 3 neurons in the upper panel fire in splay state. With 20 neurons, clusters of various sizes are seen. The clusters fire in splay state, but neurons belonging to the same cluster synchronize.

33.2. The result of this numerical experiment is in Fig. E.58. The temporal separation between E_P - and E_S -cells becomes slightly worse than in Fig. 33.7 when the strength of the E_S -to-I synapses is halved again.

33.3. The result of this numerical experiment is in Fig. E.59.

33.4. Fig. E.60 shows the voltage trace of a single cell in Fig. 33.9, scaled and shifted so that the values range from 0 to 200, and superimposed on the spike

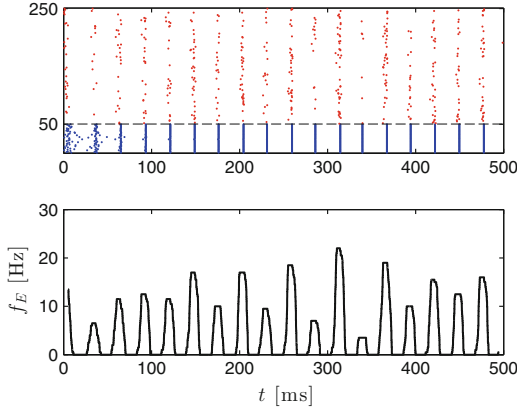


Figure E.55. Top: Spike rastergram of a weak PING network in which the E-cells are driven by independent Ornstein-Uhlenbeck processes. Bottom: Time-dependent mean firing rate of the E-cells, as defined in Section 32.1 (see eq. 32.2). The parameters are $N_E = 200$, $N_I = 50$, $\bar{I}_E = 0.9$, $\sigma_E = 0$, $\bar{I}_I = 0.8$, $\sigma_I = 0$, $\hat{g}_{EE} = 0$, $\hat{g}_{EI} = 1.0$, $\hat{g}_{IE} = 1.25$, $\hat{g}_{II} = 0.3$, $p_{EI} = 1$, $p_{IE} = 1$, $p_{II} = 1$, $\tau_{r,E} = 0.3$, $\tau_{peak,E} = 0.3$, $\tau_{d,E} = 3$, $v_{rev,E} = 0$, $\tau_{r,I} = 0.5$, $\tau_{peak,I} = 0.5$, $\tau_{d,I} = 9$, $v_{rev,I} = -75$. In addition to the constant drive \bar{I}_E , each E-cell receives stochastically fluctuating drive, a discrete Ornstein-Uhlenbeck process of mean zero characterized, in the notation of Appendix C.6, by $\tau_{noise} = 2$ ms and $\sigma_{noise} = \bar{I}_E/2$. The overall mean frequency of the E-cells (see eq. 32.3) is $\hat{f}_E \approx 4.7$ Hz, and that of the I-cells is $\hat{f}_I \approx 36$ Hz. [OU_PING]

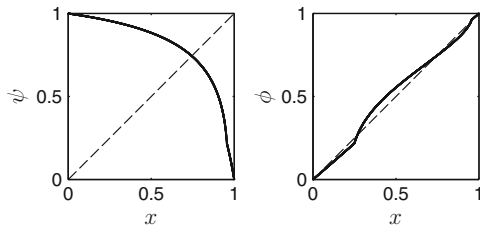


Figure E.56. Analogue of Fig. 32.14 with a 2 ms delay between the firing of an E-cell and the reset of s to 1. [PLOT_PSI_PHI_WITH_DELAY]

rastergram of Fig. 33.9. The cell skips either two or three population cycles between action potentials. This is typical; other cells behave similarly. Thus the cells fire in clusters, but membership in the clusters is far from fixed.

34.1. Figures E.61 and E.62 show the results for parts a and b, respectively. The E-to-O synapses cause the O-cells to fire continuously, and therefore there are no pauses in the gamma oscillation occurring at theta frequency. Initial approximate synchronization of the O-cells restores the nested gamma-theta rhythm.

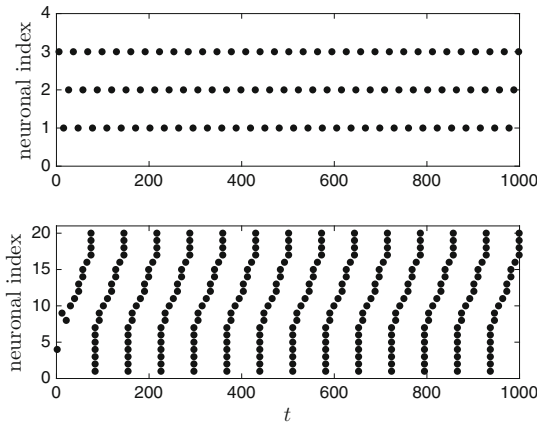


Figure E.57. Spike rastergrams for the generalization of the model given by (32.4)–(32.9) to 3 neurons (upper panel), and 20 neurons (lower panel). The neurons have been re-numbered, after the simulation, such that the last spike of neuron i occurs prior to the last spike of neuron j if and only if $i < j$. This numbering convention makes it easier to see the clusters in the lower panel. [N_LIF_NEURONS]

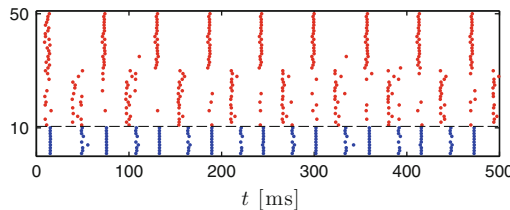


Figure E.58. Like Fig. 33.6, with the strengths of the synapses from E -cells 11 through 30 (the E_S -cells) to I -cells cut by a factor of 4. Compare with Fig. 33.7, where the E_S -to- I synapses were twice stronger than here, and twice weaker than in Fig. 33.6. [M_CURRENT_PING_9]

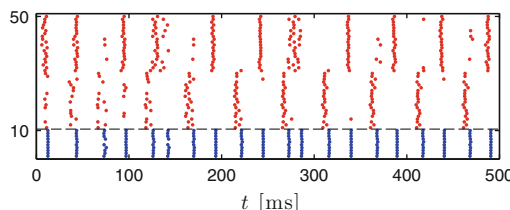


Figure E.59. Like Fig. 33.6, with the strengths of the synapses from E -cells 11 through 30 (the E_S -cells) to I -cells cut by a factor of 2, and the drive to the E_P -cells raised by 20%. [M_CURRENT_PING_10]

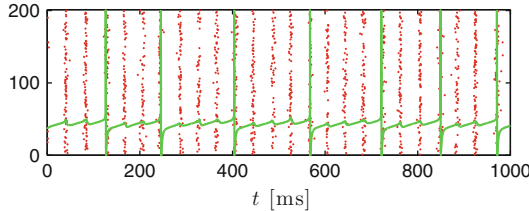


Figure E.60. The voltage trace of a single cell in Fig. 33.9, scaled and superimposed onto the spike rastergram. (Note that the simulation was continued for twice as much time as in Fig. 33.9.) [M_CURRENT_BETA_WITH_GJ_V]

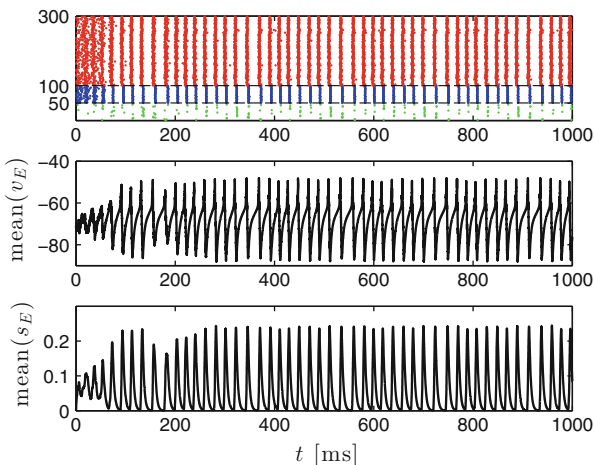


Figure E.61. Like Fig. 34.10, but with $\hat{g}_{EO} = 0.1$. [EIO_2]

34.2. Figure E.63 shows what happens when the I-to-O connection is removed in Fig. 34.10: The theta frequency pauses in the gamma oscillation have nearly disappeared.⁴⁴ Figure E.64 shows what happens when in Fig. E.63, each O-cell is initialized at a random phase uniformly distributed between 0 and 0.1, not between 0 and 1: Very clean nested gamma-theta oscillations are restored, and persist for a second of simulated time at least.

34.3. Figure E.65 shows the result. The time dependence of the A-current indeed does not matter for the nested gamma-theta rhythm. (In fact, the A-current is needed in Fig. 34.10, but only as a way of counteracting the excitatory effect of the h-current. If you omit the A-current altogether, the O-cells fire rapidly and suppress the other cells of the network.)

35.1. We note that \bar{v} is the membrane potential of a LIF neuron with I replaced

⁴⁴That they have not entirely disappeared is an accident: There is nothing to synchronize the O-cells. However, individually they fire at theta frequency, and therefore the frequency of O-cell firing, which fluctuates randomly, peaks periodically at theta frequency.

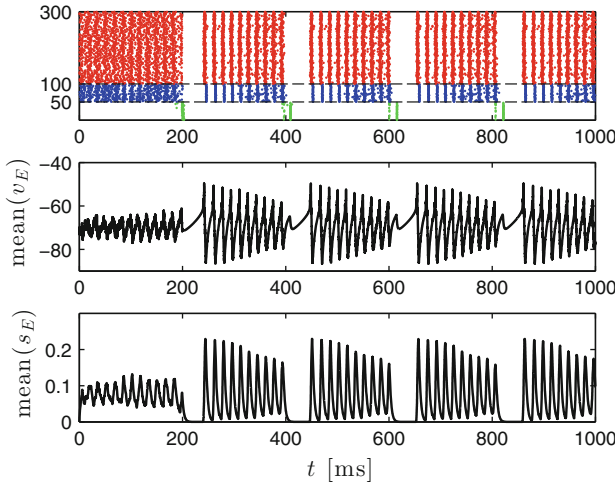


Figure E.62. Like Fig. E.61, but with nearly synchronous initialization of the O-cells, as described in exercise 34.1b. [EIO_3]

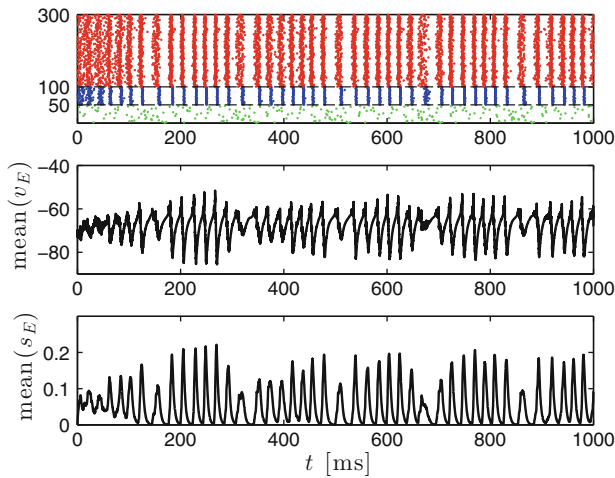


Figure E.63. Like Fig. 34.10, but with the I-to-O connection removed. [EIO_4]

by $\tilde{I} = I + \bar{g}v_{\text{rev}}$, and τ_m replaced by $\tilde{\tau}_m = \frac{1}{1/\tau_m + \bar{g}}$. The period is

$$T = \begin{cases} \tilde{\tau}_m \ln \frac{\tilde{\tau}_m \tilde{I}}{\tilde{\tau}_m \tilde{I} - 1} & \text{if } \tilde{\tau}_m \tilde{I} > 1, \\ \infty & \text{otherwise.} \end{cases}$$

The condition $\tilde{\tau}_m \tilde{I} > 1$ is clearly equivalent to $I > 1/\tau_m + \bar{g}(1 - v_{\text{rev}})$. The frequency

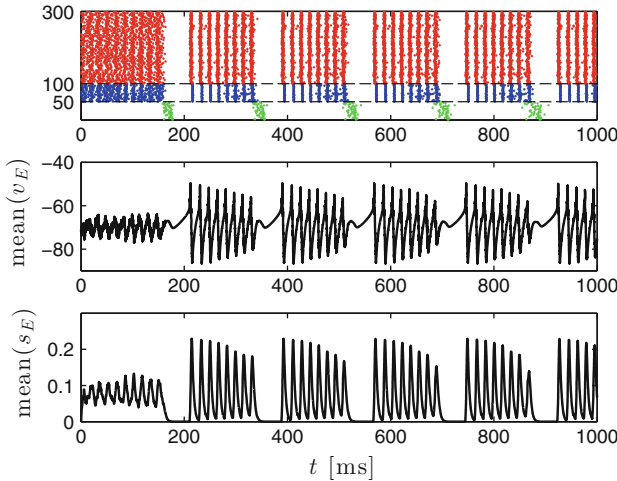


Figure E.64. Like Fig. E.63, but with the O-cells initialized in near synchrony: Each O-cell is initialized at a random phase uniformly distributed between 0 and 0.1. [EIO_5]

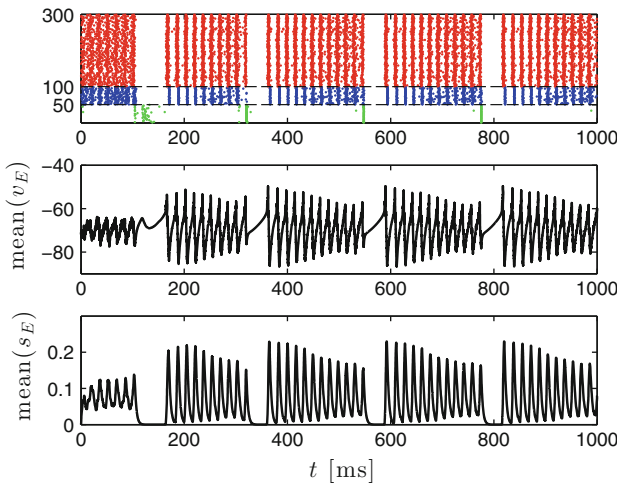


Figure E.65. Like Fig. 34.10, but with ab replaced by 0.013 — that is, with the time-dependent A-current replaced by tonic inhibition. [EIO_6]

is

$$\begin{aligned}
 f &= \frac{1000}{T} = 1000 \left(\frac{1}{\tau_m} + \bar{g} \right) \frac{1}{\ln \left(\tilde{\tau}_m \tilde{I} / (\tilde{\tau}_m \tilde{I} - 1) \right)} = \\
 &1000 \frac{1 + \tau_m \bar{g}}{\tau_m} \frac{1}{\ln \left(\tilde{\tau}_m \tilde{I} / (\tilde{\tau}_m \tilde{I} - 1) \right)} =
 \end{aligned}$$

$$1000 \frac{1 + \tau_m \bar{g}}{\tau_m} \frac{1}{\ln \left(\frac{I + \bar{g}v_{\text{rev}}}{1/\tau_m + \bar{g}} / \left(\frac{I + \bar{g}v_{\text{rev}}}{1/\tau_m + \bar{g}} - 1 \right) \right)} = 1000 \frac{1 + \tau_m \bar{g}}{\tau_m \ln \frac{\tau_m (I + \bar{g}v_{\text{rev}})}{\tau_m (I + \bar{g}v_{\text{rev}}) - 1 - \tau_m \bar{g}}}.$$

35.2. (b) Figure E.66 shows an example. When you run the code that generates Fig. E.66, you will see 200 graphs flash by; the one in Fig. E.66 is the last. The code generates 200 random triples $(I, \tau_m, v_{\text{rev}})$ with $\tau_m \in (1, 16)$, $I \in (1/\tau_m, 1.5/\tau_m)$, and $v_{\text{rev}} \in (-1, 1)$. For each of the randomly chosen triples $(I, \tau_m, v_{\text{rev}})$, the code computes the frequency $f_k = f(\bar{g}_k)$ for

$$\bar{g} = \bar{g}_k = \frac{k}{100000} \bar{g}_c, \quad k = 0, 1, 2, \dots, 99999,$$

and verifies that the graph is concave-down by verifying that $f_k > (f_{k-1} + f_{k+1})/2$ for $1 \leq k \leq 99998$. When you run the code, you will see that f , as a function of $\bar{g} \in [0, \bar{g}_c]$, is *not* always decreasing. It has a local maximum when v_{rev} is close enough to 1.

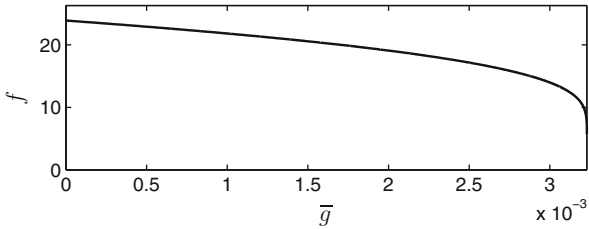


Figure E.66. The firing frequency f of the LIF neuron given by eqs. (35.5)–(35.7), as a function of \bar{g} , for a random choice of τ_m , I , and v_{rev} . [CONCAVE_DOWN]

35.3. (a) Figure E.67 shows the result. (b) For large I , in essence the neuron fires at the rate $f(0.3)$ half the time, and at the firing rate $f(0.1)$ half the time, where $f(\bar{g})$ denotes the firing rate obtained with tonic inhibition with conductance \bar{g} . (Of course the frequency also depends on I , τ_m , and v_{rev} , but that dependence is not made explicit in the notation “ $f(\bar{g})$ ”.) Since the second derivative of f with respect to \bar{g} is negative (see exercise 35.2), the average of $f(0.1)$ and $f(0.3)$ is smaller than $f(0.2)$.

36.3. Figure E.68 shows the result.

37.1. Table E.5 shows the results. Increasing \hat{g}_{IE} by 0.2 has the effect of reducing the number of sparsely firing E-cells by a factor of 2. This suggests that the number of sparsely firing E-cells, over some range of values of \hat{g}_{IE} , behaves like $e^{-c\hat{g}_{IE}}$, where $c > 0$ is determined by $e^{-0.2c} = 1/2$, so $c = 5 \ln 2 \approx 3.5$.

38.4. This is shown in Fig. E.69.

39.1. Figure E.70 shows the result.

39.2. In the limit as $\tau_{\text{rec}} \rightarrow 0$, $p + q$ must be 1, otherwise the term $(1 - p - q)/\tau_{\text{rec}}$ on the right-hand side of eq. (39.9) would become infinite. Therefore eq. (39.10)

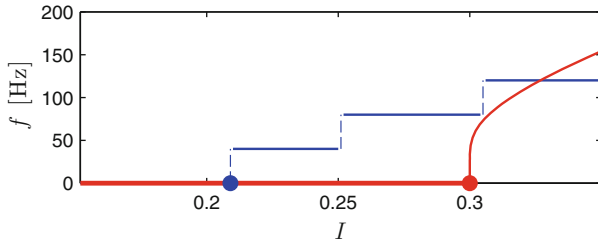


Figure E.67. The two f - I curves of exercise 35.3a.

[PERIODIC_INHIBITION_F_I_CURVE_3]

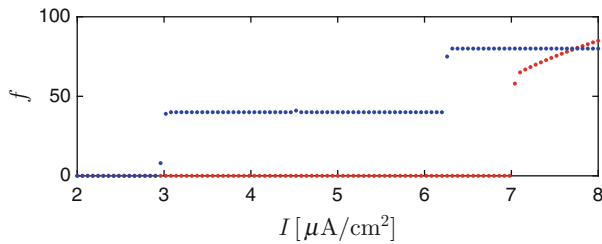


Figure E.68. Analogous to Fig. 36.3, but with the RTM neuron replaced by an Erisir neuron. [ERISIR_F_I_CURVE_PULSED_EXCITATION]

\hat{g}_{IE}	1.3	1.5	1.7	1.9
number of sparsely firing E-cells	16	8	4	2

Table E.5. The number of sparsely firing E-cells in a simulation like that of Fig. 37.1, carried out to time $t = 500$ ms, with 500 E-cells, and four different values of \hat{g}_{IE} . [PING_THR_1_TABLE]

becomes

$$\frac{dq}{dt} = -\frac{q}{\tau_{d,q}} + 1.45 \ln \frac{1}{1-U} \left(1 + \tanh \frac{v}{10}\right) (1-q).$$

This is eq. (20.9) if

$$1.45 \ln \frac{1}{1-U} = \frac{1}{0.2},$$

i.e.,

$$\frac{1}{1-U} = e^{5/1.45} = e^{1/0.29},$$

or $U = 1 - e^{-1/0.29}$.

39.3. First we solve eq. (39.14) for U :

$$U = 1 - e^{-W}. \quad (\text{E.43})$$

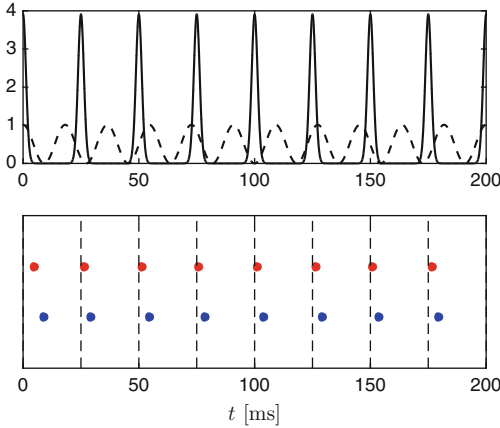


Figure E.69. Like Fig. 38.4, but with the distractor oscillating at 55 Hz instead of 25 Hz. [GAMMA_COHERENCE_3]

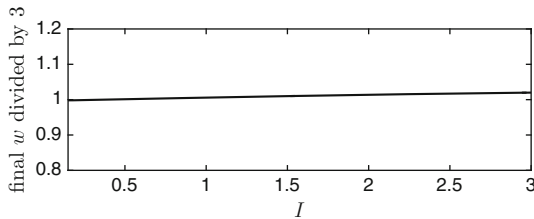


Figure E.70. Result of the numerical experiment of exercise 39.1.
[RTM_DELTA_PULSE]]

From (39.14) and (39.17),

$$\frac{dW}{dt} = -\frac{d}{dt} \ln(1-U) = \frac{1}{1-U} \frac{dU}{dt} = \frac{1}{1-U} \frac{U_0 - U}{\tau_{\text{facil}}}.$$

Now using (E.43),

$$\frac{dW}{dt} = e^W \frac{U_0 - 1 + e^{-W}}{\tau_{\text{facil}}} = \frac{1 - (1-U_0)e^W}{\tau_{\text{facil}}} = -\frac{(1-U_0)e^W - 1}{\tau_{\text{facil}}}.$$

40.4.

$$M_\delta(x) = \max_\delta(0, x) = \max(0, x) + \frac{\delta}{2} \ln \left(1 + e^{-2|x|/\delta} \right)$$

by eq. (D.6). For $x > 0$, this is

$$x + \frac{\delta}{2} \ln \left(1 + e^{-2x/\delta} \right) = \frac{\delta}{2} \left(\ln e^{2x/\delta} + \ln \left(1 + e^{-2x/\delta} \right) \right) = \frac{\delta}{2} \ln \left(e^{2x/\delta} + 1 \right).$$

For $x \leq 0$, it is

$$0 + \frac{\delta}{2} \ln \left(1 + e^{2x/\delta} \right) = \frac{\delta}{2} \ln \left(e^{2x/\delta} + 1 \right).$$

So for all $x \in \mathbb{R}$,

$$M_\delta(x) = \frac{\delta}{2} \ln \left(e^{2x/\delta} + 1 \right).$$

This is clearly an infinitely often differentiable, strictly increasing function of x . Figure E.71 shows the graph of M_δ for $\delta = 0.1$.

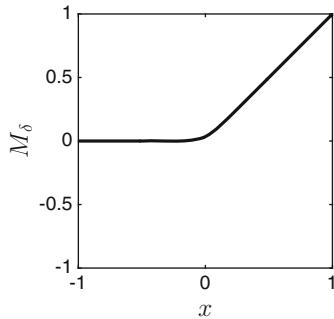


Figure E.71. The function $M_\delta(x) = \max_\delta(0, x)$ for $\delta = 0.1$. [PLOT_M_DELTA]

40.5. Figure E.72 shows the transition from $\bar{g}_{EE} < 0.23$ to $\bar{g}_{EE} > 0.23$. For \bar{g}_{EE} , the more strongly driven (second) E-cell is driven too hard to be entrained by the I-cell.

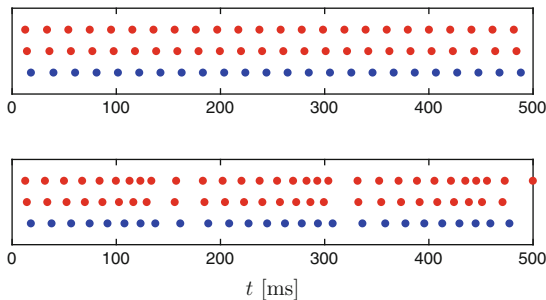


Figure E.72. Just like Fig. 40.5, but with $\bar{g}_{EE} = 0.22$ (upper panel) and $\bar{g}_{EE} = 0.24$ (lower panel). [THREE_CELL_PING_6]

40.6. $k = 0$: If $\bar{g}_{EE,ij}$ denotes the strength of the synapse from E-cell i to E-cell j , only terms related to E-cells i and j appear on the right-hand side of the equation for $\bar{g}_{EE,ij}$.

Bibliography

- [1] I. ALEKSEICHUK, Z. TURI, G. A. DE LARA, A. ANTAL, AND W. PAULUS, *Spatial working memory in humans depends on theta and high gamma synchronization in the prefrontal cortex*, Current Biology, 26 (2016), pp. 1513–1521.
- [2] R. ANDRADE, R. C. FOEHRING, AND A. V. TZINGOUNIS, *The calcium-activated slow AHP: cutting through the Gordian knot*, Frontiers in Cellular Neuroscience, 6 (2012).
- [3] D. ARION AND D. A. LEWIS, *Altered expression of regulators of the cortical chloride transporters NKCC1 and KCC2 in schizophrenia*, Arch. Gen. Psychiatry, 68 (2011), pp. 21–31.
- [4] G. J. AUGUSTINE, *How does calcium trigger neurotransmitter release?*, Current Opinion in Neurobiology, 11 (2001), pp. 320–326.
- [5] F. A. C. AZEVEDO, L. R. B. CARVALHO, L. T. GRINBERG, J. M. FARFEL, R. E. L. FERRETTI, R. E. P. LEITE, W. J. FILHO, R. LENT, AND S. HERCULANO-HOUZEL, *Equal numbers of neuronal and nonneuronal cells make the human brain an isometrically scaled-up primate brain*, J. Comp. Neurol., 513 (2009), pp. 532–541.
- [6] M. BARTOS, I. VIDA, M. FROTSCHER, J. R. GEIGER, AND P. JONAS, *Rapid signaling at inhibitory synapses in a dentate gyrus interneuron network*, J. Neurosci., 21 (2001), pp. 2687–2698.
- [7] M. BARTOS, I. VIDA, AND P. JONAS, *Synaptic mechanisms of synchronized gamma oscillations in inhibitory interneuron networks*, Nat. Rev. Neurosci., 8 (2007), pp. 45–56.
- [8] R. BERTRAM AND J. E. RUBIN, *Multi-timescale systems and fast-slow analysis*, Mathematical Biosciences, (2016).

- [9] D. BIANCHI, A. MARASCO, A. LIMONGIELLO, C. MARCHETTI, H. MARIE, B. TIROZZI, AND M. MIGLIORE, *On the mechanisms underlying the depolarization block in the spiking dynamics of CA1 pyramidal neurons*, J. Comp. Neurosci., 33 (2012), pp. 207–225.
- [10] C. BÖRGERS, S. EPSTEIN, AND N. KOPELL, *Background gamma rhythmicity and attention in cortical local circuits: A computational study*, Proc. Natl. Acad. Sci. USA, 102 (2005), pp. 7002–7007.
- [11] C. BÖRGERS AND N. KOPELL, *Synchronization in networks of excitatory and inhibitory neurons with sparse, random connectivity*, Neural Comp., 15 (2003), pp. 509–539.
- [12] ———, *Effects of noisy drive on rhythms in networks of excitatory and inhibitory neurons*, Neural Comp., 17 (2005), pp. 557–608.
- [13] C. BÖRGERS AND N. KOPELL, *Gamma oscillations and stimulus selection*, Neural Comp., 20 (2008), pp. 383–414.
- [14] C. BÖRGERS, M. KRUPA, AND S. GIELEN, *The response of a population of classical Hodgkin-Huxley neurons to an inhibitory input pulse*, J. Comp. Neurosci., 28 (2010), pp. 509–526.
- [15] C. BÖRGERS AND A. R. NECTOW, *Exponential time differencing for Hodgkin-Huxley-like ODEs*, SIAM Journal on Scientific Computing, 35 (2013), pp. B623–B643.
- [16] C. BÖRGERS, G. TALEI FRANZESI, F. E. N. LEBEAU, E. BOYDEN, AND N. KOPELL, *Minimal size of cell assemblies coordinated by gamma oscillations*, PLoS Comp. Biol., 8 (2012), p. e1002362.
- [17] C. BÖRGERS AND B. WALKER, *Toggling between gamma-frequency activity and suppression of cell assemblies*, Frontiers in Computational Neuroscience, 7, doi: 10.3389/fncom.2013.00033 (2013).
- [18] C. A. BOSMAN, C. S. LANSINK, AND C. M. A. PENNARTZ, *Functions of gamma-band synchronization in cognition: from single circuits to functional diversity across cortical and subcortical systems*, Eur. J. Neurosci., 39 (2014), pp. 1982–1999.
- [19] D. A. BROWN, *M currents*, in Ion Channels, Vo. 1, T. Narahashi, ed., Plenum Publishing Corp., New York, 1988, pp. 55–94.
- [20] P. BROWN, A. OLIVIERO, P. MAZZONE, A. INSOLA, P. TONALI, AND V. D. LAZZARO, *Dopamine dependency of oscillations between subthalamic nucleus and pallidum in Parkinson’s disease*, J. Neurosci., 21 (2001), pp. 1033–1038.
- [21] E. H. BUHL, G. TAMÁS, AND A. FISAHN, *Cholinergic activation and tonic excitation induce persistent gamma oscillations in mouse somatosensory cortex in vitro*, J. Physiol. (London), 513 (1998), pp. 117–126.

- [22] G. BUZSÁKI, *Hippocampus*, Scholarpedia, 6 (2011), p. 1468. revision #91356.
- [23] G. BUZSÁKI, C. A. ANASTASSIOU, AND C. KOCH, *The origin of extracellular fields and currents — EEG, ECoG, LFP and spikes*, Nature Reviews Neurosci., 13 (2012), pp. 407–420.
- [24] G. BUZSÁKI, D. L. BUHL, K. D. HARRIS, J. CSICSVARI, B. CZÉH, AND A. MOROZOV, *Hippocampal network patterns of activity in the mouse*, Neuroscience, 116 (2003), pp. 201–211.
- [25] G. BUZSÁKI AND J. J. CHROBAK, *Temporal structure in spatially organized neuronal ensembles: a role for interneuronal networks*, Current Opinion in Neurobiology, 5 (1995), pp. 504–510.
- [26] M. A. CASTRO-ALAMANCOS AND P. RIGAS, *Synchronized oscillations caused by disinhibition in rodent neocortex are generated by recurrent synaptic activity mediated by AMPA receptors*, J. Physiol., 542 (2002), pp. 567–581.
- [27] M. S. CEMBROWSKI, S. M. LOGAN, M. TIAN, L. JIA, W. LI, W. L. KATH, H. RIECKE, AND J. H. SINGER, *The mechanisms of repetitive spike generation in an axonless retinal interneuron*, Cell Reports, 1 (2012), pp. 155–166.
- [28] C. C. CHOW AND N. KOPELL, *Dynamics of spiking neurons with electrical coupling*, Neural Comp., 12 (2000), pp. 1643–1678.
- [29] B. W. CONNORS AND M. A. LONG, *Electrical synapses in the mammalian brain*, Annu. Rev. Neurosci., (2004), pp. 393–418.
- [30] W. E. CRILL, *Persistent sodium current in mammalian central neurons*, Ann. Rev. Physiol., 58 (1996), pp. 349–362.
- [31] S. M. CROOK, G. B. ERMENTROUT, M. C. VANIER, AND J. M. BOWER, *The role of axonal delay in the synchronization of networks of coupled cortical oscillators*, J. Comp. Neurosci., 4 (1997), pp. 161–172.
- [32] S. J. CRUIKSHANK AND N. M. WEINBERGER, *Evidence for the Hebbian hypothesis in experience-dependent physiological plasticity of neocortex: a critical review*, Brain Research Reviews, 22 (1996), pp. 191–228.
- [33] M. O. CUNNINGHAM, C. H. DAVIES, E. H. BUHL, N. KOPELL, AND M. A. WHITTINGTON, *Gamma oscillations induced by kainate receptor activation in the entorhinal cortex in vitro*, J. Neurosci., 23 (2003), pp. 9761–9769.
- [34] M. O. CUNNINGHAM, M. A. WHITTINGTON, A. BIBBIG, A. ROOPUN, F. E. N. LEBEAU, A. VOGT, H. MONYER, E. H. BUHL, AND R. D. TRAUB, *A role for fast rhythmic bursting neurons in cortical gamma oscillations in vitro*, Proc. Natl. Acad. Sci. USA, 101 (2004), pp. 7152–7157.

- [35] G. DEIDDA, M. ALLEGRA, C. CERRI, S. NASKAR, G. BONY, G. ZUNINO, Y. BOZZI, M. CALEO, AND L. CANCEDDA, *Early depolarizing GABA controls critical-period plasticity in the rat visual cortex*, Nature Neuroscience, 18 (2015), pp. 87–96.
- [36] A. DESTEXHE, Z. F. MAINEN, AND T. J. SEJNOWSKI, *Kinetic models of synaptic transmission*, in Methods in Neuronal Modeling, C. Koch and I. Segev, eds., Cambridge, MA, 1998, MIT Press, pp. 1–26.
- [37] F. DIENER, *Propriétés asymptotiques des fleuves*, C. R. Acad. Sci. Paris, 302 (1985), pp. 55–58.
- [38] M. DIENER, *Détermination et existence des fleuves en dimension 2*, C. R. Acad. Sci. Paris, 301 (1985), pp. 899–902.
- [39] D. A. DOYLE, J. M. CABRAL, R. A. PFUETZNER, A. KUO, J. M. GULBIS, S. L. COHEN, B. T. CHAIT, AND R. MACKINNON, *The structure of the potassium channel: molecular basis of K^+ conduction and selectivity*, Science, 280 (1998), pp. 69–77.
- [40] J. DROVER, J. RUBIN, J. SU, AND B. ERMENTROUT, *Analysis of a canard mechanism by which excitatory synaptic coupling can synchronize neurons at low firing frequencies*, SIAM J. Appl. Math., 65 (2004), pp. 69–92.
- [41] L. EDELSTEIN-KESHET, *Mathematical Models in Biology*, Classics in Applied Mathematics, SIAM (Philadelphia), 2004.
- [42] D. H. EDWARDS, W. J. HEITLER, AND F. B. KRASNE, *Fifty years of a command neuron: the neurobiology of escape behavior in the crayfish*, Trends in Neurosci., 22 (1999), pp. 153–161.
- [43] F. H. EECKMAN AND W. J. FREEMAN, *Correlations between unit firing and EEG in the rat olfactory system*, Brain Research, 528 (1990), pp. 238–244.
- [44] A. K. ENGEL AND P. FRIES, *Beta-band oscillations—signalling the status quo?*, Curr. Opin. Neurobiol., 20 (2010), pp. 156–165.
- [45] A. ERISIR, D. LAU, B. RUDY, AND C. S. LEONARD, *Function of specific $K(+)$ channels in sustained high-frequency firing of fast-spiking neocortical interneurons*, J. Neurophysiol., 82 (1999), pp. 2476–89.
- [46] B. ERMENTROUT, *Linearization of f-I curves by adaptation*, Neural Comp., 10 (1998), pp. 1721–1729.
- [47] G. B. ERMENTROUT, *Type I membranes, phase resetting curves, and synchrony*, Neural Comp., 8 (1996), pp. 879–1001.
- [48] G. B. ERMENTROUT, L. GLASS, AND B. E. OLDEMAN, *The shape of phase-resetting curves in oscillators with a saddle node on an invariant circle bifurcation*, Neural Comp., 24 (2012), pp. 3111–3125.

- [49] G. B. ERMENTROUT AND N. KOPELL, *Parabolic bursting in an excitable system coupled with a slow oscillation*, SIAM J. Appl. Math., 46 (1986), pp. 233–253.
- [50] ———, *Fine structure of neural spiking and synchronization in the presence of conduction delay*, Proc. Natl. Acad. Sci. USA, 95 (1998), pp. 1259–1264.
- [51] G. B. ERMENTROUT AND D. H. TERMAN, *Mathematical Foundations of Neuroscience*, Springer-Verlag, 2010.
- [52] M. A. FARRIES AND C. J. WILSON, *Phase response curves of subthalamic neurons measured with synaptic input and current injection*, J. Neurophysiol., 108 (2012), pp. 1822–1837.
- [53] D. FIORAVANTE AND W. G. REGEHR, *Short-term forms of presynaptic plasticity*, Current Opinion in Neurobiology, 21 (2011), pp. 269–274.
- [54] R. FITZHUGH, *Impulses and physiological states in theoretical models of nerve membrane*, Biophysical J., 1 (1961), pp. 445–466.
- [55] T. FREUND AND I. KATONA, *Perisomatic inhibition*, Neuron, 56 (2007), pp. 33–42.
- [56] P. FRIES, *A mechanism for cognitive dynamics: neuronal communication through neuronal coherence*, Trends in Cognitive Sciences, 9 (2005), pp. 474–480.
- [57] J. R. GIBSON, M. BEIERLEIN, AND B. W. CONNORS, *Two networks of electrically coupled inhibitory neurons in neocortex*, Nature, 402 (1999), pp. 75–79.
- [58] M. J. GILLIES, R. D. TRAUB, F. E. N. LEBEAU, C. H. DAVIES, T. GLOVELI, E. H. BUHL, AND M. A. WHITTINGTON, *A model of atropine-resistant theta oscillations in rat hippocampal area CA1*, J. Physiol., 543 (2002), pp. 779–793.
- [59] T. GILOVICH, R. VALLONE, AND A. TVERSKY, *The hot hand in basketball: On the misperception of random sequences*, Cognitive Psychology, 17 (1985), pp. 295–314.
- [60] P. S. GOLDMAN-RAKIC, *Cellular basis of working memory*, Neuron, 14 (1995), pp. 477–485.
- [61] D. GOLOMB AND D. HANSEL, *The number of synaptic inputs and the synchrony of large sparse neuronal networks*, Neural Comp., 12 (2000), pp. 1095–1139.
- [62] D. GOLOMB, X.-J. WANG, AND J. RINZEL, *Synchronization properties of spindle oscillations in a thalamic reticular nucleus model*, J. Neurophysiol., 72 (1994), pp. 1109–1126.

- [63] G. GONZALEZ-BURGOS, R. Y. CHO, AND D. A. LEWIS, *Alterations in cortical network oscillations and parvalbumin neurons in schizophrenia*, Biological Psychiatry, 77 (2015), pp. 1031–1040.
- [64] G. N. GORELOV, E. A. SHCHEPAKINA, AND V. A. SOBOLEV, *Canards and critical behavior in autocatalytic combustion models*, J. Eng. Math., 56 (2006), pp. 143–160.
- [65] A. GREENBERG AND C. T. DICKSON, *Spontaneous and electrically modulated spatiotemporal dynamics of the neocortical slow oscillation and associated local fast activity*, NeuroImage, 83 (2013), pp. 782–794.
- [66] J. S. GRIFFITH, *Mathematical Neurobiology*, Academic Press, 1971.
- [67] J. GUCKENHEIMER AND M. MYERS, *Computing Hopf bifurcations. II: Three examples from Neurophysiology*, SIAM J. Sci. Comput., 17 (1996), pp. 1275–1301.
- [68] H. H. MARKRAM, J. LÜBKE, M. FROTSCHER, AND B. SAKMANN, *Regulation of synaptic efficacy by coincidence of postsynaptic APs and EPSPs*, Science, 275 (1997), pp. 213–215.
- [69] N. HÁJOS AND I. MODY, *Synaptic communication among hippocampal interneurons: properties of spontaneous IPSCs in morphologically identified cells*, J. Neurosci., 17 (1997), pp. 8427–8442.
- [70] C. HAN, J. G. J. HOEIJKERS, S. LIU, M. M. GERRITS, R. H. M. TE MORSCHE, G. LAURIA, S. D. DIB-HAJJ, J. P. H. DRENTH, C. G. FABER, I. S. J. MERKIES, AND S. G. WAXMAN, *Functional profiles of SCN9A variants in dorsal root ganglion neurons and superior cervical ganglion neurons correlate with autonomic symptoms in small fibre neuropathy*, Brain, 135 (2012), pp. 2613–2628.
- [71] D. HANSEL, G. MATO, AND G. MEUNIER, *Synchrony in excitatory neural networks*, Neural Comp., 7 (1995), pp. 307–337.
- [72] M. E. HASSELMO, *What is the function of hippocampal theta rhythm?—Linking behavioral data to phasic properties of field potential and unit recording data*, Hippocampus, 15 (2005), pp. 936–949.
- [73] D. O. HEBB, *The Organization of Behavior*, John Wiley, New York, 1949.
- [74] M. W. HIRSCH, S. SMALE, AND R. L. DEVANEY, *Differential Equations, Dynamical Systems, and an Introduction to Chaos*, Academic Press, 2012.
- [75] A. L. HODGKIN, *The local changes associated with repetitive action in a non-medullated axon*, J. Physiol. (London), 107 (1948), pp. 165–181.
- [76] A. L. HODGKIN AND A. F. HUXLEY, *A quantitative description of membrane current and its application to conduction and excitation in nerve*, J. Physiol. (London), 117 (1952), pp. 500–544.

- [77] J. R. HUGUENARD, *Low-threshold calcium currents in central nervous system neurons*, Ann. Rev. Physiol., 58 (1996), pp. 329–348.
- [78] E. ISAACSON AND H. B. KELLER, *Analysis of Numerical Methods*, Dover, New York (reprint of 1966 edition), 1994.
- [79] T. ISHIKAWA, M. KANEKO, H.-S. SHIN, AND T. TAKAHASHI, *Presynaptic N-type and P/Q-type Ca^{2+} channels mediating synaptic transmission at the calyx of Held of mice*, J. Physiol., 568 (2005), pp. 199–209.
- [80] E. M. IZHIKEVICH, *Resonate-and-fire neurons*, Neural Networks, 14 (2001), pp. 883–894.
- [81] ———, *Simple model of spiking neurons*, IEEE Transactions on Neural Networks, 14 (2003), pp. 1569–1572.
- [82] ———, *Dynamical Systems in Neuroscience*, MIT Press, 2007.
- [83] M. E. JACKSON, H. HOMAYOUN, AND B. MOGHADDAM, *NMDA receptor hypofunction produces concomitant firing rate potentiation and burst activity reduction in the prefrontal cortex*, Proc. Natl. Acad. Sci. USA, 101 (2004), pp. 8467–8472.
- [84] C. E. JAHR AND C. F. STEVENS, *Voltage dependence of NMDA-activated macroscopic conductances predicted by single-channel kinetics*, J. Neurosci., 10 (1990), pp. 3178–3182.
- [85] J. G. JEFFERY, R. D. TRAUB, AND M. A. WHITTINGTON, *Neuronal networks for induced '40 Hz' rhythms*, Trends in Neurosci., 19 (1996), pp. 202–208.
- [86] D. T. KAPLAN, J. R. CLAY, T. MANNING, L. GLASS, M. R. GUEVARA, AND A. SHRIER, *Subthreshold dynamics in periodically stimulated squid giant axons*, Phys. Rev. Lett., 76 (1996), pp. 4074–4077.
- [87] B. KATZ AND R. MILEDI, *The role of calcium in neuromuscular facilitation*, J. Physiol., 195 (1968), pp. 481–492.
- [88] J. KEENER AND J. SNEYD, *Mathematical Physiology I: Cellular Physiology*, second edition, Springer-Verlag, 2009.
- [89] Z. P. KILPATRICK AND G. B. ERMENTROUT, *Sparse gamma rhythms arising through clustering in adapting neuronal networks*, PLoS Comput. Biol., 7 (2011), p. e1002281.
- [90] T. KLAUSBERGER, *GABAergic interneurons targeting dendrites of pyramidal cells in the CA1 area of the hippocampus*, Eur. J. Neurosci., 30 (2009), pp. 947–957.

- [91] I. C. KLEPPE AND H. P. ROBINSON, *Determining the activation time course of synaptic AMPA receptors from openings of colocalized NMDA receptors*, *Biophys. J.*, 77 (1999), pp. 1418–1427.
- [92] N. KOPELL, C. BÖRGERS, D. PERVOUCHINE, P. MALERBA, AND A. B. L. TORT, *Gamma and theta rhythms in biophysical models of hippocampal circuits*, in *Hippocampal Microcircuits: A Computational Modeler’s Resource Book*, V. Cutsuridis, B. Graham, S. Cobb, and I. Vida, eds., Springer-Verlag, 2010 (article available at <http://math.bu.edu/people/nk/papers.html>).
- [93] N. KOPELL AND B. ERMENTROUT, *Chemical and electrical synapses perform complementary roles in the synchronization of interneuronal networks*, *Proc. Natl. Acad. Sci. USA*, 101 (2004), pp. 15482–15487.
- [94] N. KOPELL AND G. LEMASSON, *Rhythmogenesis, amplitude modulation, and multiplexing in a cortical architecture*, *Proc. Natl. Acad. Sci. USA*, 91 (1994), pp. 10586–10590.
- [95] H. KORN AND D. S. FABER, *The Mauthner cell half a century later: A neurobiological model for decision-making?*, *Neuron*, 47 (2005), pp. 13–28.
- [96] T. KOSTOVA, R. RAVINDRAN, AND M. SCHONBEK, *FitzHugh-Nagumo revisited: Types of bifurcations, periodical forcing and stability regions by a Lyapunov functional*, *Int. J. of Bifurcation and Chaos*, 14 (2004), pp. 913–925.
- [97] U. KRAUSHAAR AND P. JONAS, *Efficacy and stability of quantal GABA release at a hippocampal interneuron-principal neuron synapse*, *J. Neurosci.*, 20 (2000), pp. 5594–5607.
- [98] M. KRUPA, S. GIELEN, AND B. GUTKIN, *Adaptation and shunting inhibition leads to pyramidal/interneuron gamma with sparse firing of pyramidal cells*, *J. Comp. Neurosci.*, 37 (2014), pp. 357–376.
- [99] M. KRUPA AND P. SZMOLYAN, *Relaxation oscillation and canard explosion*, *J. Differential Equations*, 174 (2001), pp. 312–368.
- [100] W. KRZYZANSKI AND J. BELL, *Modelling the geometric features and investigating electrical properties of dendrites in a fish thalamic neuron*, *Math. Med. Biol.*, 24 (2007), pp. 271–286.
- [101] S. LEE, K. SEN, AND N. KOPELL, *Cortical gamma rhythms modulate NMDAR-mediated spike timing dependent plasticity in a biophysical model*, *PLoS Comp. Biol.*, 5 (2009), p. e1000602.
- [102] M. LESZCZYŃSKI, J. FELL, AND N. AXMACHER, *Rhythmic working memory activation in the human hippocampus*, *Cell Reports*, 13 (2015), pp. 1272–1282.
- [103] T. J. LEWIS AND J. RINZEL, *Dynamics of spiking neurons connected by both inhibitory and electrical coupling*, *J. Comput. Neurosci.*, 14 (2003), pp. 283–309.

- [104] X. LI, *Cortical oscillations and synaptic plasticity — from a single neuron to neuronal networks*, PhD thesis, Hong Kong Polytechnic University, 2010.
- [105] J. E. LISMAN AND M. A. IDIART, *Storage of 7 +/- 2 short-term memories in oscillatory subcycles*, Science, 267 (1995), pp. 1512–1515.
- [106] J. E. LISMAN AND O. JENSEN, *The γ - θ neural code*, Neuron, 77 (2013), pp. 1002–1016.
- [107] A. LÜTHI AND D. A. MCCORMICK, *H-current: Properties of a neuronal and network pacemaker*, Neuron, 21 (1998), pp. 9–12.
- [108] A. LUTZ, L. L. GREISCHAR, N. B. RAWLINGS, M. RICARD, AND R. J. DAVIDSON, *Long-term meditators self-induce high-amplitude gamma synchrony during mental practice*, Proc. Natl. Acad. Sci. USA, 101 (2004), pp. 16369–16373.
- [109] G. MACCAFERRI AND C. J. MCBAIN, *The hyperpolarization-activated current (I_h) and its contribution to pacemaker activity in rat CA1 hippocampal stratum oriens-alveus interneurones*, J. Physiol., 497 (Pt. 1) (1996), pp. 119–130.
- [110] E. O. MANN, C. A. RADCLIFFE, AND O. PAULSEN, *Hippocampal gamma-frequency oscillations: from interneurones to pyramidal cells, and back*, J. Physiol., 562 (2005), pp. 55–63.
- [111] E. MARDER, *Electrical Synapses: Rectification Demystified*, Current Biology, 19 (2009), pp. R34–R35.
- [112] F. MARINO, M. CISZAK, S. F. ABDALAH, K. AL-NAIMEE, R. MEUCCI, AND F. T. ARECCHI, *Mixed-mode oscillations via canard explosions in light-emitting diodes with optoelectronic feedback*, Phys. Rev. E, 84 (2011), p. 047201.
- [113] G. MARMONT, *Studies on the axon membrane. 1. A new method*, J. Cell Physiol., 34 (1949), pp. 351–382.
- [114] N. V. MARRION, *Control of M-current*, Ann. Rev. Physiol., 59 (1997), pp. 483–504.
- [115] D. MATTIA, H. KAWASAKI, AND M. AVOLI, *Repetitive firing and oscillatory activity of pyramidal-like bursting neurons in the rat subiculum*, Experimental Brain Research, 114 (1997), pp. 507–517.
- [116] D. A. MCCORMICK AND H.-C. PAPE, *Properties of a hyperpolarization-activated cation current and its role in rhythmic oscillation in thalamic relay neurones*, J. Physiol., 431 (1980), pp. 291–318.
- [117] MERRIAM-WEBSTER DICTIONARY, *canard*, merriam-webster.com, 2016.
- [118] G. A. MILLER, *The magical number seven, plus or minus two: some limits on our capacity for processing information*, Psychol. Rev., 63 (1956), pp. 81–97.

- [119] R. E. MIROLLO AND S. H. STROGATZ, *Synchronization of pulse-coupled biological oscillators*, SIAM J. Appl. Math., 50 (1990), pp. 1645–1662.
- [120] J. MOEHLIS, *Canards for a reduction of the Hodgkin-Huxley equations*, Journal of Mathematical Biology, 52 (2005), pp. 141–153.
- [121] J. NAGUMO, S. ARIMOTO, AND S. YOSHIZAWA, *An active pulse transmission line simulating nerve axon*, Proc. IRE, 50 (1962), pp. 2061–2070.
- [122] M. OLUFSEN, M. WHITTINGTON, M. CAMPARI, AND N. KOPELL, *New functions for the gamma rhythm: Population tuning and preprocessing for the beta rhythm*, J. Comput. Neurosci., 14 (2003), pp. 33–54.
- [123] C. S. PESKIN, *Mathematical Aspects of Heart Physiology*, Courant Institute of Mathematical Sciences, New York University, New York, 1975.
- [124] V. PETROV, S. K. SCOTT, AND K. SHOWALTER, *Mixed-mode oscillations in chemical systems*, J. Chem. Phys., 97 (1992), p. 6191.
- [125] T. M. PHAM, S. NURSE, AND J. C. LACAILLE, *Distinct GABA_B actions via synaptic and extrasynaptic receptors in rat hippocampus in vitro*, J. Neurophysiol., 80 (1998), pp. 297–308.
- [126] B. R. PITTMAN-POLLETTA, B. KOCSIS, S. VIJAYAN, M. A. WHITTINGTON, AND N. KOPELL, *Brain rhythms connect impaired inhibition to altered cognition in schizophrenia*, Biological Psychiatry, 77 (2015), pp. 1020–1030.
- [127] A. R. RAU, O. J. ARIWODOLA, AND J. L. WEINER, *Postsynaptic adenosine A_{2A} receptors modulate intrinsic excitability of pyramidal cells in the rat basolateral amygdala*, Int. J. Neuropsychopharmacol., 18, doi: 10.1093/ijnp/pyv017 (2015).
- [128] S. RAY AND J. H. R. MAUNSELL, *Do gamma oscillations play a role in cerebral cortex?*, Trends in Cognitive Sciences, 19 (2015), pp. 78–85.
- [129] J. RINZEL AND G. B. ERMENTROUT, *Analysis of neural excitability and oscillations*, in Methods in Neuronal Modeling, C. Koch and I. Segev, eds., Cambridge, MA, 1998, MIT Press, pp. 251–292.
- [130] A. K. ROOPUN, S. J. MIDDLETON, M. O. CUNNINGHAM, F. E. N. LEBEAU, A. BIBBIG, M. A. WHITTINGTON, AND R. D. TRAUB, *A beta2-frequency (20-30 Hz) oscillation in nonsynaptic networks of somatosensory cortex*, Proc. Natl. Acad. Sci. USA, 103 (2006), pp. 15646–15650.
- [131] H. G. ROTSTEIN, *Subthreshold amplitude and phase resonance in models of quadratic type: nonlinear effects generated by the interplay of resonant and amplifying currents*, J. Comp. Neurosci., 38 (2015), pp. 325–354.

- [132] H. G. ROTSTEIN, T. OPPERMANN, J. A. WHITE, AND N. KOPELL, *The dynamic structure underlying subthreshold oscillatory activity and the onset of spikes in a model of medial entorhinal cortex stellate cells*, J. Comput. Neurosci., 21 (2006), pp. 271–292.
- [133] H. G. ROTSTEIN, D. D. PEROVICHINE, C. D. ACKER, M. J. GILLIES, J. A. WHITE, E. H. BUHL, M. A. WHITTINGTON, AND N. KOPELL, *Slow and fast inhibition and an H-current interact to create a theta rhythm in a model of CA1 interneuron network*, J. Neurophysiol., 94 (2005), pp. 1509–1518.
- [134] H. G. ROTSTEIN, M. WECHSELBERGER, AND N. KOPELL, *Canard induced mixed-mode oscillations in a medial entorhinal cortex layer II stellate cell model*, SIAM J. Appl. Dyn. Syst., 7 (2008), pp. 1582–1611.
- [135] M. E. RUSH AND J. RINZEL, *The potassium A-current, low firing rates and rebound excitation in Hodgin-Huxley-models*, Bull. Math. Biol., 57 (1995), pp. 899–929.
- [136] S. SAHARA, Y. YANAGAWA, D. M. O’LEARY, AND C. F. STEVENS, *The fraction of cortical GABAergic neurons is constant from near the start of cortical neurogenesis to adulthood*, J. Neurosci., 32 (2012), pp. 4755–4761.
- [137] P. A. SALIN AND D. A. PRINCE, *Spontaneous GABA_A receptor-mediated inhibitory currents in adult rat somatosensory cortex*, J. Neurophysiol., 75 (1996), pp. 1573–1588.
- [138] M. V. SANCHEZ-VIVES, V. F. DESCALZO, R. REIG, N. A. FIGUEROA, A. COMpte, AND R. GALLEGOS, *Rhythmic spontaneous activity in the piriform cortex*, Cerebral Cortex, 18 (2008), pp. 1179–1192.
- [139] J. A. SANDERS, F. VERHULST, AND J. MURDOCK, *Averaging Methods in Nonlinear Dynamical Systems*, Springer-Verlag, 2007.
- [140] S. J. SHABEL, C. D. PROULX, J. PIRIZ, AND R. MALINOW, *GABA/glutamate co-release controls habenula output and is modified by antidepressant treatment*, Science, 345 (2014), pp. 1494–1498.
- [141] P. K. SHAW, A. N. S. IYENGAR, AND M. NURUJJAMAN, *Canard and mixed mode oscillations in an excitable glow discharge plasma in the presence of inhomogeneous magnetic field*, Physics of Plasmas, 22 (2015), p. 122301.
- [142] T. P. SHEEHAN, R. A. CHAMBERS, AND D. S. RUSSELL, *Regulation of affect by the lateral septum: implications for neuropsychiatry*, Brain Research Reviews, 46 (2004), pp. 71–117.
- [143] J. H. SIEGLE, D. L. PRITCHETT, AND C. I. MOORE, *Gamma-range synchronization of fast-spiking interneurons can enhance detection of tactile stimuli*, Nature Neurosci., 17 (2014), pp. 1371–1379.

- [144] N. S. SIMONOVÍĆ, *Calculations of periodic orbits: the monodromy method and application to regularized systems*, Chaos, 9 (1999), pp. 854–864.
- [145] S. SONG AND L. F. ABBOTT, *Cortical development and remapping through spike timing-dependent plasticity*, Neuron, 32 (2001), pp. 339–350.
- [146] K. M. SPENCER, P. G. NESTOR, R. PERLMUTTER, M. A. NIZNIKIEWICZ, M. C. KLUMP, M. FRUMIN, M. E. SHENTON, AND R. W. MCCARLEY, *Neural synchrony indexes disordered perception and cognition in schizophrenia*, Proc. Natl. Acad. Sci. USA, 101 (2004), pp. 17288–17293.
- [147] C. E. STAFSTROM, *Persistent sodium current and its role in epilepsy*, Epilepsy Curr., 7 (2007), pp. 15–22.
- [148] K. M. STIEFEL, B. ENGLITZ, AND T. J. SEJNOWSKI, *Origin of intrinsic irregular firing in cortical interneurons*, Proc. Natl. Acad. Sci. USA, 110 (2013), pp. 7886–7891.
- [149] S. H. STROGATZ, *Nonlinear Dynamics and Chaos*, Westview Press, 2nd ed., 2015.
- [150] Y. SUN, A. Q. NGUYEN, J. P. NGUYEN, L. LE, D. SAUR, J. CHOI, E. M. CALLAWAY, AND X. XU, *Cell-type-specific circuit connectivity of hippocampal CA1 revealed through Cre-dependent rabies tracing*, Cell Reports, 7 (2014).
- [151] H. A. SWADLOW AND S. G. WAXMAN, *Axonal conduction delays*, Scholarpedia, 7 (2012), p. 1451.
- [152] G. TAMÁS, E. H. BUHL, A. LÖRINCZ, AND P. SOMOGYI, *Proximally targeted GABAergic synapses and gap junctions synchronize cortical interneurons*, Nature Neurosci., 3 (2000), pp. 366–371.
- [153] G. TAMÁS, E. H. BUHL, A. LÖRINCZ, AND P. SOMOGYI, *Proximally targeted GABAergic synapses and gap junctions synchronize cortical interneurons*, Nature Neurosci., 3 (2000), pp. 366–371.
- [154] G. TAMÁS, E. H. BUHL, AND P. SOMOGYI, *Massive autaptic self-innervation of GABAergic neurons in cat visual cortex*, J. Neurophysiol., 77 (1997), pp. 6352–6364.
- [155] P. TIESINGA AND T. J. SEJNOWSKI, *Cortical enlightenment: are attentional gamma oscillations driven by ING or PING?*, Neuron, 63 (2009), pp. 727–732.
- [156] P. H. E. TIESINGA, J.-M. FELLOUS, J. V. JOSÉ, AND T. J. SEJNOWSKI, *Computational model of carbachol-induced delta, theta, and gamma oscillations in the hippocampus*, Hippocampus, 11 (2001), pp. 251–274.
- [157] A. B. L. TORT, H. G. ROTSTEIN, T. D. T. GLOVELI, AND N. KOPELL, *On the formation of gamma-coherent cell assemblies by oriens lacunosum-moleculare interneurons in the hippocampus*, Proc. Natl. Acad. Sci. USA, 104 (2007), pp. 13490–13495.

- [158] R. D. TRAUB, A. BIBBIG, A. FISAHN, F. E. N. LEBEAU, M. A. WHITTINGTON, AND E. H. BUHL, *A model of gamma-frequency network oscillations induced in the rat CA3 region by carbachol in vitro*, Eur. J. Neurosci., 12 (2000), pp. 4093–4106.
- [159] R. D. TRAUB, J. G. JEFFERYS, AND M. A. WHITTINGTON, *Simulation of gamma rhythms in networks of interneurons and pyramidal cells*, J. Comp. Neurosci., 4 (1997), pp. 141–150.
- [160] R. D. TRAUB, N. KOPPELL, A. BIBBIG, E. H. BUHL, F. E. N. LEBEAU, AND M. A. WHITTINGTON, *Gap junctions between interneuron dendrites can enhance long-range synchrony of gamma oscillations*, J. Neurosci., 21 (2001), pp. 9478–9486.
- [161] R. D. TRAUB AND R. MILES, *Neuronal Networks of the Hippocampus*, Cambridge University Press, Cambridge, UK, 1991.
- [162] R. D. TRAUB AND M. WHITTINGTON, *Cortical Oscillations in Health and Disease*, Oxford University Press, 2010.
- [163] R. D. TRAUB, M. A. WHITTINGTON, E. H. BUHL, J. G. JEFFERYS, AND H. J. FAULKNER, *On the mechanism of the gamma → beta frequency shift in neuronal oscillations induced in rat hippocampal slices by tetanic stimulation*, J. Neurosci., 19 (1999), pp. 1088–1105.
- [164] M. TSODYKS, K. PAWEZIK, AND H. MARKRAM, *Neural networks with dynamic synapses*, Neural Comp., 10 (1998), pp. 821–835.
- [165] M. V. TSODYKS AND H. MARKRAM, *The neural code between neocortical pyramidal neurons depends on neurotransmitter release probability*, Proc. Natl. Acad. Sci. USA, 94 (1997), pp. 719–723.
- [166] P. J. UHLHAAS, G. PIPA, B. LIMA, L. MELLONI, S. NEUENSCHWANTER, D. NIKOLIC, AND W. SINGER, *Neural synchrony in cortical networks: history, concept and current status*, Frontiers in Integrative Neuroscience, 3 (2009).
- [167] C. VAN VREESWIJK, L. F. ABBOTT, AND G. B. ERMENTROUT, *When inhibition not excitation synchronizes neural firing*, J. Comput. Neurosci., 1 (1994), pp. 313–321.
- [168] C. A. VAN VREESWIJK AND H. SOMPOLINSKY, *Chaos in neuronal networks with balanced excitatory and inhibitory activity*, Science, 274 (1996), pp. 1724–1726.
- [169] I. VIDA, M. BARTOS, AND P. JONAS, *Shunting inhibition improves robustness of gamma oscillations in hippocampal interneuron networks by homogenizing firing rates*, Neuron, 49 (2006), pp. 107–17.
- [170] H. WACHTEL AND E. R. KANDEL, *A direct synaptic connection mediating both excitation and inhibition*, Science, 158 (1967), pp. 1206–1208.

- [171] M. WANG, Y. YANG, C.-J. WANG, N. J. GAMO, L. E. JIN, J. A. MAZER, J. H. MORRISON, X.-J. WANG, AND A. F. T. ARNSTEN, *NMDA receptors subserve persistent neuronal firing during working memory in dorsolateral prefrontal cortex*, *Neuron*, 77 (2013), pp. 736–749.
- [172] X. J. WANG, *Synaptic basis of cortical persistent activity: the importance of NMDA receptors to working memory*, *J. Neurosci.*, 19 (1999), pp. 9587–9603.
- [173] X.-J. WANG, *Pacemaker neurons for the theta rhythm and their synchronization in the septohippocampal reciprocal loop*, *J. Neurophysiol.*, 87 (2002), pp. 889–900.
- [174] X.-J. WANG AND G. BUZSÁKI, *Gamma oscillation by synaptic inhibition in a hippocampal interneuronal network model*, *J. Neurosci.*, 16 (1996), pp. 6402–6413.
- [175] X.-J. WANG, D. GOLOMB, AND J. RINZEL, *Emergent spindle oscillations and intermittent burst firing in a thalamic model: specific neuronal mechanisms*, *Proc. Natl. Acad. Sci. USA*, 92 (1995), pp. 5577–5581.
- [176] M. WECHSELBERGER, *Canards*, Scholarpedia, 2 (2007), p. 1356.
- [177] M. WECHSELBERGER, J. MITRY, AND J. RINZEL, *Canard theory and excitability*, vol. 2102 of Lecture Notes in Mathematics, Springer Verlag, 2013, pp. 89–132.
- [178] J. WHITE, C. CHOW, J. RITT, C. SOTO-TREVIÑO, AND N. KOPELL, *Synchronization and oscillatory dynamics in heterogeneous, mutually inhibited neurons*, *J. Comput. Neurosci.*, 5 (1998), pp. 5–16.
- [179] J. A. WHITE, M. I. BANKS, R. A. PEARCE, AND N. KOPELL, *Networks of interneurons with fast and slow gamma-aminobutyric acid type A (GABA_A) kinetics provide substrate for mixed gamma-theta rhythm*, *Proc. Natl. Acad. Sci. USA*, 97 (2000), pp. 8128–8133.
- [180] M. A. WHITTINGTON, I. M. STANFORD, S. B. COLLING, J. G. R. JEFFERY, AND R. D. TRAUB, *Spatiotemporal patterns of γ frequency oscillations tetanically induced in the rat hippocampal slice*, *J. Physiol. (London)*, 502 (1997), pp. 591–607.
- [181] M. A. WHITTINGTON, R. D. TRAUB, H. J. FAULKNER, I. M. STANFORD, AND J. G. JEFFERY, *Recurrent excitatory postsynaptic potentials induced by synchronized fast cortical oscillations*, *Proc. Natl. Acad. Sci. USA*, 94 (1997), pp. 12198–12203.
- [182] M. A. WHITTINGTON, R. D. TRAUB, AND J. G. R. JEFFERY, *Synchronized oscillations in interneuron networks driven by metabotropic glutamate receptor activation*, *Nature*, 373 (1995), pp. 612–615.

- [183] M. A. WHITTINGTON, R. D. TRAUB, N. KOPELL, B. ERMENTROUT, AND E. H. BUHL, *Inhibition-based rhythms: experimental and mathematical observations on network dynamics*, Int. J. of Psychophysiol., 38 (2000), pp. 315–336.
- [184] H. R. WILSON, *Spikes, Decisions, and Actions*, Oxford University Press, 1999.
- [185] H. R. WILSON AND J. D. COWAN, *Excitatory and inhibitory interactions in localized populations of model neurons*, Biophys. J., 12 (1972), pp. 1–24.
- [186] A. T. WINFREE, *The Geometry of Biological Time*, second edition, Springer-Verlag, 2001.
- [187] M. P. Y. YAARI, *Kinetic properties of NMDA receptor-mediated synaptic currents in rat hippocampal pyramidal cells versus interneurones*, J. Physiol., 465 (1993), pp. 223–244.
- [188] J. YAMAMOTO, J. SUH, D. TAKEUCHI, AND S. TONEGAWA, *Successful execution of working memory linked to synchronized high-frequency gamma oscillations*, Cell, 157 (2014), pp. 845–857.
- [189] L. ZHANG AND C. J. MCBAIN, *Voltage-gated potassium currents in stratum oriens-alveus inhibitory neurones of the rat CA1 hippocampus*, J. Physiol., 488 (Pt. 3) (1995), pp. 647–660.
- [190] L. I. ZHANG, H. W. TAO, C. E. HOLT, W. A. HARRIS, AND M. POO, *A critical window for cooperation and competition among developing retinotectal synapses*, Nature, 395 (1998), pp. 37–44.

Index

Symbols

α -amino-3-hydroxy-5-methyl-4-isoxazolepropionic acid (AMPA), 5

A

A-current, 304
acetylcholine (ACh), 5, 58
action potential, 3
activation gate, 17
activation variable, 17, 20
adaptation-based weak PING, 282, 286
afterhyperpolarization (AHP) current, 60
all-to-all coupling, 193
AMPA decay time constant, 155
AMPA receptor, 4, 154
ampere (A, unit of current), 7
anti-synchrony, 214, 218
artificial cerebrospinal fluid (ACSF), 297
asymptotics (notation), 6
asynchronous initialization, 193, 195
attention, 58
attracting fixed point, 80, 86, 89
attracting limit cycle, 26, 92
autapse, 156, 160
averaging, 235
Avogadro's number, 161
axon, 1
axon hillock, 4
axon terminal, 4

B

Banach fixed point theorem, 365
barrel cortex, 313
basal ganglia, 201, 293
basin of attraction, 96
basket cell, 33
beta oscillation, 293
beta rhythm, 293
bifurcation, 79
bifurcation diagram, 83, 92–94, 96, 394
bifurcation type 1, 85, 88
bifurcation type 2, 99
bifurcation type 3, 111
big-O notation, 7
bisection method, 75, 86, 160, 361
bistability, 96, 399
blow-up in finite time, 28
blue sky bifurcation of cycles, 97
blue sky bifurcation of fixed points, 80
Boltzmann's constant, 12
Brouwer fixed point theorem, 364
bursting, 141, 143, 144, 146, 147, 149

C

CA1, 257
CA3, 257
canard explosion, 105
Cantor function, 187
capacitor, 15
cation, 132
cell assembly, 295, 327

central difference approximation, 230
 Chebyshev's inequality, 370
 cholecystokinin, 33
 cholecystokinin-positive (CCK+), 33
 class 1 and class 2 (Hodgkin), 121,
 131
 classification of fixed points for
 two-dimensional systems, 87
 clustering, 270, 273–275, 287, 299
 coefficient of variation, 370
 column sum, 166
 communication through coherence
 (CTC), 333, 336
 condition number, 55
 conditional probability, 367
 conductance, 13
 connected graph, 167
 connectivity graph, 167
 cornu Ammonis, 257
 cortical layers, 6
 coulomb (C, unit of charge), 8
 covariance, 371

D

de-activation, 20
 de-inactivation, 20
 deep brain stimulation, 201
 delayed rectifier, 3
 dendrite, 1
 depolarization, 3
 depolarization block, 77, 85,
 89, 97, 396
 devil's staircase, 187
 diagonal symmetry, 208, 220
 diffusion, 41
 diffusion coefficient, 41
 dipole layer, 15
 Dirac delta function, 315, 343
 discrete diffusion, 167
 discrete mean value property, 172
 discrete Ornstein-Uhlenbeck process,
 292, 375
 distal dendrite, 303
 Dulac's criterion for ruling out
 periodic solutions, 180

E

E-cell, 175, 255
 E-I network, 175, 256
 EEG, 183
 electrical synapse, 165
 electroencephalography (EEG), 183
 elementary charge, 2
 elliptic bursting, 149
 entrainment, 184
 Erisir model, 34, 99, 125, 133, 326
 Erisir model, reduced to two
 dimensions, 99, 101–103
 Euler's method, 24, 28
 excitable cell, 3
 excitatory, 3
 exp, 6
 expectation (of a random variable),
 368
 expected value, 368
 exponential convergence, 17
 exponentially distributed random
 number, 375
 external drive to a neuron, 31

F

farad (F, unit of capacitance), 7, 8
 fast variable, 76
 fast-firing cells, 33
 firing of a neuron, 3, 20
 firing threshold (voltage), 4
 first law of thermodynamics, 14
 first-order accuracy, 25
 FitzHugh-Nagumo model, 76, 77, 103
 fixed point iteration, 188, 363
 fixed point of a differential equation,
 53, 77, 80
 fixed point of a function, 67, 363
 flow on a circle, 53
 frequency-current (f - I) curve, 119
 frozen noise, 197

G

GABA_A decay time constant, 155
 GABA_A receptor, 5, 154
 GABA_B decay time constant, 155
 GABA_B receptor, 5, 154

GABAergic, 5
gamma oscillation, 256
gamma rhythm, 256
gamma-aminobutyric acid (GABA),
 5
gamma-beta transition, 295
gap junction, 6, 165, 273
gating variable, 17
Gaussian, 372
Gershgorin's theorem, 172
ghost of a pair of fixed points, 83, 84,
 394, 395
glial cell, 1
global convergence, 365
globally attracting fixed point, 92
glutamate, 4
glutamatergic, 4

H

h-current, 132, 135
h-current-based weak PING, 282
hard Hopf bifurcation, 97
Heaviside function, 423
Hebb, Donald, 295
Hebbian plasticity, 295
hertz (Hz, unit of frequency), 7, 8, 48
heterogeneous conduction delays, 234
heterogeneous drives, 194
heterogeneous synaptic strengths,
 197
high-threshold potassium current,
 129
hippocampus, 1
Hodgkin, Alan, 15
Hodgkin-Huxley ODEs, 15, 18,
 99, 121, 132
Hodgkin-Huxley ODEs, reduced to
 two dimensions,
 74, 75, 99–101, 125
Hodgkin-Huxley PDEs, 39
homoclinic bifurcation, 114
homoclinic trajectory, 114
Hopf bifurcation, 91, 97
Hopf bifurcation theorem, 91
Huxley, Andrew, 15

hyperpolarization, 3
hysteresis loop, 142

I

I-cell, 175, 255
ideal gas law, 13
inactivating current, 111, 112
inactivation, 3, 20
inactivation gate, 18, 306
inactivation variable, 18, 20
independent random variables,
 179, 369
infinitesimal PRC, 202, 203
ING, 269
inhibitory, 3
integrating factor, 64, 252, 417
inter-burst interval, 141
inter-spike interval, 3
interaction function, 201, 214
interneuron, 5
intrinsic period, 194, 213
intrinsically bursting (IB) cells, 299
invariant cycle, 88
ionotropic receptor, 5
irregular entrainment, 185
Izhikevich neuron, 49

J

Jacobi matrix, 77, 87
Jahr-Stevens model, 161, 162
joule (J, unit of work and energy), 7,
 12

K

kainate, 281
kainate receptors, 281
kelvin (K, unit of temperature), 12

L

lack of memory, 375
Lapicque, Louis Édouard, 45
lateral septum, 164
layer II/III, 6
leak current, 16
leakiness, 46, 325

levodopa, 293
 limit cycle, 26, 75, 92
 linear integrate-and-fire (LIF) model, 45
 linear integrate-and-fire (LIF) neuron, 122
 little-O notation, 7
 local field potential (LFP), 183, 197
 logistic population growth, 83
 lower branch of the f - I curve, 121

M
 M-current, 58, 60, 126
 mean value (of a random variable), 368
 meditation, 256
 membrane potential, 3
 membrane time constant, 46, 47, 389
 membrane time constant of Hodgkin-Huxley-like models, 47, 50, 388, 389
 metabotropic glutamate receptor, 257
 metabotropic receptor, 5
 method of averaging, 235
 mho (unit of conductance, same as S), 8
 midpoint method, 24
 millimolar (mM), 161
 mixed-mode oscillations, 108, 109, 400
 molar (M), 161
 mole, 161
 multi-compartment model, 42
 muscarinic acetylcholine receptor, 58

N
 N-methyl-D-aspartate (NMDA), 5
 n-to-one entrainment, 185
 neocortex, 6
 Nernst equilibrium, 11, 12
 Nernst, Walther, 12
 neuromodulation, 267
 neuron, 1
 neuronal firing, 3, 20
 neurotransmitter, 4

neutrally stable, 415
 newton (N, unit of force), 7
 NMDA decay time constant, 155
 NMDA receptor, 4, 154
 non-inactivating current, 111, 112
 normal form, 81
 nullcline, 75
 number density, 13

O
 O-cells, 302
 O-LM interneurons, 302, 303
 ohm (Ω , unit of resistance), 8, 41
 Ohm's law, 12
 one-to-one entrainment, 185
 optogenetics, 313
 orbit, 75
 ordinary differential equation (ODE), 15
 oriens-lacunosum-molecular (O-LM) interneurons, 302, 303
 Ornstein-Uhlenbeck process, 292, 375

P
 Parkinson's disease, 201, 293
 partial differential equation (PDE), 15
 parvalbumin, 33
 parvalbumin-positive (PV+), 33, 303
 periodic orbit of saddle type, 101
 perisomatic inhibition, 303
 persistent current, 111, 112
 persistent gamma oscillations, 281
 persistent sodium and potassium ($I_{Na,p}$ - I_K) model, 111, 132
 persistent sodium current, 111
 phase, 193, 194
 phase plane, 74
 phase response curve (PRC), 199, 200
 phase response function, 200, 214
 phase space, 74
 phase transition curve, 202
 phase walkthrough, 241, 278, 355
 phase-locking, 173, 214
 PING, 256
 plasticity, 6, 295

Poisson process, 377
Poisson schedule, 377
post-synaptic, 4, 154
post-synaptic current, 5
post-synaptic potential, 155
potassium-chloride
cotransporter 2 (KCC2), 14
PRC, 199, 200
PRC with infinitesimal input
duration, 203
PRC with infinitesimal input
strength, 203
pre-synaptic, 4, 154
probability density function (p.d.f.),
368
probability of an event, 367
pseudo-random number, 179, 371
pulse-coupled oscillators, 213, 276
pulse-coupled oscillators with delays,
227
pyramidal neuron, 4

Q
quadratic integrate-and-fire (QIF)
neuron, 51

R
rand (Matlab command), 191, 371
randn (Matlab command), 373
random number, 367
random variable, 367
rebound firing, 131
rectifying gap junction, 165
recurrent excitation, 114, 177, 193
recurrent inhibition, 264
reduced Traub-Miles (RTM) model,
32, 123, 126
reduced Traub-Miles (RTM) model
with h-current, 135
reduced Traub-Miles (RTM) model
with M-current, 126, 134
reduced Traub-Miles (RTM) model,
further reduced to two
dimensions, 85

refractoriness, 27, 41
regular spiking (RS) cells, 299
relaxation oscillator, 76
repelling fixed point, 80, 87, 89, 92
repelling limit cycle, 94, 101
reset voltage, 46
resistance, 13
resistivity, 41
reversal potential, 16, 154
river, 251
row sum, 166
runaway firing, 354, 355

S
saddle point, 81, 87
saddle-node bifurcation, 79, 80, 82
saddle-node bifurcation of cycles, 97
saddle-node bifurcation off an
invariant cycle, 126
saddle-node bifurcation on an
invariant cycle (SNIC), 88
saddle-type periodic orbit, 101
sag current, 136
schizophrenia, 14, 143, 256
second messenger, 5
second-order accuracy, 25
self-exciting theta neuron, 114
semi-stable fixed point, 53, 80
sensorimotor areas, 293
short-term depression, 341
short-term facilitation, 341, 342
shunting inhibition, 5, 272
siemens (S, unit of conductance), 7, 8
sigmoidal function, 176
slow variable, 76
slow-fast phase plane, 76
SNIC, 88
sodium-potassium pump, 2
sodium-potassium-chloride
cotransporter 1 (NKCC1), 14
soft Hopf bifurcation, 97
soma, 1
somatostatin, 303
somatostatin-positive (SOM+), 303

- Song-Abbott model of STDP, 349
 space clamp, 15
 sparse entrainment, 185
 spike afterhyperpolarization (AHP),
 34, 129
 spike frequency adaptation, 57, 58
 spike rastergram, 178
 spike time, 120, 128
 spike timing-dependent plasticity
 (STDP), 296, 349
 splay state, 194, 244
 square-wave bursting, 144
 squid giant axon, 15
 stability threshold of Euler's method,
 28
 stable fixed point, 53
 stable manifold, 81
 stable node, 82, 86
 stable river, 251
 stable spiral, 86
 standard deviation, 369
 standard Gaussian, 372
 stochastic differential equation
 (SDE), 374
 stochastic weak PING, 281, 282
 stratum lacunosum-moleculare, 303
 stratum oriens, 303
 strong PING, 281
 subcritical Hopf bifurcation, 91, 97
 subthalamic nucleus (STN), 201
 subthreshold oscillations, 49, 108,
 399, 400
 supercritical Hopf bifurcation, 91, 97,
 179, 180
 suppression boundary, 263
 supremum, 316
 synapse, 4
 synaptic cleft, 4
 synaptic decay time constant,
 155, 157
 synaptic gating variable, 154
 synaptic plasticity, 6
 synaptic rise time constant, 155, 157
 synaptic vesicle, 341
 synchrony, 173, 193, 214
- T**
- T-current, 143
 Taylor approximation, 81
 tetanic stimulation, 257
 thermostat, 142
 theta neuron, 51, 53, 54, 122, 205
 theta neuron with synaptic input,
 249, 250
 theta oscillation, 301
 theta rhythm, 301
 Thomson, William (Lord Kelvin), 42
 threshold drive, 48, 51
 threshold voltage, 4, 45, 46
 thresholding, 297, 327, 328
 time coarse-grained Wilson-Cowan
 model, 176
 time reversal, 101
 time-discrete dynamics, 363
 time-to-peak, 159
 tonic inhibition, 308, 310, 315
 trajectory, 75
 transatlantic cable, 42
 transient current, 111, 112, 306
 Tsodyks-Markram model of
 short-term depression, 341
 Tsodyks-Markram model of
 short-term facilitation,
 341, 342
 type 1 phase response, 204
 type 2 phase response, 204
- U**
- uncorrelated, 371
 uniformly distributed random
 number, 179, 191, 371
 unstable fixed point, 53
 unstable manifold, 82
 unstable node, 87
 unstable periodic orbit, 101
 unstable river, 251

unstable spiral, 87

upper branch of the f - I curve, 121

V

variance, 369

vesicle, 341

volt (V, unit of electrical potential),

7

voltage spike, 3, 20

W

Wang-Buzsáki (WB) model, 33, 123

weak coupling, 235

weak PING, 281, 282

Wiener process, 375

Wilson-Cowan model, 175

winning streak, 279

work of compression, 13

working memory, 115, 302